eNergetics 2022

Proceedings of the 8th Virtual International Conference on Science, Technology and Management in Energy

Editor:
Velimirović, L. Z.

Publishers:
Complex System Research Centre, Niš, Serbia
Mathematical Institute of the Serbian Academy of Sciences and Arts, Belgrade, Serbia

Serbia, Belgrade, December 15-16, 2022

Editor
Velimirović, L. Z.

eNergetics 2022

8th Virtual International Conference on Science, Technology and Management in Energy

Proceedings

Publishers
Complex System Research Centre, Niš, Serbia
Mathematical Institute of the Serbian Academy of Sciences and Arts, Belgrade, Serbia

Serbia, Belgrade, December 15-16, 2022

Proceedings of the
8th Virtual International Conference
on Science Technology and Management in Energy

Serbia, Belgrade, December 15-16, 2022

Editors:
Dr. Lazar Z. Velimirović

Technical Editor:
Dr. Petar Vranić

Published by:
Complex System Research Centre, Niš, Serbia
Mathematical Institute of the Serbian Academy of Sciences and Arts, Belgrade, Serbia

Printed by:
Copy Shop, Niš, Serbia

Number of copies printed: 100
The publishing year: 2023

Printing of this edition has been financially supported by
Serbian Ministry of Education, Science and Technological Development

ISBN-978-86-82602-01-9

CIP - Каталогизација у публикацији Народна библиотека Србије, Београд

620.9(082)(0.034.2)

VIRTUAL International Conference on Science Technology and Management in Energy (8 ; 2022 ; Beograd)
Energetics 2023 [Elektronski izvor] : proceedings / 8th Virtual International Conference on Science Technology and Management in Energy, Serbia, Belgrade, December 15-16, 2022 ; editor Velimirović, L.[Lazar] Z. - Niš : Complex System Research Centre ; Belgrade : Mathematical Institute of the SASA, 2023 (Niš : Copy Shop). - 1 elektronski optički disk (DVD) ; 12 cm

Sistemski zahtevi: Nisu navedeni. - Nasl. sa naslovne strane dokumenta. - Tiraž 100. - Bibliografija uz svaki rad.

ISBN 978-86-82602-01-9 (CSRC)

a) Енергетика -- Зборници

COBISS.SR-ID 119331337

eNergetics 2022

8^{th} Virtual International Conference on Science Technology and Management in Energy

Organizer:
Mathematical Institute of the Serbian Academy of Sciences and Arts, Belgrade, Serbia

Co-organizers:

- Academy of Sciences and Arts of the Republika Srpska
- Faculty of Mining and Geology, University of Belgrade
- Faculty of Technical Sciences, UKLO University St. Climent Ohridski
- Complex System Research Centre
- National Association of Autonomous and Electric Vehicles of Serbia

Supported by:
Serbian Ministry of Education, Science and Technological Development

Program Committee

Chair:

Prof. Dr. Lazar Z. Velimrović, Mathematical Institute of the Serbian Academy of Sciences and Arts, Belgrade, Serbia

Members:

Prof. Dr. Aleksandar Janjić, Faculty of Electronic Engineering, Serbia
Prof. Dr. Detelin Markov, Faculty of Power Engineering and Power Machines, Bulgaria
Prof. Dr. Marko Serafimov, Faculty of Mechanical Engineering, Macedonia
Prof. Dr. Mileta Janjić, Faculty of Mechanical Engineering, Montenegro
Prof. Dr. Zoran Stajić, Faculty of Electronic Engineering, Serbia
Prof. Dr. Miomir Stanković, Mathematical Institute of the Serbian Academy of Sciences and Arts, Serbia
Prof. Dr. Enver Agić, Public Enterprise Electric Utility of Bosnia and Herzegovina, Bosnia and Herzegovina
Prof. Dr. Niko Majdandžić, Faculty of Mechanical Engineering, Croatia
Prof. Dr. Serkan Abbasoglu, Cyprus International University, Turkey
Prof. Dr. Bojan Srđević, Faculty of Agriculture, Serbia
Dr. Lenin Kanagasabai, PVP Siddhartha Institute of Technology, India
Prof. Dr. Abdelhak Djoudi, National Polytechnic School, Algeria
Dr. Elson Avallone, Federal Institute of Education, Science and Technology of São Paulo, Brazil
Prof. Dr. Zdravko Milovanović, Faculty of Mechanical Engineering, Bosnia and Herzegovina
Prof. Dr. Miloš Jelić, Research and Development Center Alfatec, Serbia
Prof. Dr. Zoran Markov, Faculty of Mechanical Engineering, Macedonia
Dr. Saša Milić, Institute Nikola Tesla, Serbia
Prof. Dr. Krsto Miljanović, Agromediterranean Faculty, Bosnia and Herzegovina
Prof. Dr. Lana Pantić-Ranđelović, Faculty of Sciences and Mathematics, Serbia

Organizing Committee

Chair:

Dr. Petar Vranić, Mathematical Institute of the Serbian Academy of Sciences and Arts, Serbia

Members:

Prof. Dr. Miomir Stanković, Mathematical Institute of the Serbian Academy of Sciences and Arts, Serbia

Prof. Dr. Zoran Stajić, Faculty of Electronic Engineering, Serbia

Dr. Lazar Velimirović, Mathematical Institute of the Serbian Academy of Sciences and Arts, Serbia

Dr. Dušan Tatić, Mathematical Institute of the Serbian Academy of Science and Arts, Serbia

Dr. Radmila Janković Babić, Mathematical Institute of the Serbian Academy of Science and Arts, Serbia

M.Sc. Ljubiša Stajić, Research and Development Center "ALFATEC", Serbia

M.Sc. Danijela Protić, Serbian Armed Force, Serbia

M.Sc. Jelena Velimirović, Mathematical Institute of the Serbian Academy of Sciences and Arts, Serbia

M.Sc. Ivana Veličkovska, Mathematical Institute of the Serbian Academy of Sciences and Arts, Serbia

M.Sc. Vladimir Antić, Serbian Armed Force, Serbia

Table of Contents

Numerical Study of Ceiling Fan Improvement on Heat Transfer Inside Closed Cavity

Lyes Nasseri[1], Zouhira Hireche[2], Ammar Zeghloul[3], Djamel Eddine Ameziani[4]

[1,2,3,4]Laboratory of Multiphase Flows and Porous Media, University of Sciences and Technology Houari Boumediene, FGMGP, BP 32 El Alia 16111 Bab Ezzouar, Algiers, Algeria,
[3]National Polytechnic School, BP 182, El Harrach, 16200, Algiers, Algeria

Abstract—**The convection induced by both the temperature gradient and inertial source within square enclosure has been studied. The natural convection effect is attained by temperature gradient between left and right wall (hot and cold, respectively). A ceiling fan stirs the fluid flow in the cavity to cool it. In order to investigate the effect of fan location, three different placements of fan are considered. The study has been carried out by solving numerically momentum and energy equations using the finite volume approach, with SIMPLER algorithm on the collocated arrangement. The study has been carried out for the Reynolds number in the range of $50 \le Re \le 1000$, with Rayleigh numbers $10 \le Ra \le 10^6$ for different fan position H_F, while Prandtl number is kept at 0.71. Results are presented in the form of streamlines, isotherms, and average Nusselt number. The results show that the average Nusselt number increases with increasing in Reynolds number, especially for eccentric position.**

Keywords - ceiling fan, mixed convection, ventilated cavity, momentum generation

I. INTRODUCTION

The convection induced by both the temperature gradient and inertial source within enclosure has been studied in relation to several practical applications. The most interests of these flows are encountered in building when using ceiling fan. In this situation, the interaction between the buoyancy driven and inertial source flows inside the cavity gives complexes convective regimes, and the overall transport patterns can be very different from those driven by the temperature gradients alone. Reference [1] presented numerically the influence of the thermal conductivity, Richardson and Reynolds numbers on the average Nusselt number induced by mixed convection within enclosure. Overall, they find that the heat transfer increase with increasing this controlling parameter. By adding a heat source in the ventilated rectangular cavity, the same authors [2] showed that the location of the sources strongly influences the flows structures, and a oscillatory behavior was obtained for $Gr/Re^2=50$. The influence of this parameter (Gr/Re^2) on the heat transfer is also demonstrated by [3] in the case of mixed convection within cavity with two ventilation ports. Reference [4] studied the mixed convection heat transfer in a ventilated cavity. The numerical results show the presence of a maximum interaction between the effects of the forced and natural convection, with the existence of different flow regimes, delineated in the Ra-Re plane. Reference [5], deals with the problem of mixed convection in shallow enclosure with series of heat generating components; they shown that higher Reynolds number tend to create a recirculation region of increasing strength at the core region and that the effect of buoyancy becomes insignificant beyond Re = 600. Using the LBM method, [6] investigate the effect of suspension of nanoparticles on mixed convection in square cavity with inlet and outlet ports and hot isothermal obstacle; the authors shown that the heat transfer rate is enhanced, except for Richardson numbers greater or equal 10. Reference [7] studied cooling strategy in square cavity with ventilation ports and discrete heat source; they searched the optimum heater position by maximizing the global conductance at different Rayleigh and Reynolds numbers.

ISBN: 978-86-82602-01-9

They found that the heater position is at off center in all cases, its optimum position is insensitive to the variation of Ra and Re, and it solely depends on the ventilation ports arrangement. The Nusselt number is dependent on the variation of the Richardson numbers.

On the basis of the literature review, it appears that several investigations have analyzed a number of governing parameters in natural or mixed convection in closed or open cavities, including thermal sources, fluid property, supplying fluid velocity and dimension or location of ports [8-12]. In the case of closed cavity, no work was reported on mixed convection in ventilated enclosure induced by internal inertial point (or not) sources. This work considers a rectangular cavity which may represent a local. The natural convection movement is generated by a temperature gradient between the active lateral walls. It is considered within this cavity, a volumetric fan which will brew the movement of air in order to influence heat transfer. One of the scientific challenges lies in the mathematical formulation of the physical problem. In studies cited above, jet ventilation is considered as a boundary condition modeled by an imposed velocity at the openings. This path is inadequate to model internal ventilation in a closed cavity, and then it seemed wiser to model the ventilation as a generation of momentum resulting from pressure force. In this paper, while we refer to our earlier work [13], the focus is different by examining the flow structure and the evolution of the Nusselt number for eccentric positions of the ceiling fan.

II. Mathematical Formaulation

The studied configuration is shown on Fig. 1 consider a two-dimensional square cavity (2D) of sides "L". The cavity is heated by a temperature gradient between its two vertical walls (T_h and T_c representing hot and cold temperatures, respectively for the right and left walls). The two horizontal walls are assumed to be adiabatic. An axial fan of diameter D and thickness E is placed inside the cavity. It operates in the vertical direction.

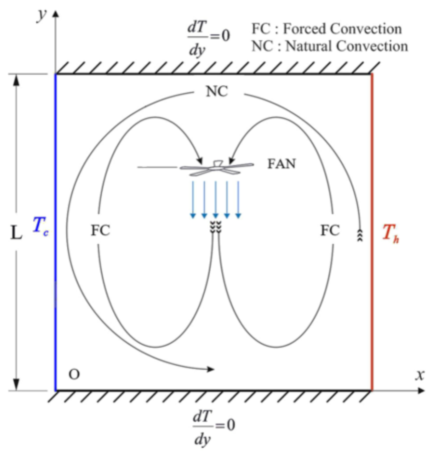

Figure 1. Physical model.

Some simplifying assumptions are taken into account in order to formulate the physical problem and facilitate its resolution. The two-dimensional flow is considered laminar, stationary, while the Boussinesq approximation has been applied to model the density variations. The thermal conductivity of the fan is assumed equal to that of the fluid and its rotational speed is considered constant. This rotation creates a kinetic energy modeled as a generation of momentum in the Navier-Stokes equations by the term ρV^2. Under theses simplifying assumptions, the dimensionless governing equations are written as follows:

$$\frac{\partial u^*}{\partial x^*}+\frac{\partial v^*}{\partial y^*}=0 \ , \quad (1)$$

$$u^*\frac{\partial u^*}{\partial x^*}+v^*\frac{\partial u^*}{\partial y^*}=-\frac{\partial p^*}{\partial x^*}+\Pr\cdot\left(\frac{\partial^2 u^*}{\partial x^{*2}}+\frac{\partial^2 u^*}{\partial y^{*2}}\right), \quad (2)$$

$$u^*\frac{\partial v^*}{\partial x^*}+v^*\frac{\partial v^*}{\partial y^*}=-\frac{\partial p^*}{\partial y^*}+\Pr\cdot\left(\frac{\partial^2 v^*}{\partial x^{*2}}+\frac{\partial^2 v^*}{\partial y^{*2}}\right), \quad (3)$$
$$+\mathrm{Ra}\cdot\Pr\cdot T^*_{moy}+F\cdot(\mathrm{Re}\cdot\Pr)^2$$

$$u^*\frac{\partial T^*}{\partial x^*}+v^*\frac{\partial T^*}{\partial y^*}=\frac{\partial^2 T^*}{\partial x^{*2}}+\frac{\partial^2 T^*}{\partial y^{*2}} \ , \quad (4)$$

$$F=\begin{cases}1: \mathit{fan}\\ 0: \mathit{fluid}\end{cases} . \quad (5)$$

The dimensionless writing of the previous equations is obtained using the following reference variables:

$$x^* = \frac{x}{L} \ , \ \ y^* = \frac{y}{L} \ , \ \ u^* = \frac{u}{\alpha/L} \ , \ \ v^* = \frac{v}{\alpha/L} \ ,$$

$$p^* = \frac{p}{\rho\left(\alpha/L\right)}, \ T^* = \frac{T - T_c}{T_h - T_c}, \qquad (6)$$

and the dimensionless numbers are respectively the Prandtl, Reynolds and Rayleigh numbers

$$\mathrm{Pr} = \frac{\nu}{\alpha}, \mathrm{Re} = \frac{V_{fan} \cdot L}{\nu}, \mathrm{Ra} = \frac{g\beta\Delta T L^3}{\nu\alpha}. \qquad (7)$$

The boundary conditions are conventional cases of natural convection in cavities:

$$\begin{cases} u^*(0, y^*) = u^*(1, y^*) = 0 \\ u^*(x^*, 0) = u^*(x^*, 1) = 0 \end{cases} , \qquad (8)$$

$$\begin{cases} v^*(0, y^*) = v^*(1, y^*) = 0 \\ v^*(x^*, 0) = v^*(x^*, 1) = 0 \end{cases} , \qquad (9)$$

$$\begin{cases} T^*\left(0, y^*\right) = 1, \quad T^*\left(1, y^*\right) = 0 \\ \left.\frac{\partial T^*}{\partial y^*}\right|_{x^*=0} = 0, \quad \left.\frac{\partial T^*}{\partial y^*}\right|_{x^*=1} = 0 \end{cases} . \qquad (10)$$

In order to make the comparison of the ventilator performances on the heat extraction, we introduce the averaged Nusselt number (averaged over the cavity length) as follows:

$$\begin{cases} Nu = \int_0^1 Nu_x dy \\ Nu_x = \int \left.\frac{dT}{dx}\right|_{x=1} \end{cases} . \qquad (11)$$

III. NUMERICAL RESOLUTION METHOD

The dimensionless conservation governing Eqs. (9)-(12) closed with the boundary conditions defined in Eqs. (8) and (9) have been transformed into algebraic equations after their discretization based on the finite volume method. The resolution of the resulting algebraic systems is assured by the TDMA line by line method. SIMPLER algorithm (i.e. Semi-Implicit Method for Pressure-Linked Equation Revised) was used for solving the velocity-pressure coupling. We should also mention that the used convergence criterion focuses on the relative error on all dependent variables $\left(\frac{|\varnothing - \varnothing^*|}{|\varnothing|} \leq 10^{-6}\right)$, where Ø* is the value of the dependent variable Ø in the previous iteration, and Ø represents the dependent variables U, V, P & T.

In developing this study, a uniform mesh grid was used to determine the required number of nodes, and ensures good ratio precision/computation-time; a test of the independence mesh was carried out for reference case (Ra = 10^{+6}, Re = 0). Four grids were tested using the average Nusselt number "Nu" as a comparison parameter. The tests results are shown in Table I.

Comparing the Nusselt number values for the considered cases demonstrates that, from a 122×122 mesh, there is no significant deviation between the results, and then we choose this last grid to launch our calculations. To ensure that the established resolution code gives coherent results, a comparison of our results with the literature should be conducted. Calculations for a square cavity filled with air (without ventilation for test cases for Ra = 10^{+3} to 10^{+6} were performed and the found heat transfer ratios are presented in Table II.

The analysis of the calculation results shows that they are very close to those found in the literature (two works were taken [14] and [15] for Pr = 0.71). The maximum difference is 2.08%, and is probably due to the nodes number, the mesh type and the calculation process.

TABLE I. .NUSSELT NUMBERS COMPARISON FOR THE FOUR GRID TESTS.

Grids	**82×82**	**102×102**	**122×122**	**142×142**
Nu	8.898	8.854	8.836	8.824
Error (%)	-	0.48	0.21	0.12

TABLE II. COMPARISON OF NUSSELT NUMBER WITH LITERATURE.

Ra	**10^{+3}**	**10^{+4}**	**10^{+5}**	**10^{+6}**
Nu [14]	1.128	2.245	4.470	8.898
Nu [15]	-	2.228	4.514	8.804
Nu (Present study)	1.114	2.235	4.506	8.835

IV. Results and Discussions

The flow structures, thermal fields, and the heat transfer rate through the hot wall will be discussed and analyzed in this section. A Rayleigh number taken within the laminar regime [$10,10^{+6}$], Reynolds number between 50 and 1000, and a Prandtl number set equal to 0.7. The both aspect ratios (radial and axial aspect ratios of the fan) are taken constant respecting the orders of magnitude for what is found in real situations (B=1/20 and C=1/5). The fan is placed at a dimensionless height HF=0.8, and horizontal positions were chosen X_F =0.2, 0.5 and 0.8 (X_F: is the distance of the fan from the cold wall).

Fig. 2 shows a typical structure of a ceiling fan airflow [13]. It can be clearly seen that it is mainly composed of two driving cells symmetrical to the central axis of the cavity. Note the presence of small recirculation cells of low acceleration. As Ra increases the structure is no longer symmetrical where buoyancy forces start to drive the fluid, and for Ra=106 the multicellular profile disappears completely and the effect of the fan is only visible in its vicinity.

For the isotherms, the figure shows that they follow the distortions caused by the stream functions for Re ⩽ 105. But for Ra=106, the isotherms are stratified in the center of the cavity with two thermal boundary layers (hot and cold) at the active walls respectively.

To investigate the effect of the horizontal position H_F on the flow structures, two positions were chosen H_F=0.2 and 0.8 with the vertical position L_F=0.8. Stream function are illustrated in Figs. 3 and 4 for different Rayleigh and Reynolds numbers.

For low values of Re (i.e. Re=10^3), we notice that the flow structure is composed of a single forced convection cell that occupies the entire cavity, and a small cell of low intensity trapped at the lower and upper left corners. Note that the main cell rotates trigonometrically (positive) for H_F=0.2 and clockwise (negative) for H_F=0.8 . As the effect of forced convection is enhanced by increasing Reynolds number, other cells trapped at the four corners of the cavity appear for Re=500 and 1000. As the Rayleigh number increases, the state of the flow is dependent on the value of the Reynolds number and the H_F parameter. For low values of Re (i.e. Re$\leqslant 10^3$), the structure is single-celled. In this situation, the flow by natural convection dominates the heat transfers. As the Reynolds number increases, the flow state depends on the H_F position. For H_F=0.2 the fan cell and the thermal gradient have the same direction of rotation, which guarantees the existence of the main cell and does not bifurcate even for high values of Ra. However, this cooperation is visible in value for the stream function even under natural convection (i.e. Ra=10^6). For H_F=0.8 the direction of rotation of the fan cell and the thermal gradient is opposite, and the fan cell is found to bifurcate and its intensity decreases with increasing Rayleigh until natural convection dominates at Ra=10^6 (Fig. 4 column c), despite the presence of recirculation in the vicinity of the fan for Re=1000.

The isotherms corresponding to the different control parameters (i.e., Reynolds and Rayleigh

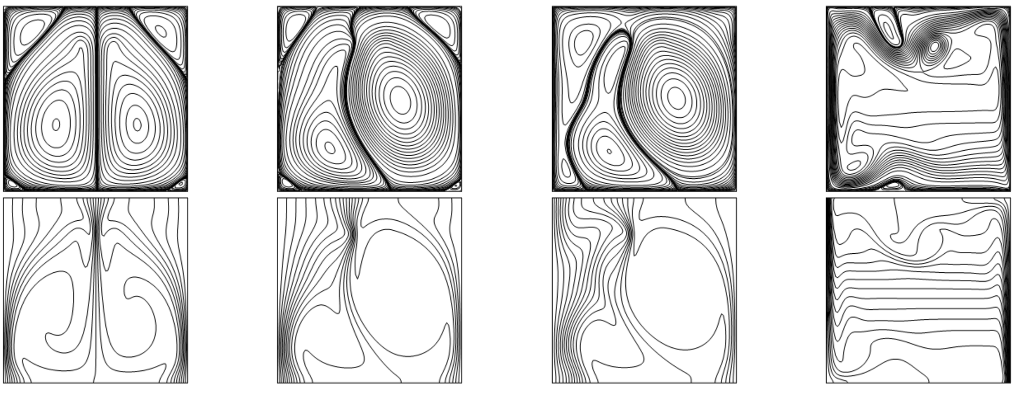

Ra=10^3 Ra=10^4 Ra=10^4 Ra=10^6

Figure 2. Evolution of the streamlines depending on Rayleigh numbers for Re=1000 and X_F = 0.5 (centered ceiling fan).

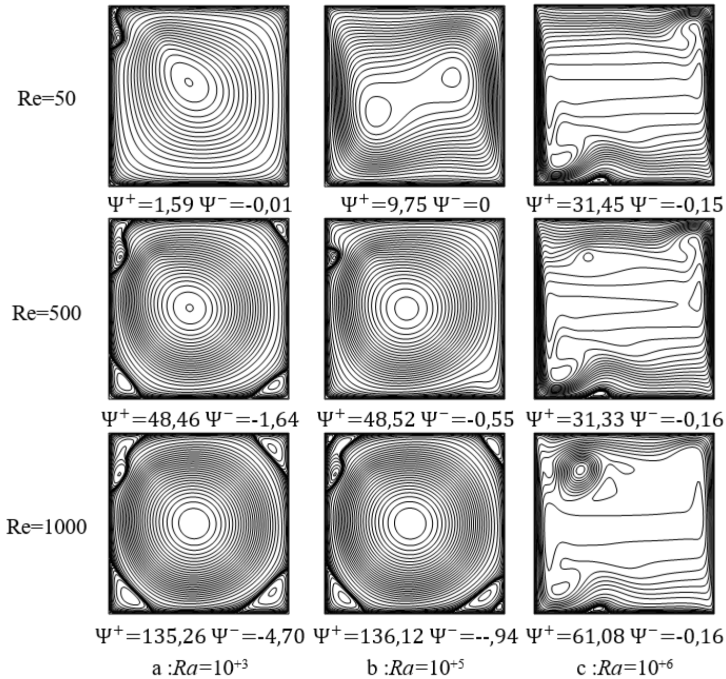

Figure 3. Evolution of the streamlines depending on Reynolds and Rayleigh numbers (X_F = 0.2).

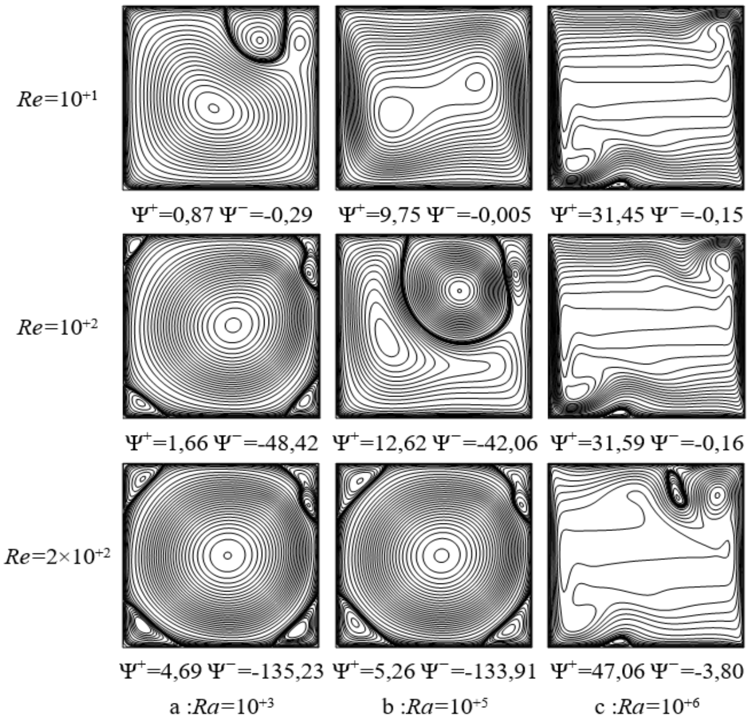

Figure 4. Evolution of the streamlines depending on Reynolds and Rayleigh numbers (X_F = 0.8).

numbers, as well as the H_F position) are shown in Figs. 5 and 6. These figures show, contrary to the case of pure natural convection, the absence of thermal stratification within the cavity except for

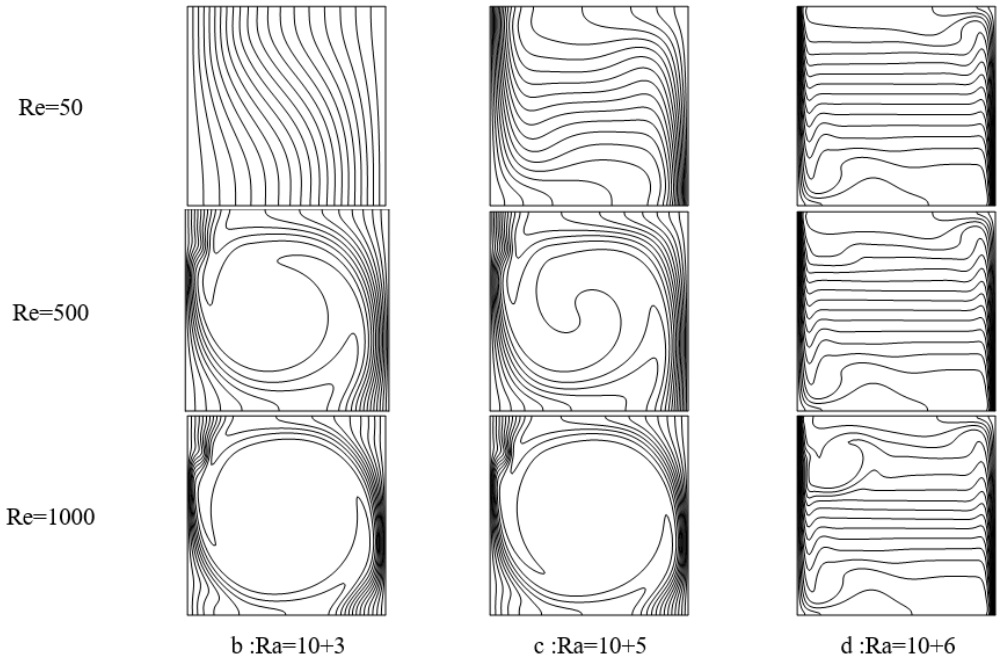

Figure 5. Isotherms evolutions depending on Reynolds and Rayleigh numbers ($X_F = 0.5$).

a low Reynolds number ($Re<10^3$) where the thermal distortions are reduced. We also notice that the temperature distribution is consistent with the fluid circulation revealed by the stream functions. This fluid flow tends to twist the isotherms and carry them along the direction of fluid flow. When buoyancy forces are large (i.e. $Ra=10^6$), the isotherms are similar to those of natural convection type and the effect of ventilation becomes negligible and its influence is limited only to the vicinity of the fan. An important difference between the two positions is that at H_F=0.2 the strong temperature gradients are directed upward, the high temperatures are near the top wall, whereas at H_F=0.8 the strong gradients are directed downward; the high temperatures are concentrated near the bottom wall.

The effect of the horizontal H_F position on the Nusselt number is shown in Fig. 7 as a function of the Rayleigh and Reynolds numbers. Three positions were chosen LF=0.2; 0.5 and 0.8 with H_F=0.5.

In general, the position L_F=0.2 gives slightly higher values for Re=10. This advantage is due to the fact that the thermal and dynamic forces are cooperating. At $Ra=10^4$ the flow tends towards a boundary layer structure and the weight of the effects of forced convection disappears.

As Re increases, the heat transfer intensifies and forced convection is dominant, thus the Nusselt number value is always higher for an eccentric position (i.e., L_F=0.2 and 0.8) for Re=500 and 1000. The domination of the forced convection regime is valid up to a critical Rayleigh value "Ra_c" which depends essentially on the pair of parameters Re and L_F. When Ra increases further (i.e., $Ra>Ra_c$), the Nussselt curve is uniformly increasing for H_F=0.2 while it is disturbed for L_F=0.5 and 0.8 due to the bifurcation of the flow cells. This passage is directly linked to the direction of rotation of the ventilation cells (with or against that imposed by the temperature gradient).

In the forced convection regime, the best transfers are obtained for a maximum Reynolds number Re=1000, with an eccentric fan (H_F=0.2 or 0.8). The Nusselt curves for the latter positions are equal for Re=500 and 1000 (Nu=4.11 and 6.04 respectively) and the transfer is found to be 27% and 31.45% better than the centered position (H_F=0.5) for the same Re values. This advantage is characteristic of a forced single-cell flow.

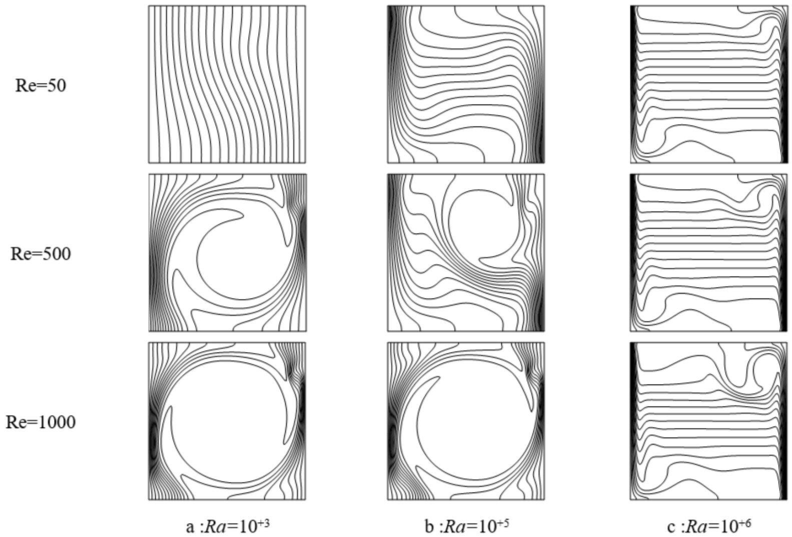

Figure 6. Isotherms evolutions depending on Reynolds and Rayleigh numbers (X_F = 0.5).

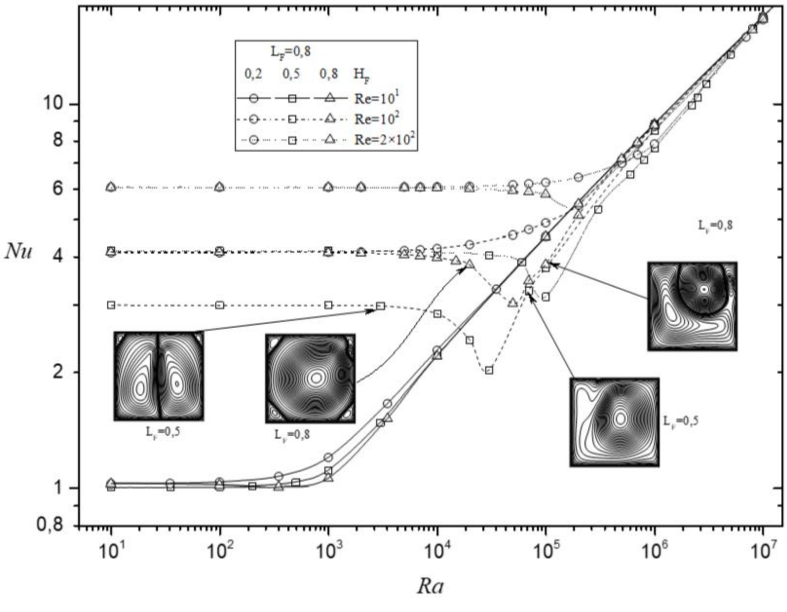

Figure 7. Nusselt number as function of Rayleigh number for different Reynolds number and fan positions H_F.

V. CONCLUSION

This paper presents a numerical study of the mixed laminar convection of a Newtonian fluid flowing in a closed square cavity. In addition to the natural convection induced by the temperature gradient between the two active walls, a ceiling fan is introduced inside the enclosure, and modeled as a momentum generator.

For low Reynolds number values, the flow is similar to the one encountered in the case of a differentially heated cavity where a boundary layer develops at the hot wall dragging the fluid upwards. The results obtained show, according to the values of Re and Ra, two types of flows in spatial competition; the movement of natural convection and that of forced convection for which the flow is multicellular, whose number of cells depends on the value of Reynolds and the position of the fan (L_F and H_F).

The heat transfer analysis shows that the heat transfer increases with increasing Rayleigh number. The average Nusselt number is sensitive to the value of the Reynolds number and the fan position, but only for low Rayleigh numbers and this dependence disappears when the thermal draft increases. The intensity of the fan jet (Reynolds number) has a greater impact on the heat transfer rate than the H_F position factor, which has very little influence on the transfer even for high Reynolds numbers. In forced convection, the maximum values of Nusselts (Nu=6.06) are achieved in the case of a single cell flow, visualized for eccentric fan positions compared to [13].

REFERENCES

[1] Papanicolaou, E., & Jaluria, Y. (1992). Transition to a periodic regime in mixed convection in a square cavity. *Journal of Fluid Mechanics*, *239*, 489-509.

[2] Papanicolaou, E., & Jaluria, Y. (1995). Computation of turbulent flow in mixed convection in a cavity with a localized heat source. *ASME. J. Heat Transfer*, *117*(3), 649–658.

[3] Hsu, T. H., & SG, W. A. (2000). Mixed convection in a rectangular enclosure with discrete heat sources. *Numerical Heat Transfer: Part A: Applications*, *38*(6), 627-652.

[4] Raji, A., Hasnaoui, M., & Bahlaoui, A. (2008). Numerical study of natural convection dominated heat transfer in a ventilated cavity: Case of forced flow playing simultaneous assisting and opposing roles. *International Journal of Heat and Fluid Flow*, *29*(4), 1174-1181.

[5] Bhoite, M. T., Narasimham, G. S. V. L., & Murthy, M. K. (2005). Mixed convection in a shallow enclosure with a series of heat generating components. *International Journal of Thermal Sciences*, *44*(2), 121-135.

[6] Mehrizi, A. A., Farhadi, M., Afroozi, H. H., Sedighi, K., & Darz, A. R. (2012). Mixed convection heat transfer in a ventilated cavity with hot obstacle: effect of nanofluid and outlet port location. *International Communications in Heat and Mass Transfer*, *39*(7), 1000-1008.

[7] Bilgen, E., & Muftuoglu, A. (2008). Cooling strategy by mixed convection of a discrete heater at its optimum position in a square cavity with ventilation ports. *International Communications in Heat and Mass Transfer*, *35*(5), 545-550.

[8] Calmidi, V. V., & Mahajan, R. L. (1998). Mixed convection over a heated horizontal surface in a partial enclosure. *International journal of heat and fluid flow*, *19*(4), 358-367.

[9] Mamou, M. (2002). Stability analysis of thermosolutal convection in a vertical packed porous enclosure. *Physics of Fluids*, *14*(12), 4302-4314.

[10] Bourich, M., Amahmid, A., & Hasnaoui, M. (2004). Double diffusive convection in a porous enclosure submitted to cross gradients of temperature and concentration. *Energy Conversion and Management*, *45*(11-12), 1655-1670.

[11] Bourich, M., Hasnaoui, M., & Amahmid, A. (2004). Double-diffusive natural convection in a porous enclosure partially heated from below and differentially salted. *International Journal of Heat and fluid flow*, *25*(6), 1034-1046.

[12] Singh, S., & Sharif, M. A. R. (2003). Mixed convective cooling of a rectangular cavity with inlet and exit openings on differentially heated side walls. *Numerical Heat Transfer: Part A: Applications*, *44*(3), 233-253.

[13] Nasseri, L., Rahli, O., Ameziani, D. E., & Bennacer, R. (2019). Study of mixed convection in closed enclosure with a ceiling fan. *The European Physical Journal Applied Physics*, *86*(2), 20902.

[14] Markatos, N. C., & Pericleous, K. A. (1984). Laminar and turbulent natural convection in an enclosed cavity. *International journal of heat and mass transfer*, *27*(5), 755-772.

[15] Ambarita, H., Kishinami, K., Daimaruya, M., Saitoh, T., Takahashi, H., & Suzuki, J. (2006). Laminar natural convection heat transfer in an air filled square cavity with two insulated baffles attached to its horizontal walls. *Thermal science and engineering*, *14*(3), 35-46.

Ant Colony Optimization Algorithm and Fuzzy Logic Controller of PEM Fuel Cell with Boost Converter

Hafid Oubouaddi[1], Adil Brouri[2], Abdelmalek Ouannou[3], Ali Bouklata[4], Chaimae Abdelaali[5], Fatima Ezzahra el Mansouri[6]

[1,2,3,4,5,6]SECNDCM Team, L2MC Laboratory ENSAM, Moulay Ismail University, Morocco

Abstract—**In this article, the control problem of output voltage of proton exchange membrane fuel cell (PEMFC) is discussed. Presently, two closed-loop methods using DC/DC boost converter are presented to improve the ripple of the PMEFC output voltage. The main objectives is to improve the reference voltage tracking and the response time. In the first method, a solution based on the ant colony optimization (ACO) proposed. However, finding appropriate values for the PI controller is not an easy task. To overcome this problem and simplify the process of tuning the PI controller parameters, a solution based on the ant colony optimization algorithm (ACO) is used. In the second approach, a fuzzy logic controller is proposed to regulate the PEMFC with boost converter output voltage. Finally, examples of simulations using a PMEFC with DC/DC converter are established showing the effectiveness of this study.**

Keywords - PEM fuel cell, DC/DC boost converter, PI controller, ant colony optimization, fuzzy logic

I. INTRODUCTION

The reliability and efficiency of DC microgrids have recently increased [1]. This is made possible by the nature of various DC loads and the use of several sources, including fuel cells, storage devices and renewable energy sources. A fuel cell (FC) system is one of the most popular components in DC microgrids [2]. The FC source is an electrochemical element that transforms the chemical energy of hydrogen and oxygen into electricity [3]. In the literature, several models that can be describe the fuel cells have been developed; the most prominent includes the proton exchange membrane FC (PEMFC) [4], the solid oxide FC (SOFC) [5], and the microbial fuel cell (MFC) [6], alkaline FC (AFC) [7], the phosphoric acid fuel cell (PAFC) [8]. However, the PEMFCs are considered the most developed [9], and thus, they have been widely utilized in a variety of application kinds, including electric vehicles. Indeed, these FCs provide significant advantages, e.g., do not cost very much, ensure efficient performance, and provide a great power. The latter benefit makes the study of the FC crucial. In addition, an accurate design and modeling of the PEMFC can help to improve the system performances [10]. Consequently, an adaptation element is necessary to enable an effective power conversion from the PEMFC to the external circuit. This device is a static DC/DC converter with a metal oxide semiconductor field effect transistor (MOSFET) or insulated gate bipolar transistor (IGBT) under command [11]. Note that numerous control techniques for DC-DC converters have been established in the literature, such as the fractional-order proportional integral-derivative (FOPID) used to control a DC/DC boost converter for PMEFC output power quality [12]. Then, a system composed by PMEFC output power quality and a DC/DC boost converter can be improved using a sliding mode control with a digital filter lowering the undesirable oscillations [13]. An adaptive technique using quasi-continuous high order sliding mode controller (QC-HOSM) to control a DC/DC boost converter is proposed by [14]. Furthermore, another approach to control the DC/DC converter using proportional-integral (PI) and a sliding mode control to maintain the fuel cell runs at an efficient PowerPoint [15].

Therefore, to maintain the output power of a fuel cell stack extremely close to its maximum, a fuzzy logic controller and particle swarm optimization (PSO) algorithm is developed by [16]. Then, another method to control the DC/DC for PMEFC using a fuzzy logic controller is proposed in [17]. The aim is that the output power of the PEM fuel cell system reaches track the maximum power.

According to a literature review, the power control of PEMFC units is one of the most attractive research topic. In order to obtain an accuracy model, it is interesting to develop new heuristic-based methods, thereby lowering the error, achieving smooth convergence, reducing computational load, and obtaining fine statistical measures. This issue is still discussed and constitutes an open research topic. One of the contributions of this work is the development of a fractional order proportional-integral is developed. In order to regulate the DC/DC converter and improving the performances of the PEM fuel cell system, an ACO algorithm and a fuzzy logic controller are used.

II. PEMFC Mathematical Model

A PEM fuel cell is an electrochemical device using two redox processes to transform the chemical energy of a fuel (often hydrogen anode) and an oxidizing agent (typically oxygen cathode) into electrical energy [18]. The PEM Fuel cells can produce electricity continuously for as long as fuel and oxygen are supplied. Figs. 1 and 2 show the structure and the equivalent circuit of the fuel cell, respectively.

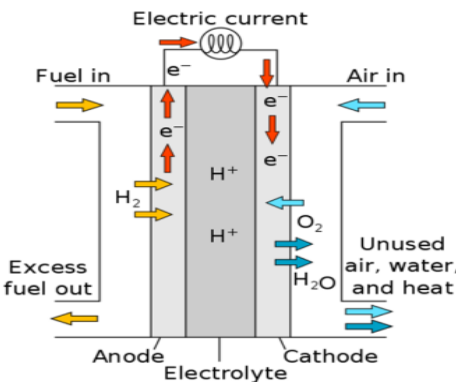

Figure 1. PEM fuel cell structure.

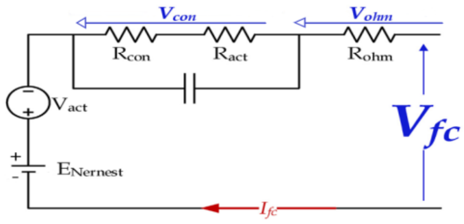

Figure 2. Equivalent circuit of PEM fuel cell.

As shown in Fig. 2, the output voltage of a fuel cell can be expressed as:

$$V_{fc} = E_{Nernest} - V_{act} - V_{con} - V_{ohm} \quad , \qquad (1)$$

where V_{act} is the activation voltage, which is given by the following expression [19]:

$$\begin{aligned} V_{act} &= -\alpha_1 - \alpha_2 T - \alpha_3, T.\ln(C_{o2}) - \\ &- \alpha_4 .T.\ln(I_{fc}) \end{aligned} \quad , \qquad (2)$$

where I_{fc} is fuel cell current, C_{o2} is the oxygen concentration, and $\alpha_i (i = 1...4)$ are semi-empirical coefficients. Note that the concentration loss V_{con} results from the change in the hydrogen and oxygen concentrations or fuel crossover. The expression of V_{con} is given as follows [20]:

$$V_{con} = -\gamma ln(1 - \frac{i}{i_{\max}}) \quad , \qquad (3)$$

where γ is an adjustable parameter, i is the fuel cell current and $i_{\max}$ stands for the maximum fuel cell current.

$E_{Nernest}$ denotes the reversible cell and is expressed by [21]:

$$\begin{aligned} E_{Nernest} &= 1.229 - 0.85.10^{-3}.(T - 298.15) + \\ &+ 4.3058.10^{-5}.(\ln(P_{H2}) + 0.5\ln(P_{O2}) \end{aligned} \quad , \qquad (4)$$

where P_{H2} is the hydrogen pressure value, P_{O2} is the oxygen pressure value, and T is the temperature of FC. Finally, the expression of the ohmic voltage drop V_{ohm} is given as [22]:

$$V_{ohm} = R_{ohm}.i = (R_m + R_c).i \quad , \qquad (5)$$

where R_m and R_c are the membrane resistance and the contact resistance, respectively. For convenience, the polarization curves corresponding to the used PEMFC are shown in Fig. 3.

To improve the output voltage of the PMEFC, a step-up converter can be used. In general, a step-up converter is featured by an excellent efficiency and is an easy solution to increase the DC power supply's voltage [23]. The diagram of the proposed closed loop control of the cell voltage is shown in Fig. 4. This solution involves the PEM fuel cell power system, a DC/DC boost converter, a load and the proposed controller.

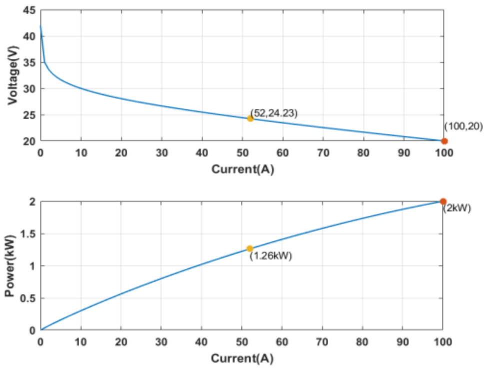

Figure 3. PEM fuel cell polarization curves.

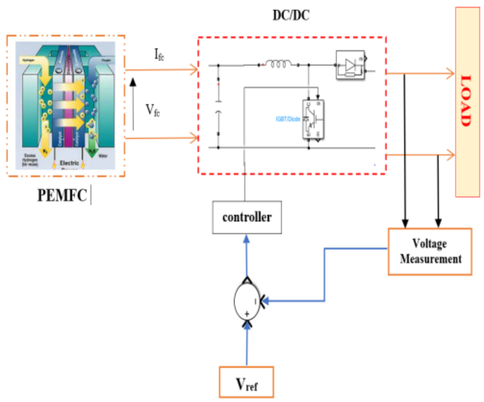

Figure 4. Diagram of the proposed closed loop control of the fuel cell voltage.

III. Description of the PEM Fuel Cell Controller

A. ACO-PI Controller

1) Description of the PI controller

A feedback-based control loop mechanism called a proportional-integral controller is widely used in many industrial applications [24]. The PI controller is composed of the integral (I) and proportional (P) actions. The PI controller output according to the error signal *ε(t)* (difference between the desired setpoint and the measured signal) is given as:

$$u(t) = K_p \varepsilon(t) + K_i \int_0^t \varepsilon(t)dt \quad . \tag{6}$$

2) Overview of the ACO algorithm

The ACO is a meta-heuristic and probabilistic method. It is frequently employed to solve challenging combinatorial optimization issues using graph representations. The aim of this method is to find the best paths based on several possible graphs. This algorithm was initially proposed by Marco Dorigo in 1992 [25]. The artificial ants used in this technique were inspired from real ant colonies and designed to search for the best path. The shorter path is obtained by analysing and comparing each ant's path in the colony. This path will be the best solution and having a higher probability of being chosen. The main steps of the proposed algorithm are summarized in Fig. 5.

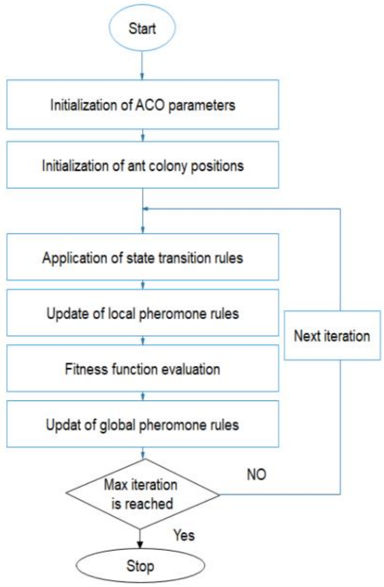

Figure 5. Description of the ACO algorithm.

3) Closed-loop control of PMEFC via ACO-PI controller

Let V_{ref} denote the reference voltage. Fig. 6 shows the closed-loop control of the fuel cells with DC/DC converter and ACO-PI. Even if the PID controller can improve the system stability, the derivative action of the PI controller would likely increase the disturbance amplitude. The algorithm of ant colony optimization (ACO) was utilized to simplify the process of tuning the PI controller parameters.

B. *Fuzzy Logic Controller*

In fuzzy logic approach, the variables are allowed to range from 0 to 1 rather than the Boolean values, i.e., true or false (or, equivalently, 1 or 0). It is employed to deal with the idea of partial truth, in which the truth value might range from absolutely true to absolutely untrue [26]. The technique of applying fuzzy logic to map a given input to output is known as fuzzy inference. The mapping then offers a foundation on which choices can be made, or equivalently, the patterns can be obtained. Generally, the fuzzy inference uses the different components mentioned in membership functions and logical operations governed by If-Then rules. Then, the aim is to reduce the error between the reference voltage and true voltage using a PI controller. In this respect, the fuzzy logic technique is used to control the DC/DC converter. The membership functions of the input and output variables of the developed controller are represented in Fig. 7. For convenience, two input signals and one output signal have been used. The first input is the error between the reference voltage and the true voltage. The second input is the derivative of this error. In this respect, note that the first and second inputs are composed by five membership functions as seen in Fig. 7. As it was mentioned before, one of the main issues is to control the error such that it remains close to zero. Then, the output of the fuzzy controller is designed to command the IGBT used in the DC/DC converter. For convenience, the output of the proposed controller is composed by five membership functions as shown in Fig. 7.

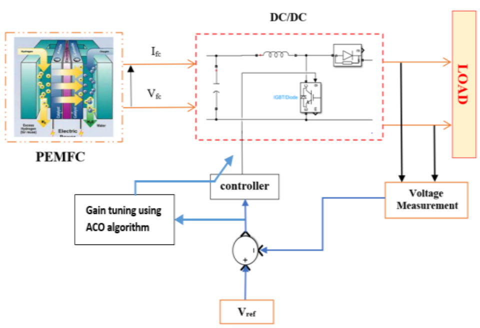

Figure 6. Fuel cell voltage control using ACO algorithm.

IV. Results and Discussion

To keep the PEMFC functioning at a maximum voltage. Then, a control technique based on ACO and fuzzy logic is applied to the DC/DC converter in order to maintain the power supplied by the fuel function at its maximum. The parameters of DC/DC boost converter, used in simulation, are as follows: $C = 5.1\ mF$ and $L = 1$.

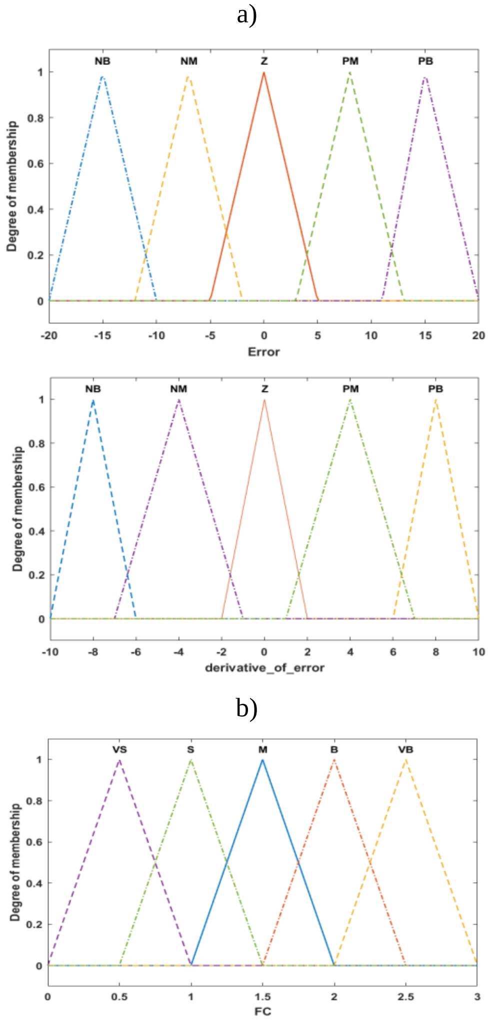

Figure 7. The membership functions of (a) the input and (b) output variables.

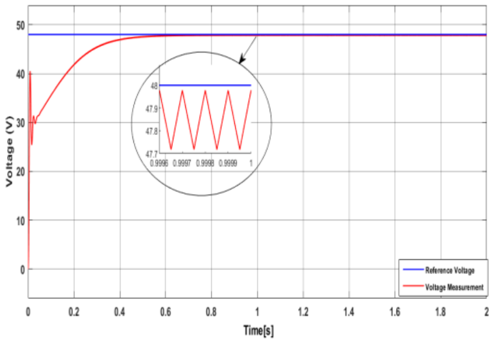

Figure 8. Output voltage and voltage reference using ACO-PI.

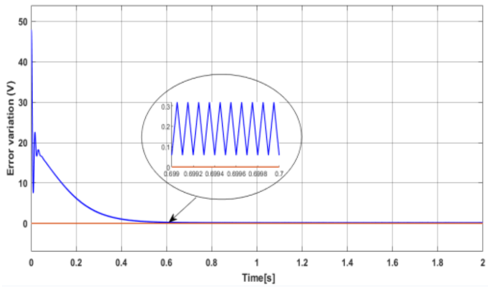

Figure 9. The error between output and reference voltages.

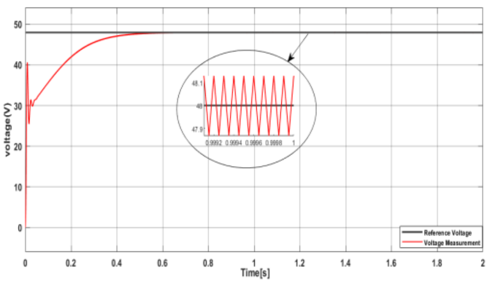

Figure 10. Output voltage and voltage reference using FLC.

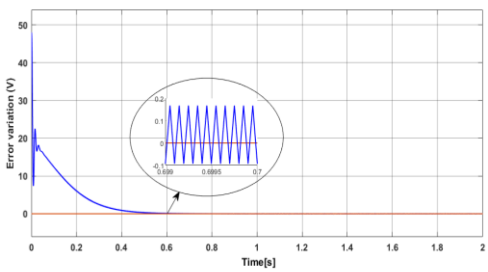

Figure 11. The error between output and reference voltages.

TABLE I. COMPARISON BETWEEN THE CONTROLLER PERFORMANCES.

Method	**Fuzzy logic**	**ACO**
Settling time (s)	0.48	0.50
Settling max (v)	48.1	47.95
Settling min (v)	47.80	47.75
Error (v)	0.1	0.2

At this stage, to show the effectiveness of the developed controllers on fuel cell output voltage, note that several simulations have been established using MATLAB/Simulink.

A. Voltage Control Using APO-PI

Example of obtained results of PEM fuel cell output voltage, for reference voltage of constant value $V_{ref}=48V$, using an ACO-PI controller have been plotted in Fig. 8. The tracking error between the reference and true voltages have been plotted in Fig. 9. As shown in these figures, the involved error in the proposed system keeps small amplitudes with a settling time nearly 0.50s.

B. Voltage Control Using Fuzzy Logic

In the second method, the ACO controller is replaced with a Fuzzy logic controller. In this respect, the response voltage of the PEM fuel cell using FLC is shown in Fig. 10, and the error variance is shown in Fig. 11.

As it is seen, the output voltage of PMEFC using FLC takes values around of the reference voltage. For convenience, in order to compare the performances of each controller, their characteristic time-domain specifications (steady-state time, peak time, overshoot) were compared. The results of this comparison are summarized in Table I. Finally, it is shown that the proposed controller using fuzzy logic approach offers better performances and high robustness compared to the ACO algorithm.

V. CONCLUSIONS

This article discusses the problem of PME fuel cell output voltage control. This PMEFC is combined with DC/DC converter and a PI controller. Here, the tuning of the PI controller parameters is based on the ACO algorithm and fuzzy logic technique. Then, an approach has been proposed to regulate the PEMFC output voltage using a DC/DC boost converter. To determine the PI controller parameters, anti-colony optimization is used. The obtained simulation results confirm that, the fuzzy logic controller improves the output voltage with small settling time. It is seen thus that the output voltage tracks the target (the reference voltage) with very small error.

REFERENCES

[1] Eason, G., Noble, B., & Sneddon, I. N. (1955). On certain integrals of Lipschitz-Hankel type involving products of Bessel functions. Philosophical *Transactions of the Royal Society of London. Series A, Mathematical and Physical Sciences, 247*(935), 529-551.

[2] Pourrahmani, H., Siavashi, M., & Moghimi, M. (2019). Design optimization and thermal management of the PEMFC using artificial neural networks. *Energy, 182*, 443-459.

[3] Tanveer, W. H., Abdelkareem, M. A., Kolosz, B. W., Rezk, H., Andresen, J., Cha, S. W., et al. (2021). The role of vacuum-based technologies in solid oxide fuel cell development to utilize industrial waste carbon for power production. *Renewable and Sustainable Energy Reviews, 142*, 110803.

[4] Sayed, E. T., Abdelkareem, M. A., Obaideen, K., Elsaid, K., Wilberforce, T., Maghrabie, H. M., et al. (2021). Progress in plant-based bioelectrochemical systems and their connection with sustainable development goals. *Carbon Resources Conversion, 4*, 169-183.

[5] Sayed, E. T., Abdelkareem, M. A., Alawadhi, H., & Olabi, A. G. (2021). Enhancing the performance of direct urea fuel cells using Co dendrites. *Applied Surface Science, 555*, 149698.

[6] Guo, X., Zhang, H., Hu, Z., Hou, S., Ni, M., & Liao, T. (2021). Energetic, exergetic, and ecological evaluations of a hybrid system based on a phosphoric acid fuel cell and an organic Rankine cycle. *Energy, 217*, 119365.

[7] Chugh, S., Chaudhari, C., Sonkar, K., Sharma, A., Kapur, G., & Ramakumar, S. (2020). Experimental and modeling studies of low-temperature PEMFC performance. *International Journal of Hydrogen Energy, 45(*15), 8866-8874.

[8] Dincer, I. (2002). Technical, environmental, and exergetic aspects of hydrogen energy systems. *International Journal of Hydrogen Energy, 27*(3), 265-285.

[9] Yau, Y. T., Hwu, K. I., & Shieh, J. J. (2021). Minimization of output voltage ripple of two-phase interleaved buck converter with active clamp. *Energies, 14*, 5215.

[10] Kravos, A., Ritzberger, D., Hametner, C., et al. (2021). Methodology for efficient parameterization of electrochemical PEMFC model for virtual observers: Model-based optimal design of experiments supported by parameter sensitivity analysis. *International Journal of Hydrogen Energy, 46*(26), 13832-13844.

[11] Kiran, S. R., Basha, C. H., Kumbhar, A., et al. (2022). A new design of single switch DC-DC converter for PEM fuel cell-based EV system with variable step size RBFN controller*. Sādhanā, 47*(3), 1-14.

[12] Pereira, L. F. D. S., Batista, E., de Brito, M. A., & Godoy, R. B. (2022). A Robustness Analysis of a Fuzzy Fractional Order PID Controller Based on Genetic Algorithm for a DC-DC Boost Converter. *Electronics, 11*(12), 1894.

[13] Silaa, M. Y., Barambones, O., Derbeli, M., Napole, C., & Bencherif, A. (2022). Fractional order PID design for a proton exchange membrane fuel cell system using an extended grey wolf optimizer. *Processes, 10*(3), 450.

[14] Silaa, M. Y., Derbeli, M., Barambones, O., Cheknane, A. (2020). Design and implementation of high order sliding mode control for PEMFC power system. *Energies, 13*, 4317.

[15] Derbeli, M., Barambones, O., Farhat, M., & Sbita, L. (2019, March). Efficiency boosting for proton exchange membrane fuel cell power system using new MPPT method. In *2019 10th International Renewable Energy Congress (IREC)* (pp. 1-4). IEEE.

[16] Luta, D. N., & Raji, A. K. (2019). Fuzzy rule-based and particle swarm optimisation MPPT techniques for a fuel cell stack. *Energies, 12*(5), 936.

[17] Harrag, A., & Messalti, S. (2018). How fuzzy logic can improve PEM fuel cell MPPT performances?. *International Journal of Hydrogen Energy, 43*(1), 537-550.

[18] Rezk, H., Ferahtia, S., Djeroui, A., Chouder, A., Houari, A., Machmoum, M., & Abdelkareem, M. A. (2022). Optimal parameter estimation strategy of PEM fuel cell using gradient-based optimizer. *Energy, 239*, 122096.

[19] Aouali, F. Z., Becherif, M., Ramadan, H. S., Emziane, M., Khellaf, A., & Mohammedi, K. (2017). Analytical modelling and experimental validation of proton exchange membrane electrolyser for hydrogen production. *International Journal of Hydrogen Energy, 42*(2), 1366-1374.

[20] Yazdani, M., & Jolai, F. (2016). Lion optimization algorithm (LOA): a nature-inspired metaheuristic algorithm. *Journal of computational design and engineering, 3*(1), 24-36.

[21] Chatrattanawet, N., Skogestad, S., & Arpornwichanop, A. (2015). Control structure design and dynamic modeling for a solid oxide fuel cell with direct internal reforming of methane. *Chemical Engineering Research and Design, 98*, 202-211.

[22] Mann, R. F., Amphlett, J. C., Hooper, M. A., Jensen, H. M., Peppley, B. A., & Roberge, P. R. (2000). Development and application of a generalised steady-state electrochemical model for a PEM fuel cell. *Journal of power sources, 86*(1-2), 173-180.

[23] Reddy, K. J., & Natarajan, S. (2018). Energy sources and multi-input DC-DC converters used in hybrid electric vehicle applications–A review. *International journal of hydrogen energy, 43*(36), 17387-17408.

[24] Deželak, K., Bracinik, P., Sredenšek, K., & Seme, S. (2021). Proportional-integral controllers performance of a grid-connected solar PV system with particle swarm optimization and Ziegler–Nichols tuning method. *Energies, 14*(9), 2516.

[25] Tarik, R., & Adil, B. (2022). Ant colony optimization algorithm and fuzzy logic for switched reluctance generator control. *AIMS Energy, 10*(5), 987-1004.

[26] Oubouaddi, H., Brouri, A., & Ouannou, A. (2022, May). Speed control of Switched Reluctance Machine using fuzzy controller and neural network. In *2022 International Conference on Intelligent Systems and Computer Vision (ISCV)* (pp. 1-6). IEEE.

Box Type Solar Oven: Analysis of Environmental Loads Associated with a Prototype

Camilla Pereira Soares[1], Silvia Guillen-Lambea[2], Monica Carvalho[3]

[1]Center for Alternative and Renewable Energies, Federal University of Paraíba, Joao Pessoa, Brazil
[2]Centro Universitario de la Defensa. Zaragoza, Spain; Department of Mechanical Engineering, University of Zaragoza, Zaragoza, Spain
[3]Department of Renewable Energy Engineering, Federal University of Paraíba, Joao Pessoa, Brazil

Abstract—**Faced with the lack of energy autonomy focused on food, precarious health conditions and quality of life, and considering climate change, recent research has focused on solar cookers and ovens. Around the world, solar ovens are a cooking strategy that has already been used, as a way out of the faced difficulties by some populations. In this sense, the objective of this study is to quantify the greenhouse gas (GHG) emissions associated with the construction of a box-type solar oven. The study has three stages: i) Build the inventory for the box-type solar oven prototype through technical visits to UFRN; (ii) Apply the life cycle assessment methodology to the solar oven to quantify GHG emissions, and iii) Analyze the GHG emissions when the destination of the product is recycling instead of the landfill (conventional destination). The results show that the solar oven has low emissions related to the equipment, achieving a reduction of approximately 70% of GHG emissions when the destination of the equipment components is recycling. The importance of understanding the environmental impact of each component of the device is highlighted here, as well as the importance of strategies for the correct disposal of waste.**

Keywords – life cycle assessment, solar oven, greenhouse gases, carbon footprint, SDG 12

I. Introduction

Solar cookers and ovens are devices that, through the captured solar energy, directly or indirectly, heat and/or cook food. The equipment has a low cost, but this technology needs political incentives that help in the accessibility and acceptance of consumers [1]. The most used types of solar ovens are: box type, panel type and concentration [2].

The use of solar ovens can be a strategy for cooking food in less favored regions [3]. Examples of use include a village in Somalia, refugee camps in Kenya, and in the Tibetan areas of China [4]. The use of solar ovens is in line with all the Sustainable Development Goals (SDGs) [5], promoted since 2015. SDG 3 stands out, which focuses on health and well-being; SDG 7 which advocates the use of clean and affordable energy; SDG 12 that values responsible consumption and production; SDG 13 that stimulates the development of actions against global climate change and, finally, SDG 15 that collaborates with the environmental, economic, and social challenges of terrestrial life.

According to the Agência Nacional do Petróleo, Gás Natural e Biocombustíveis [6], cooking gas in Brazil increased by 23.2% between March 2021 and March 2022, costing more than R$100, approximately 10% of the minimum wage in force in 2022.

Firewood gained space in the poorest homes during the pandemic [7,8] and remains today, including in Brazil. As a solution to cooking gas, wood and charcoal are used for cooking, a setback in health and quality of life because the levels of particles during the combustion process are far above those stipulated by the World

Health Organization (WHO), becoming risk factors for several types of diseases [9].

Most of the indexed publications on solar ovens and stoves, to date, present thermodynamic evaluations. Focusing on the most recent studies focused on the box-type solar oven, the study by [10] investigates the thermal performance of an improved low-cost stove to store heat and uses extended fins to increase heat exchange, while [11] studied the linear regression performance curve of this type of oven. Reference [12] presented guidelines for the design of box-type solar cookers with sensible heat storage, which can be used for both day and night cooking. The only Brazilian study found was [13], who evaluated the efficiency of a box-type solar oven made from disused recyclable elements through thermal evaluations during tests carried out with different foods such as cake, lasagna and pizza.

Another type of analysis that can be additionally developed is the environmental one, which can focus on quantifying different ecological indicators. Life Cycle Assessment (LCA) is an already consolidated methodology for quantifying potential environmental impacts, which can be applied to products, processes and even services [14]. LCA has already been applied to some types of solar ovens, as in [15] who carried out an environmental impact assessment of a parabolic solar oven in Madagascar. Reference [16] focus of study was a box-type solar oven with double mirror, for the Himalayan region. Reference [17] studied the sustainability of homemade solar ovens for use in developing regions, demonstrating the benefits of replacing microwave ovens with different types of solar ovens.

Recognizing the lack of Brazilian studies on this topic, this study aims to quantify greenhouse gas emissions associated with the construction of a box-type solar oven. First, the inventory for the box-type solar oven prototype is built, and then the LCA methodology is applied to quantify GHG emissions. Finally, the results are analyzed when the final destination of the solar oven is recycling instead of landfill. This is the first study to present a complete inventory of the material composition of the solar oven, being part of a broader project, which includes a dissertation.

II. Material and Methods

A. Solar Oven

The solar oven used in this study is an adaptation of a prototype made at the Federal University of Rio Grande do Norte (UFRN) [13]. This device was produced using materials from a disused shelf, mirrors, glass and reused expanded polystyrene. The schematic drawing is shown in Fig 1.

On June 13, 2022, a visit was made to the Laboratory of Hydraulic Machines at UFRN, when data collection was carried out on each material that makes up the solar oven. Digital scales were used for weighing, one with a capacity of up to 10 kg and the other of up to 200 kg. The measurements of each component were also measured using a caliper, ruler and tape measure. It was observed that the current version of the prototype has a reduced support height, for ergonomic reasons. Casters were also added so that the equipment could be moved easily.

B. LCA

LCA is standardized by International Organization for Standardization (ISO) in its ISO 14040 (2006) and ISO 14044 (2006) standards, which in Brazil were translated by the Brazilian Association of Technical Standards (ABNT) into

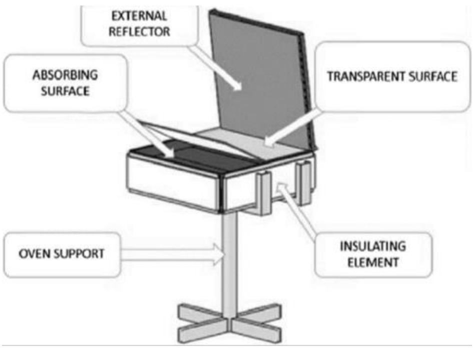

Figure 1. Schematic drawing of the studied prototype.

the same numbered standards (ABNT NBR 14040, 2014; ABNT NBR 14044, 2014) [18,19].

LCA has four steps (Fig 2): 1) definition of objectives and scope; 2) construction of the Life Cycle Inventory (LCI); 3) environmental impact assessment (choosing an environmental impact assessment method and applying it to the LCI), and 4) results and interpretation.

The LCA was developed with the Simapro 9.0.0.35 software [20], using the Ecoinvent V3.5 (2018) [21] database. Due to concerns about global warming, the environmental impact assessment method selected was the IPCC 2013 GWP 100a [22], which counts greenhouse gas (GHG) emissions over a time horizon of 100 years.

The objective of ACV was to analyze the solar oven prototype, focusing on its materials composition. The scope comprises raw material extraction, processing, manufacturing, and final disposal.

The LCA was carried out initially considering a disposal scenario representative of reality, where all materials are sent to the sanitary landfill (scenario 1). Then, it was considered that potentially recyclable materials (glass and steel) are recycled with 100% and 90% utilization, respectively (scenario 2).

III. RESULTS AND DISCUSSION

The material composition of the solar oven is shown in Table I. For the external reflector, a layer of reflective aluminum paint (50nm) on the glass of this surface was considered.

After assembling the LCI and developing the LCA, the GHG emissions related to the solar oven are obtained when the final destination is the sanitary landfill (scenario 1). Fig. 3 shows the Sankey diagram for these emissions.

TABLE I. MATERIAL COMPOSITION OF THE SOLAR OVEN.

Material	Weight (kg)
Expanded polystyrene	2.11
Wood	6.42
Steel	39.98
Glass	14.40
Rubber	0.15
Aluminum (reflective paint)	0.25
Total	**63.31**

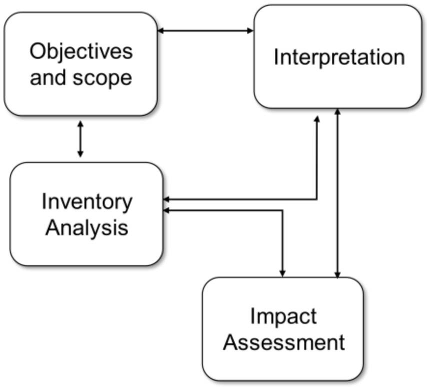

Figure 2. Stages of LCA.

Fig. 3 is a Sankey diagram, in which the thickness of the arrows indicating environmental impact is proportional to their contribution to the final impact. It is observed that from a material point of view, emissions associated with steel have the greatest contribution to the final impact, equivalent to 58% of final emissions. After steel, most emissions associated with the solar oven are related to final disposal in landfills.

Fig. 4 shows the specific emissions of each material. Aluminum is the component that has the highest CO_2-eq emission per kg, but because it is used in low amounts, it has a low impact on the product under analysis.

In scenario 2, when potentially recyclable materials (glass and steel) are effectively sent for recycling, there is a reduction of 111.73 kg CO_2 -eq in final emissions (Fig. 5).

Recycling glass and steel contribute to negative emissions of -18.73 kg CO_2-eq and -61.44 kg CO_2 -eq, respectively. The other components (wood, rubber, expanded polystyrene and non-recycled steel losses) are not recyclable and are sent to the sanitary landfill.

Recycling glass provides carbon credit, considering that the emissions associated with 14.40 kg of glass are 14.80 kg CO_2-eq and when there is recycling, avoided emissions of -18.70 kg CO_2-eq.

Comparing Figs. 3 and 5, it is observed that there was a 69.77% reduction in GHG emissions when the final disposal changes from the sanitary landfill, scenario 1, to the recycling of

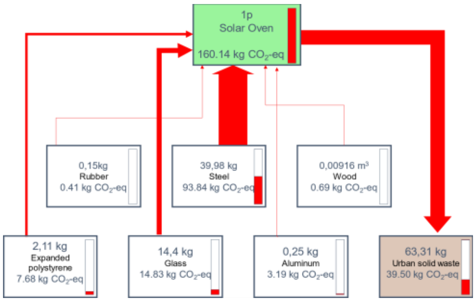

Figure 3. GHG emissions for the solar oven in scenario 1.

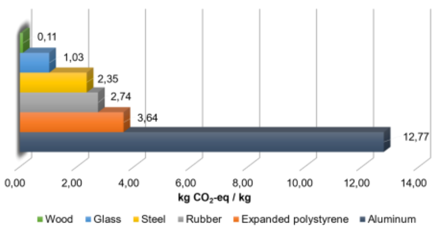

Figure 4. Material specific emissions (kg CO $_2$ -eq / kg material).

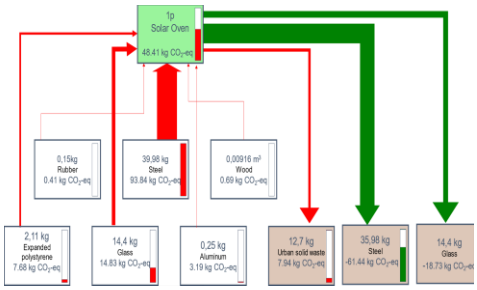

Figure 5. GHG emissions for the solar oven in scenario 2 (glass and steel recycling).

glass and steel in scenario 2 (from 160.14 kg CO_2 -eq to 48.41 kg CO_2 -eq).

The benefits associated with glass recycling had already been discussed and evidenced previously by [23] and [24], with proven benefits in terms of eco-efficiency, costs, and emissions. Both recycling and the use of the solar oven itself are broadly in line with SDG 12, related to the efficient consumption of natural (and energy) resources, as well as sustainable means of production.

Recognizing the importance of analyzing the life cycle inventory as a contribution to the management and identification of environmental impacts in production processes, the relevance of the detailed presentation of life cycle inventory data and LCA results is emphasized here as a way of complementing the existing thermodynamic analyses. LCA makes it possible to consider the environmental performance of different products, a procedure that is increasingly required by various social actors, and for LCA to be used broadly and reliably, it is necessary to build regional inventories that can be used even to benchmarking. It is noteworthy that the inventory construction stage is the basis for an LCA, and can be used in process analysis, material selection, product evaluation, product comparison, and even in policy formulation.

IV. Conclusions

This study presents the detailed life cycle inventory of a box-type solar oven, with subsequent application of the LCA methodology to quantify GHG emissions.

When considering that the landfill was the final destination of the kiln after the end of its useful life, the GHG emissions associated with this scenario were 160.14 kg CO_2 -eq. When it was considered that glass and steel could be recycled, emissions were reduced to 48.41kg CO_2 -eq.

This study demonstrated the importance of strategies for the correct disposal of waste. In this case, recycling can contribute to important reductions in GHG emissions when compared to conventional disposal (landfill).

The life cycle inventory is a topic that should be increasingly studied and discussed, as it is essential to deepen the knowledge of processes and consequent reduction of environmental impacts.

Future work is already underway, to carry out a comparison with a conventional oven in the case of cake baking.

Acknowledgment

The authors thank the Coordination for the Improvement of Higher Education Personnel (CAPES) for the master's scholarship, the National Council for Scientific and Technological Development (CNPq) for the productivity scholarship nº 309452/2021-0, and the Gobierno de Aragón (Spain) for funding from Grupo de Ingeniería Térmica y Sistemas Energéticos (GITSE) reference T55_20R.

REFERENCES

[1] Khatri, R., Goyal, R., & Sharma, R. K. (2021). Advances in the developments of solar cooker for sustainable development: a comprehensive review. *Renewable and Sustainable Energy Reviews*, *145*, 111166.

[2] Varun, K., Arunachala, U. C., & Vijayan, P. K. (2022). Sustainable mechanism to popularise round the clock indoor solar cooking–Part I: Global status. *Journal of Energy Storage*, *54*, 105361.

[3] Zubi, G., Spertino, F., Carvalho, M., Adhikari, R. S., & Khatib, T. (2017). Development and assessment of a solar home system to cover cooking and lighting needs in developing regions as a better alternative for existing practices. *Solar Energy*, *155*, 7-17.

[4] Solar cookers international - SCI. (2021). Available at: https://solarcooking.fandom.com/wiki/Category:Countries.

[5] UN - United Nations. *Transforming our world: the 2030 Agenda for Sustainable Development. 2015*. Available at: https://www.un.org/ga/search/view_doc.asp?symbol=A/RES/70/1&Lang=E.

[6] ANP, Agência Nacional de Petróleo, Gás Natural e Biocombustíveis. Available at: https://preco.anp.gov.br/.

[7] Bisaga, I., & L.S, T. (2021). *Clean Cooking in Refugee Camps and COVID-19: What Lessons Can We Learn. Modern Energy Cooking Services Programme*. Available at: https://mecs.org.uk/wp-content/uploads/2021/04/Clean-cooking-in-refugee-camps-and-COVID-19-what-lessons-can-we-learn-1.pdf.

[8] Ali, J., & Khan, W. (2022). Factors affecting access to clean cooking fuel among rural households in India during COVID-19 pandemic. *Energy for Sustainable Development*, *67*, 102-111.

[9] Gioda, A., Tonietto, G. B., & Leon, A. P. D. (2019). Exposição ao uso da lenha para cocção no Brasil e sua relação com os agravos à saúde da população. *Ciência & saúde coletiva*, *24*, 3079-3088.

[10] Kumar, A., Saxena, A., Pandey, S. D., & Joshi, S. K. (2022). Design and performance characteristics of a solar box cooker with phase change material: A feasibility study for Uttarakhand region, India. *Applied Thermal Engineering*, 118196.

[11] Ruivo, C., Apaolaza-Pagoaga, X., Coccia, G., & Carrillo-Andrés, A. (2022). Proposal of a non-linear curve for reporting the performance of solar cookers. *Renewable Energy*, *191*, 110-121.

[12] Verma, S., Banerjee, S., & Das, R. (2022). A fully analytical model of a box solar cooker with sensible thermal storage. *Solar Energy*, *233*, 531-542.

[13] Pereira Neto, R. V., de Souza, L. G. M., de Lima, J. C., de Souza, L. G. V. M., & Mendes, E. V. (2021). Theoretical-experimental study of a box-type solar oven made from disused recyclable elements. *Solar Energy*, *230*, 732-746.

[14] Michael, Z. H., Ralph, K. R., & Stig, I. O. (2018). Life Cycle Assessment: Theory and Practice.

[15] Andrianaivo, L., & Ramasiarinoro, V. J. (2014). Life cycle assessment and environmental impact evaluation of the parabolic solar cooker SK14 in Madagascar. *Journal of Clean Energy Technologies*, 2(2),191-1195.

[16] Chakma, B., Serto, L., Kharpude, S., Narale, P., & Seveda, M. S. (2021). Life cycle assessment analysis, embodied energy evaluation and economic aspect study of double mirror reflector box type solar cooker for NEH region of Sikkim. *International Journal of Green Energy*, 1-18.

[17] Mendoza, J. M. F., Gallego-Schmid, A., Rivera, X. C. S., Rieradevall, J., & Azapagic, A. (2019). Sustainability assessment of home-made solar cookers for use in developed countries. *Science of the total environment*, *648*, 184-196.

[18] Associaçâo Brasileira de Normas Técnicas. (2014a). Gestão Ambiental - Avaliação do Ciclo de Vida - Princípios e estrutura: NBR ISO 14040, Rio de Janeiro: ABNT.

[19] Associaçâo Brasileira de Normas Técnicas. (2014b). Gestão ambiental - Avaliação do ciclo de vida - Requisitos e orientações: NBR ISO 14044, Rio de Janeiro: ABNT.

[20] Pré-Sustainability. Software Simapro 9.0.0.35. (2018).

[21] Ecoinvent (2018) *Data Base*. Available at https://www.ecoinvent.org/

[22] IPCC - Intergovernmental Panel on Climate Change (2013) Report climate change 2013: the physical science basis. Cambridge University Press, NY, USA, p. 1535.

[23] Mühle, S., Balsam, I., & Cheeseman, C. R. (2010). Comparison of carbon emissions associated with municipal solid waste management in Germany and the UK. *Resources, Conservation and Recycling*, *54*(11), 793-801.

[24] Vinci, G., D'ascenzo, F., Esposito, A., Musarra, M., Rapa, M., & Rocchi, A. (2019). A sustainable innovation in the Italian glass production: LCA and Eco-Care matrix evaluation. *Journal of cleaner production*, *223*, 587-595.

Intelligent Predictive Maintenance in Electric Power System

Jasna Marković-Petrović[1], Mirjana Stojanović[2]

[1]Public Enterprise Electric Power Industry of Serbia, Belgrade, Serbia
[2]University of Belgrade, Faculty of Transport and Traffic Engineering, Belgrade, Serbia

Abstract—**Nowadays, in industrial control and management systems, large amounts of data are generated and collected. Modern comprehensive data analytics provide much information about the equipment's condition. Due to the need for processing large data sets and limited processing time, conventional maintenance methods should be substituted with intelligent ones. Modernization of maintenance should bring the following benefits: better failure tracking, early fault detection, shorter failure time prediction, and better aging estimation. The paper proposed using machine learning algorithms to improve many maintenance functions. This Intelligent Predictive Maintenance (IPdM) strategy, according to the Maintenance 4.0 concept, should short unplanned downtime, increase system efficiency, and reduce maintenance costs. In this paper, the practical application of IPdM is presented. The novel maintenance strategy and IPdM architecture are consistent with the proposed guidelines considering potential risks and implementation challenges.**

Keywords - industrial internet of things, intelligent predictive maintenance, machine learning

I. INTRODUCTION

The maintenance process plays a significant role in industrial production. Given that the maintenance range costs are between 15% and 60% of the total costs of the entire production [1], the improvement of the maintenance process enables the fulfillment of both key goals, technical and financial. Optimal maintenance should ensure the following aims in prevention of equipment failure.

- Reducing downtime and increasing the reliability of the production process with minimal costs.
- Better maintenance cost management.
- Optimization of spare parts storage.
- Timely procurement of spare parts.
- High quality of production cycle.
- Safety production cycle.
- Employee safety.
- Environmental protection.

The industrial revolution is accompanied by maintenance evolution. The following four main concepts characterize the historical development of maintenance strategies: 1) Corrective maintenance involves the equipment operation until the equipment fails, and then repair or replacement is undertaken. This way of maintenance maximizes production time, but increases repair and exchange costs due to possible catastrophic production and safety consequences and long downtime; 2) Preventive maintenance means periodic maintenance before equipment failure. The planned downtime periods are determined based on expert opinion and equipment manufacturer recommendations. In this way, catastrophic consequences are avoided, but the cost of replacing spare parts and the engagement of maintenance staff increases; 3) Condition-based maintenance (CBM) represents the first type of real-time maintenance based on online multiparameter monitoring. The parameter gradients and limits are determined by expert opinions and statistical and empirical criteria; 4) IPdM is based on an up-to-date CBM concept in which data analysis and decision-making of maintenance tasks are performed automatically, using modern information technologies (IT) that marked the fourth industrial revolution.

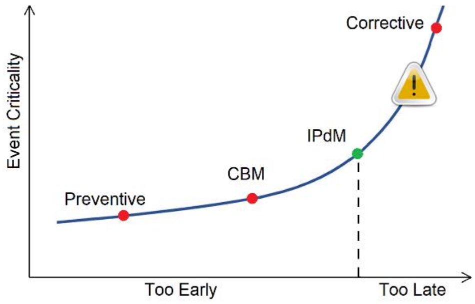

Figure 1. Maintenance strategies [2].

Fig. 1 shows the relationship between types of maintenance and the negative impact of failure.

Rapid information and telecommunication technologies development is a key driver of IPdM. Maintenance 4.0 is a twin of Industry 4.0. All the important characteristics of Industry 4.0 apply to Maintenance 4.0. Hierarchical data processing concepts are well incorporated into the Internet of Things (IoT) and Industrial Internet of Things (IIoT) strategies [3]. High-speed and large data flow and video streaming are enabled by powerful servers, workstations, as well as wireless and optical telecommunication networks. Complex data science algorithms, and artificial intelligence (AI) such as big data analytics (BDA) and machine learning (ML) methods are being developed in the IoT environment for twenty years.

Hierarchical management, control, and data processing are implemented in many strategic industrial, transport, and power systems. Edge, fog, and cloud computing have enabled the development and practical application of Maintenance 4.0. 5G telecommunication levels in IoT concepts have enabled the collection of a large amount of data in real-time. Edge computing is in charge of real-time measurement, online data processing, and database (data sets) creation. Fog computing is in charge of data analysis by using data science algorithms and data processing by using machine learning algorithms. Cloud computing is performed on powerful computers (workstations and servers) with the help of decision-making algorithms and software tools for big data analytics based on AI.

IPdM is basically based on smart sensors and systems, multiparameter real-time monitoring systems, and AI-incorporated algorithms. Modern diagnostic systems must perform online and real-time failure prediction and timely indicate the need for maintenance.

The work is divided into six chapters. In the introductory chapter, the basics of modern maintenance and hierarchical data and information processing are given. The framework of the IPdM strategy is given in chapter II. Chapter III provides maintenance guidelines for implementing an IPdM strategy. The potential risks and challenges are presented in Chapter IV. Chapter V presents case studies of the application of the IPdM maintenance strategy in power systems. Chapter VI provides concluding remarks.

II. FRAMEWORK OF IPDM STRATEGY

The main difference between CBM and IPdM is that instead of periodic maintenance (CBM), online real-time failure tracking and fault prediction are applied (IPdM). The main advantages of the IPdM strategy are real-time fault prediction and on-demand maintenance.

In contrast to the structural models of CBM, IPdM data analysis uses ML methods and information on the current state of the equipment. Such an approach is based on fault prediction and giving timely maintenance recommendations. Properly creating an IPdM strategy involves four following steps:

1. In the first step, the selection of data (multiparameter analysis) and the choice of the method for data collection and storage are made.

2. The second step involves data preprocessing and preparing data sets for the ML model:
   - data cleaning;
   - missing data treatment [4];
   - data transformations (min-max scaling, standardization, and normalization);
   - data visualizations;
   - data validation;
   - outliers detecting;
   - outlier analysis: fault detection based on outlier analysis, or outlier removing;
   - dimensionality reduction.

3. The third step implies the ML model selection and algorithms (one or more of them). This step involves training, testing, and validating the selected model.

4. The last step involves adapting and maintaining the model in accordance with the practical needs of the IPdM strategy.

The main framework of the IPdM strategy [5] is composed of four blocks presented in Fig. 2. In the process of equipment monitoring, data acquisition is performed. Data can be downloaded from existing Supervisory Control And Data Acquisition systems (SCADA), databases, knowledge bases, and online industrial IoT system sensors. Data obtained from SCADA are useful for the condition assessment of the equipment. Fault prediction, aging prediction, and remaining operational life prediction can be performed using by ML models and algorithms. Based on fault prediction, optimal maintenance plans and necessary investments are made.

The application of ML algorithms allows monitoring systems to automatically learn and improve their knowledge based on previous experience, without the need for explicit programming. ML is very useful for solving problems for which it is difficult to define a solution. ML is increasingly used in complex systems that dynamically adapt to the environment, to obtain information from large raw data sets, and to trend prediction.

There are several different types of ML algorithms (Fig. 3) [6]: supervised machine learning, unsupervised machine learning, semi-supervised machine learning, and reinforcement machine learning. ML algorithms are increasingly being applied in industry and the energy sector in: prediction of energy flows and electricity prices [7], control and management of virtual power plants [8], smart grids [9], digital twin [10], cyber risk management [11].In this research, the authors are focused on: 1) the application of ML algorithms in the maintenance of power plants, where the input data are obtained from SCADA and online monitoring systems, and 2) early fault detection by applying

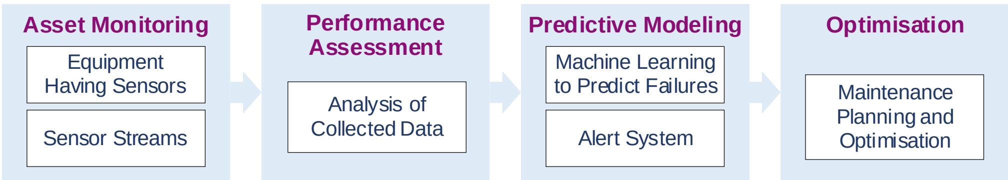

Figure 2. IPdM strategy framework.

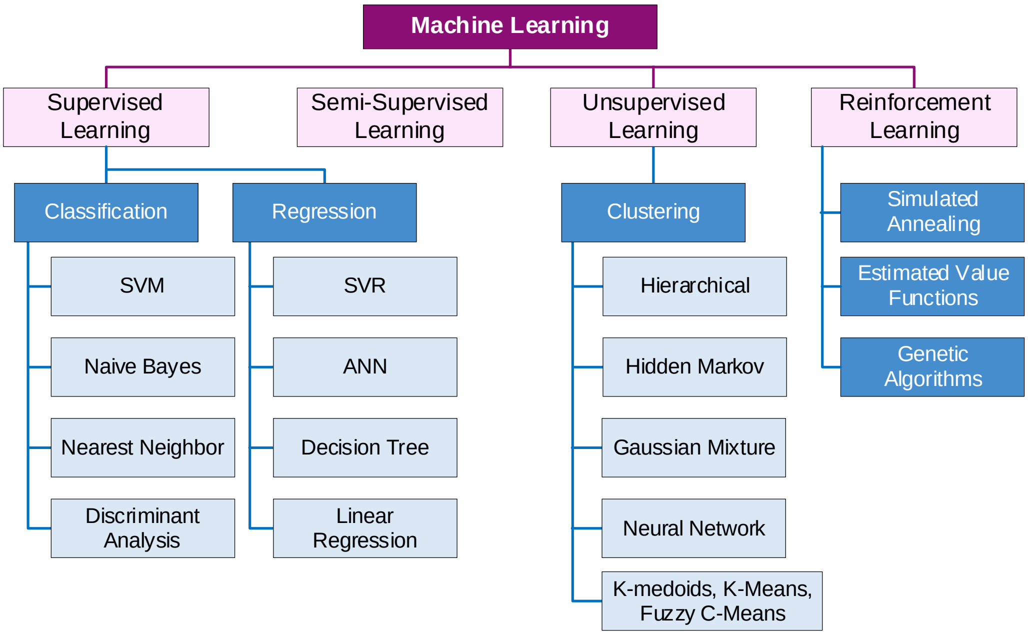

Figure 3. ML techniques classification.

different diagnostic techniques. Some of the more frequently used techniques are the following: sound and ultrasonic monitoring, chemical analysis of oil and particles, infrared and thermal imaging, partial discharges measurement, vibration analysis, frequency response analysis, etc.

Apart from the multiparameter analysis of the equipment condition, the production parameters, ambient conditions, etc. are also considered.

III. Implementation Guidelines of the IPdM Maintenance Strategy

The implementation of the IPdM strategy is proposed in [12] and is based on the gradual introduction (seven steps) of a predictive model for a set of selected equipment (Fig. 4):

1. Equipment ranking and feasibility studies. The identification of the equipment for which the application of IPdM is feasible and cost-effective is carried out. The main goal is to analyze and monitor the condition state of highly critical and medium critical equipment for which data acquisition, processing, and analysis are possible. This is also the initial step in creating a business plan and feasibility study.

2. Equipment selection, expert opinions, and experience gained for the pilot project that should be used for the IPdM system expansion. It is very important not to cover all the equipment in the initial project phase.

3. Reliability modeling is achieved using Root Cause Analysis (RCA) and Failure Mode Effects Analysis (FMEA) according to the selected equipment. It is necessary to answer the questions of what data (from sensors and external) is needed to monitor RCA and FMEA, as well as how the root causes and failure modes are interrelated.

4. The algorithm selection depends on the previous step and is important for prediction quality. In this step, data science and machine learning experts play a significant role.

5. Real-time performance monitoring: The algorithm performs data processing from different sources: SCADA systems, databases, online monitoring systems, smart sensors and failure, and maintenance reports.

6. Early fault detection and prediction (early warning). The algorithm, after the learning phase, starts fault predicting. At this stage, there is a high probability of incorrect fault detection: the algorithm can predict a fault on the correct equipment (FP - False Positive) or can not to detect a fault on the faulty equipment (FN - False Negative). Therefore, it is recommended that IPdM works in parallel with existing maintenance procedures without automatic maintenance actions based on IPdM system predictions.

7. Outage prevention. The algorithm, in addition to time-to-failure prediction, can suggest maintenance activities based on a maintenance library.

A company, that intends to implement the IPdM strategy, has to provide IT resources for the edge, fog, and cloud computing. This can be achieved by using existing own resources, new investments, public cloud solutions, or a combination thereof.

The implementation of Maintenance Strategy 4.0 requires an IoT environment, which is based on powerful computer resources, wireless communication networks, and/or optical networks between the monitored equipment on the edge level and the maintenance data center (upper than the cloud level). Establishing the necessary IoT infrastructure requires the selection of protocols, encryption methods, security solutions, and analytics platforms.

After the implementation of the IPdM system, it is necessary to continuously monitor and analyze the system operation from the aspect of achieving business goals.

The appropriate technology choice and its good application are important for the proper application of a new maintenance strategy. However, the final result depends not only on the choice of sensors, algorithms, and models, or analytical software, but also on data analysts and ML experts, digital culture, and the willingness of management and employees to change.

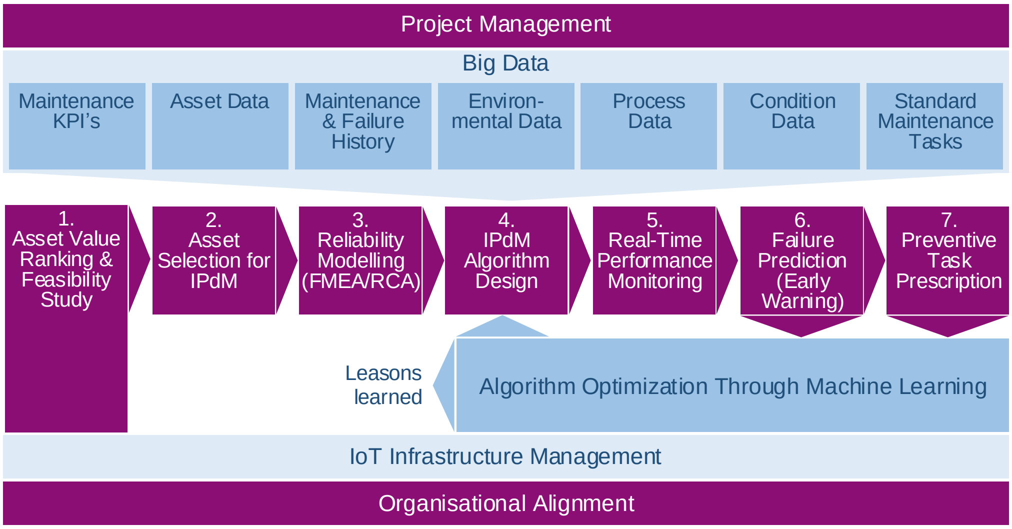

Figure 4. IPdM strategy implementation.

IV. Implementation Challenges and Risks

Despite all the advantages of the IPdM strategy, it has not been widely applied. There is an obvious difference between the possible and realized benefits of the application of the new maintenance strategy. The challenges and risks of implementation are as follows [2]:

- Data management - the process of acquisition, collecting, selecting, ingesting, organizing, transforming, storing, and maintaining the large amount of data created by various deployed measurement, monitoring, smart, and information systems. The IPdM strategy implies continuous data processing that requires the availability of web semantic technologies.

- Adopting new approaches based on AI and ML represents one of the biggest challenges in developing new maintenance strategies.

- Complex interpretation and legacy operating systems and software. Apart from complex interpretations of predictive models, the problem of IT compatibility with outdated computer systems (legacy operating systems, software, protocols, and interfaces) is also evident.

- Cyber security. Information security may be compromised because data originates from different information systems. There is also the data ownership question, given that the maintenance process often involves outsourcing companies. Multiple data owners and users (ML algorithm developers, data science experts, etc.) can present an additional security risk. Confidentiality, integrity, and availability of data can be achieved by homographic encryption and by applying Privacy-Preserving Machine Learning (PPML) algorithms.

- For now, it is difficult to talk about the economic justification of the IPdM because there are still not enough power and industry companies that accepted this strategy. Significant initial investments are required in implementing new technologies, training employees, and improving existing processes and systems. For the above reasons, it is difficult to estimate the return on investment (RoI) at the moment.

- The company structure plays a significant role in the adoption of a new maintenance strategy, due to the requirement for experts from the following fields: maintenance; hierarchical computing at the edge, fog, and cloud levels; sensor networks; etc. The issue related to company staff's ability for data processing and analysis will be of particular importance in the future.

Given that implementing a complete IPdM solution requires significant investment and organizational change, various alternatives can be adopted to capture the benefits of the strategy. Some of the development directions can be using data from traditional business and technical processes and designing new prognostic and diagnostic predictive ML models.

V. Case Studies of IPdM Strategy: A Review

Operational readiness of power plants, power distribution systems, and power grids, is very important for a reliable and safe electricity supply. Fully implementing the IPdM strategy should be contributed to raising operational readiness and fulfilling the company's strategic goals. This primarily refers to outlier detection, fault detection, aging prediction, and making equipment maintenance plans.

In the period from 2015 to 2019, the Norwegian Electricity Industry (Energi Norge) and the Swedish Center for Energy Research (Energiforsk) implemented the MonitorX project [13]. The main project goal is the development of models, algorithms, and software prototypes for the optimal use of hydropower equipment based on condition monitoring and risk analysis. The models were developed in eight case studies with the aim of anomaly detection of the following hydropower equipment in hydropower plant:

1. Rotor;
2. Drainage pumps;
3. Rotating parts and systems, by vibration analysis (vibration analysis);
4. Generator bearings;
5. Kaplan turbine hydraulic system;
6. Power transformer (temperature monitoring);
7. Servo motors (detecting force changes);
8. Various hydropower equipment (sound/noise analysis).

Special attention is paid to the data processing from the local SCADA system that is addressed in the ninth case study.

The applied ML models in the case studies learn the relationships and patterns of the equipment operation in the regular operation mode. Outlier detection is used to fault detect and trigger an alarm. The reason for using this research approach (anomaly detection) is the special design and high reliability of hydropower equipment, so learning from the database and failure reports is unfeasible. The result of these studies is a set of ML models and algorithms for condition monitoring, fault detection, aging prediction, and prediction of the remaining life of hydropower equipment. ML models have been built using different ML techniques, such as Artificial Neural Networks (ANN), Recurrent Neural Networks (RNN), Multi-Layer Perceptron (MLP) and Long Short-Term Memory (LSTM). By using these models, managers make better decisions about maintenance and investments. Norwegian power system operators recognized the following benefits of the IPdM strategy: 1) economic profit resulting from deferred investment costs, 2) economic profit due to reduced production losses due to shorter downtime, 3) lower maintenance and monitoring costs because of reduced manual maintenance, 4) shorter maintenance time due to a better condition assessment of the equipment, 5) lower corrective maintenance costs due to reduced failure probability, and 6) instant insight into the actual equipment condition and the relationship between ambient conditions, power plant operating mode, and remaining useful equipment life.

The second IPdM application is presented in a case study [14] of predictive maintenance of transformer substations. Infrared thermography was used along with AI methods for computer vision, for the early fault detection caused by bad wire connections, high load, insulation cracks, defective relays, bad clamp connections, etc. Thermal images are captured by infrared cameras in real time, and modeling is performed using a MLP artificial neural network. The result is a binary classification (failure and correct) of thermal conditions of power components of transformer substations.

The third application of ML in predictive maintenance of the water-cooling system is in the hydropower plant Nam Ngum-1 in Laos [15]. The data used for the ML algorithm are taken from three sources: data from the heat exchanger (database), a maintenance log, and daily reports for a period of 31 months. The data is divided into two sets: for training and testing. The Classification Learner Application is used to train the model. The application supports 22 types of classifiers, which can be modeled with the following six algorithms: Decision Trees (DT), Discriminant Analysis (DA), Support

Vector Machine (SVM), Logistic Regression (LR), K-Nearest Neighbor Classifiers (KNN), and Ensemble Classifiers (EM). Comprehensive analysis showed that SVM and decision trees have better predictions than other algorithms.

The fourth case study presented a novel ML algorithm intended for IPdM of nuclear power plants [16]. The remaining useful life (RUL) prediction is performed by classifying the data according to whether failure will occur in the next *n* operational cycles (probability problem). Logistic Regression (LR) and SVM algorithms were used, and their efficiency is assessed as a function of *n* cycles. These algorithms should answer the question of how early the outage will be predicted.

The fifth case study presented improvement in maintenance based on the estimation of the operating time of a turbine in a hydropower plant [17]. Guidelines are provided for sensor mapping and the input parameter selection for the ML algorithm. A comparison of four ML algorithms, determining the most favorable moment for turbine maintenance, was performed. The proposed model was implemented in five phases: 1) process mapping, 2) definition and selection of measurement quantities, 3) acquisition, preparation, and storage of data, 4) ml modeling, and 5) application in real conditions.

The model was verified in the Usina Henry Borden hydropower plant in Brazil using ANN, Deep Learning (DL), LR, and MLP algorithms. A method for determining the most important input algorithm parameters was developed within the study. In this way, the dimensionality reduction of the data set was performed.

The sixth case study presents the maintenance of photovoltaic power plants using DL [18]. The monitoring of the operation of photovoltaic panels is carried out using Convolutional Neural Networks (CNN) for the prediction of the operating curve. The difference between the actual and the predicted operating curve could indicate to defect in the photovoltaic panel. The method was verified by simulation.

The seventh case study presents outage detection of five wind turbine components using by data-centric ML algorithm [19]. Input data are obtained from three sources: 1) sensor acquisition: bearing temperature measurement, oil temperature, generator speed, tilt angle, etc., 2) meteorological data, and 3) data on previous equipment failures.

The ML algorithm performs binary classification (before failure or healthy) and linear regression for RUL. The data set is divided into a test set and a learning set. In accordance with the data-centric concept, the attention is focused on parameter selection, data preprocessing, and model hyperparameter settings. The application of several ML algorithms was analyzed, including LR, DT, Random Forest (RF), Gradient Boosted Tree (GBT), MLP and SVM. The best results were obtained using a simple DT algorithm. The model was verified with the real parameters of a wind generator.

Table I shows the summarized results of the applied ML algorithms for the needs of maintenance in the power sector.

TABLE I. APPLICATIONS OF ML IN IPDM: A BRIEF SUMMARY.

Reference	System	ML Technique	Source Data	Verification
[13]	Hydro Power Plant	ANN, MLP, RNN, LSTM	Various data depending on use case	Real use case
[14]	Power Substation	ANN	Thermal image from infrared camera	Real use case
[15]	Hydro Power Plant	DT, DA, SVM, K-NN, EM	Temperature History of operations and maintenance	Real use case
[16]	Nuclear Power Plant	LR	Temperature, power, current, speed	Simulation
[17]	Hydro Power Plant	ANN, DL, LR, MLP	Pressure in valves, water flow, position of the water injection, rotation frequency	Real use case
[18]	Photovoltaic Panels	CNN	Electrical power signals	Simulation
[19]	Wind turbine	LR, DT, RF, GBT, MLP, SVM	Sensor data: generator speed, blade pitch angle, wind speed and direction; Meteorological data; Failures data	Real use case

VI. CONCLUSION

Novel maintenance strategies have significant potential in future smart power plants. Digitization, online parameter analysis, real-time monitoring of the power equipment, as well as predictive maintenance with AI support are hot issues in Maintenance 4.0. The full implementation of Intelligent Predictive Maintenance (IPdM) requires the application of new communication and information technologies and artificial intelligence (machine learning algorithms, big data analytics, data science methodologies, etc.). The expected benefits are reflected in better maintenance planning, reduced unplanned downtime, reduction of maintenance costs, reduction of the stock of spare parts in warehouses, etc.

Equally important is the extension of the operating life of the equipment due to timely maintenance and the reduced negative impact of frequent activities related to periodic maintenance. Some limitations to the application of IPdM are related to the necessary initial investment in diagnostic equipment and operator training. The complexity of equipment and predictive mathematical models and the influence of the environment can create difficulties in condition assessment and result interpretation.

Finally, it should be pointed out that the implementation of the IPdM strategy means a paradigm shift in company maintenance and its organizational challenge.

REFERENCES

[1] Zonta, T., et al. (2020). Predictive maintenance in the Industry 4.0: A systematic literature review. *Computers & Industrial Engineering*, *150*, 106889.

[2] Bukhsh, Z. A., & Stipanovic, I. (2020). Predictive maintenance for infrastructure asset management. *IT professional*, *22*(5), 40-45.

[3] Milić, S. D., Đurović, Ž., & Stojanović, M. D. (2023). Data science and machine learning in the IIoT concepts of power plants. *International Journal of Electrical Power & Energy Systems*, *145*, 108711.

[4] Ehrlinger, L., Grubinger, T., Varga, B., Pichler, M., Natschläger, T., & Zeindl, J. (2018, September). Treating missing data in industrial data analytics. In *2018 Thirteenth International Conference on Digital Information Management (ICDIM)* (pp. 148-155). IEEE.

[5] Cachada, A., et al. (2018, September). Maintenance 4.0: Intelligent and predictive maintenance system architecture. In *2018 IEEE 23rd international conference on emerging technologies and factory automation (ETFA)* (Vol. 1, pp. 139-146). IEEE.

[6] Sarker, I. H. (2021). Machine learning: Algorithms, real-world applications and research directions. *SN Computer Science*, 2(3), 1-21.

[7] Ghoddusi, H., Creamer, G. G., & Rafizadeh, N. (2019). Machine learning in energy economics and finance: A review. *Energy Economics*, *81*, 709-727.

[8] Rouzbahani, H. M., Karimipour, H., & Lei, L. (2021). A review on virtual power plant for energy management. *Sustainable energy technologies and assessments*, *47*, 101370.

[9] Ibrahim, M. S., Dong, W., & Yang, Q. (2020). Machine learning driven smart electric power systems: Current trends and new perspectives. *Applied Energy*, *272*, 115237.

[10] Sleiti, A. K., Kapat, J. S., & Vesely, L. (2022). Digital twin in energy industry: Proposed robust digital twin for power plant and other complex capital-intensive large engineering systems. *Energy Reports*, *8*, 3704-3726.

[11] Stojanovic, M., & Markovic-Petrovic, J. (2021). Application of machine learning for cyber security risk assessment in Industrial IoT systems: A review. In *7th Virtual Int. Conf. on Science, Technology and Management in Energy –eNergetics* (pp. 209-216).

[12] Haarman, M., et al. (2018). Predictive maintenance 4.0-beyond the hype: PdM 4.0 delivers results. *PricewaterhouseCoopers and Mannovation*.

[13] Welte, W., & Foros, J. (2019). MonitorX-final report. *Technical Report Energi Norge AS*.

[14] Ullah, I., et al. (2017). Predictive maintenance of power substation equipment by infrared thermography using a machine-learning approach. *Energies*, *10*(12), 1987.

[15] Xayyasith, S., Promwungkwa, A., & Ngamsanroaj, K. (2018, November). Application of machine learning for predictive maintenance cooling system in Nam Ngum-1 hydropower plant. In *2018 16th international conference on ICT and knowledge engineering (ICT&KE)* (pp. 1-5). IEEE.

[16] Gohel, H. A., Upadhyay, H., Lagos, L., Cooper, K., & Sanzetenea, A. (2020). Predictive maintenance architecture development for nuclear infrastructure using machine learning. *Nuclear Engineering and Technology*, 52(7), 1436-1442.

[17] Vallim Filho, A. R. D. A., Farina Moraes, D., Bhering de Aguiar Vallim, M. V., Santos da Silva, L., & da Silva, L. A. (2022). A machine learning modeling framework for predictive maintenance based on equipment load cycle: An application in a real world case. *Energies*, *15*(10), 3724.

[18] Huuhtanen, T., & Jung, A. (2018, June). Predictive maintenance of photovoltaic panels via deep learning. In *2018 IEEE Data Science Workshop (DSW)* (pp. 66-70). IEEE.

[19] Garan, M., Tidriri, K., & Kovalenko, I. (2022). A data-centric machine learning methodology: Application on predictive maintenance of wind turbines. *Energies*, *15*(3), 826.

Mixed Convection of a Ferrofluid in a Vertical Channel with Porous Blocks under Magnetic Field: Effect of Permeability

Nawal Guerroudj[1], Brahim Fersadou[2], Henda Kahalerras[3]

[1,2,3]Faculty of Mechanical and Process Engineering (FGMGP), University of Sciences and Technology Houari Boumediene (USTHB), Algiers, Algeria

Abstract—**The present work is a numerical simulation of (water-Fe_3O_4) ferrohydrodynamics (FHD) mixed convection inside a vertical channel are performed. The magnetic field is produced by three sources located outside the channel's right wall, which is provided with localized heat sources surmounted by porous blocks of various shapes. The Brinkman-Forchheimer extended Darcy model is adopted for the flow in the porous regions. The governing equations with the appropriate boundary conditions are solved by the finite volume method. The effects of some pertinent parameters such as the magnetic number, shape of porous blocks and the permeability of porous blocks is examined. The results reveal essentially, that specific choices in the governing parameters cited above, can produce a significant heat transfer enhancement when an oscillating component is added to the mean flow.**

Keywords – ferrohydrodynamics, mixed convection, ferrofluid, porous blocks, blocks shape

I. Introduction

A promising method to improve heat transfer in the several thermal systems encountered in industry is the use of ferrofluids. Indeed, with this type of fluid which represents a special class of nanofluids, the flow can be manipulated in an appropriate way to enhance the convective exchanges. Ferrofluids can be employed in a variety of technology fields, including micro-scale heat exchangers, aerospace and electronic packaging.

For this purpose, they have been the subject of numerous experimental and numerical studies in the presence of an external magnetic field [1-6]. Ferrofluid heat transfer enhancement caused by the introduction of a line dipole was explored by [7]. They found that under the ferrohydrodynamic (FHD) effect, a vortex is formed locally at the wall where the dipole is located, which impacted energy transport favorably. Both magnetohydrodynamic (MHD) and ferrohydrodynamic effects were considered by [8] while studying the flow and heat transfer of a ferrofluid in a semi-annular enclosure. Ferrofluid non-uniform MHD mixed convection within a lid-driven cavity containing a solid backward step at the enclosure's bottom was investigated by [9].

Mixed convective heat transfer in porous media was intensively investigated because of its relevance in many practicle applications such as nuclear reactors, ground water, drying processes, heat exchangers, solar collectors, geophysical systems, electronic cooling, etc. A great number of research have been conducted in the literature to handle this topic under a variety of settings [10-14]. Reference [15] examined numerically the mixed convection flow of a water-alumina nanofluid in a lid-driven cavity containing two adherent porous blocks. The effects of an inclined magnetic field and rotating circular cylinder on nanofluid mixed convection in a trapezoidal porous enclosure was studied by [16].

The present work is a numerical simulation of (water-Fe_3O_4) ferrohydrodynamics (FHD) mixed convection inside a vertical channel are performed. The magnetic field is produced by three sources located outside the channel's right wall, which is provided with localized heat sources surmounted by porous blocks of various shapes.

II. PHYSICAL DOMAIN

The study domain, shown in Fig. 1, is a vertical channel consisting of two parallel plates of length ℓ and separated by a distance W. The left plate is thermally insulated, while on the right one are mounted porous blocks each having a base width *wp*, a height hp and are spaced by a distance sp. Localized heat sources are placed at block level providing a constant heat flux density q. The first block is placed in the channel so that inlet effects are avoided, while the length behind the last one is chosen large enough to satisfy the condition of a fully developed flow at the exit. Three porous blocks shapes are considered; namely rectangular, trapezoidal and triangular.

A ferrofluid (water - Fe_3O_4), which thermophysical properties are given in Table I, enters the channel at uniform velocity, temperature and nanoparticles volume fraction.

A non-uniform magnetic field is created by three sources each consisting of a wire crossed by an electric current I. These sources are placed outside the channel so that their axial coordinate a corresponds to the middle of a block, while the transverse distance b from the plate is 0.25W.

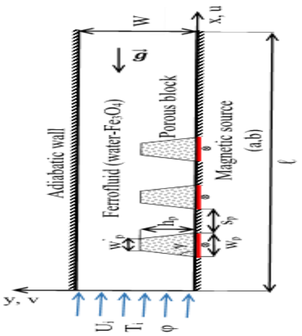

Figure 1. Physical domain.

TABLE I. THERMOPHYSICAL PROPERTIES OF WATER AND Fe_3O_4.

Properties	Water	Fe_3O_4
Cp (J/kg K)	4179	670
ρ(kg/m3)	997.1	5200
k (W/m K)	0.613	6
$\beta(K^{-1})$	21×10^{-5}	1.3×10^{-5}

III. MATHEMATECAL FORMULATION

A. Governing Equations

Some assumptions are considered to simplify the problem: the flow is two-dimensional, laminar, and incompressible with no internal heat generation and neglecting viscous dissipation. The thermo-physical properties of the fluid are assumed to be constant, and the porous medium is considered homogeneous, isotropic, and saturated with a single-phase fluid in local equilibrium with the solid matrix. The flow is modeled by the Brinkman-Forchheimer extended Darcy model in the porous regions to incorporate the viscous and inertia effects. The dimensionless equations can be written as follows:

Continuity

$$\frac{\partial U}{\partial X}+\frac{\partial V}{\partial Y}=0 \quad (1)$$

Momentum

$$U\frac{\partial U}{\partial X}+V\frac{\partial U}{\partial Y}=-\frac{\partial P}{\partial X}+\frac{\rho_f}{\rho_{nf}}\frac{\mu_{nf}}{\mu}\frac{\varepsilon R_\mu}{Re}\times$$
$$\times\left(\frac{\partial^2 U}{\partial X^2}+\frac{\partial^2 U}{\partial Y^2}\right)-\frac{\rho_f}{\rho_{nf}}\frac{\mu_{nf}}{\mu}\frac{\varepsilon}{Re\,Da}U-\frac{C}{\sqrt{Da}}\times \quad (2)$$
$$\times\left|\vec{V}\right|U+Ri\theta+\frac{\rho_f}{\rho_{nf}}Mn\left(\Upsilon_c-\theta-\Upsilon_i\right)\bar{H}\frac{\partial\bar{H}}{\partial X}$$

$$U\frac{\partial V}{\partial X}+V\frac{\partial V}{\partial Y}=-\frac{\partial P}{\partial Y}+\frac{\rho_f}{\rho_{nf}}\frac{\mu_{nf}}{\mu}\frac{\varepsilon R_\mu}{Re}\times$$
$$\times\left(\frac{\partial^2 V}{\partial X^2}+\frac{\partial^2 V}{\partial Y^2}\right)-\frac{\rho_f}{\rho_{nf}}\frac{\mu_{nf}}{\mu}\frac{\varepsilon}{Re\,Da}V- \quad (3)$$
$$-\frac{C}{\sqrt{Da}}\left|\vec{V}\right|V+\frac{\rho_f}{\rho_{nf}}Mn\left(\Upsilon_c-\theta-\Upsilon_i\right)\bar{H}\frac{\partial\bar{H}}{\partial Y}$$

Energy

$$U\frac{\partial\theta}{\partial X}+V\frac{\partial\theta}{\partial Y}=\frac{\left(\rho C_p\right)_f}{\left(\rho C_p\right)_{nf}}\frac{k_{nf}}{k_f}\frac{R_k}{\varepsilon RePr}\times$$
$$\times\left(\frac{\partial^2\theta}{\partial X^2}+\frac{\partial^2\theta}{\partial Y^2}\right)+\frac{\left(\rho C_p\right)_f}{\left(\rho C_p\right)_{nf}}Mn\,Ec\left(\Upsilon_c+\theta\right)\times \quad (4)$$
$$\times\bar{H}\left(U\frac{\partial\bar{H}}{\partial X}+V\frac{\partial\bar{H}}{\partial Y}\right)$$

$\mu_0 M\vec{\nabla}H$ and $-\mu_0 T\dfrac{\partial M}{\partial T}\vec{V}.\vec{\nabla}H$ represent the Kelvin force and the magnetocaloric effect respectively. These two terms depend on the existence of the magnetic field gradient and the material magnetization which expression is:

$$M = K'\left(T_c - T\right)H \ . \tag{5}$$

In the non-porous region, the previous equations remain valid by taking: $\varepsilon = 1$, $K \to \infty$, $\mu_{eff} = \mu_{nf}$, and $k_{eff} = k_{nf}$.

B. Boundary Conditions

The associated boundary conditions are:

$$Inlet: \quad U = 1; V = 0; \ \theta = 0 \ , \tag{6}$$

$$Exit: \quad \frac{\partial U}{\partial X} = 0; \ V = 0; \ \frac{\partial \theta}{\partial X} = 0 \ , \tag{7}$$

$$Right\ wall: \quad U = V = 0 = \\ = \begin{cases} \dfrac{\partial \theta}{\partial Y} = -\dfrac{1}{R_k}\dfrac{k_f}{k_{nf}} & under\ the\ blocks \\ \dfrac{\partial \theta}{\partial Y} = 0 & elsewhere \end{cases} \ , \tag{8}$$

$$Left\ wall: \quad U = V = 0; \ \frac{\partial \theta}{\partial Y} = 0 \ . \tag{9}$$

C. Ferrofluid Properties

The ferrofluid properties are calculated using the following expressions:

- *Density*

$$\rho_{nf} = \left(1-\varphi\right)\rho_f + \varphi\rho_p \ , \tag{10}$$

- *Heat capacity*

$$\left(\rho C_p\right)_{nf} = \left(1-\varphi\right)\left(\rho C_p\right)_f + \varphi\left(\rho C_p\right)_p \ . \tag{11}$$

- *Viscosity and thermal conductivity*

The Corcione model [17] is used to determine the viscosity and the thermal conductivity of the ferrofluid:

$$\mu_{nf} = \frac{\mu}{1 - 34.87\left(d_p / d_f\right)^{-0.3}\varphi^{1.03}} \ , \tag{12}$$

$$\frac{k_{nf}}{k_f} = 1 + 4.4 Re_B^{0.4} Pr^{0.66}\left(\frac{T}{T_{fr}}\right)^{10}\left(\frac{k_P}{k_f}\right)^{0.03}\varphi^{0.66} \\ \mathrm{Re}_B = \frac{\rho_f d_p}{\mu}\frac{2k_B T}{\pi\mu d_p^2} \ , \tag{13}$$

df and T_{fr} are the molecule diameter ($df = 3.85\times10^{-10}$m) and the base fluid freezing temperature (T_{fr} = 273.15K) respectively.

The expressions for the various dimensionless groupings are as follows:

$$Re\frac{\rho_f U_i W}{\mu}; Da\frac{K}{W^2}; Ri\frac{g\beta \, qW/k_f \, W}{U_i^2}; Pr\frac{\mu C_p}{k_f}; \\ Mn = \frac{\mu_0 K' H_0^2 \, qW/k_f}{\rho_f U_i^2}; \\ Ec\frac{U_i^2}{C_{pf}\, qW/k_f}; \mathrm{Y}_c\frac{T_c}{qW/k_f}; \mathrm{Y}_i\frac{T_i}{qW/k_f}; \\ R_\mu\frac{\mu_{eff}}{\mu_{nf}}; R_k\frac{k_{eff}}{k_{nf}} \ . \tag{14}$$

D. Nusselt Number

The local Nusselt number is given by:

$$Nu = \frac{hW}{k_f} = \frac{1}{\theta_w - \theta_m}, \\ \theta_m = \frac{\int_0^1 |U|\theta\, dY}{\int_0^1 |U|\, dY} \ . \tag{15}$$

The mean Nusselt number at the level of each block is calculated as follows:

$$Nu_{mi} = \frac{1}{W_p}\int_{X_i}^{X_i+W_p} Nu\, dX \ , \tag{16}$$

where X_i is the position of block "*i*" relative to the channel inlet.

The global Nusselt number is defined as follows:

$$Nu_g = \frac{1}{3}\sum_{i=1}^{3} Nu_{m_i} \quad . \tag{17}$$

E. Friction Coefficient

The local friction coefficient is given by:

$$f = -\frac{dp_m}{dx}\frac{H}{\rho_f \bar{u}^2} = -\frac{\rho_{nf}}{\rho_f}\frac{dP_m}{dX}\frac{1}{\varepsilon^2 \bar{U}^2} \quad , \tag{18}$$

$$P_m = \int_0^1 P\, dY \quad . \tag{19}$$

The mean friction coefficient is expressed as:

$$f_m = \frac{1}{L}\int_0^L f\, dX \quad . \tag{20}$$

IV. Numerical Procedure

The previous conservation equations with the associated boundary conditions are solved numerically using the finite volume method, based on integrating the conservative differential equations over control volumes enclosing the nodal points. A staggered grid is used, such that velocity components are located at the control volume faces, whereas pressure and temperature are located at the centers of the control volumes. The velocity and pressure fields are linked by the SIMPLE Algorithm, and the power-law scheme is used in the discretizing procedure.

The obtained system of algebraic equations is then solved using a line-by-line technique, combining the tridiagonal matrix algorithm and the Gauss-Seidel method. A non-uniform grid in the two directions is employed. The finer meshes are placed in both the interfacial regions of the porous blocks and near the regions of the solid walls. For the Convergence criteria of the iterative process, the relative variations of velocity components and temperature between two successive iterations are required to be smaller than the value of 10^{-5}.

Since the parameters that govern the problem under investigation are numerous, some of them have been fixed: the base fluid is water $P_r = 6.62$, the porosity $\varepsilon = 0.97$, the inertial coefficient $C = 0.1$, the Reynolds number $R_e = 200$, the viscosity ratio $R_\mu = 1$ and the thermal conductivity ratio $R_k = 1$. The geometrical parameters are such that the length of the channel is $L = 29$, the base width of a porous block is $W_p = 1$ and the spacing between two successive blocks is $S_p = 1$. Furthermore, we focused on the effect of the magnetic number ($0 \le M_n \le 50$), the porous blocks shape (rectangular, trapezoidal and triangular) and the Darcy number ($1 \le D_a \le 10^{-6}$).

In Fig. 2, the isocontours plots are shown for different Darcy numbers. The flow resistance is particularly high when the porous medium permeability is low, the blocks behave like solids, and the ferrofluid motion occurs primarily outside of them. The heat sources are poorly cooled and the heat is transferred mainly by conduction in the blocks; in this case the effect of the magnetic field is negligible. By augmenting the Darcy number and therefore decreasing the flow resistance, the amount of fluid penetrating the blocks becomes increasingly relevant, resulting in an improvement in heat transfer at the heat sources level. The magnetic field impact gets stronger, and the flow becomes more disrupted. The impact study of the blocks shape clearly shows that the triangular blocks are the most efficient from a dynamic and thermal viewpoint, since they have the lowest flow resistance at each permeability. However, increasing Da reduces the difference between the various shapes, since the influence of the porous medium becomes negligible in this case, and nearly similar streamlines and isotherms structures are obtained.

As expected, the global Nusselt number, shown in Fig. 3, increases with the porous medium permeability and this enhancement is more noticeable up to Da around 10^{-2}, where the heat transfer rate tends towards a constant value due to the disappearance of the porous medium effect.

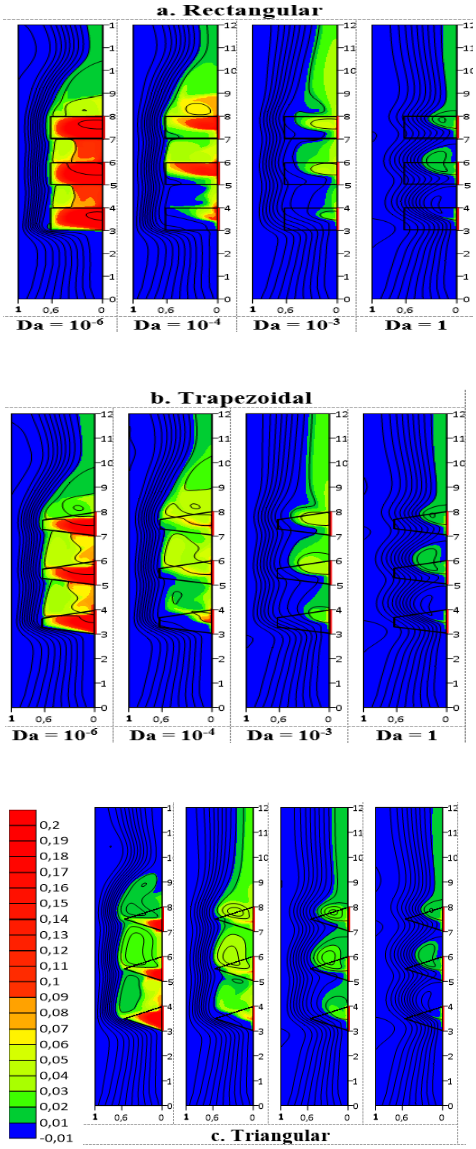

Figure 2. Evolution of Nu_g and fm with D_a for different blocks shapes : $R_i = 1$ and $M_n = 30$.

In comparison to the other two shapes, the triangular shape with low flow resistance produces the maximum heat transfer rate. By increasing the Darcy number, the difference is reduced, and the Nu_g values tend to be almost similar. This improvement in heat transfer, in respect to the Darcy number and the porous blocks shape, is accompanied by a decrease of the mean friction coefficient as it appears in Fig. 3b.

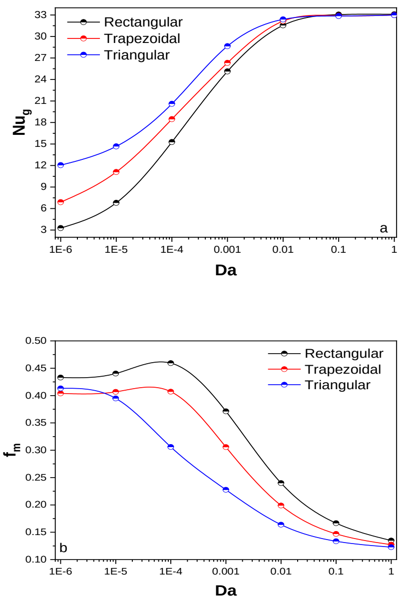

Figure 3. Evolution of Nug and fm with Da for different blocks shapes: $R_i = 1$ and $M_n = 30$.

The analysis of the combined effect D_a-M_n, depicted in Fig. 4, reveals a similar behavior regardless of the magnetic field strength. However, at low Darcy numbers, the Nu_g values are nearly identical due to the negligible influence of the magnetic field. As D_a increases, the impact of the magnetic number becomes more important and the porous medium effect disappears at progressively lower permeabilities. Thus at $M_n = 15$, the effect of the porous medium on the global Nusselt number persists until $D_a = 1$, while at $M_n = 50$, its effect disappears from $D_a = 10^{-2}$.

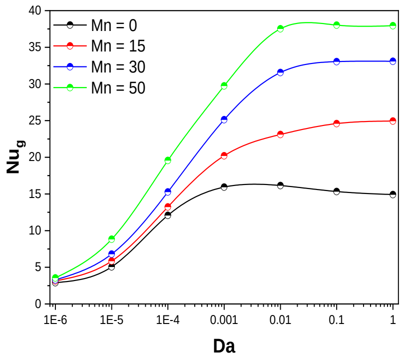

Figure 4. Evolution of Nug with Da for the rectangular shape and different values of M_n at $R_i = 1$.

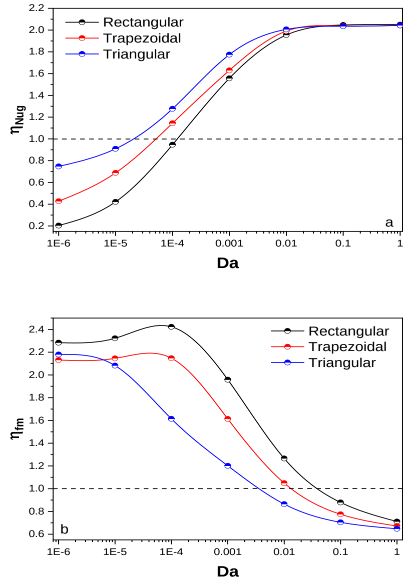

Figure 5. Evolution of η_{Nug} and η_{fm} with D_a for different blocks shapes: R_i = 1 and M_n = 30.

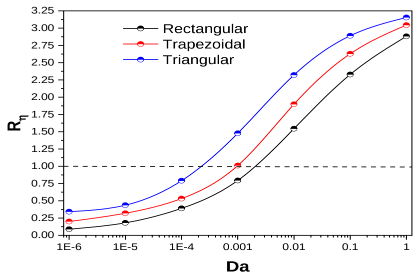

Figure 6. Evolution of Rη with Da for different blocks shapes: Ri = 1 and Mn = 30.

Fig. 5 reveals that the reference system is the most efficient at low porous medium permeabilities, and it is surpassed from a Darcy number that decreases with the block volume reduction. From the thermal point of view, the magnetic field - block shapes combination becomes attractive from $D_a \approx 2\times10^{-5}$, 5×10^{-5}, and 1.5×10^{-4} for the triangular, trapezoidal, and rectangular shapes, respectively. From the pressure drop viewpoint, these Darcy numbers are shifted to 3.5×10^{-3}, 1.5×10^{-2}, and 3.5×10^{-2}. The highest gains in heat transfer and mean friction coefficient are about 105% and 35% respectively.

Fig. 6, depicting the evolution of the performance factor with D_a, indicates that combining different techniques to improve the performance of the physical system under consideration is advantageous from a Darcy number of about 10^{-3}. The maximum R_η value, around 2.03, is obtained from $D_a = 10^{-2}$ whatever the shape of the blocks.

V. Conclusion

FHD mixed convection flow of (Fe_3O_4-water) ferrofluid inside a vertical channel containing variously shaped heated porous blocks has been numerically investigated. The key findings are as follows:

- The impact study of the blocks shape clearly shows that the triangular blocks are the most efficient from a dynamic and thermal viewpoint, since they have the lowest flow resistance at each permeability.
- The increase of Da, allowing a better penetration of the fluid in the porous medium
- The simultaneous employment of porous medium of various shapes, the permeability of porous blocks and magnetic field to improve the thermal-hydraulic performance of some industrial thermal systems seems promising. However, the control parameters must be carefully chosen to optimize the heat transfer while limiting pressure losses.

References

[1] Ghasemian, M., Ashrafi, Z. N., Goharkhah, M., & Ashjaee, M. (2015). Heat transfer characteristics of Fe3O4 ferrofluid flowing in a mini channel under constant and alternating magnetic fields. *Journal of Magnetism and Magnetic Materials*, *381*, 158-167.

[2] Larimi, M. M., Ghanaat, A., Ramiar, A., & Ranjbar, A. A. (2016). Forced convection heat transfer in a channel under the influence of various non-uniform transverse magnetic field arrangements. *International Journal of Mechanical Sciences*, *118*, 101-112.

[3] Ghorbani, B., Ebrahimi, S., & Vijayaraghavan, K. (2018). CFD modeling and sensitivity analysis of heat transfer enhancement of a ferrofluid flow in the presence of a magnetic field. *International Journal of Heat and Mass Transfer*, *127*, 544-552.

[4] Shah, R. K., & Khandekar, S. (2019). Exploring ferrofluids for heat transfer augmentation. *Journal of Magnetism and Magnetic Materials*, *475*, 389-400.

[5] Aly, A. M., & Ahmed, S. E. (2020). ISPH simulations for a variable magneto-convective flow of a ferrofluid in a closed space includes open circular pipes. *International Communications in Heat and Mass Transfer*, *110*, 104412.

[6] Mehrez, Z., & El Cafsi, A. (2021). Heat exchange enhancement of ferrofluid flow into rectangular

channel in the presence of a magnetic field. *Applied Mathematics and Computation*, *391*, 125634.

[7] Ganguly, R., Sen, S., & Puri, I. K. (2004). Heat transfer augmentation using a magnetic fluid under the influence of a line dipole. *Journal of Magnetism and Magnetic Materials*, *271*(1), 63-73.

[8] Sheikholeslami, M., & Ganji, D. D. (2014). Ferrohydrodynamic and magnetohydrodynamic effects on ferrofluid flow and convective heat transfer. *Energy*, *75*, 400-410.

[9] Gibanov, N. S., Sheremet, M. A., Oztop, H. F., & Nusier, O. K. (2017). Convective heat transfer of ferrofluid in a lid-driven cavity with a heat-conducting solid backward step under the effect of a variable magnetic field. *Numerical Heat Transfer, Part A: Applications*, *72*(1), 54-67.

[10] Mejni, F., & Ouarzazi, M. N. (2009). Global instabilities in inhomogeneous mixed convection flows in semi-infinite porous media. *Mechanics Research Communications*, *36*(2), 260-264.

[11] Pal, D., & Talukdar, B. (2011). Combined effects of Joule heating and chemical reaction on unsteady magnetohydrodynamic mixed convection of a viscous dissipating fluid over a vertical plate in porous media with thermal radiation. *Mathematical and Computer Modelling*, *54*(11-12), 3016-3036.

[12] Alves, L. D. B., Barletta, A., Hirata, S., & Ouarzazi, M. N. (2014). Effects of viscous dissipation on the convective instability of viscoelastic mixed convection flows in porous media. *International Journal of Heat and Mass Transfer*, *70*, 586-598.

[13] Chakkingal, M., de Geus, J., Kenjereš, S., Ataei-Dadavi, I., Tummers, M. J., & Kleijn, C. R. (2020). Assisting and opposing mixed convection with conjugate heat transfer in a differentially heated cavity filled with coarse-grained porous media. *International Communications in Heat and Mass Transfer*, *111*, 104457.

[14] Yerramalle, V., Premachandran, B., & Talukdar, P. (2021). Mixed convection from a heat source in a channel with a porous insert: A numerical analysis based on local thermal non-equilibrium model. *Thermal Science and Engineering Progress*, *25*, 101010.

[15] Bondarenko, D. S., Sheremet, M. A., Oztop, H. F., & Abu-Hamdeh, N. (2019). Mixed convection heat transfer of a nanofluid in a lid-driven enclosure with two adherent porous blocks. *Journal of Thermal Analysis and Calorimetry*, *135*, 1095-1105.

[16] Ali, F. H., Hamzah, H. K., Hussein, A. K., Jabbar, M. Y., & Talebizadehsardari, P. (2020). MHD mixed convection due to a rotating circular cylinder in a trapezoidal enclosure filled with a nanofluid saturated with a porous media. *International Journal of Mechanical Sciences*, *181*, 105688.

[17] Corcione, M. (2011). Empirical correlating equations for predicting the effective thermal conductivity and dynamic viscosity of nanofluids. *Energy conversion and management*, *52*(1), 789-793.

Quantification and Characterization of Cotton Residues as Fuel: The Case of Cukurova

İbrahim Halil Yılmaz[1]

[1]Mechanical Engineering Department, Adana Alparslan Turkes Science and Technology University, Adana, Turkey

Abstract—**Cotton is one of the products having an important place in agriculture, industry, and trade sectors in the world with its different usage areas. The Cukurova region is located in southern Turkey where 15.0−20.7% of Turkish cotton was produced according to the 2017−2021 data of the Turkish Statistical Institute. After harvesting cotton fields, agricultural residues of cotton are not effectively evaluated but could be the primary feedstocks for generating fuel and electricity from bioenergy. This research presents the biomass fuel properties of cotton stalks collected from agricultural activities in the Cukurova region since biomass fuel resources are extremely heterogeneous and variable and the determination of fuel properties and the results of quantity/quality manipulations is essential for planning such as waste transportation, plant capacity and control purposes, particularly direct combustion processes of highly engineered bioenergy power plants. For this reason, proximate analysis, ultimate analysis, anions, ash minerals, alkali metal concentration, and ash fusion temperatures were performed according to ISO and ASTM standards to determine the compatibility of the residue to a combustor system and its co-combustion with another residue. Results indicate that the fuel and ash contents of the residues are appropriate for various combustion processes however transportation of cotton stalks would be costly due to the high moisture content (~40%), relatively low ash content (~2%) and calorific value (~2500 kcal/kg) thus the optimum distance should be considered for the quantification and qualification of a biomass power plant.**

Keywords - cotton residues, biomass, fuel properties, direct combustion, Cukurova region

I. INTRODUCTION

Biomass is a carbon-neutral source and used as a heating material since ancient times. Nowadays, it is used in modern technologies as fuel or fuel-deriving entities [1]. Turkey is one of the largest cotton-planting countries [2]. The Cukurova region shown in Fig. 1 is located in southern Turkey where 15.0−20.7% of Turkish cotton is produced according to the 2017−2021 data. The region covers the provinces of Adana, Mersin, Osmaniye, and Hatay. These provinces have both growing agricultural and industrial activities and thus seek alternative ways like biomass to fulfill their energy deficit. However, cotton residues are not effectively evaluated to produce biofuel or electricity.

Predicting cotton availability is an important issue for the quantification of biomass potential [4]. Biomass is an alternative to other conventional energy sources in Turkey [5] and has the potential to be replaced fossil fuels in terms of environmental issues [6]. Reference [7] estimated that Turkey's available agricultural residual potential was 142.4 mton/yr and this potential corresponds to ~15.9 mTPE.

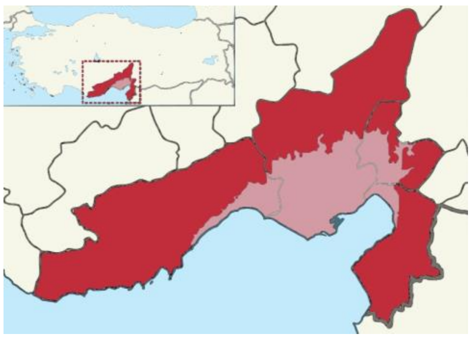

Figure 1. The Cukurova region [3].

Reference [8] estimated the theoretical energy values of the field and orchard residues as 908.119 TJ and 90.354 TJ, respectively for Turkey. Reference [9] provided an overview of the biomass energy potential in Turkey and estimated the usable bioenergy as ~17.2 mTPE.

Reference [10] estimated that the maximum available cotton stalk in Turkey was 4.41 mton/yr which corresponded to 75.62 PJ by 1999. Hepbasli et al. [11] estimated Turkey's total energy and exergy gain from cotton stalks as about 49,146 and 59,395 MJ/ha, respectively. On the other hand, some researchers evaluated the cotton stalk for different products like xylitol [12] and acetic acid [13].

According to the 2017−2021 data of the Turkish Statistical Institute, the average cotton production in Turkey is 4.43 mton/yr. The amount of cotton residue can theoretically double cotton production. This study aims to evaluate the quantification of cotton residue in Cukurova and its characteristics whether being used in direct combustion processes of highly engineered bioenergy power plants.

II. Material and Method

For the quantification of cotton feedstock, the statistics of the Turkish Statistical Institute were considered. For qualification, ISO and ASTM standards were performed to conduct proximate analysis, ultimate analysis, anions, ash minerals, alkali metal concentration, and ash fusion temperatures of the stalks collected from the Cukurova region to determine its compatibility with the biomass combustion systems.

III. Results and Discussion

Fig. 2 shows the cotton harvested in the provinces of Cukurova between 2017−2021. Hatay is the biggest producer among them but its production amounts have declined in recent years. Osmaniye makes the least contribution to the cotton production of the region. The average cotton production in Cukurova is 0.82 mton/yr. The available stalk derived from this production refers nearly to 1.63 mton/yr which is a good potential to recover it for bioenergy plants.

The proximate analysis is the simplest analysis based on mass fractions. Table I gives the results of the as-received proximate analysis for cotton residues. The moisture content is high and can lead to ignition and combustion problems such as flame instability. On the other hand, it can increase transportation costs for long distances and thus needs route planning for optimum transport. Relatively low ash content and medium calorific value would make the residues feasible in using biomass power plants.

The ultimate analysis lists the mass fractions of elements. Table II shows the as-received ultimate analysis of cotton residues. As seen, only 28.56% of the composition can be converted into heat. On the other hand, this analysis is beneficial to determine air requirements for combustion, in turn, to size the draft systems and calculate the emissions to the environment after burning the residuals.

Inorganic components in biomass have a direct effect on the formation of slag deposits, corrosion of boiler components, aerosol formation, and ash utilization. Table III gives the ash minerals present in the ash. The molar ratios of the chlorine and sulfur to alkali (Na and K given in Table IV) in the deposits indicate that the majority of the deposit alkali does not occur as chloride or sulfate, but presumably as a silicate [14].

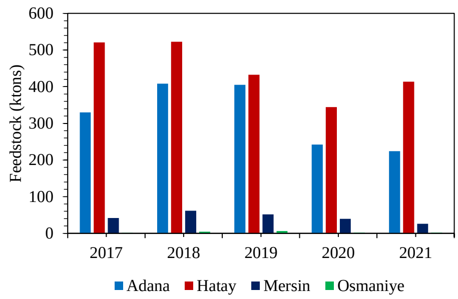

Figure 2. Cotton production in Cukurova by years.

TABLE I. PROXIMATE ANALYSIS.

Analysis	Result	Test method
Moisture	41.49%	ISO 589
Ash	2.08%	ISO 1171
Volatile matter	43.96%	ISO 562
Fixed carbon	12.46%	ASTM D 3172
Gross cal. value	2595 kcal/kg	ISO 1928
Net cal. value	2206 kcal/kg	ISO 1928

TABLE II. ULTIMATE ANALYSIS.

Analysis	Result	Test method
C	25.31%	ASTM D 5373
H	3.14%	ASTM D 5373
N	0.67%	ASTM D 5373
S	0.11%	ASTM D 4239
O	27.20%	ASTM D 3176
C	25.31%	ASTM D 5373

The most critical parameter is the ratio of sulfur to chlorine or, more specifically, to the maximum amount of Cl in the fuel. The ratio of 2×S/(max available alkali, available Cl) should be greater than 2 to reduce corrosion potential and avoid significant deposit Cl levels. As seen, the ratio is below 2 thus the most widely used combustion technology of reciprocating grate is not suitable for the residues. Fluidized bed combustion technology is more appropriate and can provide co-combustion with other biomass residues but the size of the particles should be lower than 10 mm.

Ash fusion is applied to rank the ash in terms of its propensity to form fused slag deposits and is widely used in the industry for fuel specification, combustion equipment design, and plant operational purposes. Table V lists the ash fusion temperatures for the residue. A reduction in fusion temperature results in a higher potential of furnace slag otherwise the heat transfer performance in the convective section of boiler tube bundles lowers with increasing fouling over time due to high silica/high potassium/low calcium ashes [15]. One of the key factors is to manage the flue gas temperature and avoid excessive slag formation.

TABLE III. ASH MINERALS.

Analysis	Result	Test method
CaO	33.65%	ASTM D 4326
K_2O	28.52%	
MgO	10.60%	
SiO_2	6.71%	
Na_2O	4.70%	
SO_3	4.63%	
Cl	4.15%	
Al_2O_3	2.60%	
P_2O_5	2.51%	
Fe_2O_3	1.38%	
Others	<0.55%	

TABLE IV. ALKALI METAL CONCENTRATION.

Analysis	Result	Test method
Na	0.124%	ASTM D 4326
K	0.843%	

TABLE V. ASH FUSION TEMPERATURE.

Analysis	Result	Test method
Deformation	1407 °C	ASTM D 1857
Sphere	1439 °C	
Hemisphere	1468 °C	
Flow	1479 °C	

This study reveals that quantification and characterization of a biomass residue are important for both determining the boiler capacity and boiler properties. Based on the analysis performed, cotton residues in Cukurova can be evaluated for energy recovery but many challenges are available which can be minimized by making proper decisions. Otherwise, some combustion problems would occur during the operation of the plant.

IV. CONCLUSION

Waste valorization and resource recovery are two important subjects for energy alternative policy and circular economy [16]. These are the motivations of this study where laboratory analyses were performed using cotton straws to examine their technological suitability for conventional combustion systems and possible problems. These analyses are essential for characterizing the combustion system design and the control of particle collection efficiency. Since biomass power plants operate for more than 25 years, possible issues should be determined before installation. The interactions between the alkali Cl and the sulfur might reduce the stickiness of the fly ash and deposit material thus careful considerations for fuel properties must be taken.

ACKNOWLEDGMENT

The author is thankful to Bemka Energy Inc. for supporting this research.

REFERENCES

[1] Yılmaz, İ. H., & Abdulvahitoğlu, A. (2019). Evaluation of municipal solid waste options in Turkey: Scenarios for energy recovery, carbon mitigation and consequent financial strategies. *Resources, Conservation and Recycling, 147*, 95-110.

[2] Hamawand, I., Sandell, G., Pittaway, P., Chakrabarty, S., Yusaf, T., Chen, G., ... & Hopf, J. (2016). Bioenergy from cotton industry wastes: A review and potential. *Renewable and Sustainable Energy Reviews, 66*, 435-448.

[3] The Wikipedia website. (2022). *Çukurova*. Available at: https://en.wikipedia.org/wiki/%C3%87ukurova.

[4] Wanjura, J. D., Barnes, E. M., Kelley, M. S., Holt, G. A., & Pelletier, M. G. (2014). Quantification and characterization of cotton crop biomass residue. *Industrial Crops and Products*, *56*, 94-104.

[5] Yılmaz, İ. H., & Saka, K. (2018). Exploitable biomass status and potential of the Southeastern Anatolia Region, Turkey. *Energy Sources, Part B: Economics, Planning, and Policy, 13*(1), 46-52.

[6] Bilgen, S., Keleş, S., Sarıkaya, İ., & Kaygusuz, K. (2015). A perspective for potential and technology of bioenergy in Turkey: present case and future view.

Renewable and Sustainable Energy Reviews, *48*, 228-239.

[7] Saka, K., & Yılmaz, İ. H. (2017). Agricultural biomass potential in Turkey. *International Journal of Management and Applied Science*, *3*(2), 79-81.

[8] Avcıoğlu, A. O., Dayıoğlu, M. A., & Türker, U. (2019). Assessment of the energy potential of agricultural biomass residues in Turkey. *Renewable Energy*, *138*, 610-619.

[9] Guresci, E. (2020). A general view of the biomass energy potential and its use in Turkey. *Proceedings of the Institution of Civil Engineers-Energy*, *173*(4), 141-149.

[10] Akdeniz, R. C., Acaroglu, M., & Hepbasli, A. (2004). Cotton stalk as a potential energy source. *Energy Sources*, *26*(1), 65-75.

[11] Hepbasli, A., Utlu, Z., & Akdeniz, R. C. (2007). Energetic and exergetic aspects of cotton stalk production in establishing energy policies. *Energy Policy*, *35*(5), 3015-3024.

[12] Sapcı, B., Akpinar, O., Bolukbasi, U., & Yilmaz, L. (2016). Evaluation of cotton stalk hydrolysate for xylitol production. *Preparative Biochemistry and Biotechnology*, *46*(5), 474-482.

[13] Sayar, N. A., Kazan, D., Pinar, O., Akbulut, B. S., & Sayar, A. A. (2018). Retro-techno-economic evaluation of acetic acid production using cotton stalk as feedstock. *Journal of Material Cycles and Waste Management*, *20*(4), 2077-2088.

[14] Robinson, A. L., Junker, H., & Baxter, L. L. (2002). Pilot-scale investigation of the influence of coal−biomass cofiring on ash deposition. *Energy & Fuels*, *16*(2), 343-355.

[15] Koppejan, J., & van Loo, S. (1st Ed.). (2008). *The handbook of biomass combustion and co-firing*. Earthscan.

[16] Kale, M., Yılmaz, İ. H., Kaya, A., Çetin, A. E., & Söylemez, M. S. (2022). Pilot-scale hydrogen generation from the hydrolysis of black aluminum dross without any catalyst. *Journal of the Energy Institute*, *100*, 99-108.

Life Cycle Assessment in Breweries – A Systematic Review

Daniel de Paula Diniz[1], Monica Carvalho[2]

[1]Graduate Program in Mechanical Engineering, Federal University of Paraiba, João Pessoa, Brazil

[2]Departament of Renewable Energy Engineering, Federal University of Paraiba, João Pessoa, Brazil

Abstract—**The beer market is one of the fastest-growing industrial sectors in Brazil and the world. Making all this production sustainable is very well seen by society, and breweries are adapting to this proposal. Quantifying emissions is very important to achieve the objective of cleaner industrial production. The Life Cycle Assessment (LCA) is an internationally recognized and standardized tool for this purpose. This review focuses on the application of LCA in the international beer market. Studies were selected from two databases, Web of Science (WoS) and Scopus, encompassing 1999-2022. Comparing the results of the studies is a complex task, as each study used specific tools, different software, and databases. There has been an increase in the keywords employed and the number of studies published recently.**

Keywords – beer, LCA, bibliometric review

I. Introduction

China, United States, Brazil, Mexico, and Germany: At first glance, this eclectic group of countries may seem to have little in common, but on closer inspection, one element stands out: beer. They are the five largest beer producers in the world [1]. In 2020, global beer production reached 1.82 billion hectoliters, and the five largest producers reached 930 x 10^6 hL [1].

The craft beer market is also growing: in the United States, there was an expansion of 8% in the volume produced between 2020 and 2021, reaching 124,000 hL of craft beer [2]. The Brazilian market follows this increasing trend, and despite the Covid-19 pandemic, at the end of 2020, Brazil counted with 1,383 breweries registered with the Ministry of Agriculture, Livestock, and Supply [3].

Beer production has an intensive use of energy, both thermal and electrical, as several processes are energy-intensive with long execution times [4]. This intensive energy use brings a significant environmental impact that must be quantified.

LCA is a powerful tool for this purpose, as it is a methodology for assessing and determining inputs, outputs, and potential environmental impacts throughout the life cycle of a product, process, or activity [5]. LCA can evaluate systems performance and its effects on the life cycle phases, identifying improvement opportunities [6]. Depending on the scope of the study, LCA can take into account the extraction of raw materials, manufacture, transportation, operation or use, and final disposal. LCA has different applications [7]: to help develop products and processes with fewer environmental impacts, promote improvements in the ecological aspects of products and processes, and even for benchmarking purposes.

LCA was initially standardized in 1997 by the International Organization for Standardization (ISO) [8]. The standards were reviewed in 2006, yielding ISO 14040 [9] and ISO 14044 [10]. In Brazil, the standards were translated by the Brazilian Association of Technical Standards (ABNT) into NBR 14040 [11] and NBR 14044 [12].

This study aims to carry out a systematic literature review (SLR) based on indexed studies (Scopus and Web of Science) on the application of LCA in the global beer market. The overarching aim is to understand the importance of quantifying the environmental impacts associated with this industrial sector.

II. METHODOLOGY

In this study, two methodologies were used, one of a bibliometric nature and the other of a systematic nature.

Bibliometrics is defined as all studies that attempt to quantify the processes of written communication [13]. Therefore, the bibliometric review can be applied to different areas of knowledge, being an application of statistics to the bibliography. The literature review is conducted according to the steps: (i) definition of the research scope, (ii) choice of the research question, (iii) identification of relevant studies, (iv) selection of studies, (v) data processing and (vi) analysis of results.

An SLR is used to identify, evaluate and interpret available and relevant studies on a specific research question [14].

The first stage of an SRL is the exploratory stage, when research is planned. The second stage is the development stage, when the review is conducted. The third stage is the analysis stage, when the research report is disclosed.

In the first stage, the question related to the objective of this research was defined: "*What are the characteristics, amplitude, and results of the research conducted on Life Cycle Assessment in the brewing industry?*". Based on this question, the study object was defined, exploring how LCA has been approached and analyzed in the brewing industry. This preliminary study is significant as it evaluates the relevance of the research question and delimits the study area and research platforms to be chosen [15]. The main words used in the studies were identified, later used to define the search strings.

In the second stage, the portfolio was defined as a detailed description of the research procedure (this guarantees the method can be replicated). It was based on the preparation of search strings delimited by the study topic [16].

The Web of Science (WOS) and Scopus databases were selected for this research, two of the most relevant academic literature databases in the academic field [17]. Besides being the most prestigious databases, they also cover a wide range of indexed journals, encompassed by the Journal Citation Report (JCR) [17]. The databases include tools that automatically analyze their information and process the initial samples and their references, enabling accurate analysis of the data obtained in their databases.

Works published until May 2022 were included, without setting an initial date in the search, to obtain the highest possible number of relevant studies.

The search was carried out in English and used the *title, abstract, and keywords* research fields. The following keywords were used: "Life Cycle Assessment", "Life Cycle Analysis", "LCA", "Carbon Footprint", "Beer", "Brewing", "Brewery".

The final search string was: (TITLE-ABS-KEY ("life cycle assessment" OR "life cycle analysis" OR "lca" OR "carbon footprint") AND TITLE-ABS-KEY ("beer" OR "brewery " OR "brewing")).

Initial analyses focused on establishing a relationship between the research theme and the titles, abstracts, and keywords selected [15,18].

Inclusion and exclusion criteria included research studies (papers) and review studies and excluded any other type of document.

As the research was carried out in two different databases, it was expected to find repeated studies, which were eliminated.

Then the titles and abstracts were read, including the studies related to the theme, even if in a general way. Finally, the selected studies were fully read, including in the final sample those studies that applied or focused on LCA within the brewing industry.

III. RESULTS AND DISCUSSION

First, 230 papers were found, 102 on the Scopus platform and 128 on WoS. The first selection criterion was the type of work, including articles and review articles and excluding any other type of work. At this stage, 23 papers were excluded, leaving 207 for the next phase. As the research was carried out on two platforms, the next criterion was the exclusion of works published on both platforms. Here, 41 works were excluded, leaving 166 for the next phase. The next inclusion criterion was the relationship with the theme by reading the title and abstract. Here, 96 papers were excluded, leaving 70 for the next criterion. The last criterion was to find the relationship with the topic of application of LCA concepts in breweries with the complete reading of the articles that passed the previous criterion. In the end, 46 articles were excluded, leaving this systematic review with 24 works to analyze.

A. *Bibliometric Analysis*

The sample was divided into four periods (1999-2005, 2006-2011, 2012-2017, 2018-2022) for better visualization. Fig. 1 shows the number of publications throughout time.

After a decline in the second period (2006-2011) with only one published study, the following two periods showed an increase in the number of studies, with 17 published works on LCA in breweries.

Although the first LCA on the beer production process was carried out in 2001 [4], the first paper was published in 1999 [19], focusing on beer packaging.

Of the 24 published studies, six were published in the International Journal of Life Cycle Assessment. Two studies were published in the Journal of Cleaner Production. The remaining 16 studies were published in different journals.

The development of keywords in the four analyzed periods is shown in Fig. 2. The numbers inside the rectangles show the number of keywords used in the period. The ascending arrows indicate the number of keywords that are not used in the following time period. Descending arrows indicate the number of new keywords that were introduced in the period. The horizontal arrows indicate the number of keywords that are used again in the next period.

Fig.2 shows an increase in the number of keywords, mainly in the last two periods, demonstrating the process of formation of the research line, incorporating a high number of keywords.

Fig. 3 demonstrates the interactions of the keywords divided into the four periods studied. The Jaccard index generated a thematic evolution of research related to LCA and Breweries [20]. This index develops relationships between the themes, which can be a conceptual connection (solid line) or a non-conceptual connection based on keywords, demonstrated in the figure by the dashed lines. Line thicknesses indicate the number of overlapping keywords or themes.

Analysis of Fig. 3 indicates a growth in the number of keywords used in the studies during the periods studied and that there are many links between them, especially in the last two periods.

B. *Systematic Analysis*

Of the 24 studies identified herein, 11 focused on large multinational brewing organizations [4], [19], [21-29].

Eleven studies focused on small companies [30-40]. These studies were motivated by the growth of the craft beer market and with the simpler access to data necessary for research.

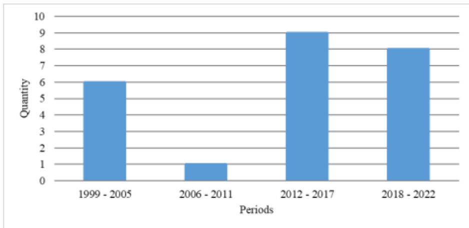

Figure 1. Number of publications per period.

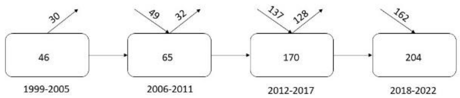

Figure 2. Development of keywords through time.

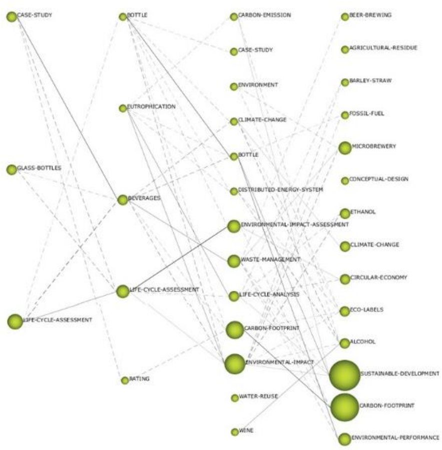

Figure 3. Thematic evolution of research related to LCA and breweries.

Two comparison studies were also identified, which compared different size breweries, seeking to understand how the size of the company influences its environmental impacts [41,42].

The scope of most studies was the beer brewing process, with 18 studies. Two studies verified the packaging stage, and the remainder covered other aspects such as energy, land use, by-products, and a comparison between beer and wine.

The first two studies involving LCA and breweries compared returnable and non-returnable beer bottles [19,24]. The authors conclude that regarding the distribution of beer in returnable and non-returnable bottles, it is necessary to analyze the environmental and economic, technological, and social aspects.

The first study of the LCA of breweries, focusing on beer production, was carried out in Estonia [4]. This pioneering study adapted the software and the KCL-ECO database, initially prepared for the timber industry.

In Greece, [22] studied LCA in breweries and found the manufacture of packaging as the most significant environmental impact.

An LCA study regarding the grain supply for three different products (barley for beer, wheat for bread, and canola for cooking oil) was carried out by [37]. It was verified that the grain supply for brewing beer had the highest environmental impact, and canola oil production had the lowest impact.

In another study developed in a brewery in Galicia, Spain [28], production and transport of raw materials and packaging presented the highest impacts and should be considered in further actions to reduce the effects of the brewery [28].

For a Lager-style beer in an Italian microbrewery, an LCA study was conducted investigating two packaging options: 20-liter returnable stainless steel kegs and 330 mL non-returnable bottles. The analysis identified the relevance of the consumption phase and the choice of packaging in the life cycle. It also showed that beer producers and consumers are active and responsible actors in pursuing the goal of environmental sustainability [35].

In 2011 [21] investigated land use indicators in life cycle assessment, using beer production in Finland as a case study. The interpretation of the results was hindered due to the limited understanding of the environmental impacts of land use. Another work by the same author [29] explored the uncertainty in consumer decision-making regarding the decision to drink wine or beer. After applying the LCA concepts to the two beverages, the carbon footprint of beer was higher but with a negligible difference.

In one of the few studies carried out in Latin America, a carbon footprint analysis was carried out in a microbrewery in Chile [40]. The authors used as a case study four styles of beer (Ale, Bock, Lager, and Weizen), all packaged in 330 mL bottles. They concluded that a 5-10% decrease in bottle weight could reduce the carbon footprint of beers by about 5%.

Regarding beer production in China [23], a series of indicators were studied: Global Warming Potential (GWP), Acidification Potential (AP), Eutrophication Potential (EP), Abiotic Depletion Potential (ADP), Human Toxicity Potential (HTP), and Photochemical Ozone Creation Potential (POCP). The results indicated that the GWP was the highest contributor to the overall environmental impact in producing Chinese beer, corresponding to 43.75% of the potential environmental effects.

In an Italian microbrewery [30], a survey was carried out on the direct and indirect greenhouse gas (GHG) emissions of three high-fermentation and three low-fermentation beer production processes and packaging systems (0.33cL and 0.75cL glass bottles) [30]. Emissions related to the production plant management were considered, such as lighting, electricity, employee mobility, and waste treatment. Ultimately, 57% of total GHG emissions were related to direct emissions from plant management.

In a comparative study between different beer packages, [31] evaluated the environmental impacts of the production and distribution of 1hL of a Lager-style beer. Several packaging types were compared: 660mL glass bottles, 330mL glass bottles wrapped in cardboard or cluster packaging, 330mL aluminum cans, and 30-liter stainless steel kegs. Due to the high reuse rate, the 30-liter steel barrel had the lowest carbon footprint, and the 330 ml glass bottles with cardboard packaging had the most significant environmental impact.

In an LCA focused on the industrial stages of production, two beer styles were compared: Ale (high fermentation) and Lager (low fermentation). The boiling and hopping of Ale beer produced a more significant environmental impact than Lager beer, but Lager fermentation presented higher impacts [36].

When assessing the life cycle environmental impacts and the costs of producing and consuming beer in the UK, [25] found that beer packaged in steel cans had the lowest environmental impacts in five of the 12 impact categories considered in the study. Beer in glass bottles was the worst option in nine of the 12 categories studied.

Nine breweries were studied by [41] to understand the effects of brewery size on the carbon footprint of the brewing processes. The carbon footprint increased by 45% when comparing the largest brewery ($10x10^6$hL/year) with the smallest brewery (500hL/year). Regardless of the size of the brewery, the use of PET (polyethylene terephthalate) bottles instead of glass bottles reduced the carbon footprint by about 2.7%.

In Romania, [26] conducted an LCA study at a local brewery. It was concluded that PET bottles are more environmentally friendly than glass bottles. However, this changes if glass bottles are reused and PET bottles are recycled, incinerated, or landfilled.

An LCA was developed to explore options to mitigate the environmental impacts of the main hotspots of the production of 1hL of beer, in Italian breweries of different sizes and with beer packaged in different formats [42]. By progressively replacing virgin glass bottles with recycled glass or PET, road transport with rail, importing barley with locally grown barley, and traditional energy with solar, breweries can effectively reduce their carbon footprint.

The environmental impacts of waste management for a UK brewery were studied by [27]. Initially, three types of waste were identified: barley straw, malt waste, and used grains. Barley straw was chosen as the case study. Extracting the wax from the straw using supercritical CO_2 was identified with the highest impact due to the high energy requirements.

A study on the economic and environmental performance of an instantaneous water heating system for production processes in a craft brewery was carried out by [32]. The results showed that the investment in the water heating system was not economically profitable due to the current productivity of the microbrewery. But in the case of environmental impacts, the water heating system reduced the beer production's GWP by about 22.4%.

Reference [33] studied the environmental performance of different stabilization methods of brewer grains (dehydration, separation, lactofermentation, lyophilization, refrigeration, freezing, methanation, and use for animal feed) [33]. The results show the importance of strategic choices and provide trends and recommendations on parameters for the valuation of food by-products in the circular economy context.

In Brazil, [34] quantified the GHG emissions associated with the supply of thermal and electrical energy to a craft brewery [34]. The results indicate that photovoltaic electricity resulted in 66% fewer emissions per kWh consumed. In the case of thermal energy, the use of solar energy decreased by 95% the emissions, when compared to the use of fossil fuels.

Seven microbreweries participated in the study of craft beer production in Wales [38]. Beer distribution to the consumer has become a hotspot due to the inefficient use of light commercial vehicles for this purpose. Packaging was not as impactful because most production is distributed in reusable packaging or stainless steel barrels. Reference [39] studied the choice of packaging and the coordination of distribution logistics to reduce the environmental footprint of craft beer value chains. The results showed that breweries could achieve reductions in several environmental impact categories by adopting returnable bottles and aluminum cans. Additional reductions are possible if transportation is changed from small vans to trucks. PET kegs have not achieved satisfactory results when beer is delivered over short distances.

Methods Used. The most used method by the authors was ReCiPe [43]. ReCiPe was developed in 2008, and its main objective is to transform the life cycle inventory results into indicator scores that can express the relative severity of an impact category [43]. There are 18 midpoint indicators and three endpoint indicators. Each level contains factors according to three perspectives (Individualist, Hierarchical and Egalitarian). In the individualist perspective, the short term is considered, with optimism that technology will be able to avoid problems in the future. The hierarchist perspective is the consensus model often found in scientific studies. The egalitarian perspective considers the long term, based on the precautionary principle [43].

The second most used method was the IPCC (Intergovernmental Panel on Climate Change) method for GWP quantification [44]. This method groups GHG emitted into the atmosphere by anthropogenic action into a single equivalent gas, CO_2-eq.

The third most used method was PAS (Publicly Available Specification) 2050 [45], prepared by the BSI (British Standards), Carbon Trust, and the Department of Environment, Food and Rural Affairs (DEFRA). PAS 2050 groups GHGs into a common metric, CO_2-eq, to facilitate the interpretation of results.

Other methods, such as DAIA 1998, CML 2001, and IMPACT 2002, are no longer used.

Software. The most used software was Simapro [46], launched in 1990 by Pré Sustainability and has users in more than 80 countries.

The second most used software was GaBi [47], which also carries out LCC (Life Cycle Cost), LCR (Life Cycle Reports), and LCWE (Work Environment Life Cycle).

Other software employed include KCL-ECO, initially designed for LCA studies in wood and forest products [4]. OPEN –LCA is free and open-source software with high compatibility with current databases, including about 100,000 different datasets [48].

Databases. The most used database was Ecoinvent [49]. The first Ecoinvent database was published in 2003 through a cooperation between Swiss research institutes. The objective was to harmonize and update the various public LCA databases developed by different institutes in Switzerland, thus becoming one of the best-known databases in the world [50].

Other databases used by the authors are part of the software used for the calculations, such as the KCL-ECO and GaBi databases.

IV. CONCLUSION

The LCA methodology has been in the spotlight recently, with more than 40,000 works published in various lines of research. LCA has been consolidated as a tool to quantify several classes of environmental impacts, being an internationally recognized methodology. LCA can help demonstrate the environmental benefit of energy transition in various segments of society, such as the brewing industry.

In the brewing sector, the number of publications is high. Papers are mainly published in Europe, but the number of works carried out in the Americas, Asia, and Oceania is growing. There is still difficulty in comparing the results found in the published studies because the authors use different software and databases. Few works present the same methodologies that would accurately compare results.

ACKNOWLEDGMENT

The authors wish to thank FAPESQ (Foundation for the Support of Research in the state of Paraíba) for the Ph.D. scholarship and CNPQ (National Council for Scientific and Technological Development), productivity grant 309452/2021-0.

REFERENCES

[1] BarthHass. (2022). *The Industry Report of the Year 2022* Available at: https://www.barthhaas.com/en/campaign/barthhaas-report-2022

[2] Brewers Association. (2022). *Promoting Independent Craft Brewers.* Available at: www.brewersassociation.org

[3] Ministry of Agriculture, Livestock and Supply. (2022). Available at: https://www.gov.br/agricultura/pt-br

[4] Talve, S. (2001). Life cycle assessment of a basic lager beer. *The International Journal of Life Cycle Assessment, 6*(5), 293-298.

[5] Boulay, A. M., Bouchard, C., Bulle, C., Deschênes, L., & Margni, M. (2011). Categorizing water for LCA

inventory. *The International Journal of Life Cycle Assessment*, *16*(7), 639-651.

[6] Benetto, E., Nguyen, D., Lohmann, T., Schmitt, B., & Schosseler, P. (2009). Life cycle assessment of ecological sanitation system for small-scale wastewater treatment. *Science of the total environment*, *407*(5), 1506-1516..

[7] Monteiro, M. F. (2008). Avaliação do ciclo de vida do fertilizante superfosfato simples. *DEA (Departamento de Engenharia Ambiental)–UFBA Salvador*.

[8] de Sousa, M. N., da Rocha Geremia, A., & Rodrigues, L. J. (2018). Análise da Viabilidade Econômica e Dimensionamento de Sistemas de Aquecimento Solar de Água para o Processo de Mosturação de Cerveja. In *VII Congresso Brasileiro de Energia Solar-CBENS 2018*.

[9] International Organization For Standardization – ISO (2006) ISO 14040: Environmental management - Life cycle assessment - Principles and framework. Genebra.

[10] International Organization For Standardization – ISO (2006) ISO 14044: Environmental management - Life cycle assessment - Requirements and guidelines. Genebra.

[11] Brazilian Association of Technical Standards. (2014). Environmental Management. Life Cycle Assessment - Principles and structure: NBR ISO 14040. Rio de Janeiro

[12] Brazilian Association of Technical Standards. (2014) Environmental Management Life cycle assessment - Requirements and guidelines: NBR ISO 14044. Rio de Janeiro.

[13] Pritchard, A. (1969). Statistical bibliography or bibliometrics. *Journal of documentation*, *25*, 348.

[14] Kitchenham, B. (2004). Procedures for performing systematic reviews. *Keele, UK, Keele University*, *33*(2004), 1-26.

[15] Tranfield, D., Denyer, D., & Smart, P. (2003). Rumo a uma metodologia para desenvolver conhecimento de gestão baseado em evidências por meiode revisão sistemática. *British Journal of Management*, *14*(3), 207-222.

[16] Emodi, N. V., Chaiechi, T., & Beg, A. R. A. (2019). The impact of climate variability and change on the energy system: A systematic scoping review. *Science of the total environment*, *676*, 545-563.

[17] Wang, Q., & Waltman, L. (2016). Large-scale analysis of the accuracy of the journal classification systems of Web of Science and Scopus. *Journal of informetrics*, *10*(2), 347-364..

[18] Ensslin, L., Ensslin, S. R., Dutra, A., Nunes, N. A., & Reis, C. (2017). BPM governance: a literature analysis of performance evaluation. *Business Process Management Journal*..

[19] Mata, T. M., & Costa, C. A. (1999). LCA: Comparison Between Recycle and Reuse of Glass Beer Bottles. In *Tools and Methods for Pollution Prevention* . Springer, Dordrecht (pp. 85-96).

[20] Real, R., & Vargas, J. M. (1996). The probabilistic basis of Jaccard's index of similarity. *Systematic biology*, *45*(3), 380-385.

[21] Mattila, T., Helin, T., & Antikainen, R. (2012). Land use indicators in life cycle assessment. *The International Journal of Life Cycle Assessment*, *17*(3), 277-286.

[22] Koroneos, C., Roumbas, G., Gabari, Z., Papagiannidou, E., & Moussiopoulos, N. (2005). Life cycle assessment of beer production in Greece. *Journal of Cleaner Production*, *13*(4), 433-439.

[23] Yu, J., Zhang, Y., Zhang, S., & Li, J. (2015). Life cycle assessment of beer production *Huanjing Kexue Xuebao/Acta Scientiae Circumstantiae*, *35*(4), 1217-1223.

[24] Mata, T. M., & Costa, C. A. (2001). Life cycle assessment of different reuse percentages for glass beer bottles. *The International Journal of Life Cycle Assessment*, *6*(5), 307-319.

[25] Amienyo, D., & Azapagic, A. (2016). Life cycle environmental impacts and costs of beer production and consumption in the UK. *The International Journal of Life Cycle Assessment*, *21*(4), 492-509.

[26] Ghinea, C., & Leahu, A. (2017). Life cycle environmental impacts of Romanian beer production. In *International Multidisciplinary Scientific GeoConference: SGEM*, *17*, (pp. 115-122).

[27] Garcia-Garcia, G., & Rahimifard, S. (2019). Life-cycle environmental impacts of barley straw valorisation. *Resources, Conservation and Recycling*, *149*, 1-11.

[28] Hospido, A., Moreira, M. T., & Feijoo, G. (2005). Environmental analysis of beer production. *International journal of agricultural resources, governance and ecology*, *4*(2), 152-162.

[29] Mattila, T., Leskinen, P., Soimakallio, S., & Sironen, S. (2012). Uncertainty in environmentally conscious decision making: beer or wine?. *The International Journal of Life Cycle Assessment*, *17*(6), 696-705.

[30] Masotti, P., Campisi, B., & Bogoni, P. (2016). Carbon footprint evaluation of an Italian microbrewery. *Procedia Environmental Science, Engineering and Management*, *3*(3-4), 119-127.

[31] Cimini, A., & Moresi, M. (2016). Carbon footprint of a pale lager packed in different formats: assessment and sensitivity analysis based on transparent data. *Journal of Cleaner Production*, *112*, 4196-4213.

[32] San Martín-González, M. F., Cai, H., & Huang, J. Y. (2021). Economic and environmental performance of instantaneous water heating system for craft beer production. *Food and Bioproducts Processing*, *127*, 472-481.

[33] Petit, G., Korbel, E., Jury, V., Aider, M., Rousselière, S., Audebrand, L. K., ... & Mikhaylin, S. (2020). Environmental evaluation of new brewer's spent grain preservation pathways for further valorization in human nutrition. *ACS Sustainable Chemistry & Engineering*, *8*(47), 17335-17344.

[34] de Paula Diniz, D., Carvalho, M., & Abrahao, R. (2021). Greenhouse gas accounting for the energy transition in a brewery. *Environmental Progress & Sustainable Energy*, *40*(2), e13563.

[35] Cordella, M., Tugnoli, A., Spadoni, G., Santarelli, F., & Zangrando, T. (2008). LCA of an Italian lager beer. *The International Journal of Life Cycle Assessment*, *13*(2), 133-139.

[36] De Marco, I., Miranda, S., Riemma, S., & Iannone, R. (2016). Life cycle assessment of ale and lager beers

production. *Chemical Engineering Transactions*, *49*, 337-342.

[37] Narayanaswamy, V., Altham, W., Van Berkel, R., & McGregor, M. (2005, February). Application of life cycle assessment to enhance eco-efficiency of grains supply chains. In *Proc. Aust. Conf. on Life Cycle Assessment, 4th, Sydney, Australia* (pp. 23-25).

[38] Morgan, D. R., Styles, D., & Lane, E. T. (2021). Thirsty work: Assessing the environmental footprint of craft beer. *Sustainable Production and Consumption*, *27*, 242-253.

[39] Morgan, D. R., Styles, D., & Lane, E. T. (2022). Packaging choice and coordinated distribution logistics to reduce the environmental footprint of small-scale beer value chains. *Journal of Environmental Management*, *307*, 114591.

[40] Muñoz, E.; Riquelme, C.; Cardenas, J.P. (2012). Carbon footprint of beer – Analysis of a small-scale processing plant in Chile. *Proceedings 2nd LCA Conference.* Lille France.

[41] Cimini, A., & Moresi, M. (2018). Effect of brewery size on the main process parameters and cradle- to-grave carbon footprint of lager beer. *Journal of Industrial Ecology*, *22*(5), 1139-1155.

[42] Cimini, A., & Moresi, M. (2018). Mitigation measures to minimize the cradle-to-grave beer carbon footprint as related to the brewery size and primary packaging materials. *Journal of Food Engineering*, *236*, 1-8.

[43] Pre-Sustainability. (2022) *ReCiPe Method*. Available at: https://pre-sustainability.com/articles/recipe/

[44] Intergovernmental Panel on Climate Change. (2022) Available at: https://www.ipcc.ch/

[45] PAS2050. (2008) *PAS 2050 Method*. Available at: https://aggie-horticulture.tamu.edu/faculty/hall/publications/PAS2050_Guide.pdf

[46] Simapro. (2022). *Simapro Software*. Available at: https://simapro.com/

[47] Sphera. (2022) *GaBi Software*. Available at: https://gabi.sphera.com/international/

[48] OpenLCA. (2022). *OpenLCA Software*. Available at https://www.openlca.org/

[49] Ecoinvent. (2022). *Ecoinvent Database*. Available at https://ecoinvent.org/

[50] Takano, A., Winter, S., Hughes, M., & Linkosalmi, L. (2014). Comparison of life cycle assessment databases: A case study on building assessment. *Building and Environment*, *79*, 20-30.

New Technologies of Optical Telecommunications and Their Application in Electro Power Systems

Slađana Pantelić[1], Saša Milić[2], Alekandar Ilić[3]

[1,2,3]Faculty of Diplomacy and Security, Belgrade, Serbia

Abstract—**Fiber optic telecommunication systems have been used in high-voltage facilities and power grids for many years. These systems have become very important in smart grids. The paper analyzes the new technologies of optical fibers and the possibilities of their application in optoelectronic systems, sensor systems, and modern telecommunication networks that are used in power systems. Today's power transmission networks use fiber optic cables for data transfer, system monitoring, and transmission control. The basic principles were used for signal analysis in a certain bandwidth. Multiplexing by wavelengths (WDM) and optical fiber connection issues, as well as optoelectronic signal conversion, signal attenuation, and signal transmission, are described. The dependence of the signal on temperature, ambient conditions (external installation), and the presence of high-voltage lines, were analyzed.**

Keywords - optical fiber, optical sensor, power systems

I. INTRODUCTION

In recent decades, in many highly developed countries, the sharing economy of personal property and funds has been increasingly prevalent, with the aim of their full use and the realization of additional income. This idea is increasingly represented in infrastructure economics, where the level of asset utilization is important for the final cost result (lower unit price for all consumers).

The telecommunications and power systems connect consumers in a similar way. Both systems require a wide distribution network, and the investment of their construction or expansion is quite high. By sharing network capacity, these two systems can achieve the goals of quality services they provide, while simultaneously sharing costs.

The joint use of passive equipment (concrete towers, channels and poles) began to be applied due to the adopted regulations of electronic communications, with the aim of improving the development of telecommunication systems. However, the sharing of active equipment, as is the case with the excess capacity of optical cables, remains at a lower level. The possibility of using fiber optic cables in power systems is great and it will be described how today's power transmission networks use fiber optic cables.

II. OPTICAL SIGNAL TRANSMISSION SYSTEMS AND COMPONENTS

A long time has passed since the first attempts to send information remotely. From the smoke signals of Indian fires, through Bell's first works in the field of communications, to the idea of transmitting signals around our planet, which was to be covered with lenses formed based on thermal distributions of air masses with the aim of preserving routes around the Earth.

The functioning of the transmission system had to take place in different ambient, weather and temperature conditions, which changed the idea of air lenses. From the radio and microwave areas, the technology of transmission, reception and modulation had to be changed. By moving the area of the electromagnetic spectrum for signal transmission to the optical area, it brought several advantages, with the expansion of the transmission capabilities of the channel and the change in the modulation depth, everything began to change. Practically, it was necessary to achieve the required reliability of the signal transmission system, to solve the problem of noises, to achieve the greatest possible length of signal transmission without repeaters...

All of this underwent changes, and it was about functioning on a large scale and replacing the previous transmission systems. Theoretically, many new components and many other theoretical foundations were arrived at, so that both Raman and Rayleigh scattering, and electro-optical, electromagnetic, and opto-acoustic effects, soon gained their new significance [1].

Although there were many doubts from the beginning of the development in the USA and in the eastern parts of our planet, it seems that everything went at breakneck speed with the installation of underwater optical cables, which connect America and Europe. Fiber optic fibers and other signal transmission systems have become indispensable elements of everyday life

A. Materials for Making Optical Fibers

Commercial optical fibers are made from a variety of materials. One of the types of optical fibers are multi-component glass optical fibers, whose core and sheath are made of glass with different chemical composition. They are obtained by fusing ultrapure powders. The glasses, which make up the shell and the core, are fused separately, and then combined into a compact fiber by a special process. The most used optical fibers are the so-called PCS (polymer coated silica), which consists of a fiber made of doped quartz glass (Fig. 1), with a protective polymer coating of polyethylene [2].

Polyethylene has excellent physical parameters (high strength, wear resistance, resistance to ultraviolet radiation, oxidation, and other chemical influences) and good dielectric properties. It is resistant to moisture penetration and does not change its physical properties under the influence of environmental temperature changes.

The characteristics of these optical fibers are:

- High bandwidth
- Minimal signal loss (low attenuation)
- Resistance to temperature
- Flexibility

Plastic optical fibers are also produced, where the core is made of organic glass, and the protective layer is made of fluoroplastic.

Figure 1. Microscopic appearance of quartz glass for making optical fibers.

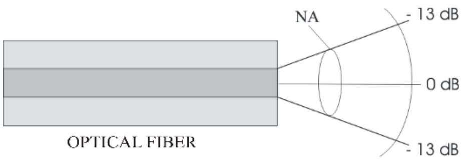

Figure 2. The imaginary cone with acceptance angle (NA).

B. Method of Optical Signal Transmission Through Optical Fiber, Types of Optical Fibers, and Areas of Their Application

Optical fiber transmits light on the principle of total internal reflection. Light is bent, or reflected, as it travels from the middle of one refractive index to the middle of another refractive index. If light passes from the center of lower refractive index to the center of higher refractive index, the light "bends" toward the normal, and if the light passes from the center of higher to the center of lower refractive index, the light moves away from the normal. The change in the amount of light during its passage through two media of different refractive indices is defined by Snell's law [3].

The core of the optical fiber has a higher index of refraction than the index of refraction of the cladding ($n1 > n2$), which allows total internal reflection to occur. Light entering the fiber core at an angle sufficient for total internal reflection is transmitted through the core and reflected at the junction between the core and the cladding. Light entering the fiber at an angle smaller than the critical angle is refracted into the fiber sheath and thus lost.

The imaginary cone with acceptance angle alpha (α), which is determined by the critical angle, refers to a parameter called the numerical aperture (NA) of the fiber, Fig. 2.

The numerical aperture describes the characteristic of the fiber to collect light, and is given as:

$$NA = \sin\alpha = \sqrt{n_1^2 - n_2^2} \quad . \qquad (1)$$

According to the number of modes, optical fibers are divided into:

- single mode, and
- multimode fibers.

Single mode fibers support the propagation of only one basic mode (Figs. 3 and 4), while several thousand modes can be propagated through multimode fibers (Fig. 5).

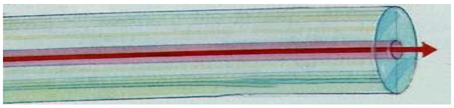

Figure 3. Single mode fibers.

Figure 4. Single mode fibers used in the experimental part.

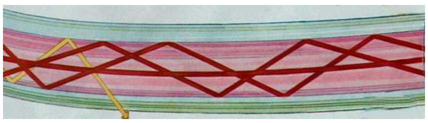

Figure 5: Step-indeks multimode fibers.

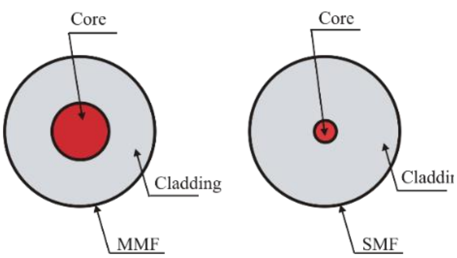

Figure 6. Cross section of SM and MM optical fiber.

According to the spatial distribution of the refractive index, single-mode and multi-mode optical fibers are divided into:

- gradient and
- with graded refractive index.

The most common dimensions and applications of the presented optical fibers are, Fig. 6:

- 9/125 μm (single mode optical fiber (SM)): used in systems for the transmission of large amounts of data and long-distance applications.
- 50/125 μm (multimode optical fiber (MM)): mainly used in military applications, but also in commercial applications such as computer networks.
- 62.5/125 μm (multimode optical fiber (MM)): very popular in most commercial applications; it has high usage with low and moderate speed data links and video links.

Multimode optical fibers offer several advantages over single mode fibers. The first is that the larger diameter of the core of multimode fibers enables their easier connection and connection, as well as more efficient introduction of light from the light source.

Another advantage is that multimode fibers, in addition to laser diodes, allow the use of light-emitting diodes - LEDs as a light source during transmission, while single mode fibers can only work effectively in combination with laser diodes, which complicates and makes the transmission system more expensive. However, single-mode optical fibers have a significant advantage - they allow the transmission of a much larger amount of information per unit of time. This advantage is due to a significantly higher bandwidth (the range of frequencies that can be spread through the fiber). The bandwidth of multimode optical fibers is reduced by the occurrence of the so-called “intermodal” dispersion, which limits the transmission speed. Intermodal dispersion occurs due to different group velocities of individual modes, which results in a difference in their arrival times.

The technology of optical fiber transmission itself developed rapidly thanks to the development of new methods (techniques) of transmission, which from day to day enabled the transmission of higher capacity over longer distances without a regenerator [4].

If different wavelengths are used for transmission, one optical fiber can transmit two or more signals in the same or opposite direction. It is usual that if the wavelengths are quite different (e.g.1310 nm and 1550 nm), it is called WDM transmission (wavelength division multiplexing), and if the “packing” of wavelengths is denser, it is called OFDM transmission (optical frequency division multiplexing).

The OFDM technique makes it possible to transmit hundreds of independent signals (each of them can carry several Gb/s) in the range of 1500-1600 nm (corresponds to a bandwidth of 12.5 THz). To achieve this, extremely stable light sources are needed, then optical separation filters (if using IMDD transmission) or separation is done with the help of electrical filters in heterodyne detection (coherent transmission) when a local optical variable oscillator is needed. This is why the technology and measuring equipment is extremely expensive.

C. *Basic Fiber Optic Splicing Techniques and Characteristics*

Optical fiber connection and splicing techniques are often of great importance in the process of designing optical fibers and cables because the attenuation of the transmitted power, which is lost at one joint, is equivalent to the attenuation of hundreds of meters of optical fiber, which greatly contributes to the overall attenuation. Therefore, it is important to gain a complete understanding of the mechanisms in the process of connecting optical fibers, the way of measuring the attenuation that occurs on that occasion and the possible causes that lead to it.

There are several ways in which splicing techniques applicable to optical fiber can be categorized. The divisions are partly arbitrary, but the main ways of joining are [5]:

- connecting optical fibers using the fusion-melting method (electric arc),
- splicing of optical fibers by mechanical adjustment (straightening method),
- splicing of optical fibers using the laser welding method (method under development).

Fusion splicing is a proven technique in which optical fibers are prepared, joined and welded with an electric arc, using a special splicer device Fig. 7.

Optical fibers connected in this way form a continuous element, where the connection point is invisible to the naked eye and cannot be determined by modern devices for testing optical lines.

Fig. 8 shows an example of a realized permanent connection.

Mechanical tuning, on the other hand, is a very broad term, referring to:

Figure 7. Fujikura optical splicer.

Figure 8. A joint of optical fibers created by splicing.

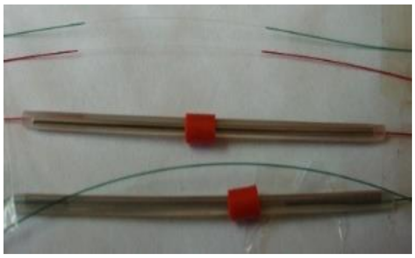

Figure 9. Coupling with connectors for optical fibers.

- mechanical connection using a connector with fiber optic connectors, Fig. 9.
- front connection of non-contact connectors, which can be dismantled, Fig. 10.
- front connection of contact connectors, which can be dismantled, Fig. 11,

and all other techniques, which are not listed above [6].

A single bad connector can give much greater attenuation than the attenuation of a 1km length of optical fiber. That's why connector testing is mandatory after installation, Fig. 12 shows an SM fiber optic cable with FC/PC connectors on its ends, and Fig. 13 shows how to test the fiber optic connector. Thus, the value of attenuation and back reflection, which the connector enters, is obtained. High back reflection can cause unreliable operation of the light source [7].

The mentioned optical fiber splicing techniques have their own names: fusion splicing with an electric arc produces a high-quality splice with the least attenuation; Mechanical couplers are removable and are used for temporary connection of optical fibers and optical connectors are used for splicing optical sections and connecting fibers to optical devices [8].

The optical performance of each fiber optic connection can be viewed from two aspects:

- its performance in the transmission of optical power, known as the introduced attenuation and represents the ratio of the transmitted power, which is obtained at the output of the receiving core of the optical fiber and the incident-transmitting power at the output of the transmitting core of the optical fiber,

- and its performance in reflection, known as return attenuation, which is proportional to the reflected power from the optical fiber junction back into the core of the transmitting optical fiber.

The continuation of optical fibers, regardless of the way in which it is performed, requires the performance of certain actions:

- preparation of connecting cables where the primary protection is removed from

Figure 10. Mechanical coupling.

Figure 11. Optical connector with coupling.

Figure 12. SM fiber optic cable with FC/PC connectors on its ends.

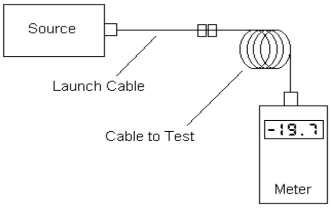

(a)

(b)

Figure 13. Measurement scheme (a) and experimental method (b), for testing optical connectors.

the end of the fiber, after which the fiber is straight cut to the appropriate length and placed in a connecting device, an optical connector (the connecting process is more complex and requires additional operations in laboratory conditions) or a mechanical connector;

- Splicing of optical fibers using the provided technique.

Mandatory control of attenuation at the connection with OTDR (Optical Time Domain Reflectometer), Fig. 14.

- In case of great weakening, repetition of connection.
- Appropriate protection of the realized connection.

The OTDR method of measuring joint attenuation is very convenient because:

Access to the optical fiber from only one end is sufficient.

- Is a high measurement speed.
- Has high resolution and accuracy.
- Enables monitoring of all events on the section.

The causes of attenuation at the optical fiber connection can depend on internal and external factors. Internal factors include geometrical deviations in the manufacture of optical fibers, which cause an increase in attenuation at the joint, and cannot be influenced during splicing. External factors include those that can be influenced during splicing, by careful handling of the fibers and splicing device, using good fiber cutting tools, and taking care of the cleanliness and roughness of the fiber surface. These include cases when there is: lateral displacement, married asymmetry, or separation of cores at the connection of optical fibers. On the screen of the splicer, the ends of the optical fibers are visible, magnified enough to adjust and avoid errors, that is, to reduce the attenuation of the connection.

Figure 14. NetTest - Optical Time Domain Reflectometer.

Finally, complete content and organizational editing before formatting. Please take note of the

D. Advantages of Fiber Optic Sensors

Fiber optics, in combination with other fields of quantum electronics, laser technology, laser electronics and related fields, started a “technological” and “innovation offensive” 20 years before the new millennium. This also applies to its integration into telecommunications, semiconductors, and many areas and segments that electronics serves. Fiber sources, fiber sensors, fiber waveguides, and finally fiber optic lidars. The dimensions and prices of the components were also reduced. Optical sensors required ever smaller dimensions, and lighter weight components, than the electronics used until then, but they introduced high operating speeds, high sensitivity, and specific working widths.

The reason for these, as well as many other advantages, can be seen in the fact that both sensitivity and signal propagation functions are related to photons rather than electrons. Based on this, a unique segment of electronics is created in which sensors with distributed or matrix forms are formed, covering extensive locations, with the possibility of sending information to a remote station. With small modifications, signal processing devices, signal dividers (splitters), combiners, multiplexers, filters, delay lines can be implemented, thus forming a group of “all-fiber” measuring elements [9].

Dielectric and dichroic glasses or plastic materials make fibers passive and immune to electromagnetic interference (EMI), and through them, large systems, and electrical equipment, such as generators and motors, very reliable, with minimal possibility of damage to sensitive elements (or remote electronics), in the case of close electron discharge. Fiber sensors do not generate heat or arcs, they are also reliable for working in dangerous environments and spaces, such as oil refineries, warehouses (silos), mines, chemical plants, etc. Standard glass fibers do not have any corrosive properties in corrosive environments and temperatures above 232°C. Special fibers withstand temperatures higher than 232°C, and some even temperatures of 648°C.

III. APLICATION OF OPTICAL FIBERS IN POWER SYSTEMS

We don't have time to go into a lot of details, so we are moving to the field of energy/power, which with its problems introduced in new ways of conversion: types of energy, its transmission, sources, and control, which inevitably come to the fore, and we have just come out of the pandemic! The pandemic has instructed and set us that work must be preserved from home or from remote places and reminded us (although we are still unaware of all the roles of optical fibers), of the importance of optics in computer systems and in the transmission of low or high power [10].

In our country, the role of optical fibers in energy has been talked about or worked on for at least three decades, and from the usual roles, it has changed to the present state, where optical cables are installed along with energy cables.

Electricity is transmitted and distributed over large geographical areas through networks. In those areas there are power plants, alternative energy sources (solar, wind...), distribution substations and microgrids [11]. To ensure reliable distribution of electricity, grids must be monitored and managed [12]. To monitor the operation and manage the networks, various means of communication are used, including running optical cables along transmission and distribution towers, radio links and contracting communication services from telecom operators [13]. Fig. 15 shows the types of optical cables that are installed on transmission lines.

OPGW (Optical Power Ground Wire), Fig. 16, is the most used type of optical cable in telecommunication systems of power companies [14].

OPGW optical cable (known as optical fiber composite overhead ground wire), the optical fiber is placed in the ground wire of the overhead high voltage transmission line to form the optical fiber communication network on the transmission line. This structure has the dual function of a ground wire and a communication wire. Since the optical fiber has the characteristics of anti-electromagnetic interference, light weight, etc., it can be installed on top of the transmission line tower. OPGW has significant features such as higher reliability, superior mechanical performance, and lower cost. OPGW fiber optic cable is reliable, stable, and strong due to the metal wire sheath. As the overhead grounding wire and optical cable are combined as a whole, the construction period is equivalent to installing a good conductor of the overhead grounding wire, which can reduce the submerged current of the transmission line and

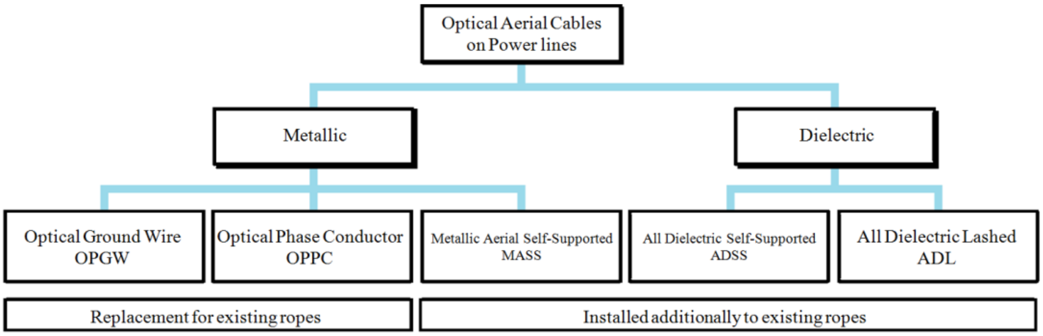

Figure 15. The types of optical cables that are installed on transmission lines.

Figure 16. OPGW (Optical Power Ground Wire) optical cable.

the current frequency surge, and improve the transmission line to the communication line.

A special optical fiber placed in the OPPC (Optical Phase Conductor) conductor enables determination of the actual temperature of the phase conductors in given weather conditions. Monitoring allows the dispatcher to dynamically load line I in a broader perspective, the so-called intelligent network management or “smart grids”.

MASS (metal self-supporting antenna) - Self-supporting cables made of aluminum steel wire in combination with optical fibers. They are very similar to OPGW cables, but they are not lightning rods. For this reason, MASS cables usually hang slightly lower than the phase conductors, Fig. 17.

Optical cables without metal elements are made of a centrally positioned core in the form of a rod, surrounded by several tubes containing optical fibers, and the most applicable are ADSS cables (All-Dielectric Self-Supporting cables) Fig. 18.

Between the inner and outer sheath of the cable there are very strong aramid fibers, which give ADSS cables adequate mechanical strength. When choosing a connection for ADSS cables, it is necessary to take into account the distribution of the electric field between the phase conductors, because in case of rain or high air humidity, the outer sheath is exposed to micro-discharges. Placing wires in an area with too much electric field leads to rapid destruction of their sheath. The solution to this problem is the use of semiconductor cables, which, due to the high strength of the electromagnetic field, are usually used in lines with a voltage of no more than 110 kV. When designing the installation of ADSS cables on existing transmission lines, it is necessary to take into account the additional stresses acting on the supporting structures and provide for appropriate reinforcements.

ADL (All-Dielectric Lashed Cables) is a non-metallic fiber optic cable that is wrapped around an earth wire. They provide a faster and cheaper network.

In Figs. 19-22, there are examples of the installation of optical cables on transmission lines, which were realized on the territory of our country. It can be noticed that reserves of fiber optic cable (on transmission lines in the form of a circle) have been left everywhere in case of damage, and the possibility of their continuation.

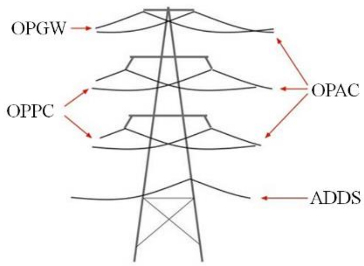

Figure 17. Optical cables on transmission lines.

.

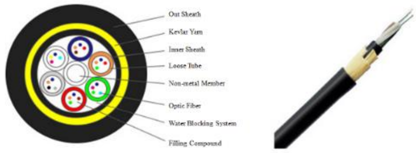

Figure 18. ADSS cables.

Figure 19. High-voltage transmission line before installation of optical fiber.

Figure 20. High-voltage transmission line during installation of optical fiber.

IV. EFFECT OF TEMPERATURE CHANGE ON OPTICAL FIBER JOINTS

The application of optical cables in transmission lines implies their exposure to various temperature influences, from the lowest to the highest.

For the experimental investigation of the effect of temperature change on the permanent connections of optical fibers, which is reflected in the stability of the optical line, samples of single-mode optical fiber (Fiber Optics HQ, 9/125/250/900 μm) with a quartz glass core were used.

The process of permanent joining of optical fibers was realized using a Fujikura device (FSM-16S). The display, as an integral part of the device, enables monitoring of the process of positioning and welding of optical fibers.

The commercial single-mode optical fiber with FC/PC optical connectors (Fig. 11) samples were 9/125/3000 μm thick and made of quartz glass. It is produced to work in so called second and third window (1300 nm and 1550 nm). The fiber length varied from 1 m to 10 m. Produced by MOLEX. According to the literature, data fibers have insertion loss of 0.34 dB/km and 0.21 dB/km in second and third window, respectively. Insertion loss given by producer was <0.4 dB and return loss > -30 dB.

The technical conditions for the attenuation at the joints provide that the measurement of the attenuation at the joints is carried out by the reflectometer method with the use of an OTDR. The measurement block diagram is given in Fig. 23.

OTDR Methods were applied for backscattering and reflections measuring and monitoring. The backscatter is directly related to the signal in the test pulse. As the signal decreases, so does the backscatter. The

Figure 21. High-voltage transmission line after installation of optical fiber.

Figure 22. High-voltage transmission line with optical cable and left reserve, for 10 renewable connections.

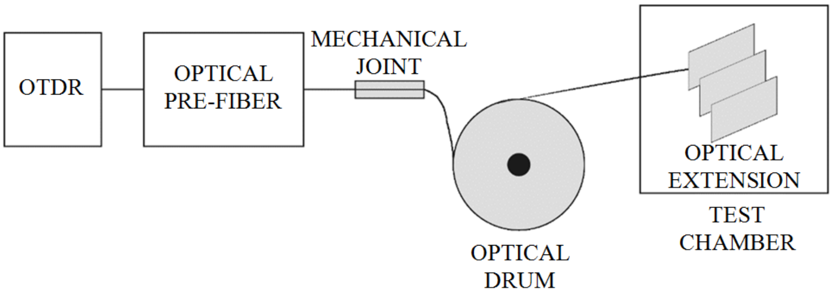

Figure 23. Block diagram of measurement of attenuation on a permanent connection of an optical fiber.

TABLE I. RESULTS OF EXPERIMENTAL MEASUREMENT AFTER TEMPERATURE CYCLE.

Connection sequence number	**Wavelength 1310 nm**		**Wavelength 1550 nm**	
	Losses (dB)	***Reflection (dB)***	***Losses (dB)***	***Reflection (dB)***
1	0.41	- 39.10	1.10	- 49.65
2	0.48	- 36.70	1.24	- 46.60
3	0.48	- 36.75	1.22	- 46.53
4	0.50	-34.48	1.62	-39.53
5	0.40	- 39.90	1.09	- 50.00
6	0.45	- 37.98	1.14	- 48.30
7	0.35	- 40.25	0.85	- 61.00

TABLE II RESULTS OF EXPERIMENTAL MEASUREMENT BIFOR TEMPERATURE CYCLE.

Connect.sequence number	**Wavelength 1310 nm**		**Wavelength 1550 nm**	
	Losses (dB)	***Reflection (dB)***	***Losses (dB)***	***Reflection (dB)***
1	0.39	- 36.70	0.41	- 41.25
2	0.45	- 33.90	0.46	- 36.75
3	0.43	- 34.50	0.46	- 38.30
4	0.48	-33.45	0.42	-40.25
5	0.35	- 39.45	0.38	- 42.30
6	0.42	- 35.40	0.42	- 38.80
7	0.31	- 40.20	0.39	- 45.05

difference in strength between two points of backscatter is the same as the difference in strength (intensity) between the test pulse at the same two points. The OTDR procedure was done on the GN Nettest instrument. The wavelength was 1310 nm.

After basic measurements, all connectors and optical joints are subjected to artificial aging in a climate chamber. The aging process consisted of temperature changes from -40°C to +80°C,

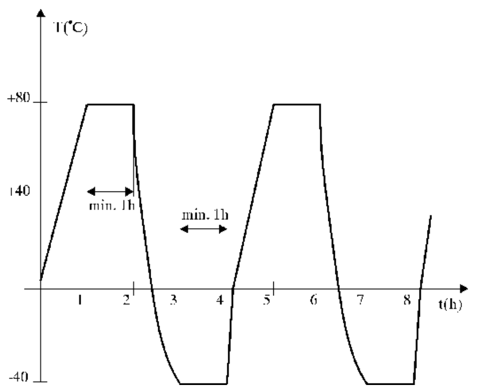

Figure 24. Temperature cycle.

which represents the working temperature range of the used connectors. The chamber was programmed in cycles of two hours at low temperature and two hours at high temperature, and its quality ensured that the connectors were at the set low and high temperatures for one hour each.

V. CONCLUSION

The results of measuring connector attenuation and back reflection, before and after aging, at 1310 nm, show great stability depending on the temperature change. This means that there is no increase in attenuation at the connector joints depending on temperature changes and aging, which is very important for proper operation and use of the entire optical system.

By comparing the results obtained before and after aging, at 1550 nm, it can be stated that there is a drastic increase in attenuation at the connectors. The increase occurred after exposing the connector to low temperatures. In practical applications, this can be expressed especially when switching to work in the winter months. Therefore, for working with such systems, it is necessary to provide rooms with a constant temperature, unless special applications require something else.

The temperature cycle of artificial aging in the climate chamber is shown in Fig. 24. After completing several continuous temperature cycles, the characteristics of the optical connectors were re-measured. The obtained results are given in Table I and Table II.

ACKNOWLEDGMENT

The authors would like to thank their colleague Rade Sekulić, Head of Design and Consulting Department at KBV Datacom d.o.o., without whose support the photographs from the field, which show the installation of optical fibers on power lines, would not exist.

REFERENCES

[1] Ghatak, A., & Thyagarajan, K. (1998). *An introduction to fiber optics*. Cambridge university press.

[2] DeCusatis, C. (Ed.). (2013). *Handbook of fiber optic data communication: a practical guide to optical networking*. Academic Press, San Diego, USA.

[3] Elliott, B., Elliott, B. J., & Gilmore, M. (2002). *Fiber Optic Cabling*. Newnes,UK.

[4] Agrawal, G. P. (2001). *Applications of nonlinear fiber optics*. Elsevier.

[5] De Rosa, M., Carberry, J., Bhagavatula, V., Wagner, K., & Saravanos, C. (2002). High-power performance of single-mode fiber-optic connectors. *Journal of Lightwave Technology*, *20*(5), 851.

[6] Pantelić, S., Srećković, M. Janićijević, A., Davidović, M., Jevtić, S., Karastojković, Z., & Rajković, V. (2018). Effects of ND3+: YAG laser on optical components made from glass, ceramic and plastic materials. In *proceedings of the conference Contemporary Materials*, (pp. 33-48).

[7] Pantelić, S., Borna, N., Srećković, M., Kovačević, A., Bugarinović, A., Kovačević, M., Lazarević, Đ. (2011). Influence of nuclear radiation and laser beams on optical fibers and components. Nuclear technology & Radiation protection, 26(1), 32-38.

[8] Sreckovic, M. Z., Pantelic, S. N., Stanković, S. J., Polić, S. R., Ivanović, N., Bugarinović, A. R., & Ostojić, S. M. (2017). Gamma irradiation effects in optical fibres, splitters, and connectors. *Nuclear technology and radiation protection*, *32*(4), 375-380.

[9] Travica, S., Tomic, M., Aleksic, O., Srećkovic, M., & Pantelić, S. (1999). Optically powderd Fiber Optic temperature thick film resistor NTC Sensor. In Proceedings of Lasers 98, Ed. W. Corcoran and T. Goldman, SoQuE, McLain, 562-567.

[10] Anatory, J., Theethayi, N., & Thottappillil, R. (2009). Channel characterization for indoor power-line networks. *IEEE Transactions on Power Delivery, 24* (4), 1883–1888.

[11] Wang, W., Xu, Y., & Khanna, M. (2011). A survey on the communication architectures in smart grid. *Computer Networks 55*, 3604–3629.

[12] Ahuja, K., & Khosla A. (2019). Network selection criterion for ubiquitous communication provisioning in smart cities for smart energy system. *Journal of Network and Computer Applications, 127*, 82-91.

[13] Borges, R.M., de Souza Lopes, C.H., Lima, E.S., de Oliveira, M.A., Cunha, M.S.B., Alexandre, L.C., da Silva, L.G., Pereira, L.A.M., Spadoti, D.H., Romero, M.A., & Sodré Junior, A.C. (2021). Integrating Optical and Wireless Techniques towards Novel Fronthaul and Access Architectures in a 5G NR Framework. *Applied Sciences, 11*, 5048.

[14] Koonen, T. (2018). Indoor optical wireless systems: Technology, trends, and applications. *Journal of Lightwave Technology, 36*, 1459–1467.

Improved Algorithm for FET Analysis of Transient Linear Circuit Problems

Ivica Jurić-Grgić[1], Marin Mandić[2], Tonći Modrić[3]

[1,2,3]University of Split, Faculty of Electrical Engineering, Mechanical Engineering and Naval Architecture, R. Boskovica 32, HR-21000 Split, Croatia

Abstract—**Most of the circuit simulators such as SPICE apply the backward differentiation formulae (BDF) integration method to the system of differential algebraic equations (DAEs) that is defined after applying the well-known modified nodal analysis (MNA) to the considered linear circuit/network. To provide a fast and accurate circuit/network analysis, many efforts have been made to improve integration algorithms. In general, time-domain circuit analysis demands solving a system of ordinary differential equations (ODEs), which represent the mathematical model and give transient behavior of the considered linear circuit/network. The aim of this paper was to establish a novel algorithm for a transient linear circuit analysis based on the Finite Element Technique (FET). The FET procedure is based on the Finite Element Method (FEM) approach and allows a straightforward solution for complex electric circuits. The developed algorithm enables selection of different types of time integration schemes when forming a local system of equations for a coupled circuit finite element. To illustrate the basic principle of the developed FET-based algorithm and to perform transient analysis, a random coupled linear circuit was analyzed. Numerical solutions obtained using FET procedure were compared to the solution obtained by Matlab Simulink software. It was shown that the accuracy of results depends on the employed time integration scheme when performing the FET procedure.**

Keywords - circuit analysis; finite element technique; time domain; time integration schemes

I. INTRODUCTION

The aim of this paper was to establish a novel algorithm for a transient linear circuit analysis based on the FET. The FET procedure allows a straightforward solution for complex electric circuits since it is based on the Finite Element Method (FEM) approach. Using an assembling procedure based on the FEM approach, it is quite straightforward to develop a numerical model (i.e. simulator) of a complex electric circuit by focusing on the modeling of a single finite element (FE) in a linear electric circuit.

In general, time-domain circuit analysis demands solving a system of ordinary differential equations (ODEs), which represent the mathematical model and give the transient behavior of the considered linear circuit/network.

Most of the circuit simulators such as SPICE apply the BDF integration method to the system of DAEs that is defined after applying the well-known MNA to the considered linear circuit/network. To provide a fast and accurate circuit/network analysis, many efforts have been made to improve integration algorithms. The most used methods in modern circuit simulators for time integration of the DAEs are the BDF methods, improved BDF method (yields less damping) in combination with the Trapezoidal Rule [1], Implicit Runge–Kutta methods such as the Radau [2], Choral methods [3], and Modified Extended BDF methods [4]. The FEM is the standard procedure for solving ordinary or partial differential equations (ODEs or PDEs) when dealing with continuum field problems. The continuum needs to be divided into finite elements where each FE is defined by an appropriate algebraic system of equations as an approximation of the original ODEs or PDEs [5].

FEM has been widely used for solution of a great number of engineering problems in structural analysis problems [5] as well as multiconductor transmission line (MTL) problems [6,7].

In [6], which is based on the classical FEM procedure, an algebraic local system of equations for a MTL transient analysis was obtained using the generalized trapezoidal rule (ϑ-method) for the time integration scheme. In [7], an algorithm was developed for electromagnetic transient calculations on the MTL achieved by improvement of the time integration when forming the local system of equations for the finite element. Improvement of accuracy was obtained by using Heun's method. Heun's method is one of the variants of the Runge–Kutta second order time integration method. In this paper, the local system of equations of a coupled circuit finite element was obtained using the generalized trapezoidal rule (ϑ-method) as well as using Heun's method.

II. FET PROCEDURE

According to the FET terminology (based on the FEM approach), each circuit element can be defined as a single finite element (FE) with a corresponding local system of algebraic equations that are obtained in the time domain. The FE model of a coupled circuit finite element can be defined as a finite element with 2n local nodes as is shown in Fig. 1, where 'n' is the number of coupled circuit element branches.

The coupled circuit finite element shown in Fig. 1 is defined by the following system of coupled ordinary differential equations (ODE-s):

$$\{\varphi_1\}-\{\varphi_2\}=[R]\cdot\{i\}+ [L]\cdot\frac{d\{i\}}{dt}+\{U_c\}+\{e\}\ , \tag{1}$$

$$\{i\}=[C]\cdot\frac{d\{U_c\}}{dt}, \tag{2}$$

where:
[R]-resistance matrix,
[L]-inductance matrix,
[C]-capacitance matrix,
{i_1}-nodal current vector of currents entering the finite element at local nodes '11'…'1n',
{i_2}-nodal current vector of currents entering the finite element at local nodes '21'…'2n',
{φ_1}-nodal potential vector at local nodes '11'…'1n',
{φ_2}-nodal potential vector at local nodes '21'…'2n',
{e}-electromotive force vector,
{U_c}-capacitance voltage vector.

A. Coupled Circuit Finite Element—Theta Method Time Integration Scheme

The general principles of the time integration of Eqs. (1) and (2) using the ϑ-method time integration scheme can be found in [6]. To obtain a system of algebraic equations, it is necessary to perform a time integration of the system of coupled ordinary differential Eqs. (1) and (2):

$$\int_t^{t+}\left(\{\varphi_1\}-\{\varphi_2\}-[R]\cdot\{i\}-[L]\cdot\left\{\frac{di}{dt}\right\}- -\{U_c\}-\{e\}\right)\cdot dt=0\ , \tag{3}$$

$$\int_t^{t+}\left(\{i\}-[C]\cdot\frac{d\{U_c\}}{dt}\right)\cdot dt=0\,. \tag{4}$$

The time integration based on the ϑ-method can be described by the following equations:

$$\int_t^{t+} f(t)\cdot dt\approx\left[(1-\vartheta)\cdot f+\vartheta\cdot f^{+}\right]\cdot\Delta t\,, \tag{5}$$

$$\int_t^{t+}\frac{df(t)}{dt}dt=\int_t^{t+}df(t)=f^{+}-f\ . \tag{6}$$

Vectors marked by '+' denote the variables' state at the end of the time interval, while vectors without the mark denote the variables' state at the beginning of the time interval *Δt*.

With the application of the ϑ-method on Eqs. (3) and (4), based on the same procedure described in [6], the following system of algebraic equations suitable for assembly procedure (FEM approach) can be defined as follows:

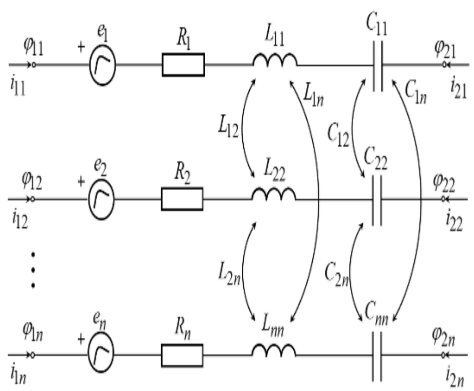

Figure 1. Coupled circuit finite element.

$$\begin{bmatrix} [B] & -[B] \\ -[B] & [B] \end{bmatrix} \cdot \begin{bmatrix} \{\varphi_1^+\} \\ \{\varphi_2^+\} \end{bmatrix} =$$

$$= \begin{bmatrix} -[D] & [D] \\ [D] & -[D] \end{bmatrix} \cdot \begin{bmatrix} \{\varphi_1\} \\ \{\varphi_2\} \end{bmatrix} + \begin{bmatrix} [K] \\ -[K] \end{bmatrix} \cdot \{U_c\} +$$
$$+ \begin{bmatrix} [D] \\ -[D] \end{bmatrix} \cdot \{e\} + \begin{bmatrix} [B] \\ -[B] \end{bmatrix} \cdot \{e\}^+ + \quad , (7)$$
$$+ \begin{bmatrix} -[H] & [0] \\ [0] & -[H] \end{bmatrix} \cdot \begin{bmatrix} \{i_1\} \\ \{i_2\} \end{bmatrix} + \begin{bmatrix} \{i_1\}^+ \\ \{i_2\}^+ \end{bmatrix}$$

where:

$$[A] = \vartheta \cdot \Delta t \cdot [R] + [L] + (\vartheta \cdot \Delta t)^2 \cdot [C]^{-1}, \quad (8)$$

$$[G] = -(1-\vartheta) \cdot \Delta t \cdot [R] + [L] - (\vartheta \cdot \Delta t) \cdot (1-\vartheta) \cdot \Delta t \cdot [C]^{-1}, \quad (9)$$

$$[B] = [A]^{-1} \cdot \vartheta \cdot \Delta t, \quad (10)$$

$$[D] = [A]^{-1} \cdot (1-\vartheta) \cdot \Delta t, \quad (11)$$

$$[H] = [A]^{-1} \cdot [G], \quad (12)$$

$$[K] = \Delta t \cdot [A]^{-1}, \quad (13)$$

$$\{i_1\}^+ = \{i\}^+, \quad (14)$$

$$\{i_2\}^+ = -\{i\}^+. \quad (15)$$

B. Coupled Circuit Finite Element—Heun's Method Time Integration Scheme

The general principles of the time integration of Eqs. (1) and (2) using Heun's method time integration scheme can be found in [7]. To perform the time integration according to Heun's method, it is necessary to rewrite Eqs. (1) and (2) in the following form:

$$\frac{d\{i\}}{dt} = f_1(\{i\}, \{U_c\}, \{\varphi_1\}, \{\varphi_2\}, \{e\}), \quad (16)$$

$$\frac{d\{U_c\}}{dt} = f_2(\{i\}), \quad (17)$$

$$f_1(\{i\}, \{U_c\}, \{\varphi_1\}, \{\varphi_2\}, \{e\}) = -[L]^{-1} \cdot [R] \cdot \{i\} + [L]^{-1} \cdot \{\varphi_1\} - [L]^{-1} \cdot \{\varphi_2\} - [L]^{-1} \cdot \{U_c\} - [L]^{-1} \cdot \{e\}, \quad (18)$$

$$f_2(\{i\}) = [C]^{-1} \cdot \{i\}. \quad (19)$$

With the application of the Heun's method on Eqs. (16)-(19), based on same procedure described in [7], the following system of algebraic equations suitable for assembly procedure (FEM approach) can be defined as follows:

$$\begin{bmatrix} [A] & [B] \\ -[A] & -[B] \end{bmatrix} \cdot \begin{bmatrix} \{\varphi_1^+\} \\ \{\varphi_2^+\} \end{bmatrix} = \begin{bmatrix} -[D] & -[E] \\ [D] & [E] \end{bmatrix} \cdot$$
$$\cdot \begin{bmatrix} \{\varphi_1\} \\ \{\varphi_2\} \end{bmatrix} + \begin{bmatrix} -[F] \\ [F] \end{bmatrix} \cdot \{U_c\} + \begin{bmatrix} -[H] \\ [H] \end{bmatrix} \cdot \{e^+\} +$$
$$+ \begin{bmatrix} -[K] \\ [K] \end{bmatrix} \cdot \{e\} + \begin{bmatrix} -[J] & [0] \\ [0] & -[J] \end{bmatrix} \cdot \begin{bmatrix} \{i_1\} \\ \{i_2\} \end{bmatrix} + \quad , (20)$$
$$+ \begin{bmatrix} \{i_1\}^+ \\ \{i_2\}^+ \end{bmatrix}$$

$$[G] = [I] + \frac{\Delta t^2}{4} \cdot [L]^{-1} \cdot [C]^{-1}, \quad (21)$$

$$[A] = \frac{\Delta t}{2} \cdot [G]^{-1} \cdot [L]^{-1}, \quad (22)$$

$$[B] = -\frac{\Delta t}{2} \cdot [G]^{-1} \cdot [L]^{-1}, \quad (23)$$

$$[D] = \frac{\Delta t}{2} \cdot [G]^{-1} \cdot [L]^{-1} - \frac{\Delta t^2}{2} \cdot [G]^{-1} \cdot [L]^{-2} \cdot [R], \quad (24)$$

$$[E] = -\frac{\Delta t}{2} \cdot [G]^{-1} \cdot [L]^{-1} + \frac{\Delta t^2}{2} \cdot [G]^{-1} \cdot [L]^{-2} \cdot [R], \quad (25)$$

$$[F] = -\Delta t \cdot [G]^{-1} \cdot [L]^{-1} + \\ + \frac{\Delta t^2}{2} \cdot [G]^{-1} \cdot [L]^{-2} \cdot [R] , \quad (26)$$

$$[H] = \frac{\Delta t}{2} \cdot [G]^{-1} \cdot [L]^{-1}, \quad (27)$$

$$[K] = -\frac{\Delta t}{2} \cdot [G]^{-1} \cdot [L]^{-1} + \\ + \frac{\Delta t^2}{2} \cdot [G]^{-1} \cdot [L]^{-2} \cdot [R] , \quad (28)$$

$$[J] = [G]^{-1} - \Delta t \cdot [G]^{-1} \cdot [L]^{-1} \cdot [R] + \\ + \vartheta \cdot \Delta t^2 \cdot [G]^{-1} \cdot [L]^{-2} \cdot [R]^2 - \\ - \frac{\Delta t^2}{4} \cdot [G]^{-1} \cdot [L]^{-1} \cdot [C]^{-1} , \quad (29)$$

$$\{i_1\}^+ = \{i\}^+ , \quad (30)$$

$$\{i_2\}^+ = -\{i\}^+ . \quad (31)$$

C. Assembling Procedure

The general principles of the FET assembling procedure based on the FEM approach can be found in [6,7]. To perform the assembling procedure, local systems Eq. (7) in the case of the ϑ-method time integration scheme and Eq. (20) in the case of Heun's method time integration scheme, each FE must be set in the following form:

$$\begin{Bmatrix} \{i_1\}^+ \\ \{i_2\}^+ \end{Bmatrix} = [Q] \cdot \begin{Bmatrix} \{\varphi_1\}^+ \\ \{\varphi_2\}^+ \end{Bmatrix} + \\ + \begin{Bmatrix} F_1(\{\varphi_1\},\{\varphi_2\},\{i_1\},\{i_2\}) \\ F_2(\{\varphi_1\},\{\varphi_2\},\{i_1\},\{i_2\}) \end{Bmatrix} . \quad (32)$$

The global system must be solved for each time step, evaluating unknown nodal potentials. The value of the current of each finite element is then computed by using Eq. (32) for each time step.

III. Numerical Example

To present the basic principle of the developed FET-based algorithm and to perform transient analysis, the following coupled linear circuit was analyzed. A coupled linear electrical circuit, shown in Fig. 2 has four branches and two global nodes.

Fig. 3 shows the entire coupled linear circuit as a unique finite element (FE) prepared for the FET procedure. It has eight local nodes and four branches. The first branch contains an electromotive force that is a ramp function (in the time interval 0–100 ms increases its value from 0 up to 10 V). The value of the time interval *Δt* was taken as 0.1 ms. The values of the circuit elements were assumed to be as follows: R_2 = 1 Ω, R_3 = 2 Ω, R_4 = 1 Ω, C_2 = 1 mF, L_3 = 0.1 H, L_4 = 0.01 H, L_{34} = 0.1 mH.

Fig. 4 shows the current in the first branch during the 9.8-11 ms time interval as well as during the entire simulation, while Fig. 5 shows the second branch capacitor voltage during the 10.8-12 ms time interval, as well as during the entire simulation. Numerical solutions obtained using Heun's method and using the generalized trapezoidal rule were compared to the solution obtained by Matlab Simulink software.

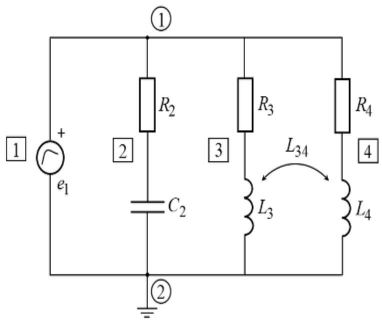

Figure 2. Example of coupled linear electrical circuit.

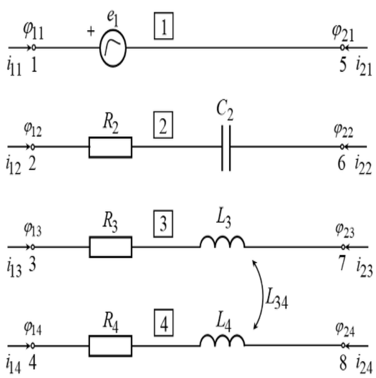

Figure 3. Coupled linear circuit finite element.

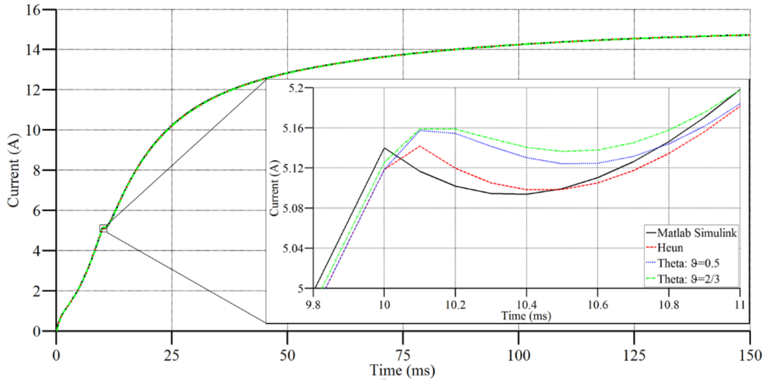

Figure 4. First branch current during the 9.8-11 ms time interval.

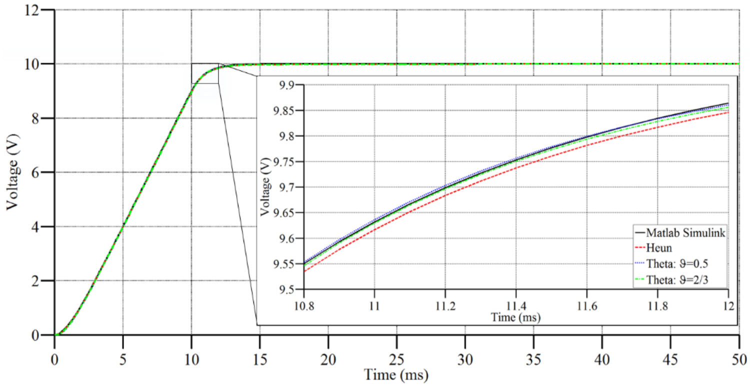

Figure 5. Capacitor voltage during the 10.8-12 ms time interval.

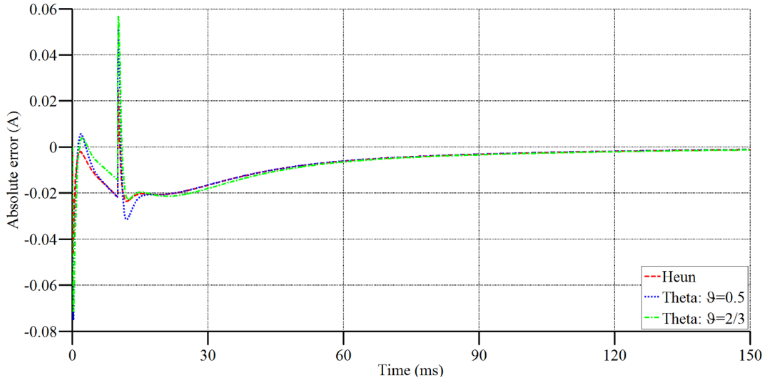

Figure 6. Absolute errors of the current in the first branch.

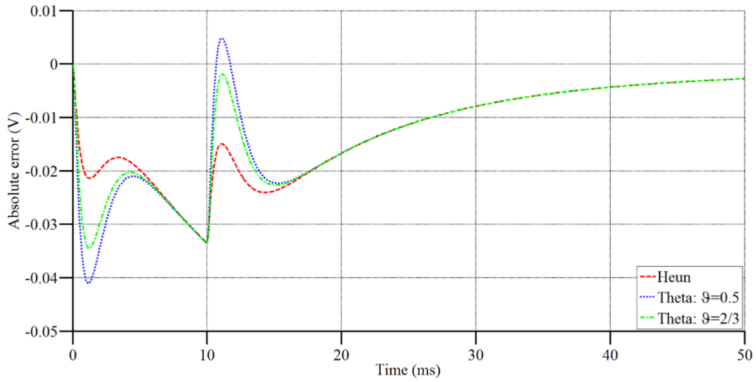

Figure 7. Absolute errors of the capacitor voltage in the second branch.

Absolute errors of numerical solutions related to the Matlab Simulink solution are shown in Figs. 6 and 7. Maximum values of these errors are presented numerically in Table I.

TABLE I. MAXIMUM ABSOLUTE ERRORS OF THE CURRENT IN THE FIRST BRANCH AND CAPACITOR VOLTAGE IN THE SECOND BRANCH.

Methods	**Current**	**Capacitor Voltage**
Heun	0.046789	0.033552
Theta: $\vartheta = 0.5$	0.074807	0.041031
Theta: $\vartheta = 2/3$	0.071435	0.034416

It was shown that the accuracy of results depends on the type of time integration scheme when performing the FET procedure.

IV. CONCLUSION

In this paper, a novel algorithm for a transient linear circuit analysis based on the Finite Element Technique (FET) was established. The FET procedure allows a straightforward solution of complex electric circuits since it is based on the Finite Element Method (FEM) approach. Using an assembling procedure based on the FEM approach, it is quite straightforward to develop a numerical model of a complex electric circuit by focusing on the modeling of a single element in a linear electric circuit. The algorithm allows us to choose various types of time integration schemes when forming a local system of equations for a coupled circuit finite element.

In this paper, a local system of equations of a coupled circuit finite element was obtained using the generalized trapezoidal rule (ϑ-method) as well as using Heun's method.

To show the basic principle of the developed FET based algorithm and to perform transient analysis, the random coupled linear circuit was analyzed. Numerical solutions obtained using Heun's method and using the generalized trapezoidal rule were compared to the solution obtained by Matlab Simulink software. It was shown that the accuracy of results depends on the type of time integration scheme when performing the FET procedure.

REFERENCES

[1] Hosea, M. E., & Shampine, L. F. (1996). Analysis and implementation of TR-BDF2. *Applied Numerical Mathematics*, *20*(1-2), 21-37.

[2] Swart, J. J. B. (1997). Parallel software for implicit differential equations. [Doctoral dissertation, University of Amsterdam].

[3] Günther, M., Rentrop, P., & Feldmann, U. (2001). CHORAL — A one step method as numerical low pass filter in electrical network analysis. In *Scientific Computing in Electrical Engineering* (pp. 199-215).

[4] Bruin, S. M. A. (2001). Modified extended BDF applied to circuit equations. [Master's thesis, Vrije Universiteit Amsterdam].

[5] Zienkiewicz, O. C., & Taylor, R. L. (1989). *The finite element method, Volume 1: The basis* (4th ed.). McGraw-Hill.

[6] Lucić, R., Jurić-Grgić, I., & Kurtović, M. (2010). Time domain finite element method analysis of multi-conductor transmission lines. *European Transactions on Electrical Power*, *20*, 822-832.

[7] Jurić-Grgic, I. Lucic, R., & Krolo, I. (2019). Improving time integration scheme for FEM analysis of MTL problems. *International Journal of Wiley journal Circuit Theory and Applications*, *47*, 1800-1811.

Two-Phase Gas-Liquid Flow through a Venturi Tube, an Experimental Study

Ammar Zeghloul[1], Zouhira Hireche[2], Lyes Nasseri[3]

[1,2,3]Laboratory of Multiphase Flows and Porous Media, University of Sciences and Technology Houari Boumediene, FGMGP, BP 32 El Alia 16111 Bab Ezzouar, Algiers, Algeria

[1]National Polytechnic School, BP 182, El Harrach, 16200, Algiers, Algeria

Abstract—**This paper highlights the measurement results of air-water two-phase flow by means of a Venturi meter. The presented device can be applied within a continuous and accurate measurement of the gas-liquid mass flow rate with no need for a phase separator. The effect of the Venturi geometry on the flow behaviour was evaluated by using three different Venturis with inlet to throat diameter ratios of 0.40, 0.55 and 0.75, respectively, placed in a vertical air-water test section. The void fraction time series were measured along the test section by nine different electrical conductance sensors covering the converging, throat and diverging sections. The void fraction measurement along the Venturi (before, at the throat, and after) showed that the void fraction after the Venturis throat with a bigger diameter ratio appears to quickly restore itself when compared to that of a lower diameter ratio. It is further found that the void fraction oscillation for all Venturi diameter ratios was uniquely located in the 10D area prior to and after the Venturi throat. The comparison of the experimental data with the two-phase mass flow rate models from the literature shows that the correlation given by Chisholm with a Venturi diameter ratio β=0.55, present the best accuracy among other correlations.**

Keywords - gas-liquid flow, venturi tube, pressure drop, electrical conductance probe

I. INTRODUCTION

The direct measurement of the mass flow of two-phase mixtures is an essential procedure in many sectors, such as chemical industry, power generation and oil and gas industries).

Controlling and improving oil production at wellbore sites and continuous monitoring of wells requires real-time measurement of multiphase flow. The Venturi meter is extensively used in the oil and gas industry to measure flow in single-phase flow systems. In particular, in gas well-being whether the well generates dry gas or wet gas with lower than 5% liquid [1].

The conventional procedure used in large petroleum industries is to separate the different phases and then measuring the flow rate of each phase separately. This technique involves costly and additional equipment and, in many circumstances, causes an interruption in the production line. In addition, this method is not convenient for offshore platforms due to the constraints of the operation area and the clutter of the machine parts. Nowadays, multi-phase flow meters are often used because of their high efficiency and small size. The Venturi meter is one of the most trusted devices used to measure multiphase mass flow. This choice is motivated by the cost, the form and design of the venturi tube, the absence of moving parts and lower causing pressure drop in comparison to other devices [2]. This small pressure drop is caused by the smooth dynamic profile in the venturi, which also enhances the pressure regeneration. The idea behind 2-phase flow metering is based on the relation between the mass flow rate of the mixture and the pressure drop. On-line mass quality measurement is a challenge. Thus, rather than focusing on the mass flow quality, a more practical approach is to focus on the measurement of the void fraction parameter [3]. The latter constitutes the main parameter to determine the mass flow rate of each phase.

The objective of this study is to investigate new experimental findings for air-water two-phase flow with venturis. The geometry of venturi has been considered with three different throat diameters. The hydrodynamic influence of the venturi on the flow behavior was assessed by embedding a series of conductance probes prior to, post and at the throat of the venturis. The implementation of conductance probes in the Venturis allows for real-time void fraction measurement, which is required in two-phase flow measurement.

II. Theoretical Overview

A. *Single and Two-Phase Flow Estimation*

Flow measurement by means of a Venturi tube is primarily driven from the differential pressure measurement of the flowing fluid between the Venturi inlet and the Venturi throat.

The flow rate can be calculated from the difference pressure measurement and the properties of the fluid and the geometrical characteristics of the Venturi meter. The mass flow rate of a single-phase flow through a venturi is linked to the differential pressure by the following equation [4]:

$$\dot{m}_{SP} = \frac{F_a Y C \pi d^2 / 4}{\sqrt{1-\beta^4}} \sqrt{2 \Delta P_{SP} \rho_{SP}} \quad , \qquad (1)$$

where F_a is the thermal expansion factor (F_a=1 for water); Y is the compressibility coefficient of the fluid (Y=1 for water); C is the discharge coefficient (depend on the Venturi geometry); *d* is diameter of the venturi throat; β is the Venturi diameter ratio; ΔP_{SP} is the measured pressure drop of the single phase fluid; ρ_{SP} is the single phase fluid density.

The single-phase flow correlation was reconfigured to fit two-phase flow forms by taking Eq. (1) and multiplying it by a factor K, which gives:

$$\dot{m}_{SP} = \frac{F_a Y C \pi d^2 / 4}{\sqrt{1-\beta^4}} \sqrt{2 \Delta P_{SP} \rho_{SP}} K \quad . \qquad (2)$$

In general, the K factor is dependent on the mass quality or the void fraction and the fluid densities, ρ_{SP} is the density of the liquid or gas phase (according to the correlation).

Many correlations have been suggested to predict the factor, K. The most widely reported correlations in the literature are presented in Table I.

B. *Estimation of the Mass Flow Quality*

The mass flow quality, x specifies the weight ratio of the gas phase to the total weight of the two-phase flow through the pipe, while the void fraction, α specifies the area covered by the gas over the cross-section of the pipe. The last is more convenient and measurable in two-phase flow with Venturis. The function between the mass quality and the void fraction is defined by:

$$x = \frac{1}{1 + \frac{\rho_L}{\rho_G} \frac{1}{S} \frac{1-\alpha}{\alpha}} \quad , \qquad (3)$$

where ρ_L and ρ_G are the density of the liquid and gas respectively; *S* is the slippage between phases and α is the void fraction.

C. *Estimation of the Slippage between phases*

The slippage, S, is defined as the ratio of the mean gas and liquid velocities, U_G and U_L , respectively. The slippage expression is defined as:

$$S = \frac{U_G}{U_L} \quad . \qquad (4)$$

Thus, the liquid and gas velocities U_G and U_L are linked to the surface velocities U_{GS} and U_{LS} by:

$$U_G = \frac{U_{GS}}{\alpha} \quad \textit{and} \quad U_L = \frac{U_{LS}}{(1-\alpha)} \quad . \qquad (5)$$

From (3), (4) and (5) the slip ratio can be arranged as shown in Table I:

TABLE I. CORRELATIONS OF TWO-PHASE FLOW COEFFICIENT.

Reference	Correlation
Homogeneous model	$$K=\sqrt{\frac{1}{x\left(\frac{\rho_L}{\rho_G}-1\right)+1}} \quad (6)$$
[5]	$$K=\frac{1}{x+1.26\,(1-x)\left(\frac{C_G Y_G}{C_L}\right)\sqrt{\frac{\rho_G}{\rho_L}}} \quad (7)$$
[6]	$$K=\sqrt{\frac{1}{x^{1.5}\left(1-\frac{\rho_G}{\rho_L}\right)+\frac{\rho_G}{\rho_L}}} \quad (8)$$
[7]	$$K=\left(\frac{1}{1-x}\right)\left[1+\left(\frac{\frac{1}{S}\sqrt{\frac{\rho_L}{\rho_G}}+S\sqrt{\frac{\rho_G}{\rho_L}}}{\left(\frac{1-x}{x}\right)\sqrt{\frac{\rho_G}{\rho_L}}}\right)+\left(\frac{1}{\left(\frac{1-x}{x}\right)^2\frac{\rho_G}{\rho_L}}\right)\right]^{-\frac{1}{2}} \quad (8)$$ For: $X \geq 1$ $$S=\left(1+x\left(\frac{\rho_L}{\rho_G}-1\right)\right)^{1/2} \quad (9)$$ For: $X < 1$ $$S=\left(\frac{\rho_L}{\rho_G}\right)^{1/4} \quad (10)$$ With: $$X=\frac{\sqrt{\Delta P_L}}{\sqrt{\Delta P_G}}=\left(\frac{1-x}{x}\right)\left(\frac{\rho_G}{\rho_L}\right)^{1/2} \quad (11)$$
[8]	$$K=\frac{1}{(1-x)\theta+x\sqrt{\frac{\rho_L}{\rho_G}}} \quad (12)$$ $$\theta = 1.48625-9.26541\,\gamma + 44.6954\,\gamma^2 - 60.6150\,\gamma^3 - -5.12966\,\gamma^4 - 26.5743\,\gamma^5$$
[9]	$$K=\sqrt{\frac{1}{x^n\left(\frac{\rho_L}{\rho_G}-1\right)+1}} \qquad n=1.25+0.26\,x^{1/3} \quad (13)$$
[10]	$$K=\sqrt{\frac{1}{c\left(\frac{\alpha}{1-\alpha}\right)^n\left(\frac{\rho_L}{\rho_G}\right)^m+1}} \qquad With:\ c=0.50,\ n=0.95,\ m=0.02 \quad (14)$$

III. EXPERIMENTAL SETUP AND THE METHODOLOGY

A series of two-phase flow experiments has been performed to study the two-phase air-water flows through the Venturi. Fig. 1 depicts the experimental test setup. The letter was the same experimental test facility used previously by [11,12].

Experiments were run by pumping tap water from the storage tank to the water rotameters by means of a centrifugal pump.

A series of monitoring valves upstream of the rotameters were operated to allow for water flow control. Pressurized air supplied by the compressor was initially conditioned by the pressure controller to nearly atmospheric pressure, and then the gas mass flow rate was obtained by controlling the air rotameters. The uncertainties of the air and water rotameters are less than 2% of the respective full scale. Air and water are mixed in the mixing device and generate the two-phase flow. Details on the mixing device are discussed by [12]. Following the mixer, the air-water mixture flows across the venturi tube through the vertical testing section, then across a 90° bend, a horizontal pipe, then another vertical 90° bend, and finally to the phase separator tank. Under gravity, the water flows back through the bottom of the tank then recirculated, while the air is discharged to the ambient.

The height of the test section is about 7 m with an inner diameter of 34 mm which is made of transparent acrylic resin material. Thus, the flow configuration and behaviour in the pipe can be observed (Fig. 2). The Venturi tube is placed 4.5 m upstream of the mixing device which is a sufficient length to consider flow pattern as fully developed. A total of nine conductance probes were mounted throughout the test section to collect time series of the void fraction. These conductance probes are are positioned as shown in Fig. 2.

Three venturis manufactured of polyvinyl chloride (PVC) were tested, which designed according to ISO 5167-4 [13]. These venturis are composed of three sections: the convergent, the throat and the divergent section. A pair of stainless-steel plate electrodes were used to measure the void fractions at the venturi throat. The pressure taps positions are considered in the designed venturi. According to ISO 5167-4 [13], the pressure taps are situated 1D and 0.5D before and after the converging section respectively. The geometric details of these venturis are presented in Table II.

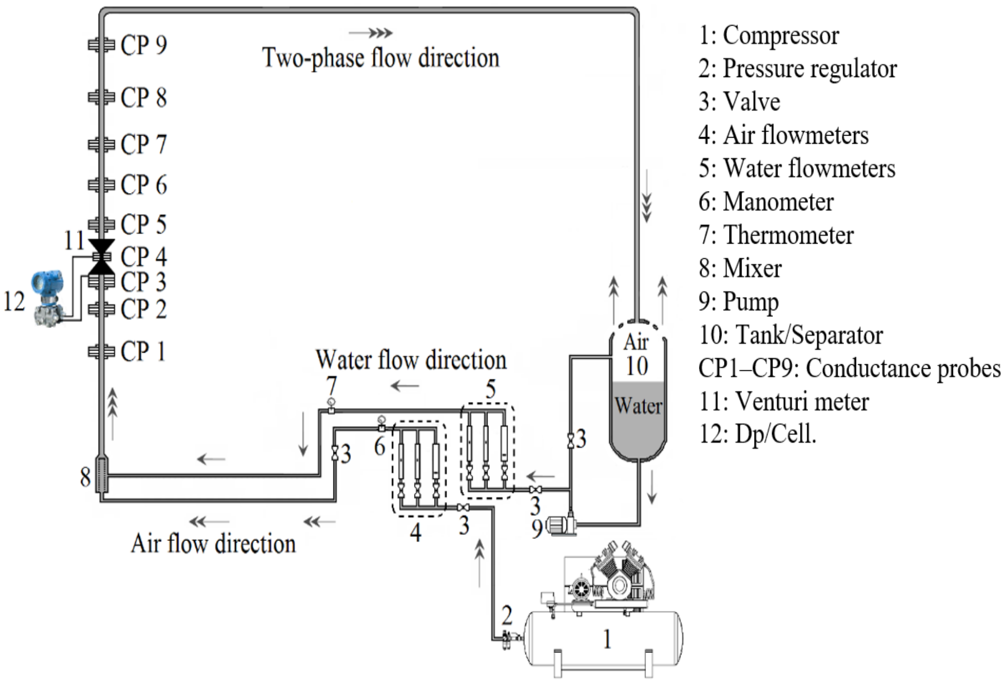

Figure 1. Schematic of the experimental test facility.

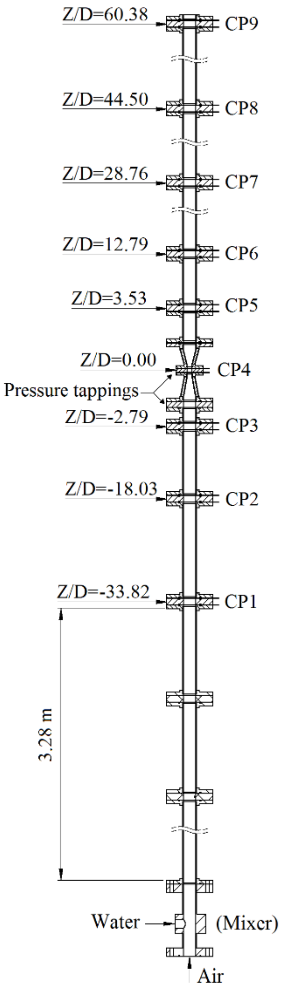

Figure 2. Schematic of the experimental test facility.

A. Flow Pattern

The gas and liquid flow conditions used for the experiments were found to be up to 3.5 m/s and 1 m/s respectively. Observations of the flow pattern through the test section showed three flow patterns, including bubbly, slug, and churn

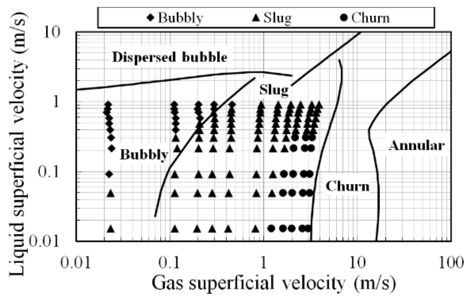

Figure 3. Flow pattern map of Shoham [14].

flows. As shown in Fig. 3, a number of 125 experimental data were displayed on the Shoham38 flow maps. It is worth noting that all 125 experimental conditions were used for each individual venturi tube.

B. Void Fraction Time Series

Fig. 4 illustrates sample time series of void fraction acquired through the test section for the venturi 1 (β=0.40). The time series of void fraction measured from the CP1 to CP9 in Fig. 4 (a), indicates that the flow is a bubbly flow. The void fraction taken from CP4 corresponds to the Venturi throat. One can see that the flow at the Venturi throat exhibits more turbulence, demonstrating more bubble coalescence as a result of flow acceleration.

Fig. 4 (b) shows the time series of the slug flow that is acquired from the nine conductance probes. The signals from the initial three probes (CP1 to CP3), correspond to the upstream of the Venturi, show the behavior of the slug flow, in which the signal show high values of the void fraction correspond to Taylor bubbles and lower values to liquid slug. The void fraction data extracted from CP5 (i.e., immediately following the Venturi throat) shown that there is a breakup of Taylor bubbles into smaller bubbles due to the effect of flow acceleration, this finding can be confirmed by the interrupted shape within the Taylor bubble signal. Furthermore, the Taylor bubbles returned to their original shape after approximately 30 D below the Venturi tube.

From Fig. 4 (c), the acquired signals from the conductance probes indicate that the flow is classified as churn. It is known that the churn flow can be distinguished by a chaotic character of the flow and a significant void fraction [15, 11]. Furthermore, the flow pattern from the probes shows a similar tendency. In addition, it can be noticed that the amplitude of the void fraction in the Venturi throat is less than the others (CP4). This could be due to the impact of the diverging section on the Venturi throat where there might be more liquid film falling into the Venturi throat, leading to a reduction in the void fraction.

C. Slippage Between Gas and Liquid Phases

The slippage coefficient, S, against the mixture velocity $U_m = U_{LS} + U_{GS}$ for the nine conductance probes is plotted in Figs. 5 (a)-(i).

According to these plots, it can be seen that the geometry of Venturi is found to affect the

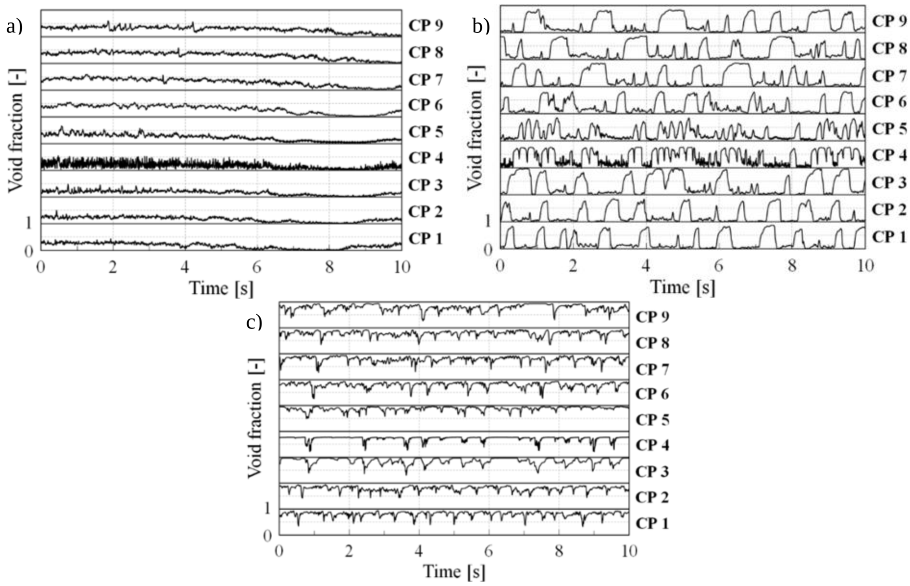

Figure 4. The time series from the conductance probes upstream and downstream of the Venturi 1.

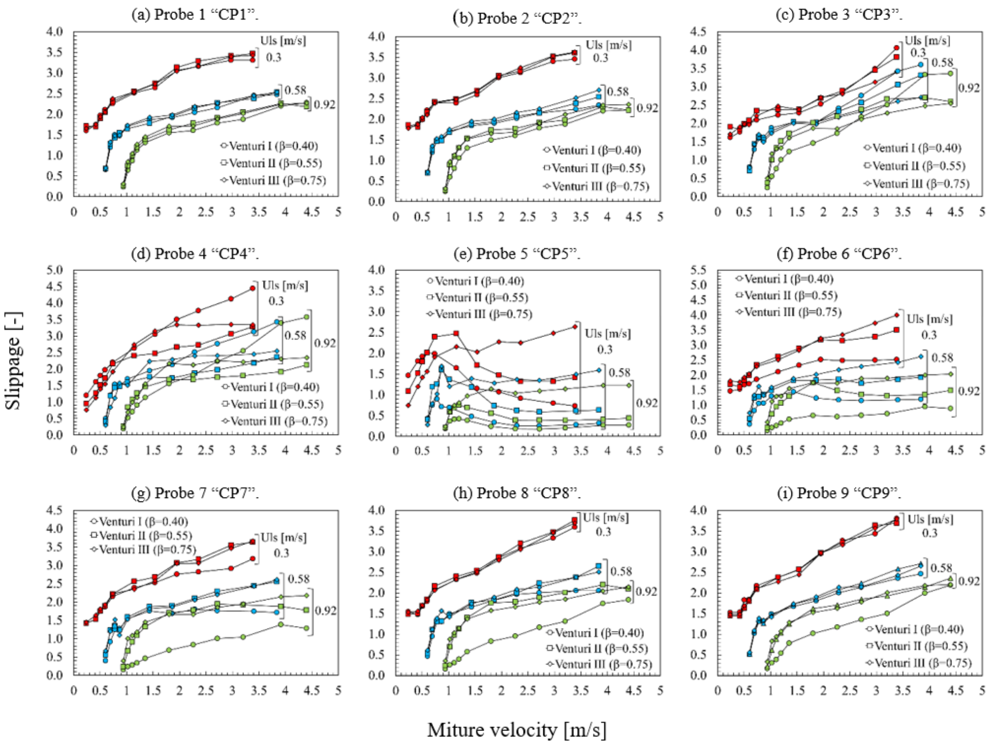

Figure 5. Slippage coefficient against the mixture velocity.

slippage for a given mixture velocity condition. The slippage profile upstream of the Venturi are clearly different from those downstream of the Venturi. Similarly, if we compare the trends in slippage with mixture velocity at CP1 to that downstream the Venturi, we can see that the

TABLE II. GEOMETRICAL DETAILS OF THE TESTED VENTURI.

Venturi	Throat diameter, d (mm)	Diameter ratio, β (-)	Convergent length (mm)	Throat length (mm)	Divergent length (mm)	Total Venturi length (mm)
1	13.60	0.40	55.03	13.60	97.05	205.58
2	18.70	0.55	41.28	18.70	72.79	173.56
3	25.50	0.75	22.93	25.50	40.44	128.87

slippage curves begin to return to their initial trends from CP7 and beyond. For the CP4 probe (positioned in the Venturi throat), and for every liquid superficial velocity condition, it can be seen that the slippage trends are different for the four Venturi and that it decreases with increasing liquid superficial velocity. At low to medium mixing velocity, the slippage is increased mono-functionally. At the fifth probe CP5 and with a liquid velocity of 0.58 m/s, the slippage is approximately unity over a large mixing velocity range, thus showing a good homogenizing effect of the Venturi at this location. Even more downstream, at the sixth probe CP6, at medium to high mixture velocity, the slippage becomes mostly regardless of the mixture velocity and exhibits a strong homogenization effect at a liquid superficial velocity of 0.92 m/s especially for the Venturi 1 where the slippage is nearly equal to unity.

From the previous analysis, it is clear that the homogenizing phenomenon will require a minimum liquid velocity of approximately 0.58 m/s (in the current investigation) to take place, and therefore the location of good homogeneity will be dependent on this critical velocity as well as on the Venturi throat section.

D. *Evaluation of the Two-Phase Mass Flow Correlations*

To quantify the discrepancy between both experimental data and those from the two-phase mass flow correlations synthesized in Table II, the root mean square (RMS) and the average relative absolute error (ABE) were both computed as indicated in Eqs. (15) and (17).

$$\mathrm{RMS}=\sqrt{\frac{1}{n}\sum_{i=0}^{n}\left[\frac{K_{i,calculated}-K_{i,measured}}{K_{i,measured}}\right]^2}\ , \quad (15)$$

$$x_i=\frac{\left|K_{i,calculated}-K_{i,measured}\right|}{K_{i,measured}}\ , \quad (16)$$

$$\mathrm{ABE}=\frac{1}{n}\sum_{i=0}^{n}x_i\ , \quad (17)$$

where $K_{i,calculated}$ is the predicted two-phase flow coefficient and $K_{i,measured}$ is the experimental two-phase flow coefficient.

Table III provides a synthesis of the computed RMS and ABE obtained for the theorical correlations as well as the homogeneous model. The correlation of [7] yields to the smallest deviation value for the Venturi with a diameter ratio of 0.55 which matches the RMS and ABE of 8.17% and 5.29%, respectively. Furthermore, acceptable accuracy was achieved for the Venturi in diameter ratio of 0.4 corresponding to the RMS and ABE of 15.71% and 12.50% respectively. The correlation of [6] resulted in best RMS and ABE accuracy for the Venturi diameter ratio of 0.75 corresponding to 16.58% and 11.88%, respectively. It is worth noting that the matching errors for β=0.4 and β=0.75 are still regarded as being acceptable in the context of two-phase flow metering.

TABLE III. CALCULATED RMS AND ABE (%) FOR TWO-PHASE MASS FLOW RATE.

	RMS (%)			**ABE (%)**		
	Venturi I (β=0.4)	***Venturi II (β=0.55)***	***Venturi III (β=0.75)***	***Venturi I (β=0.4)***	***Venturi II (β=0.55)***	***Venturi III (β=0.75)***
Homogeneous	28.15	25.01	39.87	22.07	19.39	34.77
Murdock [5]	18.25	13.93	22.53	14.42	11.42	20.41
James [6]	30.40	30.25	16.58 *	25.42	27.21	11.88*
Chisholm [7]	15.71*	8.17*	26.77	12.50*	5.29*	23.58
Lin [8]	20.01	16.24	31.89	17.65	13.85	30.59
Zhang et al. [9]	20.47	18.02	20.71	17.86	15.85	14.33
Zhang et al. [10]	23.80	13.03	19.63	19.18	10.44	15.85

*Best accuracy.

IV. CONCLUSIONS

A comprehensive void fraction measurement along the Venturi (before, at the throat, and after) showed that the void fraction after the Venturis throat with a bigger diameter ratio appears to quickly restore itself when compared to that of a lower diameter ratio. It is further found that the void fraction oscillation for all Venturi diameter ratios was uniquely located in the 10D area prior to and after the Venturi throat. Evaluation of the models in the literature also indicated that the versions that include the slippage are more effective than the models that ignore the slippage effect. Hence, the slippage is a highly relevant parameter to be taken into consideration for each correlation in the two-phase mass flow calculation by Venturi tube. The findings also showed that the correlation of [7] gives better accordance with the actual experimental data for smaller diameter ratios and the correlation of James shows good accordance with the experimental data for the larger diameter ratio.

REFERENCES

[1] Arsalan, M., Ahmad, T. J., Black, M. J., & Noui-Mehidi, M. N. (2015, November). Challenges of permanent downhole water cut measurement in multilateral wells. In *Abu Dhabi International Petroleum Exhibition and Conference*. OnePetro.

[2] [2] Huang, Z., Xie, D., Zhang, H., & Li, H. (2005). Gas–oil two-phase flow measurement using an electrical capacitance tomography system and a Venturi meter. *Flow measurement and Instrumentation*, *16*(2-3), 177-182.

[3] Hasan, A., & Lucas, G. (2009). Modelling and Measurement of the Gas Flow Rate in Vertical Annular Gas-Water Flow Using a ‘Conductance Multiphase Venturi meter’.

[4] Oliveira, J. L. G., Passos, J. C., Verschaeren, R., & Van Der Geld, C. (2009). Mass flow rate measurements in gas–liquid flows by means of a venturi or orifice plate coupled to a void fraction sensor. *Experimental Thermal and Fluid Science*, *33*(2), 253-260.

[5] Murdock, J. W. (1962). Two-phase flow measurement with orifices. *J. Basic Eng.*, *84*, 419-433.

[6] R, James (1965). Metering of steam-water two-phase flow by sharp-edged orifices. *Proceedings of the Institution of Mechanical Engineers*, *180*(1), 549-572.

[7] D. Chisholm. (1983). Two-Phase Flow in Pipelines and Heat Exchangers, Longman Gr. London: G. Godwin in association with Institution of Chemical Engineers.

[8] Lin, Z. (1982). Two-phase flow measurements with sharp-edged orifices. *Int. J. Multiph. Flow*. *8*, 683-693.

[9] Zhang, H. J., Lu, S. J., & Yu, G. Z. (1992). An investigation of two-phase flow measurement with orifices for low-quality mixtures. *International journal of multiphase flow*, *18*(1), 149-155.

[10] Hong-jian, Z., Wei-ting, Y., & Zhi-yao, H. (2005). Investigation of oil-air two-phase mass flow rate measurement using Venturi and void fraction sensor. *Journal of Zhejiang University-SCIENCE A*, *6*(6), 601-606.

[11] Zeghloul, A., Azzi, A., Saidj, F., Azzopardi, B. J., & Hewakandamby, B. (2015). Interrogating the effect of an orifice on the upward two-phase gas–liquid flow behavior. *International Journal of Multiphase Flow*, *74*, 96-105.

[12] Zeghloul, A., Azzi, A., Hasan, A., & Azzopardi, B. J. (2018). Behavior and pressure drop of an upwardly two-phase flow through multi-hole orifices. *Proceedings of the Institution of Mechanical Engineers, Part C: Journal of Mechanical Engineering Science*, *232*(18), 3281-3299.

[13] International Organization for Standardization. (2003) .Measurement of fluid flow by means of pressure differential devices inserted in circular cross-section conduits running full — Part 4: Venturi tubesitle,” *ISO 5167-4*.

[14] O. Shoham. (2006). Mechanistic Modelling of Gas–Liquid Two-Phase Flow in Pipes. USA.

[15] Costigan, G., & Whalley, P. B. (1997). Slug flow regime identification from dynamic void fraction measurements in vertical air-water flows. *International Journal of Multiphase Flow*, *23*(2), 263-282.

Identifying the Multidimensional Energy Literacy Levels of Elementary School Students of Kerala, India: A Measure of Knowledge, Attitude and Behaviour

Annie Feba Varghese[1] Divya Chandrasenan[2]

[1,2]Department of Education, University of Kerala, India

Abstract—**Only by understanding what energy is, which are its sources and production processes, ways of use and conservation strategies, it is possible to make informed decisions about the best use of energy. However, knowledge alone does not determine a more conscious use of energy. It is necessary that people be able to translate this knowledge into concrete actions. Energy literacy is an important tool that empowers individuals, allowing them to make better decisions concerning energy. Energy literacy encompasses broad content knowledge as well as affective and behavioral characteristics empowering people to make appropriate energy-related choices. Energy Literacy of elementary school students of Kerala was measured with an Energy Literacy Questionnaire (ELQ). Results indicate that the students have a low level of cognitive scores (cognitive subscale mean of 39.43% of the maximum attainable score) but have relatively higher scores for affective subscale (72.95% of the maximum) and behavioral subscales (68.31% of the maximum). This indicates that though the students may lack the knowledge about energy aspects there is a positive attitude towards the use of energy which is reflected in their behavioral scores as well. The knowledge, attitude and behaviour domains of Energy Literacy are correlated, with the attainment level of one influencing the other. The correlations co-efficient (0.51, 0.65 and 0.59) between the knowledge and attitude subscales, knowledge and behavioral subscale and attitude and behaviour subscale respectively indicate that the domains are related to each other and enhancement in one affects the other. These findings necessitate enhancing Energy Literacy by reorganizing the formal and non-formal education of students by emphasizing on content knowledge as well as attitude and behaviour.**

Keywords - energy literacy, knowledge, attitude, behaviour, elementary

I. Introduction

Energy Literacy is an awareness of the nature and role of energy in the world and in our daily lives, as well as the capacity to apply this knowledge to our daily lives in order to solve energy-related problems [1]. It is the capacity to have access to energy and make prudent use of it. Literacy denotes knowledge or skill in a specific area, but Energy Literacy takes into account an individual's Knowledge, Attitude, and Behavior [2]. Historically, the primary energy sources have been primarily petroleum, coal, and natural gas. The use of these fuels irresponsibly has resulted in climate change and the accompanying increase in global temperature [3]. National Oceanic and Atmospheric Administration reports indicate that the annual global temperature has risen by an average of 0.18°C (0.32°F) per decade [4]. Existence of the human species requires an immediate transition to renewable energy sources such as biomass, solar, wind, geothermal, and hydropower, as well as energy conservation.

II. Need and Significance

Energy education focuses primarily on all of these aspects, and energy-literate citizens appear to be the only path out of the current energy crisis. India is the third-largest consumer of electricity in the globe and is developing methods to meet its ever-increasing demand for it. Considering the aforementioned factors, it is evident that energy literacy and a positive attitude towards energy conservation are the only ways to combat this crisis. Conscious steps can be taken to include energy literacy in the citizen's right from the earliest phases of development, which can be most effectively addressed by introducing energy education in elementary school. Individual behaviour is a crucial component of sustainability, as evidenced by the rise in individual energy consumption and greenhouse gas emissions from residential households. Energy literacy encompasses the cognitive (knowledge, understanding, skills), affective (sensitivity, attitudes), and behavioral (intention, participation, action) acquisitions of individuals in regards to energy [5,6]. In order to envision a society with a high level of energy literacy, it is necessary to know the energy literacy level of the subjects under consideration. Due to the paucity of research on energy literacy in India, it was necessary to devise a tool for measuring energy literacy and determining where the average Indian student stands on the energy literacy scale.

III. Materials and Methods

A. Tool

With the understanding that Energy Literacy involves the individual's Cognitive (Knowledge), Psychomotor (Behavior), and Affective domains, an Energy Literacy Questionnaire has been designed to test elementary school pupils' energy literacy. Through an elaborate review of existing energy education and cognitive/ attitude/ behaviour research and studies, the construct definition and measurement criteria were developed [2]. The general criteria for energy literacy were defined based on essential principles and concepts put forward by Department of Energy, USA. Cognitive items were formulated into five-option multiple choice questions with one correct answer choice. Affective and behavioural scales were constructed using a variation of the Summated Ratings Method used by Likert, with a five-part response format that included one neutral option. Positive or favorable statements were given scores 5,4,3,2,1 for Strongly Agree, Agree, Undecided, Disagree, Strongly Disagree respectively and negative or unfavorable statements were scored in the reverse order. The Energy Literacy Questionnaire suitable for use with elementary school students as developed, covers all the critical benchmarks that define energy literacy was standardized for validity and reliability.

TABLE I. Summaries, item analysis.

	Knowledge	**Attitude**	**Behavior**
N	303	303	303
Average Item Difficulty	0.40	–	–
Average Discrimination index	0.43	0.35	0.28
Reliability	0.67	0.68	0.78

The final version of the Energy Literacy Questionnaire included 49 questions, 19 of which belonged to the “cognitive” subscale, 10 to the “attitude,” and 20 to the “behavioral” subscale. Table I reveals that the average item difficulty on the cognitive scale was 0.40, while the discrimination indices for the behavioral and affective subscales were 0.28 and 0.35, and the subscale’s reliability was calculated to be 0.67, 0.68 and 0.78 for the cognitive, attitude and behaviour subscales respectively.

B. Sample, Data Collection and Analysis

The sample comprised of 303 students from various elementary schools in Kerala. The sample was given the questionnaire, and their responses were collected. The item responses were converted into numeric scores based on their respective subscale. Each correct answer was worth one point, while each erroneous or blank response was worth zero points. To calculate rating sums for each subscale, Likert-type responses on the affective and behavioral subscales were converted to numeric values according to a predetermined preferred direction of response, with values ranging from 1 (least preferred response) to 5 (most preferred response). The 16th version of the Statistical Package for the Social Sciences (SPSS) was used to conduct statistical analyses.

The descriptive results regarding the students’ scores with respect to Energy Literacy and the constituent subscales are given in Table II.

TABLE II. DESCRIPTIVE RESULTS REGARDING THE STUDENTS' ENERGY LITERACY SCALE SCORES.

Scale /Subscale	Energy Literacy	Knowledge	Attitude	Behaviour
Mean	60.23%	39.43%	72.95%	68.31%
Median	59.28%	36.84%	72.0%	68.0%
Mode	52.35%	36.84%	68.0%	65.0%
Standard Deviation	24.4	1.20	9.05	8.17
Skewness	0.09	-0.10	-0.11	0.03
Kurtosis	-0.59	-0.94	-0.49	-0.45

The values given in Table II shows that the mode median and arithmetic mean have values that are close to each other. In addition, when the kurtosis and skewness values are examined, it is observed that these values are between -2 and +2. In this case, it can be stated that the data show a normal distribution [7]. The total average score of the students for the scale was 60.23 %. It was concluded that the energy literacy level of students was moderate.

IV. COMPOSITION OF THE INDICATORS OF ENERGY LITERACY

A. Scores of Energy Knowledge

The average cognitive scores of the students were discouragingly low as seen from Table II. The energy-related knowledge of the students seems very low which indirectly points out the fallings of the energy education imparted to the students. The students are not even able to reach the average level of 50% which is a call to revise the methods of teaching and revision of curriculum with respect to energy to meet the need of the hour. Detailed examination of the scores indicated that the students knew the basic concepts of energy like sources and types but were missing on higher concepts mainly.

B. Scores of Attitude Towards Energy

The average attitude scores of the students are much better than cognitive or behavioral scores (Table II), indicating that the students generally accept that energy crisis and problems exist and accept the need to conserve it. An average score of 72.95 % indicates a positive attitude of students towards wise and prudent use of energy and increased awareness of the urgency of our energy problems.

C. Scores of Behaviour Towards Energy

An average score of 68.31 % indicates a positive behaviour of students. The findings suggest that the students are adopting habits that help in conserving energy. The students did report that they were more likely to put into practice ways of saving and conserving energy in their homes than in school.

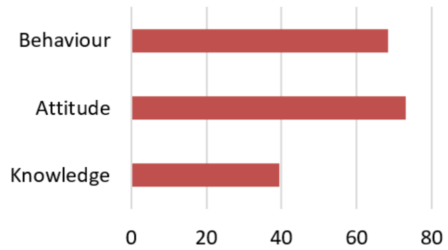

Figure 1. Overview of Energy Literacy Score with respect to each indicator.

A graphical representation of the extent of energy literacy score with respect to knowledge, attitude and behaviour is shown in Fig. 1.

V. RELATIONSHIP BETWEEN COGNITIVE, AFFECTIVE, AND BEHAVIORAL ASPECTS OF ENERGY LITERACY

One of the main objectives of energy education is to create favorable attitudes towards energy conservation and to strengthen students' critical thinking and decision-making skills. This is because energy literacy comprises not just knowledge but also attitudes, values, decisions, and actions. Studies demonstrating improvements in energy-related behaviors following participation in educational programs, such as those by [8,9], frequently involve initiatives that emphasize a change in students' values, beliefs, and attitudes through the use of pertinent projects, case studies, decision-making exercises, and action strategies. Energy literacy encompassing the cognitive (knowledge, understanding, skills), affective (sensitivity, attitudes), and behavioral (intention, participation, action) acquisitions of individuals in regards to energy is influenced by the nature of attainment in each of these individual domains. The acquisitions in the individual domains are correlated to each other which is apparently reflected in the total energy literacy score. Intercorrelations between average cognitive, affective and behavioral, subscale scores are summarized in Table III.

TABLE III. INTERCORRELATIONS BETWEEN AVERAGE COGNITIVE, AFFECTIVE AND BEHAVIORAL, SUBSCALE SCORES.

Inter-correlation between	**Pearson Correlation coefficient**
Knowledge and Attitude subscale	0.51
Knowledge and Behavioral subscale	0.65
Attitude and Behavioral subscale	0.59

Pearson correlation coefficient value: ± 0.50 and ± 1(strong correlation), ± 0.30 and ± 0.49 (medium correlation) and < ±. 29 (small correlation)

The inter-correlations are all significant between the subscales as seen in Table III. The positive and high values of the correlation values obtained clearly indicates a strong positive correlation between the domains which implies that an increase in the knowledge of the students determines to change the attitude and behaviour of the students in a positive manner. The results described in this study tend to suggest that the Indian educational system could be doing more by revising their curriculum to increase knowledge related to energy to impact student attitudes toward energy issues, which may in turn help improve their conservation behaviour.

VI. DISSCUSSION

Numerous studies on elementary school students' energy literacy have focused on their knowledge, attitudes, and behaviour regarding energy use and conservation. In a study conducted in the United States, researchers used a pre- and post-test design to evaluate the energy literacy of fourth and fifth grade students. After participating in a six-week energy curriculum that focused on energy sources, energy use, and conservation strategies, students' energy literacy significantly increased. The study also found that after completing the curriculum, students were more likely to engage in energy-saving behaviour at home. Students had a rudimentary understanding of energy sources, but lacked knowledge of energy efficiency and renewable energy, according to a study of the energy literacy of Turkish elementary school students. The study also revealed that students had favorable attitudes towards energy conservation and were willing to take measures to conserve energy.

In a study conducted in Canada, researchers developed a set of energy literacy indicators for elementary school pupils and assessed their knowledge, attitudes, and behaviour regarding energy use and conservation. The study revealed that students had a strong grasp of energy sources and fundamental energy concepts, but lacked knowledge regarding energy efficiency and renewable energy. The study also revealed that students had favorable attitudes towards energy conservation and were willing to take measures to conserve energy. This current study also demonstrates that elementary school students have a moderate level of energy literacy but a discouragingly low level of knowledge-based energy literacy.

In accordance with the findings of a study conducted by Dewaters & Powers on energy literacy, the degree of literacy in terms of attitude and behaviour is comparatively higher than the knowledge scores [10]. Low levels of theoretical knowledge and awareness of the effects of energy consumption on societies and the environment were reported [11]. These findings highlight the need for enhanced energy education programmes in schools, with a broader focus on current events and practical issues, such as how we use energy in our daily lives. A similar study of energy literacy among nursing students in Taiwan found high correlations between students' energy-related knowledge, attitude, and behavior [6]. However, an earlier study by the same researchers on high school students found a significant discrepancy between students' attitude and their behaviour. These findings suggest that effective educational programmes should target not only content knowledge, but also the attitudes, beliefs, and values of students.

The energy curriculum should be hands-on, inquiry-based, and experiential, providing students with the opportunity to learn about real-world issues while engaging in activities that are relevant to their own lives. Thus, energy-related education that can hone students' energy literacy and synergize its domains need to develop to improve students' energy literacy.

VII. Conclusion

Overall, these studies indicate that elementary school students have a fundamental comprehension of energy sources and energy conservation, but may be lacking in knowledge of energy efficiency and renewable energy. However, providing students with energy education and encouraging them to engage in energy-saving behaviours can increase their energy literacy and encourage them to be more environmentally responsible.

Acknowledgment

The work was financially supported by Indian Council for Social Science Research (No. RFD/21-22/Short-Term/GEN/15), funded by Ministry of Education, Government of India. The findings and opinions presented here do not necessarily reflect the opinions of the funding agency.

References

[1] U. S Department of Energy (2011). *Energy Literacy: Essential Principles for Energy Education.* Available at: https://www.energy.gov/eere/education/energy-literacy-essential-principles-energy-education

[2] DeWaters, J., & Powers, S. (2013). Establishing measurement criteria for an energy literacy questionnaire. *The Journal of Environmental Education*, *44*(1), 38-55.

[3] Lindsey, R., & Dahlman,L.(2022). *Climate Change: Global Temperature. NOAA's National Centers for Environmental Information. National Oceanic and Atmospheric Administration*, USA. Available at: https://www.climate.gov/news-features/understanding-climate/climate-change-global-temperature.

[4] NOAA National Centers for Environmental Information (2022). *Monthly Global Climate Report for Annual2021.* Available at: https://www.ncei.noaa.gov/access/monitoring/monthly-report/global/202113.

[5] Lay, Y. F., Khoo, C. H., Treagust, D., & Chandrasegaran, A. (2013). Assessing secondary school students' understanding of the relevance of energy in their daily lives. *International Journal of Environmental and Science Education*, *8*(1), 199-215.

[6] Lee, L. S., Lee, Y. F., Altschuld, J. W., & Pan, Y. J. (2015). Energy literacy: Evaluating knowledge, affect, and behavior of students in Taiwan. *Energy Policy*, *76*, 98-106.

[7] George, D., & Mallery, M. (2003). Using SPSS for Windows step by step: a simple guide and reference. (4th ed.). London: Pearson Education.

[8] Volk, T. L., & Cheak, M. J. (2003). The effects of an environmental education program on students, parents, and community. *The Journal of Environmental Education*, *34*(4), 12-25.

[9] Zografakis, N., Menegaki, A. N., & Tsagarakis, K. P. (2008). Effective education for energy efficiency. *Energy Policy*, *36*(8), 3226-3232.

[10] DeWaters, J. E., & Powers, S. E. (2011). Energy literacy of secondary students in New York State (USA): A measure of knowledge, affect, and behavior. *Energy policy*, *39*(3), 1699-1710.

[11] van den Broek, K. L. (2019). Household energy literacy: A critical review and a conceptual typology. *Energy Research & Social Science*, *57*, 101256.

Optimization of Some Physical Properties of a New Solar Cell Structure based CIGS and CZTSe Absorber Layers Study: A Numerical Simulation

Naceur Selmane[1], Feriha Afrah Boukhelkhal[2], Ali Cheknane[3], Fakhereddine Khemloul[4]

[1,2,3]Electronic Department, Laghouat University, Laghouat, Algeria
[4]Physics Department, Laghouat University, Laghouat, Algeria

Abstract—**CuInGaSe (CIGS) based solar cells are promising, but involve costly and hazardous and costly indium element. This work aims at solving these problems, without sacrificing the benefits of CIGS systems. The approach is to use thinner CIGS layers. However, very thin layers minimize absorption and lower cell performance. Adding a second CuZnSnSe (CZTSe)-layer absorber should maintain high cell performance. The new proposed cell that has been simulated is MgF2/ZnO/Al/ZnO:i/CdS(n)/CZTSe(p)/CIGS(p)/ Mo, with MgF2 antireflection layer, ZnO:i passivating layer, CdS emitter layer, CZTSe/CIGS double absorber layer, ZnO-Al transparent conductor oxide(TCO) and element almolybdenum (Mo) back contact. TCAD SILVACO using ATLAS module has been used in the simulation. Various parameters, including layer-thickness and doping-concentration, are optimized,. The results show that increasing the one-absorber CIGS-layer thickness by 2.5-fold, increases conversion efficiency from 22.3 to 24.3% only, which does not justify the extra costs. Alternatively, efficiency improves from 22.40 to 29.22% by adding CZTSe to a thin 1.0 µm CIGS layer. In conclusion, the study highlights the added value for the second-absorber layer.**

Keywords - CIGS, CZTSe, solar cell, optimization, absorber layer, thickness

I. INTRODUCTION

Solar energy is green and sustainable, as long as the Sun exists. Therefore, extensive efforts are devoted to solar energy technology, specifically in thin-layer p-n photovoltaic cells. Binary cells, such as metal chalcogenides [1,2], ternary cells e.g. CIS [3,4] and quaternary cells [5,6] are paramount areas of photovoltaic research. In this work, the electrical properties of new thin-film solar cells, using Cu2ZnSn(S, Se) 4 (written here as CZTSe) and Cu(In, Ga)Se2 (written here as CIGS), as combined absorbent layers, are simulated. CdS is used as the emitter layer, and experimentally electrodeposited ZnO-Al as TCO [7,8]. Effect of inserting CZTSe, as an additional absorber layer to a thin CIGS layer, on cell performance is the focal issue. The goal of the study is three-fold: firstly, using smaller CIGS layer thickness to minimize the drawbacks described above, namely high cost of indium element and its hazardous effects to environment. This is for future practical purposes. Using thinner CIGS layer lowers the negative impact on the environment especially in case of wide-spreading applications of CIGS. With lower layer thickness, cost saving will surely be achieved as well. Cu, Zn and S elements are being used in the added CZTSe at the expense of the CIGS layer thickness. Secondly, studying the effects of various parameters, including thickness and doping concentration, for different layers, with special focus on the two absorber layers, without sacrificing the benefits of CIGS systems themselves. Thirdly, to design a new solar cell, based on combined CZTSe and CIGS with efficiency significantly higher than earlier reported, for future applications [9].

II. STRUCTURE AND SIMULATION DETAILS

The simulation has beenmade with the environment of TCAD SILVACO using Atlas module. It is a very useful two-dimensional component modelling simulator [10] with the ability to predict the electrical characteristics of most semiconductors. In addition to external electrical properties, the software gives information about the internal distributions of variables such as lines of current, electric field and potentials. This is achievable by numerically solving the Poisson equation together with the continuity equations of electrons and holes at a finite number of points forming the structure mesh defined by the program. All materials properties involved in the present solar cell are defined. The cell involves an array of thin semiconductor layers of MgF_2/ZnO/ZnO:i/n-CdS/p-CTZS/p-CIGS/Moto simulate by TCAD Silvaco-Atlas. The complete device structure is schematically shown in Fig. 1. In the present study, molybdenum element (Mo) is used here as back contact, CIGS and CZTSe as two absorber layers, CdS as a buffer layer, undoped ZnO:i as an intrinsic layer, ZnO-Al as TCO, and MgF2 as antireflection coating (ARC) layer. The ZnO:i layer is intentionally included based on earlier literature. The highly resistive ZnO:i layer furnishes field-effect passivation. As reported earlier, this enhanced the power conversion efficiency from 11.0 to 12.1% [11]. In search to find highest performance cells, the passivation layer has been included here. All optical parameters used have been extracted from earlier reports. AM1.5 radiation, with power density of 1000 W/m^2, is employed as an illumination source in the simulation and all physical parameters for each layer are presented below in Table I.

III. RESULTS AND DISCUSSIONS

A. *One-absorber Layer (CIGS)*

The conventional ZnO-Al(TCO)/ZnO (i)/CdS/CIGS/Mo structure, with no CZTSe second layer or (MgF2) ARC layer, are simulated first. The ZnO-Al (TCO) layer inserted here is obtained by electrodeposition. The physical parameters for each layer are presented above in Table1. The CIGS absorber layer thickness has been varied from 1.0 to 2.5 µm, keeping the CdS buffer layer thickness fixed at 0.05 µm. Effects of CIGS layer thickness on the cell parameters are summarized in Fig. 2. Fig. 2a-c show that cell performance values are improved with increased CIGS absorber layer thickness. Fig. 2b shows that both open circuit voltage (V_{OC}) and short-circuit current density (J_{SC}) reaches high values of 0.784 V and 39.7 mA/cm^2, respectively, with increasing absorber layer thickness to 2.5 µm. Fig. 2c shows that both fill factor (FF) and conversion efficiency (η) values continued to increase with increased CIGS layer thickness. Similarly, Fig. 2d shows increased quantum efficiency (QE) value with increased CIGS layer thickness.

The enhancement in cell performance by increased CIGS layer thickness still does not justify using higher thicknesses, by any means. For instance, when the layer thickness is more

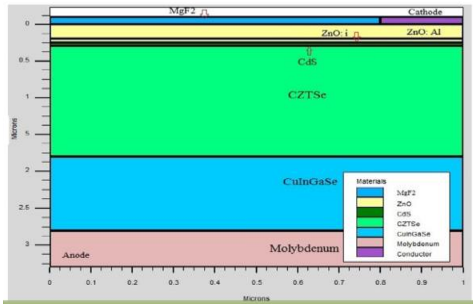

Figure 1. Solar cell structure simulated by TCAD Silvaco Atlas.

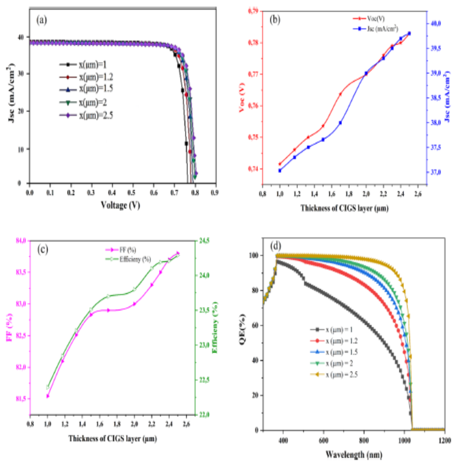

Figure 2. Effect of CIGS absorber monolayer thickness on ZnO(TCO)/ZnO:i/CdS/CIGS/Mo cell performance. (a) J-V plots, (b) Jsc &Voc, (c) Efficiency &FF, (d) Quantum efficiency vs. wave length plots.

TABLE I. MAJOR SIMULATION PARAMETERS EMPLOYED FOR VARIOUS LAYERS IN THE SOLAR CELL.

Layers properties	**Semiconductor type**				
	n-ZnO	***n-CdS***	***p-CZTSe***	***p-CIGS***	***ZnO:i***
Dielectric permittivity	10.000	10.000	13.600[13]	10.000	10.000
Thickness (μm)	0.2	Variable	Variable	Variable	0.05
Band gap(eV)	3.400	2.450	1.096	1.200	3.400
Electronic affinity (eV)	4.550	4.450	4.100	4.500	4.550
Effective conduction band density Nc (cm^{-3})	4×10^{18}	2×10^{18}	2.2×10^{18}	2×10^{18}	4×10^{18}
Effective conduction band density Nv (cm^{-3})	9×10^{18}	1.5×10^{19}	1.8×10^{19}	2×10^{18}	9×10^{18}
Electron mobility μ_n(cm^2/V.s)	5×10^1	5×10^1	5×10^2	5×10^1	5×10^1
Hole mobility μ_p (cm^2/V.s)	2×10^1	2×10^1	2.5×10^1	2×10^1	2×10^1
Doping concentration of donors N_d(cm^{-3})	5×10^{18}	1×10^{17} [13-15]	0	0	1.1×10^{18}
Doping concentration of acceptors N_a(cm^{-3})	0	0	5×10^{16} [16]	1×10^{15}	1.1×10^{18}

than doubled, from 1.0 to 2.5 μm, the conversion efficiency η exhibits increase from ~22.3 to ~24.3% only. Similarly, other cell parameter values increase but to a certain extent. The issue that arises is that enhancements in cell parameters do not justify higher thicknesses of the costly CIGS materials, notably indium and gallium. There should be another more feasible way to achieve higher performance, as described below.

B. Two-absorber Layers

The solution to the above issue is described here. If the cell performance can be increased, without hazards and higher cost inherited by higher CIGS layer thickness that should then be the best strategy. Using thinner CIGS layer, and low-cost CZTSe layer as another additional adsorbent, could be the way out to achieve higher cell performance without cost increase. The CIGS layer thickness of 1.0 μm is used here based on literature [12].

Simulation studies of the proposed two-absorber layer cell are shown here. Optimizing various parameters of the solar cell components to yield highest performance is paramount.

C. Effects of CdS and CZTSe Layer Hicknesses

The default thicknesses for CZTSe and CIGS layers are 1.5 and 1 μm, respectively, with total thickness of 2.5 μm used in the simulation, CdS emitter layer thickness is assessed here. The CdS emitter layer thickness values in the range 0.05 to 0.5 μm have been used, as described in Fig. 3. Other optimal parameter values for other remaining layers have been kept unchanged. All cell performance parameters, J-V plots, V_{OC}, J_{SC}, FF and η, are higher with thinner CdS layer thickness. The thickness 0.05 μm yields the optimal conversion efficiency value of 25.88%, in congruence with earlier experimental studies [17] [13]. The FF decreases from 84.4% to 79.3% for CdS layer thicknesses 0.05 μm and 0.5 μm, respectively. The J_{SC} also decreases from 41.3 to 33.3 mA/$cm^2$with increased CdS emitter thickness. The results are justifiable. The CdS is n-type semiconductor has a bandgap energy (Eg) 2.3 eV that is higher than those of CIGS (p-type 1.2 eV) and CZTSe (p-type 1.0 eV).Thus. As the CIGS first absorber layer is responsible for converting photons into electron-hole excitons, the total absorber layer must have a high absorption, particularly in the visible. The band gap for the absorber layer material must be suitable to various incident wave lengths to maximize cell conversion efficiency. The two absorber layers of CIGS and CZTSe, with two different band gaps of 1.2 and 1.0 eV, respectively, are therefore useful, the CIGS thickness is kept to a minimal value to avoid unnecessary costs. In the optimization study of the CZTSe layer thickness here, the range 0.1 to 1.5 μm has been used in the simulation. Effect of CZTSe layer thickness on solar cell performance is examined, and the resulting J-V plots are described in Fig.4a. Fig. 4a and b show that the V_{OC} remains approximately constant at 0.79 V. That is because the V_{OC} is determined by the narrowband gap of CZTSe. The effect of absorber layer thickness on resulting J_{SC} has been reported in other types of heterojunction solar cells [18,19]. The FF value increases from 84% to 86.2% with the increasing CZTSe layer thickness, Fig. 4c. The conversion efficiency significantly changes from 19.3% (for 0.1 µm thickness) to 27.54% (for 1.5 µm). Measuring the quantum efficiency (QE), which helps understand solar cell performance at various incident wavelengths, has also been studied here. Fig. 4d shows improvement in quantum efficiency, at various wavelengths, with increased absorber layer thickness.

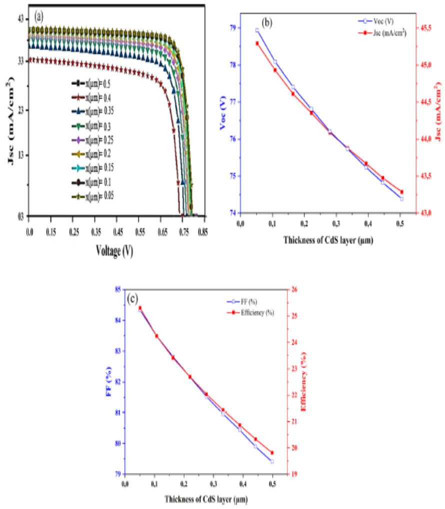

Figure 3. Effect of CdS buffer layer thickness on MgF_2/ZnO/ZnO:i/n-CdS/p-CTZS/p-CIGS/Mo solar cell (a) J-V plots,(b) J_{sc}&V_{oc}values, (b) FF & conversion efficiency values.

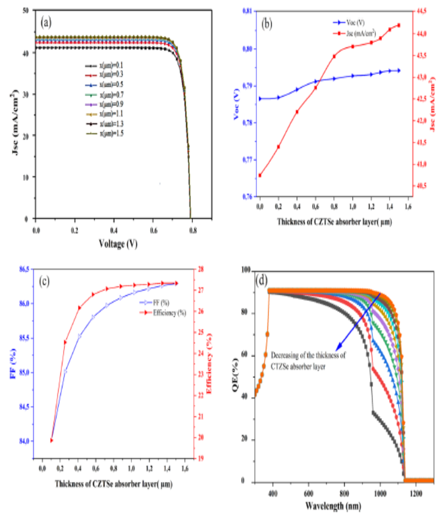

Figure 4. Effect of thickness of CZTSe absorber layer on the performance of the MgF2/ZnO/ZnO:i/n-CdS/p-CTZS/p-CIGS/Mo solar cell. a) J-V plots, b) JSC & VOC, c) Efficiency & FF, d) Quantum efficiency vs wave length plots.

Within wavelength range 300–1000 nm, the quantum efficiency value remains constant at 90%, with absorber layer thickness less than 1.0 µm. Additional response also occurs at 1150nm in the IR region, with thickness 1.15µm or higher.

IV. Conclusion

A solar cell of the type MgF_2/ZnO-Al/ZnO:i/n-CdS/p-CTZS/p-CIGS/ Mo involving two absorber layers CZTSe and CIGS has been simulated here using the SILVACO TCAD (ATLAS module) software.. CdS has been used as buffer layer, CZTSe/CIGS a double absorber layer and Mo as a back contact. MgF2 is used as anti-reflective coating (ARC) layer. Including CZTSe absorber layer here, with its abundant components, is to minimize thickness of costly CIGS layer, without sacrificing solar cell performance. Effects of layer thicknesses have been optimised to yield a solar cell with performance parameters of: efficiency 29.22%, V_{CO} 0.79 V, J_{SC} 43.5 mA/cm^2 and FF 85.7%.

References

[1] Laoufi, A. M., Dennai, B., Kadi, O., & Fillali, M. (2021). Study of the Effect of Absorber Layer Thickness of CIGS Solar Cells with Different Band Gap Using SILVACO TCAD. *Journal of nano- and electronic physics*, *13*(4).

[2] Moon, D. G., Rehan, S., Yeon, D. H., Lee, S. M., Park, S. J., Ahn, S., & Cho, Y. S. (2019). A review on binary metal sulfide heterojunction solar cells. *Solar Energy Materials and Solar Cells*, *200*, 109963.

[3] Ahmad, F., Anderson, T. H., Monk, P. B., & Lakhtakia, A. (2019). Efficiency enhancement of ultrathin CIGS solar cells by optimal bandgap grading. *Applied optics*, *58*(22), 6067-6078.

[4] Rasal, A. S., Chang, T. W., Korupalli, C., & Chang, J. Y. (2022). Composition engineered ternary copper chalcogenide alloyed counter electrodes for high-performance and stable quantum dot-sensitized solar cells. *Composites Part B: Engineering*, *232*, 109610.

[5] Benmansour, A. (2012). *Effect of CIGS thin layers on the efficiency of the photovoltaic cells with heterostructures.*

[6] Benmir, A., & Aida, M. S. (2013). Analytical modeling and simulation of CIGS solar cells. *Energy Procedia*, *36*, 618-627.

[7] Selmane, N., Cheknane, A., Aillerie, M., & Hilal, H. S. (2019). Effect of ZnO - based TCO on the

performance of a ‐ Si H (n)/a ‐ Si H (i)/c ‐ Si H (p)/Al BSF (p+)/Al heterojunction solar cells. *Environmental Progress & Sustainable Energy, 38*(4), 13114.

[8] Selmane, N., Cheknane, A., Gabouze, N., Maloufi, N., & Aillerie, M. (2017). Experimental study of optical and electrical properties of ZnO nano composites electrodeposited on n-porous silicon substrate for photovoltaic applications. In *E3S Web of Conferences* (Vol. 22, p. 00155). EDP Sciences.

[9] Heriche, H., Rouabah, Z., & Bouarissa, N. (2017). New ultra thin CIGS structure solar cells using SCAPS simulation program. *International Journal of Hydrogen Energy, 42*(15), 9524-9532.

[10] Selmane, N., Cheknane, A., Khemloul, F., Helal, M. H., & Hilal, H. S. (2022). Cost-saving and performance-enhancement of CuInGaSe solar cells by adding CuZnSnSe as a second absorber. *Solar Energy, 234*, 64-80.

[11] Li, H., Chen, J., Zhang, Y., Wang, W., & Gu, H. (2020). Efficiency enhancement of CIGS solar cells via recombination passivation. *ACS Applied Energy Materials, 3(*9), 9459-9467.

[12] Rezaei, N., Isabella, O., Vroon, Z. A. E. P., & Zeman, M. (2019). Optical optimization of a multi-layer wideband anti-reflection coating using porous MgF2 for sub-micron-thick CIGS solar cells. *Solar Energy, 177*, 59-67.

[13] Xu, J., Lin, J., & Zhuang, C. (2018). Analysis of the open-circuit voltage of Cu2ZnSn (S, Se) 4 thin film solar cell. *Solar Energy, 164*, 231-242.

[14] Ouédraogo, S., Zougmoré, F., & Ndjaka, J. M. (2013). Numerical analysis of copper-indium-gallium-diselenide-based solar cells by SCAPS-1D. *International Journal of photoenergy*.

[15] Parisi, A., et al. (2015). Graded carrier concentration absorber profile for high efficiency CIGS solar cells. *International Journal of Photoenergy, 2015*.

[16] Olopade, M. A., Oyebola, O. O., & Adeleke, B. S. (2012). Investigation of some materials as buffer layer in copper zinc tin sulphide (Cu2ZnSnS4) solar cells by SCAPS-1D. *Advances in Applied Science Research, 3*(6), 3396-3400.

[17] Muhammad, A. J., Salih, A. I., & Fadel, G. (2016). Numerical analysis of graded band gap CZT (S, Se) solar cells using AMPS-1D. *International Jurnal of Electrical Engineering, 4*(10).

[18] Saha, U., Biswas, A., & Alam, M. K. (2021). Efficiency enhancement of CZTSe solar cell using CdS (n)/(AgxCu1–x) 2ZnSnSe4 (p)/Cu2ZnSnSe4 (p+) structure. *Solar Energy, 221*, 314-322.

[19] Selmane, N., Cheknane, A. L. I., & Hilal, H. S. (2020). Optimization of al-doped ZnO transparent conducting oxide and emitter layers for enhanced performance of Si heterojunction solar cells. *Journal of Electronic Materials, 49*, 2179-2190.

Predicting GDP of a Country using Different Energy Measures based on Machine Learning Approach

Mohd Amiruddin Abd Rahman[1], Caceja Elyca Anak Bundak[2]

[1,2]Department of Physics, Faculty of Science, Universiti Putra Malaysia, UPM Serdang, Malaysia

Abstract—**Gross Domestic Product (GDP) is an important indication for every country in the world to determine the performance of its economy. However, it is unknown how different types of energy utilization affect different country's GDP. Here, we propose a machine learning based technique using optimized Support Vector Regression (SVR) algorithm to predict a country's GDP using different energy measures. The algorithm uses up to two combinations of energy measures input. Our results show that unique energy types drive different country's GDP based on correlation study. We obtained accuracy of up to 93.64% in predicting the last 10-year GDP of a country using the developed SVR algorithm. This shows that energy measures are reliable indicators to predict a country's GDP. The study also reveals that the type of energy that drives the GDP of developed nations is different from developing and least developed nations.**

Keywords – gross domestic product, machine learning, energy, support vector regression

I. Introduction

GDP is often used as a gauge of a country's economic performance and is often compared between country to country to evaluate its relative economic strength. It measures the total value of goods and services produced within a country's borders in a given period, typically a year. Predicting GDP can be challenging, as it is influenced by many variables and can be impacted by unexpected events such as natural disasters or political instability. However, there are several methods and tools that can be used to forecast GDP. One common method is to use economic indicators, such as unemployment rates [1], national income and product accounts [2], and industrial production [3]. These indicators can provide valuable information about the current state of the economy and can help analysts forecast future economic performance.

Other way to forecast GDP is by using energy measurements, as energy consumption is often tied to economic activity and changes in energy consumption can be an early sign of changes in GDP. There are several factors that can influence the relationship between energy consumption and GDP. Energy measures, such as electricity production or consumption, can be important indicators of a country's economic activity and can provide valuable information for predicting GDP. These include technological advances that increase energy efficiency, changes in energy prices, and shifts in economic structure. One of the best approaches to predict GDP using energy measures is by using machine learning techniques. A study in [4] use deep learning algorithms for predicting GDP in Indonesia. The study used long short-term memory (LSTM) and recurrent neural network (RNN) models to analyze economic indicators such as GDP, inflation, population, and oil imports from 1980-2011. While in [5], a machine learning causal direction from dependency algorithm is used to find relationship between solar and wind energy production, coal consumption, and CO_2 emission. It has been shown that the use of machine learning techniques and energy measures as predictors of GDP offers a promising approach for forecasting economic growth and understanding the factors that contribute to a country's prosperity.

ISBN: 978-86-82602-01-9

In this paper, the relationship between the energy measure and GDP using correlation coefficient is examined. Then, the most important energy measures are chosen and used to estimate the GDP using the machine learning based Particle Swarm Optimization – Support Vector Regression (PSO-SVR) algorithm. The key contribution of this paper is as follows: 1) To examine the relationship between the energy measure and GDP using correlation coefficient; 2) To identify the most important energy measures for predicting GDP; 3) To accurately estimate the GDP based on chosen energy measures on GDP using PSO-SVR.

II. METHODOLOGY

The flowchart in Fig. 1 illustrates the process for predicting GDP using a dataset obtained from GitHub [6]. The dataset consists of two types of data, energy and GDP, and countries are grouped into three categories based on their level of economic development: developed economies, developing economies, and least developed countries. The correlation between different factors and GDP is analyzed and the factors that have the highest correlation with GDP (cc>0.75) are chosen as inputs for the prediction. The prediction is made using the PSO-SVR algorithm, which employs three different types of kernel functions.

A. Dataset Description

Table I summarizes the energy dataset that was used to predict GDP. The dataset includes data from 10 countries, grouped into different categories based on their level of economic development. For example, Japan, Germany, and the USA are part of the major developed economies (G7) group. The dataset is divided into training and testing sets, with the testing data covering the years from 2010 to 2021 and the training data specific to each level of economic development. The training data for each category is different as some country's data is relatively small, especially for the least developed countries. The input factors for the prediction are chosen based on the correlation analysis results, selecting only factors that have a correlation coefficient greater than 0.75.

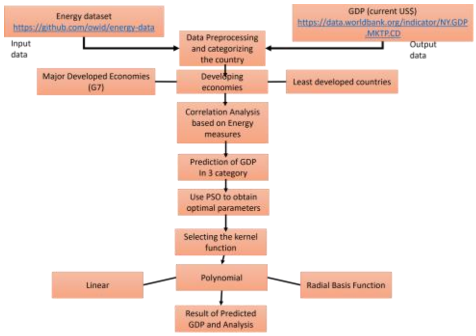

Figure 1. Flowchart of the GDP prediction using PSO-SVR algorithm.

B. Support Vector Regression Algorithm

SVR is a type of Support Vector Machine (SVM) that is used for regression tasks, rather than classification. It is a supervised learning algorithm that uses a linear or non-linear function to model the relationship between the input data and the output value. The aim is to find a linear regression function in this space that can accurately predict output values for new input data. SVR can be expressed as a convex optimization problem, which involves finding the optimal solution to a mathematical problem where the constraints are in the form of convex functions.

In SVR, a set of input-output pairs, represented by $X_i, X_j, \ldots, X_i, X_j$ are used to train the model, where i and j is the number of samples. The model includes parameters such as the weight factor w, the threshold value b, and the error cost C. The input samples are transformed into a higher dimensional space using a kernel function (φ), which allows for nonlinear mapping between the input space and the feature space. The ξ_i and ξ_i^* values represent the upper and lower training errors, respectively, which are subject to constraints defined by the ε-insensitive tube. This predicted value would be resulted after:

$$Minimize \frac{1}{2}\|w\|^2 + C\sum_{i=1}^{l}\left(\xi_i + \xi^*\right). \quad (1)$$

Subject to

$$\left\{\begin{array}{ccc} y_i - \left[w\cdot\Psi\left(x_i\right)\right] - b & \leq & \varepsilon + \xi_i \\ b - y_i + \left[w\cdot\Psi\left(x_i\right)\right] & \leq & \varepsilon + \xi_i^* \\ \xi_i,\ \xi_i^* & \geq & 0 \end{array}\right\}. \quad (2)$$

TABLE I. DATASET DESCRIPTION FOR PREDICTING GDP

Country's Economy Category	Country	Number of Input factors	Train Data	Test Data
Major Developed (G7)	Japan	17	40 (1970-2009)	12 (2010-2021)
	German	17		
	USA	23		
Developing	Malaysia	22	45(1965-2009)	
	India	31		
	Brazil	18		
	Serbia	4	15 (1995-2009)	
Least developed	Sudan	14	30(1980-2009)	
	Angola	5		
	Myanmar	3		

In addition to that, kernel function is used to map the input data into a higher-dimensional space, where it can be more easily modeled using a linear function. In our work, we used linear, polynomial and Radial Basis Function (RBF). Description of each kernel function is mentioned in the following:

- *Linear*. Simply takes the dot product of the input data and a set of weights. $K(X, X_i) = X \times X_{ji}$.
- *Polynomial*. Like the linear kernel function but it also includes a parameter that raises the dot product to a specified power. $K(X_i, X_j) = (X_i \times X_j + 1)^d$
- *RBF*. More complex function that uses the Euclidean distance between the input data and a set of prototype vectors. $K(X_i, X_j) = exp(-\gamma X_i - X_j)^2$

C. *Optimised SVR Parameters Using PSO*

Particle Swarm Optimization (PSO) is an optimization algorithm that is inspired by the collective behavior of swarms of animals, such as birds or bees. It can be used to solve a wide range of optimization problems, including those involving Support Vector Regression (SVR). Fig. 2 shows how Particle Swarm Optimization (PSO) process the parameters and select features for support vector regression (SVR). This approach involves using PSO to optimize the values of certain control parameters to improve the accuracy and convergence behavior of the SVR model.

D. *Model Evaluation*

In this study, three different estimation methods were used to compare their performance: root mean square error (RMSE), mean absolute percentage error (MAPE), mean absolute error (MAE) and correlation coefficient (cc). These metrics were used to evaluate the consistency between the original value and the predicted value. The goal is to have low values when comparing the results using these methods. By comparing the results obtained from these three metrics, we can have a more complete understanding of the performance of the estimation methods used in the study.

III. RESULTS AND DISCUSSIONS

Table II presents the results of predicting GDP based on basic economic conditions of each country. The input factors were chosen for each country to achieve the best prediction accuracy. We limit our result to only one and two-input factor predictions as to avoid complex computation process. From the table, the most accurate GDP prediction could be made for USA, with a MAPE of 1.5% which translate to 98.5% accuracy when using two input factors. The best prediction using one input factor could be

TABLE II. RESULT OF PREDICTION OF GDP FOR CLASSIFIED COUNTRIES.

Country's Economies Category	Country	Number of Input factors	Train Data	Test Data	Best prediction for one input	Best prediction for two inputs
Major Developed (G7)	Japan	17	40 (1970-2009)	12 (2010-2021)	gas share energy (MAPE=6.27)	coal share elec'+'gas share energy' (MAPE=5.30)
	German	17			Low carbon share energy (MAPE=5.04)	low_carbon_consumption+'low_carbon_share_energy' (MAPE=4.32)
	USA	23			Low carbon consumption (MAPE=3.20)	**electricity demand'+wind electricity' (MAPE=1.50)**
Developing	Malaysia	22	45(1965-2009)		fossil fuel consumption (MAPE=8.28)	coal share energy+'oil consumption (MAPE=6.36)
	India	31			wind energy per capita' (MAPE=4.80)	gas energy per capita'+'wind consumption' (MAPE=3.60)
	Brazil	18			fossil energy per capita'(MAPE=11.94)	fossil fuel consumption'+'hydro consumption' (MAPE=6.13)
	Serbia	4	15 (1995-2009)		per capita electricity (MAPE=13.38)	electricity generation'+'per capita electricity' (MAPE=11.62)
Least developed	Sudan	14	30(1980-2009)		energy per capita (MAPE=32.86)	electricity demand'+'energy per capita' (MAPE=34.71)
	Angola	5			Population (MAPE=20.62)	population'+'energy per capita' (MAPE=30.06)
	Myanmar	3			population (MAPE=18.29)	population+gas_prod_per_capita' (MAPE=26.18)

observed for Germany and USA where low carbon energy is used as the sole input.

Fig. 3 shows the correlation heatmap between GDP and various energy measures for Malaysia. We chose only input that have correlation above 0.75 as to make filtering the input easier. Based on the figure, the energy measures that highly correlated with Malaysian's GDP are fossil fuel, oil, and coal energy. This suggests that the GDP in Malaysia is strongly influenced by traditional energy resources.

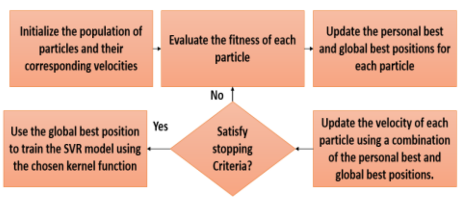

Figure 2. PSO algorithm decision based on given parameters.

Table III compares various input factors used to predict GDP in Malaysia, as well as the results of different kernel functions (linear, polynomial, and RBF) used in the predictions. The lowest prediction error is achieved when using the PSO-SVR algorithm with the RBF kernel function and an input factor of fossil fuel consumption, with a mean absolute percentage error (MAPE) of 8.28 and a correlation value of 0.69. The results in Table III suggest that using fossil fuel consumption as an input factor in combination with the RBF kernel function is particularly

TABLE III. PREDICTION OF MALAYSIAN'S GDP USING ONE INPUT FACTOR.

	Linear				Polynomial				RBF			
Variable	***RMSE***	***MAE***	***MAPE***	***CC***	***RMSE***	***MAE***	***MAPE***	***CC***	***RMSE***	***MAE***	***MAPE***	***CC***
'coal share energy'	5.00E+10	4.30E+10	13.14	0.42	5.02E+10	4.34E+10	13.14	0.42	5.20E+10	4.50E+10	13.65	0.42
'fossil energy per capita'	1.80E+11	1.70E+11	52.91	0.24	1.75E+11	1.72E+11	52.82	0.24	9.50E+10	8.20E+10	24.96	0.24
'fossil fuel consumption'	1.20E+11	1.20E+11	36.56	0.69	1.22E+11	1.20E+11	36.61	0.69	**3.10E+10**	**2.60E+10**	**8.28**	**0.69**
'gas consumption'	1.50E+11	1.50E+11	45.63	0.3	1.52E+11	1.49E+11	45.63	0.3	1.10E+11	1.00E+11	32.04	0.31
'gas energy per capita'	1.90E+11	1.90E+11	57.68	-0.2	1.91E+11	1.88E+11	57.63	-0.2	1.70E+11	1.60E+11	50.24	-0.18
'gas prod per capita'	2.00E+11	2.00E+11	62.08	-0.17	2.05E+11	2.02E+11	62.06	-0.17	1.80E+11	1.70E+11	52.89	-0.14
'gas production'	1.70E+11	1.70E+11	50.78	0.47	1.68E+11	1.66E+11	50.77	0.47	8.80E+10	7.70E+10	23.78	0.46
'hydro consumption'	1.20E+11	9.60E+10	31.25	0.76	1.18E+11	9.67E+10	31.36	0.76	1.20E+11	9.20E+10	29.95	0.76
'hydro elec per capita'	1.60E+11	1.40E+11	45.61	0.76	1.48E+11	1.31E+11	42.06	0.76	1.70E+11	1.70E+11	52.23	0.76
'hydro electricity'	1.20E+11	1.00E+11	32.64	0.76	1.18E+11	1.02E+11	32.58	0.76	1.10E+11	9.60E+10	30.14	0.57
'hydro energy per capita'	1.70E+11	1.60E+11	51.23	0.76	1.70E+11	1.62E+11	51.23	0.76	1.90E+11	1.80E+11	56.97	0.76
'low carbon consumption'	1.10E+11	9.70E+10	31.07	0.78	1.11E+11	9.63E+10	30.82	0.78	6.70E+10	5.40E+10	17.43	0.4
'low carbon elec per capita'	1.40E+11	1.20E+11	39.85	0.77	1.34E+11	1.11E+11	35.96	0.77	1.50E+11	1.40E+11	43.84	0.77
'low carbon electricity'	1.10E+11	9.90E+10	31.77	0.77	1.14E+11	9.94E+10	31.77	0.77	6.80E+10	5.30E+10	17.46	0.47
'low carbon energy per capita'	1.50E+11	1.40E+11	45.52	0.77	1.54E+11	1.43E+11	45.4	0.77	1.60E+11	1.60E+11	49.45	0.77
'oil consumption'	1.60E+11	1.60E+11	49.99	0.61	1.65E+11	1.63E+11	50.04	0.61	7.00E+10	6.20E+10	19.32	0.64
'oil energy per capita'	2.10E+11	2.10E+11	64.54	0.09	2.12E+11	2.10E+11	64.44	0.09	2.00E+11	2.00E+11	59.93	0.09
'renewables consumption'	1.10E+11	9.60E+10	30.79	0.78	1.11E+11	9.72E+10	31.03	0.78	6.60E+10	5.20E+10	17.06	0.48
'renewables elec per capita'	1.40E+11	1.20E+11	39.86	0.77	1.34E+11	1.11E+11	35.96	0.77	1.50E+11	1.40E+11	43.98	0.77
'renewables electricity'	1.10E+11	9.90E+10	31.77	0.77	1.14E+11	9.94E+10	31.77	0.77	6.80E+10	5.30E+10	17.52	0.48
'renewables energy per capita'	1.50E+11	1.40E+11	45.43	0.77	1.54E+11	1.43E+11	45.48	0.77	1.60E+11	1.60E+11	49.82	0.77

effective for predicting GDP in Malaysia. The correlation value of 0.69, which measures the relationship between changes in GDP and changes in fossil fuel consumption, supports the idea that fossil fuel is a useful indicator for predicting GDP in Malaysia. This is consistent with the findings from the correlation heatmap discussed earlier which suggested that fossil fuel,

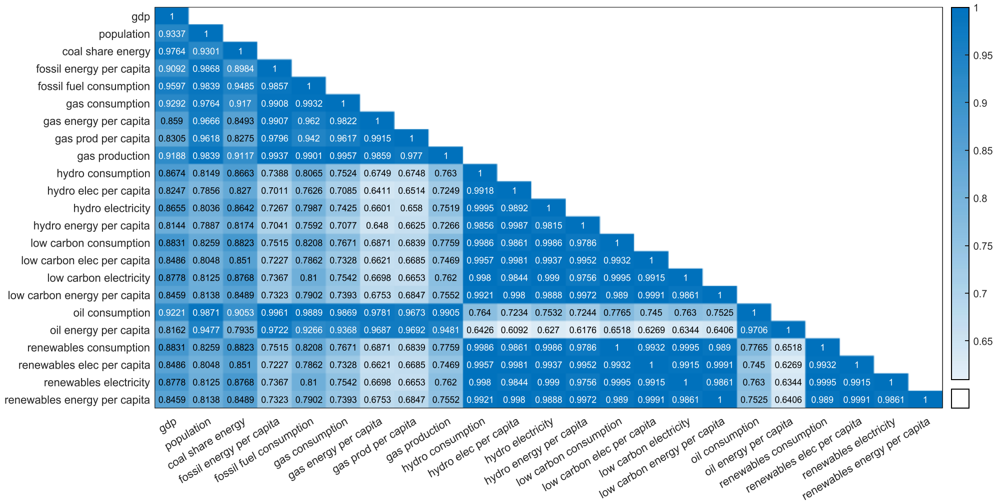

Figure 3. Correlation heatmap of energy measures in Malaysia.

oil and coal energy are strongly related to Malaysian's GDP.

Table IV shows the results of predicting GDP using two input factors as opposed to just one. The table compares the results and shows that using two input factors improves the prediction accuracy. Specifically, it shows that using two input factors results in a lower mean absolute percentage error (MAPE) of 6.36 compared to using one input factor, which had a

TABLE IV. PREDICTION OF MALAYSIAN'S GDP USING ONE TWO FACTOR.

	Linear			
Variable	***RMSE***	***MAE***	***MAPE***	***CC***
coal share energy+'hydro elec per capita'	4.26E+10	3.51E+10	10.726	0.533
'coal share energy+ 'low carbon elec per capita'	4.43E+10	3.64E+10	11.113	0.550
'coal share energy+'renewables elec per capita'	4.43E+10	3.65E+10	11.123	0.551
'coal share energy+'hydro consumption'	4.43E+10	3.47E+10	10.657	0.632
'coal share energy+'hydro energy per capita'	4.48E+10	3.72E+10	11.330	0.499
	Polynomial			
Variable	***RMSE***	***MAE***	***MAPE***	***CC***
'coal share energy+'hydro elec per capita'	4.26E+10	3.52E+10	10.738	0.553
'coal share energy+'low carbon elec per capita'	4.38E+10	3.60E+10	10.999	0.551
'coal share energy+'renewables energy per capita'	4.40E+10	3.64E+10	11.107	0.525
'coal share energy+'low carbon energy per capita'	4.40E+10	3.65E+10	11.115	0.525
'coal share energy+'renewables elec per capita'	4.40E+10	3.63E+10	11.067	0.546
	RBF			
Variable	***RMSE***	***MAE***	***MAPE***	***CC***
'coal share energy+'oil consumption'	**2.38E+10**	**2.05E+10**	**6.361**	**0.706**
fossil energy per capita+'fossil fuel consumption'	2.69E+10	2.24E+10	7.113	0.726
coal share energy+'fossil fuel consumption'	2.69E+10	2.21E+10	6.880	0.704
oil consumption+'oil energy per capita'	2.88E+10	2.51E+10	8.133	0.809
'coal share energy+'low carbon consumption'	2.90E+10	2.46E+10	7.650	0.625

MAPE of 8.28. The table suggests that the best prediction is obtained when using a combination of coal share energy and oil energy as input factors. However, it also indicates that the relationship between energy and GDP, as seen in heatmap correlation, is consistent whether using one or two input factors or not.

Fig. 4 shows the prediction graph comparison between the actual value of GDP with each of the kernel functions used in PSO-SVR where we used input dataset from 2010 until 2021. From the figure, it can be observed that RBF kernel function fits very well with the actual value of the GDP compared to the other two kernels.

Fig. 5 shows the comparison of predicted and actual GDP for the major developed economies when using PSO-SVR with RBF kernel function. The GDP is mostly correlated with the low carbon energy. However, Japan's economy appears to be driven by coal and gas energy. This discrepancy could be due to increasing awareness of the negative impacts of climate change and the desire for sustainable long-term economic growth. While non-renewable energy sources have been the primary contributors to economic development in the past, access to fossil fuel-based energy is expected to be limited and difficult to obtain in the future, hence the shift towards low-carbon energy.

Fig. 6 shows a comparison between the predicted and actual GDP for a group of economies classified as developing. The graph shows that for many of these countries, non-renewable energy sources are the primary drivers of economic growth. For example, Malaysia's economy appears to be closely tied to the use of coal and oil energy, while Brazil's economy is linked to the use of fossil fuels. However, there are also examples of developing economies where renewable energy sources play a significant role in driving economic growth. For instance, India's economy is driven by wind energy, Serbia's economy by low carbon energy, and Brazil also uses hydro energy.

Fig. 7 shows the predicted and actual value of GDP for the least develop countries. The GDP prediction deviated so much from the actual value. Interestingly, the GDP does not correlate with energy measures where population gives the best indicator. This implies that energy related factors, as an input to predict GDP, may not have a significant impact on economic growth for the least developed countries.

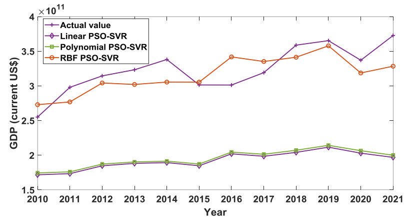

Figure 4. Comparison of algorithm performance using different kernel for predicting Malaysia’s GDP with the best prediction input factor (coal share energy+oil consumption).

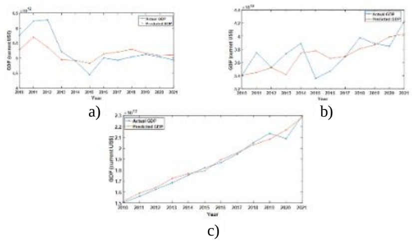

Figure 5. Comparison of Predicted and Actual GDP for Major Developed Economies (G7): (a) Japan (coal share elec and gas share energy), (b) Germany (low carbon consumption and low carbon share energy), (c) USA (: low carbon consumption and low carbon share energy).

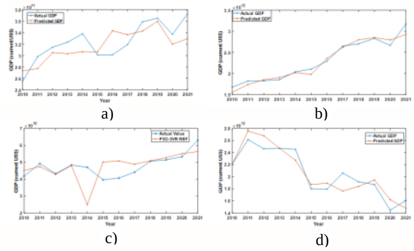

Figure 6. Comparison of Predicted and Actual GDP for Developing economies: (a) Malaysia (coal share energy and oil consumption), (b) India (gas energy per capita and wind consumption), (c) Serbia (low carbon consumption and low carbon share energy), (d) Brazil (fossil fuel consumption and hydro consumption).

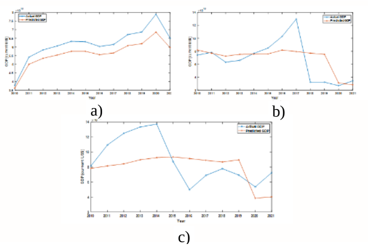

Figure 7. Comparison of Predicted and Actual GDP for Least Develop Countries: (a) Myanmar (population and gas prod per capita), (b) Sudan (: electricity demand and energy per capita), (c) Angola (population and energy per capita).

IV. CONCLUSIONS

The results show that unique energy types drive different country's GDP based on correlation study. From predicting the last 10-year GDP of a country using the developed PSO-SVR algorithm, we found that the country that have good number of datasets with multiple energy measures such as the major developed economies (G7) would give the best prediction accuracy compared to the small datasets of energy measures from least developed countries. The study also reveals that the type of energy that drives the GDP of developed nations is different from developing and least developed nations. PSO-SVR using RBF give better results compared to the other kernel functions when predicting the GDP of a country.

ACKNOWLEDGMENT

Authors would like to thank Universiti Putra Malaysia for supporting this research under funding of Geran Putra IPM Scheme with reference number of GP-IPM/2020/9694700.

REFERENCES

[1] Kingnetr, N., Tungtrakul, T., & Sriboonchitta, S. (2017). Forecasting GDP growth in Thailand with different leading indicators using MIDAS regression models. *In Robustness in Econometrics* (pp. 511-521). Springer, Cham.

[2] Garciga, C., & Knotek II, E. S. (2019). Forecasting GDP growth with NIPA aggregates: In search of core GDP. *International Journal of Forecasting, 35(4)*, 1814-1828.

[3] Lehmann, R., & Wohlrabe, K. (2015). Forecasting GDP at the regional level with many predictors. *German Economic Review, 16(2)*, 226-254.

[4] Sa'adah, S., & Wibowo, M. S. (2020, December). Prediction of gross domestic product (GDP) in Indonesia using deep learning algorithm. *In 2020 3rd International Seminar on Research of Information Technology and Intelligent Systems (ISRITI)* (pp. 32-36). IEEE.

[5] Magazzino, C., Mele, M., & Schneider, N. (2021). A machine learning approach on the relationship among solar and wind energy production, coal consumption, GDP, and CO2 emissions. *Renewable Energy*, *167*, 99-115.

[6] *Owid. Energy Data*. Available at: https://github.com/owid/energy-data.

CFD Based Optimization of Different Types of Fractal Systems

Abdulmuttalib A. Muhsen[1], Bashar Hassan Attiya[2]

[1]Faculty of Power and Aeronautical Engineering, Warsaw University of Technology, Warsaw, Poland
[1,2]Haditha Hydropower Station, Ministry of Electricity, Haditha, Iraq

Abstract—**Fractal-type structures are increasingly being used in cooling systems or heat sinks. They perform better than straight (parallel)/serpentine channels. Optimizing these structures is very difficult as many parameters needed to be observed and examined carefully. This paper discusses the optimization of three different types of fractal-type structures by utilizing CFD analysis to predict the performance of optimized fractals. In this study the optimized model was created simply by increasing the number of sub-levels.**

Keywords - fractal-type structure, optimization, computational fluid dynamics, performance

I. Introduction

Optimizing the design of any fractal-type channel is a hard task, since many variables affect its geometry. Branch angle and aspect ratio play an important role during the design phase. Aspect ratio affects the formation of vortices in the fluid, causing an improvement in heat transfer efficiency. The fractal systems are mainly studied for creating heat sinks for different electronics as they provide better temperature uniformity [1-2].

In" Compact Modeling of Fractal Tree-Shaped Microchannel Liquid Cooling Systems." A technique called Flow Network Modeling (FNM) approach is utilized since the complete simulation of such systems can sometimes be very complex due to the number of fields (flow and temperature). This technique substantially improves the efficiency of analyzing different network structures and the influence of geometric variables on the performance. Element-based CFD model is constructed to validate the accuracy of this approach. It can be used along with an optimization algorithm to optimize the geometry of a fractal microchannel network. It provides an optimum geometry with a favorable total flow rate and acceptable uniformity. FNM can be expected to execute an effective and efficient analysis and optimization for other fractal microchannel networks. This method can be used with thermal analysis to predict system flow uniformity and temperature distribution. The CFD model can only validate FNM simulation in terms of velocity distribution along the channel [3]. After the model is built; then the following boundary conditions are specified:

- Pressure drop is specified as a constant value.
- Fluid is water and has constant material properties at 300 K.
- Pressure at outlets is defined as zero.

The FNM results resemble the CFD analysis outcomes. Optimization of structures with respect to most degrees of freedom leads to robustness. In the case of a radial disc, it means to distribute the imperfections related to constructal theory and not uniform distribution over an area [3].

Three independent geometry parameters determine rhombus Fractal-like Units for Electronic Chip Cooling: the branch angle and the length and width ratio under the specified external sizes. Therefore, the geometry parameters with minimum pumping power can be optimally designed by establishing the pumping power calculation method based on these independent geometry parameters and then finding the optimal branch angle and the length and width ratio through an iterative procedure, and then comparing the performance.

A triangular finned heat sink provides a faster cooling rate than other finned heat sinks at all values of the investigated Reynolds number. In descending order, triangle, square, rectangle, hexagon, and circular finned heat sinks perform better in terms of heat transfer performance. The circle-finned heat sink has the lowest pressure drop, followed by the hexagon, rectangle, square, and triangle. In relation to heat transfer performance and pressure drop differential, square and triangular finned heat sinks function in similar pattern. In every scenario, staggered designs outperform inline geometries by about 4%. Circular fins perform best when the pressure drop, and pumping power are modest. Triangular pin-fins provide the best performance at higher pressure drop and pumping power values [4].modified in MS Word 2013 provides authors with most of the formatting specifications needed for preparing electronic versions of their papers. All standard paper components have been specified for three reasons: (1) ease of use when formatting individual papers, (2) automatic compliance to electronic requirements that facilitate the concurrent or later production of electronic products, and (3) conformity of style throughout a conference proceedings. Margins, column widths, line spacing, and type styles are built-in; examples of the type styles are provided throughout this document and are identified in italic type, within parentheses, following the example.

II. Optimization Analysis

The normal models of fractals were selected to be the simplest structure of the fractal for ease of comparison. The optimized model was designed to check how they can improve or decline in performance if the number of levels is increased. All the analysis was done on Ansys Fluent by assuming that all the investigated systems have similar flow conditions.

A. *Maintaining Normal Versus Optimized Model (Y-Shaped)*

The normal Y-shaped consists of only the 1st level, while the optimized model is up to the 2nd level, as shown in Figs. 1 and 2.

B. *Pressure Distribution in Normal versus Optimized Y-shape geometry*

In both cases, the maximum pressure appears at the stagnation point. However, the pressure drop in the optimized geometry is more significant than the normal geometry. This may be because of the greater number of bifurcations of optimized geometry.

C. *Temperature Distribution Plot of Normal Versus Optimized Y-shape Geometry*

In Figs. 5 and 6 the temperature distribution remains almost the same but slightly declines at the 2nd level branch of optimized geometry.

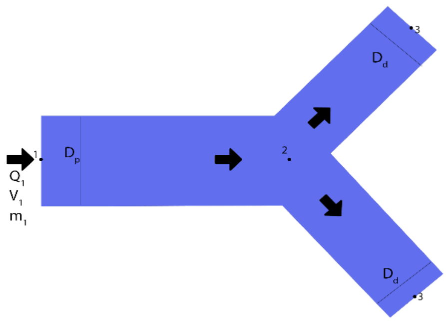

Figure 1. Normal Y-shaped fractal.

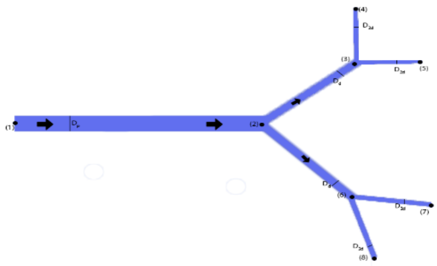

Figure 2. Optimized Y-shaped fractal.

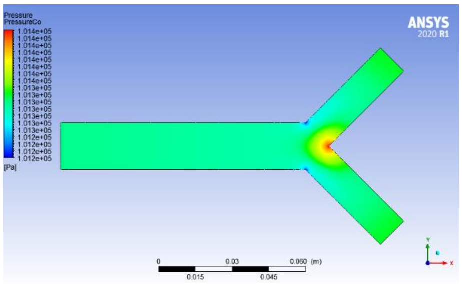

Figure 3. Y-shaped pressure contour (normal).

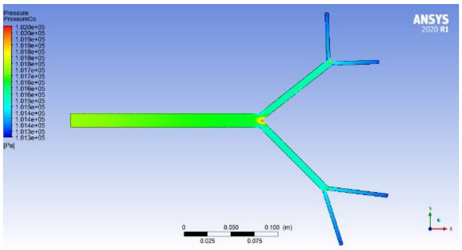

Figure 4. Y-shaped pressure contour (optimized)

D. Velocity Based Analysis of Normal Versus Optimized Y-shape Geometry

The flow uniformity across the optimized y-shaped fractal geometry Fig. 8 is more homogenous than the normal geometry (Fig. 7).

E. Normal versus Optimized Geometry (T-shaped)

The normal T-shaped fractal (Fig. 9) has only one level branch, while the optimized one (Fig. 10) has up to three level sub-branches.

F. Pressure Distribution in Normal versus Optimized T-shape Geometry

Fig. 11 shows that the pressure drops rapidly after the main branch in normal T-shaped fractal geometry while the pressure drops slowly in the

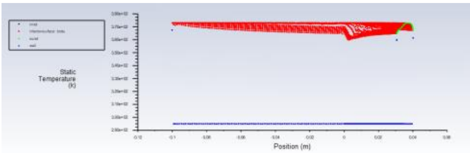

Figure 5. (normal) Y-shaped temperature plot.

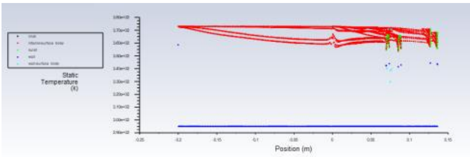

Figure 6. (optimized) Y-shaped temperature plot.

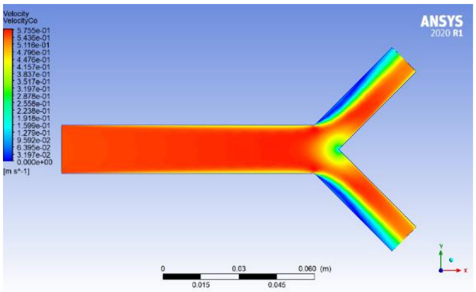

Figure 7. Y-shaped velocity contour (normal).

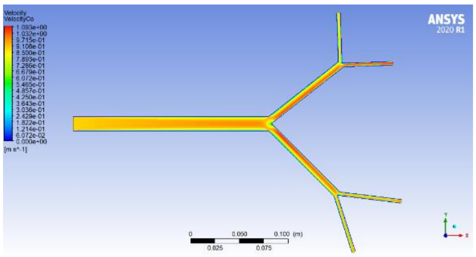

Figure 8. Y-shaped velocity contour (optimized).

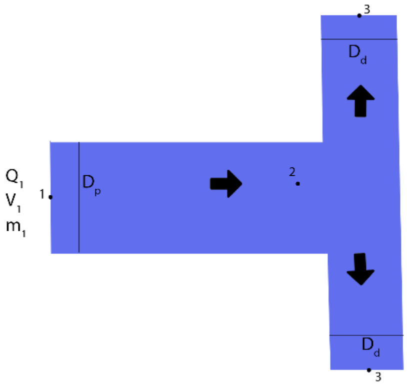

Figure 9. Normal T-shaped fractal.

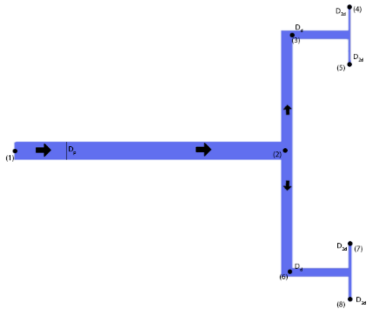

Figure 10. Optimized T-shaped fractal.

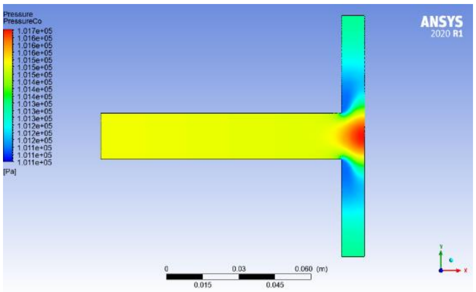

Figure 11. T-shaped pressure contour (normal).

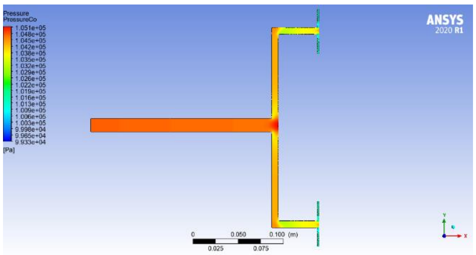

Figure 12. T-shaped pressure contour (optimized).

3rd level of bifurcation in optimized T-shaped fractal (Fig. 12).

G. *Temperature Velocity Based Analysis of Normal versus Optimized Y-shape Geometry*

In Figs. 13 and 14, the temperature distribution remains almost the same but slightly declines at the 3rd level branch of optimized geometry.

H. *Temperature Distribution Plot of Normal versus Optimized Y-shape Geometry*

The flow uniformity is better in optimized T-fractal geometry (Fig. 16) than normal geometry (Fig. 15).

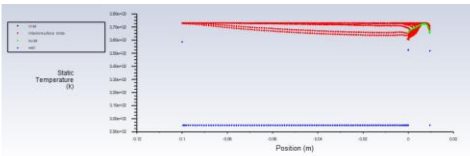

Figure 13. (normal) T-shaped temperature plot.

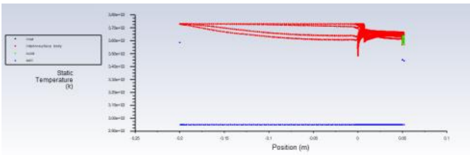

Figure 14. (optimized) T-shaped temperature plot.

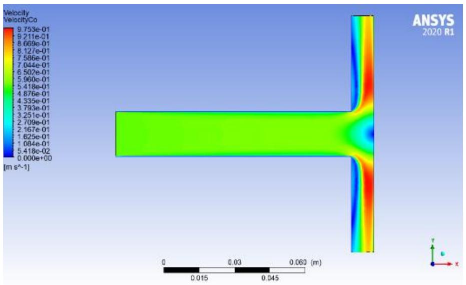

Figure 15. T-shaped velocity contour (normal).

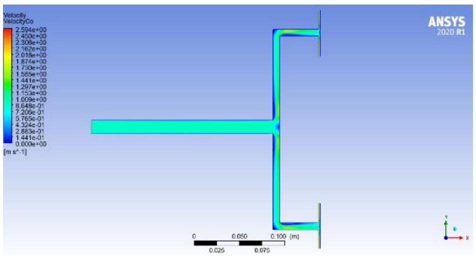

Figure 16. T-shaped velocity contour (optimized).

I. *Normal versus Optimized Geometry (Irregular-shaped)*

Figs. 17 an 18 show the normal irregular fractal geometry and optimized irregular fractal with sub-branches that are also irregular.

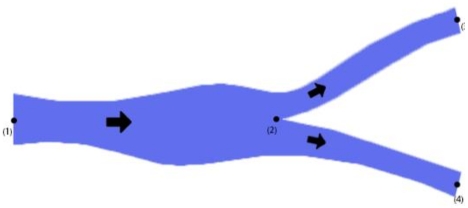

Figure 17. Irregular Fractal (Normal).

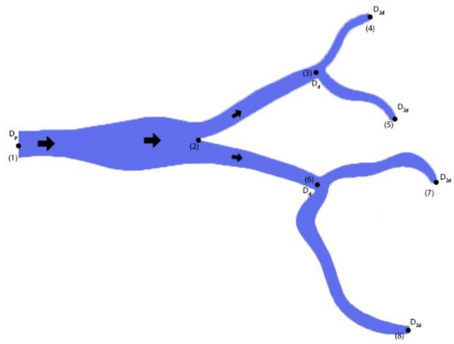

Figure 18. Irregular Fractal (optimized).

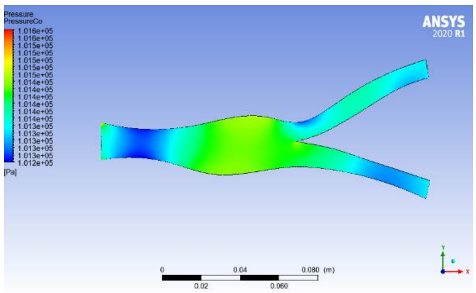

Figure 19. Irregular pressure contour (normal)

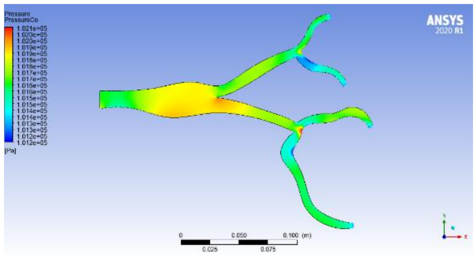

Figure 20. Irregular pressure contour (optimized).

J. *Pressure Distribution in Normal versus Optimized Irregular Fractal Geometry*

The pressure drop appears to be more in the normal irregular fractal (Fig. 19) than in Fig. 20, which shows an optimized irregular fractal.

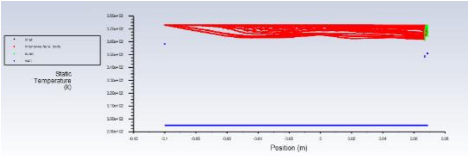

Figure 21. (normal) irregular fractal temperature plot

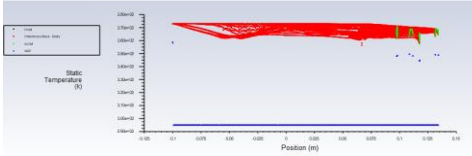

Figure 22. (optimized) irregular fractal temperature plot

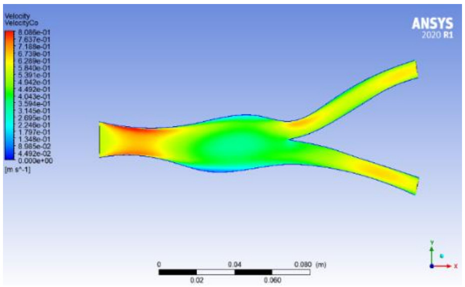

Figure 23. Irregular velocity contour (normal).

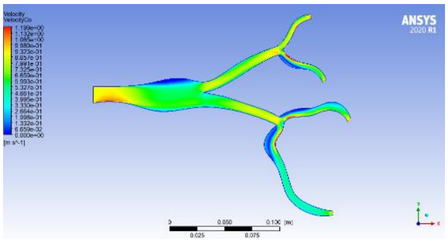

Figure 24. Irregular velocity contour (optimized).

K. *Temperature Distribution Plot of Normal versus Optimized Irregular Fractal Geometry*

Although the temperature does not change throughout the system, the temperature uniformity is better in normal (Fig. 21) than in the optimized one (Fig. 22).

L. *Velocity Based Analysis of Normal versus Optimized Irregular Shaped Geometry*

The flow uniformity of normal and optimized are shown in Fig. 23 and Fig. 24, respectively.

III. CONCLUSSION

- For Y-shaped geometry, the pressure distribution is more uniform in the normal fractal, while the temperature distribution has almost similar behavior. Flow uniformity is better in the optimized fractal.
- The pressure distribution is better in an optimized fractal for T-shaped geometry, while the temperature distribution is almost identical. Flow uniformity is better in an optimized one.
- Pressure drop is higher in optimized irregular fractal maybe because of the change in diameter, the temperature distribution is better in a normal irregular fractal, and flow is not uniform in both the cases of the irregular fractal.

REFERENCES

[1] Muhsen, A. A., & Kizilova, N. The Advanced Cooling System of Generator for Hydropower Plant. *changes*, *8*, 10.

[2] Muhsen, A. A., Attiya, B. H., & Algburi, H. A. Theoretical Analysis of Different Fractal-Type Pipelines.

[3] Chen, C., Samadiani, E., & Sammakia, B. (2011, January). Compact Modeling of Fractal Tree-Shaped Microchannel Liquid Cooling Systems. In *ASME International Mechanical Engineering Congress and Exposition* (Vol. 54969, pp. 997-1006).

[4] Arjun, K. S., & Kumar, R. (2018). Optimization of micro pin-fin heat sink with staggered arrangement. *Thermal Science*, *22* (6 Part B), 2919-2931.

Construction of Hydropower Plants in Transition Economies Example of BiH and "JP Elektroprivreda BiH"

Enver Agić[1], Damir Šljivac[2], Bakir Agić[3]

[1]Court Expert Electrical Engineer, Tuzla, BiH
[2]Electrical Faculty, The University J. J. Strossmayer of Osijek, Osijek, Croatia
[3]Faculty of Electrical Engineering Tuzla, Tuzla, BiH

Abstract—**The paper briefly discusses that sustainable development can be realized parallel and balanced development of the economy and the preservation of ecosystems in the case of public company "Elektroprivreda BiH", dd Sarajevo. Therefore, methods of analysis of the environmental impact should evolve in accordance with the current changes in society. The balance of the environment we have significantly disrupted, more often the various concession arrangements foreign investor gives local natural resource for a period of use, and requires serious review and change the direction of the vector of interest in the method of assessing the environmental impact and give the necessary approvals. Comparative cited manufacturing methods analysis used in the former country and in the world today, with the proposal of making, in particular with regard to hydroelectric resources that are given to investors to use. The meaning and the degree of feasibility of the necessary measures to protect the environment must influence the choice of the concept of technical solutions, each nation builds its existence perspective special attention and responsibility for the environment. The method of defining the conditions and limitations of environmental protection, development of appropriate analysis of the impact on the environment, during the design of hydropower facilities, the law and superior to the method of solving the problem after the fact, after the appearance of the problem of adverse environmental impact.**

Keywords - hydropower, sustainable development, systematic and responsible development planning

I. Planning the Construction of Hydropower Plants

Systematic and responsible development planning, in the design and execution of hydropower facilities, area prerequisite for environmental protection. An important instrument is the environmental impact analysis, which at the initial stage of planning and design of hydropower facilities and systems, provides information about the consequences that environmental interventions in space may have. Hydrotechnical facilities are built today exclusively as multipurpose facilities, for the following purposes [1]:

- water supply,
- production of cheap and clean electricity,- protection from flooding,
- improving the water regime at the appearance of small waters,
- prevention of uncontrolled transmission and deposit of driftwood and driftwood,
- water transport,
- development of commercial and sport fishing tourism and recreation on the landscaped banks of reservoirs, canals and rivers.

Environmental parameters physically and economically, condition national energy policy and must be incorporated at all stages at bilateral, regional and global levels. Environmental protection is crucial for the sustainable development of society, lasting without adverse effects on the environment [2]. Today, the development of energy sources and

ISBN: 978-86-82602-01-9

consumers globally in the world does not enable sustainable development, the method of sustainable development, new technologies, and the use of RES must be applied.

The mandatory practice of making environmental impact assessments of hydropower facilities, in the world today is carried out by government institutions and international organizations, the UN, the EU. Environmental impact assessment took on official global importance at the 1992 UN Conference on Environment and Development. Making such analyses is the most important means of achieving the goals of the concept of sustainable development.

The concept of sustainable development represents the harmonization of human activities with natural resources, through development that will cause minimal negative impacts on the environment, through increasing efficiency in the process of production and consumption in terms of the use of natural resources and raw materials, and the development of clean and environmentally sound technologies.

Recently, countries have been introducing legislation on the development of environmental impact assessment scrutiny. The character and effectiveness of their application are different in individual countries, depending on the sincerity of the attitude of the particular society towards the environment, and on the available personnel and material resources for the development and use of a complex method of impact assessment [3].

In practice in the world, three concepts are most often encountered when preparing environmental impact studies:

- EA – Environmental Assessment,
- EIA – Environmental Impact Assessment,
- EAP – Environmental Action Plan

EIA, according to the Criteria of the WB is a more complex study than the previous Detailed Analysis of environmental impact, and today it is the Environmental Impact Study. In addition to the previously listed, even more complexly processed content, there are numerous detailed appendices, where: attached are the minutes of at least two public hearings organized with local NGOs, dealing with environmental protection and the mandatory involvement of the local population, whose life is affected by the construction of the hydropower facility in question, as well as all interested, numerous and large tables with detailed data, appropriate reports whose statements were used in the study (e.g. displacement), defined list of participants in the preparation of the study, individually and by institution, the literature used [4].

The EAP according to the WB criteria should include:

- definition of protection measures with cost price, technical protection solution project and detailed dynamics of the implementation of the same;
- monitoring of certain influences with a detailed description of the technical details, parameters that need measure, by what methods and dynamics, with a description of the sampling locations;
- the necessary personnel structure and training, if necessary, a technical assistance program and orientation and provision of the necessary equipment;
- method of application of prescribed protection measures, with a dynamic plan of activities and engagement the necessary funds, with a clear definition of the source of funding;
- proof that The EAP is an integral part of the entire hydropower project and that the investor is all the necessary environmental measures foresee, financially secured and facilitated their in advance, or in parallel with the project of the execution of works.

II. Methods of Drafting Environmental Studies in BiH

In engineering practice, environmental impacts have not been taken into account before. Later, the procedure for designing hydropower facilities and systems was adopted. In environmental issues, it had its place in the following stages of design:

- environmental conditions and limitations are defined at the beginning, after water management conditions and are an integral part of the terms of reference for the system study and general design,

- the previous environmental impact analysis was carried out in the phase of drafting the general project and the approval of the competent ministry for environmental protection is necessary,

- detailed environmental impact analysis was carried out in the preliminary design phase and adopted by the competent ministry. Today, environmental procedures are tightened and aligned with the regulations of EU countries.

III. Environmental Impact Study in Transition

In the transition, when ceding to a foreign investor of natural resources for long term use, today is the time to review and change the direction of vectors of interest in environmental impact analysis and giving the necessary consents [5]. The public is aware of the preservation of the environment, the stability in the field of environmental impact is equal to the static, hydraulic and geotechnical stability of the building. The transition has also brought new relations in financing models, project preparation, construction and exploitation of hydropower facilities and systems. Concession arrangements and numerous BOT models are new forms of project financing in the field of hydropower [6].

The general model BOT (Build, Operate and Transfer, or Build, Own and Transfer) has as variants:

- BOO (Build, Own and Operate),
- BOOT (Build, Own, Operate and Transfer)
- BOR (Build, Operate and Renewal of concession),
- BLT (Build, Lease and Transfer)
- BRT (Build, Rent and Transfer),
- BT (Build and Transfer immediately),
- BTO (Build, Transfer and Operate),
- DBFO (Design, Build, Finance and Operate),
- DCMF (Design, Construct, Manage and Finance),
- MOT (Modernize, Own/Operate and Transfer),
- ROO (Rehabilitate, Own and Operate),
- ROT (Rehabilitate, Own and Transfer.

Within the new models of project financing, the method of drafting environmental impact studies should be changed and adapted to the resulting conditions. If an investor takes a concession for many years over a natural resource, in any of the above forms of project financing, it is important to present and “weight” define environmental impacts and necessary protection measures. Hydropower potential and waters are renewable waters, quality must not be jeopardized, especially in concession BOT arrangements [7].

The past is unconditional support for the construction of power facilities. If today, when preparing the necessary environmental impact analyses, within the framework of concession and BOT arrangements, the negative impact is underestimated, the state and society irrevocably lose much. The concessionaire exploits hydropower potential, and during this time the local community is left with the permanent consequences of the malpractice relationship on the environment.

In these cases, the problem is solved by all possible influences:

Critically and thoroughly analyzed.

- with maximum methodological and mathematical, modeling support,
- with adequately prescribed and timely implemented protection measures and
- with proper monitoring.

When analyzing the environmental impact of hydropower facilities, the designer should require that:

- use separate water intakes to release minimum guaranteed flows,
- provide control fasteners with discharges,
- ensure the management of the oxygen regime with monitoring, in accumulation and downstream,
- continuously monitors the behavior of accumulation, constant measurement of

certain parameters, the development of adequate mathematical models and their taring,

- Locate loans in the future reservoir (if biological remediation is not possible),
- solve ichthyology,
- dynamize the filling of the reservoir, with prior cleaning and rehabilitation of the accumulation space,
- provide for all technically adequate and appropriate coastal protection systems,
- combining anti-erosion works and the concept of evacuation of large waters through strong foundation discharges, slow down the process of filling the reservoir,
- pay special attention to tourist and ecological valorization of the waters, and the like.

The condition, before proving the techno-economic justification of the construction of the facility is - to examine whether and if so, how the facility endangers the environment. This determines what environmental measures will be implemented. In terms of concession arrangements, it is necessary to prepare the bases, studies and studies in accordance with the regulations of the WB.

According to the criteria of the WB Environmental Impact Study, HPP is specified and should contain [WB]:

- Political, legal and administrative framework of the project
- Description of the technical solution
- Analysis of considered alternatives
- Zero - natural state of the environment
- Environmental impacts of buildings
- Protection measures
- Concluding considerations
- Adverbs (Appendices)

No environmental impact should be underestimated, and the basic approach to the method of drafting environmental impact studies in hydropower must be aligned with four fundamental criteria, defined in the EU Environmental Action Programmes:

- Prevention is better than measures to repair the state of the environment,
- Environmental degradation should be prevented or minimized at source,
- The polluter should pay the price of the measures taken to protect the environment,
- Environmental policy should be an integral part of other EU policies,

These four principles represent the basis of EU environmental policy, and in concession and BOT project financing arrangements, they should be applied in this form or more stringently. A responsible attitude towards the environment can ensure sustainable development.

IV. An Example of Investments in the Construction of HPP in BiH in the Company JP EPBIH DD Sarajevo

The cessation of operation of existing production facilities in JP “Elektroprivreda BiH” dd Sarajevo, and especially TPP is based on age, years of operation and planned extension of life after reconstructions (Table I). The blocks reach 47 to 55 years of operation, except for block 7 in Kakanj, whose stopping (or new revitalization?) will depend on the realization of the new block in The Kakanj TPP (G9). Existing thermoblocks must exit the operation both due to environmental limitations, and low heat η.

The construction of the EEE is based on the Decisions of the Government of the FBiH on the proclamation of public interest and the preparation of the construction of energy facilities:

- Decision on the proclamation of public interest and accession to the preparation and construction of EEE, the selection of strategic partners and accession to the award of concessions (V. No. 553/2006 of 28.09.2006, Official Gazette of the FBiH No. 60/06);
- Decision on declaring public interest and accession to the preparation and

TABLE I. DYNAMICS OF CONSTRUCTION OF EE BUILDINGS.

		Installed power	Possible power	Total power		Investments
		Total power MW	*Yearly production GWh*	*Investments mil.KM*	*2012 mil. KM*	*2013 mil. KM*
	HPP					
1	HPP VRANDUK	20	96	126	15.8	29.5
2	HPP JANJICI	13	60	65	2.4	5.6
3	HPP USTIKOLINA	60	247	240	0.6	3.5
4	HPP CAPLJE	12	57	65	1.0	1.8
5	HPP KRUSEVO/ZEL.VIR				1.2	1.4
6	Development and preparation of HPP				2.0	4.0
	TOTAL HPP	105	460	496	23.0	45.7
	Small HPP					
7	mHPP na Neretvici	26.1	102	97	10.0	25.0
8	mHPP Una Kostela - Anex	6.4	21	20	2.0	6.0
9	mHPP Kakanj	4.5	22	12		
	WPP					
10	WPP Podvelezje	46	93	125	19.5	80.0
11	WPP Vlasic	48	98	125		
12	New projects OiE			4	1.5	1.5
13	OIE Konjic			1	1.0	
		2012-2014.				
		2014 mil. KM	total mil. KM	Construction start		Start of work
	HPP					
1	HPP VRANDUK	45.4	90.7	2012		2015
2	HPP JANJICI	18.0	26.0	2013		2017
3	HPP USTIKOLINA	13.3	17.4	2014		2017
4	HPP CAPLJE	10.0	12.8	2014		2017
5	HPP KRUSEVO/ZEL.VIR	5.6	8.2	2014		2018
6	Development and preparation of HPP	5.0	11.0			
	TOTAL HPP	97.3	166.0			
	Small HPP					
7	mHPP na Neretvici	29.5	64.5	2012		2014/15/16
8	mHPP Una Kostela - Anex	8.0	16.0	2013		2015
9	mHPP Kakanj	2.0	2.0	2014		2016
	WPP					
10	WPP Podvelezje	24.5	124.0	2012		2014
11	WPP Vlasic		0.0	2015		2017
12	New projects OiE	1.0	4.0			
13	OIE Konjic		1.0			
	Total mHPP and WPP	65.0	211.5			

construction of EEE in the FBiH (Official Gazette of the FBiH No. 8/10);

- Decision on the preparation and construction of HPP Vranduk 23 MW, or 19.63 MW on the River Bosna (Official Gazette of the FBiH No. 13/10 and 34/11);

- Decision on granting consent for accession to the concession award procedure for the construction of HPP Vranduk 23 (19.63) MW, on the River Bosna (Official Gazette of the FBiH No. 13/10);

- Decision on preparation and construction of HPP Kruševo 9,75MW with HPP Zeleni Vir 2, 13MW, on the river Bioštica (Official Gazette of FBiH No. 17/10);

- Decision on granting a concession for the construction of HPP "Vranduk 19.63MW" (FBiH Official Gazette No. 62/11)

The new capacities are replacement for the existing ones and should ensure the production and satisfaction of balance sheet needs and continuity of operation of hydropower plants, reduction of operation of thermoblocks, achievement of optimal mix of "thermo-hydro" in this company, fulfillment of environmental regulations.

In the second iteration, the dynamics of the implementation of OI projects changed The corrected scenario predicts the realization of projects in a period of 11 years.

The optimistic scenario is, 2 to 3 new projects would be released annually, 9 to 11 projects are in implementation at the same time. All renewable projects have been retained as the ultimate goal, and the more "stretched" dynamics are realistic.

V. The Problem of Building New Hydro Capacities in EP BIH DD Sarajevo

The construction of priority production capacities of EPBiH should begin, parallel to continue with the preparation of the following projects due to:

- meeting the needs of EE,

- the survival of the mine and

- capacity in The Hague.

The priority is to build new replacement thermo-capacities that are necessary for:

- replacement of existing capacities whose age expires,

- meeting balance sheet energy needs and

- the possibility of increasing mine production.

The construction of other renewable energy production facilities has less significance from the balance point of view because these facilities account for 20% of the total production of new facilities from this analysis, but it is necessary for the purpose of:

- utilization of OE and

- works that will employ the domestic industry and enable economic growth and employment.

VI. Scenario without Construction

The scenario without the construction of new buildings or with the construction of only the OI indicates that it is impossible to meet the needs of consumption without the construction of new capacities, since they need to stop working G3 and G4 in TPP Tuzla and G5 in TPP Kakanj. And, if the planned OI were built, the total production in 2020 would be lower than consumption. In a scenario like this, coal needs would drop drastically.

In 2020, only 624,000 tons of lignite and 170,000 tons of brown 1 would need for TPP Tuzla, which means closing most of the mining capacity. This scenario indicates the necessary construction of new capacities, as well as that delays can have severe consequences.

VII. Method of Realization of Capital Investments

The possible volume of capital investment for production facilities amounts to €2.02 billion and includes:

- 14 OI projects (€0.62 billion) and

- two thermal projects with accompanying mining capacity (€1.41 billion).

In addition to the new capacities, EPBiH has the need for ongoing investments in existing production capacities, in distribution and mining capacities and common and systemic needs, which in 10 years amount to € 0.713 billion, the total investment needs are over 2.72 billion euros. There is a disproportion between need and opportunity. Own resources are limited to depreciation, which is further reduced due to loan servicing obligations and part of any profit.

The solution of the financial structure-model for the construction of new production capacities is:

Increase credit indebtedness and joint construction with strategic partners.

This means the application of two basic financing models:

- corporate financing-taking of loans by EPBiH for capacity expansion,
- project financing with an ownership stake and/or energy right of a strategic partner.

The first model is possible for small OI projects for which favorable loans can be obtained. EpBiH's indebtedness is low, there is a significant space for a new long-term debt. An additional reason for not building with the partners of these projects is time, since the process of selecting partners significantly prolongs the beginning of realization, because some projects can be built this year.

In the case of new TPP with mines, the investment volume is significantly growing and exceeds the possible loan insurance, from the point of view of financial indicators of operations and due to the complexity, size and risk of these projects. The solution for these projects is in the construction models with a strategic partner.

The dynamics of the realization of new projects is conditioned by the possibilities of financing and the fulfillment of other formal preconditions. Taking into account the objective time required for the preparation of projects, for negotiations and obtaining permits, the extension of realization and the limitation of the number of projects should be considered.

VIII. Priorities

Regardless of the above, at this time, the priority should be:

- the beginning of the realization of one project from the renewable energy portfolio and the new block of TPP Tuzla,
- restructuring of mines, development of a long-term restructuring plan,
- continuation of preparatory activities for other projects, establishing a model for the realization and closure of the financial structure.

In accordance with the possibilities of financing and the expected reduction of production of existing capacities, for each project determine the date of entry into operation and the start of construction. Specific priority projects and target dynamics are given in Table II.

The implementation of priority projects is important for BiH and EPBiH as a company.

There is a delay in the implementation of projects. The cause of frequent political pretumbations in BiH, which leads to delays in all planned projects, the problem of ownership, everything is public and there is a great influence of political entities on all investments, which is unsustainable. Precious years have been lost to invest.

These delays have been around for about 5-10 years, the planned projects should have been implemented and put into operation a long time ago. An important problem is the “restraint” by the state of private entrepreneurs in order to invest private capital in the energy sector, which is inadmissible through various bylaws.

TABLE II. PRIORITY PROJECTS AND TARGETED DYNAMICS.

	Object	Install. Total power (MW)	Possible annual production (GWh)
1	HPP Vranduk	20	96
2	mHPP Neretvica	26	102
3	VPP Podveležje	46	93
	Total renewable	**92**	**291**
4	Tuzla G7	450	2535
	Total	**653**	**2826**

Declarative support to EU accession, private entrepreneurship and the restraint of that same private entrepreneurship in investing in energy, has obviously led to delays in the realization of investments. The realization of certain projects is questionable, due to shortcomings in procedures, “deliberate” transition from one project to another, which is unsustainable and will certainly lead to a decline in production in the future.

All these wanderings in the way of realization of investments cost the Federation of BiH dearly and lead to a chronic lack of money and investments, a decline in employment and a decline in the standards of citizens.

The opening of this sector to private capital to invest will certainly in the future be the impetus for the economic development of BiH and the achievement of the desired economic growth. Only private capital has access to all financial institutions, the problems of “public procurement” in the private sector are eliminated and the goal is clearly reached.

REFERENCES

[1] Agić, E. (2014). *Procjena rizika ulaganja elektroprivrede na otvorenom tržištu s ekonomskim i okolišnim ograničenjima* (Doctoral dissertation, Electrical Faculty, The University J. J. Strossmayer of Osijek).

[2] Heydt, G. T., Liu, C. C., Phadke, A. G., & Vittal, V. (2001). Solution for the crisis in electric power supply. *IEEE Computer applications in Power*, *14*(3), 22-30.

[3] Kundur, P. (1994). *Power System Stability and Control*, McGraw-Hill.

[4] Gomes, P., de Lima, A. C. S., & de Pádua Guarini, A. (2004). Guidelines for power system restoration in the Brazilian system. *IEEE Transactions on Power Systems*, *19*(2), 1159-1164.

[5] www.eia.org/grd/policy/electres.htm

[6] Directive, C. (1990). 90/377/EEC of 29 June 1990 concerning a Community procedure to improve the transparency of gas and electricity prices charged to industrial end-users. *Official Journal L*, *185*(17), 07.

[7] http://appsso.eurostat.ec.europa.eu/nui/show.do?dataset=nrg_pc_204&lang=en]

Comparison between Two Ventilated Cavities by using the Lattice Boltzmann Method, a Case Study of Thermal Comfort

Zouhira Hireche[1], Ammar Zeghloul[2], Lyes Nasseri[3]

[1,2,3]Laboratory of Multiphase Flows and Porous Media, University of Sciences and Technology Houari Boumediene, FGMGP, BP 32 El Alia 16111 Bab Ezzouar, Algiers, Algeria
[2]National Polytechnic School, BP 182, El Harrach, 16200, Algiers, Algeria

Abstract—**In this work, we have presented a numerical study on the heat transfer phenomenon by convection in a ventilated square cavity. Two configurations have been considered: in the first one, the hot wall is the left one, and in the second configuration is the right one. While the other walls are considered adiabatic for both cases. The governing equations have been modeled by the Lattice Boltzmann method on multi-relaxation time (MRT) lattice. The numerical simulations were performed in the laminar regime, for values of Reynolds number, Re, [20-500], Rayleigh number, Ra, [10-106] and Prandtl number for air (Pr = 0.7). The analysis of the results in forced convection regime obtained on the flow structure, the isotherms, the evolution of the average Nusselt number as a function of Ra and Re, as well as the average temperature, allowed us to establish correlations of the average temperature and the heat transfer rate as a function of the Reynolds number, for the two configurations. A comparison of the two cases' results was made to deduce the conditions that provide the best thermal comfort in the cavity.**

Keywords - forced convection, mixed convection, ventilated cavity, Lattice Boltzmann method, MRT method

I. INTRODUCTION

The study of heat transfer by forced or mixed convection in ventilated cavities has been the subject of several theoretical and experimental works. The main control parameters that dominate the analysis of heat transfer in ventilated cavities are: the position of the openings, thermal boundary conditions and the direction and intensity of the ventilation jet. Reference [1], numerically studied the mass and heat transfers by mixed convection in a square room, whose walls are adiabatic except for the bottom wall where a heat flow is applied over a distance L/2. The purpose of this study is to evaluate the efficiency of displacement ventilation, while ensuring good comfort conditions in the work area. They showed that the best position of the air outlet to optimize its quality with an efficient heat release should be on the same side as the inlet. Reference [2] took the same configuration, only, the heating source is applied on the whole bottom wall, three typical values of Reynolds numbers based on the height of the enclosure are chosen as Re= 50, 100 and 200, and stable laminar results are obtained in the Richardson range as $0 \leqslant R_i \leqslant 10$ and a fixed Prandtl number of 0.71. The computational results indicate that the heat transfer coefficient is strongly influenced by the Reynolds number and Richardson number. For the same conditions [3], numerically studied the effect of nano fluid (water-copper) on heat transfer. They found that the average Nusselt number increases with Ri for a given Re, and the effect of nanoparticles for low values of Re is more apparent when Ri is high. The average temperature within the cavity decreases when the concentration of solid nanoparticles increases because the presence of the latter leads to a good temperature penetration to the cavity.

Reference [4], considered heat transfer by natural convection, the left wall of the ventilated cavity is subjected to several heat sources, and the other walls are adiabatic. The maximum global conductance depends strongly on the Rayleigh number. It increases with the value of Ri, as well as the number and size of the hot sources. Similarly, for the Nusselt number and the volumetric flow rate. The same authors [5] reproduced the same system to study the cooling for three arrangements of the ventilation ports. They found that the optimal position of the heater is insensitive to the variation of the Reynolds and Rayleigh numbers. It is strongly dependent on the arrangement of the ventilation ports. Reference [6], conducted a numerical study of turbulent mixed convection in a ventilated cavity by combining the finite volume method with the k-ε turbulence model, the left wall is kept at a warm temperature and the air jet passes vertically through the cavity, through two openings (inlet/outlet). The average Nusselt number undergoes a drop when forced convection is dominant ($0.1<Ri<1$), and varies linearly for $Ri>1$. When natural convection dominates ($Ri \geqslant 10$), heating has no influence on the mean Nusselt number, it remains almost constant. For the case of heated straight wall [7], studied the heat transfer in a ventilated cavity in order to analyze the temperature distribution, and to determine the right ventilation configuration. Four configurations depending on the exhaust opening were examined, and two different materials of the hot wall (Brick and Adobe Brick) are analyzed with three thicknesses 0.1, 0.2 and 0.3m. The analysis of the average Nusselt number shows that the highest heat transfer rate is relative to the cases where the outlet is on the top wall on the side of the active wall, where the average temperatures are the lowest, thus a high temperature gradient between the hot surface is the fluid, causing an increase in the average heat flux. The finite element method was used by [8], to solve the two-dimensional mass, momentum and energy equations for a steady state mixed convection problem in a ventilated square cavity with a square heat conducting obstacle inside. The right vertical wall is heated and the other walls are adiabatic. The jet inlet and on the low side of the active wall and the outlet is at the top of the right wall. They deduced that the locations of the block have a significant effect on the thermal flux and fields. Reference [9], Carried out a numerical study for a mixed convection problem, Ri (0.1-10), to analyze the influence of the solid-fluid thermal conductivity ratio, K (0.2 - 50), as well as the obstruction (block) diameter, D (0.1 - 0.7), centered on the flow and thermal fields in a vented cavity. From this study it was concluded that a smaller block size and lower thermal conductivity coefficient are more effective for the phenomenon of heat transfer of the enclosure. For a cylindrical obstruction, [10] used the finite element method, The results show that the average Nusselt number at the heated surface is highest for the lowest value of the cavity aspect ratio "AR", but the average temperature of the fluid in the cavity and the temperature at the center of the cylinder are lower for the highest value of "AR". Reference [11] presented a numerical study of stationary laminar mixed convection with heat conduction at the active wall of the ventilated square cavity. The air inlet space is located at the bottom of a vertical glazing wall and air outlets through a space at the top surface. Three locations for the opening at the top surface are considered. The remaining surfaces are adiabatic. The conservation equations of momentum, energy and mass, were solved by the finite volume method for a range of Rayleigh numbers: $104<Ra<106$ and range Reynolds number: $100<Re<700$. The configurations gave different results. Reference [12], studied numerically the same phenomenon, with a cylindrical obstacle as heat source, and placed in the center of a ventilated square cavity, the two openings are diagonally opposed. All the walls of the cavity are considered adiabatic. The results show that the heat transfer rate and the friction force increase with the diameter and the heat generation while they decrease if the conductivity ratio increases, while the average temperature of the fluid increases with the increase of the three parameters (diameter, heat generation and conductivity ratio). For the present work, the Lattice Boltzmann method [13] with several relaxation times (LTM) has been chosen to solve the transfer equations.

II. Mathematical Modelling

A. Physical Model

The model includes two ventilated square cavities are shown in Fig. 1 (A) and (B). All walls are adiabatic except for the left wall in the first cavity, and the right wall for the second cavity which are maintained at a fixed temperature. The generalized model was used to solve the governing equations. The cavity is crossed by a jet of air assumed incompressible. All properties were assumed to be constant except the density, except the density, where the Boussinesq approximation is applied.

B. Conservation Equations

- Continuity equation:

$$\frac{\partial \rho}{\partial t}+\frac{\partial U}{\partial X}+\frac{\partial V}{\partial Y}=0 \; . \qquad (1)$$

- Momentum equation along the X direction:

$$\frac{\partial U}{\partial t}+\frac{\partial (UU)}{\partial X}+\frac{\partial (UV)}{\partial Y}= =-\frac{\partial P}{\partial X}+\frac{1}{Re}\left[\frac{\partial^2 U}{\partial X^2}+\frac{\partial^2 U}{\partial Y^2}\right] \; . \qquad (2)$$

- Momentum equation along the Y direction:

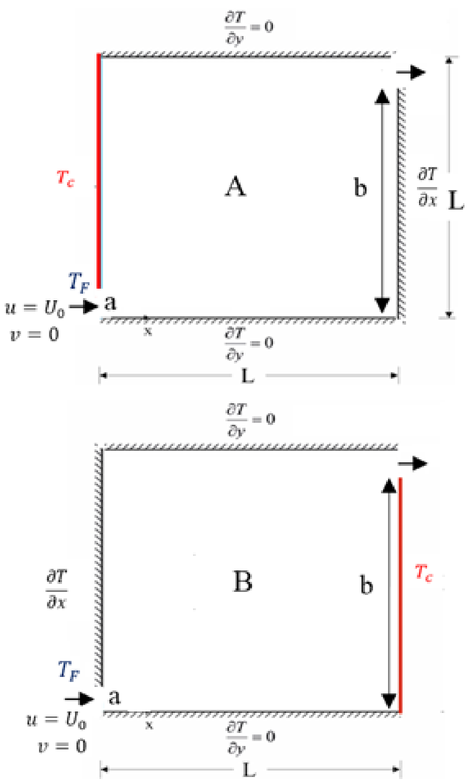

Figure 1. Geometrical configuration.

$$\frac{\partial V}{\partial t}+\frac{\partial (UV)}{\partial X}+\frac{\partial (VV)}{\partial Y}= =-\frac{\partial P}{\partial Y}+\frac{1}{Re}\left[\frac{\partial^2 V}{\partial X^2}+\frac{\partial^2 V}{\partial Y^2}\right]+ \; . \; +\frac{1}{Pr}\,.\frac{1}{Re^2}\,.R_a.\theta \qquad (3)$$

- Energy equation:

$$\frac{\partial \theta}{\partial t}+\frac{\partial (U\theta)}{\partial X}+\frac{\partial (V\theta)}{\partial Y}= =\frac{1}{Re.Pr}\left[\frac{\partial}{\partial X}\left(\frac{\partial \theta}{\partial X}\right)+\frac{\partial}{\partial Y}\left(\frac{\partial \theta}{\partial Y}\right)\right] \; . \qquad (4)$$

- The heat transfer rate at the wall is defined as follows:

$$Nu=\frac{L-a}{L}\int_{a/L}^{1} Nu_x \, dy \; . \qquad (5)$$

Nu: represents the average Nusselt number calculated at the hot wall.

- The dimensionless variables are given as:

$$X=\frac{x}{L}\;;\; Y=\frac{y}{L}\;; \quad U=\frac{u}{U_0}\;;\; V=\frac{v}{V_0}\;;\; P=\frac{p}{\rho V_0^2} \; , \qquad (6)$$

$$\theta=\frac{T-T_F}{\Delta T}\;;\quad \Delta T=T_c-T_F\;;\; t=\frac{t}{L/V_0} \; . \qquad (7)$$

- The dimensionless numbers are given as:

$$Pr=\frac{\nu}{\alpha}\;;\; Ra=\frac{g\,\beta\,\Delta T L^3}{\nu\alpha}\;; \quad Re=\frac{\rho V_0 L}{\mu} \; . \qquad (8)$$

C. The Considered Boundary Conditions

The hydrodynamic boundary conditions are the same for both configurations and are as follows:

The inlet $X=0$ and $0 \leq Y \leq a/L$

$$\begin{cases} U=1 \\ V=0 \end{cases}. \quad (9)$$

The Outlet $X=1$ and $a/L \leq Y \leq 1$

$$\begin{cases} U=\dfrac{\partial u}{\partial x} \\ V=0 \end{cases}. \quad (10)$$

<u>The walls</u>

$$\begin{cases} U=0 \\ V=0 \end{cases}. \quad (11)$$

The thermal boundary conditions for the two configurations are as follows:

Configuration (A)

$$X=0 \begin{cases} 0 \leq Y \leq a/L & : \theta=0 \\ a/L \leq Y \leq 1 & : \theta=1 \end{cases}, \quad (12)$$

$$\begin{gathered} X=1 \text{ and } 0 \leq Y \leq 1 : \dfrac{\partial \theta}{\partial x}=0 \\ \begin{cases} 0 \leq X \leq 1 \\ Y=0 \text{ and } Y=1 \end{cases} : \dfrac{\partial \theta}{\partial y}=0 \end{gathered}. \quad (13)$$

Configuration (B)

$$X=0 \begin{cases} 0 \leq Y \leq a/L & : \theta=0 \\ a/L \leq Y \leq 1 & : \dfrac{\partial \theta}{\partial x}=0 \end{cases}, \quad (14)$$

$$X=1 \begin{cases} 0 \leq Y \leq b/L & : \theta=1 \\ b/L \leq Y \leq 1 & : \dfrac{\partial \theta}{\partial x}=0 \end{cases}. \quad (15)$$

The difference with configuration (A) is in the vertical walls, which are reversed. The Eqs. (2) and (5) are solved with the Lattice Boltzmann method with several relaxation times (LBM-MRT).

III. Results and Discussion

A mechanical analysis is carried out in order to determine the effects of the different parameters involved, i.e. the Rayleigh number which characterizes the heating power.

The results are expressed in terms of streamlines and isotherms, in order to visualize the flow of the fluid in the cavity and the thermal field, and in terms of the evolution of the average Nusselt number, to quantify the exchanges and evaluate the difference between the two configurations.

A. *Validation of the Computing Program*

The computational code has been validated by comparing our results for the average Nusselt number with those of [9]. The comparison was made for the limiting case of unobstructed cavity, for different Richardson numbers: $Ri = Ra/Pr \cdot Re^2$, Fig. 2.

B. *The Thermal Comfort*

Fig. 3 represents the evolution of the average temperature as a function of the Reynolds number at the free zone of the cavity for the two configurations studied. Two standard values of the height: 1.1 m (for a sedentary seated occupation) and 1.8 m (for an active and essentially standing occupation) have been adopted [13]. These values correspond to the dimensionless heights Y=0.3 and Y=0.6 respectively. The figure shows decreasing curves for the two heights considered. They characterize the effect of cooling in the cavity. As the Reynolds number increases, the effect of cooling is important, because the cold air jet favors the evacuation of heat to the outside. The average temperature increases with the increase of the height, this is explained by the heating of the fluid particles which tend to go up thanks to the decrease of their densities by thermal thrust effect. These hot particles give way at the bottom of the cavity to cold particles of higher density,

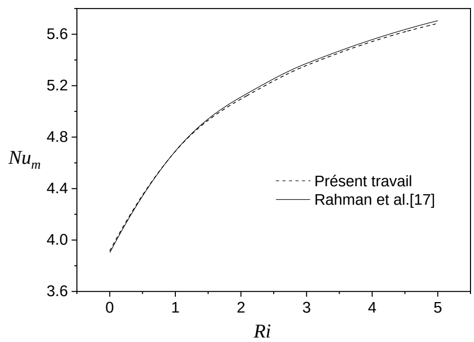

Figure 2. Evolution of Num as a function of Ri with and that of Rahman et al. [8].

which come to warm up in turn and so on. This result is very reasonable, knowing that by increasing the speed of the cold flow, more heat is evacuated towards the outside.

In configuration (B), the cooling is more efficient, because the fresh air jet is in front of the hot wall. The new fluid cools the entire active wall after passing through the bottom wall. In this case the two forces (thermal and dynamic) are cooperating. Whereas in configuration (A), the presence of recirculation reduces the cooling of the active wall. Therefore configuration (B) is the most convenient.

The mean temperature curves are correlated by the following expressions:

- Configuration (A)

For $Re[20-100]$.

Y=0.3 $T_{moy} = 3{,}156 \times Re^{-0{,}572}$

Y=0.6 $T_{moy} = 3{,}322 \times Re^{-0{,}528}$

For $Re[100-500]$

Y=0.3 $T_{moy} = 0{,}78787 \times Re^{-0{,}26428}$

Y=0.6 $T_{moy} = 1{,}01056 \times Re^{-0{,}26437}$

- Configuration (B)

For Y=0.3:

$Re[20-130]$ $T_{moy} = +0.788 - 1.115 \times Re$

$Re[130-500]$ $T_{moy} = -0.354 - 0.570 \times Re$

For Y=0.6:

$Re[20-500]$ $T_{moy} = = +0.504 - 0.766 \times Re$

Fig. 4 shows the evolution of the peak Rayleigh number as a function of the Reynolds number for the two configurations. This curve marks the comfort zones in the cavity, it is located below the curve since the average air temperatures are lower. Below the curve, the average temperature depends only on the Reynolds number (controlled comfort). However, above this curve, both parameters (Reynolds and Rayleigh) are involved. For the configuration (A), the values of the critical Rayleigh number decrease for low values of the Reynolds number (i.e., Re<100). As Re increases, the curve passes through an optimum (minimum) from which it changes trend. While for the configuration (B) the value of the critical Rayleigh number is directly proportional to the value of the Reynolds number according to two linear laws. The curve of the second configuration (B) is composed of two lines, for values of Re>100 the slope is important while for values of Re< 100 the slope is very weak. This different result is due to the structure of the flow where the existence of recirculation requires larger values of the Ra_c number.

The two curves cross for Ra=4720 and Re=257. For Reynolds number values between [10-257] and for configuration (A) (where the thermal forces and the flow of air have a different direction), it can be seen that the values of the critical Rayleigh number are higher than for the second configuration (where the thermal forces and the flow of air are cooperating). After the point of intersection of the two curves, the critical Rayleigh number values for the second configuration (B) become higher than the critical

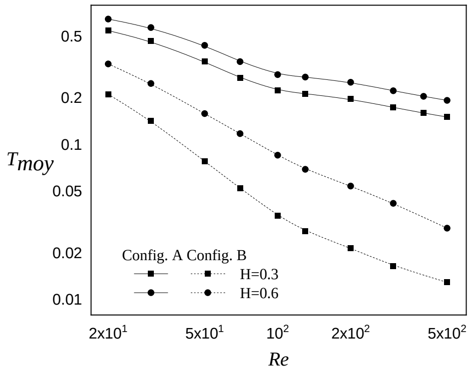

Figure 3. Variation of the mean temperature as a function of Re, in forced convection regime (i.e. Ra=10).

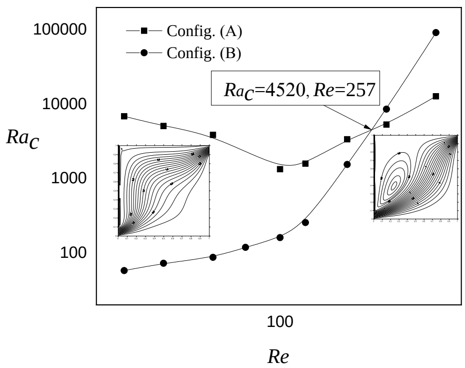

Figure 4. Pairs (Re-Rac) achieving the comfort zone curves.

Rayleigh number values for the first configuration (A).

Fig. 5 shows that the increase of Re enhances the transfer for both cases. For configuration (A), the evolution of Nusselt shows three distinct zones: in the first one we have higher values than in configuration (B), while for the other two the transfer rate is significantly lower. This reduction is due to the appearance of the recirculation cell as soon as the ventilation flow becomes less important.

IV. CONCLUSIONS

In the present work, the heat transfer in a ventilated square cavity is studied. One of the vertical walls is assumed to be hot, while the other walls are assumed to be adiabatic. The Lattice Boltzmann method with several relaxation times "MRT" has been used to solve the conservation equations. The heat transfers are expressed as a function of the different parameters that characterize the heat transfer by forced, natural or mixed convection, including the Rayleigh number, Ra, and the Reynolds number, Re. The influence of these two numbers as well as the position of the active wall on the transfer, mean temperature was discussed.

For low Reynolds number values, the effect of natural convection is evident, but remains relatively weak. As the Reynolds number increases, the flow accelerates; the effect of natural convection becomes negligible compared to forced convection.

Comparing the results of the two configurations, it can be deduced that the second configuration offers the best comfort conditions, as the lowest mean temperatures related to the two heights of the clean zone (Y=0.3 and 0.6) are

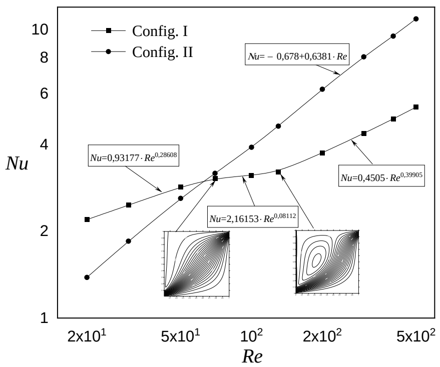

Figure 5. Variation of the mean Nusselt number as a function of Reynolds in forced convection regime (i.e., Ra=10).

obtained in this configuration. The variation of the average temperature and the average Nusselt number were correlated with the Reynolds number. Also, maps summarizing the transfer regime as a function of Num, Ra_c and Re have been established.

REFERENCES

[1] Deng, Q. H., & Tang, G. F. (2002). Numerical visualization of mass and heat transport for mixed convective heat transfer by streamline and heatline. *International Journal of Heat and Mass Transfer, 45*(11), 2387-2396.

[2] Saha, S., Saha, G., Ali, M., & Islam, M. Q. (2006). Combined free and forced convection inside a two-dimensional multiple ventilated rectangular enclosure. *ARPN Journal of Engineering and Applied Sciences, 1*(3), 23-35.

[3] M. Shahi, A. H. Mahmoudi, and F. Talebi. (2010). Numerical study of mixed convective cooling in a square cavity ventilated and partially heated from the below utilizing nanofluid. International Communications in Heat and Mass Transfer. 37. 201-213.

[4] Bilgen, E., & Balkaya, A. (2008). Natural convection on discrete heaters in a square enclosure with ventilation ports. *International journal of heat and fluid flow, 29*(4), 1182-1189..

[5] E. Bilgen & Muftuoglu. A. (2008). Cooling strategy by mixed convection of a discrete heater at its optimum position in a square cavity with ventilation ports. *International Communications in Heat and Mass Transfer. 35,* 545-550.

[6] Bouaraour, K., Kholai, O., & Boudebous, S. (2008). simulation numérique de la conevction mixte turbulente dans une cavité ventilée. *Algerian Journal of applied fluid mechanics, 1*.

[7] Xamán, J., Tun, J., Álvarez, G., Chavez, Y., & Noh, F. (2009). Optimum ventilation based on the overall ventilation effectiveness for temperature distribution in ventilated cavities. *International journal of thermal sciences, 48*(8), 1574-1585.

[8] Rahman, M. M., Alim, M. A., Saha, S., & Chowdhury, M. K. (2009). Effect of the presence of a heat conducting horizontal square block on mixed convection inside a vented square cavity. *Nonlinear Analysis: Modelling and Control, 14*(4), 531-548.

[9] Ahammad, M. U., Rahman, M. M., & Rahman, M. L. (2013). Mixed convection flow and heat transfer behavior inside a vented enclosure in the presence of heat generating obstacle. *International journal of innovation and applied studies, 3*(4), 967-978.

[10] Rahman, M. M., Elias, M., & Alim, M. A. (2009). Mixed convection flow in a rectangular ventilated cavity with a heat conducting square cylinder at the center. *Journal of Engineering and Applied Sciences, 4*(5), 20-29.

[11] Arce, J., Xamán, J., & Álvarez, G. (2011). Numerical study of mixed convection and conduction in a 2-D square ventilated cavity with an inlet at the vertical glazing wall and outlet at the top surface. *Heat and mass transfer, 47*, 223-236.

[12] Rahman, M. M., Parvin, S., Hasanuzzaman, M., Saidur, R., & Rahim, N. A. (2013). Effect of heat-generating solid body on mixed convection flow in a ventilated cavity. *Heat transfer engineering, 34*(15), 1249-1261.

[13] A. A. Mohamad. (2011). *Lattice Boltzmann method: fundamentals and engineering applications with computer codes*. Springer.

Study of Couette Microflow around a Rectangular Obstacle

Youssef Elguennouni[1], Mohamed Hssikou[2], Jamal Baliti[3], Younes Oulahou[4], Ahmed Moussaoui[5], Mohammed Alaoui[6]

[1,4,5,6]Moulay Ismail University of Meknes, Faculty of Sciences, Morocco
[2,3]University of Sultan Moulay Slimane, Polydisciplinary Faculty, Beni Mellal, Morocco

Abstract—**The multi-relaxation time lattice Boltzmann method (MRT-LBM) was applied in this work to study gas flow in the slip regime. The presence of a rectangular obstacle is addressed in two cases. First, we investigate the Couette flow, with a bottom wall immovable and a top wall on the move, whereas, In the second, the bottom wall moves in the inverse direction according to the other one. To calculate slip velocity at walls, simulations of such microflows need adequate boundary conditions. On the barriers, bottom and top walls, diffuse scattering boundary conditions (DSBC) are applied. However, periodic boundary conditions are used on the inlet and outflow. The effects of the Knudsen number (*Kn*) and the rectangular obstacle on streamlines and both components of velocity contours are investigated. According to this study, the MRT method has been shown to be capable of treating such microflows even in the slip regime.**

Keywords - MRT, DSBC, Couette flow, Knudsen number, rectangular obstacle

I. INTRODUCTION

The study of the gas microflow that occurs in devices with nano- and micro-electro-mechanical systems (NEMS) and MEMS has received a lot of attention [1]. To simulate Couette flow in the transition regime, the linear Boltzmann equation [2], direct simulation Monte Carlo (DSMC) [3,4], and Burnett equation [5] have all been used. In addition, the lattice Boltzmann method (LBM) has been utilized in several studies to simulate Couette flow in the slip flow regime [6,7], although transitional and free molecular regimes have not yet seen this type of simulation.

When compared to macro-geometries, flow behavior in nano- and micro-geometries is different. These devices' extremely small sizes cause the fluids they are interacting with to exhibit a rarefaction property. The dimensionless Knudsen number (Kn) is employed in this study to quantify how rarefied the gas is. Based on this amount, which equals the mean free route of the gas molecules (ƛ) divided by the usual length scale of the flow domain, four flow regimes are identified (l). The continuum regime is valid for Kn $\lesssim$ 0.001, the slip regime is suitable for 0.001$\lesssim$ Kn $\lesssim$ 0.1, the transition regime is valid for 0.1 $\lesssim$ Kn $\lesssim$ 10, and the free molecular regime is suitable for Kn > 10. When Kn is greater than unity in some micro-configurations, particle/wall collisions must be taken into account also, since in this case, the gas is rarefied. This situation has drawn the attention of recent microfluidic research.

A fresh option to model fluid flow has arrived with the LBM. This method combines the advantages of the moment equation, which speeds up computing, with the benefit of DSMC, it gives the Boltzmann equation a more accurate approximation. The new technique LBM, which is mesoscopic method, warrants a relationship between the micro- and macroscopic-scale descriptions of flow, and merges the kinetic description provided by the Boltzmann equation with the traditional computational fluid dynamics (CFD). For such flows, accurate selection and implementation of the boundary conditions (BC) is a crucial stage in the LBM simulation. Different boundary conditions are tested in this context; the most popular ones are bounce-back boundary conditions [6,8], specular reflection boundary conditions [9], a combine between specular reflection and bounce-back boundary conditions [10], and diffuse scattering boundary conditions [11,12]. The Boltzmann equation is solved using the Bhatnagar, Gross, and Krook (BGK) model [13], where a linear discretization approximation of the collision term is applied.

With or without a rectangular barrier, the MRT-LBM technique is used in this study to model Couette gas flow in a rectangular microchannel in the slip regime that is frequently present in MEMS devices [14]. The results are presented as plots of velocity profiles, contours of both velocity components, and streamlines based on the Knudsen number.

II. Problem Statement

By neglecting the term of the force of gravity, Couette gas flow will be studied in two cases. In the first case, Couette flow with a moving top wall and a fixed bottom wall is explored, while in the second case the walls move in opposite directions at the velocities U_0 and $-U_0$ (Fig. 1). The effect of having a rectangular obstacle in the microchannel's center on the components of the velocity (u/U_0, v/U_0) and the streamlines will be studied.

III. Numerical Part

A. MRT-LBM Method

By disregarding the force term, the LBM governing equation in the BGK model for the distribution function density f is expressed as follows:

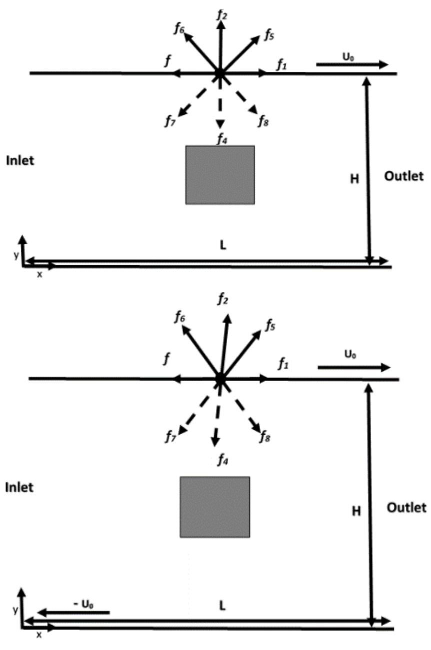

Figure 1. Studied domains configuration ($Ar = H/L$ =3/8), (a) case 1 and (b) case 2.

$$f_k(\mathrm{x}+\mathrm{c}_k\Delta t, t+\Delta t) = \\ = f_k(\mathrm{x},\mathrm{t}) - \frac{1}{\tau}(\mathrm{f}_k(\mathrm{x},\mathrm{t}) - \mathrm{f}_k^{eq}(\mathrm{x},\mathrm{t})) \quad , \qquad (1)$$

where τ is the relaxation time. The Maxwell distribution function in the equilibrium state f_k^{eq} at the second-order of Taylor expansion is written as follows:

$$f_k^{eq} = w_k \rho \left[1 + 3\frac{\mathrm{c}_k.\mathrm{u}}{c^2} + \frac{9}{2}\frac{(\mathrm{c}_k.\mathrm{u})^2}{c^4} - \frac{3}{2}\frac{\mathrm{u}^2}{c^2} \right], \quad (2)$$

where w_k are the weight factors defined by: $w_0 = 4/9$, $w_{1-4} = 1/9$, and $w_{5-8} = 1/36$. The lattice speed c is determined by: $c = \frac{\Delta x}{\Delta t} = \frac{\Delta y}{\Delta t}$.

There are nine discrete velocities in the discrete scheme D2Q9, defined by (Table I):

TABLE I. Discrete velocities in the discrete scheme D2Q9.

	c₀	**c₁**	**c₂**	**c₃**	**c₄**	**c₅**	**c₆**	**c₇**	**c₈**
$\binom{x}{y}$	$\binom{0}{0}$	$\binom{1}{0}$	$\binom{0}{1}$	$\binom{-1}{0}$	$\binom{0}{-1}$	$\binom{1}{1}$	$\binom{-1}{1}$	$\binom{-1}{-1}$	$\binom{1}{-1}$

At the MRT-LBM model, the distributions do not relax at the same velocity to their equilibrium states [15] unlike the previous model. The lattice Boltzmann equation for this approach is written as follows:

$$f_k(\mathrm{x}+\mathrm{c}_k\Delta t, t+\Delta t) = \\ = f_k(\mathrm{x},\mathrm{t}) - \mathrm{S}(\mathrm{f}_k(\mathrm{x},\mathrm{t}) - f_k^{eq}(\mathrm{x},\mathrm{t})) \quad , \qquad (3)$$

where **S** is a diagonal relaxation matrix that replaces the term $\frac{1}{\tau}$ of the BGK collision operator.

The MRT-LBM model assumes that although the collision phase takes place in a macroscopic space created by the moments m of the distribution functions f, the propagation phase takes place at the microscopic level in the space established by the discrete velocities $\mathbf{c}_k$. The matrix M ensures the transition between these two areas [16], which is defined by:

$$\mathrm{m} = \mathrm{M}f \quad , \qquad (4a)$$

$$f = M^{-1}m \ . \qquad (4b)$$

Equation (3) becomes:

$$\begin{aligned} f_k(x + c_k\Delta t, t+\Delta t) = f_k(x,t) - \\ - M^{-1}S(m(x,t) - m^{eq}(x,t)) \end{aligned} , \qquad (5)$$

where $m(x,t)$ and $m^{eq}(x,t)$ are respectively the vectors of the moments corresponding to the distribution functions f_k and f_k^{eq} .

The diagonal matrix S's relaxation times have significant effects on the collision phase. At the distribution that one wants to preserve, a relaxation time of unity is allocated. According to the BGK approximation, the equilibrium states of its non-conservative moments are defined by the following equation:

$$m'(x,t) = m(x,t) - S(m(x,t) - m^{eq}(x,t)) \ , \qquad (6)$$

where $m'(x,t)$ is the vector of moments after the collision, and $m^{eq}(x,t)$ is its equilibrium vector of moments correspond.

Following the diagonal, the parameters of the matrix S are given by:

$$S = diag(S_k)^T , \qquad k = 0-8 \ , \qquad (7)$$

where $s_7 = s_8 = \frac{1}{\tau}$, the values of the parameters *s_0*, *s_3* and *s_5* are taken equal to 1. For the sake of ensuring calculation stability *s_1*, *s_2*, *s_4* and *s_6* are a little bit higher than 1 [16].

The macroscopic space in which the collisions occur is characterized by the vector of moments *m* provided by:

$$m = (\rho \ \ e \ \ \varepsilon \ \ \rho u \ \ q_x \ \ \rho v \ \ q_y \ \ p_{xx} \ \ p_{xy})^T , \qquad (8)$$

where *e* is the energy, $\varepsilon = e^2$, $q(q_x, q_y)$ is the vector of heat flux, $j(j_x, j_y) = (\rho u, \rho v)$ is the momentum of density, and (p_{xx}, p_{xy}) are the components of the stress tensor.

The moment vector m^{eq} at the equilibrium state is given by [16]:

$$\begin{aligned} m^{eq} = (\rho \ \ -2\rho + 3(j_x^2 + j_y^2) \ \ \rho - 3(j_x^2 + j_y^2) \ \ j_x \ \ - \\ -j_x \ \ j_y \ \ -j_y \ \ j_x^2 + j_y^2 \ \ j_x j_y)^T . \end{aligned} \qquad (9)$$

The following relations yield the macroscopic density ρ and velocity u(*u*, *v*):

$$\rho = \sum_{k=0}^{8} f_k \ , \qquad (10)$$

$$u = \frac{1}{\rho}\sum_{k=0}^{8} c_k f_k \ . \qquad (11)$$

B. *Relationship Between Kn and τ*

Number equations consecutively.

The ratio of the mean free path λ to the mean thermal velocity $< v >$ can be used to define the relaxation time as follows:

$$\tau = \frac{\lambda}{< v >} = \lambda\sqrt{\frac{\pi}{8RT}} \ . \qquad (12)$$

The rarefaction degree of gas flows in microfluidic devices is measured by the Knudsen number $Kn = \frac{\lambda}{H}$, and in the LBM, $c = \sqrt{3RT} = 1$ for the D2Q9 model, so [9]:

$$\tau = \lambda\sqrt{\frac{3\pi}{8}} \cong KnH \ . \qquad (13)$$

C. *Boundary Conditions*

In the present work, the diffuse scattering boundary condition (DSBC) is applied to the bottom and top walls as well as the sides of the obstruction, whereas periodic boundary conditions are utilized at the inlet and outlet. To implement the DSBC condition at the top wall which moves with horizontal velocity $u_w(U_0, 0)$ (Fig. 1), the unknown distribution functions (f_4, f_7, f_8) are determined from the known distribution function (f_2, f_5, f_6) and $(f_4^{eq}, f_7^{eq}, f_8^{eq})$ by the following equations [17]:

$$f_4 = \frac{A_n}{\rho_w} f_4^{eq}(\mathrm{u}_w, \rho_w)(f_2 + f_5 + f_6) \ , \quad (14)$$

$$f_7 = \frac{A_n}{\rho_w} f_7^{eq}(\mathrm{u}_w, \rho_w)(f_2 + f_5 + f_6) \ , \quad (15)$$

$$f_8 = \frac{A_n}{\rho_w} f_8^{eq}(\mathrm{u}_w, \rho_w)(f_2 + f_5 + f_6) \ , \quad (16)$$

for the D2Q9 scheme adopted in this work, the value of A_n is taken equal to 6 [18].

IV. RESULTS AND DISCUSSION

A Couette flow is considered, first, the bottom plate is fixed, and the top plate is moving (U_0 = 0.1) and in the second one, both plates move at velocity U_0 in opposite directions (Fig. 1). Afterward, the presence of a rectangular obstruction that is centered in the microchannel is studied in both scenarios. The micro-aspect cavity's ratio is assumed to be Ar=3/8 (rectangular surface) [19].

A. Mesh Indepence Study

The choice of the mesh is related to the first case. Using the MRT-LBM approach, for Kn = 0.05, Fig. 2 shows the influence of the mesh size on the profiles of (u/U_0) the horizontal component of the velocity. According to the results obtained, a mesh of 320×120 has been adopted for the following simulations.

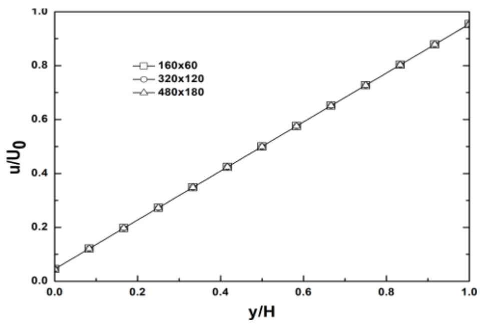

Figure 2. Profiles of u/U_0 for Kn = 0.05 obtained by the MRT-LBM method for different mesh grids – case 1.

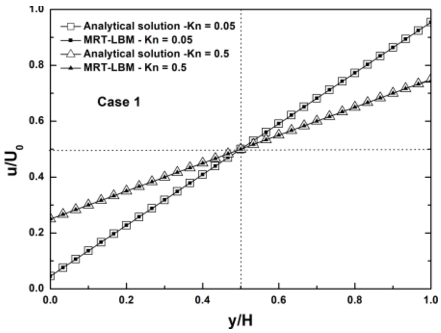

(a)

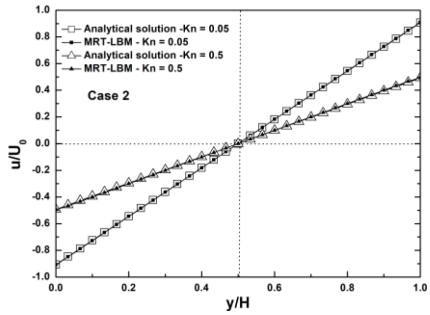

(b)

Figure 3. Profiles of u/U_0 for Kn = 0.05 and Kn = 0.5 obtained by the MRT-LBM method and compared with the analytical solutions (a) case 1 and (b) case 2.

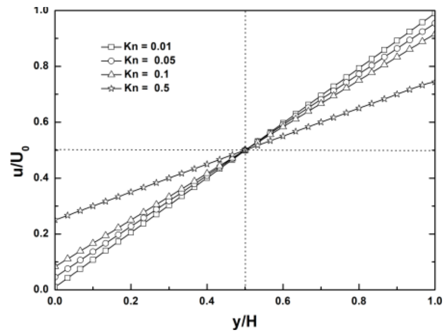

(a)

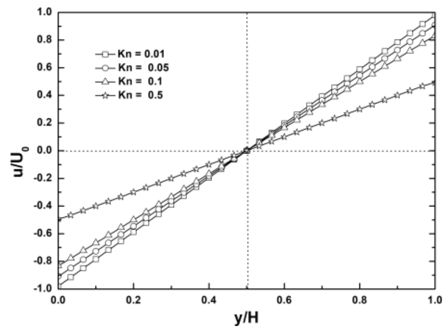

(b)

Figure 4. Profiles of u/U_0 for different values of Kn (a) case 1 and (b) case 2.

B. Validation

The following equations [14] describe how to obtain the dimensionless horizontal velocity component in the slip regime:

- For the first case:

$$u(y) = \frac{U_0(y/H + (2-\sigma_v/\sigma_v)Kn)}{1+2(2-\sigma_v/\sigma_v)Kn}\ , \qquad (17)$$

- For the second case:

$$u(y) = \frac{2U_0(y/H)}{1+2(2-\sigma_v/\sigma_v)CKn}\ , \qquad (18)$$

where y is the distance from the bottom wall, H is the number of lattice in the vertical direction, and the coefficient C is fixed at C = 1.03. The tangential momentum accommodation coefficient, denoted by the symbol σ_v, is set to 1 in the case of diffuse reflection.

The MRT-LBM model utilized in this study needs to be validated. Figs. 3a and 3b show the profiles of analytical solutions (17 and 18) and the numerical solutions obtained by the MRT-LBM approach for the values of Kn = 0.05 and 0.5. By comparing, it is clear that our findings are in accord with analytical results, with good accuracy being displayed even for Kn = 0.5 in the transition regime.

C. Numerical Results

The horizontal velocity component profiles are plotted for Kn = 0.01, 0.05, 0.1, and 0.5 without an obstacle. These profiles are linear and intersect at the height y/H = 0.5 of the microchannel for both cases. For the first case, the intersection value of the profiles of (u/U_0) is equal to 0.5 (normalized), however, for the second case, it has the value 0. By increasing the degree of rarefaction Kn, slip velocity at the walls (moving and fixed) is increasing (Figs. 4a-4b). Note that the component u/U_0 keeps the same value according to the direction x and the vertical component of the velocity (v/U_0) is equal to zero. The horizontal velocity profiles are traced as a function of time steps number for the degrees of rarefaction Kn = 0.01, 0.05, 0.1, and 0.5 in order to compare the transient time of the MRT-LBM technique. With increasing the value of Kn, the number steps iteration necessary to the horizontal velocity to reach the stationary state decreases (Fig. 5).

By placing a square obstacle in the middle of the microchannel in the first case, the profile of the horizontal component along the vertical central line completely loses its linearity. As the degree of rarefaction Kn increases, the slip velocity at both walls increases (Fig. 6a). For $Kn = 0.5$, by comparing figures 4a and 6a, the value of the component u/U_0 of the velocity decreases from *0.25* to *0.11* at the bottom wall and also

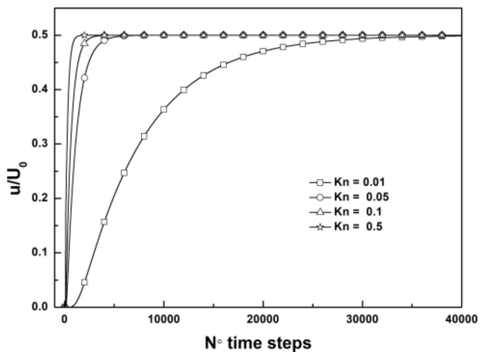

Figure 5. Evolution of the horizontal velocity component at the center of the microchannel for different values of Kn - case 1.

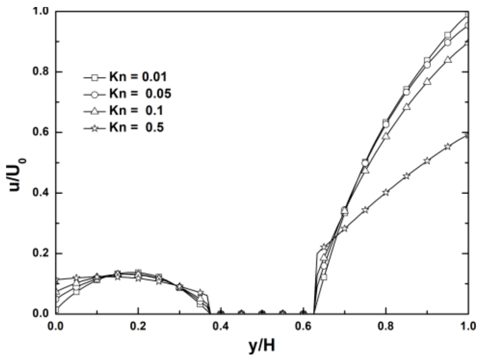

(a)

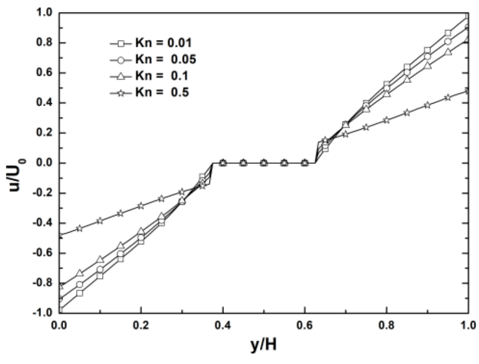

(b)

Figure 6. Profiles of u/U_0 along the vertical centerline in presence of square obstacle for Kn = 0.01-0.5 (a) case 1 and (b) case 2.

decreases from *0.75* to *0.59* at the upper wall. For the second case, far from the obstacle, the component u/U_0 keeps its linearity, also as *Kn* increases, the slip velocity increases (Fig. 6b). The value of u/U_0 at the two moving walls undergoes a slight decrease that can be neglected (from *0.5* to *0.48*).

Figures (7a-7d) show the effect of the presence of the rectangular obstacle on the streamlines and *u*-velocity component, for values of *Kn* = 0.01 and 0.1 in both cases. In the first case, two vortices appear near the stationary

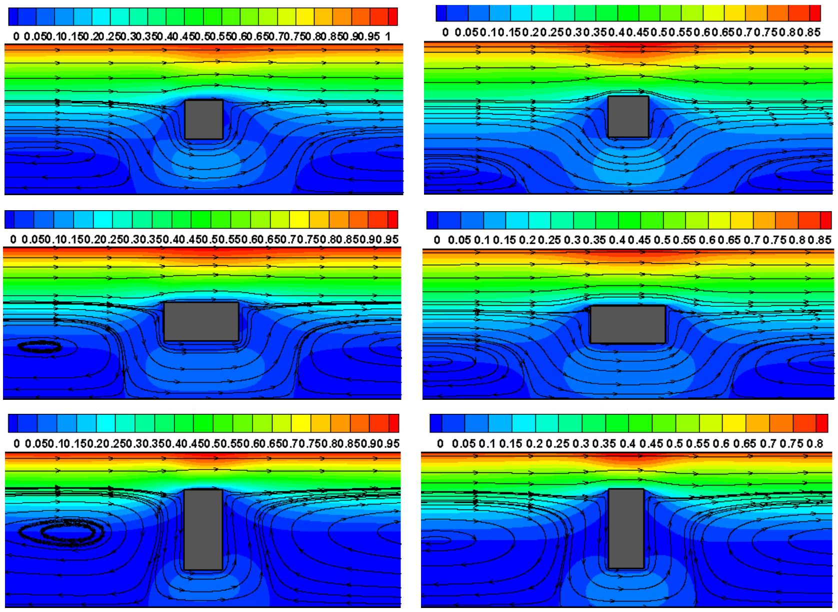

(a) Case 1 – *Kn*=0.01. (b) Case 1 – *Kn*=0.1.

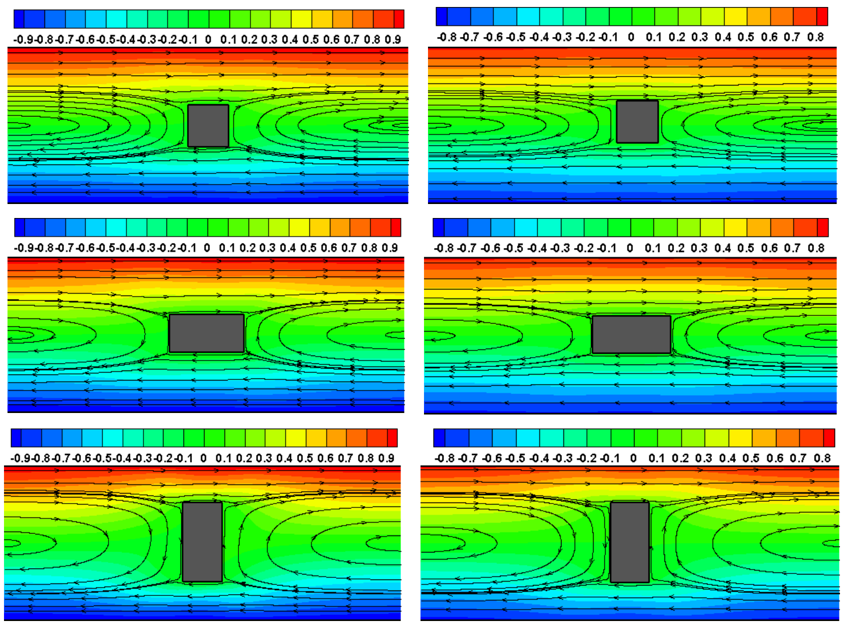

(c) Case 2 – *Kn*=0.01. (d) Case 2 – *Kn*=0.1.

Figure 7. Streamlines and *u*-velocity component obtained for *Kn* = 0.01 and 0.1 in presence of three types of obstacles.

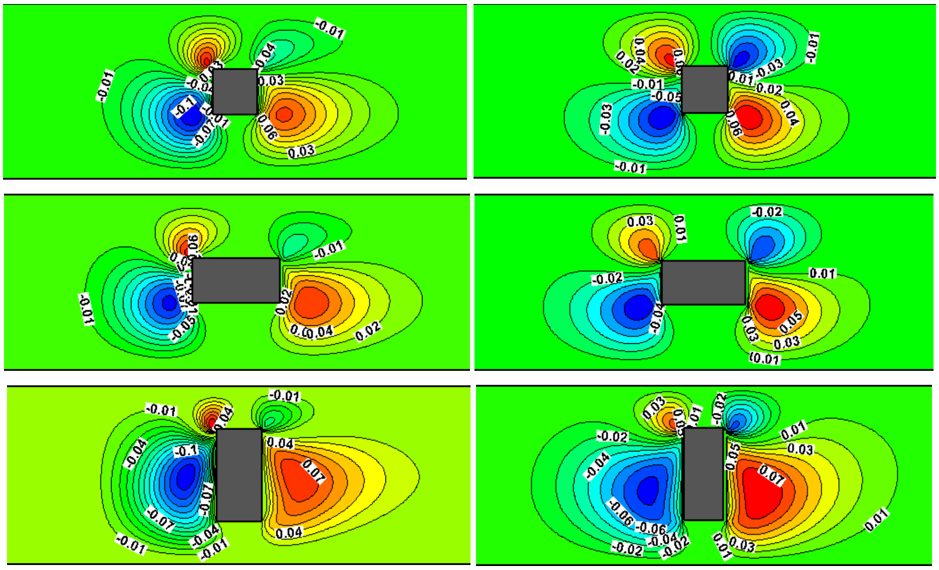

(a) Case 1 – *Kn*=0.01. (b) Case 1 – *Kn*=0.1.

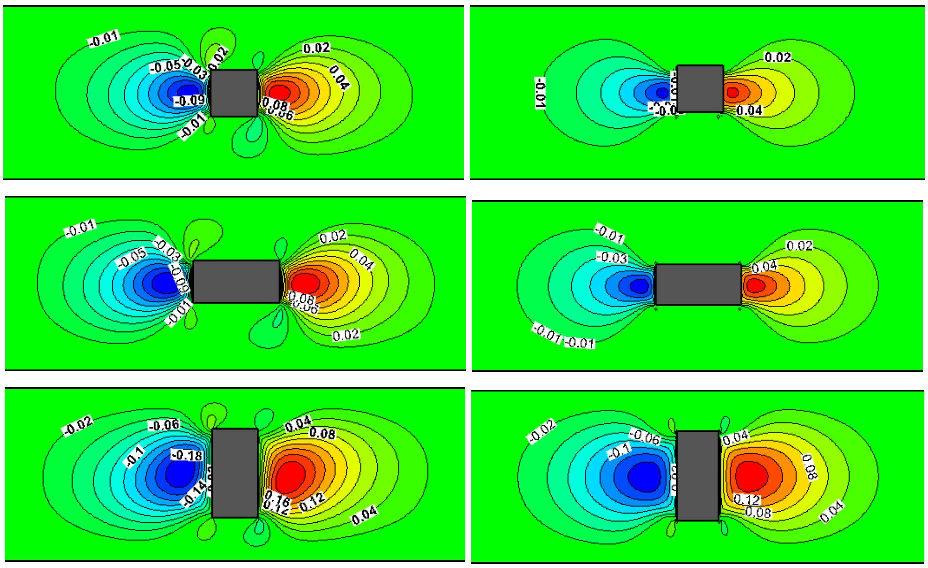

(c) Case 2 – *Kn*=0.01. (d) Case 2 – *Kn*=0.1.

Figure 8. Contours of *v*-velocity component obtained for *Kn* = 0.01 and 0.1 in presence of three types of obstacles.

wall, which are not totally symmetrical with respect to the central vertical line. The shape of the vortices narrows by increasing the value of *Kn* (Figs. 7a-7b). Figs. (7c-7d) show the effect of the presence of the obstacle on the streamlines for *Kn* = 0.01 and 0.1 in the second case. Because of the antisymmetry of the problem, the streamlines are symmetrical with respect to the horizontal centerline for the different values of *Kn*. We also observe the presence of two vortices caused by the obstacle, their centers are located respectively in the middle of the entrance and exit of the microchannel. As *Kn* increases, the shape of these vortices decreases and becomes more spread out. All these observations show the great influence of the presence of the obstacle on the flow. In the first case, the type of obstacle according to its length and width has an effect on the position of the vortices. Fig. 7a, for *Kn* = 0.01, the center of the vortex that forms on the right is formed at positions (*x/H*;*y/H*)=(0.26;0.28), (0.26;0.34) and (0.45; 0.48) respectively from top to bottom. In the second case, because of the antisymmetry of the problem, the type of obstacle has no effect on the position of the vortices (Figs. 7c and 7d). For both cases, by increasing the value of *Kn*, the slip velocity of the horizontal component (u/U_0) at the moving walls increases.

Without obstacle, the vertical component of the velocity is zero throughout the domain and for the different values of *Kn*. By placing an obstacle in the center of the domain (Figures 8a-8d), the length and width of the obstacle have effects on the v/U_0 component for both cases. The negative values are found after the first choc with the obstacle, more precisely on its left, while the positive values are on the right of the obstacle. We can also observe only in the first case that at the left/top corner of the obstacle, positive values of v/U_0 have appeared while at the right/top corner of the obstacle, negative values of v/U_0 are formed. By increasing the degree of rarefaction *Kn*, the values of v/U_0 decrease in both cases, since the gas becomes more ratified.

V. CONCLUSION

The MRT-LBM is employed in this investigation to examine gas flow in micro-geometries. The slip velocity measured in micro-Couette flow at various Knudson number values was demonstrated to be extremely precise and comparable to that of analytical solutions (without obstacles). The degree of rarefaction *Kn* and the type of obstacle placed in the middle of the microchannel have great effects on both components of the velocity (u/U_0, v/U_0) and the streamlines in both cases. The approach used maintains its stability in the slip regime for Kn = 0.01 and 0.1. Thus, to describe the gas micro-flows usually encountered in the devices of micro/nano-electromechanical systems, the MRT-LBM approach stands out as a good numerical calculation tool.

REFERENCES

[1] Gad-el-Hak, M. (1999). *The fluid mechanics of microdevices—the Freeman scholar lecture.*

[2] Sone, Y., Takata, S., & Ohwada, T. (1990). Numerical analysis of the plane Couette flow of a rarefied gas on the basis of the linearized Boltzmann equation for hard-sphere molecules. *European Journal of Mechanics B Fluids*, *9*(3), 273-288.

[3] Fan, J., & Shen, C. (2001). Statistical simulation of low-speed rarefied gas flows. *Journal of Computational Physics*, *167*(2), 393-412.

[4] Hssikou, M., Baliti, J., & Alaoui, M. (2016). The planar Couette flow with slip and jump boundary conditions in a microchannel. *Monte Carlo Methods and Applications*, *22*(4), 337-347.

[5] Xue, H., Ji, H. M., & Shu, C. (2001). Analysis of micro-Couette flow using the Burnett equations. *International Journal of Heat and Mass Transfer*, *44*(21), 4139-4146.

[6] Nie, X., Doolen, G. D., & Chen, S. (2002). Lattice-Boltzmann simulations of fluid flows in MEMS. *Journal of statistical physics*, *107*(1), 279-289.

[7] Yang, L. M., Shu, C., Wu, J., & Wang, Y. (2017). Comparative study of discrete velocity method and high-order lattice Boltzmann method for simulation of rarefied flows. *Computers & Fluids*, *146*, 125-142.

[8] Gallivan, M. A., Noble, D. R., Georgiadis, J. G., & Buckius, R. O. (1997). An evaluation of the bounce-back boundary condition for lattice Boltzmann simulations. *International journal for numerical methods in fluids*, *25*(3), 249-263.

[9] Lim, C. Y., Shu, C., Niu, X. D., & Chew, Y. T. (2002). Application of lattice Boltzmann method to simulate microchannel flows. *Physics of fluids*, *14*(7), 2299-2308.

[10] Tang, G. H., Tao, W. Q., & He, Y. L. (2005). Thermal boundary condition for the thermal lattice Boltzmann equation. *Physical Review E*, *72*(1), 016703.

[11] Elguennouni, Y., Hssikou, M., Baliti, J., Ghafiri, R., & Alaoui, M. (2020, April). SRT-LBM and MRT-LBM comparison for a lid-driven gas microflow. In *2020 1st International Conference on Innovative Research in Applied Science, Engineering and Technology (IRASET)* (pp. 1-6). IEEE.

[12] Elguennouni, Y., Hssikou, M., Baliti, J., & Alaoui, M. (2020). Numerical study of gas microflow within a triangular lid-driven cavity. *Advances in Science, Technology and Engineering Systems Journal*, *5*(5), 578-591.

[13] Bhatnagar, P. L., Gross, E. P., & Krook, M. (1954). A model for collision processes in gases. I. Small amplitude processes in charged and neutral one-component systems. *Physical review*, *94*(3), 511.

[14] Karniadakis, G., Beskok, A., & Aluru, N. (2006). *Microflows and nanoflows: fundamentals and simulation*, *29*. Springer Science & Business Media.

[15] d'Humières, D. (1992). Generalized lattice-Boltzmann equations. *Rarefied gas dynamics*.

[16] Baliti, J., Elguennouni, Y., Hssikou, M., & Alaoui, M. (2022). Simulation of Natural Convection by Multirelaxation Time Lattice Boltzmann Method in a Triangular Enclosure. *Fluids*, *7*(2), 74.

[17] Ansumali, S., & Karlin, I. V. (2002). Kinetic boundary conditions in the lattice Boltzmann method. *Physical Review E*, *66*(2), 026311.

[18] Niu, X. D., Shu, C., & Chew, Y. T. (2005). Numerical simulation of isothermal micro flows by lattice Boltzmann method and theoretical analysis of the diffuse scattering boundary condition. *International Journal of Modern Physics C*, *16*(12), 1927-1941.

[19] Ghatreh Samani, S., & Meghdadi Isfahani, A. H. (2019). A new relaxation time model for lattice Boltzmann simulation of nano couette flows in wide range of flow regimes. *Journal of Applied Fluid Mechanics*, *12*(6), 1781-1790.

Study the Effects of Vanadium (V) Concentration Doped with Tin Disulfide (SnS_2)

Shafi Ullah[1], Hanif Ullah[2], Vicente Compañ[3], Bernabe Mari Soucase[4]

[1,4]Instituto de diseño y Fabricación (IDF)-Universitat Politècnica de València (UPV), Camino de Vera, s/n, 46022 Valencia, Spain

[2]Department of Electrical Engineering, Federal Urdu University (FUUAST) Islamabad, Pakistan

[3]Departamento de Termodinámica Aplicada (ETSII), Universitat Politècnica de València, Camino de Vera s/n, 46022 Valencia, Spain

Abstract—**Tin disulfide (SnS_2) is a non-toxic and earth-abundant element with a direct band gap of about 2.2 to 2.4 eV, for these reasons the SnS_2 is a possible nominee to use as a buffer layer for photovoltaic applications. Here, we report the successful low-cost and easily available synthesis of non-toxic semiconductor materials SnS_2 prepared by hydrothermal technique. In order to realize and maximize the effect of incident photons in the visible light range, the low band gap and earth-abundant material vanadium (V) atoms have been incorporated in different atomic percentages (V = 0%, 2%, 4%, and 6%) into the SnS_2 compound. The synthesized compound was characterized by X-ray spectroscopy (XRD), Scanning electron microscopy (SEM), Energy dispersive microscopy (EDS), UV-Vis, and electrochemical measurements have been performed. The XRD analysis confirmed the dominant peaks related to SnS_2 and SnS_2 doped V without any impurities. The SEM and elemental composition analysis revealed the incorporation of V contents affects the morphology where the V contents were found homogeneously dispersed over the surface. Moreover, the optical analysis demonstrates that after the incorporation of V contents the transmission of film decreases, and absorption increases where the band gap is gradually decreased to the lower energy wavelength. The photoelectrochemical analysis was performed in three-electrode setups where the SnS_2; V photoanode exhibits 2.89 μA/cm^2 as compared to the SnS_2. Our results demonstrate the V content played important role when it's mixed with SnS_2 compound which may be a promising candidate for optoelectronic applications such as photoelectrochemical catalysts, photodetectors, and especially for photovoltaic applications.**

Keywords - tin disulfide, structural and photoelectrochemical performance

I. Introduction

Currently, binary, ternary, and quaternary composites have achieved enormous ability in optoelectronic applications [1]. Among the different ternary (CIS), quaternary (CIGS) and binary (CdTe) binary chalcogenide materials accessible for the large-scale photovoltaic application. In the field of photovoltaic some of them have the main difficulties such as elevated manufacture cost, toxicity of Se, shortage of In, Te and Ga, purity, mechanical deficiencies, stoichiometry, and high cost were extremely limited the usage of these composites for large scale commercial development [2]. Though, binary CdS based thin film solar cells (CdTe/CdS) have been developing some recreation of the above limitations, because of their easy stoichiometry protection with enhanced photoconversion productivity. In addition to this, CdS is an n-type semiconductor material with band gap energy ~2.45 eV has broadly examined as the window layer in several device applications [3]. To solve the above-mentioned restriction for using CdS we proposed and replaced the SnS_2 can be placed to substitute CdS materials due to its enhanced optical and structural properties [4]. SnS/SnS_2 are simple binary, inexpensive, non-toxic and earth abundant compounds with easily controllable stoichiometry and environment friendly material.

However, they have acceptable optoelectronic and electrical properties for thin film solar cells. Particularly, SnS is a favorable absorber material with good carrier mobility and shows a p-type electrical conductivity. According to literature review the SnS thin films demonstrated a direct optical band gap in the range of 1.2-1.5 eV and indirect optical transition in the range of 1.0-1.2 eV [5]. However, the reported conversion efficiency is 4.4% which is still away from its theoretical efficiency of about 33%. Probably, this different is mainly due to the mismatching of the band gape alignment between the absorber and buffer layer interface [6]. Therefore, the proposed SnS_2 buffer layer can play an important role due to their polycrystalline nature, non-toxic, earth abundant, high absorption coefficient of $>10^4$ cm^{-1}, varying energy band gape from 0.8-2.88 eV with n-type conductivity make it suitable candidate to use as a buffer layer for photovoltaic applications [7].

Many studies have been reported and using different technique for SnS_2 buffer layer preparation, such as vacuum evaporation, solvothermal, reactive evaporation, chemical vapour deposition (CVD), physical vapour deposition (PVD) and molecular beam epitaxy (MBE) [8], chemical spray pyrolysis [9], vacuum evaporation, solvothermal [10], reactive evaporation [11]. Though, the above techniques are based on high-cost vacuum techniques which lead to excessive production cost. Nevertheless, very few reports are available online based on synthesis of SnS_2 thin films by hydrothermal technique for solar cell application. In this work we synthesized SnS_2 thin films for solar cell application by using reasonably inexpensive, simple, and vacuum free method, which is hydrothermal technique which could lay down significantly the fabrication cost of the device.

II. Experimental Setup

All the starting materials were used without further refinement as received. For tin source 0.005 M of $SnCl_4$. $5H_2O$ solution was prepared in 20 ml of H_2O in previously dissolved tartaric acid ($C_4H_6O_6$) solution. For the Sulphur source 0.02 M thioacetamide (CH_3-CS-NH_2) was dissolved in same way as for the Sn ions. Both solutions were mixed and stirred for 30 minutes and then the mixed solution was transferred to 50 ml of Teflon stainless autoclave. The autoclave was kept in electric oven at 200 °C for 12 hours. Finally, the product washed with water and ethanol by centrifugation (4000 rpm) and subsequently the obtained product dried at 100°C for 5 hours.

III. Results and Discussions

The structural analysis was performed by using X-ray diffraction (XRD) from 10-60º at 2 theta range. The XRD assessment shows the polycrystalline nature of the samples with multiple diffraction peaks Fig. 1. The main peaks are corresponding to (001), (100), (101), (003), (110), (111), (200) and (112) of brendite structure JCPDS (00-23-677). It was observed from the analysis that the intensities of the characteristic peaks slightly decrease after the incorporation of V contents, probably it can be suggesting that the bigger ion size of Sn (225 pm) are being replaced by the smaller size of V ions (205 pm). After the analysis it's confirmed that there are no secondary phases detected and all the main peaks are correlated to pure SnS_2. All the diffraction peaks are well match with the reported data and JCPDS (00-23-677) reference card. The average crystalline size D (nm) of SnS_2 was calculated by using the famous Scherrer formula. The structural parameter was also calculated and summarized in Table I.

Fig. 2. shows the SEM analysis of the obtained samples along with their elemental composition images. The surface morphology revealed that the topography of the films changed from big grain size to smoother surface as increased the doping concentration. The Vanadium incorporation leads the surface to the small grain size from 45 nm, 34 nm, and 28 nm for SnS_2, 2% and 4% respectively. It was observed that the elemental composition of SnS_2 was almost near stoichiometric 42 ± 5 and 58 ± 5

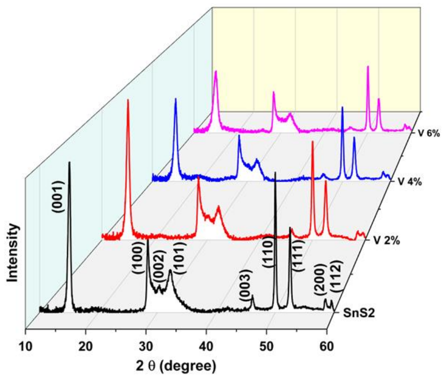

Figure 1. XRD spectra of SnS_2 doped Vanadium.

TABLE I. STRUCTURAL PARAMETER OF SnS_2 DOPED VANADIUM CONCENTRATION.

Peaks	2 θ	FWHM	D (nm)	Average	δ x 10^{-3} (nm^{-2})	ε x 10^{-3}
SnS_2-110	50.04	0.44	20.23	18.63	0.0025	0.00089
111	52.53	0.53	17.02		0.0035	0.0012
V-2% 110	50.03	0.31	22.17	20.52	0.003	0.0009
111	52.52	0.47	18.87		0.0029	0.0011
V-4% 110	50.07	0.43	20.64	18.16	0.0024	0.0009
111	52.55	0.57	15.69		0.0041	0.0013

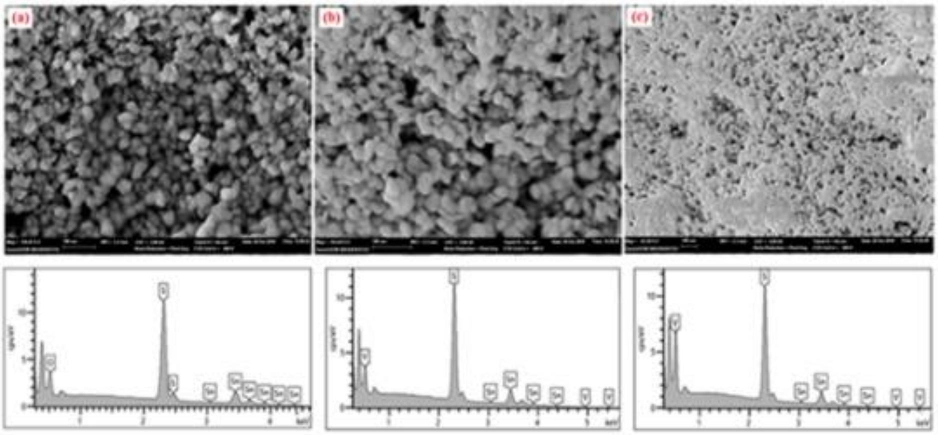

Figure 2. SEM images of the surface of SnS_2 doped Vanadium along with EDS analysis.

at % for Sn and S, respectively. The obtained results are in good agreement with the XRD analysis.

IV. OPTICAL ABSORPTION AND TRANSMISSION

The optical absorption and transmission of the synthesis thin films were recorded in the wavelength range of 350-1000 nm by using UV-vis-NIR spectrometer. Fig. 3(a,b) showed that the extreme light absorption observed in the visible wavelength range from 400-500 nm. Furthermore, by introducing the V content which played an important role and significantly increased the SnS_2 as we increased the V concentration. Moreover, the optical transitions from the incident photon energy hv (direct band gap) are calculated by using the following expression:

$$\alpha hv = A(hv - Eg)^{1/2} , \qquad (1)$$

where, α is the absorption coefficient, hv is the incident photon energy, A is constant and Eg is the energy band gap. The optical bandgap of the SnS_2 doped V examined from absorption spectrum by the extrapolated intercept on the straight section of the αhυ vs hv plot onto the energy axis. The optical bandgap of different V concentration illustrated in the Fig. 3(c), where the band gap is gradually decreases and we increased the V content to the SnS_2 precursor. The bandgap energy for SnS_2 is 2.40 eV, V 2% 2.38 eV, V 4% 2.36 eV and for V 6% 2.28 eV, respectively.

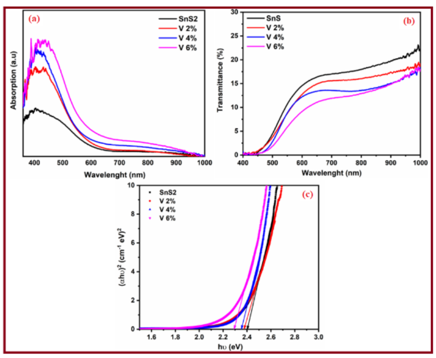

Figure 3. (a) Optical absorption, (b) transmission and (c) energy bandgap of SnS2 doped V.

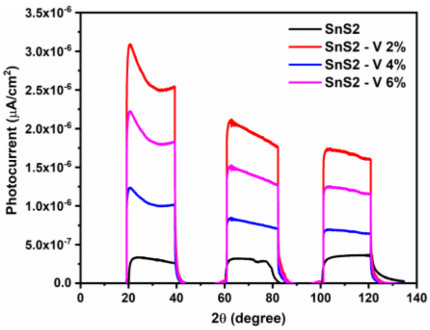

Figure 4. Photocurrent response of SnS2 and doped different V (2%, 4% and 6 %) concentration.

V. Electrochemical Analysis

Photocurrent (I vs t) measurements of the SnS_2 doped V thin films were recorded in a three electrode potentiostat setup, where the working is SnS_2, a saturated calomel is a reference electrode and platinum plate is a counter electrode under a bias voltage of 0.5 V at time scale from 20 to 120 seconds. the light source was a Xenon lamp (PLSSXE300/300UV) equipped with a UV cut-off filter ($\lambda > 420$ nm). The photocurrent response of various samples demonstrated with a current change from 0μA to 3 μA approximately under UV illumination. It's noted from the outcomes that vanadium 6% shows a significant photocurrent response ($3.0*10^{-6}$A cm^{-2}) as compared to the pure SnS_2 ($4.0*10^{-7}$A cm^{-2}) thin films.

The improvement of the light response by introducing the dopant concentration of V (2%, 4% and 6%) promoted the electron transport and film conductivity. The increases in the photocurrent response upon V concentration can be concluded by two reasons. First, pure SnS_2 is powerless to attract high wavelengths above 650 nm energy. Secondly, which may occur due to sub-band (intermediate band).

VI. Conclusion

The SnS_2 doped V thin films were successfully prepared on ITO substrate by simple and low-cost hydrothermal technique for large scale production. Structural, morphological, compositional, optical, and electrochemical analysis revealed that SnS_2 doped V thin film could be suitable as a buffer layer for the fabrication of solar cells. The flexibility of the tunable band gap determined that the SnS_2 can be good choice to mitigate the mismatching of the band gap between the absorber and window layer. The electrochemical analysis of various samples demonstrated that doped V 6% shows a remarkable photocurrent response ($3.0*10^{-6}$A cm^{-2}) as compared to the pure SnS_2 ($4.0*10^{-7}$A cm^{-2}) thin films. It can be concluded that SnS_2 doped V will be a suitable candidate for using it as a buffer layer for photovoltaic applications.

Acknowledgment

This work was supported by the, RRHH, postdoctoral contract (PAID-10-20), UNIVERSIDAD POLITECNICA DE VALENCIA and Ministerio de Economía y Competitividad (Grant Number PID2019-107137RB-C21), Valencia (Spain).

References

[1] Ghanwat, V. B., Mali, S. S., Bagade, C. S., Mane, R. M., Hong, C. K., & Bhosale, P. N. (2016). Thermoelectric Properties of Indium (III) ‐ Doped Copper Antimony Selenide Thin Films Deposited Using a Microwave ‐ Assisted Technique. *Energy Technology*, 4(7), 835-842.

[2] Jackson, P. et al. (2011). New world record efficiency for Cu (In, Ga) Se2 thin ‐ film solar cells beyond 20%. *Progress in Photovoltaics: Research and Applications*, *19*(7), 894-897.

[3] Khot, K. V. et al. (2014). Novel-approach for fabrication of CdS thin films for photoelectrochemical solar cell application. *Journal of Materials Science: Materials in Electronics*, 25(12), 5606-5617.

[4] Shi, C., Yang, P., Yao, M., Dai, X., & Chen, Z. (2013). Preparation of SnS2 thin films by close-spaced sublimation at different source temperatures. *Thin Solid Films*, *534*, 28-31.

[5] Reddy, V. R. M., et al(2015). Development of sulphurized SnS thin film solar cells. *Current Applied Physics*, *15*(5), 588-598.

[6] Jiang, F., Shen, H., Wang, W., & Zhang, L. (2011). Preparation of SnS film by sulfurization and SnS/a-Si heterojunction solar cells. *Journal of the Electrochemical Society*, *159*(3), H235.

[7] George, J., & Kumari, C. V. (1983). Growth and characterization of tin disulphide crystals grown by physical vapour transport method. *Journal of crystal growth*, *63*(2), 233-238.

[8] Kawano, K., Nakata, R., & Sumita, M. (1989). Effects of substrate temperature on absorption edge and photocurrent in evaporated amorphous SnS2 films. *Journal of Physics D: Applied Physics*, *22*(1), 136.

[9] Thangaraju, B., & Kaliannan, P. (2000). Spray pyrolytic deposition and characterization of SnS and SnS2 thin films. *Journal of Physics D: Applied Physics*, *33*(9), 1054.

[10] Du, W., Deng, D., Han, Z., Xiao, W., Bian, C., & Qian, X. (2011). Hexagonal tin disulfide nanoplatelets: a new photocatalyst driven by solar light. *CrystEngComm*, *13*(6), 2071-2076.

[11] Price, L. S., et al. (1999). Atmospheric pressure chemical vapor deposition of tin sulfides (SnS, Sn2S3, and SnS2) on glass. *Chemistry of materials*, *11*(7), 1792-1799.

Distribution Grid Reliability Improvement Considering Electricity Customers' Satisfaction based on the Kano Model

Amir Niromandfam[1], Ramin Niromandfam[2]

[1]Sahand University of Technology, Tabriz, Iran
[2]Azad Islamic University, Bonab, Iran

Abstract—**Current electricity service providing models are oblivious the customers individual perspectives and needs in which the main criteria is average of the customers' service quality. These models strive to provide a higher average service as possible which leads to a higher service cost to all the customers. Today, the concept that providing higher service leads to more customer satisfaction is becoming obsolete and instead the idea that the level of service should be provided based on the customer's point of view has been replaced. This paper utilizes the Kano model to identify the customers' individual viewpoints. The Kano model is used widely for measuring customer satisfaction which offers an overview of what features delight, want, need, indifferent, or are dissatisfy the customers. This model tries to understand the emotional impact of different functionalities on customers based on a special questionnaire and a Kano evaluation table. In this paper, the identified viewpoints regard to the electricity service will be mapped to the electricity grid's equipment. The selected functionalities in this paper are reduction of outage duration, outage frequency, and voltage fluctuations. In the numerical section, a multi objective programming model is utilized to allocation different equipment in the grid in with the goals of the customers' satisfaction maximization, the investment minimization and the hardness of work minimization. The hardness of work is adopted to consider the distribution network viewpoint in the equipment allocation problem.**

Keywords - customer request, Kano model, distribution network, goal programming model

I. INTRODUCTION

Current electricity services are designed based on the incentive-based model for Distribution Companies (Disco). Also, these models are oblivious the customers' perspective. Distribution companies optimize the location of equipment by considering technical and financial constraints to achieve the maximum service level. In the incentive-based model, the average level of service is utilized to penalize or incentive the Disco [1-2]. In these models, the customer's perspective has not considered in the service. Hence, it seems that a new model needs to be introduced to provide the service based on the customers' perspectives. Reference [3] expressed that service providing regardless the consumer vision is inefficient and suggested that technical insurance mechanism is used to upgrade distribution grid. Where, Disco provides different service levels and customers choose their desired reliability levels through the insurance contract.

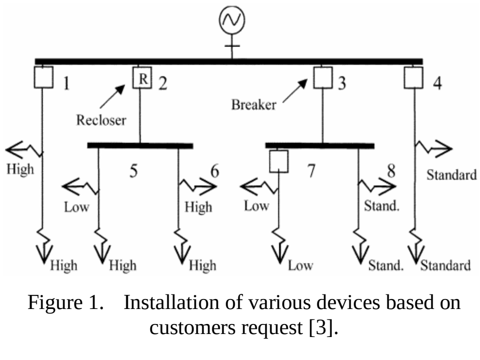

Figure 1. Installation of various devices based on customers request [3].

Disco uses the insurance premium to improve the grid or pay reimbursement (Fig. 1). These contracts enable Disco to provide service level according to the customers' vision by installing equipment based on the request.

Kano proposed a model for estimating the Customer Requests (CR) based on the operational and non-operational questions. Previous definition of quality was one dimensional, for instance good or bad quality and high or low social welfare. But Kano model propose a two-dimensional definition of quality. Putting together operational parameters of quality and satisfaction of customers in a two dimensional space, allows us to define quality in a sophisticated method utilizing two dimensional questionnaire. The vertical axis is the value of the customer satisfaction and the horizontal axis is the quality of service from the customer viewpoint. Reference [4] has utilized one more question about the importance of each customer's need. This paper has been used positive and negative coefficient to transform the qualitative request to the quantitative needs to plot a two dimensional curve. Kano polar model can provide a better investigation of the customers' needs and classify the customers' needs in a polar system. In this paper, we will utilize the polar Kano model to identify electricity customer's perspective regards electricity service. In addition to the customers' perspectives, we strive to consider distribution Company's vision to allocate optimally the equipment in the grid. Because these selected objectives cannot be expressed through the same unit, this paper will utilize a multi-objective programming to solve the allocation problem.

The rest of this paper has been organized as follows: In the next section, the overall view of the proposed allocation procedure will be described. Section III and IV are dedicated to describe the Kano model and detail of the proposed allocation model. Multi-objective goal programming will be described in Section V. The numerical results and paper concluded are discussed in Section VI, VII.

II. PROPOSED ALLOCATION MODEL

This paper proposes a new allocation model to install equipment in electricity grid based on the customers' requests. To this end, these requests have been mapped to technical needs such as fuse, breaker, re-closer and capacitor installation. To identify consumer requests and convert them into the technical requests, this paper utilizes the following steps.

1) First step: Investigation each customer requirement and its' importance.
2) Second step: Determination level of the customer's request by the Kano model $W(CRi)$.
3) Third step: Correcting $W(CRi)$ considering the service level that customers had been received (d_i).
4) Fourth step: Investigation technical needs and determination the relation between them and the customer request (R_{ij}).
5) Fifth step: Specifying the dependency matrix (r_{ij}).
6) Sixth step: Specifying the importance of technical needs (w_j).
7) Seventh step: Modeling Distribution Company views and equipment costs.
8) Eighth step: Formulating and optimization multi-objective programming to specify the equipment initialization value.

The first step in the decision algorithm is dedicated to investigate the customer requests which are often general and ambiguous. So, it is necessary to simplify these tasks by defining these requests in a standard and clear form. The customer's request interpretation is a difficult task hence this paper tries to translate them to the corresponding features. To this end, we ask experts to define the relation between customer requirement and technical needs and also define internal relation of technical needs. These relations often are general equations and show the general effect of a device on the customer requirement.

III. KANO MODEL

Through the Kano model, customer requirements can be categorized in five groups: must-be quality element, one dimensional quality element, attractive quality element, indifferent quality element and reverse quality element [5].

Must-be quality element: Existence of this element is essential for customer's satisfaction.

On the other hand, customer's satisfaction cannot improve through increasing these elements because the customer assumes the service includes them definitely.

One-dimensional quality element: In this case, customer satisfaction improvement is proportional to increase these elements.

Attractive quality element: Provision of these elements will improve customer's satisfaction extremely, but the lake of them cause no dissatisfaction.

Indifferent quality element: Some features of product or service cannot change viewpoint of the customer about the products. In the other word, the customer is neither satisfied nor dissatisfied whether the features implemented or not implemented.

Reverse quality element: Implementation of these features of product not only increases the customer satisfaction, but also decreases the consumer satisfaction.

Two dimensional Kano quality model is an effective tool for analysing the customer requests. This model utilizes functional and non-functional questionnaires to understand the customer requests (Table I). Also, Kano evaluation table (Table II) is a guiding tool for discovering the type of needs. Kano model explore customer views about products and services from questionnaires. First question is about the customer's reaction, when product has that property (functional aspect of the question). The second one is about the customer's reaction when the product hasn't that property (non-functional aspect of the question). After answering the questions, the importance of the request should be evaluation.

TABLE I. KANO QUESTIONNAIRE.

Kano question	**Answer**
Functional form of the question (*e.g., if the outage hours reduce, how do you feel*?)	□ I like it that way □ It must be that way □ I am neutral □ I can live with it that way □ I dislike it that way
Dysfunctional form of the question (*e.g., if the outage hours do not reduce, how do you feel*?)	□ I like it that way □ It must be that way □ I am neutral □ I can live with it that way □ I dislike it that way

For example, it is possible that outage hours decreasing is very welcome for many of customers but each one interprets different importance for it and pays different price to decrease his/her outage. So in addition to the original question, each customer should answer to the importance question as shown in Table III.

The terms (x_{ij}, y_{ij}, w_{ij}) represent the response of j^{th} consumer in the i^{th} feeder to the non-functional, functional and the importance question of the certain request of the consumer, respectively. From the other words, x_{ij} and y_{ij} mean "*What* are your feels?", w_{ij} means "How much do you estimate the value of your needs?".

TABLE II. KANO EVALUATION [5].

		Dysfunctional form of the question				
		Like	**Must-be**	**Neutral**	**Live with**	**Dislike**
Functional form of the question	Like	Q	A	A	A	O
	Must-be	R	I	I	I	M
	Neutral	R	I	I	I	M
	Live with	R	I	I	I	M
	Dislike	R	R	R	R	Q

A, Attractive; O, One-dimensional; M, Must-be; I, Indifferent; R, Reverse; Q,Questionable.

TABLE III. SCORES FOR SELF-STATED IMPORTANCE.

Not important		Somewhat important		Important		Very important		Extremely important	
0.1	0.2	0.3	0.4	0.5	0.6	0.7	0.8	0.9	1.0

Now, the mean value of the answers in each bus can be determined as follows:

$$\bar{X}_i = \frac{1}{J}\sum_{j=1}^{J} w_{ij} x_{ij}, \quad \bar{Y}_i = \frac{1}{J}\sum_{j=1}^{J} w_{ij} y_{ij} \quad . \tag{1}$$

Now $\left(\bar{X}_i, \bar{Y}_i\right)$ can be plotted in a two-dimensional diagram, so the various needs of the customers in each bus can compare with the other buses where the horizontal and vertical axes indicate the dissatisfaction and satisfaction value of the needs (Fig. 2).

The characteristic of customer request (CR) can be represented as a polar vector, $\vec{r}_i \equiv \left(r_i, \phi_i\right)$, where $r_i = |\vec{r}_i| = \sqrt{\bar{X}_i^2 + \bar{Y}_i^2}$ is the magnitude of $\vec{r}_i$ and $\phi_i = \tan^{-1}\left(\bar{Y}_i / \bar{X}_i\right)$ is the angle between $\vec{r}_i$ and the horizontal axis. The magnitude of the vector (r_i) is called the importance index and the angle (ϕ_i) is called the satisfaction index where, $0 \le r_i \le \sqrt{2}$ and $0 \le \phi_i \le \pi/2$. The extreme situation, $\phi_i = 0$ means that the CR causes dissatisfaction, while functioning of CR does not enhance satisfaction, and hence it is an ideal must-be element. Conversely, $\phi_i = \pi/2$ means that customer request is an ideal attractive element (Fig. 3).The following equation can aggregate these two indices into a unique index [6]:

$$\mathrm{K}_i = \frac{2\sqrt{2}}{3}\left(1-\varphi_i/\pi\right)\times r_i \ . \qquad (2)$$

In general, value of the request depends on current level of it. Assume that for a customer decreasing of outage reduction is more important than voltage quality. So, the outage is decreased. Now the question is that how long the quality of other component be ignored and only the outage decreased.

TABLE IV. SCORES FOR FUNCTIONAL/DYSFUNCTIONAL FEATURE.

Answer to the Kano question	**Functional form of the question**	**Dysfunctional form of the question**
I like it that way (like)	1	-0.5
It must be that way (must be)	0.5	-0.25
I am neutral (neutral)	0	0
I can live with it that way (live with)	-0.25	0.5
I dislike it that way (dislike)	-0.5	1

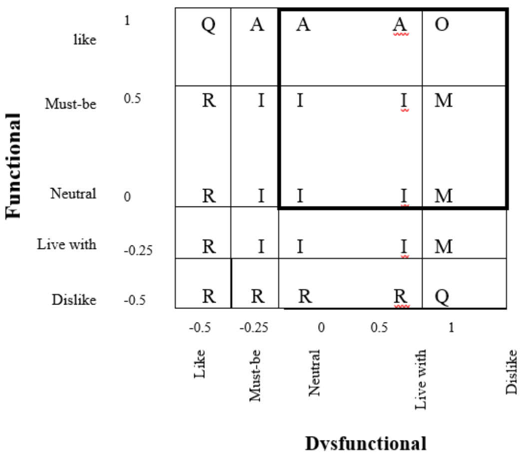

Figure 2. Tow dimensional Kano model.

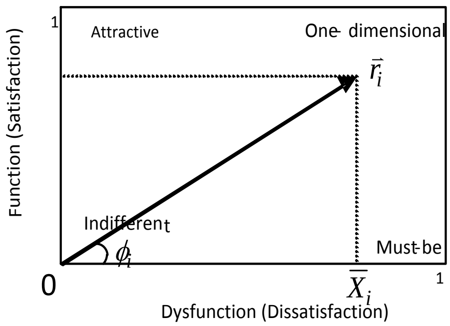

Figure 3. Polar representation of customer perception based on the Kano model [6].

In this paper, the slope of the request curve, d_i, is utilized to evaluate the current service level impact in the request as formulated (3).

$$d_i = \frac{\left(S_{\max_i} - S_i\right)}{\left(S_{\max_i} - S_{\min i}\right)} \ , \qquad (3)$$

where, $S_{\max_i}$ $S_{\min_i}$ and S_i represent the maximum, minimum and current level of customer service, respectively.

After specification of customer requests, the relationship between each request and technical needs should be determined. In this paper, the these relationship are identified by the expert team which are illustrated in Table IV.

IV. CALCULATION OF CUSTOMER REQUIREMENT WEIGHT

The customer requirement importance is extracted by a weighting factor which is defined as follows [7]:

TABLE V. RELATION BETWEEN CUSTOMERS REQUESTS AND TECHNICAL NEEDS.

	Capacitor	**Recloser**	**Breaker**	**Fuse**
Reduce Outage	Without correlation	Medium Correlation	High correlation	High Correlation
Reduce outage	Without correlation	High correlation	Low correlation	Medium correlation
Voltage fluctuatio	High correlation	Low correlation	Low correlation	Low correlation

$$W\left(CR_i\right)=\frac{d_i \times \mathrm{K}_i}{\sum_{l=1}^{L} d_l \times \mathrm{K}_l} \quad , \tag{4}$$

where, K is the satisfaction index from Kano model and d is the slope of customer request.

Relationship between customer request with technical needs and internal relation of technical needs can calculated from below equation:

$$R'_{ij}=\frac{\sum_{k=1}^{n} R_{ik} \times r_{kj}}{\sum_{j=1}^{n}\sum_{k=1}^{n} R_{ik} \times r_{kj}} \quad , \tag{5}$$

where, R_{ij} is the normalized relation between i^{th} customer requirement and j^{th} technical needs (see Table V). r_{ij} represents internal relation by technical needs (Table VI). Also, for each customer request we have $\sum R'_{ij}=1$.

Fuzzy system is used for assessment of degree of dependency, because these relations have inherent imprecise. So, $\tilde{\Re}_{ik}$ and $\tilde{\gamma}_{ik}$, are fuzzy numbers that indicate the relation of customer request with technical needs and indicate the internal relation of technical needs. To define the fuzzy relation of membership function $\tilde{\Re}_{ik}$, the concept of cut α is used in this paper. The lower and upper limits of cuts α of $\tilde{\Re}'_{ij}$ are shown in a simplified form as follows [8]:

$$\tilde{\Re}'_{ij}=\frac{\sum_{k=1}^{n} \tilde{\Re}_{ik} \times \tilde{\gamma}_{kj}}{\sum_{j=1}^{n}\sum_{k=1}^{n} \tilde{\Re}_{ik} \times \tilde{\gamma}_{kj}} \quad , \tag{6}$$

$$\left(\tilde{\Re}'_{ij}\right)_a^l=\frac{\sum_{k=1}^{n} \left(\tilde{\Re}_{ik}\right)_a^l \times \left(\tilde{\gamma}_{kj}\right)_a^l}{\sum_{j=1}^{n}\sum_{k=1}^{n} \left(\tilde{\Re}_{ik}\right)_a^u \times \left(\tilde{\gamma}_{kj}\right)_a^u} \quad , \tag{7}$$

$$\left(\tilde{\Re}'_{ij}\right)_a^u=\frac{\sum_{k=1}^{n} \left(\tilde{\Re}_{ik}\right)_a^u \times \left(\tilde{\gamma}_{kj}\right)_a^u}{\sum_{j=1}^{n}\sum_{k=1}^{n} \left(\tilde{\Re}_{ik}\right)_a^L \times \left(\tilde{\gamma}_{kj}\right)_a^L} \quad . \tag{8}$$

Now importance of j^{th} technical needs can be determine for each bus separately as follows:

$$\tilde{W}_j=\sum W\left(CR_i\right).\tilde{\Re}'_{ij} \quad . \tag{9}$$

So, the upper and lower limits of $\tilde{w}_j$ in each cut α can be calculated from the below equation:

$$\left(W_j\right)_a=\left[\left(W_j\right)_a^L,\left(W_j\right)_a^u\right]= \\ =\left[\sum_{i=1} W\left(CR_i\right)\times\left(\Re'_{ij}\right)_a^l, \sum_{i=1} W\left(CR_i\right)\times\left(\Re'_{ij}\right)_a^u\right] . \tag{10}$$

It is assumed that the member function is a fuzzy triangular number that can be calculated by linearization. For example if $\tilde{\Re}_{ij}$ would be considered strong, it can show by fuzzy number $s=(0.8,0.9,1)$ then, the membership function would be as:

$$\mu_s(R_{ij})=\begin{cases}\dfrac{\left(R_{ij}-0.8\right)}{\left(0.9-0.8\right)} & 0.8 \le R_{ij} \le 0.9 \\ \dfrac{\left(1-R_{ij}\right)}{\left(1-0.9\right)} & 0.9 \le R_{ij} \le 1\end{cases} \quad , \tag{11}$$

where, μ_s is the membership function. The cuts α of the membership function will be as (12):

$$\left[\left(R_{ij}\right)_a^L,\left(R_{ij}\right)_a^u\right]=\left[0.8+0.1a, 1-0.1a\right] \quad . \tag{12}$$

Also, if $\tilde{\Re}_{ij}$ evaluated as medium, it can be shown by fuzzy number $s=(0.2,0.3,0.4)$ then, the membership function would be as:

$$\mu_s(R_{ij})=\begin{cases}\dfrac{\left(R_{ij}-0.2\right)}{\left(0.3-0.2\right)} & 0.2 \le R_{ij} \le 0.3 \\ \dfrac{\left(0.4-R_{ij}\right)}{\left(0.4-0.3\right)} & 0.3 \le R_{ij} \le 0.4\end{cases} \quad . \tag{13}$$

The cuts α of membership function are:

$$\left[\left(R_{ij}\right)_a^L,\left(R_{ij}\right)_a^u\right]=\left[0.3+0.1a, 0.4-0.1a\right] \quad . \tag{14}$$

Also, if $\tilde{\Re}_{ij}$ will be evaluated as weak, it can be shown by fuzzy number of s = (0.0,0.1,0.2) in which the membership function would be as follows:

$$\mu_s(R_{ij}) = \begin{cases} \dfrac{(R_{ij} - 0.0)}{(0.1 - 0.0)} & 0.0 \le R_{ij} \le 0.1 \\ \dfrac{(0.2 - R_{ij})}{(0.2 - 0.1)} & 0.1 \le R_{ij} \le 0.2 \end{cases} . \quad (15)$$

The cuts α of the membership function would be as follows:

$$\left[(R_{ij})_a^L , (R_{ij})_a^u \right] = [0.0 + 0.1a, 0.2 - 0.1a] . \quad (16)$$

Now equations' values can be changed to the fuzzy numbers as shown in Table VII. Similarly, the internal relation of technical needs can be written as a fuzzy number.

TABLE VI. DEPENDENCY MATRIX.

	C	R	B	F
F	Low correlation	Medium correlation	High correlation	-
B	Low correlation	Medium correlation	-	-
R	Low correlation	-	-	-
C	-	-	-	-

F, Fuse; B, Breaker; R, Recloser; C, Capacitor

V. GOAL PROGRAMMING MODEL

To install the equipment, the viewpoint of Distribution Company cannot be disregarded. To this end, in this paper, the function of cost and hardness of work are defined as indices for Distribution Company satisfaction that expert determine their levels. The function of cost is selected to consider different equipment cost and the function of hardness is selected to consider the hardness of work. Same as the customers' perspective, Disco's perspective will be converted to the fuzzy quantity. Because these objectives, customers' satisfaction, equipment cost, and the hardness of work, are not in a same unit, we need a multi-objective programming model to solve the equipment allocation problem. To this end, this paper utilizes the goal programming model to solve the problem, which formulated as follows:

$$\max \sum_{j=1}^{n} \tilde{W}_j x_j \ \min \sum_{j=1}^{n} \tilde{C}_j x_j \ \min \sum_{j=1}^{n} \tilde{T}_j x_j , \quad (17)$$

where, x is decision variable vector and $\tilde{W}_j, \tilde{C}_j, \tilde{T}_j$ are the description of implementation of j^{th} technical needs, costs and hardness of work in the fuzzy form respectively.

Different weight for each objective function can be assumed. For example from the regulator points of view, customer satisfaction and cost reduction are more important than the hardness of work. In this paper, membership degree of customer satisfaction and costs are assumed greater than the membership degree of hardness of work.

$$\begin{aligned} \mu_1(x) &\ge \mu_3(x) \\ \mu_2(x) &\ge \mu_3(x) \end{aligned} . \quad (18)$$

Based on the three fuzzy objects and their importance, multi-objective programming can be formulated as equation (19), where, L_j indicates the minimum estimation of technical needs that achieved by mapping the minimum available service to the customer.

VI. CASE STUDY

To represent the effectiveness of the proposed model, we develop a questioner and collect answers from 100 household customers. For simplicity, all the customers have been choice from one feeder. Then we solve 21 linear programming model using 11 a-cuts. By using the model and consumers' answers, the Kano and sensitivity coefficients are calculated

TABLE VII. FUZZY RELATION BETWEEN CUSTOMERS REQUEST AND TECHNICAL NEEDS.

	C	R	B	F
Reduce outage hours	0+0.1α 0.2-0.1α	0.2+0.1α 0.4-0.1	0.8+0.1α 1-0.1α	0.8+0.1α 1-0.1α
Reduce outage frequency	0+0.1α 0.2-0.1α	0.8+0.1α 1-0.1α	0+0.1α 0.2-0.1α	0.2+0.1α 0.4-0.1
Voltage fluctuations	0.8+0.1α 1-0.1α	-	-	-

according to Table VIII. Utilizing these coefficients, the degree of relative importance can be obtained.

After determining consumer's requests, expert team had been asked to express the hardness and cost of different equipment by fuzzy numbers. Table IX and X illustrate the cost and hardness from the experts' vision in fuzzy representations.

$$
\begin{aligned}
&\tilde{z} = \max \sum_{h=1}^{3} \tilde{\mu}_h(x) \\
&st: \\
&\tilde{\mu}_1(x) = \frac{\sum_{j=1}^{n} \tilde{W}_j x_j - G_1^{\min}}{G_1^{\max} - G_1^{\min}} \\
&\tilde{\mu}_2(x) = \frac{G_2^{\max} - \sum_{j=1}^{n} \tilde{C}_j x_j}{G_2^{\max} - G_2^{\min}} \\
&\tilde{\mu}_3(x) = \frac{G_3^{\max} - \sum_{j=1}^{n} \tilde{T}_j x_j}{G_3^{\max} - G_3^{\min}} \\
&\tilde{\mu}_1(x) \geq \tilde{\mu}_3(x) \\
&\tilde{\mu}_2(x) \geq \tilde{\mu}_3(x) \\
&\tilde{\mu}_i(x) \leq 1 \\
&\tilde{\mu}_i(x) \geq 0 \qquad i = 1,2,3 \\
&x_j \geq L_j \qquad j = 1,\ldots,n \\
&0 \leq x_j, L_j \leq 1
\end{aligned} \tag{19}
$$

TABLE VIII. KANO'S COEFFICIENTS, SLOP OF REQUEST AND DEGREE OF RELATIVE BASE ON CUSTOMER'S ANSWER (CR).

CR	K	d	W(CR)
Reduce Outage hours	0.94	0.91	0.3667
Reduce outage frequency	0.85	0.92	0.3352
Voltage fluctuations	0.81	0.86	0.2986

TABLE IX. THE COST OF TECHNICAL REQUIREMENTS BASED ON THE EXPERT TEEM'S ANSWERS.

a	F	B	R	C
0	0.2-0.4	0.8-1	0.8-1	0.6-0.9
0.5	0.25-0.35	0.85-0.95	0.85-0.95	0.7-0.8
1	0.30	0.90	0.90	0.75

TABLE X. THE HARDNESS OF TECHNICAL REQUIREMENTS BASED ON THE EXPERT TEAM'S ANSWERS.

a	F	B	R	C
0	0.2-0.5	0.6-0.9	0.6-0.9	0.8-0.1
0.5	0.35-0.45	0.7-0.8	0.7-0.8	0.85-0.95
1	0.35	0.75	0.75	0.90

Upper and lower limits of each goal have been determined by solving optimization in cut zero (a=0). The result of optimization for customer's satisfaction (G_1), cost (G_2) and hardness (G_3) are (0.247, 1.43), (1.61, 5) and (1.76, 5) respectively. It is clear that the object level of cost and hardness are closer to each other and achievement them is easier than the object of customer's satisfaction.

Then by solving 21 linear programming model and using 11 a-cuts, can be determine level of each goals and theirs membership degree. Also, (z_a^l , z_a^h) and levels of each request can be calculate. Table XI shows the results of solving model for each goal for X_1. Table XII illustrates upper and lower levels of each technical requests. The fuzzy numbers can be reverted to scalar form as shown in Table XII.

This numbers can be used as a factor in equipment placement. For example, requirement to installing the Fuse in the studied feeder is calculated between (0.77, 0.92). It means that fuse installation cannot go lower than 0.77 and upper than 0.92 to achieve the defined goals. Finally, it should be noted that these numbers are unit less and are only used to compare and measure the importance of different equipment installation impact.

TABLE XI. UPPER AND LOWER LIMITS FOR OBJECTIVE FUNCTION FOR X1.

a	μ_1		μ_2		μ_3	
	L	U	L	U	L	U
0.0	0.57	0.73	0.32	0.75	0.30	0.75
0.1	0.56	0.76	0.33	0.73	0.33	0.74
0.2	0.61	0.78	0.34	0.70	0.35	0.71
0.3	0.62	0.74	0.37	0.67	0.38	0.69
0.4	0.67	0.79	0.38	0.65	0.38	0.65
0.5	0.70	0.82	0.40	0.62	0.40	0.62
0.6	0.71	0.76	0.43	0.60	0.44	0.74
0.7	0.72	0.78	0.44	0.58	0.44	0.59
0.8	0.73	0.77	0.47	0.56	0.47	0.57
0.9	0.73	0.74	0.52	0.52	0.53	0.53
1	0.74	0.74	0.52	0.52	0.53	0.53

TABLE XII. UPPER AND LOWER LIMITS AND DEFUZZY LEVEL OF TECHNICAL REQUEST (TR).

	Low Band	High Band	Defuzzy
F	0.77	0.92	0.85
B	0.59	0.84	0.71
R	0.61	0.82	0.72
C	0.72	0.79	0.75

VII. CONCLUSIONS

This paper utilized the Kano model to improve the quality and reliability of distribution network by installing various equipment from electricity customers' needs. These needs have been expressed by the qualitative phrase. So, at first these needs have been changed to the quantitative data with fuzzy method and then these data have been mapped to the technical needs for installing equipment. Also, for acquiring customers' satisfaction and increasing efficiency, the satisfaction of Distribution Company also has considered. Output of this model is the numbers that indicate the benefit of equipment installation from the various customers' vision. Furthermore, these numbers can be used to determine the placement of various devices that satisfy the customers and the distribution companies by financial and technical consideration.

REFERENCES

[1] Niromandfam, A., Yazdankhah, A. S., & Kazemzadeh, R. (2020). Design of reliability insurance scheme based on utility function for improvement of distribution grid reliability. *Journal of Operation and Automation in Power Engineering*, *8*(3), 257-272.

[2] Niromandfam, A., Karimizare, P., Sheikh-El-Eslami, M., & Haghifam, M. (2012). Distribution network upgrading base on expected utility by using insurance model.

[3] Niromandfam, A., Choboghloo, S. P., Yazdankhah, A. S., & Kazemzadeh, R. (2020). Electricity customers' financial and reliability risk protection utilizing insurance mechanism. *Sustainable Energy, Grids and Networks*, 24, 100399.

[4] Ho, H. H., & Tzeng, S. Y. (2021). Using the Kano model to analyze the user interface needs of middle-aged and older adults in mobile reading. *Computers in Human Behavior Reports*, 3, 100074.

[5] Bhardwaj, J., Yadav, A., Chauhan, M. S., & Chauhan, A. S. (2021). Kano model analysis for enhancing customer satisfaction of an automotive product for Indian market. *Materials Today: Proceedings*, 46, 10996-11001.

[6] Lai, X., Tan, K. C., & Xie, M. (2007). Optimizing product design using quantitative quality function deployment: a case study. *Quality and reliability engineering international*, *23*(1), 45-57.

[7] Temponi, C., Yen, J., & Tiao, W. A. (1999). House of quality: A fuzzy logic-based requirements analysis. *European Journal of Operational Research*, *117*(2), 340-354.

[8] Chen, L. H., & Ko, W. C. (2008). A fuzzy nonlinear model for quality function deployment considering Kano's concept. *Mathematical and Computer Modelling*, *48*(3-4), 581-593.

Renewable Hydrogen Production by Bioconversion Process and Pyrolysis of Biomass

Victor Carlos de L. Arruda[1], Philip Alexandre A. V. dos Santos[2], Taynara Geysa Silva do Lago[3], Flávia de Medeiros Aquino[4], Joelda Dantas[5], Silvia Layara Floriani Andersen[6]

[1,2]Postgraduate Program in Renewable Energy - UFPB, João Pessoa - PB, Brazil
[3,4,5,6]Department of Renewable Energy Engineering, Federal University of Paraíba, João Pessoa-PB, Brazil

Abstract—**Biomass is one of the alternatives to fossil fuels because it is renewable and can be a sustainable source of energy. Biofuels are forms of bioenergy obtained through renew-able sources. Biomass is less polluting than fossil fuels, thus reducing greenhouse gas emissions, as well as enabling waste treatment. From treatment to processing, biomass can be used to produce green hydrogen, either from the electrolysis of water using electricity from biomass. One of the processes for obtaining H2 from biomass is anaerobic digestion (AD). AD converts biomass into biogas, digested material and renewable energy such as bioelectricity and biofuels. Another process is pyrolysis or thermolysis. It is a thermochemical reaction system in which dehydration and decomposition of matter occur in an oxygen-free atmosphere. Pyrolysis products are bio-oil, gas and bio-char, and can be applied in the energy sector. This work aims to introduce the production of bioenergy, especially green H2 through AD and Pyrolysis from biomass, and its main conditions and technological arrangements seen in the literature.**

Keywords – bioenergy, anaerobic digestion, pyrolisys, green hydrogen

I. INTRODUCTION

Currently the highest percentage of energy consumed by humans originates from fossil fuels (about 81% in 2019). The use of fossil fuels generates environmental impacts that can affect human well-being and health. Global concern for new energy sources has been increasing in recent years due to the numerous climate changes caused by air pollution [1].

Renewable energy sources (ER) are those considered inexhaustible by human standards of use. They are supported through natural resources that do not decrease over time. Renewable energy sources examples are solar energy, hydroelectric, geothermal, tidal and biomass. Such technologies offer minimal environmental impact and present the economy with a means for carbon neutralization. The concept of clean energy is often associated with renewable sources, when compared to fossil fuels they reduce environmental impacts and generate virtually no waste or emissions of pollutants [2].

Through the Paris Agreement (2015), the international community has set targets to reduce the effects of climate change. The world needs to reduce carbon dioxide emissions in the atmosphere and thus reduce the temperature increase by up to 1.5 °C or even 2 °C by the end of the century. The decarbonization of the energy matrix is one of the frontlines of the countries. ER sources had a 14% share in the world's primary energy supply in 2019, so, to meet the Paris Agreement itinerary, the share of direct electricity in total final energy consumption is expected to increase from 21% in 2019 to more than 50% in 2050. Furthermore, the share of renewables in electricity generation would have to increase from 26% in 2019 to 90% in 2050 [1,3].

Several countries have innovated and encouraged research on renewable energy to find economically viable and less polluting alternatives. Several technological methods have been developed in commercial projects,

ISBN: 978-86-82602-01-9

such as solar thermal, photovoltaic systems and biomass energy. The photovoltaic solar system uses photovoltaic cells (SF) that convert solar energy into electricity. The solar thermal system (ST) uses solar thermal collectors that convert solar energy into heat through heat transfer, which can be used for heating or cooling purposes. Water heating technology using solar radiation is an economical choice for developing countries. Energy derived from biomass, bioenergy, plays a significant role in the future by reducing the amount of CO_2 in the atmosphere compared to fossil fuels [4,5].

This template, modified in MS Word 2013 provides authors with most of the formatting specifications needed for preparing electronic versions of their papers. All standard paper components have been specified for three reasons: (1) ease of use when formatting individual papers, (2) automatic compliance to electronic requirements that facilitate the concurrent or later production of electronic products, and (3) conformity of style throughout a conference proceedings. Margins, column widths, line spacing, and type styles are built-in; examples of the type styles are provided throughout this document and are identified in italic type, within parentheses, following the example.

A. Biomass Energy

Biomass has been used by humans for millennia and was the main source of energy before the discovery of fossil fuels. Bioenergy is obtained by traditional means through the direct combustion of biomass. Recently biomass has been reintegrated in the world's largest-scale energy supply, by modern means, through the gasification of wood and other materials, carbon sequestration and biofuels such as biogas and biodiesel [2,6,7].

Biomass becomes one of the alternatives to fossil fuels and it can reduce fuel imports and promote energy security. Biomass energy is obtained in direct and indirect consumption. Direct consumption is based on burning by heating, cooling and industrial processes. While indirect consumption consists in the conversion of biomass into secondary energy. Biomass resources are accessible worldwide, in its various forms, such as animal manure, municipal solid waste, agricultural waste – its most abundant form, industrial effluents and wastewater [42,7,8].

RenovaBio is a policy for the use of biofuels in Brazil, in which it recognizes the important contribution to the implementation of the agreements made by Brazil in the Paris Agreement, thus providing an expansion of biofuel production in the country and, consequently, reducing the production of fossil fuels. Renova Bio's policy involves the creation of objectives aimed at the decarbonization of the fuel sector, issuance of certificates to biofuel producers and generation of decarbonization credits and can make the sale of these credits in the market, stimulating the expansion of the production and commercialization of biofuels in Brazil [9].

Brazil is one of the largest producers of renewable energy in the world; by the year 2021, 44.7% of its energy matrix will come from clean and sustainable sources [10].

The transport sector in Brazil has a very diversified energy matrix (Ethanol, Biodiesel, Diesel Oil, Natural Gas, Gasoline, Aviation Kerosene and other biofuels). Biofuels were responsible for replacing about 22% of the percentage of petroleum-derived fuels in Brazil in 2021. Ethanol and biodiesel are consolidated in the national scenario and play a fundamental and strategic role in direct relation to the Brazilian decarbonization project [10].

B. Renewable H_2

Hydrogen is a simple, colorless, and odorless chemical element, its atom is composed of a single electron orbiting around a single proton. It has a lower density than air, and because it has low molecular weight and low viscosity, it is very susceptible to leaks. Its leakage rate is 50 times higher than that of water and 10 times higher than that of the liquid nitrogen. The energy power of hydrogen is seven times greater than that of fossil fuels. It is estimated that 1 kg of hydrogen has an equivalent energy of more than 2.75 kg of gasoline [11,12]. When compared to other fuels, hydrogen is shown to have higher energy power, as shown in Table I [14].

When produced by low- and zero-carbon production routes, then stored, and subsequently used in zero-emission energy conversion devices such as fuel cells, hydrogen can be used as a fuel source. It has great flexibility as an energy carrier and can be used as fuel for heavy road and rail transport, ships and aircraft. As well as it can be used in industrial processes and as a vector of domestic energy for cooking and heating [13,14].

Homes can also be powered locally, employing hydrogen fuel cells. It can also be burned to produce heat (thermal energy) for heating environments and hot water [15].

There are different routes for hydrogen production. For [16].hydrogen can be produced conventionally, from fossil fuels through the reform or pyrolysis of hydrocarbons, or alternatively through renewable sources.

When H_2 is produced from natural gas (NG) and other fossil fuels, being the result and by-product of industrial processes, accompanied by CO_2 emission, it is called Gray hydrogen. With the modification of the production process enabling the sequestration and storage of CO_2 (SSC) and at the same time preventing pollution the Gray hydrogen is often called Blue hydrogen. Green hydrogen is produced through water electrolysis using electricity from renewable sources, such as hydroelectric, wind, photovoltaic solar (PV) or biomass energy [17,18].

Currently, almost all the world's hydrogen is produced by a "gray" route. However, to achieve sustainable development hydrogen production must become increasingly green. Lower costs to produce green or renewable H_2 will increase hydrogen potential. That is, if solar and wind energy costs become cheaper, primary energy will be a mixture of renewable sources [19].

TABLE I. COMPARISON OF FUELS ENERGY POTENTIAL.

Fuel	(MJ/kg)
Hydrogen	120
Liquefied petroleum gas - LPG	54.4
Propane	49.6
Aviation gasoline	46.8
Automotive gasoline	46.4
Automotive diesel	45.6
Ethanol	29.6
Methanol	19.7
Dry wood	16.2
Bagasse	9.6

II. ANAEROBIC BIODIGESTION TO RENEWABLE H_2

Anaerobic Digestion (AD) is a process derived from microbial metabolism that produces biogas (methane) from the conversion of organic matter. The process occurs in the absence of oxygen, involving different microbial groups, each of them being responsible for the degradation of a category of organic compounds present in the system. The process occurs in 4 stages, which are hydrolysis, acidogenesis, acetogenesis and methanogenesis [20].

During (i) Hydrolysis, hydrolytic enzymes decompose complex organic substrates (proteins, carbohydrates, and fats) into amino acids and monomers. In (ii) Acidogenesis, solubilized monomers released from the hydrolysis process are further degraded to short-chain fatty acids, alcohols and keton as by acidogenic bacteria. At (iii) Ketogenesis, products produced in the previous phase are converted into acetic acid, hydrogen and carbon dioxide. Finally, in (iv) Methanogenesis; methane and CO_2 are produced under strict anaerobic conditions [21].

AD is a traditional route for the conversion of biomass into biogas, digestive and renewable energy. Biogas consists mainly of CH_4 (50-75% volume), CO_2 (25-50%) and trace gases (1-2%). Its composition and quantity depend on the efficiency of the biochemical process, influenced by temperature, pressure and pH. Biogas can be easily stored and distributed to any location. It is also a good source to produce H_2 by means of water vapor change reaction, which can be used also to produce ammonia [22-24].

The AD of biomass can be done on individual materials (mono-digestion) or mixtures of numerous materials (mixed-digestion or co-digestion). The co-digestion enhances waste bioconversion and energy generation by increasing availability of nutrients for microbes and organic load while reducing inhibitory chemical toxicity through co-substrate dilution [25].

In [26], the co-digestion enhanced biogas production compared to mono-digestion. The co-digestion of the Water hyacinth (WH) with Food Waste (FW) improved the biogas production by 5%, 9%, 15%, 53%, and 58% for mix proportions of 85:15, 30:70, 15:85, 55:45, and 70:30 (WH: FW) respectively. Another example of co-digestion was introduced by [27], and showed up the anaerobic co-digestion of wood vinegar using domestic sewage as an inoculum. It presented a higher efficiency in the process, pointing out that the continuous domestication of substrates promoted the enrichment of related functional microbiological communities.

III. H_2 PRODUCTION BY AD

Reference [28] used co-digestion, with a mixture of the biomass of sorgo with liquid wave manure in a two-stage CSTR reactor. The effect of pH and hydraulic retention on the biodigestion process was evaluated. The combination of 5 days of hydraulic retention with pH 5.0 showed the highest rate of hydrogen production.

A research carried out by [29] showed that pH is a critical parameter for the optimization of the degradation process of the organic substrate of food residues. It was found that first, the anaerobic fermentation, enriched the effluent, and second of anaerobic digestion using the remaining fraction increased the bioconversion efficiency by 51.3%. A fermentation temperature of 55ºC, pH of 5.8 and 20.1 days of hydraulic retention produced 98.8 mL of H_2 per gram of digested organic compound.

Reference [30] found that the addition of grass clippings to the food waste substrate can inhibit the rapid fall of pH, functioning as eco-friendly buffering agents. The results of anaerobic co-digestion experiments revealed that the addition of 2 to 6% of grass clippings promoted a better acidogenesis with increased acetic and butyl acids, as well as hydrogen production. While the addition of 8 to 10% promoted ethyl alcohol solvetogenesis. The hydrogen production observed in the experiments was 27 to 30% of the total biogas.

According to [31], the AD of sugarcane leaves pretreated with deep eutectic solvent is more efficient when saccharification and fermentation occur simultaneously (SSF), when compared to separate hydrolysis and fermentation (SHF), both in single-stage reactors. SSF and SHF produced 3187±202 and 2135±315 mL H_2/L, respectively.

Pretreatment of biomass using diluted sulfuric acid method is promising in biohydrogen production when compared to biomethane production. The hydrogen production was observed when initially 4% (w/v) and 6% (w/v) spent coffee grounds containing hydrolysates were used as substrates at pH 5.5, yielding 2.9±0.09 dm^3kg $V.S^{-1}$and 3.85±0.12 dm^3kg $V.S^{-1}$, respectively [32].

Others pieces of work evidence different forms and combination of biomass conversion into hydrogen through AD, Table II.

IV. PYROLYSIS FOR THE PRODUCTION OF RENEWABLE H_2

Pyrolysis, also known as thermolysis, is a thermochemical reaction in which dehydration and decomposition of matter occurs in an oxygen-free atmosphere. The products of pyrolysis are divided into bio-oil, gas and biochar, and are applied in the energy sector, in the transport industry, in the generation of electrical energy, fuel production, in agriculture, among other sectors [36,37]. Decomposition is a predominant process in pyrolysis, occurring at temperatures above 300°C and involving the degradation of the macromolecule into smaller particles, gas, oil or biochar [38].

Slow pyrolysis allows the production of bio-oil, gas and biochar. In this type of reaction, a heating rate ranging from 0.1°C/sec to 1°C/sec is applied, the feedstock particles used in the reaction range from 5 mm to 50 mm and the reaction time is longer than 5 minutes. In slow pyrolysis the temperature can reach 600°C, generating a higher percentage of biochar and in smaller proportions gas and bio-oil [39].

Intermediate pyrolysis technology is a process that enables a high yield of biochar and bio-oil. The reaction characteristics involve temperatures between 400°C and 700°C, the reaction time to produce volatiles is from 1 second to 30 seconds and to produce solids ranges from 30 seconds to 1500 seconds. The heat transfer rate is higher compared to slow pyrolysis, ranging from 10°C/min to 100°C/min [40].

Fast pyrolysis is a thermochemical reaction, which aims to produce bio-oil. It works with the following reaction conditions, heating rate of 100°C/second, and takes place at a temperature between 400°C and 600°C [41].

The operational characteristics used in flash pyrolysis are temperature between 800°C and 1200°C, feedstock size should be below 0.1 mm, eliminating the production of solids, reaction time for the complete process is around 0.1 second to 0.5 second and heating rate higher than 1000°C/sec [42].

TABLE II. HYDROGEN YIELD FROM BIOMASS BIOCONVERSION.

Substrate	Reactor	pH	H_2	Source
Corn steep liquor	CSTR, 2 stages	5.25	0.74 dm^3/L. 32.6% vol.	[33]
Sorghum biomass solution with liquid cow manure (in a ratio 95:5v/v)	CSTR, 2 stages	5.0	0.13 L/LR·d.	[28]
Sewage sludge, wine vinasse, poultry manure	single stage	7.5	0.41 mL/gVS	[34]
Palm oil mill effluent (POME)	Up-flow anaerobic sludge fixed-film	5.0-5.5	10.39 L H_2/L	[35]

TABLE III. PERCENTAGE OF HYDROGEN IN SOME PYROLYSIS TECHNIQUES.

Substrate	Reactor	Temperature (°C)	H_2 vol% in gas	Source
Sugarcane bagasse	Slow	480	9.6%	[44]
Sugarcane bagasse	Slow	780	28.8%.	[44]
Rice husk	Intermediate	800	8.6%	[45]
Sugarcane bagasse	Fast	480	8.7%	[44]
Sugarcane bagasse	Fast	780	45.3%	[44]
Microalgae	Flash	800	44.3%	[43]
Wood waste	Catalytic	650	80.71%	[46]
Sewage sludge	Microwave	800	48%	[36]

A. Hydrogen Production by Pyrolysis

Few studies have pointed out the production of hydrogen from conventional pyrolysis techniques. Higher temperatures and feedstock used are essential parameters to have a significant hydrogen conversion [43]. The advanced pyrolysis methods achieved higher conversion rates of the feedstock into H_2. The microwave method achieved satisfactory results at 800°C using sewage sludge as feedstock [36].

Table III shows some pyrolysis methods found in the literature and their respective results for hydrogen conversion.

V. CONCLUSIONS

According to the literature, anaerobic digestion and pyrolysis technologies are promising routes for hydrogen production.

Approaches such as catalytic pyrolysis and microwave-assisted pyrolysis may increase the potential of the technology for hydrogen manufacturing.

The anaerobic digestion in two stages favors the production of hydrogen with regard to pretreatment and enrichment of the subtreatment or effluent. The co-digestion of substrates of animal waste with plant material is a path for the treatment of waste and that also favors the production of hydrogen. Anyway, the different substrates should be analyzed for administration for the best technologic arrangement.

ACKNOWLEDGMENT

The authors acknowledge the financial support of the Postgraduate Research Grant, Term No. 16/2022, Paraíba State Research Foundation (FAPESQ). The opinions, hypotheses and conclusions or recommendations expressed in this material are those of the author(s) and do not necessarily reflect the views of FAPESQ.

REFERENCES

[1] World Bioenergy Association – WBA (2021), Global Bioenergy Statistics 2021.

[2] Majeed, M. T., Luni, T., & Tahir, T. (2022). Growing green through biomass energy consumption: the role of natural resource and globalization in a world economy. *Environmental Science and Pollution Research*, *29*(22), 33657–33673.

[3] Internacional Renewable Energy Agency - IRENA, *Renewable energy and jobs annual review 2021*. (2022).

[4] Deep Singh, A., Gajera, B., & Sarma, A. (2022). Appraising the availability of biomass residues in India and their bioenergy potential. *Waste Management*, *152*, 38–47.

[5] Tembhare, S. P., Barai, D. P., & Bhanvase, B. A. (2022). Performance evaluation of nanofluids in solar thermal and solar photovoltaic systems: A

comprehensive review. *Renewable and Sustainable Energy Reviews*, *153*, 111738.

[6] Archer, S. A., & Steinberger-Wilckens, R. (2018). Systematic analysis of biomass derived fuels for fuel cells. *International Journal of Hydrogen Energy*, *43*(52), 23178–23192.

[7] Thiruselvi, D., Kumar, P. S., Kumar, M. A., Lay, C. H., Aathika, S., Mani, Y., Jagadiswary, D., Dhanasekaran, A., Shanmugam, P., Sivanesan, S., & Show, P. L. (2021). A critical review on global trends in biogas scenario with its up-gradation techniques for fuel cell and future perspectives. *International Journal of Hydrogen Energy*, *46*(31), 16734–16750.

[8] Amin, F. R., Khalid, H., Zhang, H., Rahman, S. U., Zhang, R., Liu, G., & Chen, C. (2017). Pretreatment methods of lignocellulosic biomass for anaerobic digestion. *AMB Express*, *7*(1).

[9] N. G. & B. National Agency for Petroleum, “RenovaBio,” *ANP*, 2022. Available at: https://www.gov.br/anp/pt-br/assuntos/renovabio.

[10] Energy Research Company (2022). *National Energy Balance - BEN, EPE, 2022*. Available at: https://www.epe.gov.br/pt/publicacoes-dados-abertos/publicacoes/balanco-energetico-nacional-ben.

[11] Ke, L., Wu, Q., Zhou, N., Xiong, J., Yang, Q., Zhang, L., Wang, Y., Dai, L., Zou, R., Liu, Y., Ruan, R., & Wang, Y. (2022). Lignocellulosic biomass pyrolysis for aromatic hydrocarbons production: Pre and in-process enhancement methods. *Renewable and Sustainable Energy Reviews*, *165*, 112607.

[12] Agyekum, E. B., Nutakor, C., Agwa, A. M., & Kamel, S. (2022). A Critical Review of Renewable Hydrogen Production Methods: Factors Affecting Their Scale-Up and Its Role in Future Energy Generation. *Membranes*, *12*(2), 173.

[13] Hajji, Y., Bouteraa, M., Bournot, P., & Bououdina, M. (2022). Assessment of an accidental hydrogen leak from a vehicle tank in a confined space. *International Journal of Hydrogen Energy*, *47*(66), 28710–28720.

[14] Qazi, U. Y. (2022). Future of Hydrogen as an Alternative Fuel for Next-Generation Industrial Applications; Challenges and Expected Opportunities. *Energies*, *15*(13), 4741.

[15] Mukelabai, M. D., Wijayantha, U. K., & Blanchard, R. E. (2022). Renewable hydrogen economy outlook in Africa. *Renewable and Sustainable Energy Reviews*, *167*, 112705.

[16] Reed, J., Dailey, E., Fong, A., & Samuelsen, G. S. (2022). Time-phased geospatial siting analysis for renewable hydrogen production facilities under a billion-kilogram-scale build-out using California as an example. *International Journal of Hydrogen Energy*, *47*(66), 28224–28243.

[17] Ishaq, H., Dincer, I., & Crawford, C. (2022). A review on hydrogen production and utilization: Challenges and opportunities. *International Journal of Hydrogen Energy*, *47*(62), 26238–26264.

[18] Gregorie, E. F. J., Lamb, J. J., Lien, K. M., Pollet, B. G., & Burheim, O. S. (2020). Hydrogen and Biogas. *Micro-Optics and Energy*, 131–155.

[19] Bauer, C., et al. (2022). On the climate impacts of blue hydrogen production. *Sustainable Energy & Fuels*, *6*(1), 66–75.

[20] Zhou, Y., Li, R., Lv, Z., Liu, J., Zhou, H., & Xu, C. (2022). Green hydrogen: A promising way to the carbon-free society. *Chinese Journal of Chemical Engineering*, *43*, 2–13.

[21] Von Zuben, T., Moreira, D., Germscheidt, R., Yoshimura, R., Dorretto, D., de Araujo, A., Salles Jr., A., & Bonacin, J. (2022). Is Hydrogen Indispensable for a Sustainable World? A Review of H2 Applications and Perspectives for the Next Years. *Journal of the Brazilian Chemical Society*.

[22] Ottoni, J. R., Bernal, S. P. F., Marteres, T. J., Luiz, F. N., dos Santos, V. P., Mari, N. G., Somer, J. G., de Oliveira, V. M., & Passarini, M. R. Z. (2022). Cultured and uncultured microbial community associated with biogas production in anaerobic digestion processes. *Archives of Microbiology*, *204*(6).

[23] Chozhavendhan, S., Karthigadevi, G., Bharathiraja, B., Praveen Kumar, R., Abo, L. D., Venkatesa Prabhu, S., Balachandar, R., & Jayakumar, M. (2023). Current and prognostic overview on the strategic exploitation of anaerobic digestion and digestate: A review. *Environmental Research*, *216*, 114526.

[24] Andreides, D., Fliegerova, K. O., Pokorna, D., & Zabranska, J. (2022). Biological conversion of carbon monoxide and hydrogen by anaerobic culture: Prospect of anaerobic digestion and thermochemical processes combination. *Biotechnology Advances*, *58*, 107886.

[25] Emebu, S., Pecha, J., & Janáčová, D. (2022). Review on anaerobic digestion models: Model classification & elaboration of process phenomena. *Renewable and Sustainable Energy Reviews*, *160*, 112288.

[26] Sharma, K. (2019). Carbohydrate-to-hydrogen production technologies: A mini-review. *Renewable and Sustainable Energy Reviews*, *105*, 138–143.

[27] Kunatsa, T., & Xia, X. (2022). A review on anaerobic digestion with focus on the role of biomass co-digestion, modelling and optimisation on biogas production and enhancement. *Bioresource Technology*, *344*, 126311.

[28] Oduor, W. W., Wandera, S. M., Murunga, S. I., & Raude, J. M. (2022). Enhancement of anaerobic digestion by co-digesting food waste and water hyacinth in improving treatment of organic waste and bio-methane recovery. *Heliyon*, *8*(9), e10580.

[29] Fan, Q., Fan, X., Fu, P., Li, Y., Zhao, Y., & Hua, D. (2022). Anaerobic digestion of wood vinegar wastewater using domesticated sludge: Focusing on the relationship between organic degradation and microbial communities (archaea, bacteria, and fungi). *Bioresource Technology*, *347*, 126384.

[30] Dareioti, M. A., Tsigkou, K., Vavouraki, A. I., & Kornaros, M. (2022). Hydrogen and Methane Production from Anaerobic Co-Digestion of Sorghum and Cow Manure: Effect of pH and Hydraulic Retention Time. *Fermentation*, *8*(7), 304.

[31] Greses, S., Tomás-Pejó, E., & González-Fernández, C. (2022). Food waste valorization into bioenergy and bioproducts through a cascade combination of bioprocesses using anaerobic open mixed cultures. *Journal of Cleaner Production*, *372*, 133680.

[32] Chakraborty, D., Palani, S. G., Ghangrekar, M. M., Anand, N., & Pathak, P. (2022). Dual role of grass clippings as buffering agent and biomass during anaerobic co-digestion with food waste. *Clean*

Technologies and Environmental Policy, *24*(9), 2787–2799.

[33] Miftah, A. K., Sittijunda, S., Imai, T., Salakkam, A., & Reungsang, A. (2022). Biohydrogen and Methane Production from Sugarcane Leaves Pretreated by Deep Eutectic Solvents and Enzymatic Hydrolysis by Cellulolytic Consortia. *Fermentation*, *8*(8), 396.

[34] Vanyan, L., Cenian, A., & Trchounian, K. (2022). Biogas and Biohydrogen Production Using Spent Coffee Grounds and Alcohol Production Waste. *Energies*, *15*(16), 5935.

[35] Chorukova, E., Hubenov, V., Gocheva, Y., & Simeonov, I. (2022). Two-Phase Anaerobic Digestion of Corn Steep Liquor in Pilot Scale Biogas Plant with Automatic Control System with Simultaneous Hydrogen and Methane Production. *Applied Sciences*, *12*(12), 6274.

[36] Sillero, L., Perez, M., & Solera, R. (2023, January). Temperature-phased enhanced the single-stage anaerobic co-digestion of sewage sludge, wine vinasse and poultry manure: Perspetives for the circular economy. *Fuel*, *331*, 125761.

[37] Zainal, B. S., Gunasegaran, K., Tan, G. Y. A., Danaee, M., Mohd, N. S., Ibrahim, S., Chyuan, O. H., Nghiem, L. D., & Mahlia, T. I. (2022). Effect of temperature and hydraulic retention time on hydrogen production from palm oil mill effluent (POME) in an integrated up-flow anaerobic sludge fixed-film (UASFF) bioreactor. *Environmental Technology & Innovation*, *28*, 102903.

[38] Kim, D., Kim, G., Oh, D. Y., Seong, K. W., & Park, K. Y. (2022). Enhanced hydrogen production from anaerobically digested sludge using microwave assisted pyrolysis. *Fuel*, *314*, 123091.

[39] Yoon, K., Lee, S. S., Ok, Y. S., Kwon, E. E., & Song, H. (2019). Enhancement of syngas for H2 production via catalytic pyrolysis of orange peel using CO2 and bauxite residue. *Applied Energy*, *254*, 113803.

[40] Arun, J., Raghu, R., Suhail Madhar Hanif, S., Thilak, P., Sridhar, D., Nirmala, N., Dawn, S., Sivaramakrishnan, R., Chi, N. T. L., & Pugazhendhi, A. (2022). A comparative review on photo and mixotrophic mode of algae cultivation: Thermochemical processing of biomass, necessity of bio-oil upgrading, challenges and future roadmaps. *Applied Energy*, *325*, 119808.

[41] Arantes, H. T., Machado, M. A., Santoro, M. C., Freitas, J. C., Ronconi, C. M., Ligiero, C. B., Cassini, S. T., Sampaio, I. C., & Luz, P. P. (2023). Effect of activated biochar as a low-cost catalyst on the quality of catalytic intermediate co-pyrolysis oil from waste polystyrene and green coconut pericarp. *Fuel Processing Technology*, *240*, 107539.

[42] Sun, J., Norouzi, O., & Mašek, O. (2022). A state-of-the-art review on algae pyrolysis for bioenergy and biochar production. *Bioresource Technology*, *346*, 126258.

[43] Mishra, K., Singh Siwal, S., Kumar Saini, A., & Thakur, V. K. (2023). Recent update on gasification and pyrolysis processes of lignocellulosic and algal biomass for hydrogen production. *Fuel*, *332*, 126169.

[44] Lee, D., Nam, H., Won Seo, M., Hoon Lee, S., Tokmurzin, D., Wang, S., & Park, Y. K. (2022). Recent progress in the catalytic thermochemical conversion process of biomass for biofuels. *Chemical Engineering Journal*, *447*, 137501.

[45] Allende, S., Brodie, G., & Jacob, M. V. (2022). Energy recovery from sugarcane bagasse under varying microwave-assisted pyrolysis conditions. *Bioresource Technology Reports*, *20*, 101283.

[46] Vuppaladadiyam, A. K., Vuppaladadiyam, S. S. V., Awasthi, A., Sahoo, A., Rehman, S., Pant, K. K., Murugavelh, S., Huang, Q., Anthony, E., Fennel, P., Bhattacharya, S., & Leu, S. Y. (2022). Biomass pyrolysis: A review on recent advancements and green hydrogen production. *Bioresource Technology*, *364*, 128087.

Advanced Hydrogen Fuel Cell Vehicle Technologies

Milan Prokin[1], Dragana Prokin[2]

[1]University of Belgrade – School of Electrical Engineering, Belgrade, Serbia
[2]Academy of Technical and Art Applied Studies, School of Electrical and Computer Engineering, Belgrade, Serbia
[1,2]National Association of Autonomous and Electric Vehicles, Belgrade, Serbia

Abstract—**The major problems with hydrogen fuel cell vehicles (FCVs) are fuel cells cost, hydrogen cost, carbon dioxide emission during lower cost hydrogen production methods, hydrogen delivery, hydrogen storage and power efficiency. The fuel cell cost can be decreased using improved catalyst. The hydrogen cost and carbon dioxide emission can be reduced by producing synthetic fuels for the remaining internal combustion engines as side effects. The hydrogen delivery and hydrogen storage cost can be significantly decreased using optional storage of solid substances and water instead of compressed hydrogen. The power efficiency can be increased by using regenerative braking with special batteries using lithium purification in combination with hybrid supercapacitors instead of state-of-the-art lithium ion batteries with or without ultracapacitors.**

Keywords – hydrogen fuel cell vehicles, regenerative braking, hybrid supercapacitors

I. INTRODUCTION

There is a renewed interest for hydrogen powered vehicles (Figs. 1-2), primarily “green” hydrogen [1-3]. Hydrogen fuel cells provide favorable efficiency in comparison with internal combustion engines, but smaller than lithium-ion batteries [4]. Some authors claim that hydrogen saves semi-truck weight in comparison with lithium-ion batteries [5]. Fuel cells were studied as range extenders for electric vehicles [6,7]. Types of DC-DC converters for fuel cell vehicles were also discussed [8,9]. Energy management of fuel cell electric vehicles have already been developed and are applicable to circuits presented in this paper [10,11].

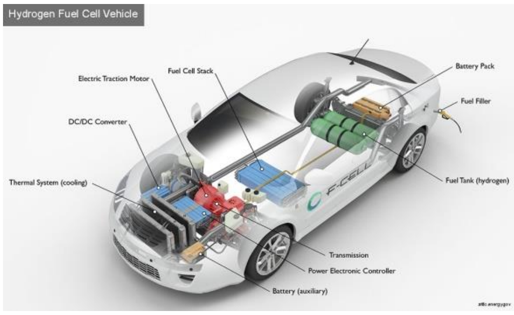

Figure 1. Hydrogen fuel cell vehicle.

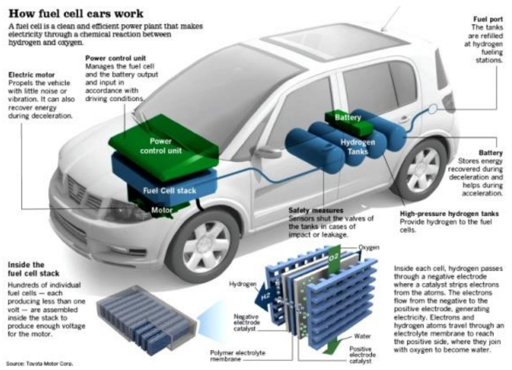

Figure 2. Hydrogen fuel cell vehicle.

II. ENERGY STORAGE VARIANTS

These three regenerative braking energy storage variants are used in EVs (from the most used to the least used) [12]:

- Lithium batteries have good energy density (can store a lot of energy), but have relatively low power density, which translates to longer vehicle acceleration and deceleration cycles.
- Supercapacitors have higher power density (can charge and discharge at

ISBN: 978-86-82602-01-9

much faster rates than chemical batteries), have longer lifetime without deterioration and wide operational temperature range (both freezing and hot), but have lower energy density, which translates to larger units than lithium-ion batteries for acceleration and deceleration.

- Hybrid supercapacitors are half way between lithium batteries and supercapacitors. They can also utilize lithium chemistry.

III. REGENERATIVE BRAKING ENERGY

Hydrogen fuel cell vehicles cannot return braking energy into fuel cells, so they use lithium ion batteries, thus extremely increasing the efficiency in city driving via regenerative braking:

- Regenerative braking is the process of deceleration with energy return to energy storage instead of heating brakes.
- Batteries are too slow to be charged from regenerative braking, rendering the complete regenerative braking inefficient.
- High surge currents during regenerative braking decrease battery lifetime.
- Supercapacitors are sufficiently fast to be charged from regenerative braking, making the complete regenerative braking highly efficient.
- City driving with frequent acceleration and deceleration will be highly efficient due to regenerative braking.

Major components for regenerative braking energy systems are batteries, ultracapacitors and DC/DC converters [13-18].

There are several electrical schematics for combining fuel cell(s) with a unidirectional boost DC/DC converter, ultracapacitors with lithium ion batteries and DC/DC converters [19-24], spanning two decades of the continuous research and development interest.

An ultracapacitor can be simply connected in parallel with a battery, which essentially inhibits quick ultracapacitor charging to voltage higher than battery voltage, while the power distribution between the ultracapacitor and the battery is uncontrollable (Fig. 3) [25-29].

Decoupling an ultracapacitor and a battery from an inverter by a bidirectional DC/DC converter doesn't help much in resolving the previous problem, but it stabilizes inverter voltage at the expense of high surge current rating of the DC/DC converter (Fig. 4) [27].

Decoupling an ultracapacitor from a battery by a bidirectional DC/DC converter enables ultracapacitor voltage to be different from battery voltage, at the expense of high surge current rating of the bidirectional DC/DC converter and decreased battery lifetime due to high charging and discharging currents (Fig. 5) [30-40].

Decoupling a battery from an ultracapacitor by a bidirectional DC/DC converter decreases surge currents through the bidirectional DC/DC converter and increases battery lifetime, but enables ultracapacitor voltage to be too much different from battery voltage, thus increasing breakthrough voltage rating of an inverter (Fig. 6) [26,41-43].

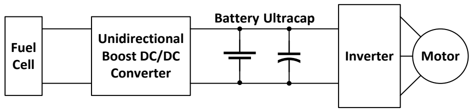

Figure 3. A fuel cell with a boost converter, and an ultracapacitor in parallel with a battery.

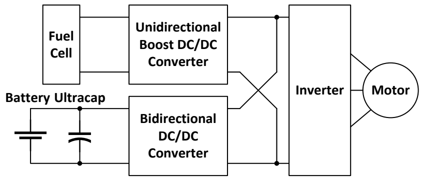

Figure 4. A fuel cell with a boost converter, and an ultracapacitor and a battery decoupled from an inverter by a bidirectional DC/DC converter.

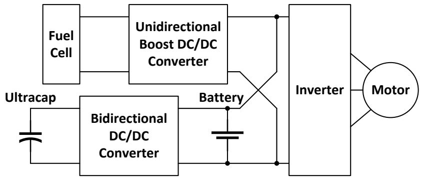

Figure 5. A fuel cell with a boost converter, and an ultracapacitor decoupled from a battery by a bidirectional DC/DC converter.

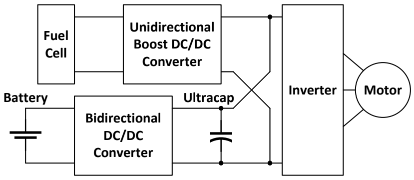

Figure 6. A fuel cell with a boost converter, and a battery decoupled from an ultracapacitor by a bidirectional DC/DC converter.

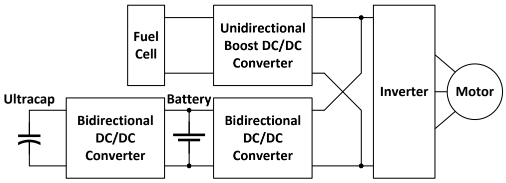

Figure 7. A fuel cell with a boost converter, and an ultracapacitor, a battery and an inverter decoupled by two serial bidirectional DC/DC converters.

Decoupling an ultracapacitor, a battery and an inverter can be performed by two serial bidirectional DC/DC converters in order to provide different ultracapacitor and battery voltages, but stable inverter voltage at the same time (Fig. 7) [44,45].

Decoupling a battery, an ultracapacitor and an inverter can be performed by two serial bidirectional DC/DC converters in order to provide different battery and ultracapacitor voltages, but stable inverter voltage at the same time (Fig. 8) [27,46].

The problem with the configurations in Figs. 7 and 8 is lower efficiency due to currents passing through two serial bidirectional DC/DC converters. This problem is solved by decoupling a battery, an ultracapacitor and an inverter by two parallel bidirectional DC/DC converters enabling different ultracapacitor and battery voltages (Fig. 9) [27,47-53]. The configuration in Fig. 9 can be improved by using a multiple input bidirectional DC/DC converter instead of two parallel bidirectional DC/DC converters (Fig. 10) [24,47,54-62].

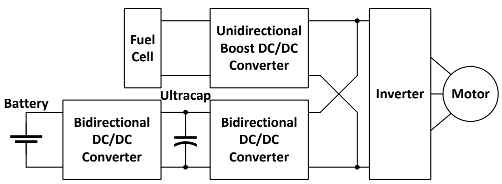

Figure 8. A fuel cell with a boost converter, and a battery, an ultracapacitor and an inverter decoupled by two serial bidirectional DC/DC converters.

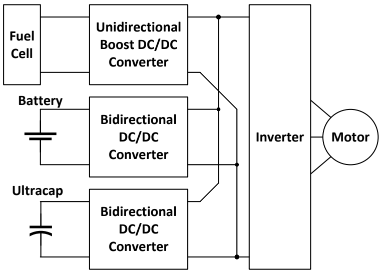

Figure 9. A fuel cell with a boost converter, and a battery, an ultracapacitor and an inverter decoupled by two parallel bidirectional DC/DC converters.

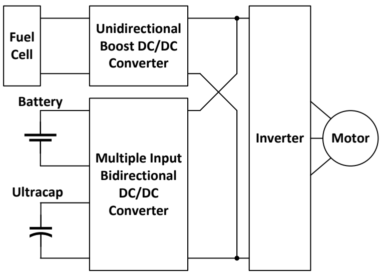

Figure 10. A fuel cell with a boost converter, and a battery, an ultracapacitor and an inverter by one multiple input bidirectional DC/DC converter.

IV. HYBRID SUPERCAPACITORS

Hybrid supercapacitors (Fig. 11) are halfway between lithium batteries (Fig. 12) and carbon supercapacitors (Fig. 13) [63-71].

Hybrid supercapacitor features are:

- One lithium compound electrode.
- The other graphene electrode.
- There is no chemical reaction.
- There is no free flow of lithium ions floating in the battery that can form potentially dangerous lithium dendrites shortcircuiting electrodes, producing explosion and fire.
- They are inherently fire safe.
- The charges are stored statically, like in a supercapacitor.
- There is some electrolyte involved, but as a filler that allows the charges to move.
- The electrolyte is soaked up by the nano-carbon electrode material, so if the cells are ruptured, very little or none will leak out.

- Operating temperatures are from -40°C to +80°C.
- No active thermal management is needed.
- The same assembling and packaging process already used for state-of-the-art lithium batteries and carbon supercapacitors can be also used for hybrid supercapacitors (Fig. 14).

A. Power Type Version of Hybrid Supercapacitors [71-73]

- Specific energy of 80-100 Wh/kg.
- Specific power of 1,000-1,500 W/kg.
- Lifetime 20,000-50,000 full charging cycles.

B. Energy Type Version of Hybrid supercapacitors [71-73]

- Specific energy of 200-230 Wh/kg.
- Specific power of 300-500 W/kg.
- Lifetime over 10,000 full charging cycles.

C. Lithium Ion Battery for Comparison [72-73]

- Specific energy of 180-250 Wh/kg.
- Specific power of 100-500 W/kg.
- Lifetime over 2,000 full charging cycles.

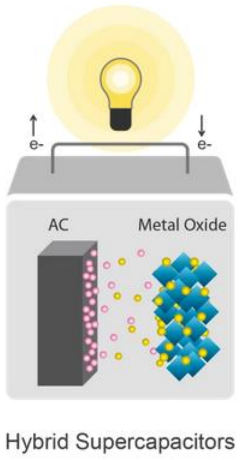

Figure 11. Hybrid supercapacitor.

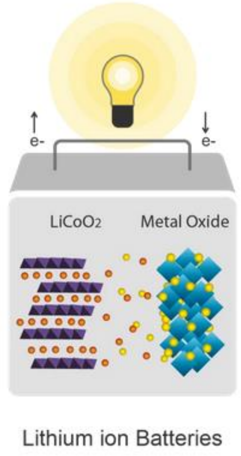

Figure 12. Typical lithium ion battery.

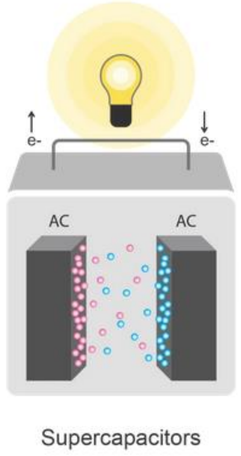

Figure 13. Typical supercapacitor.

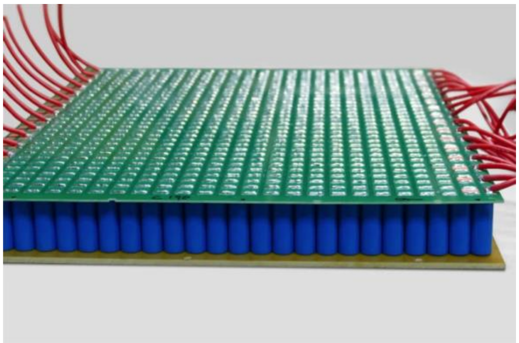

Figure 14. Hybrid supercapacitor pack.

A hybrid supercapacitor can be used instead of an ultracapacitor, a battery and bidirectional DC/DC converters in all configurations in Figs. 3-10 (Figs. 15-16).

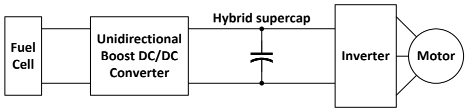

Figure 15. A fuel cell with a boost converter, and a hybrid supercapacitor instead of an ultracapacitor, a battery and DC/DC converter(s).

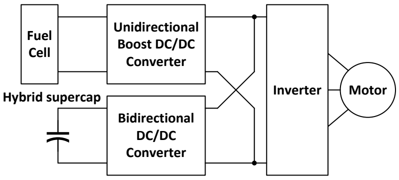

Figure 16. A fuel cell with a boost converter, and a bidirectional DC/DC converter, a hybrid supercapacitor instead of an ultracapacitor and a battery.

V. Conclusions

The hybrid supercapacitors increase vehicle range by capturing regenerative braking energy during deceleration and releasing it during acceleration, while inherently solving regenerative braking efficiency problem without any additional components: ultracapacitors and bidirectional DC/DC converter(s), thus increasing the reliability and decreasing size and weight of hybrid fuel cell vehicle subsystems.

Acknowledgment

This work was partially supported by European Institute of Innovation & Technology Urban Mobility (EIT UM) under grant no. SGA22 22374, as well as Ministry of Education, Science and Technological Development of Republic of Serbia under grant nos. TR32039 and TR32047.

References

[1] A hydrogen strategy for a climate-neutral Europe, COM (2020) 301 final, *European Commission*.

[2] Veziroglu, A., & Macario, R. (2011). Fuel cell vehicles: State of the art with economic and environmental concerns. *International Journal of Hydrogen Energy*, *36*, 25-43

[3] Sooriarachchi, V. (Feb. 2021). Green hydrogen and transportation industry – An overview of its applications. *IEEE Smart Grid Bulletin*.

[4] Bhagavathy, S., & Thakur, J. (Feb. 2021). Green hydrogen: Challenges for commercialization. *IEEE Smart Grid Bulletin*.

[5] Houseman, D. (Feb. 2021). Using curtailed renewable energy to produce green hydrogen. *IEEE Smart Grid Bulletin*.

[6] Brooker, P., (2015). Fuel cells as electric vehicle range extenders. *FSEC Report: FSEC-CR-1995-14*.

[7] Fernandez R. A., Cilleruelo F. B., & Martinez I. V. (2016). A new approach to battery powered electric vehicles: A hydrogen fuel-cell-based range extender system. *International Journal of Hydrogen Energy*, *41*, 4808-4819.

[8] Bhaskar, M. S., Ramachandaramurthy, V. K., Padmanaban, S., Blaabjerg, F., Ionel, D. M., Mitolo, M., & Almakhles, D. (2020). Survey of DC-DC non-isolated topologies for unidirectional power flow in fuel cell vehicles. *IEEE Access*, *8*, 178130.

[9] Gurz, M., Baltacioglu, E., Hames, Y., & Kaya, K. (2017). The meeting of hydrogen and automotive: A review. *International Journal of Hydrogen Energy*, 1-13.

[10] Sayed, K., Abdel-Khalek, S., Zakaly, H. M. H., & Aref, M. (2022). Energy management and control in multiple storage energy units (battery–supercapacitor) of fuel cell electric vehicles. *Materials*, *15*, 8932.

[11] Yuan, H.-B., Zou, W.-J., Jung, W., & Kim, Y.-B. (2022). A real-time rule-based energy management strategy with multi-objective optimization for a fuel cell hybrid electric vehicle. *IEEE Access*, *10,* 102168.

[12] Prokin, M, & Prokin, D. (2021, Dec. 16-17). Advanced electric vehicle technologies. In *eNergetics 2021 – 7th Virtual Conference on Science, Technology and Management in Energy* (pp. 325-332).

[13] Liu, D., & Li, H. (2006, Nov. 6-10). A three-port three-phase DC-DC converter for hybrid low voltage fuel cell and ultracapacitor. In *IECON 2006 - 32nd Annual Conference on IEEE Industrial* Electronics (pp. 2258-2563).

[14] Lukic, S. M., Cao, J., Bansal, R. C., Rodriguez, F., & Emadi A. (2008, June). Energy storage systems for automotive applications. *IEEE Transactions on Industrial Electronics*, *55*(6), 2258-2267.

[15] Alireza, K., & Li, Z. (2010, July). Battery, ultracapacitor, fuel cell, and hybrid energy storage systems for electric, hybrid electric, fuel cell, and plug-in hybrid electric vehicles: State of the art. *IEEE Transactions on Vehicular Technology*, *59*(6), 2806–2814.

[16] Siang, F. T., & Chee, W. T. (2013, April). A review of energy sources and energy management system in electric vehicles. *Renewable and Sustainable Energy Reviews*, *20*, 82–102.

[17] Ding, N., Prasad, K., & Lie, T. T. (2017, Jan.). The electric vehicle: a review. *Int. Journal of Electric and Hybrid Vehicles*, *9*(1), 49-66.

[18] Un-Noor, F., Padmanaban, S., Mihet-Popa, L., Mollah, M. N., & Hossain, E. (2017, Aug. 17). Comprehensive study of key electric vehicle (EV) components, technologies, challenges, impacts, and future direction of development. *Energies*, *10*, 1217-1301.

[19] Cao, J., & Emadi, A. (2009, Sep. 7-10). A new battery/ultra-capacitor hybrid energy storage system for electric, hybrid and plug-in hybrid electric vehicles. In *2009 IEEE Vehicle Power and Propulsion Conference*, Dearborn, MI, USA.

[20] Cao, J., & Emadi, A. (2012, Jan. 1). A new battery/ultra-capacitor hybrid energy storage system for electric, hybrid and plug-in hybrid electric vehicles. *IEEE Transactions on Power Electronics*, *27*(1), 122-132.

[21] Bobba, P. B., & Rajagopal, K. R. (2012, Dec. 16-19). Modeling and analysis of hybrid energy storage systems used in electric vehicles. In *2012 IEEE Int. Conference on Power Electronics, Drives and Energy Systems*, Bengaluru, India.

[22] Xiang, C., Wang, Y., Hu, S., & Wang, W. (2014, Apr. 29). A new topology and control strategy for a hybrid battery-ultracapacitor energy storage system. *Energies*, *7*(5), 2874-2896.

[23] Chakraborty, S., Vu, H.-N., Hasan, M. M., Tran, D.-D., Baghdadi, M. E., & Hegazy, O. (2019, Apr. 25). DC-DC converter topologies for electric vehicles, plug-in hybrid electric vehicles and fast charging stations: State of the art and future trends. *Energies*, *12*(8), 1569-1612.

[24] Lai, C.-M., Teh, J., Lin, Y.-C., & Liu, Y. (2020, Mar. 6). Study of a bidirectional power converter integrated with battery/ultracapacitor dual-energy storage. *Energies*, *13*(5), 1234-1257.

[25] Pay, S., & Baghzouz, Y. (2003, June 23-26) Effectiveness of battery-supercapacitor combination in electric vehicles. In *2003 IEEE Bologna Power Tech Conference,* Bologna, Italy.

[26] Gao, L., Dougal, R. A., & Liu, S. (2005, Jan. 10). Power enhancement of an actively controlled battery/ultracapacitor hybrid. *IEEE Transactions on Power Electronics, 20*(1), 236-243.

[27] Lukic, S. M., Wirasingha, S. G., Rodriguez, F., Cao, & J., Emadi A. (2006, Sep. 6-8). Power management of an ultracapacitor/battery hybrid energy storage system in an HEV. In *2006 IEEE Vehicle Power and Propulsion Conference,* Windsor, UK.

[28] He, H.-W., Xiong, R., Chang, Y.-H. (2010, Nov. 22). Dynamic modeling and simulation on a hybrid power system for electric vehicle applications. *Energies*, *3*(11), 1821–1830.

[29] Ding, S., Wei, B., Hang, J., Zhang, P., & Ding, M. (2017, Aug. 11-14). A multifunctional interface circuit for battery-ultracapacitor hybrid energy storage system. In *2017 20th Int. Conference on Electrical Machines and Systems (ICEMS)*, Sydney, NSW, Australia.

[30] Dixon J., Ortuzar M., & Wiechmann E. (2000, Oct. 15-18). Regenerative braking for an electric vehicle using ultracapacitors and a buck-boost converter. In *The 17. International Electric Vehicle Symposium and Exposition: Driving New Visions*, Montreal, PQ (Canada).

[31] Ortuzar M., Moreno J., & Dixon J. (2007, Aug.). Ultracapacitor-based auxiliary energy system for an electric vehicle: implementation and evaluation. *IEEE Transactions on Industrial Electronics, 54*(4), 2147-2156.

[32] Niemoeller, B. A., & Krein, P. T. (2010, Feb. 12-13). Battery-ultracapacitor active parallel interface with indirect control of battery current. In *2010 Power and Energy Conference*, Urbana-Champaign, IL, USA (pp. 12-19).

[33] Miller, J. M., & Sartorelli, G. (2010, Sep. 1-3). Battery and ultracapacitor combinations - Where should the converter go? In *2010 IEEE Vehicle Power and Propulsion Conference*, Lille, France.

[34] Pan, C., Chen, L., Chen, L., Chen H., & Xie M. (2013, Jan.). Research on energy management of dual energy storage system based on the simulation of urban driving schedules. *Int. Journal of Electrical Power and Energy Systems. 44*(1), 37-42.

[35] Machado, F., Antunes, C. H., Dubois, M. R., & Trovao, J. P. (2015, Oct. 19-22). Semi-active hybrid topology with three-level DC-DC converter for electric vehicle application. In *2015 IEEE Vehicle Power and Propulsion Conference (VPPC)*, Montreal, QC, Canada (pp. 1-6).

[36] Shen, J., & Khaligh, A. (2015, Oct.). A supervisory energy management control strategy in a battery/ultracapacitor hybrid energy storage system. *IEEE Transactions on Transportation Electrification*, *1*(3), 223-231.

[37] Hinov, N. L., Penev, D. N., & Vacheva, G. I. (2016, Sep. 12-14). Ultra capacitors charging by regenerative braking in electric vehicles. In *2016 XXV International Scientific Conference Electronics (ET),* Sozopol, Bulgaria.

[38] Castaings, A., Lhomme, W., Trigui, R., & Bouscayrol, A. (2016). Practical control schemes of a battery/supercapacitor system for electric vehicle. *IET Electrical Systems in Transportation*, *6*(1), 20-26.

[39] Naseri, F., Farjah, E., Ghanbari, T. (2017, May). An efficient regenerative braking system based on battery/supercapacitor for electric, hybrid and plug-in hybrid electric vehicles with BLDC motor. *IEEE Transactions on Vehicular Technology*, *66*(5), 3724-3738.

[40] Adib, A., & Dhaouadi, R. (2018). Performance analysis of regenerative braking in permanent magnet synchronous motor drives. *Advances in Science, Technology and Engineering Systems Journal*, *3*(1), 460-466.

[41] Lhomme, W., Delarue, P., Barrade, P., Bouscayrol, A., & Rufer, A. (2005, Oct. 2-6). Design and control of a supercapacitor storage system for traction applications. In *2005 Industry Applications Conference* (pp. 2013-2020).

[42] Liu, X., Zhang, Q., & Zhu, C. (2009, Sep. 7–10). Design of battery and ultracapacitor multiple energy storage in hybrid electric vehicle. In *2009 IEEE Vehicle Power and Propulsion Conference,* Dearborn, MI, USA.

[43] Kuperman, A., Aharon, I., Malki, S., & Kara, A. (2013, Feb.). Design of a semiactive battery-ultracapacitor hybrid energy source. *IEEE Transactions on Power Electrononics*, *28*(2), 806-815.

[44] Miller, J. M., McCleer, P. J., Everett, M., & Strangas, E. G. (2005, June 20-23). Ultracapacitor plus battery energy storage system sizing methodology for HEV power split electric CVT's. In *2005 IEEE International Symposium on Industrial Electronics*, Dubrovnik, Croatia.

[45] Jing, W., Lai, C. H., Wong, S. H. W., & Wong, M. L. D. (2017). Battery-supercapacitor hybrid energy storage system in standalone DC microgrids: A review. *IET Renewable Power Generation*, *11*(4), 461–469.

[46] Onar, O., & Khaligh, A. (2008, Sep. 3-5). Dynamic modeling and control of a cascaded active battery/ultra-capacitor based vehicular power system. In *2008 IEEE Vehicle Power and Propulsion Conference (VPPC),* Harbin, China.

[47] Di Napoli, A., Crescimbini, F., Capponi, F. G., & Solero, L. (2002, July 8-11). Control strategy for multiple input DC-DC power converters devoted to hybrid vehicle propulsion systems. In *2002 IEEE International Symposium on Industrial Electronics*, L'Ayuila, Italy (pp. 1036-1041).

[48] Li, Z., Onar, O., Khaligh, A., & Schaltz, E. (2009-01-1387). Design, control, and power management of a battery/ultra-capacitor hybrid system for small electric vehicles. In *SAE World Congress & Exhibition*, Detroit, MI, USA.

[49] Dixon, J., Nakashima, I., Arcos, E. F., & Ortuzar, M., 2010, Mar.). Electric vehicle using a combination of ultracapacitors and ZEBRA battery. *IEEE Transactions on Industrial Electronics*, *57*(3), 943-949.

[50] Allegre, A. L., Bouscayrol, A., & Trigui, R. (2013). Flexible real-time control of a hybrid energy storage system for electric vehicles. *IET Electrical Systems in Transportation*, *3*(3), 79-85.

[51] Trovão, J. P. F., & Pereirinha, P. G. (2015). Control scheme for hybridised electric vehicles with an online power follower management strategy. *IET Electrical Systems in Transportation*, *5*(1), 12-23.

[52] Trovão, J. P., Silva, M. A., & Dubois, M. R. (2017). Coupled energy management algorithm for MESS in urban EV. *IET Electrical Systems in Transportation*, *7*(2), 125-134.

[53] Livreri, P., Castiglia, V., Pellitteri, F., & Miceli, R. (2018, Sep. 10-13). Design of a battery/ultracapacitor energy storage system for electric vehicle applications. In *2018 IEEE 4th International Forum on Research and Technologies for Society and Industry (RTSI)*, Palermo, Italy (pp. 1-5).

[54] Napoli, A., Crescimbini, F., Rodo, S., & Solero, L. (2002, June 23-27.). Multiple input DC-DC power converter for fuel-cell powered hybrid vehicles. In *2002 IEEE 33rd Annual Power Electronics Specialists Conference*, Cairns, QLD, Australia (pp. 1685-1690).

[55] Gummi, K., & Ferdowsi, M. (2010, Feb.). Double-input DC–DC power electronic converters for electric-drive vehicles - Topology exploration and synthesis using a single-pole triple-throw switch. *IEEE Transactions on Industrial Electronics*, *57*(2), 617-623.

[56] De Castro, R., Pinto, C., Araujo, R. E., Melo, P., & Freitas, D. (2012, Oct. 9-12). Optimal sizing and energy management of hybrid storage system. In *2012 IEEE Vehicle Power and Propulsion Conference (VPPC)*, Seoul, Korea.

[57] Kumar, L., & Jain, S. (2013). Multiple-input DC/DC converter topology for hybrid energy system. *IET Power Electronics*, *6*(8), 1483-1501.

[58] Lai, C.-M., & Yang, M.-J. (2016). A high-gain three-port power converter with fuel cell, battery sources and stacked output for hybrid electric vehicles and DC-microgrids. *Energies*, *9*(3), 180-195.

[59] Hintz, A., Prasanna, U. R., & Rajashekara, K. (2015, May). Novel modular multiple-input bidirectional DC-DC power converter (MIPC) for HEV/FCV application. *IEEE Transactions on Industrial Electronics*, *62*(5), 3163-3172.

[60] Momayyezan, M., Hredzak, B., & Agelidis, V. G. (2015, Nov. 9-12). A new multiple converter topology for battery/ultracapacitor hybrid energy system. In *IECON 2015 - 41st Annual Conference of the IEEE Industrial Electronics Society*, Yokohama, Japan (pp. 464-468).

[61] Lai, C.-M., Cheng, Y.-H., Hsieh, M.-H., & Lin, Y.-C. (2018, Feb.). Development of a bidirectional DC/DC converter with dual-battery energy storage for hybrid electric vehicle system. *IEEE Transactions on Vehicular Technology*, 67(2), 1036-1052.

[62] Lai, C.-M., Yang, C.-Y., & Cheng, Y.-H. (2018, Dec. 1). Power supply system and power supply method for electric vehicle including a supercapacitor to receive power from a motor and capable of extending the battery life. *Taiwan Patent no. I642575*.

[63] Scrosati, B., Abraham, K. M., Van Schalkwijk, & W. Hassoun, J. (ed.) (2013). Lithium batteries: Advanced technologies and applications. ECS-The Electrochemical Society.

[64] Pistoia, G. (ed.) (2014). Lithium-ion batteries: Advances and applications. Elsevier.

[65] Gulbinska, M. K. (ed.) (2014). Lithium-ion battery materials and engineering: Current topics and problems from the manufacturing perspective. Springer.

[66] Julien, C., Mauger, A., Vijh, A., & Zaghib, K. (2015). Lithium batteries. Science and technology. Springer.

[67] Wu, Y. (2015). Lithium-ion batteries: Fundamentals and applications. CRC Press.

[68] Warner, J. (2015). The handbook of lithium-ion battery pack design: Chemistry, components, types and terminology. Elsevier.

[69] Korthauer, R. (ed.) (2018). Lithium-ion batteries: Basics and applications. Springer.

[70] Eftekhari, A. (ed.) (2019). Future lithium-ion.batteries. The Royal Society of Chemistry.

[71] Liu, S., Ouyang, X., & Zheng, Y. (2016, Aug. 24). Carbon back capacity battery and carbon back capacity battery group. *China Patent No. 205751881*.

[72] *Batteries are dead, long live Carbon based Power Capacitors!* Available at: https://kurt.energy/wp-content/uploads/2019/04/WHITE-PAPER-Carbon-based-power-caps.pdf

[73] *Hybrid carbon-based supercapacitor cell specifications*. Available at: https://kurt.energy/wp-content/uploads/2020/01/Hybrid-C-Supercaps-Datasheet08012020.pdf

[74] Zheng, Y., & Zheng. D. (2017, Jul. 11). New energy automobile charging station based on carbon back capacity battery group. *China Patent No. 206323188*.

Study of Responsivity for InP/InGaAs Heterojunction Bipolar Phototransistor Intended for Optoelectronic Applications

Jihane Ouchrif[1], Abdennaceur Baghdad[2], Aicha Sahel[3], Abdelmajid Badri[4]

[1,2,3,4]Electrical Engineering Department, EEA&TI Laboratory, Faculty of Sciences and Techniques of Mohammedia, Hassan II University of Casablanca, Morocco

Abstract—**Phototransistors are excellent devices used as photodetectors in optical fiber communication systems. In this work, we studied the responsivity of InP/InGaAs Heterojunction Bipolar Phototransistor (HPT) at two wavelengths 1310nm and 1550nm. The HPT structure is mainly based on an optimised structure of HBT of our research work. We used TCAD-Silvaco tools to design the structure and also to simulate the electrical characteristics, we integrated the physical models to consider physical phenomena occurring within the studied device. We simulated the photocurrent and the collector current as a function of light intensity, and then we extracted the responsivity. The obtained results are promising, this HPT can be used for optoelectronic applications.**

Keywords - InP/InGaAs heterojunction bipolar phototransistor, light intensity, optical fiber communication systems, optoelectronic applications, TCAD-Silvaco

I. INTRODUCTION

Nowadays, semiconductor devices are requested in communication and information systems. There is a growing demand for devices based on III-V semiconductor materials because of their interesting properties.

Indium Phosphide (InP) and Indium Gallium Arsenide (InGaAs) are semiconductor materials of the III-V family of semiconductors. Heterojunction bipolar transistors based on InP and InGaAs have shown to be excellent electronic devices, they are characterized by high electrical performances of speed and high frequency [1,2].

The Heterojunction Bipolar Phototransistor (HPT) has almost the same epitaxial layer as the HBT, but the difference is in the electrode structure which enables illumination in the top of the device structure [3,4].

Heterojunction Bipolar Phototransistors (HPTs) are attractive alternatives to devices as metal-semiconductor-metal (MSM), the PIN and avalanche photodiodes [5].

Among the various applications where photodetectors based on InP are required, there is the biomedical field, the firms of chemistry for near infrared (NIR) light detection, the environment and the optical communication systems [6].

The aim of this work is to study the responsivity of InP/InGaAs Heterojunction Bipolar Phototransistor at two wavelengths 1310nm and 1550nm using TCAD-Silvaco.

II. INP/INGAAS HPT MODELLING

A. *InP/InGaAs HPT Device Structure*

We were based on the optimized HBT structure of our research work [1,7] to design InP/InGaAs shown in the Fig. 1. The HBT was changed in such a way that can intercept light. Table I presents in order the epitaxial layers characteristics (doping profiles, thicknesses and the semiconductor materials). It is an npn heterojunction bipolar phototransistor, the contacts are made from material gold.

ISBN: 978-86-82602-01-9

TABLE I. EPITAXIAL LAYER STRUCTURE OF THE PHOTOTRANSISTOR HPT INP/INGAAS.

Layer	Material	Doping (cm^{-3})	Thickness (nm)
Cap	$In_{0.47}Ga_{0.53}As$	$n = 1x10^{19}$	135
Emitter 1	InP	$n = 1x10^{16}$	135
Emitter 2	InP	$n = 1x10^{17}$	40
Spacer	$In_{0.47}Ga_{0.53}As$	-	5
Base	$In_{0.47}Ga_{0.53}As$	$n = 1x10^{19}$	55
Collector	$In_{0.47}Ga_{0.53}As$	$n = 1x10^{16}$	630
Sub-collector	$In_{0.47}Ga_{0.53}As$	$n = 1x10^{19}$	500
Buffer	$In_{0.47}Ga_{0.53}As$	-	10
Substrate	Semi-insulating InP		

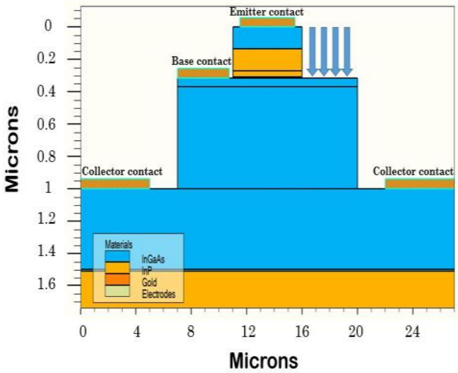

Figure 1. Schematic Diagram of InP/InGaAs HPT.

Regarding the fabrication of this device, there are different techniques for the growth of epitaxial layers such as Metal Organic Chemical Vapor Deposition (MOCVD) [8], and Molecular Beam Epitaxy (MBE) [9].

The Fig. 1 illustrates a schematic cross-section of the top-illuminated InP/InGaAs HPT, incident radiation striking the base surface through the optical window whose dimension is equal to 4µm by 4µm. The light beams are emitted at the two wavelengths 1310nm and 1550nm.

In this phototransistor, the optical signal is absorbed exponentially decreasing in the base, collector and sub-collector regions. The photogenerated electron-hole pairs are separated by the electric field in the absorption region, the electrons are drifting to the n-type collector and sub-collector, and the holes to the p-type base region.

The photogenerated holes accumulate in the base region, due to a large potential barrier in the valence band at the base-emitter heterostructure until they recombine with the injected electrons from the emitter. To maintain the charge neutral condition in the base, a large injection of electrons takes place from the emitter to the base resulting in a high current flow between the emitter and the collector.

B. Physical Modelling

To take into consideration the different physical mechanisms happening within this electronic device, we have added some physical models [10] included in the simulator ATLAS such as mobility models, recombination models, impact ionization, tunneling models and carrier injection models, etc.

Among the physical models integrated in the simulation, the carrier statistical model (BGN), the recombination model (SRH), the Selberherr's model of the impact of ionization (IMPACT SELB), the Band-to-Band model (BBT.STD), the optical recombination model (OPTR), the Parallel Electric Field Dependence model (FLDMOB), the Fermi-Dirac model (FERMI), etc.

C. Numerical Modelling

The Newton method was used to solve numerically semiconductor equations. Below are these equations [11]:

Poisson’s equation:

$$div\ (\varepsilon \nabla \psi) = \rho\ , \tag{1}$$

where,

ε : the dielectric constant of the material,
ψ : the local voltage potential,
and ρ : the local charge density.

The electric field $\vec{E}$:

$$\vec{E} = -\nabla\psi . \tag{2}$$

The carrier continuity equations for electrons and holes:

$$\frac{\partial n}{\partial t} = \frac{1}{q} div(\mathrm{J}\vec{\mathrm{n}}) + G_n - R_n , \tag{3}$$

$$\frac{\partial p}{\partial t} = -\frac{1}{q} div(J\vec{p}) + G_p - R_p , \tag{4}$$

where, $J\vec{n}$ and $J\vec{p}$ are the electron and hole currents. G_n , G_p , R_n and R_p are respectively the generation and recombination rates for the electrons and holes.

The drift and diffusion currents for electrons and holes:

$$J\vec{n} = n q \mu_n \vec{E} + q D_n \tilde{N} n , \tag{5}$$

$$J\vec{p} = p q \mu_p \vec{E} - q D_p \tilde{N} p , \tag{6}$$

where, μ_n and μ_p are the carrier mobilities, and D_n , D_p are the diffusion coefficients for electrons and holes.

III. Results and Discussions

This study was at room temperature (300 K). The figures in this part show the simulation results of InP/InGaAs HPT in the photodiode and phototransistor mode for the two wavelengths 1310nm and 1550nm. We simulated the photocurrent and the collector current as a function of light intensity for different bias conditions for the two modes, and we then extracted the responsivity of the studied phototransistor.

A. Responsivity of InP/InGaAs HPT

1) Responsivity in photodiode mode $R_{pd}\,(A/W)$

The responsivity in photodiode mode [12] allows to analyze the photocurrent generated in the active area of the HPT for detection. Its study, therefore, requires "cutting off" the transistor effect by short-circuiting the base-emitter junction while the base-collector junction is polarized in its normal conditions of use.

The photodiode mode is the mode when $V_{be} = 0V$, the responsivity in photodiode mode $R_{PD}\,(A/W)$ is expressed as follows:

$$I_{ph} = R_{PD}.P_{opt} . \tag{7}$$

2) Responsivity in phototransistor mode R_{HPT}

The responsivity in phototransistor mode considers the normal operation of the transistor, and it is therefore given according to the bias since it adds the transistor effect to the detection. It is defined by the following equation [12]:

$$\mathrm{R}_{HPT}(\lambda) = \frac{I_{c-opt}}{P_{opt}}\,(A/W) , \tag{8}$$

where, I_{c-opt} is the collector current due to photodetection, and P_{opt} is the optical power,

B. Simulation results of InP/InGaAs HPT

According to Fig.2, the photocurrent I_{ph} varies in a linear way for each applied power density. The responsivity R_{PD} of InP/InGaAs HPT in photodiode mode is equal to 0.8A/W at λ = 1310nm. This responsivity in photodiode mode remains the same by changing V_{be} from 0 to 3V with a step of 0.5.

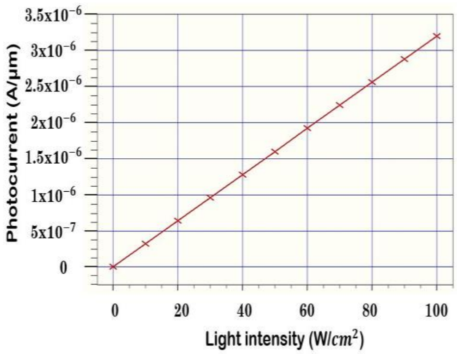

Figure 2. Photocurrent as a function of light intensity for the wavelength 1310nm at $V_{be} = 0V$ and $V_{ce} = 0V$.

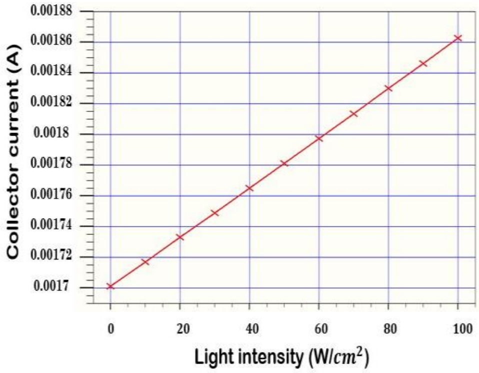

Figure 3. Collector current as a function of light intensity for the wavelength 1310nm at $V_{be} = 0.86V$ *and* $V_{ce} = 1.6V$.

Fig. 3 shows a linear evolution, the collector current increases gradually with the growth of the applied optical intensity (W/cm^2) .The responsivity R_{HPT} in phototransistor mode is approximately equal to 10A/W at 1310nm.

As shown in the Fig. 4, the photogenerated current varies in a linear manner with increasing application of light intensity. Therefore, the responsivity R_{PD} in photodiode mode of the studied HPT is of the order of 0.7A/W at $\lambda = 1550$nm. For different values of V_{be} (0 to 3V) with a step of 0.5, we obtain the same responsivity in photodiode mode for 1550nm.

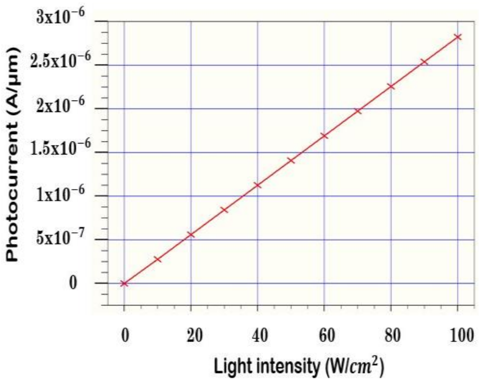

Figure 4. Photocurrent as a function of light intensity for the wavelength 1550nm at $V_{be} = 0V$ et $V_{ce} = 0V$.

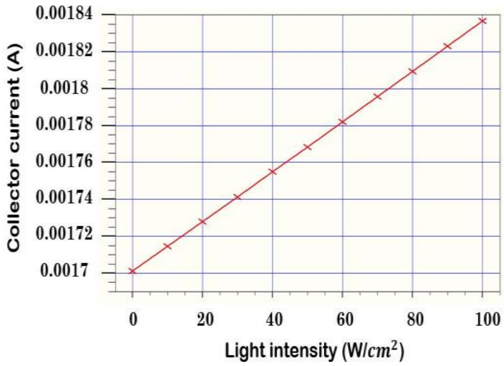

Figure 5. Collector current as a function of light intensity for the wavelength 1550nm at $V_{be} = 0.86V$ *and* $V_{ce} = 1.6V$.

Fig. 5 presents the linear evolution of the collector current as a function of the light intensity (W/cm^2) for the wavelength 1550nm. The responsivity R_{HPT} of HPT InP/InGaAs is equal to 8.4A/W in phototransistor mode.

IV. CONCLUSION

We used the simulator TCAD-Silvaco to model the electronic device InP/InGaAs Heterojunction Bipolar Phototransistor. We have integrated the physical models included in the simulator such as SRH, OPTR, BBT.STD, etc. to take into consideration the various physical mechanisms occurring inside this device. We then simulated the photocurrent and the collector current as a function of the light intensity for the photodiode and phototransistor mode. We extracted the responsivity of the studied photodetector at two wavelengths 1310nm and 1550nm. According to the obtained results, this phototransistor can be used in optoelectronic applications.

ACKNOWLEDGMENT

We are grateful to L'Oréal and UNESCO for their financial support and encouragement through their scholarship "L'Oréal-UNESCO Young Talents Maghreb For Women in Science Maghreb."

REFERENCES

[1] Tauqeer, T., Sexton, J., Amir, F., & Missous, M. (2008, October). Two-dimensional physical and numerical modelling of InP-based heterojunction bipolar transistors. In *2008 International Conference on*

Advanced Semiconductor Devices and Microsystems (pp. 271-274). IEEE.

[2] Yu, D., Choi, K., Lee, K., Kim, B., Zhu, H., Vargason, K., Kuo, J. M., Pinsukanjana, P., & Kao, Y. (2004). Ultra high-speed 0.25-µm emitter InP-InGaAs SHBTs with f(max) of 687 GHz. In 2004 *International Electron Devices Meeting* (pp. 557–560). IEEE.

[3] Khan, H. A., Rezazadeh, A. A., Sohaib, S., & Tauqeer, T. (2012). Detailed analysis on the spectral response of InP/InGaAs HPTs for optoelectronic applications. *IEEE Journal of Quantum Electronics*, *48*(5), 576-580.

[4] Chennafi, N., Rumelhard, C., Gonzalez, C., & Thuret, J. (1998). Modelling the photoresponse characteristics of InP/InGaAs heterojunction phototransistor with different incident directions of beam light.

[5] Ściana, B., Panek, M., Borczuch, A., & Tłaczała, M. (2011). Simulations of AlGaAs/GaAs heterojunction phototransistors. *Open Physics*, *9*(4), 1114-1121.

[6] Jo, Y. C., Song, H. J., Choi, Y. S., Kim, H., Park, H. D., Kwon, Y. S., & Choi, P. (2007). Design and optical characterization of passive pixel with sensitivity-improved InGaAs/InP phototransistors considering light-dependent shunt resistance for near infrared imaging applications. *Japanese Journal of Applied Physics*, *46*(9S), 6222.

[7] Ouchrif, J. (2019). *Conception d'un photodétecteur à base du transistor HPT InP/InGaAs pour les applications de télécommunications fibrées numériques et microondes* [Doctoral thesis, Faculty of Sciences and Techniques of Mohammedia, Hassan II University of Casablanca]. N° d'ordre : 53/2019/CED.

[8] Kamitsuna, H., Shibata, T., Kurishima, K., & Ida, M. (2003, September). Direct Optical Injection Locking of InP/InGaAs HPT Oscillator Circuits for Millimeter-Wave Photonics and Optoelectronic Clock Recovery. *MWP2003*. *IEEE International Topical Meeting on Microwave Photonics*, Budapest, Hungary.

[9] Sexton, J., Tauqeer, T., Mohiuddin, M., & Missous, M. (2008). GHz Class Low-Power Flash ADC for Broadband Communications. In *2008 International Conference on Advanced Semiconductor Devices and Microsystems*, (pp. 235–238).

[10] ATLAS (2012). User's Manual DEVICE SIMULATION SOFTWARE. *SILVACO*.

[11] Ouchrif, J., Baghdad, A., Sahel, A., Badri, A., & Ballouk, A. (2019). How does technological parameters impact the static current gain of InP-based single heterojunction bipolar transistor?. *International Journal of Electrical and Computer Engineering*, *9*(5), 3432.

[12] Polleux, J. L. (2001). *Contribution à l'étude et à la modélisation de phototransistors bipolaires à hétérojonction SiGe/Si pour les applications opto-microondes* [Thèse de doctorat]. CNAM Paris.

A Simple Model for Estimation of Tortuosity of Sandstone Formations as a Function of Porosity

Pratiksha D. Khurpade[1], Somnath Nandi[2]

[1]School of Chemical Engineering, Dr. Vishwanath Karad MIT World Peace University, Pune, India

[2]Department of Technology, Savitribai Phule Pune University, Pune - 411007, India

Abstract—**Tortuosity is one of the important petrophysical properties of petroleum reservoir rocks which has a great influence on movement of hydrocarbon through interconnected pore flow channels. Various factors such as scale deposition in pore channels, fines migration and presence of clay minerals lead to plugging of pores inside reservoir rock matrix and hence, reduces the pore connectivity. Although qualitatively tortuosity concept is simple, it is difficult to measure experimentally effective fluid flow path length due to inherent pore structure heterogeneity of sedimentary rocks. In addition, various existing empirical correlations in literature are based on porosity which typically varies from one reservoir to another. In this study, a simple and generalized equation to estimate tortuosity as a function of easily measurable property of porous media namely porosity of the form $\tau = a \times \phi^{b}$ is targeted. Model was developed by utilizing forty training data points and randomly selected seven validation data points among total forty-seven data set of tortuosity – porosity from sandstone formations in Ordos Basin of China. The developed model as $\tau = 1.327 \times \phi^{-0.127}$ can predict tortuosity with good accuracy with percentage of error less than 15% compared with published result of sandstone reservoir of China. The efficacy of model was then tested with wide range of data sets of other sandstone reservoirs available from open literature. The results indicate good agreement between our model predicted tortuosity values and published literature results (with less than 20% error). Moreover, comparison study was carried with various existing tortuosity – porosity correlations in literature. The results revealed that the developed model exhibits reasonably good accuracy as compared to other previous models.**

Keywords - tortuosity, porosity, pore structure, sandstone formation

I. INTRODUCTION

Among the key characteristics, tortuosity is one of the important properties of petroleum reservoir rock formations. The flowability of oil and gas through reservoir rock is strongly dependent on tortuosity as it represents the interconnectivity of pore flow channels [1]. Thus, it plays a key role in the understanding of transport of fluids through subsurface porous media [2]. Higher pore network connectivity of reservoir rock matrix results in less tortuous flow channels and thus, contributes more to improve the fluid flow through it [3].

The concept of tortuosity was first introduced by Kozney and Carman as a factor that illustrates the departure of fluid flow paths in porous material than straight flow channels. The well-known Kozney-Carman equation relates permeability with porosity, tortuosity and specific surface area. Although qualitatively tortuosity concept is simple, it is difficult to measure experimentally effective fluid flow path length due to inherent pore structure heterogeneity of sedimentary rocks.

Several researchers have reported various tortuosity measurement techniques namely experimental methods, numerical methods, image analysis methods along with theoretical and empirical correlations between tortuosity and porosity [4,5]. Two widely used experimental approaches of tortuosity estimation are electrical resistivity and diffusivity measurements but these methods are expensive, requires specialized equipment and time consuming [6]. However, in past few years, image analysis method utilizing two-dimensional microscopic thin section, scanning electron microscopic (SEM) or three-dimensional X-ray computed tomographic (X-ray CT) images have been used for estimation of tortuosity of sandstone, carbonate or shale rock samples, as it is less time consuming than electrical resistivity, diffusivity techniques and numerical methods as well [7-10]. Several researchers have developed numerous image-based algorithms to estimate the tortuosity of porous media from two or three-dimensional digital images namely medial axis [11,12], A-star algorithm [13] and Dijkstra shortest path algorithm [14] etc. However, most of these algorithms are employed using commercial software such as Avizo and 3-Dimensional Medial Axis Rock (3DMA-Rock) software which are costlier and are not easily available for researchers [9,15]. In addition, these software tools work on different methods for calculation of tortuosity which often leads to inconsistency in results.

Moreover, various theoretical or empirical models between tortuosity and porosity have also been proposed in literature [5]. In theoretical model studies, researchers assume only ideal geometry of porous media (porous medium with cubic, cylindrical or spherical particles) even though actual subsurface petroleum bearing rocks are anisotropic in nature [6,16]. As a result, theoretical models will incur more errors when applied to anisotropic formations. On the contrary, empirical models exhibit better accuracy compared to theoretical model despite of adjustable parameters involved in it [6]. It should be noted that tortuosity is mainly affected by pore structure heterogeneity of petroleum reservoir rocks such as wide variations in pore size, pore structure and pore size distribution along with grain size, shape and sorting. Such pore structure complexities make it challenging to develop mathematical model that can estimate tortuosity for hydrocarbon reservoir rock as a function of parameter representative of its microstructure heterogeneity [16]. Additionally, in-depth analysis of pore network characteristics of reservoir rock is time consuming and requires sophisticated instruments such as mercury injection capillary pressure (MICP) analysis, low pressure nitrogen adsorption and thin section or scanning electron microscopy (SEM) analysis [17]. In this aspect, empirical models have been utilized for tortuosity estimation.

Hence, there is need for the development of simple and generalized methodology to infer tortuosity of complex porous rock matrix using easily measurable petrophysical property which in absence of other pore structure properties. In this study, tortuosity and porosity data of sandstone formations from published literature along with tortuosity – porosity empirical correlations available in the literature is used to develop new, simpler and useful model for tortuosity estimation in terms of porosity for sandstone reservoirs.

II. Model Development for Estimation of Tortuosity as a function of Porosity

In this study, a simple and generalized model to estimate tortuosity (the targeted output) as a function of easily measurable property of porous media namely porosity was developed.

The following generalized model is targeted:

$$\tau = a \times \phi^{\mathbf{b}} \qquad (1)$$

where, τ: tortuosity of porous medium (–), ϕ: porosity in fraction (–) and defined as ratio of pore volume to total volume of porous material. (sometimes it is expressed in percentage %), a and b : model coefficients

Model was developed by utilizing forty training data points and randomly selected seven validation data points among total forty-seven data set of tortuosity – porosity from sandstone formations of China published by [8]. The studied sandstone reservoir data of [8] belongs to low and medium porosity sandstone formation in the Ordos Basin in China, having porosity ranging from about 3% to 20%. The optimal parameters a and b of the proposed model (1) were found using multivariate regression analysis in EXCEL.

A. Description of Multivariate Regression Approach

Multivariate regression is a standard statistical method used to estimate the relationship between the one dependent variable of interest (also known as response variable, i.e., the targeted output) and multiple independent variables (called as predictor variables).

The multivariate regression model can be written in the general form as:

$$Y = \beta_0 + \beta_1 X_1 \pm \ldots + \beta_i X_k + \varepsilon , \qquad (2)$$

where, Y represents the targeted outputs (τ), X represents the experimental input (ϕ), β_i's are the coefficients of the proposed model ($i = 1, 2, \ldots, n$) and ε stands for the residuals (errors) between model predictions and corresponding experimental values.

In multivariate analysis, the optimal parameters for the model that best fit the data points are estimated using least square method that minimizes the square of residuals (SSR).

$$SSR = \sum_{i=1}^{n} \varepsilon_i^2 = = \sum_{i=1}^{n} (Y_i - \beta_0 - \sum_{j=1}^{k} \beta_j X_{ij})^2 . \quad (3)$$

In this study, the present nonlinear model Eq. (1) was converted to linear form using logarithms and then model parameters were found using multivariate regression method in EXCEL.

B. *Statistical Error Analysis*

To assess the efficiency and accuracy of the developed regression-based model, percentage relative error was utilized.

Percentage relative error or percentage error: it is measure of the relative deviation of predicted tortuosity from the experimental value.

$$E_i = \left(\frac{\tau_{pred.} - \tau_{\text{expt.}}}{\tau_{\text{expt.}}} \right) \times 100, \mathrm{i} = 1, 2, \ldots, \mathrm{n} \quad (4)$$

III. Results and Discussion

The developed generalized model was utilized to estimate the tortuosity of porous medium as a function of important petrophysical property of rock namely porosity. The optimal parameters of model Eq. (1) were estimated using multivariate regression using EXCEL based on published data set of [8] and is represented by Eq. (5) as follows:

$$\tau = 1.327 \times \phi^{-0.127} \quad (5)$$

The results of model predicted tortuosity Eq. (5) along with [8] reported tortuosity versus porosity are presented in Fig. 1 (a) forty training data set and Fig. 1 (b) seven validation data set. As evident from Fig. 1 a and b, simple developed model can predict the tortuosity quite accurately.

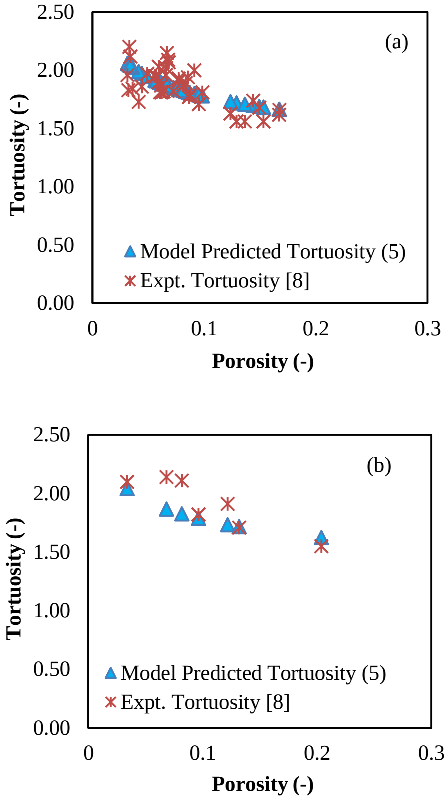

Figure 1. Model predicted tortuosity (using 5) and experimental tortuosity values [8] versus porosity data for (*a*) forty training data set (*b*) seven validation data set.

TABLE I. PERCENTAGE RELATIVE ERROR OF TORTUOSITY USING DEVELOPED MODEL (1).

Data set	Relative percentage error [E_i]
Training data set (40)	14.98 %
Testing data set (7)	13.49 %

Furthermore, to quantify the efficiency and accuracy of the developed model, percentage relative error (E_i) was calculated for all the predictions and the obtained values are provided in Table I.

As evident from Table I, the developed model predicts the tortuosity of 40 training data points [8] with accuracy of 85.02% and subsequently validated with randomly selected 7 data points [8] with accuracy of 86.51%. It is important to note that the tortuosity estimated by developed model exhibits more variation compared to tortuosity data of [8] especially for the samples having lower range of porosity values. Typically, reservoir rocks with low porosity values (<8–10%), exhibits poor pore connectivity due to higher proportion of micropores. On the contrary, petroleum reservoirs rock samples with less complex pore structure and good pore connectivity is dominated by higher percentage of macropores and thus have higher porosity range (>10%). Therefore, more deviation is observed for core samples with low porosity value due to poor pore structure. Although pore structure characterization was not carried out in this study, these findings were confirmed with the results of relationship between important petrophysical properties (porosity and permeability) of Xujiahe sandstone formation samples of [18] with different types of pores (macro, meso or micropores) and their proportions using MICP and thin section analysis. Also, it should be noted that, this complex pore structure leads to distinct porosity term exponent for different types of reservoir rocks. Therefore, it can be concluded that developed model (5) shows a good match with the experimental data [8] of wide porosity range with the accuracy >85% and thus, tortuosity can be effectively estimated from porosity in sandstone formations using developed simple model.

A. *Testing of Developed Model*

Developed model was later tested with the published data sets of sandstone reservoir of [18] and [19]. Reported the tortuosity data of 36 core samples [18] belongs to Xujiahe Formation in Sichuan basin, southwest China which is low permeability sandstone reservoir with porosity ranges from 4 to 22%, whereas Berea and synthetic sandstone cores data were reported by [19] have porosity values 19 to 29%. Fig. 2 a and b illustrates the results of our model predicted tortuosity (5) with reported tortuosity data sets [18, 19]. It is clearly observed from Fig. 2 a and b that the prediction of our developed model (5) exhibits good agreement with experimental data of [18] with 81.63% accuracy. Additionally, developed model shows good agreement with experimental data of [19] for Berea sandstone with 75.65% accuracy and for synthetic sandstone with 79.03% accuracy.

The percentage relative error of present model for data sets [18,19] are shown in Fig. 3 a and b. As presented in Fig. 3 a and b, the developed tortuosity model gives % relative error of less than 20% for 36 data points of [18] and less than 25% for 20 data points of [19]. Thus, results shown in Fig. 3 a and b of sandstone reservoir data sets from two different fields further confirms the validity of developed model for estimation of tortuosity of sandstone formations with good accuracy.

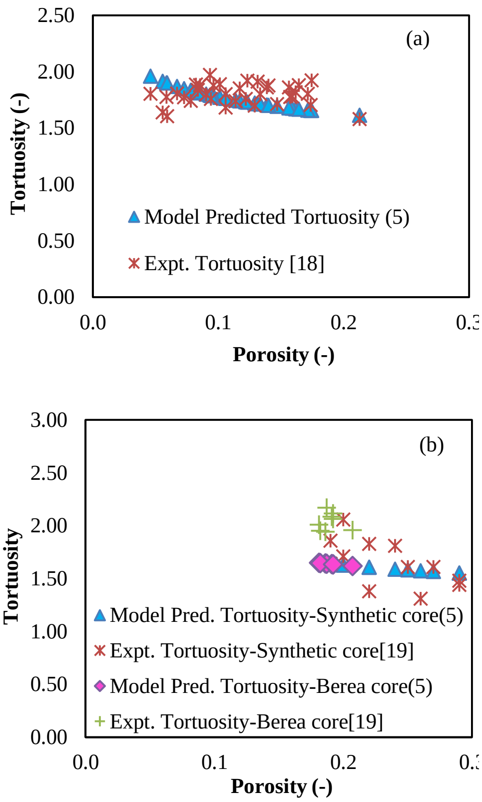

Figure 2. Model predicted tortuosity (5) with experimental tortuosity values of (*a*) [18] (*b*) [19] versus porosity data set.

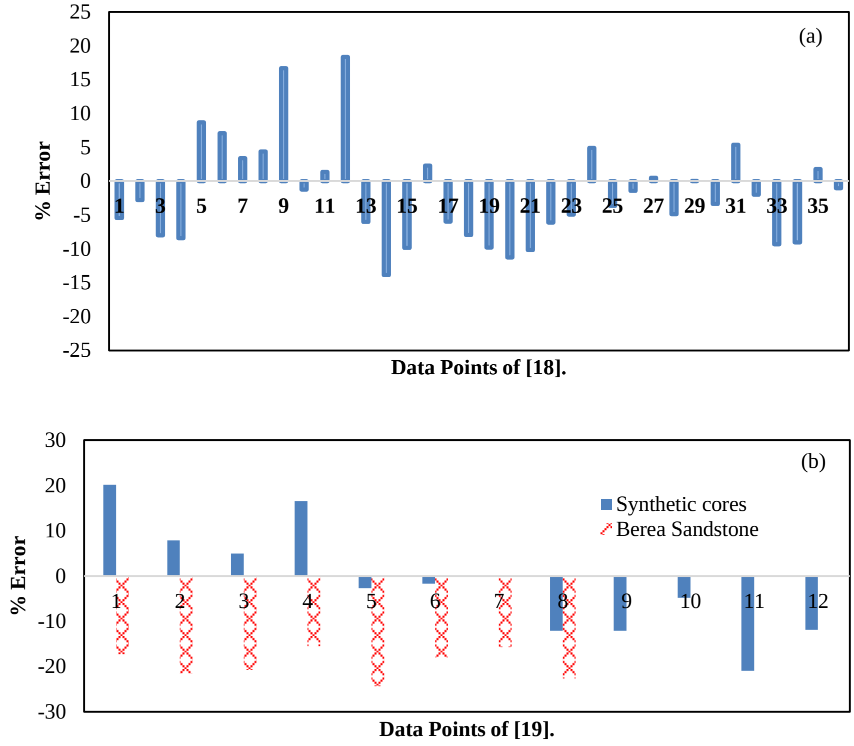

Figure 3. % Error in prediction of our developed model in comparison with tortuosity data set (*a*) [18] (*b*) [19].

B. *Comparison Between the Correlations Reported in the Literature and Developed Model*

Furthermore, comparison study was carried out between various existing tortuosity – porosity correlations in literature which are listed in Table II and present model utilizing the same data set of model development [8].

TABLE II. VARIOUS EXISTING TORTUOSITY–POROSITY EMPIRICAL CORRELATIONS IN LITERATURE.

Correlation	Reference
$\tau = 1.5 - 0.5 \times \Phi$	[20]
$\tau = \Phi^{0.5}$	[21]
$\tau = 1 - 0.5 \times \ln \Phi$	[22]
$\tau = \sqrt{1 - \ln \Phi^2}$	[6]
$\tau = 1 - 0.41 \times \ln \Phi$	[23]
$\tau = 1/\sqrt{\Phi}$	[24,25]

Figs. 4 and 5 illustrates the comparison between various empirical correlations listed in the Table II and developed model Eq. (5) in this study and obtained % relative error. As can be seen in Fig. 5, % relative error of all previous correlations is noticeably greater than our developed model. The result analysis revealed that the predictions obtained with developed model were found to be in good agreement, with an error less than 15% as compared to previous models (Maxwell: –32.57 %, Archie's: 116.25%, Weissberg: 49.84%, Boudreau: 56.91%, Comiti and Renaud: - 29.49%, Bruggeman: 204%).

In addition, tortuosity results presented in Fig. 4 clearly indicates that Bruggeman (1935) and Archie (1942) correlations gives the highest estimates and Comiti and Renaud (1989) and Maxwell (1873) model provides the lowest estimates. The results of Weissberg (1963) and Boudreau (1996) models fall in between. In all these correlations, tortuosity values have large

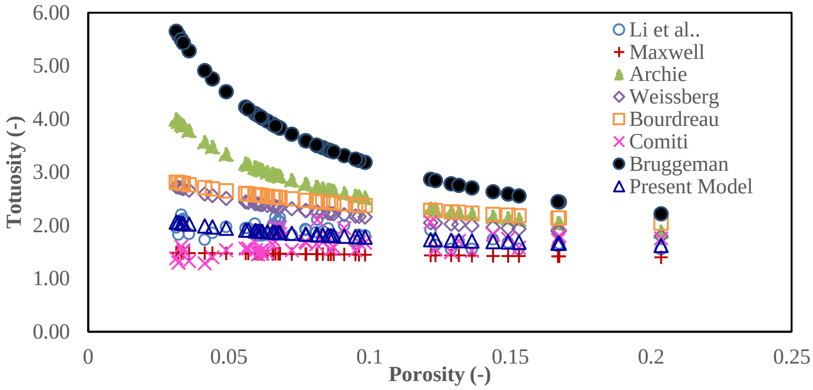

Figure 4. Tortuosity estimation using present model (5) in comparison with previous empirical correlations.

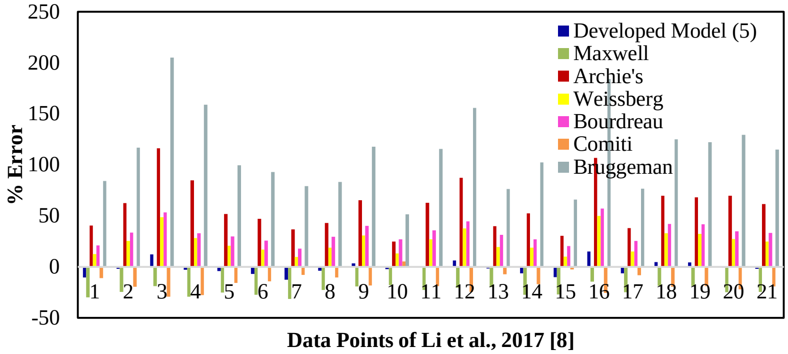

Figure 5. Percentage error in prediction of developed model (5) in comparison with previous empirical Correlations.

scattering at lower porosity values. As porosity increases, the scattering decreases. From these comparisons, it is observed that our developed model provides the better agreement between predicted and actual reported tortuosity values for wide range of porosity of formations.

It can be concluded that the developed tortuosity – porosity model exhibits better performance as compared to all previous empirical correlations and thus applicable to predict the tortuosity of sandstone formations with reasonable accuracy.

IV. CONCLUSIONS

A simple tortuosity model as a function of porosity for sandstone formation has been developed using multivariate regression analysis. A published literature data set including forty-seven samples from Ordos Basin in China were utilized in our study for training and validation of tortuosity – porosity model. Later model was tested with other published sandstone formations belongs to Xujiahe Formation in Sichuan basin, Southwest China, along with Berea and synthetic sandstone cores reported in literature. The result analysis demonstrated that the correlations between the tortuosity and the easily measurable petrophysical rock property namely porosity would yield a better relationship with better accurate coefficients. Overall, the tortuosity prediction is in reasonably good agreement with the earlier published results (less than 20% relative error) for low as well as medium porosity sandstone formations. The comparison study of developed model with previous correlations confirms the applicability for estimation of tortuosity of sandstone formations using easily measurable petrophysical property of reservoir rocks namely porosity.

REFERENCES

[1] Saomoto, H., & Katagiri, J. (2015). Direct comparison of hydraulic tortuosity and electric tortuosity based on finite element analysis. *Theoretical and Applied Mechanics Letters*, *5*(5), 177-180.

[2] Graczyk, K. M., & Matyka, M. (2020). Predicting porosity, permeability, and tortuosity of porous media from images by deep learning. *Scientific reports*, *10*(1), 21488.

[3] Goral, J., Panja, P., Deo, M., Andrew, M., Linden, S., Schwarz, J. O., & Wiegmann, A. (2020). Confinement effect on porosity and permeability of shales. *Scientific reports*, *10*(1), 49.

[4] Delgado, J. M. P. Q. (2006). A simple experimental technique to measure tortuosity in packed beds. *The canadian Journal of chemical engineering*, *84*(6), 651-655.

[5] Ghanbarian, B., Hunt, A. G., Ewing, R. P., & Sahimi, M. (2013). Tortuosity in porous media: a critical review. *Soil science society of America journal*, *77*(5), 1461-1477.

[6] Boudreau, B. P. (1996). The diffusive tortuosity of fine-grained unlithified sediments. *Geochimica et cosmochimica acta*, *60*(16), 3139-3142.

[7] Chen-Wiegart, Y. C. K., DeMike, R., Erdonmez, C., Thornton, K., Barnett, S. A., & Wang, J. (2014). Tortuosity characterization of 3D microstructure at nano-scale for energy storage and conversion materials. *Journal of Power Sources*, *249*, 349-356.

[8] Li, W., Zou, C. C., Wang, H., & Peng, C. (2017). A model for calculating the formation resistivity factor in low and middle porosity sandstone formations considering the effect of pore geometry. *Journal of Petroleum Science and Engineering*, *152*, 193-203.

[9] Zhang Y. (2019). Comparative Study of Pore Structure Characterization for Different Rock Samples Using Digital Images. MSc thesis, Melbourne School of Petroleum and Geological Engineering.

[10] Roque, W. L., & Costa, R. R. (2020). A plugin for computing the pore/grain network tortuosity of a porous medium from 2D/3D MicroCT image. *Applied Computing and Geosciences*, *5*, 100019.

[11] Lindquist, W. B., Lee, S. M., Coker, D. A., Jones, K. W., & Spanne, P. (1996). Medial axis analysis of void structure in three- dimensional tomographic images of porous media. *Journal of Geophysical Research: Solid Earth*, *101*(B4), 8297-8310.

[12] Al-Raoush, R. I., & Madhoun, I. T. (2017). TORT3D: A MATLAB code to compute geometric tortuosity from 3D images of unconsolidated porous media. *Powder Technology*, *320*, 99-107.

[13] Montes, J. M., Cuevas, F. G., & Cintas, J. (2007). Electrical and thermal tortuosity in powder compacts. *Granular Matter*, *9*, 401-406.

[14] Shanti, N. O., Chan, V. W., Stock, S. R., De Carlo, F., Thornton, K., & Faber, K. T. (2014). X-ray micro-computed tomography and tortuosity calculations of percolating pore networks. *Acta Materialia*, *71*, 126-135.

[15] Cheon, D. S., Takahashi, M., & Kim, T. (2021). Permeability differences based on three-dimensional geometrical information of void spaces. *Journal of Rock Mechanics and Geotechnical Engineering*, *13*(2), 368-376.

[16] Fu, J., Thomas, H. R., & Li, C. (2021). Tortuosity of porous media: Image analysis and physical simulation. *Earth-Science Reviews*, *212*, 103439.

[17] Kashif, M., Cao, Y., Yuan, G., Asif, M., Javed, K., Mendez, J. N., ... & Miruo, L. (2019). Pore size distribution, their geometry and connectivity in deeply buried Paleogene Es1 sandstone reservoir, Nanpu Sag, East China. *Petroleum Science*, *16*, 981-1000.

[18] Xiao, L., Zou, C. C., Mao, Z. Q., Shi, Y. J., Jin, Y., Guo, H. P., & Hu, X. X. (2013). Estimation of water saturation from nuclear magnetic resonance (NMR) and conventional logs in low permeability sandstone reservoirs. *Journal of Petroleum Science and Engineering*, *108*, 40-51.

[19] Attia, A. M. (2005). Effects of petrophysical rock properties on tortuosity factor. *Journal of Petroleum Science and Engineering*, *48*(3-4), 185-198.

[20] Maxwell, J. C. (1873). *A treatise on electricity and magnetism* (Vol. 1). Oxford: Clarendon Press.

[21] Archie, G. E. (1942). The electrical resistivity log as an aid in determining some reservoir characteristics. *Transactions of the AIME*, *146*(01), 54-62.

[22] Weissberg, H. L. (1963). Effective diffusion coefficient in porous media. *Journal of Applied Physics*, *34*(9), 2636-2639.

[23] Comiti, J., & Renaud, M. (1989). A new model for determining mean structure parameters of fixed beds from pressure drop measurements: application to beds packed with parallelepipedal particles. *Chemical Engineering Science*, *44*(7), 1539-1545.

[24] Bruggeman, D. A. G. (1935). Calculation of different physical constants of heterogeneous substances I: dielectric constant and conductivity of media of isotropic substances. *Ann. Phys.(Leipzig)*, *24*, 636-664.

[25] Sen, P. N., Scala, C., & Cohen, M. H. (1981). A self-similar model for sedimentary rocks with application to the dielectric constant of fused glass beads. *Geophysics*, *46*(5), 781-795.

Piece-wise Fourier Transform of Electrostatic Discharge Currents

Vesna Javor[1]

[1]Faculty of Electronic Engineering, University of Niš, Niš, Serbia

Abstract—**This paper presents a new procedure to obtain the Piece-wise Fourier transform (PWFT) of pulse waveforms. In the first step, the pulse waveform is approximated by the Multi-peaked analytically extended (MP-AEF) function, and in the second step, its Fourier transform is obtained part by part i.e. by integrating from peak to peak of the waveshape. Results of this procedure are presented for the single-wave and multiple-waves cosine functions, for the IEC 60060-1 standard waveshape 1.2/50 μs/μs, and for the IEC 61000-4-2 standard electrostatic discharge current. The advantage of the procedure is that it is suitable for aperiodic functions with multiple and sharp peaks.**

Keywords - Fourier transform, electrostatic discharge currents, piece-wise functions

I. Introduction

Pulse signals may be represented by their waveshapes and parameters in time domain or by their frequency spectrum in frequency domain. Frequency spectra of voltages' and currents' waveshapes are important in their analysis and in their measurements [1,2]. Fourier transform (FT) is used for periodic waveshapes, whereas Piece-wise Fourier transform (PWFT) may be used for aperiodic waveshapes with multiple and sharp peaks. For all periodic functions, frequency spectrum has spectral components at the zero frequency and at the discrete frequencies that are harmonics of the fundamental frequency. FT magnitudes at these frequencies are so called spectral components and represent the signal strength at these frequencies. However, FT of aperiodic waveshapes results in continuous spectra. That implies the use of Discrete Fourier transform (DFT) or Fast Fourier transform (FFT), as well as window functions. In fact, DFT is a discrete time approximation of FT, whereas FFT is just a wise implementation of DFT in a certain number of discretization points [3]. For the FFT application, a sample interval in time domain has to be small to provide representation of the signal accurately. Besides, the signal value has to be the same at the beginning and at the end of time window to avoid Gibb's phenomenon.

For an energy signal, $x(t)$, it is important to determine its energy spectral density that is proportional to the square of its FT magnitude, $\left|X(f)\right|^2$. The total energy of such signal is the integral of the energy spectral density in frequency domain that is equal to the integral of the squared signal in time domain, as given by the Parseval's equation:

$$\int_{-\infty}^{+\infty} x^2(t)\,dt = \int_{-\infty}^{+\infty} \left|X(f)\right|^2 df \quad . \qquad (1)$$

Electrostatic discharge (ESD) currents are energy signals and their total energy is finite. Before applying the PWFT procedure to such a signal, its waveshape is approximated by the Multi-peaked analytically extended function (MP-AEF), [4,5]. In order to present the PWFT [6], examples of single-wave and multiple-waves cosine functions are analyzed in this paper.

As an example of electrostatic discharge (ESD) current, the IEC 60060-1 standard testing pulse waveform [7] in high-voltage technique T_1/T_2=1.2/50μs/μs is approximated by double-exponential function, and its FT is obtained by using Gamma functions. In order to apply the PWFT procedure, the pulse is approximated by MP-AEF by applying the Marquardt Least-Squares Method (MLSM), and the Fourier transform is obtained by integrating from peak to peak. PWFT may be also used for measured ESD currents [8-12]. In this paper, results are given also for the IEC 61000-4-2 standard ESD current.

II. PWFT Procedure

MP-AEF [4] is a piece-wise function that is used for the ESD current $i(t)$ approximation for the chosen number of time intervals, e.g. $p=4$ in Eq. (2), between the current peaks $\sum_{n=1}^{r} I_{\mathrm{m}n}$ at the time moments t_{mr}, for $r=1,\ldots,p-1$ (*m* stands for maximum) and the chosen number of parameters for these intervals: a_i, b_i, c_i, d_i, weighting coefficients e_i, f_i, g_i, h_i, and the chosen number of terms in these intervals j, k, l, and n, for $\sum_1^j e_i = \sum_1^k f_i = \sum_1^l g_i = \sum_1^n h_i = 1$.

$$
i(t) = \begin{cases}
I_{m_1} \sum_{i=1}^{j} e_i \left[\dfrac{t}{t_{m_1}} \exp\left(1 - \dfrac{t}{t_{m_1}}\right) \right]^{a_i}, & 0 \le t \le t_{m_1}, \\
I_{m_1} + I_{m_2} \sum_{i=1}^{k} f_i \left[\dfrac{t - t_{m_1}}{t_{m_2} - t_{m_1}} \exp\left(1 - \dfrac{t - t_{m_1}}{t_{m_2} - t_{m_1}}\right) \right]^{b_i}, & t_{m_1} \le t \le t_{m_2}, \\
I_{m_1} + I_{m_2} + I_{m_3} \sum_{i=1}^{l} g_i \left[\dfrac{t - t_{m_2}}{t_{m_3} - t_{m_2}} \exp\left(1 - \dfrac{t - t_{m_2}}{t_{m_3} - t_{m_2}}\right) \right]^{c_i}, & t_{m_2} \le t \le t_{m_3}, \\
\left(I_{m_1} + I_{m_2} + I_{m_3}\right) \sum_{i=1}^{n} h_i \left[\dfrac{t}{t_{m_3}} \exp\left(1 - \dfrac{t}{t_{m_3}}\right) \right]^{d_i}, & t_{\mathrm{m}3} \le t < \infty .
\end{cases} \tag{2}
$$

The expression for single time interval is denoted as MP-AEF term $y_{term}(t)$, and is written also as:

$$
\begin{aligned}
y_{term}(t) &= C_1 + (C_2 - C_1)\left[\frac{t - t_b}{t_e - t_b} \exp\left(1 - \frac{t - t_b}{t_e - t_b}\right) \right]^a = C_1 + (C_2 - C_1) \times \\
&\times \left[\left(\frac{1}{t_e - t_b} t - \frac{t_b}{t_e - t_b} \right) \exp\left(-\frac{t}{t_e - t_b} + \frac{t_e}{t_e - t_b} \right) \right]^a = C_1 + (C_2 - C_1)\left[(D_1 t + D_2) \exp(1 - D_1 t - D_2) \right]^a
\end{aligned} \tag{3}
$$

for C_1 equal to the value of $y(t_b) = y(t_{mr})$ at the beginning, and C_2 equal to $y(t_e) = y(t_{mr+1})$ at the end of using approximation term in *r*-th interval $D_1 = (t_e - t_b)^{-1}$, $D_2 = -t_b (t_e - t_b)^{-1} = -t_b D_1$.

Single-wave of the cosine function $cos(2\pi t / T)$, for $T = 1s$, is approximated by the four terms of MP-AEF given by Eq. (3) with satisfying accuracy of the approximation, presented in Fig.1, and given by:

$$
y_{\cos}(t) = \begin{cases}
1 - 2\left[(2t)\exp(1 - 2t)\right]^a, & 0 \le t < 0.25, \\
-1 + 2\left[(2t - 1)\exp(2 - 2t)\right]^a, & 0.25 \le t < 0.5, \\
1 - 2\left[(2t - 2)\exp(3 - 2t)\right]^a, & 0.5 \le t < 0.75, \\
-1 + 2\left[(2t - 3)\exp(4 - 2t)\right]^a, & 0.75 \le t < 1 .
\end{cases} \tag{4}
$$

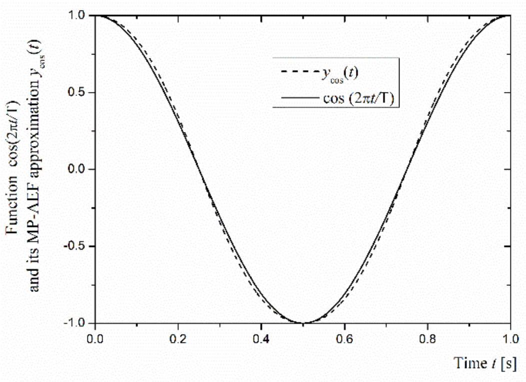

Figure 1. Single-wave cosine function (full line) $\cos(2\pi t/T)$ and its MP-AEF approximation (dash-lines).

Parameter a is calculated so that $y_{cos}(t_2)=0$ at $t_2=0.25$ and $y_{cos}(t_4)=0$ at $t_4=0.75$.

$$a=\frac{\ln(0.5)}{\ln[0.5\exp(0.5)]}\cong 3.5887 \quad . \qquad (5)$$

At $t_3=T/2=0.5s$ the function has its minimum $y_{\cos}(t_3)=-1$, whereas at the beginning, at $t_1=0$, the function has its maximum $y_{\cos}(t_1)=1$. At the end of approximation interval, at $t_5=T$, the function is at its maximum.

Exponential function is represented by AEF terms Eq. (3), for $a=1$, after using:

$$\begin{aligned}&\exp(-Dt)=(Dt+1-Dt)\exp(-Dt)=\\&=(Dt+1)\exp(-Dt)-Dt\exp(-1)\exp(1-Dt)\end{aligned}\ , \quad (6)$$

so that the double-exponential (DEXP) function is represented without error as:

$$\begin{aligned}&\exp(-\alpha t)-\exp(-\beta t)=\\&=(\alpha t+1)\exp(-\alpha t)-\alpha t\exp(-1)\exp(1-\alpha t)-\\&-(\beta t+1)\exp(-\beta t)+\beta t\exp(-1)\exp(1-\beta t)\end{aligned} \quad (7)$$

The DEXP function for approximating pulse voltage functions is given by:

$$u(t)=U_m\left(e^{-\alpha t}-e^{-\beta t}\right)=\frac{U}{\eta}\left(e^{-\alpha t}-e^{-\beta t}\right)\ , \quad (8)$$

for U the voltage value that divided by the peak correction factor η results in the maximum voltage U_m, whereas α and β are the parameters of the DEXP function. The peak correction factor is the function of α and β:

$$\eta=e^{-\alpha t_m}-e^{-\beta t_m}\ , \qquad (9)$$

for t_m the time of the maximum value U_m and:

$$t_m=\frac{1}{\beta-\alpha}\ln\frac{\beta}{\alpha}\ . \qquad (10)$$

TABLE I. DEXP PARAMETERS [3].

T_1/T_2 [$\mu s/\mu s$]	Parameters		
	η	α (s^{-1})	β (s^{-1})
1.2/50	0.95847	14732.18	2080312.7
10/350	0.9511	2121.76	245303.6
10/700	0.97423	1028.39	257923.7
10/1000	0.98135	712.41	262026.6
250/2500	0.9055184	316.9572	16003.33

The IEC 60060-1 standard voltage waveform 1.2/50 $\mu s/\mu s$ (Table I) can be also approximated by the two MP-AEF terms:

$$y_{1.2/50}(t)=\begin{cases}\left[\dfrac{t}{t_m}\exp\left(1-\dfrac{t}{t_m}\right)\right]^a, & 0\le t<t_m,\\[2ex] \left[\dfrac{t}{t_m}\exp\left(1-\dfrac{t}{t_m}\right)\right]^b, & t_m\le t\end{cases} \ ,(11)$$

for the maximum value at $t_m=1.9\mu s$, parameters $a=4$ and $b=0.03126$. Other ESD waveshapes (Table I) and experimentally measured currents can also be approximated by MP-AEF, and the procedure to obtain the parameters is given in [5]. FT of each term Eq. (2) is obtained analytically from the definition of this integral transformation, so that the following equation is used $(C_1\neq 0)$:

$$\begin{aligned}&Y(p)=\frac{C_1}{p}+\left(C_2-C_1\right)\times\\&\times\frac{\exp\left(a+D_2p/D_1\right)}{D_1\left(a+p/D_1\right)^{a+1}}\gamma\left[a+1,z_1,z_2\right]\end{aligned}\ . \quad (12)$$

for the arguments $a+1, z_1 = (D_1 t_1 + D_2)(a + p/D_1)$, and $z_2 = (D_1 t_2 + D_2)(a + p/D_1)$ of the Gamma function, defined by:

$$\gamma[a+1, z_1, z_2] = \int_{z_1}^{z_2} t^a \exp(-t)\, dt \quad . \qquad (13)$$

Results for PWFT amplitudes versus frequency, for one-wave, two-, three-, four- and five-waves cosine functions, are given in Figs. 2-6.

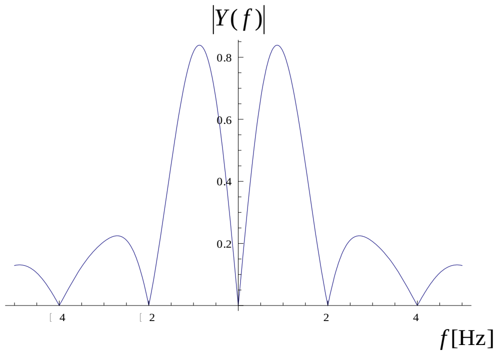

Figure 2. PWFT modulus of one-wave cosine function.

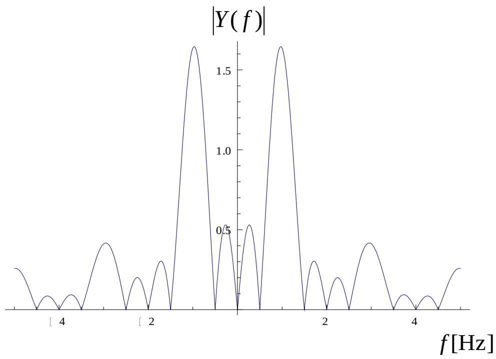

Figure 3. PWFT modulus of two-waves cosine function.

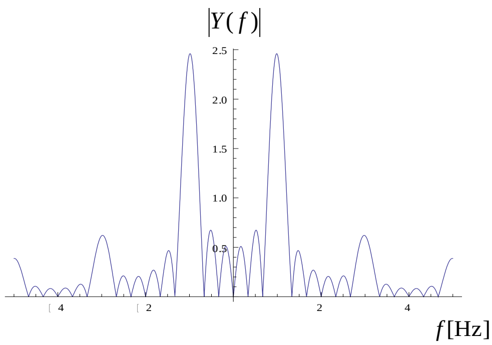

Figure 4. PWFT modulus of three-waves cosine function.

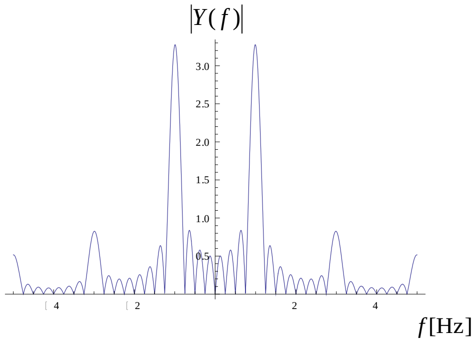

Figure 5. PWFT modulus of four-waves cosine function.

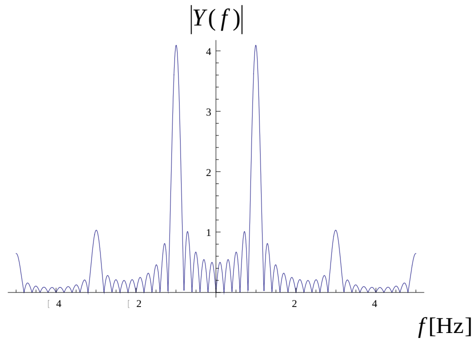

Figure 6. PWFT modulus of five-waves cosine function.

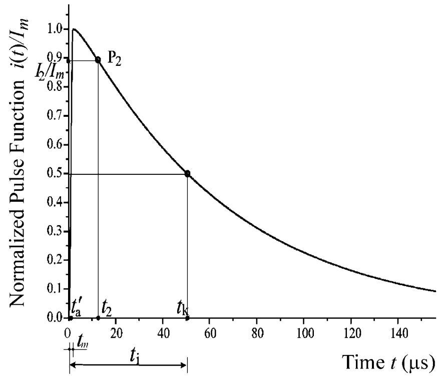

Figure 7. IEC 60060-1 standard function 1.2/50 µs/µs approximated by 1P-AEF(1,1).

Modulus $|Y(f)|$ of the Fourier transform versus frequency for the pulse function 1.2/50 $\mu s/\mu s$ (given in Fig. 7) is given in Fig. 8. It can be noticed that above frequency $f_2 = 0.2 MHz$, the modulus decreased below 1% of the value at low frequencies. IEC 6100-4-2 standard ESD current is represented by 3P-AEFs (with 10 coefficients) and by the sum of the three 1P-AEFs (with 6 coefficients) in Fig. 9. Its FT is given in Fig. 10.

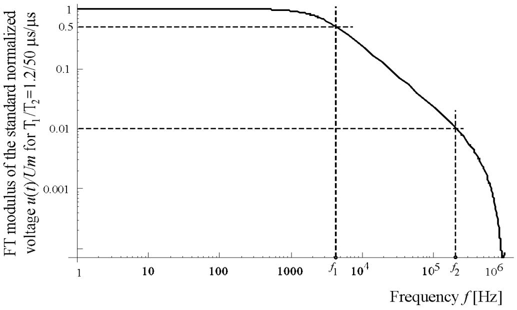

Figure 8. FT modulus of the standard voltage 1.2/50μs/μs versus frequency *f* [Hz].

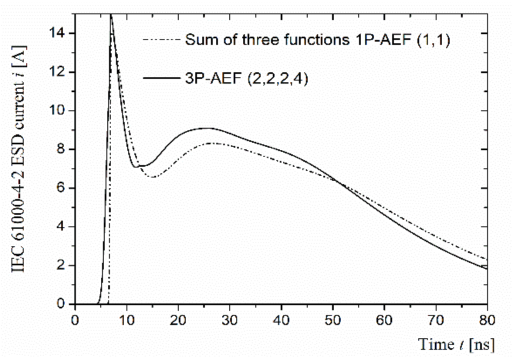

Figure 9. IEC 61000-4-2 standard function approximated by the sum of three 1P-AEF(1,1) and by 3P-AEF(2,2,2,4).

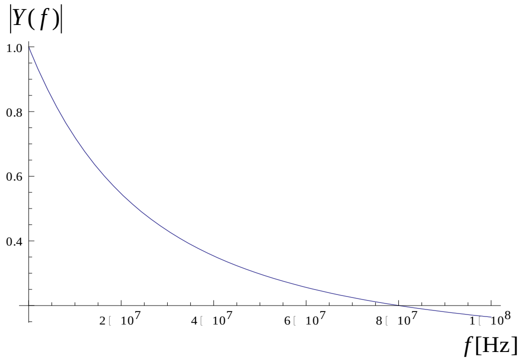

Figure 10. FT modulus of the IEC 61000-4-2 standard function approximated by 3P-AEF(2,2,2,4).

III. Conclusion

Classical Fourier transform gives better results if applied to periodic waveshapes, whereas Piece-wise Fourier transform is suitable for aperiodic pulse waveshapes with sharp peaks. Electrostatic discharge currents are functions with many peaks in the measured waveforms. The terms of MP-AEF are used in this paper to approximate pulse functions in time domain, and afterwards, the PWFT is applied. In this paper the procedure is used for single- and multiple-wave cosine function, for the IEC 60060-1 standard voltage 1.2/50 $\mu s/\mu s$, and for IEC 61000-4-2 standard ESD current. This enables the analysis of the energy spectrum of pulse signals, estimation of their effects on circuits and systems, as well as choice of measurement equipment.

Acknowledgment

The paper is a part of the research done within the project no. 451-03-68/2022-14 of the Faculty of Electronic Engineering in Niš, supported by the Ministry of Education, Science and Technological Development of the Republic of Serbia.

References

[1] Schon, K. (2013). *High impulse voltage and current measurement techniques*. Berlin: Springer. Chapter 2.

[2] Schon, K. (2013). *High impulse voltage and current measurement techniques*. Berlin: Springer, Chapter 8.

[3] Kaiser, K. L. (2004). *Electromagnetic compatibility handbook*. CRC press. Chapter 12.

[4] Javor, V. (2012, September). Multi-peaked functions for representation of lightning channel-base currents. In *2012 International Conference on Lightning Protection (ICLP)* (pp. 1-4). IEEE.

[5] Lundengård, K., Rančić, M., JavorR, V., & Silvestrov, S. (2017, August). Electrostatic discharge currents representation using the Multi-peaked analytically extended function by interpolation on a D-optimal design. In *2017 IEEE International Symposium on Electromagnetic Compatibility & Signal/Power Integrity (EMCSI)* (pp. 25-30). IEEE.

[6] Javor, V. (2022, March). Piece-Wise Fourier Transform of Aperiodic Functions. In *2022 21st International Symposium Infoteh-Jahorina (INFOTEH)* (pp. 1-4). IEEE.

[7] Techniques—Part, H. V. T. (2010). 1: General definitions and test requirements. *IEC Standard*, 60060-1.

[8] EMC – Part 4-2: Testing and Measurement Techniques – Electrostatic Discharge Immunity Test. *IEC Int. Standard*, 61000-4-2, Ed. 2, 2008-2012.

[9] Javor, V., Lundengård, K., Rančić, M., & Silvestrov, S. (2019, October). A study on frequency spectrum of electrostatic discharge currents and lightning currents. In *2019 14th International Conference on Advanced Technologies, Systems and Services in Telecommunications (TELSIKS)* (pp. 198-201). IEEE.

[10] Fotis, G. P., Asimakopoulou, F. E., Gonos, I. F., & Stathopulos, I. A. (2006). Applying genetic algorithms for the determination of the parameters of the electrostatic discharge current equation. *Measurement Science and Technology*, *17*(10), 2819.

[11] Abdel-Salam, M. (2018). *High-voltage engineering: theory and practice, revised and expanded*. CRC Press.

[12] Kuffel, J., & Kuffel, E. (2000). *High voltage engineering fundamentals*. Elsevier.

eNergetics 2022

Silicon Carbide-based Power Electronics as an Enabler for 100% Green Energy Transition

Prahaladh Paniyil[1], Vishwas Powar[1], Naireeta Deb[1], Rajendra Singh[1,2]

[1]Holcombe Dept of Electrical and Computer Engineering, Clemson, USA 29634
[2]Dept. of Automotive Engineering, Clemson, 29607 USA

Abstract—**The necessity of implementing an end-to-end DC power network with green and renewable energy sources like PV and wind energy with battery systems to solve the climate emergency has been illustrated in [1]. In such a network, Silicon Carbide (SiC)-based power electronics can become the key enabler in the three major DC power stages of (a) generation (PV/wind and battery) to transmission (HVDC), (b) distribution (EV DC fast charging), and (c) utilization (EV powertrain). This paper emphasizes the role of SiC-based power electronics in each of these three stages. Also, negative prices for electricity in the grid are the most recent challenge faced by power networks with major renewable energy penetration. This paper investigates submarine power transmission to export electricity across borders as a possible solution to reduce the impact of negative pricing scenarios in the grid. In this regard, the power and cost advantages of SiC-based power converters in HVDC transmission to enable submarine power transmission are discussed.**

Keywords - photovoltaics, batteries, local DC power, transportation, access to all

I. INTRODUCTION

The adverse effects of Climate Change have become more and more evident in recent times. The increase in the frequency and intensity of natural disasters like droughts, wildfires, hurricanes, flooding, etc. is an indicator of the effects of climate change. The world can no longer ignore climate change as a global crisis. CO_2 emissions have been on an all-time high in 2021 as seen in Fig.1 [2]. There is an immediate need to reduce global carbon emissions. Fig.2 [3] showcases the global greenhouse emissions classified into sectors. It can be seen that the Energy sector is the highest contributor to greenhouse emissions. Therefore, concrete steps must be taken to reduce the greenhouse emission rate from this sector.

There has been tremendous growth in the implementation of solar and wind power globally in the past decade. In 2021, solar saw an increase of 23% and wind saw an increase of 14% globally [4]. However, inspite of this increase in renewable power like solar and wind, power generated from coal has also seen an increase in the last two yeas. This is attributed mainky to the increase in global energy demand in the post-pandemic era as well as the reliance on natural gas generated power. Due to the current political situations in Ukraine, the countries relying on Russian natural gas have been forced to refire their coal plants to compebsate for Russian gas. This has caused the recent increase in the global greenhouse emissions. Therefore, in addition to increasing the implementation of renewable energy, the most efficient utilization must also be taken into consideration. The effieicnt utilization of wind and solar combined with battery systems for storage will enable us to not rely on natural

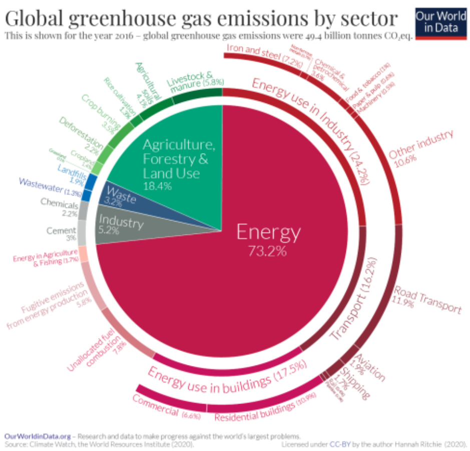

Figure 1. Greenhouse gas emissions by sector [3].

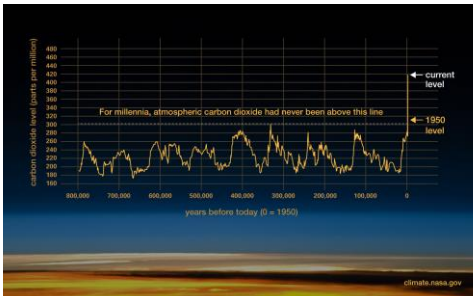

Figure 2. The relentless rise of carbon dioxide (NASA) [2].

gas power plants even for peak load demands. This article focuses on the significance of end-to-end DC power networks in the implementation and utilization of renewable energy. It identifies the role of SiC-based power electronics in enabling such an end-to-end DC power network. The argument for an SiC power electronics enabled end-to-end DC power network is reinforced by illustrating it as a solution for the upcoming negative oricing challenge faced by the grid due to increased penetration of renewable energy into the grid.

II. SIGNIFICANCE OF END-TO-END DC POWER NETWORK

Solare energy converted to electric power by Photocvoltaics (PV) systems in DC form undergoes losses when converted to AC power for penetration into the grid. Although wind energy systems generate AC power, they can be converted to DC power for signal conditioning. And reducing the intermittent nature of wind energy generation. The viability of lithium-ion battery systems as the most viable storage system for PV and wind power is discussed in [5]. Li-ion battery storage systems also store electrical energy in DC form. Thus, the generation and storage of clean energy from these rebnewable sources exclusively deals with DC power. If the power network is implemented at a local level as a micro/nano-grid, the only requirement for AC power will be at load-level for existing loads catered towards the existing AC system. Thus, a novel local power network involving novel and smart DC loads like Data centers, EV charging systems, DC-powered residential and commercial buildings, etc. can be implemented utilizing DC power only. The conceptual design of such a power network is shown in Fig.3 [5]. Such a local interconnected network does not involve any transmission system and hence is limited to the maximum allowalble range through MVDC power distribution between the micro/nano-grids and loads.

The upper hand for the AC power network has always been in the ability to transmit electrical power over long distances with reduced losses i^2R losses. This is enabled by the transformer's capability to seamlessly step-up/step-down voltage levels. The high voltage levels (in the order of hundreds of kVs) reduces the current (I) in the transmission system leading to minimal transmission losses attributed by the resistance

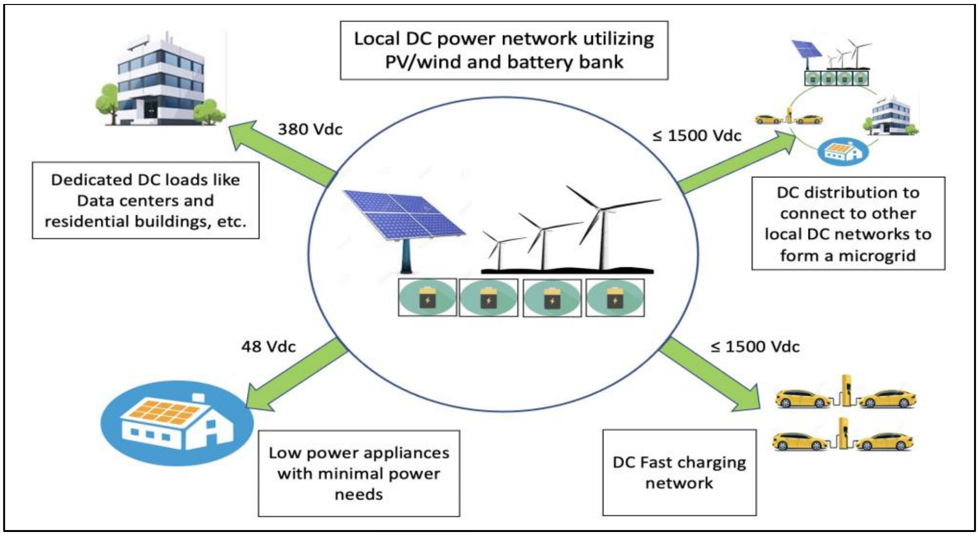

Figure 3. Local interconnected DC power network with different types of loads [5].

of the cables. Thus, the existing AC power infrastructure is the result of this advantage of AC systems over the DC system's inability to step-up/step-down voltage levels. The AC power infrastructure has a robust and reliable power transmission system in place for the several decades. However, recently, there has been an increase in the adoption of high voltage DC (HVDC) transmission for long-distance as well as submarine transmission of power [6]. The conversion mechanicsm from an HVAC voltage level to an HVDC voltage level has enabled an HVDC transmission system which is more effiecient than its AC counterpart. However, there is a significant investment as well as a large footprint in the HVAC-to-HVDC converter stations. Thus, such HVDC systems are only employed in very long haul transmission systems where the feasibility of such an expensive HVDC can be justified. HVDC systems do not require repeater systems like their HVAC counterparts and hence, no additional costs are added with increasing distance in an HVDC system as compared to an HVAC system. The HVDC transmission systems have a break-even distance after which they become feasible because the converter station's cost per mile keeps linearly decreasing with increasing distance. However, in our end-to-end DC power network, the generation, storage, and utilization (load-level DC-to-AC conversion for AC loads) are all in DC form. Thus, if HVDC transmission can be enabled for our system without the need for HVAC-to-HVDC conversion, the cost and footprint of the converter station can be replaced with the cost for DC-to-DC conversions. Thus, a feasible end-to-end long-distance DC power network as shown in Fig.4 [5] can be realized by leveraging the efficient HVDC transmission system. Fig.4 [5] also showcases the implementation of novel high power DC loads by leveraging the HVDC levels. The increased power level can be utilized to implement these high power loads at the MVDC distribution level. However, in order to implement such an end-to-end DC power network as shown in Fig.4 [5], there is need for DC-to-DC converters at various levels of implementation.

III. ROLE OF SIC-BASED POWER ELECTRONICS IN DC POWER NETWORK

Owing to the demand from the EV and power sector, there has been immense growth in the demand for WBG power electronics. The superior physical characteristics of WBG devices and modules over their Silicon counterparts have enabled the reductions in system cost, energy consumption, as well as weight and size. These paramters are the driving force in the growth of wide badgap (WBG) power electronics in a

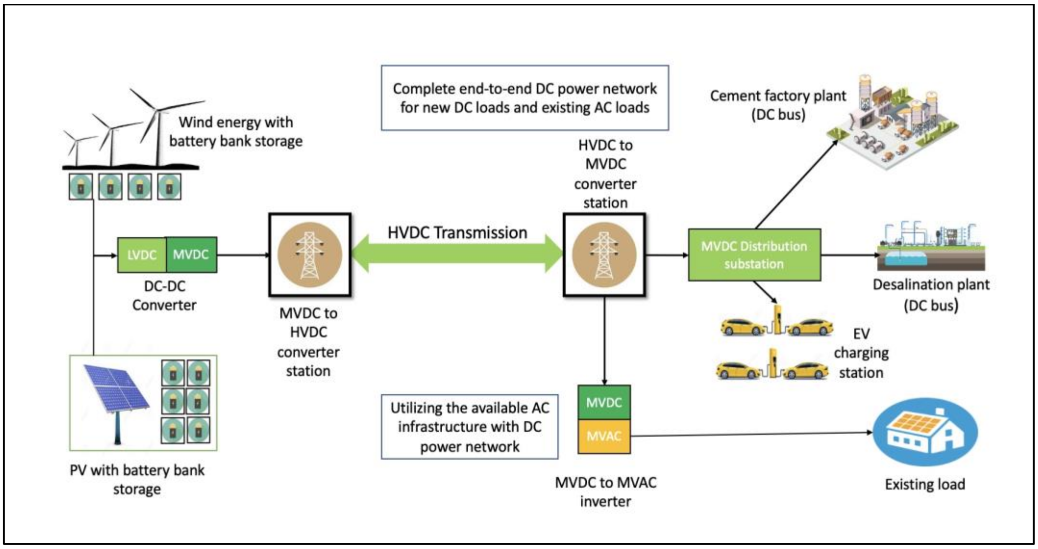

Figure 4. Proposed end-to-end DC power netowork including HVDC transmsission systems [5].

power system as shown in Fig.5. Similar operational characteristics will be required in our proposed end-to-end DC power network for the implementation of DC-DC converters with a high voltage ratio in a cost-effective and footprint effective manner. The paarmeters required for such converters would be a high breakdown field and high thermal conductivity. The high breakdown field would enable devices to operate at higher voltage levels requiring fewer devices to achieve the same level of voltage conversions. The higher thermal conductivity would be effective in reducing the requirement of cooling mechanisms and thus, lowering the total footprint of the converter systems. In this regrad, SiC power electronics would be the ideal choice in our systems. Even though SiC devices have a lower breakdown field compared to Gallium nitride (GaN) devices, their superior thermal conductivity makes them extremely attractive for high power converters. The only factor where Si devices have a major advantage over SiC devices is the device-level cost. However, with the adoption of mature manufacturing techniques as well as a reduction in the defect density, the forecast for SiC devices is looking positive on this end as well as shown in Fig.6 [7]. The role of SiC devices in converter implementation in the proposed power network can be divided into the following subsections:

a) Generation and Transmission stage
b) Distribution stage
c) Utilization stage

A. Generation and Transmission stage:

The generation and transmission have been comibined into a single stage of implementation as the generation and storage system consisting of PV, wind energy, and Li-ion battery storage do not require significant voltage ratios. The conversion from LVDC to MVDC stages can be implemented using Si IGBTs due to the maturity of this technology as well as the lower cost benefits. However, in the transmission stage, conversion ratios ranging from LVDC to MVDC, MVDC to HVDC, or even LVDC to HVDC may be required. In this space, the SiC devices can enable immense benefits in terms of system costs and footprints. An SiC-based converter concept is shown in [5]. An HVDC transmission system deployed with the utilization of this concept as a module in the system is shown in Fig.7 [8]. This system also showcases the reduction in modules/ components due to the implementation of the SiC-based DC-DC converter module. The reduction in component/module count is facilitated by the elimination of AC filtering passive components, reduction in the transformer form factor (linear vs high-frequency transformer), as well as the reduction in active cooling mechanisms due to lower conversion losses and superior thermal characteristics for SiC devices. Thus, the over system complexity is greatly reduced.

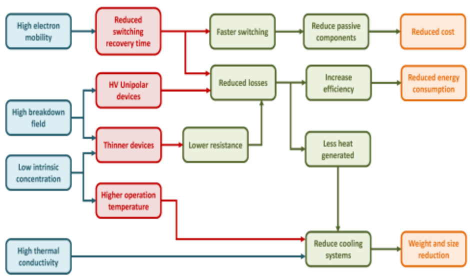

Figure 5. Impact of WBG power electronics in a power system.

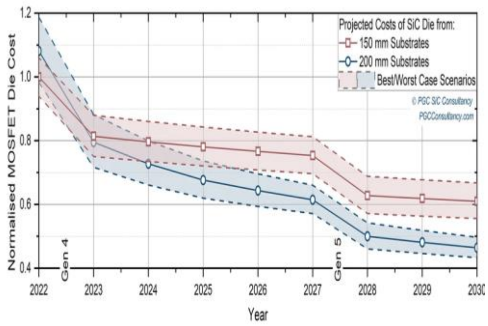

Figure 6. Projected normalized die cost for state-of-the-art 2021 1200V/100A SiC MOSFET (PGC Consukltancy) [7].

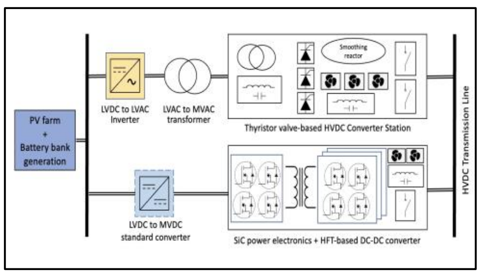

Figure 7. Proposed vs Current Practice for HVDC transmission systems in generation to transmission in a power network [8].

Some device-level considerations which enable the SiC converter in the system are as follows:

1. Superior thermal characteristics of SiC devices
2. Higher operating voltage and switching frequency than Si IGBTs.
3. Lower ON resistance and lower switching losses than Si IGBTs.

Some system level considerations for the converter are as follows:

1. The converter is a bidirectional soft switching resonant modular converter.
2. The modularity of the converter enables maximum scalability and reducing system complexity.
3. The modularirty also increases the flexibility of implementation for the system.

In addition to the considerations there a few challenges associated with device and system level isolation and protection, device level gate control techniques, and trade-offs between insulation and thermal management for the high frequency transformer.

B. Distribution Stage

The distribution stage in the power network can be effectively illustrated by considering the emaple of EV charging mechanisms. With the increasing adoption of EV systems in recent times, there will be a proportional increase in the electricity demand from the charging requirements for EVs. The grid is already saturated with the current load demand and is not equipped to handle this substantial increase from the EV charging sector. Thus, our proposed end-to-end DC network can efficiently implement DC-to-DC charging by utilizing the generated and stored DC power. However, there are significant challenges in deploying a EV charging infrastructure at the MVDC distribution stage as shown in Fig.4 [5]. The charging infrastructure will be limited by the radial distance dictated by the i^2R losses for the implemented power cables. The system size and complexity will be a key factor in EV charging platforms due to the space limitations in residential/commercial areas. The DC fast charging mechanisms will also require appropriate cooling mechanisms for the generated heat during fast charging. The charging power requirement is currently in the

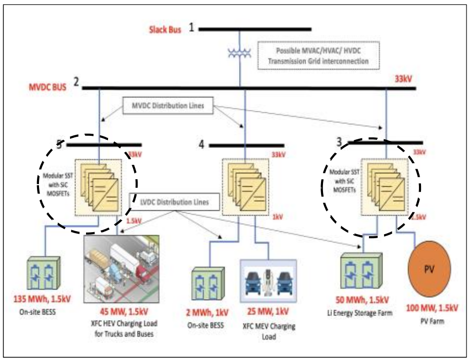

Figure 8. DC distribution network for EV fast charging with PV farm and co-located battery storage [8].

range of 250-300kW for DCFC. However, with the advent of electric semis and trucks, this DCFC power requirement is alos going to increase to the range of 500kW-1MW. Therefore there is an attractive opportunity for the modular SiC based converter in this MVDC distribution stage as well. This is illustrated in Fig.8 [8]. The HVDC transmission is not included in this sub-section as it deals with only the distribution-level implementation. Thus, the PV farm and battery bank are co-located to facilitate the MVDC distribution bus.

An analysis was conducted on the operating characteristics of SiC vs Si devices in the DCFC systems. Clear advantages can be seen in the SiC device-level implementation in regard to temperature, power, themal loss, and energy efficiency. These results are summarized in Fig.9 [9]. The percentage capacity for an SiC device is higher in both extremes of the operating temperature range. The charging time is an indication of the time taken to charge an EV with respect to increasing power levels of charging. The SiC device-based system shows reduced charging times with increasing power level. As already discussed, the SiC devices have superior thermal characteristics compared to their Si counterpart. This is illustrated in Fig.9(c). Lastly, the energy efficiency for an SiC device-based system is also superior compared to the Si device-based system with increasing power levels. Thus, the SiC devices have the necessary charcteristics to support the increasing overall charging demand as well as the increased rate of charging (power level) with the oncoming electric semis and trucks.

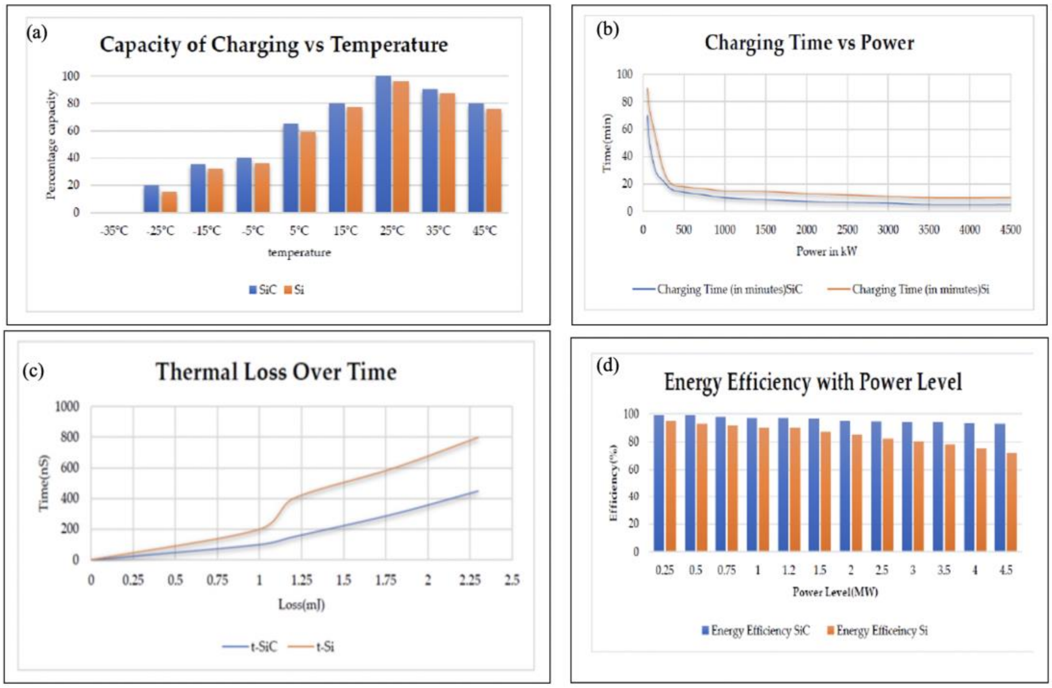

Figure 9. Si vs SiC operating characteristicsin DCFC: (a) Temperature (b) Power (c) Thermal loss (d) Energy efficiency [9].

C. *Utilization Stage*

As seen in the previous subsection, the advent of electric semis and trucks will also harbor the need for a higher voltage powertrain. Major EV companies like Tesla have indicated the adoption of a 1000V powertrain [10]. Other companies are also experiencing the shift from a 400V powertrain to 800V/900V. The advatages of SiC devices in current handling capability as well as power transmitted to the powertrain is illustrated in Fig.10 [10]. Thus, the superior characteristics of SiC devices make them the most efficient and cost-effective choice in our system for all three stages of transmission, distribution, and utilization in an end-to-end DC power network (Table 1).

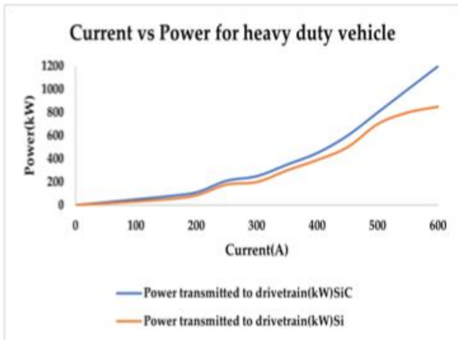

Figure 10. Power delivered to the output for heavy-duty vehicles with higher power rated components vs the current transmitted in the powertrain [10].

IV. NEGATIVE PRICING IN THE GRID: CHALLENGE AND MITIGATION

As mentioned before in this article, there has been tremendous increase in the implementation of PV and wind energy-based power systems in recent times. However, their penetrations in the grid have given rise to some challenges. In this article, we would like to focus on the novel emerging challenge of negative pricing in the in

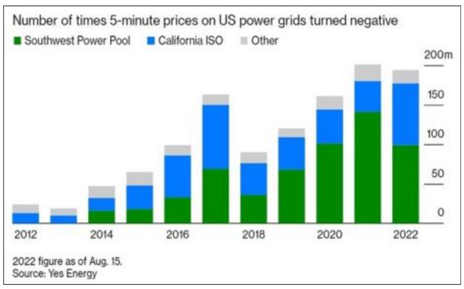

Figure 11. Increasing frequency of neagtive pricing scenarios in major US grid networks [11].

TABLE I. COMPARISON OF EXTREMELY FAST CHARGING (XFC) WITH EXSITING CHARGING TECHNIQUES [9]

Unit of measure	**Charging techniques**				
	Level 1 (110V, 1.4 kW)	***Level 2 (220V, 7.2 kW)***	***DC Fast Charger (480V, 50kW)***	***Tesla SuperCharger (480V, 140 kW)***	***XFC (800+V, 400 kW)***
Range per minute of charge (miles)	0.0082	0.42	2.92	8.17	23.3
Time to charge for 200 miles (minutes)	2.143	417	60	21	7.5

the wholesale market for the electricity grid in numerous locations [11].

The increased supply from the renewable energy sources like solar and wind has led to the situation of more supply than demand in the grid. In such a scenario, the wholesale electricity prices can go negative leading to the negative pricing challenge. As the current electricity grid is heavily congested, the excess upply from renewable energy sources are trapped in the distribution grids. An argument can be made that the non-renewable energy sources can be curbed to utilize only the renewable energy generated power in this scenario to gain maximum advantage of these clean resources. However, major non-renewable energy sources such as coal, natural gas, and even nuclear energy systems are inertial systems and it would be a greater cost to the grid to restart these inertial systems after they are curbed than to keep them running. Renewable energy sources like PV and wind energy based systems are not inertial and hence can be easily curbed and restarted. Thus, in order to reduce the negative pricing scenarios, the renewable energy sources are curbed at peak generation. There is immense wastage of clean power due to the lack of infrastructure to support them. Also, this excess supply can be utilized in regions with power deficit if the appropriate infrastructure can deliver the excess power to the regions with deficits. Fig.11 [11] illustrates the increasing frequency of negative pricing scenarios in major US electricity grids.

The mitigation strategies for these scenarios must be cenetered around transmission of excess supply instead of curbing peak power generating sources. Such a mitigation strategy must also ensure the transmission of excess power across national boundaries. The proposed SiC converter-based HVDC transmission network can provide a low-cost and efficient solution to the negative pricing challenge. A proposed concept of an end-to-end DC power network with mitigation of negative pricing scenarios through transmission of excess PV/wind supply is illustrated in Fig.12.

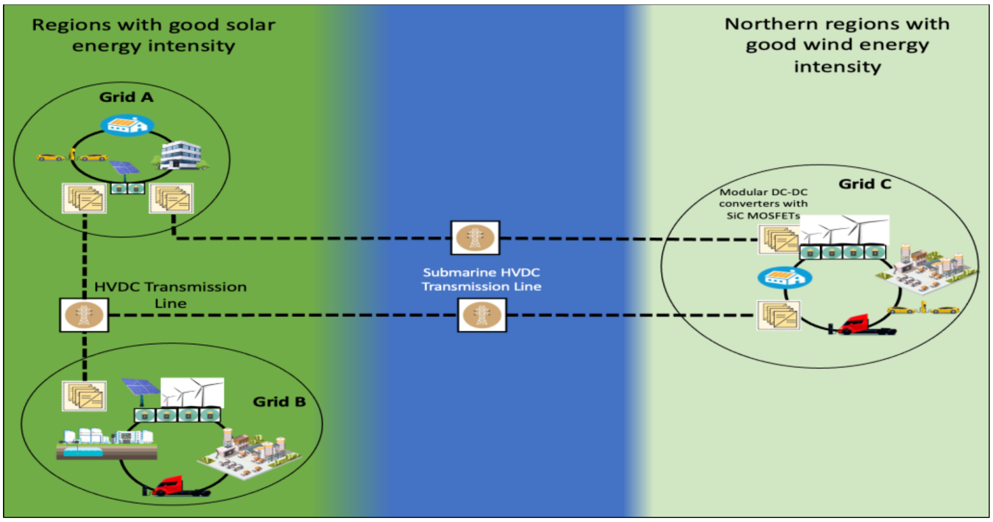

Figure 12. Interconnected end-to-end DC power network enabled by SiC-based modular converter.

V. CONCLUSION

SiC-based power electronics has the potential to be an enabler for a cost-effective and energy-efficient transition to renewable energy across the globe. The role of SiC power electronics is of utmost significance in the local utilization of green power, transmitting green power most efficiently from generation to utilization, extreme fast charging infrastructure, efficient powertrains of oncoming heavy duty EVs, and avoiding grid penetration challenges like negative pricing.

REFERENCES

[1] Singh, R., Paniyil, P., & Zhang, Z. (2022). Transformative role of power electronics: in solving climate emergency. *IEEE Power Electronics Magazine*, *9*(2), 39-47.

[2] NASA. *The relentless rise of carbon dioxide.* Available at: https://climate.nasa.gov/climate_resources/24/graphic-the-relentless-rise-of-carbon-dioxide/

[3] Our World in Data. *Emissions by sector*. Available at: https://ourworldindata.org/emissions-by-sector

[4] Reuters. *Global wind and solar growth on track to meet climate targets*. Available at: https://www.reuters.com/business/sustainable-business/global-wind-solar-growth-track-meet-climate-targets-2022-03-30/

[5] Paniyil, P., Singh, R., Powar, V., Deb, N., Zhang, J., Bai, K., & Dubey, A. (2021, June). Batteries and free fuel based photovoltaics and complimentary wind energy based DC power networks as 100% source of electric power around the globe. In *2021 IEEE 48th Photovoltaic Specialists Conference (PVSC)* (pp. 1821-1828). IEEE.

[6] R. Patel. *Underwater HVDC-based Grid: Pushing the Limits of Power Transmission*. Available at: https://www.allaboutcircuits.com/news/underwater-HVSC-based-grid-pushing-the-limits-of-power-transmission/

[7] P. Gammon. *Taking Stock of SiC, Part 1: a review of SiC cost competitiveness and a roadmap to lower costs*. Available at: https://www.pgcconsultancy.com/post/taking-stock-of-sic-part-1-a-review-of-sic-cost-competitiveness-and-a-roadmap-to-lower-costs

[8] Powar, V., & Singh, R. (2023). End-to-End Direct-Current-Based Extreme Fast Electric Vehicle Charging Infrastructure Using Lithium-Ion Battery Storage. *Batteries*, *9*(3), 169.

[9] Deb, N., & Singh, R. (2023). An 800V End to End SiC Powertrain to Accommodate Extremely Fast Charging. *Journal of Energy and Power Technology*, *5*(1), 1-19.

[10] InsideEVs. *Tesla launches 1000-Volt Powertrain: Semi is first but not the last.* Available at: https://insideevs.com/news/624822/tesla-1000volt-powertrain-semi-first/

[11] N. Malik. *Negative Power Prices? Blame the US Grid for stranding Renewable Energy*. Available at: https://www.bloomberg.com/news/articles/2022-08-30/trapped-renewable-energy-sends-us-power-prices-below-zero?leadSource=uverify%20wall#xj4y7vzkg

Comparative Analysis of Energy Loss and Flow Uniformity of Different Fractals

Abdulmuttalib A. Muhsen[1], Bashar Hassan Attiya[2]

[1]Faculty of Power and Aeronautical Engineering, Warsaw University of Technology, Warsaw, Poland
[1,2]Haditha Hydropower Station, Ministry of Electricity, Haditha, Iraq

Abstract—**Different types of fractal structures have been proven to improve the efficiencies of many systems, and further research is being conducted. This paper is a comparative study of three types of fractals: T-shaped, Y-shaped, and irregular fractals. The main premise of the study is CFD analysis. The analysis of all fractals will determine how much energy loss happens and how much flow uniformity is present. The branching was kept to the least possible level to clearly understand how fractals behave at more minor scales. The same constant flow conditions are applied for all the fractals, and the pressure distribution, temperature distribution, and flow uniformity are found.**

Keywords - fractal shaped structures, computational fluid dynamics, flow uniformity, energy loss

I. INTRODUCTION

Fractals have been studied profusely to replace straight and serpentine channel systems in recent years. CFD analysis of a fractal-like shell for a shell and tube heat exchanger showed that the pressure drops increased as the number of bifurcations increased, and the pressure drop increased exponentially. The area of fractal shape was kept constant. The temperature increased on the shell side when the bifurcation increased, and the increment was linear. The higher number of bifurcations decreased the coefficient of performance of the fractal-like shell. This proved that the fractal-like structures are suitable while acting as a heat sink but should not be utilized in shell tube heat exchangers as the performance declines [1-3].

CFD analysis between a straight channel and fractal-shaped structure was conducted while keeping the following parameters constant between the two configurations:

- Length of a single flow path from inlet to exit.
- The convective surface area.
- The terminal hydraulic diameter.
- The applied heat flux and the required pumping power.
- All constant and temperature-dependent properties.

After the following considerations, the pressure drop in the fractal-shaped structures was 50 percent less than the one in straight channels. However, a difference in pressure drop was observed between the 3D model and the one-dimensional model of the same fractal shaped. The pressure drops slightly when the thermos-physical properties are kept constant instead of variable. This was due to less shear stress on walls caused by less viscosity of the fluid [4].

A comparison of heat transfer and pressure drop is made between fractal branching channel nets with the traditional parallel channel network. It is found that the fractal net can increase the total heat transfer rate while it reduces the total pressure drop in the fluid. Furthermore, a larger fractal dimension or a more significant total number of branching levels is found to have a stronger heat transfer capability with a minor pumping power requirement. Thus, the fractal branching channel net enhances the efficiency of a micro heat exchanger. This was done without considering the effect of bifurcation on pressure drop and assuming a fully developed laminar flow conditions [5].

II. Comparison Between Different Fractal Systems

It is clear that when compared with straight or serpentine channels, the fractal channels are more efficient, and they cause less pressure drop and thermal resistance. But the fractals can be of many different types. This leads to the question of which fractal system is better.

A study in "Simulation of Fractal Like Branching Microchannel Network on Rectangular Heat Sink for Single Phase Flow" compared fractal-shaped and T-shaped fractals. Many different parameters affect the fractals' performance like pressure drop, temperature, and geometry of fractal channel network. The results showed that the temperatures increase due to heat transfer from the heat sink wall to the fluid. This fluid is confined near the surface of the heat sink while cold fluid moves between these branches. But the temperature distribution remained the same [4].

The study showed that the T-shape fractal heat sink has reduced pressure drop and decreased heat transfer compared to the Fractal-shape fractal. Small pressure drops and high average heat transfer coefficient in Fractal shape were better than other results. The results shows a small pressure drop compared to previous studies, with high average heat transfer coefficient. The highest value of pressure appears at the stagnation point [6].

A comparative study between single-layered, double-layered, and truncated double-layered heat sinks showed the double-layered heat sink is changed to a truncated one. It improves temperature uniformity around the inlet and requires less power. But as pressure drop increases, the double-layered heat sink performs better than the truncated double-layered heat sink. The relationship between heat and flow distribution is discussed by the authors, and it's revealed that only when heat distribution is accordant with flow distribution can the truncated double-layered (TDL) heat sink achieve the best cooling performance [7].

III. CFD Analysis and Results

The analysis of all chosen systems is performed under the same flow conditions. The fluid considered is water at 373K. Ansys Fluent commercial software was used to perform all the analyses in this study.

A. *Two-dimensional Model of Fractals*

The Y-shaped, T-shaped, and irregular fractal model is considered in its simplest form in order to correctly predict the behavior of fluid flowing them at a very smaller scale. This will help determine whether the pressure drops and energy losses at a smaller scale should be taken into account.

The Y-fractal model was considered only up to its 1st level, as shown in Fig.1. Similarly, only the 1st level was taken for T-shaped and irregular shaped fractals, as shown in Fig. 2 and Fig. 3, respectively.

B. *Pressure Distribution Comparison*

The maximum pressure was obtained at the stagnation point for fractals. In the Y-shaped fractal, the pressure distribution appears to be more uniform from inlet to outlet. See Fig. 4.

The pressure in Fig. 5 T-shaped fractal decreases rapidly after stagnation point and

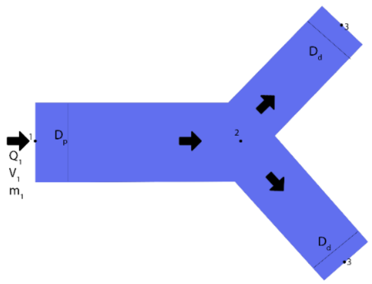

Figure 1. Y-shaped fractal.

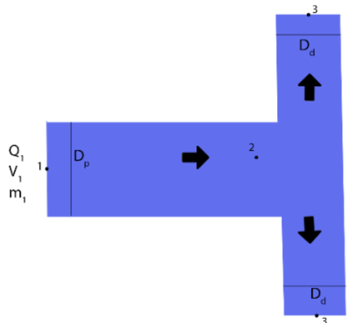

Figure 2. T-shaped fractal.

enters the sub-branch levels. This indicates that the pressure decreases more in T-shaped and irregular fractals than in Y-shaped fractals. In the case of the irregular fractal, the pressure increases when the breadth of the main branch increases, as shown in Fig. 6.

C. *Temperature Distribution Comparison*

In order to observe the temperature resistance in each fractal system, boiling water flowing at 373K is utilized. As a result, the temperature distribution in all the fractal systems appeared to be almost identical regardless of their difference in shapes. See Figs. 7-9 for contours.

The temperature distribution plots show how the temperature change remains the same in all fractals throughout the system, as shown in Figs. 10-12 and represent.

D. *Flow Distribution Comparison*

The flow distribution in the Y-shaped fractal appears to be the most consistent and becomes zero at the stagnation point in Fig. 13. There is an increase in the fluid velocity when passing through the sub-branch of the T-shaped fractal, as contours show in Fig. 14. A decrease in the velocity of the irregular fractal was observed when the breadth of the main branch increases; otherwise, the flow distribution appears to be

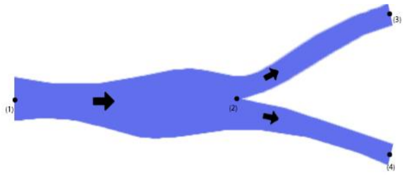

Figure 3. Irregular fractal.

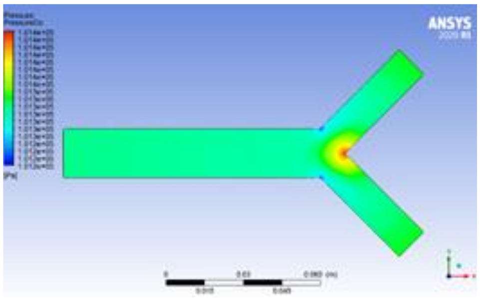

Figure 4. Y-shaped Pressure contour.

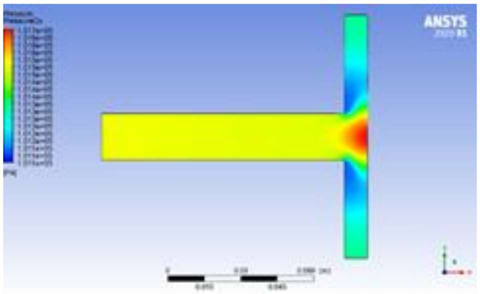

Figure 5. T-shaped (Pressure contour).

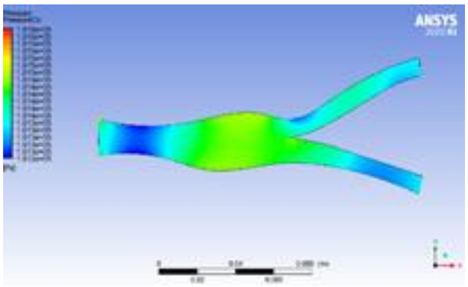

Figure 6. Irregular fractals (Pressure contour).

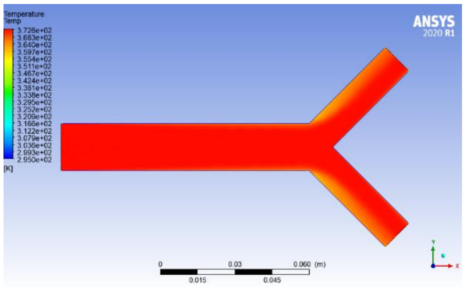

Figure 7. Y-shaped fractal (Temperature Contour).

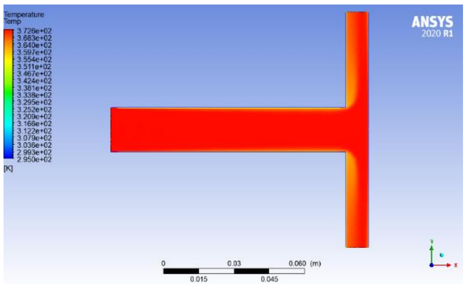

Figure 8. T-shaped fractals (Temperature Contour).

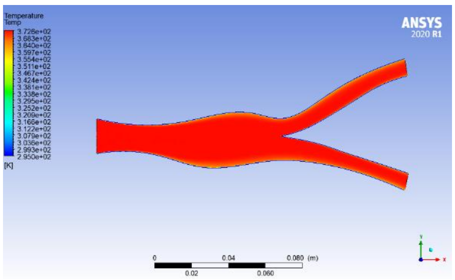

Figure 9. Irregular Fractal (Temperature Contour).

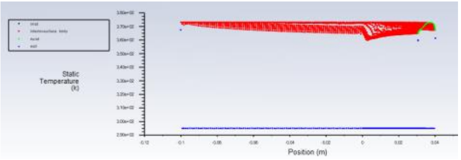

Figure 10. Y-shaped Temperature plot.

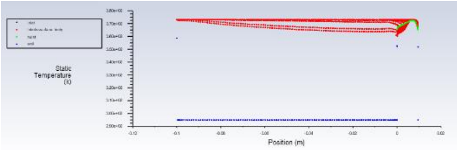

Figure 11. T-shaped Temperature plot.

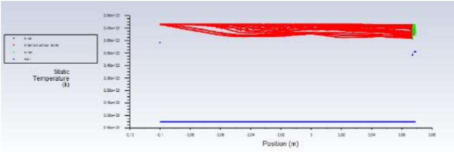

Figure 12. Irregular shaped Temperature plot.

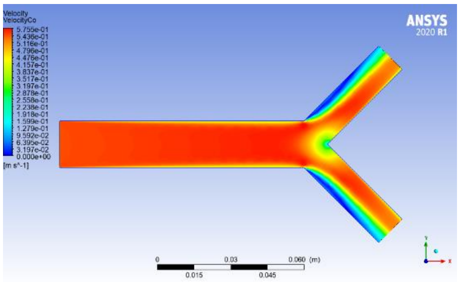

Figure 14. Y-shaped fractal (Velocity contour).

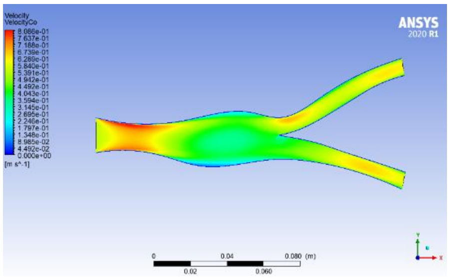

Figure 15. Irregular fractals (Velocity contour).

uniform, and the velocity appears to be lower than Y-shaped fractal but greater than T-shaped fractal throughout the simulation as shown by the velocity contours in Fig. 15.

IV. DISSCUSION

- As shown by the simulation, the pressure drop occurs in T-shaped fractal the most, then comes the irregular fractal and drops the least in the Y-shaped fractal.
- The temperature distribution results prove that the uniformity remains almost the same throughout the system regardless of the fractal design.
- The flow remains most consistent and uniform in Y-shaped fractals. The velocity becomes minimum at the stagnation point of the system. Finally, complete content and organizational editing before formatting. Please take note of the following items when proofreading spelling and grammar:

V. CONCLUSION

After analyzing the 2D models through CFD analysis, it can be stated that, for the investigated cases, the most efficient fractal system is the Y-shaped fractal as the pressure drops at its minimum, the temperature is uniform throughout, and flow uniformity is the most consistent. The Y-shaped fractal can be used in heat sinks instead of conventional channels like straight and serpentine. A 3D analysis may give us a deeper insight into what type of fractal works best in different situations, as the 2D analysis does not consider the varying fluid properties.

REFERENCES

[1] Foster, N., Sebastia-Saez, D., & Arellano-Garcia, H. (2019). Fractal branch-like fractal shell-and-tube heat exchangers: A CFD study of the shell side performance. *IFAC-PapersOnLine*, *52*(1), 100-105.

[2] Muhsen, A. A., Attiya, B. H., & Algburi, H. A. Theoretical Analysis of Different Fractal-Type Pipelines.

[3] Muhsen, A. A., & Kizilova, N. The Advanced Cooling System of Generator for Hydropower Plant. *changes*, 8, 10.

[4] Alharbi, A. Y., Pence, D. V., & Cullion, R. N. (2003). Fluid flow through microscale fractal-like branching channel networks. *J. Fluids Eng.*, *125*(6), 1051-1057.

[5] Jacobs, I. S. (1963). Fine particles, thin films and exchange anisotropy. *Magnetism*, 271-350.

[6] Manshoor, B., Sapit, A., Nordin, N., Hariri, A., Salleh, H., Razali, M. A., ... & Alsayed, M. K. (2020). Simulation of fractal like branching microchannel network on rectangular heat sink for single phase flow. *CFD Letters*, *12*(2), 69-79.

[7] Yan, Y., Yan, H., Feng, S., & Li, L. (2019). Thermal-hydraulic performances and synergy effect between heat and flow distribution in a truncated doubled-layered heat sink with Y-shaped fractal network. *International Journal of Heat and Mass Transfer*, *142*, 118337.

Thermoelectric Properties of Binary Lithium-Based Compounds Li_3Pn (Pn= Sb, Bi)

Fakhereddine Khemloul[1], Mohamed Halit[2], Abdennour Benmakhlouf[3], Said Maabed[4], Mohamed Bouchenafa[5], Naceur Selmane[6]

[1,2,3,4,5]Laboratoire pour Application et Valorisation des Energies Renouvelables (LMAVER), Laghouat, Algeria
[6]Laboratoire Matériaux, Systèmes Énergétiques, Énergies Renouvelables et Gestion de l'Énergie (LMSEERGE) Boulevard des Martyrs, Laghouat, Algeria

Abstract—**By performing first-principles DFT calculations combined with the Boltzmann transport equation, we investigated the electronic structures and thermoelectric properties of the binary lithium-based compounds Li_3Pn $\left(Pn = Sn, Bi\right)$. The computed electronic band structure indicates narrow and indirect band-gap features of the studied compounds. Within the semi-classical Boltzmann transport approach and the relaxation time approximation, transport properties of Li_3Sb and Li_3Bi compounds at different temperatures were estimated. The optimal values of the Seebeck coefficient are 2.09 mV/K for Li_3Sb and 1.65 mV/K for Li_3Bi, respectively, which are comparable to those of many promising thermoelectric materials. As a consequence, a maximum ZT value of 0.99/1.00 can be realized for Li_3Sb / Li_3Bi at room temperature. These findings suggest that the binary lithium-based compounds Li_3Sb and Li_3Bi are promising candidates for thermoelectric materials at room temperature.**

Keywords - thermoelectric parameters, lithium-based pnictides, first-principles calculation, Boltzmann transport theory

I. INTRODUCTION

Thermoelectric materials have received renewed attention in recent years due to their vast applicability in the field of device and high temperature components.

The binary lithium-based compounds Li_3Pn ($Pn = Sn, Bi$) have been known for their potential applications as electronic and optoelectronic devices [1-3]. However, to date, the study on lithium-based compounds for thermoelectric application is scarce. Therefore, we take the lithium-based semiconductor materials Li_3Sb and Li_3Bi as an example to systematically investigate the electronic structures and thermoelectric properties.

In this paper, we aim to present a theoretical insight into the structural, electronic, charge transport and thermoelectric properties of the binary lithium-based compounds Li_3Pn ($Pn = Sn, Bi$).

The paper is divided as follows. We briefly introduce the Computational Method in Sec. II. The results on our calculations are presented in Sec. III. In Sec. IV is a conclusion of our work.

II. COMPUTATIONAL METHOD

The structural, electronic and thermoelectric properties of the synthesized Li_3Sb and Li_3Bi crystals in the ground state were investigated by the Wien2k code [4] based on the density functional theory. The basis functions are expanded up to $R_{MT}K_{max} = 8.5$, and up to $l_{max} = 10$ in the expansion of the non-spherical charge and potential. The values of muffin-tin radii R_{MT} for the Li , Sb , and Bi atoms are chosen to be 1.8, 2.3, and 2.3 a.u, respectively. For the exchange and correlation interactions we used the standard Perdew, Burk and Ernzerhof functional for the generalized gradient approximations [5] and the modifed Becke and

Johnson potential [6]. For the integration we used 20 × 20 × 20 Monkhorst-Pack [7] *k*-points mesh in the first Brillouin zone.

Investigation of thermoelectric efficiency of both compounds was performed by using BoltzTraP code [8].

III. RESULTS AND DISCUSSION

A. *Structural Properties*

Fig. 1 gives the crystal structure of Li_3Sb and Li_3Bi unit cell. They have a face-centered cubic structure with the $Fm\bar{3}m$ (*No.225*) space group and twelve (12) atoms in the conventional cell. The four-equivalent antimony (bismuth) atoms occupy *4a* (0, 0, 0) Wyckoff position, four lithium atoms occupy the *4b* (1/2, 1/2, 1/2) position, and other eight lithium atoms occupy position *8c* (1/4, 1/4, 1/4) in a unit cell, respectively.

The equilibrium structural parameters are determined by fitting the total energy as a function of volume to the Birch-Murnaghan's equation of state (Fig. 2). The deduced structural parameters obtained with the GGA-PBE approximation are presented in Table I, which are accompanied with some experimental data and theoretical results for comparison.

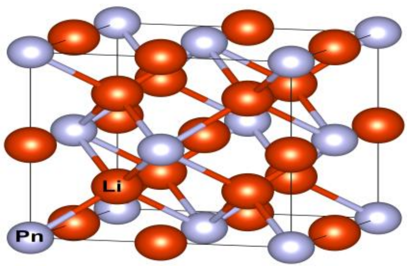

Figure 1. The conventional cells of Li_3Pn. (Pn= Sb, Bi).

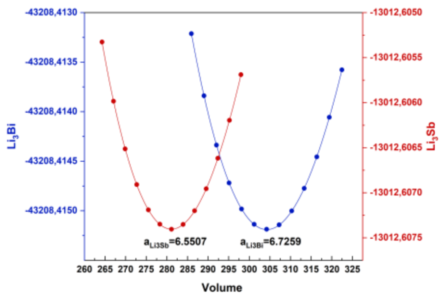

Figure 2. The total energy as a function of volume.

TABLE I. CALCULATED VALUES OF LATTICE PARAMETERS FOR THE Li_3Pn COMPOUNDS.

System		Structural parameters		
		Lattice constant	***Density (g/cm^3)***	$d_{Li\text{-}Pn}$
Li_3Sb	Cal.	6.551	3.369	2.837
	Exp.	6.565 [9]		
	Cal.	6.566 [10]		
Li_3Bi	Cal.	6.726	5.015	2.912
	Exp.	6.722 [11]		
	Call.	6.738 [10]		

The optimized lattice constants are 6.55Å and 6.72Å for Li_3Sb and Li_3Bi , respectively, which are in good agreement with the previous experimental and theoretical results [9-11]. The length of Li-Sb and Li-Bi bond in crystal structure are 2.837 and 2.912, respectively.

B. *Electronic Properties*

The calculated electronic band structures and total electron density of states of these materials are plotted in Figs. 3 and 4. Through comparing, one can see that the energy bands have same features and the conduction band maxima state is located at the high-symmetry X point, the valence band minima state is located along the Γ - K line, which clearly depicts that these materials are indirect band gap semiconductors. Li_3Sb and Li_3Bi are narrow band gap semiconductors with the GGA-PBE band gaps of 0.715 eV and 0.382 eV,

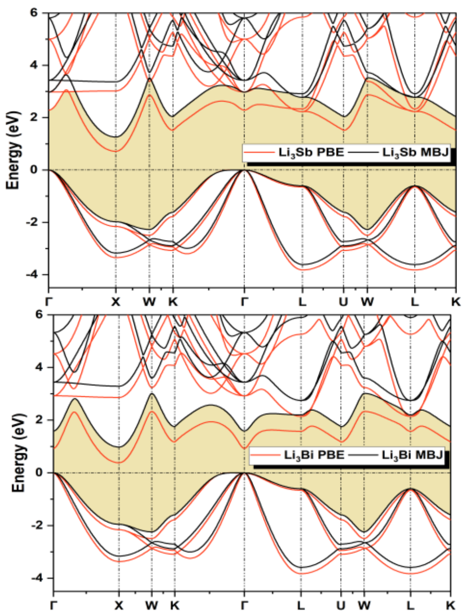

Figure 3. Electronic band structure of Li_3Pn (Pn= Sb, Bi).

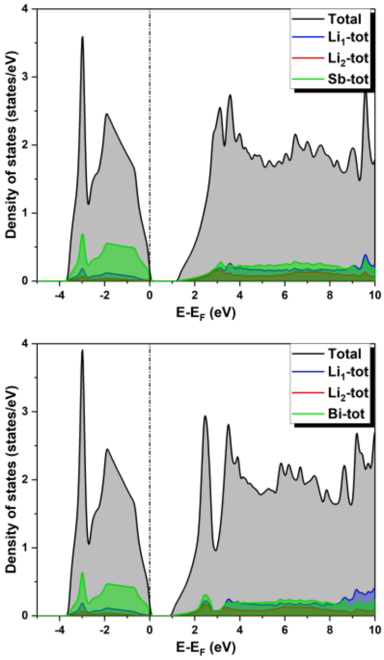

Figure 4. The total electron density of states of Li_3Pn (Pn= Sb, Bi).

respectively, which are consistent with other works [10]. Th TB-mBJ calculation predicts a larger band gap of 1.258 eV for Li_3Sb and of 0.978 eV for Li_3Bi .

The main feature of the density of states is that the conduction and the valence bands predominated by the pnictide (Sb and Bi) states.

C. Thermoelectric Properties

In this section, we calculated the thermoelectric properties of Li_3Pn materials such as Seebeck coefficient and figure of merit. Fig. 5 show the transport properties as a function of the chemical potentials (μ) in the range of -1.7 to 1.7 eV at different temperatures (*T*) of 300 K, 600 K, and 900 K. The Seebeck coefficient shown in Fig. 5a and b, is very large and positive which shows the presence of p-type charge carriers. The investigated compounds have a larger Seebeck coefficient at room temperature compared to that at 600 and 900 K. In the selected range of μ , two peaks with maximum values of *S* are observed, one at positive μ and another at negative μ . The maximum peaks in *S* are obtained at $\mu = -0.04$ and -0.09 V with values 2.11, and 1.66 mV/K, respectively for Li_3Sb and Li_3Bi . The other maxima having S

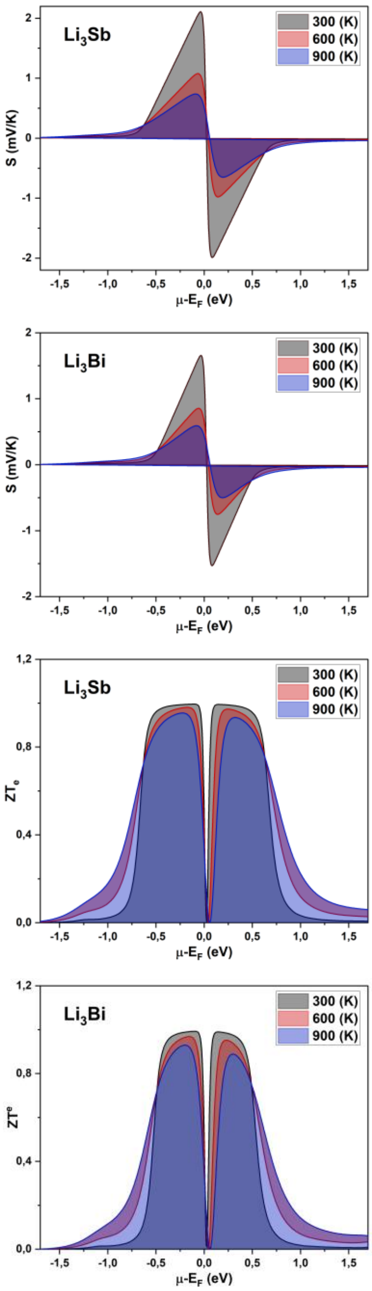

Figure 5. The Seebeck coefficient and figure of merit for Li_3Pn (Pn= Sb, Bi).

equal to -1.99 and -1.53 mV/K were obtained at $\mu = +0.08$ and + 0.19 eV for Li_3Sb and Li_3Bi , respectively, which means that Li_3Sb ($Pn = Sn, Bi$) compounds are p-type materials.

Fig. 5c and d show the electronic figure of merit ZTe curves of Li_3Sb and Li_3Bi ,

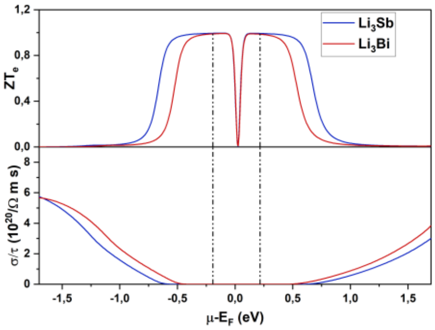

Figure 6. The electrical conductivity and figure of merit for Li_3Pn (Pn= Sb, Bi).

respectively as a function of the chemical potential at temperatures of 300 K, 600 K, and 900 K. From these figures, we notice that both compounds exhibit the same behavior with ZT_e value around unity. For Li_3Sb and Li_3Bi the predicted maximum value for the figure of merit is about 0.99 at room temperature, which means that these studied lithium-based compounds are excellent candidates for thermoelectric devices.

The ZT_e rises dramatically in both n-type and p-type as chemical potential goes to zero, and the critical points are obtained between $\mu\{-0.11 \textit{ and } +0.15\, eV\}$ for Li_3Sb and $\mu\{-0.10 \textit{ and } +0.14\, eV\}$ for Li_3Bi. Although the Li_3Pn compounds possess very small electrical conductivity in these regions (see Fig. 6), the high ZT_e values arise due to the high Seebeck coefficient values. These results clearly suggest that the Seebeck coefficient plays more important role on the thermoelectric performance of these materials than the electrical conductivity.

IV. Conclusion

We systematically investigated the geometric, electronic and thermoelectric properties of Li_3Pn ($Pn = Sn, Bi$) by employing the first principal calculations combined with semi-classical Boltzmann transport theory. Our results reveal that both compounds are semiconductors and have moderate band gaps. Li_3Pn ($Pn = Sn, Bi$) exhibits the maximum ZT value ($ZT = 1$) for n-type and p-type doping at room temperature. Higher power factors could be achieved in these compounds, making them promising candidates for efficient thermoelectric materials.

Acknowledgment

Financial support by Université Amar Telidji de Laghouat, Algeria, is acknowledged.

References

[1] Moolayadukkam, S., Bopaiah, K. A., Parakkandy, P. K., & Thomas, S. (2022). Antimony (Sb)-Based Anodes for Lithium–Ion Batteries: Recent Advances. *Condensed Matter*, *7*(1), 27.

[2] Guo, S. D. (2014). Electronic structures and elastic properties of X3Sb (X= Li, K, Cs) from the first-principles calculations. *Materials Research Express*, *1*(1), 015906.

[3] Ha, V. A., Yu, G., Ricci, F., Dahliah, D., van Setten, M. J., Giantomassi, M., ... & Hautier, G. (2019). Computationally driven high-throughput identification of CaTe and Li 3 Sb as promising candidates for high-mobility p-type transparent conducting materials. *Physical Review Materials*, *3*(3), 034601.

[4] Blaha, P., Schwarz, K., Tran, F., Laskowski, R., Madsen, G. K., & Marks, L. D. (2020). WIEN2k: An APW+ lo program for calculating the properties of solids. *The Journal of Chemical Physics*, *152*(7), 074101.

[5] Perdew, J. P., Burke, K., & Ernzerhof, M. (1996). Generalized gradient approximation made simple. *Physical review letters*, *77*(18), 3865.

[6] Tran, F., & Blaha, P. (2009). Accurate band gaps of semiconductors and insulators with a semilocal exchange-correlation potential. *Physical review letters*, *102*(22), 226401.

[7] Monkhorst, H. J., & Pack, J. D. (1976). Special points for Brillouin-zone integrations. *Physical review B*, *13*(12), 5188.

[8] Madsen, G. K., & Singh, D. J. (2006). BoltzTraP. A code for calculating band-structure dependent quantities. *Computer Physics Communications*, *175*(1), 67-71.

[9] Zintl, E., & Brauer, G. (1935). Konstitution der Lithium‐Wismut‐Legierungen: 14. Mitteilung über Metalle u. Legierungen. *Zeitschrift für Elektrochemie und angewandte physikalische Chemie*, *41*(5), 297-303.

[10] Kalarasse, L., Bennecer, B., & Kalarasse, F. (2011). Elastic and electronic properties of the alkali pnictide compounds Li3Sb, Li3Bi, Li2NaSb and Li2NaBi. *Computational materials science*, *50*(10), 2880-2885..

[11] Leonova, M. E., Sevast'yanova, L. G., Gulish, O. K., & Burdina, K. P. (2001). New Cubic Phases in the Li–Na–Sb–Bi System. *Inorganic materials*, *37*(12), 1270-1273.

Power Factor and Frequency Measuring in Single-phase Power Systems

Đorđe Lazarević[1], Marko Živković[2], Đorđe Kocić[3], Jovan Ćirić[2]

[1,2,3]Faculty of Electronic Engineering, 18000 Niš, Serbia
[4]Toplica Academy of Vocational Studies – Department of Agricultural and Food Studies, 18400 Prokuplje, Serbia

Abstract—**Measuring power factor and frequency in AC power systems is a necessary part of determining the value power of the load. Also, frequency and power measurements are widely used in power and frequency regulator circuits for their improvement. Frequency and power factor are required for correct results of AC values measurement. This paper describes the theoretical aspect of frequency and power factor measurement and offers an explanation of methods for measurement and appropriate calculation. Lastly, this paper also presents the practical implementation of measurement systems by using a microcontroller system and high-precision power analyzer which provides high accuracy in the measurement process.**

Keywords – power factor, frequency, microcontroller, power analyzer

I. INTRODUCTION

The efficiency and power consumption of equipment are directly proportional to its power factor. The energy consumption of the equipment is higher if the power factor is lower and vice-versa [1]. The indicator of power quality in AC power systems is the power factor. The value of the power factor is between 0 and 1. In the ideal case, where the given load is pure resistance, voltage and current are in phase and the power factor is equal to 1. So the apparent and real power of the load are equal to each other and because of pure resistance of the load, reactive power is equal to 0. For loads, such as lighting ballasts, power transformers, and induction motors, the minimization of reactive power is very essential [2]. The average power consists of real and reactive power. If the phase angle between the voltage and current are the same, that means that the load is only resistive, and complete power will be absorbed by the load. In the case where the load is reactive, the average power will be reflected back to the source. In the situation where the phase difference is 90°, the load can be taken as reactive and the average power is reflected back to the AC (alternating current) source.

$$\begin{aligned} P &= V_{RMS} I_{RMS} \angle\left(\Theta_v - \Theta_i\right) = \\ &= V_{RMS} I_{RMS} cos\left(\Theta v - \Theta i\right) \end{aligned} , \tag{1}$$

$$S = V_{RMS} I_{RMS} , \tag{2}$$

$$I_{RMS} = \sqrt{\sum_{n=0}^{N-1} \frac{i^2(n)}{N}} , \tag{3}$$

$$V_{RMS} = \sqrt{\sum_{n=0}^{N-1} \frac{v^2}{N}} . \tag{4}$$

Apparent power (S) is calculated by multiplying voltage and current. It can be calculated by multiplication of RMS voltage and RMS current, as shown in Eq. (2) and it is expressed in units of volt-amperes (VA). The RMS values are calculated using Eqs. (3) and (4). The number of samples, Eqs. (5) and (6), present the samples of the electrical voltage and current signals. The capability of the circuit for performing work at a time is real power (P). The real power can be calculated by multiplying measured voltage and current and their averaging over time:

ISBN: 978-86-82602-01-9

$$P = \frac{1}{N}\sum_{n=0}^{N-1} v(n)i(n) \,, \tag{5}$$

$$PF = \cos(\theta) = = \frac{\mathrm{Re}\,alPower(W)}{ApparentPower(VA)} = \frac{P}{S} \,. \tag{6}$$

The ratio of Real Power to Apparent Power presents the power factor (PF) and it represents the capability of the electrical system to convert electric current into useful workloads such as heat, rotation, or light [3].

The frequency is one of the most important parameters in electrical circuits. The basic principle of the frequency meter is based on comparing a high-frequency stabilized source as a reference clock and the measured frequency of other signals. The gate time of 1 second in normal conditions represents a number of pulses per second. Gate time can also be greater than or less than one second. With the longer gate time obtained more accurate resulting frequency value. The longer the gate time is, the longer intervals after every measurement frequency are. The shorter the gate time gives faster frequency values of the measured refresh rate. A shorter gate time directly affects the accuracy of the measured frequency. The instrument which is used for the digital display of the frequency of the measured signal is a digital frequency meter. The measured signal can be a sine wave, square wave, or another signal with circuit changes. Frequency represents the number of changes in the periodic signal in a time frame (1s). The number of iterations of the modulation of the periodic signal measured in a certain time interval T is N. The frequency can be expressed as [7]:

$$f = \frac{N}{T} \,. \tag{7}$$

II. METHODS FOR POWER FACTOR AND FREQUENCY MEASUREMENT

Alternating Current (AC) electrical system is a system where values of electrical signals are oscillating in time. A small difference in oscillation time between two wave patterns is a phase shift. It is a delay between two waves that have the same period or frequency. The phase angle is the phase shift in the positive or negative angle which is within the -180 to 180-degree range. In a particular electrical system phase shift can be observed between voltage and current signal. This method is often used in measurement systems for determining the quality of the loads/generator. Power Factor, Real Power, Apparent Power, and Reactive Power can be defined by using the value of the phase angle, between the voltage and current waves. In a 3-Phase system, the phase shift can also be used between voltage and current waves. The phase angle is an important electrical parameter. It is also often used in 3 phase systems to determine the phase sequence. Phase angle can be determined by using 2 methods. The first method is using the same starting time value for measuring the time difference to reach the peak value (or 0 value) between both waves. This method is the simplest method for comparing phase angles. Using this method implies measuring 2 reference points only (the starting point and peak value point). It is particularly suitable for pure waves and distorted or high-disturbance waves. The first wave is taken as a reference to the other for the phase angle comparison. The current wave is always altered based on the applied load so the wave that is always taken as a reference is the voltage wave. It is also possible to compare 2 or 3 voltage waves in a 3-phase electrical system [5]. Fig. 1 shows determining the phase angle by using the start and end points.

The most direct method for frequency detection is the zero-crossing algorithm. The calculation method is simple and has fast execution and it is not necessary to use complex mathematical formulas. The period between two zero crossing points is half a signal period for the signals of one cycle. The actual frequency of the

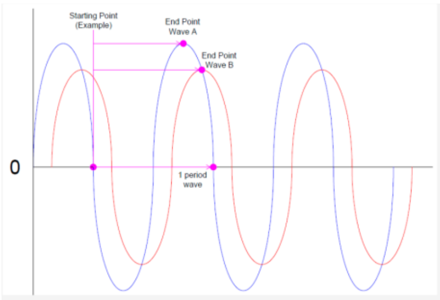

Figure 1. Determining the phase angle by using start and end point [5].

signal is obtained by using the signal before and after the zero crossing position. Also, this method requires numerical computation, converted into units of time, and seeking the reciprocal value.

Zero-crossing algorithm schematics of the electric signal is shown in Fig. 2.

In practice typically, the sampling frequency is not an integer multiple of the actual signal frequency. Therefore signal period is not an integer multiple of the sampling period and the accurately calculated m value is not an integer value. In Fig. 3, zero crossing points (Yi-1, Yi) from negative to positive are shown, and, zero crossing points (Yi+m, Yi+m+1) from negative to positive, respectively.

The accurate period of the sine wave can be expressed as:

$$T = mT_s + \delta_2 + \delta_3 = m_A T_s = m_A \Delta\Theta \quad , (8)$$

where:

$$T_s = \Delta\Theta \ . \qquad (9)$$

Given that the sampling interval is not an integer multiple of the signal cycle, and is not an integer, according to Fig. 3, can be expressed as (10):

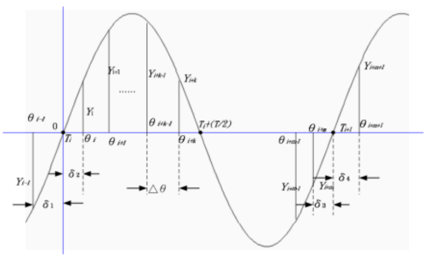

Figure 2. Zero crossing algorythm schematic [6].

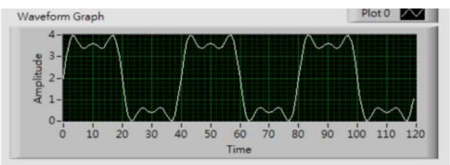

Figure 3. Simulated mixed signals with 3rd and 5th harmonics with different amplitudes 1V, 0.4V and 0.2V [6].

$$m_A = m + \frac{\delta_2}{\Delta\theta} + \frac{\delta_3}{\Delta\theta} = m + \frac{\delta_1}{\delta_1\delta_2} + \frac{\delta_3}{\delta_3\delta_4} \ . (10)$$

The time difference between the sampling point and zero point (Ti) is δ_2. By using a definition similar to trigonometric in Fig. 3 and (10) can be expressed as:

$$m_A = m + \frac{|y_i|}{|y_i| + |y_{i-1}|} + \frac{|y_m|}{|y_m| + |y_{m+1}|} \ . (11)$$

The true frequency of the test signal can be expressed as (12):

$$f = \frac{1}{m_A T_s} = f_a \frac{m}{m_A} \ . \qquad (12)$$

Equations (10) and (11) still can be used for frequency detection, even if Yi or Ym is separately located in the condition of Ti and Ti+1 (zero amplitude value). The zero crossing algorithm is very simple and fast and it is usually used as an algorithm for electric power measurement [6].

III. Systems for PF and Frequency Measurement

For power factor and frequency measurement usually used devices are power analyzers or custom-made electronic systems which are usually based on microcontrollers. Power analyzers are commercial products with high accuracy, high price, and high quality with the possibility of measuring power factor and frequency. However, they also can measure all electrical parameters. This type of device can be used for checking electrical equipment in the laboratory as well as for checking the quality of electrical energy in facilities. A typical power analyzer for laboratory use is shown in Fig. 4.

Figure 4. Laboratory power analyzer [7].

For low-cost measurement and acceptable accuracy, it is possible to use a more simple device as a microcontroller system which is based on an 8-bit microcontroller and can measure power factor and frequency also. Fig. 5 shows a low-cost microcontroller system that can be used for measuring power factor and frequency.

IV. Laboratory Work With Practical Implementation by Using a Microcontroller System and Power Analyzer

For practical measurement and research designed an 8-bit microcontroller system which is based on an 8-bit microcontroller Atmega328P [9]. This system consists also of RS232, CAN bus, and USB interface, and so the information can be sent and received on a computer. For voltage, sensing used current type voltage sensor module ZMPT101B [10]. This module contains an operational amplifier with all necessary components for amplification signal from the voltage transformer and sensor calibration. Current is sensed by using the ACS712 Hall-effect sensor module [11]. This type of sensor is fully integrated with an offset voltage of 2.5V with a power supply of 5V which is very useful for application in microcontroller systems that are operating with 5V without voltage translation. The sensitivity of this type of sensor is 66mv/A for the 30A version. Figure 6 shows the prototype board of the microcontroller system which is used for this experiment.

As a reference instrument for this research and measurement is used power analyzer Chauvin Arnoux C.A. 8335 [12]. This type of power analyzer is suitable for laboratory as well as outdoor use, thanks to its construction. Fig. 7 shows the connection of the system which is consist of a prototype board of a microcontroller system, a power analyzer, and an oscilloscope with the computer.

Checking of work of the system is done with three types of electrical loads. For measuring are used resistive and inductive loads which are most common in industrial systems. Voltage and current signals for all types of loads are taken from the ZMPT101B and ACS712 sensors, respectively.

The resistive load is a classic heater with a power of 1000W. In this case, voltage and current are in phase so the power factor is equal to 1. On this type of load because of its low parasitic inductance and capacitance almost all power consumption is by active power and reactive power is practically very small.

Fig. 8 shows voltage and current shapes for resistive load. In the case of resistive loads voltage and current are in phase so the angle between them is zero and the power factor is 1.

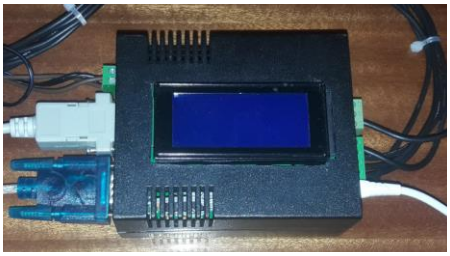

Figure 5. Low cost microcontroller system [8].

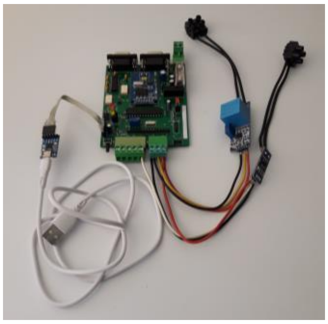

Figure 6. Prototype board of microcontroller system.

Figure 7. Connection of the system.

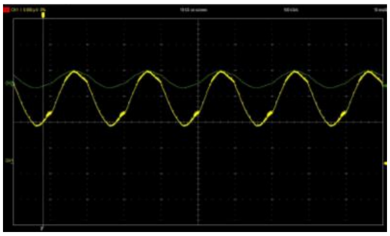

Figure 8. Voltage and current signals for resistive load.

TABLE I. POWER FACTOR AND FREQUENCY MEASURING BY DIFFERENT LOADS WITH MEASURING ERROR.

N.M.	**Type of electrical load**	**Microcontroller system**		**Power analyzer C.A. 8335**		**Error (%)**	
		PF	***f(Hz)***	***PF***	***f(Hz)***	***PF***	***f***
1.	Heater 1000W	0.99	49.99	1	50.01	1	0.03
2.	AC motor	0.5	50	0.51	50.01	1.9	0.01
3.	Fan with heater	0.98	50.01	0.99	50	1.01	0.02

The second electrical load is low power single-phase asynchronous electromotor. By measurement, the power factor is determined to be very low. This is not the case with electromotors with higher values of power. That means that the motor consumes more reactive than active power which is solved by adding a system for power factor correction.

The third type of device is an electrical fan with a heater of 1800W. Using this type of device provides correction of power factor to 1 because of the heater which is used in it. Without heating, this type of device is typically inductive with a small power factor.

Fig. 9 shows voltage and current signals for inductive loads.

It is clearly visible that voltage and current are not in phase, and the voltage is shifted in relation to the current for a certain angle. It implies that the power factor is lower than 1.

All measurements are shown in Table I which also presents measurement errors. Measuring is done by using a microcontroller board and high-precision power analyzer and it shows measuring errors.

Results in the table show that results of measuring with a microcontroller system are very close to results which are provided by high precision power analyzer. That means this type of device can be used for measuring with enough accuracy rate for a lot of applications.

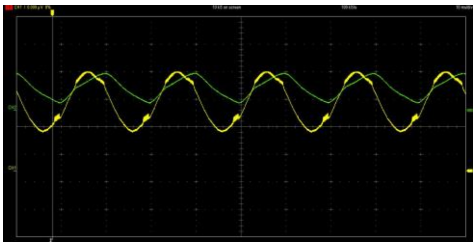

Figure 9. Voltage and current signal for inductive loads.

V. CONCLUSIONS

Power factor and frequency measurement, for single-phase circuits, are done in this research using a microcontroller system by the method of determining phase difference of voltage and current signal and zero crossing algorithm. For power factor determination a statistical method can also be used with average values of RMS values of voltage and current. Given that frequency is the strictest criterion for power quality the need for frequency measurement is great. This research presents a low-cost and efficient method for checking and determining the value of power factor and frequency with acceptable accuracy for the calculation of power in single-phase systems.

REFERENCES

[1] Mukaila, A. A., Olugbemi, I., & Sule, E. E. (2020). Design and Construction of A Single-Phase Power Factor Meter. *Electrical Science & Engineering*, *2*(2), 11-14.

[2] Rija, B. M., Hussain, M. K., & Vural, A. M. (2020). Microcontroller Based Automatic Power Factor Correction for Single-Phase Lagging and Leading Loads. *Engineering, Technology & Applied Science Research*, *10*(6), 6515-6520.

[3] Gunawan, T. S., Anuar, M. H., Mira, K., & Zuriati, J. (2020). Design of power factor meter using internet of things for power factor improvement remote monitoring and data logging. *Indones. J. Electr. Eng. Comput. Sci*, *17*, 700-709.

[4] Zheng, W. Q. (2014). Design and Implementation of Digital Frequency Meter Based on SCM. In *Applied Mechanics and Materials* (Vol. 687, pp. 3466-3469). Trans Tech Publications Ltd.

[5] *How to measure Power Factor and Phase Angle with Arduino?* (2019). Available at: https://solarduino.com/how-to-measure-power-factor-and-phase-angle-with-arduino/.

[6] Chen, Y. C., Shen, H. Y., Chen, H. Y., & Hsu, C. H. (2016, July). Low cost Arduino DAQ development and implementation on an Android app for power frequency measurement. In *2016 International Symposium on Computer, Consumer and Control (IS3C)* (pp. 99-102). IEEE.

[7] *Power analyzer Hioki PW3390*. (2021). Available at: https://www.hioki.com/sites/default/files/2021-04/product_image6413.png.

[8] Lazarević, Đ., Živković, M., Kocić, Đ., & Ćirić, J. (2022). The utilizing Hall effect-based current sensor ACS712 for true RMS current measurement in power electronic systems. *Scientific Technical Review*, *72*(1), 27-32.

[9] *ATMega328P microcontroller, datasheet*. (2015). Available at: https://ww1.microchip.com/downloads/en/DeviceDoc/Atmel-7810-Automotive-Microcontrollers-ATmega328P_Datasheet.pdf.

[10] *ZMPT101B current-type Voltage Transformer, datasheet* (2021). Available at: https://5nrorwxhmqqijik.leadongcdn.com/ZMPT101B+specification-aidijBqoKomRilSqqokpjkp.pdf.

[11] *ACS712, Fully Integrated, Hall Effect-Based Linear Current Sensor with 2.1 kVRMS Voltage Isolation and a Low-Resistance Current Conductor, datasheet* (2007). Available at: https://www.sparkfun.com/datasheets/BreakoutBoards/0712.pdf.

[12] *Power and energy quality analysers C.A 8332B - C.A 8334B - C.A 8335, datasheet*. (2008). Available at: https://www.testequipmenthq.com/datasheets/CHAUVIN%20ARNOUX-CA8335-Datasheet.pdf.

Multiport Converters' usual Topologies and Applications: A Review

Walklis Victor Lima da Penha[1], Rafael Pereira do Nascimento[2], Romero Leandro Andersen[3]

[1,2,3]Universidade Federal da Paraíba, João Pessoa, Brazil

Abstract—**In general, a multiport converter is built by integrating different types of converters to connect multiple energy sources to one or more outputs, which can be a battery pack, a load, or the grid, along with other possibilities. The review was made to collect data regarding the current viable applications and topologies used for this type of converter and to catalog the usual topologies into three separate categories, isolated, nonisolated, and partially isolated converters, each one of them was exemplified in this article. In addition, a final consideration was made concerning the limitations and benefits of the topologies proposals applications studied by this paper.**

Keywords - multiport converter, converter topologies, dc-dc converters, renewable energy

I. Introduction

The energy demand is increasing globally [1], and countries are looking for alternative energy sources in response to this increase [2]. To minimize this problem, there has been an expansion in renewable energy sources and technological advances in energy storage systems. As a result, there was a need to manage the generation and distribution of electricity. Furthermore, Microgrids are becoming more popular as a way to combine renewable energy with a battery bank, as they can enable integration with the power grid [3]. This way, converters are used to manage the energy flow so that this integration can be carried out. Because of this, it uses a multiport converter (MPC), an integrated converter capable of connecting multiple loads. Multiport converters have various topologies, including single input multiple outputs (SIMO), multiple inputs and single output (MISO), and multiple inputs with multiple outputs (MIMO) [4].

In the face of these new developments, the study of MPCs is also increasing in order to create options on how to integrate numerous DC sources. Studies are focusing on using fewer switches to make the system less complex and cheaper. The topologies of a multiport converter can also be divided into nonisolated, partially isolated, and isolated. Table I classifies the topologies mentioned in this article. Standalone PV systems are an example of a nonisolated converter application, [5] describes an MPC based on a phase-shift-switched capacitor converter for this purpose. Moreover, [6] and [7] introduce a partially isolated MPC to reduce the complexity of an isolated structure by isolating only the necessary ports. Furthermore, the applications of an MPC are not limited to PV systems generation to the grid, but they are used for other purposes as well. In [8] is proposed a DC-DC converter capable of transferring energy from PV to electric vehicles (EV), PV to grid, grid to vehicles, and vehicles to grid. The topology consists of a bidirectional isolated CLLLC converter for off-board vehicles charging and linking the PV system to the grid. This paper approached the benefits of each topology and when each one is best suited for use.

The multiport interface approach in these systems is interesting because it can integrate storage batteries used to maintain the excess energy and to supply the load with this energy stored when necessary; it also has a shutdown process to stop conduction to the battery bank in cases of instability or failure in the general system.

TABLE I. MULTIPORT CONVERTERS CLASSIFICATION.

Applications	Topologies		
	Isolated	***Nonisolated***	***Partially Isolated***
Reference	Ref. [8,10,15, 16]	Ref. [5,19,20]	Ref. [6,7,27]

In addition, using multiple ports makes it possible to utilize a more significant number of renewable energy sources, making the system more reliable.

This study aims to review the topologies applications of multiport converters and to encourage the research concerning this topic. The topologies observed in this paper, and their specifications are presented in Sections II, III, and IV, followed by a critical analysis of the results in Section V.

II. ISOLATED APPLICATIONS

As previously mentioned, some different MPC topologies are being studied and proposed. The most used topology is the isolated one, with no direct conductor path between a potential voltage differences. In [9] is mentioned an isolated MPC, where a multi-winding transformer can be shared by different full- and/or half-bridge converters, having multiple input/output ports. However, this structure increases circuit design difficulty; furthermore, isolated MPCs require a significant number of switches, which increases the circuit's complexity and control difficulty.

Despite these cons, some appliances require isolation; in [10] an implementation of multilevel inverters and multiport DC-DC converters for microgrids is presented. A MISO MPC is used with three inputs and one single output. Fig. 1 indicates the schematic of the micro-grid system suggested by the last previously mentioned paper.

One PV system, one fuel cell component, and a bank of batteries are the system's inputs, and the only output of the MPC is connected to the multilevel inverter, which is linked to the microgrid. One of the advantages of the structure proposed is that the current flow is bidirectional, which means that batteries may be charged by the sources during the day and feed the load at night, giving more reliability to the system.

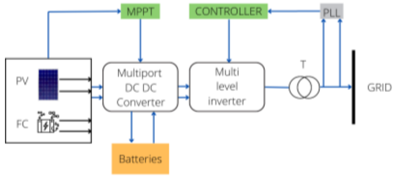

Figure 1. Schematic of the micro-grid system [10].

Another application was approached in [8]. Besides, the study modeled and simulated a bidirectional isolated CLLLC converter for the off-board plug-in electric vehicles (PEV) charger. The main goal of this proposal is to communicate a PV system, a PEV, batteries, and a grid. Previous topologies were reviewed by the study [11-13]; however, the majority of these converters require more switches and do not offer isolation. Therefore, the integrated MPC proposed in [8] does not have the problems mentioned earlier and can connect its ports in a bidirectional way for all possible links. Furthermore, this topology can be applied to parking areas and work as a standalone electric parking lot, charging vehicles with maximum power point tracking.

One more relevant application for isolated multiport converters is combining PV, electric vehicles, and the grid. When it is possible to add bidirectional power capability to this topology, it increases the benefits of its use [14]. Many studies are presented in the literature discussing MPC for EV applications alongside PV and grid integration [8,15].

The authors in [15] proposed a multiport reconfigurable converter for a grid-integrated hybrid PV/EV/battery system. The proposed converter can operate in multiple modes, including PV/grid to the vehicle, and PV/battery to the vehicle, for when the EV needs to charge faster, PV to vehicle, in case there is no energy stored in the batteries, battery to the vehicle, and grid to the vehicle, in case the PV source is not available, and PV to the battery, in order to store energy. The converter is designed for charging EVs at 10 kW and to share components across different power flow paths, achieving increased component utilization and high power density. To exchange power between the EV and the rest of the sources a single transformer is used to guarantee EV isolation standards and attain reduced magnetic elements. The schematic of the circuit is illustrated in Fig.2.

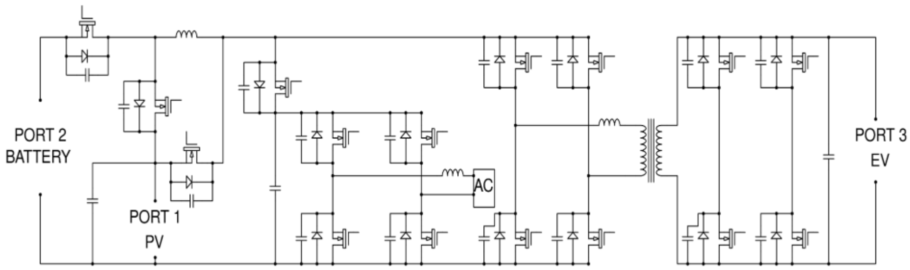

Figure 2. Reconfigurable converter for integration of PV, EV, battery and the grid; modified from [15]

Another topology is a three-port Multilevel converter shown in Fig. 3 having a concentrated PV port 1, a battery bank connected to port 2, and the load is connected to the remaining port. The topology proposed a converter to an hourly dispatch scheme to deliver a predetermined constant PV power to the utility grid from the variable photovoltaic system, seeking the optimum value of the DOD that yields the most cost-effective battery energy storage system (BESS). From this topology, we can highlight their attractive solution for integrating a large-scale PV-BESS into the grid, having a high efficiency with flexible control for power flow, allowing operation at high voltage [16].

III. NONISOLATED APPLICATIONS

The discussion of this section concerns the nonisolated MPCs, where none of the ports are galvanic isolated. Therefore, the converters are coupled using a DC-link integrator capacitor or inductor.

On the other hand, switched capacitor converters (SCC) are known for their high power density in nonisolated applications.

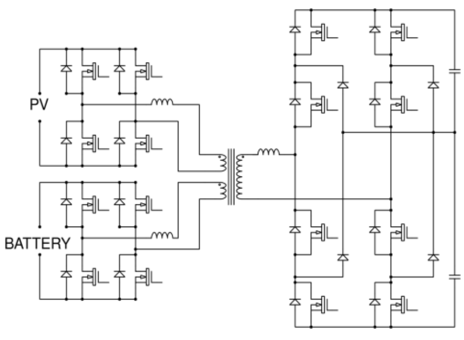

Figure 3. Structure of the hourly dispatching PV system; modified from [16]

SCCs mainly use capacitors instead of inductors as an energy-storage element in circuits because the energy density of discrete capacitors is 100 to 1000 times greater than similarly scaled inductors [17,18].

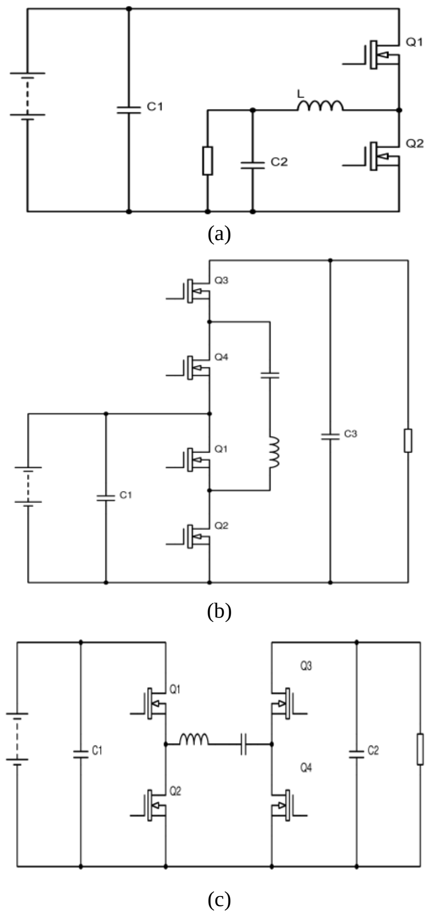

Figure 4. Key elements for the proposed MPCs. (a) Bidirectional PWM converter. (b) PS-SCC. (c) Nonisolated DAB converter; modified from [5].

Taking into account the preceding, [5] proposes nonisolated MPCs based on phase-shift-switched capacitor converters (PS-SCC) for standalone PV systems, using a traditional bidirectional pulse width modulation (PWM) converter and PS-SCC integrated with sharing active switches. Although the structure still contains one inductor, the number of capacitors is far greater. Fig. 4 illustrates the key elements for constructing the last MPC mentioned.

The proposed nonisolated MPC is derived from an integration of a traditional PWM converter and the PS-SCC shown in Fig. 4(a) and (b). This same PS-SCC can be transformed into a dual active bridge (DAB) converter, as depicted in Fig. 4(c). These fundamental elements are combined by disconnecting the source pin of Q4 in the PS-SCC and connecting it to the ground; that way, the PS-SCC can be transformed into the nonisolated DAB converter. The significant features and operation principles of the PS-SCC are identical to those of the nonisolated DAB.

In the same perspective, a family of five novel nonisolated multiport dc–dc converters with bipolar symmetric outputs (MBDC) was proposed in [19] for integrating multiple renewable energy sources into bipolar dc grids. The proposed converters have high voltage gain or voltage transformation factor and naturally symmetrical bipolar outputs or require a simple open-loop PWM control of 50% duty cycle to keep the output voltages balanced. Furthermore, the models can increase the number of input ports to accommodate more renewable energy resources by adding only the respective active switch for the introduced source.

An application that can be mentioned is in power generation; in this situation, the topology [20] combines two inputs; the first is dedicated to the primary voltage source, and the second is connected to the battery bank. Through this topology, a simplified and compact design for a DC converter; however, due to this, it can only be used for low load voltages. Fig. 5 illustrates the key elements for constructing the last mentioned MPC. As a result, the system's power quality problems are resolved.

Fig. 6 illustrates a topology of a multiport converter with two bidirectional inputs and one unidirectional output. This is used for power generation systems and storage systems. The main goal of this topology is to solve power

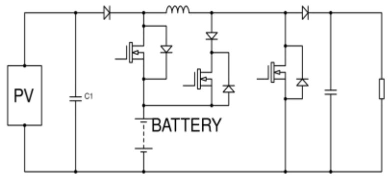

Figure 5. Reconfigurable converter for integration of PV, EV, battery and the grid; modified from [20].

quality problems and promote a continuous flow of energy with good performance. For this reason, the concept of LES (Local Energy System) or ESS (Energy Storage System) [21,22] has been introduced. The energy is forked and sent to both the load and the ESS. In case of overvoltage, the necessary voltage goes to the load and the rest of it goes to the ESS.

This topology achieved constant power flow and good output power efficiency, ensuring smooth operation for low and medium voltage levels. However, this model still needs ways to improve its stability and optimize efficiency [23].

The next topology is a four-port converter shown in Fig. 7 having a concentrated PV port 1, a fuel cell connected to port 2, a battery bank connected to port 3, and the load is connected to the remaining port. From this topology, we can highlight their very significant gain; having a small number of switches. However, due to its high gain, this model has a low efficiency compared to other topologies converters, ranging from 85% to 90%; the converter cannot be operated at minimum load; By using a pulsed charge/discharge method for the battery, it will

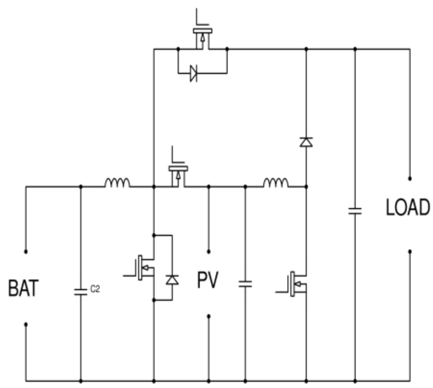

Figure 6. Circuit diagram of proposed converter without IOT; modified from [23].

need a short time between charge pulses for it to stabilize [24].

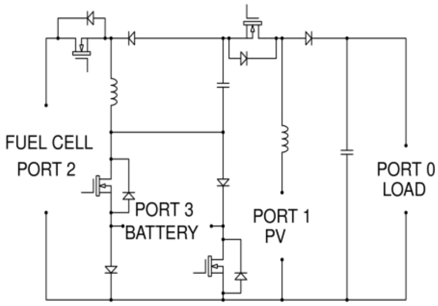

Figure 7. Circuit diagram of three input DC-DC converter; modified from [24]

IV. PARTIALLY ISOLATED APPLICATIONS

This section will discuss partially isolated converters, which combine the characteristics of the other two [25]. Only some of the converter ports will be galvanically isolated.

As the main benefits of partially isolated converters, we can highlight the possibility of output isolation, which enables better output security and can isolate some of the inputs. However, such a topology has high switching stress, making it challenging to minimize transformer leakage currents [26].

Even with some cons, there are numerous applications for this type of topology, mainly within power generation systems.

An application can be cited in hybrid energy systems; in this situation, we can mention the topology [27]. This topology is suitable for applications like EVs and smart buildings. Such a topology combines three inputs. However, the converter provides a different path for the inputs to feed the load directly. The first input is dedicated to the primary voltage source, not needing components between it and the converter, being connected directly to the DC link; in the second, most DC power sources can be connected, being necessary to isolate such input; the third input is a PV system, being necessary to isolate it galvanically to avoid leakage currents. The topology proposed addresses the problems of excessive switch interaction and low battery life, proposing an extensible MPC that benefits from a HESS and using the methods proposed by [28] and [29] to elaborate its design. HESS will help MPC with a fast dynamic response and improve the main battery's performance life. Through this topology, it achieved a shorter response time, as well as allowing an alternative path to be able to feed the load that helps with overload problems directly. Fig. 8 illustrates the key elements for constructing the last mentioned MPC.

The authors in [6] brought a new idea for partially isolated topologies, they proposed a novel partially-isolated MPC with automatic current balancing capability and improved transformer utilization [30], and it presented the fully developed work of [30]. A flying capacitor (FC) is added to the interleaved PWM converter to realize the automatic current balancing and an enhanced voltage conversion ratio. Moreover, the added FC allows the interleaved PWM converter to operate with a nominal duty cycle of 0.5 for the 12- V LVB and 48-V HVB, consequently improving the transformer utilization and reducing the RMS current of the transformer winding. During its analysis, it was noted that the automatic current balancing was successfully made, and the added FC achieved a voltage conversion ratio double that of conventional interleaved PWM converters.

A single-magnetic partially isolated MPC was studied in [7]. The MPC proposed integrating a series-resonant converter (SRC) and a bidirectional PWM converter by sharing switches. This process is illustrated in Fig. 9.

The magnetizing inductance of the transformer is utilized as a filter inductor for the PWM converter. In contrast, the leakage inductance plays a role of a resonant inductor for the SRC, hence achieving the single-magnetic topology. The experimentation made to test the efficiency of this topology used a 150-W prototype, and it demonstrated through measuring voltage conversion and transient response characteristics that using pulse frequency modulation and PWM controls it was possible to independently control the output and battery voltages without interdependence.

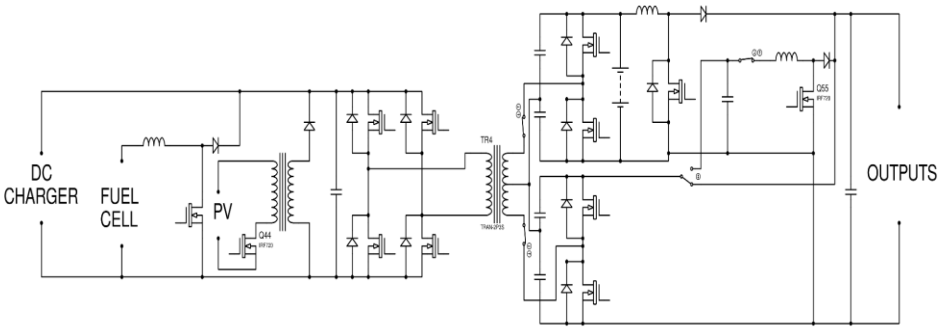

Figure 8. Circuit diagram of four port DC-DC converter; modified from [27]

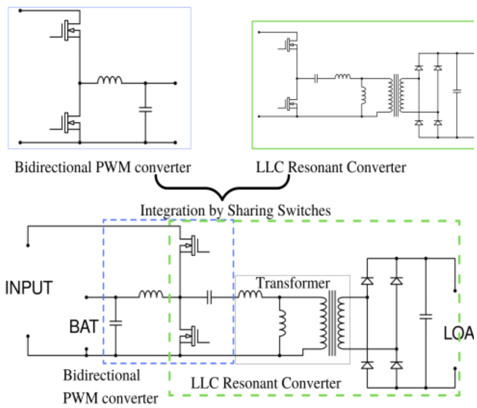

Figure 9. Derivation of conventional partially isolated MPC from the integration of bidirectional PWM converter and LLC resonant converter; modified from [7]

V. FINAL CONSIDERATIONS

Recent papers on multiport dc-dc converters and their applications were analyzed in this review. A wide variety of topologies can be divided into three large groups depending on their isolation: fully isolated, partially isolated, and non-isolated. This variability is a consequence of the different applications and their needs. According to literature, multiport converters have a reduced size with a higher power density and greater efficiency when compared to traditional converters. Thus, to reduce the sizes of multiport converters, a high switching frequency can be used to reduce the sizes of transformers and magnetic components.

REFERENCES

[1] Panwar, N. L., Kaushik, S. C., & Kothari, S. (2011). Role of renewable energy sources in environmental protection: A review. *Renewable and sustainable energy reviews*, *15*(3), 1513-1524.

[2] Lowitzsch, J. (2019). Investing in a renewable future–renewable energy communities, consumer (Co-) ownership and energy sharing in the clean energy package. *Renewable Energy Law and Policy Review*, *9*(2), 14-36.

[3] Burmester, D., Rayudu, R., Seah, W., & Akinyele, D. (2017). A review of nanogrid topologies and technologies. *Renewable and sustainable energy reviews*, *67*, 760-775.

[4] Dhananjaya, M., & Pattnaik, S. (2022). Review on multi-port DC–DC converters. *IETE Technical Review*, *39*(3), 586-599.

[5] Sato, Y., Uno, M., & Nagata, H. (2019). Nonisolated multiport converters based on integration of PWM converter and phase-shift-switched capacitor converter. *IEEE Transactions on Power Electronics*, *35*(1), 455-470.

[6] Uno, M., Sato, M., Tada, Y., Iyasu, S., Kobayashi, N., & Hayashi, Y. (2022). Partially Isolated Multiport Converter With Automatic Current Balancing Interleaved PWM Converter and Improved Transformer Utilization for EV Batteries. *IEEE Transactions on Transportation Electrification*, *9*(1), 1273-1288.

[7] Uno, M., Oyama, R., & Sugiyama, K. (2018). Partially isolated single-magnetic multiport converter based on integration of series-resonant converter and bidirectional PWM converter. *IEEE Transactions on Power Electronics*, *33*(11), 9575-9587.

[8] Ebadpour, M. (2021, February). A Multiport Isolated DC-DC Converter for Plug-in Electric Vehicles Based on Combination of Photovoltaic Systems and Power Grid. In *2021 12th Power Electronics, Drive Systems, and Technologies Conference (PEDSTC)* (pp. 1-5). IEEE.

[9] Uno, M., & Sugiyama, K. (2018). Switched capacitor converter based multiport converter integrating

bidirectional PWM and series-resonant converters for standalone photovoltaic systems. *IEEE Transactions on Power Electronics*, *34*(2), 1394-1406.

[10] Herrera, M. A., & Balal, A. (2021, October). Implementing Multilevel Inverters and Multiport DC-DC Converters for Microgrids. In *2021 IEEE 18th International Conference on Smart Communities: Improving Quality of Life Using ICT, IoT and AI (HONET)* (pp. 61-65). IEEE.

[11] Li, W., Xiao, J., Zhao, Y., & He, X. (2011). PWM plus phase angle shift (PPAS) control scheme for combined multiport DC/DC converters. *IEEE Transactions on Power Electronics*, *27*(3), 1479-1489.

[12] Pinto, J. G., Monteiro, V., Gonçalves, H., & Afonso, J. L. (2013). Onboard reconfigurable battery charger for electric vehicles with traction-to-auxiliary mode. *IEEE Transactions on vehicular technology*, *63*(3), 1104-1116.

[13] Wu, H., Sun, K., Ding, S., & Xing, Y. (2012). Topology derivation of nonisolated three-port DC–DC converters from DIC and DOC. *IEEE Transactions on Power Electronics*, *28*(7), 3297-3307.

[14] Zhang, Y., He, J., & Ionel, D. M. (2019, June). Modeling and control of a multiport converter based EV charging station with PV and battery. In *2019 IEEE Transportation electrification conference and EXPO (ITEC)* (pp. 1-5). IEEE.

[15] Khan, O., Hredzak, B., & Fletcher, J. E. (2022, June). A Reconfigurable Multiport Converter for Grid Integrated Hybrid PV/EV/Battery System. In *2022 IEEE 16th International Conference on Compatibility, Power Electronics, and Power Engineering (CPE-POWERENG)* (pp. 1-6). IEEE.

[16] Roy, P., He, J., & Cramer, A. (2021, October). Three-Port Multilevel Converter for Hourly Dispatching Solar PV Power with Battery Energy Storage System. In *2021 IEEE Energy Conversion Congress and Exposition (ECCE)* (pp. 489-496). IEEE.

[17] Sanders, S. R., Alon, E., Le, H. P., Seeman, M. D., John, M., & Ng, V. W. (2012). The road to fully integrated DC–DC conversion via the switched-capacitor approach. *IEEE Transactions on Power Electronics*, *28*(9), 4146-4155.

[18] Uno, M., & Kukita, A. (2018). PWM switched capacitor converter with switched-capacitor-inductor cell for adjustable high step-down voltage conversion. *IEEE Transactions on Power Electronics*, *34*(1), 425-437.

[19] Jiya, I. N., Van Khang, H., Kishor, N., & Ciric, R. M. (2022). Novel family of high-gain nonisolated multiport converters with bipolar symmetric outputs for DC microgrids. *IEEE Transactions on Power Electronics*, *37*(10), 12151-12166.

[20] Mohapatra, S., & Mohapatro, S. (2021, December). Non-Isolated Bidirectional Multiport Converter for LVDC Microgrid. In *2021 National Power Electronics Conference (NPEC)* (pp. 01-06). IEEE.

[21] Han, D., Noppakunkajorn, J., & Sarlioglu, B. (2014). Comprehensive efficiency, weight, and volume comparison of SiC-and Si-based bidirectional DC–DC converters for hybrid electric vehicles. *IEEE Transactions on vehicular technology*, *63*(7), 3001-3010.

[22] Ding, S., Wu, H., Xing, Y., Fang, Y., & Ma, X. (2013, March). Topology and control of a family of non-isolated three-port DC-DC converters with a bidirectional cell. In *2013 Twenty-Eighth Annual IEEE Applied Power Electronics Conference and Exposition (APEC)* (pp. 1089-1094). IEEE.

[23] Sivasankar, N., & Devabalaji, K. R. (2022, February). Smart Multiport Bidirectional Non-Isolated DC-DC Converter for Solar PV-Battery Systems. In *2022 First International Conference on Electrical, Electronics, Information and Communication Technologies (ICEEICT)* (pp. 1-8). IEEE.

[24] Haghighian, S. K., Tohidi, S., Feyzi, M. R., & Sabahi, M. (2017). Design and analysis of a novel SEPIC-based multi- input DC/DC converter. *IET Power Electronics*, *10*(12), 1393-1402.

[25] Alhatlani, A., & Batarseh, I. (2019, October). Review of Partially Isolated Three-Port Converters for PV-Battery Systems That Interface a PV, Bidirectional Battery, and Load. In *2019 IEEE Conference on Power Electronics and Renewable Energy (CPERE)* (pp. 465-472). IEEE.

[26] Qian, Z., Abdel-Rahman, O., & Batarseh, I. (2010). An integrated four-port DC/DC converter for renewable energy applications. *IEEE Transactions on Power Electronics*, *25*(7), 1877-1887.

[27] Vahid, S., & Ayman, E. R. (2020, October). A novel topology for an extendable isolated DC-DC multi-port power converter with a multipurpose hybrid energy storage system. In *2020 IEEE Energy Conversion Congress and Exposition (ECCE)* (pp. 1259-1266). IEEE.

[28] Vahid, S., & El-Refaie, A. (2020, February). Generalized systematic approach applied to design a novel three-port power converter. In *2020 IEEE International Conference on Industrial Technology (ICIT)* (pp. 542-548). IEEE.

[29] Vahid, S., & El-Refaie, A. (2020, December). A Generalized Systematic Approach to Design a Multi-Port Power Converter, to be presented at *International Conference on Power Electronics, Machines and Drives (PEMD)* 2020, Nottingham, UK. IEEE.

[30] Sato, M., Tada, Y., & Uno, M. (2020, October). Multi-Port Converter Integrating Automatic Current Balancing Interleaved PWM Converter and Dual Active Bridge Converter with Improved Transformer Utilization. In *IECON 2020 The 46th Annual Conference of the IEEE Industrial Electronics Society* (pp. 1377-1382). IEEE.

Numerical Study of the Melting Process of Phase Change Material Inside a Latent Heat Storage Unit Partially Filled with a Metal Matrix

Manal Hariss[1], Ayoub Gounni[2], Mustapha El Alami[3]

[1,2,3]LPMAT Laboratory, Université Hassan 2, FSAC, Km8 Casablanca, Marocco

Abstract—**To bridge the gap between energy supply and demand, thermal energy storage utilizing Phase Change Materials (PCMs) can be employed. The key factor impeding their broad use is the poor thermal conductivity of PCMs, which causes the systems to have sluggish energy storage and recovery rates. To shorten the melting time of a phase change material, PCM(n-eicosane), a honeycomb structure was used in this work to depict a two-dimensional numerical simulation. Investigations focused on the phase change behavior of a two-dimensional rectangular thermal storage unit that included PCM and a honeycomb structure HCS that partially filled the tank. The current study represents a comparative analysis of the thermal behavior during the melting process in a rectangular enclosure filled with (Pure PCM only, Bottom, and top HCS configurations) subjected to a constant heat flux. Thanks to the solidification/melting module of the commercial CFD software, which is based on the enthalpy-porosity model, the modeling is based on a transient calculation that enables analysis of the phase change of eicosane. For each of the three configurations, the development of the liquid fraction is addressed. The use of partly filled honeycomb structures (HCS) enhances thermal performance within the storage unit, according to numerical results. The implementation of top-HCS configuration results in the best decrease in overall melting time.**

Keywords - latent heat storage, PCM, melting, enhancement technique, honeycomb structure

I. INTRODUCTION

Thermal energy storage (TES) has seen widespread use of latent heat thermal energy storage (LHTES) systems utilizing liquid-solid phase change. These are triggered by the high storage density in a small volume, the wide range of melting temperatures of phase change materials, and the broad latent heat of fusion (PCMs). However, the limited heat conductivity of these organic PCMs is a clear drawback. This limited thermal conductivity prevents LHTES from responding quickly to thermal absorption and dissipation, which restricts their ability to be used widely.

Effective thermal conductivity enhancers (TCE) must be used effectively to improve heat transport in PCMs[1]. Fins [2], encapsulations [3], nanoparticles [4], and metallic foams [5][6], are the most often utilized TCEs.

The use of a metal matrix with excellent thermal conductivity embedded in PCM appeared to significantly increase the total energy transfer rate because of the extremely high surface area to volume ratio. Metal matrix-based augmentation for speeding the phase change rate of PCMs has been the subject of a considerable number of studies. The effect of metal foam porosity on the heat transfer procedure was examined experimentally and numerically by [7]. According to research, the outcomes of the experiment and mathematical analysis were largely consistent. Additionally, the melting of PCMs can be accelerated more effectively for metal foams with high porosity. The use of copper foam and aluminum wire as woven foam in phase change procedures was described by Prasanth et al.[8]. When the PCM was filled with copper foam or aluminum wire woven foam, they claimed there was minimal change in the melting time. In a two-dimensional rectangular tube, Sheng and Xing [9] simulated the melting processes of PCMs with or without metal foam filling. They discovered that metal foam improved PCM conductivity and the heat storage system's capacity. Additionally, Lei et al. [10] investigated the effect of foamed copper with various porosities on heat transfer. They discovered that the performance of heat storage was greatly enhanced by the use of copper foam. The total melting time as well as the average heat flow for the case with varying porosity reduced by 6.8% and increased by 4.3%, respectively, when compared to the constant porosity.

The present study takes into consideration a metal matrix construction because of its excellent/robust performance in boosting heat transmission. To enhance the heat transfer rate, we propose a numerical study based on the numerical simulation of the charging process of a phase change material within a rectangular enclosure of two different partially-filled configurations. A comparison with a reference case was done

II. NUMERICAL PROCEDURE

A. *Assumptions*

The transient two-dimensional model of heat transfer during the PCM melting process was governed by the following general assumptions:

- The thermophysical properties of PCM are constant for the temperature.
- The fluid is Newtonian and incompressible;
- We neglect convection in the liquid phase due to the great value of the PCM viscosity.

B. *Heat Equation*

The only mode of heat transfer considered during the fusion process is conduction. The effects of natural convection at the solid-liquid interface are neglected. The guiding equation considered here is the classical heat equation:

$$\rho C_p \frac{\partial T}{\partial t} + div(-k\overrightarrow{\nabla T}) = 0\,. \qquad (1)$$

C. *Discretization Method*

A two-dimensional transient model based on the finite volume method using an enthalpy-porosity technique is implemented to analyze the performance of a thermal energy storage unit within a rectangular metal matrix enclosure.

The CFD method was used to solve and calculate the governing equations. The Second Order Upwind scheme and the SIMPLE method for pressure-velocity coupling are used to solve the momentum and energy equations. The "Second-order" scheme is also adopted for the pressure correction equation.

III. VALIDATION

To ensure the accuracy of the current numerical approach, the average liquid fraction is verified with the experimental results of H.Shokouhmand, B. Kamkari [11]. The lauric acid is filled into a rectangular enclosure with an inside dimension of 120 mm in height and 50mm in width & depth. The PCM is initially at a constant temperature of 299 K. The right wall of the cavity is subjected to a constant temperature (70°C) while adiabatic boundary conditions are set on the other walls. Fig. 1 depicts a comparison of numerical results (present study) and experimental results of melt fraction variation for a constant temperature. It can be seen that the numerical model is very consistent with the experiment results.

The need to better understand the heat transfer of the thermal energy storage system during the charging phase, which makes use of the latent heat of PCM melting, is the motivating factor behind this research.

We present a similar comparison of three configurations (as seen in Fig. 2) under the same boundary conditions.

A. *Studied Configuration*

In the current study, the latent heat thermal energy storage system is a two-dimensional rectangular enclosure filled with PCM that was

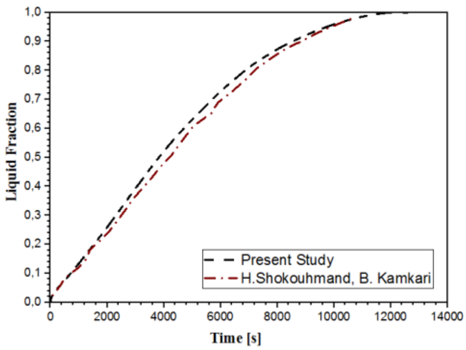

Figure 1. Comparison of numerical results (present study) and experimental results (H.Shokouhmand, B. Kamkari [11]).

initially in a solid state. Eicosane was deployed as the phase-change material. A partly filled metal matrix was incorporated to increase the rate of heat transfer during the charging process. SolidWorks software was used to represent the honeycomb structure as a distinct domain. Three different configurations are examined to better understand the phase change behavior of partly honeycomb structures contained in a rectangular container. The specific structure is illustrated in Fig. 2. The PCM's starting temperature was adjusted to be just a little below the melting point, therefore the liquid phase percentage was set at 0 (298 K).

A predetermined convection condition was applied to the top horizontal wall of the two-dimensional model (Fig. 2), while the left and right sides (shown in red color) were adjusted to adiabatic conditions. The bottom wall of the model was subjected to continuous heat flow.

In this study, an aluminum honeycomb structure was adopted; Table I. represents the thermo-physical properties of aluminum used in the numerical model. The phase change material used in this study is eicosane. Table II. represents the different thermophysical properties used in the numerical simulation.

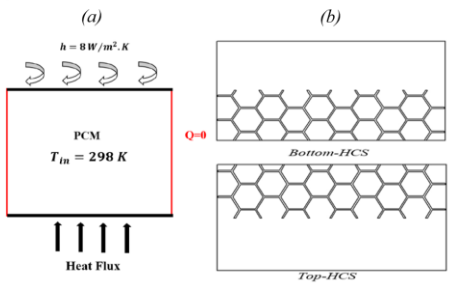

Figure 1. Schematic of the computational region (a) thermal boundary condition and dimension (b) two partially-filled HCS scenarios.

TABLE I. THERMOPHYSICAL PROPERTIES OF ALUMINUM USED IN THE NUMERICAL MODEL.

Property	Units	Value
ρ	kg/m^3	2719
λ	$W/m.K$	202.2
C_p	$J/kg.K$	871

TABLE II. THERMOPHYSICAL PROPERTIES OF EICOSANE [12].

Property	Units	Value
ρ	kg/m^3	790
λ	$W/m.K$	0.23
L	J/kg	241000
C_p	$J/kg.K$	2050
β	$1/K$	0.0001
μ	$kg/m.s$	0.00355
T_m	K	309.5
T_s	K	308.5
T_l	K	310.5

B. *Phase Change Interface*

The following image represents the shape and movement of the fusion interface over time. First, I would like to point out that the color blue and red represent the condition when the material is completely solid and liquid, respectively. We notice that the first stages of the charging process start from the zone which is near to the source. For the three studied configurations the PCM in the honeycomb structure melt more quickly whatever the position of the metal matrix. This makes it possible to say that this structure can increase the exchange surface and improve heat transfer within the latent storage system. Fig. 3 (b) and (c) represent the evolution of the solid-liquid interface when the metal matrix is at the bottom, and top respectively.

It was observed that before the 2000s, the evolution of the phase change is faster for the second configuration, i.e., the bottom honeycomb structure compared to the other configuration, the configuration that contains only pure PCM and top HCS. This is explained by the fact that the metal matrix is mainly located in the lower half; therefore the heat transfer is boosted in this area. However, for the time between the 2000s and 4000s. The charging process is faster for the Top-HCS configuration because of the presence of the honeycomb structure in the upper half, while the same area contains only pure PCM in the other configurations.

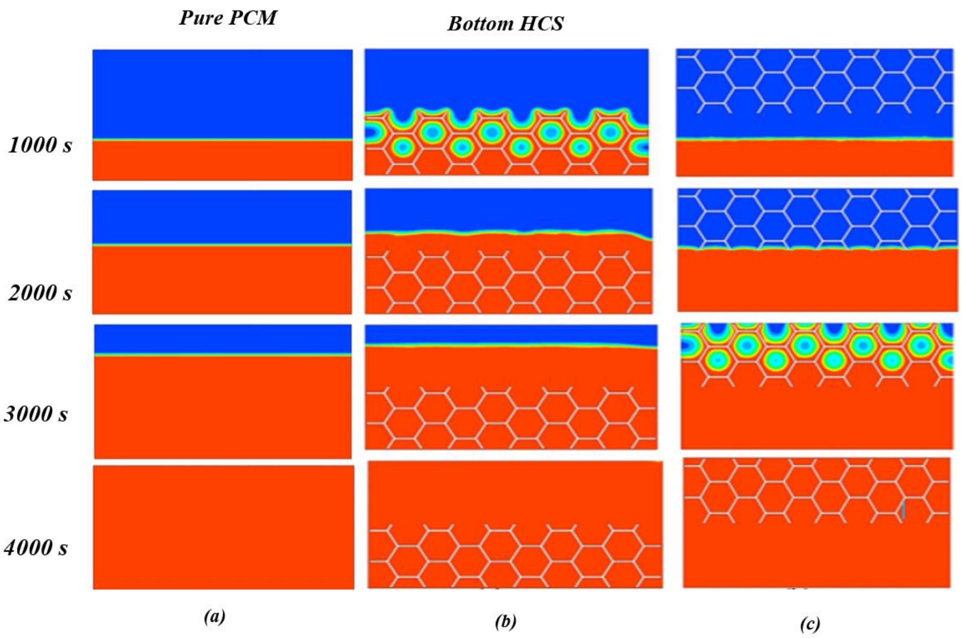

Figure 3. Graphic representation of the spatial distribution of the liquid fraction (= 1, red, in the fluid; = 0, blue, in the solid).

C. Evolution of the Liquid Fraction

The liquid fraction is a typical dimensionless parameter that characterizes the charging characteristic of a latent heat storage unit. Fig. 4 depicts the variation of liquid fraction for eicosane in a rectangular enclosure with two partially filled honeycomb structure scenarios and a comparison with a reference case. The impregnation of the honeycomb matrix makes it possible to reduce the complete melting time by 3.77%, and 11.11% for the bottom and right configurations, respectively.

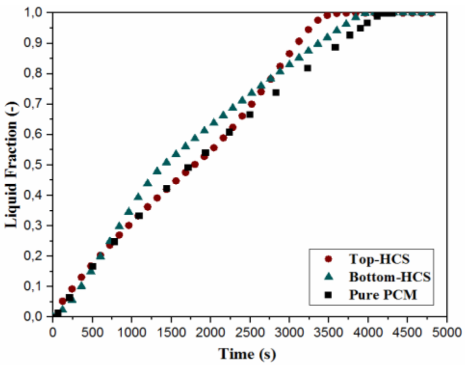

Figure 4. Evolution of liquid fraction.

IV. Conclusion

The suggested research tries to comprehend the phenomena of heat energy transfer in rectangular enclosures with honeycomb structures partially filled in. On the one hand, the numerical outcomes produced by the CFD Software for the three configurations under investigation demonstrate that the phenomenology of phase changes is the same. One test can only be distinguished from another by its computed characteristic time (slower). The introduction of the honeycomb structure, on the other hand, is similar to boosting and enhancing the system's performance. especially if the enclosure's top part contains the HCS. We came to the conclusion that the honeycomb matrix impregnation allows for a reduction in the total melting time of 3.77% for the bottom configuration and 11.11% for the right configuration.

References

[1] Hariss, M., Gounni, A., & El Alami, M. (2022). A practical guide on numerical and experimental investigations of solid-liquid phase-change heat transfer using some heat transfer enhancement techniques: Case study in Morocco. *Journal of Energy Storage, 52*, 105070.

[2] Khedher, N. B., Ghalambaz, M., Alghawli, A. S., Hajjar, A., Sheremet, M., & Mehryan, S. (2022, July). Study of tree-shaped optimized fins in a heat sink filled by solid-solid nanocomposite phase change material. I*nternational Communications in Heat and Mass Transfer, 136*, 106195.

[3] Fukahori, R., Nomura, T., Zhu, C., Sheng, N., Okinaka, N., & Akiyama, T. (2016, May). Macro-encapsulation of metallic phase change material using cylindrical-type ceramic containers for high-temperature thermal energy storage. *Applied Energy, 170*, 324–328.

[4] Sun, H., Khalifa, N. T., Saad, H. A., Othman, H. A., Hussin, A. M., & Helmi, M. M. (2022, October). Investigation of behavior of heat storage system including paraffin with involving MWCNT nanoparticles. *Journal of Energy Storage, 54*, 105250.

[5] Liu, G., Xiao, T., Wei, P., Meng, X., Yang, X., Yan, J., & He, Y. L. (2023, January). Experimental and numerical studies on melting/solidification of PCM in a horizontal tank filled with graded metal foam. *Solar Energy Materials and Solar Cells, 250*, 112092.

[6] Hariss, M., El Alami, M., & Gounni, A. (2021, September). Role of honeycomb structure in improving the melting process of a phase change material inside a latent heat storage unit. *Renewable Energy and Power Quality Journal, 19*, 589–592.

[7] Huang, X., Sun, C., Chen, Z., & Han, Y. (2021, December). Experimental and numerical studies on melting process of phase change materials (PCMs) embedded in open-cells metal foams. *International Journal of Thermal Sciences, 170*, 107151.

[8] Prasanth, N., Sharma, M., Yadav, R. N., & Jain, P. (2020, December). Designing of latent heat thermal energy storage systems using metal porous structures for storing solar energy. *Journal of Energy Storage, 32*,

[9] Shu, G., Xiao, T., Guo, J., Wei, P., Yang, X., & He, Y. L. (2023, February). Effect of charging/discharging temperatures upon melting and solidification of PCM-metal foam composite in a heat storage tube. I*nternational Journal of Heat and Mass Transfer, 201*, 123555.

[10] Lei, J., Tian, Y., Zhou, D., Ye, W., Huang, Y., & Zhang, Y. (2021, June). Heat transfer enhancement in latent heat thermal energy storage using copper foams with varying porosity. *Solar Energy, 221*, 75–86.

[11] Shokouhmand, H., & Kamkari, B. (2013, October). Experimental investigation on melting heat transfer characteristics of lauric acid in a rectangular thermal storage unit. *Experimental Thermal and Fluid Science, 50*, 201–212.

[12] Arshad, A., Jabbal, M., Sardari, P. T., Bashir, M. A., Faraji, H., & Yan, Y. (2020, August). Transient simulation of finned heat sinks embedded with PCM for electronics cooling. *Thermal Science and Engineering Progress, 18*, 100520.

First-principles Study of Optoelectronic and Transport Properties of BCs_3Pn_2 (Pn= P, As) Materials for Solar Cells Applications

Fakhereddine Khemloul[1], Mohamed Halit[2], Abdennour Benmakhlouf[3], Said Maabed[4], Mohamed Bouchenafa[5], Naceur Selmane[6]

[1,2,3,4,5]Laboratoire pour Application et Valorisation des Energies Renouvelables (LMAVER), Laghouat, Algeria
[6]Laboratoire Matériaux, Systèmes Énergétiques, Énergies Renouvelables et Gestion de l'Énergie (LMSEERGE) Boulevard des Martyrs, Laghouat, Algeria

Abstract—**By using density-functional theory (DFT) based first-principles calculations, we have systematically investigated the structural, electronic and optical properties of the alkali metal dipnictidoborates $BCs_3Pn_2\left(Pn = P, As\right)$. Both compounds are predicted to be indirect gap semiconductors of 1.82 eV and 1.94 eV respectively. Moreover, the optical spectra of $BCs_3Pn_2\left(Pn = P, As\right)$ obtained from the Heyd-Scuseria-Erzenhof hybrid functional (HSE06) demonstrate strong anisotropy between different light polarizations. Our findings reveal that the $BCs_3Pn_2\left(Pn = P, As\right)$ is an attractive candidate for optoelectronic applications as it is a semiconductor with an indirect band gap, a relatively high carrier mobility, and strong optical absorption energy in the visible light range. Our studies provide a better understanding of electronic and optical properties of dipnictidoborates $BCs_3Pn_2\left(Pn = P, As\right)$ and might shed light on their potential electronic and optoelectronic applications.**

Keywords - first-principles calculation, optical properties, dipnictidoborates, electronic structures, effective masses

I. Introduction

Photovoltaics and photochemical systems have received a lot of interest in recent years as clean and sustainable energy sources. The semiconductors used in these systems have a variety of properties, including a low band gap (generally less than 3 eV, which falls within the visible spectrum), a low effective mass ($m^* < 0.5m_0$) and strong optical absorption of $10^4\,cm^{-1}$ in the visible region [1].

The alkali metal dipnictidoborates BM_3Pn_2 (*M* = alkali metal, *Pn* = pnictides) are fascinating materials with excellent physicochemical properties. Many of them are known to be semiconductors with gaps varying between 1.2 eV and 1.9 eV and an onset optical absorption energy in the visible light range [2-4]. In this context, the ternary dipnictidoborates BM_3Pn_2 (*M* = alkali metal, *Pn* = pnictides) are very likely to show a wide range of application in various opto-electronic devices including solar energy conversion, infrared lasers, light-emitting diodes (LEDs) and photocatalysts for solar water splitting.

Herein, the structural, electronic, charge transport and optical properties of $BCs_3Pn_2\left(Pn = P, As\right)$ have been studied as a member of the BM_3Pn_2 family. The aim of the present work is to determine the suitability of these materials for photovoltaic applications.

II. COMPUTATIONAL DETAILS

Ab-initio calculations are performed using pseudopotential plane–wave (PP-PW) method in the framework of density functional theory (DFT) as implemented in CASTEP (Cambridge Serial Total Energy Package) software [5]. The GGA-PBE (generalized gradient approximation of the Perdew–Burke–Ernzerhof) functional is used for the exchange correlation term [6]. The plane wave cutoff energy was set to 450 eV and the Brillouin zone (BZ) was sampled on a $4 \times 4 \times 4$ Monkhorst–Pack.

As it is well known that the standard semi local GGA approximation underestimates the band gaps of semiconductors, we employ the more accurate HSE06 (nonlocal exchange with the Heyd-Scuseria-Erzenhof hybrid functional) [7] approach to calculate the electronic band structures.

III. RESULTS AND DISCUSSION

A. *Structural Properties*

The alkali metal dipnictidoborates $BCs_3Pn_2\left(Pn = P, As\right)$ compounds crystallize in a monoclinic structure, space group $C2/c$ (No.15), with two formula units per unit-cell $\left(Z = 2\right)$. Its asymmetric unit contains two crystallography independent alkaline metal atoms (Caesium), one Boron atom and one Phosphid (Arsenide) atom. Structures for these systems are shown in Fig. 1.

The obtained equilibrium lattice parameters (a, b and c) and unit cell volume are reported in Table I along with the available experimental data for comparison. What is interesting in the data obtained in this study by the GGA-PBE approximation is the fairly good agreement with the experimental values. The error is generally less than 2% for both compounds.

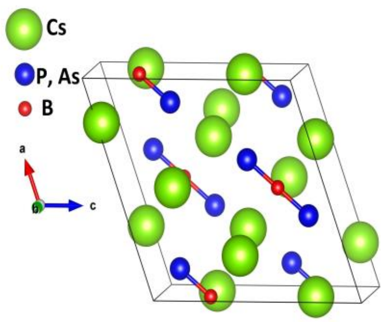

Figure 1. Crystal structure of BCs_3Pn_2 (Pn= P, As).

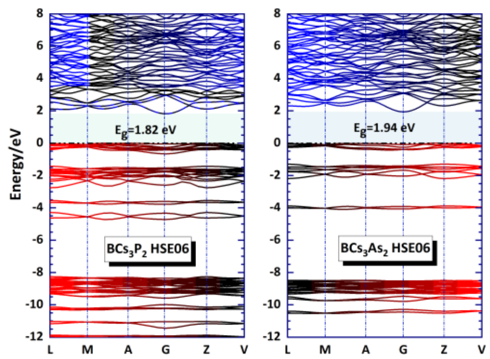

Figure 2. Calculated band structure for BCs_3Pn_2.

TABLE I. CALCULATED STRUCTURAL PARAMETER.

Structural parameters		Dipnictidoborates	
		BCs_3P_2	BCs_3As_2
Unit-cell parameters	a (Å)	9.77[a], 9.83[b]	9.98[a], 10.05[c]
	b (Å)	9.80[a],9.67[b]	9.85[a],9.87[c]
	c (Å)	9.95[a], 9.86[b]	10.03[a], 10.17[c]
Cell volume		891.4[a], 882.7[b]	922.2[a], 944.7[c]
Density		3.513[a], 3.548[b]	4.028[a], 3.931[c]

[a]this work. [b][3]. [c][4].

B. *Electronic Properties*

In this section, we discuss the electronic properties of $BCs_3Pn_2\left(Pn = P, As\right)$ compounds from both the electronic band structure and density of states point of view.

The calculated electronic band structures performed by the HSE06 hybrid functional method for BCs_3P_2 and BCs_3As_2 are shown in Fig. 2. As it can be seen from Fig. 2, the investigated compounds show the same features. It can also be seen from this figure that the conduction band minimum (CBM) locates at the gamma point, and the valence band maximum (VBM) locates along the M - A direction, which clearly depicts that these materials are indirect band gap semiconductors. The calculated HSE06 band gaps values for BCs_3P_2 (1.82) and BCs_3As_2 (1.94) are ideal for photovoltaic applications.

The analysis of the total and partial density of states (Fig. 3) close to the Fermi level suggests that the upper part of the valence bands arises mainly from the pnictide (P, As) atom states with a contribution of Cs states. Whereas the conduction band is predominantly occupied by the Cs states and some contributions from B and As atoms can be seen respectively.

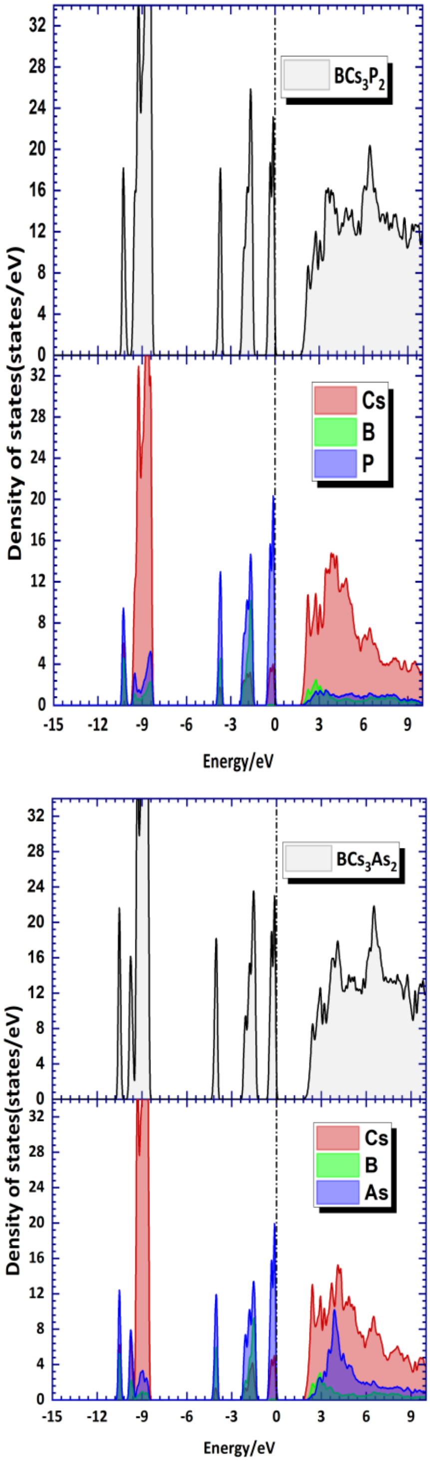

Figure 3. Total and partial density of states for the BCs_3Pn_2 (Pn= P, As) compounds.

TABLE II. EFFECTIVE MASS IN M_0 FOR BCs_3PN_2 (PN=P, AS).

System	Efective mass	
	Electron	***Hole***
BCs_3P_2	0.38	0.22
BCs_3As_2	0.72	0.32

C. *Effective Masse*

The value of electron effective mass at CBM and hole effective mass at the VBM can be found from the curvature of respective bands. The calculated effective masses for the investigated materials for $BCs_3Pn_2\left(Pn = P,\ As\right)$ are reported in Table II. As can be seen from the table, the electron effective masses are greater than hole effective masses for both studied compounds, which leads us to classify these semiconductors as n-type conducting materials.

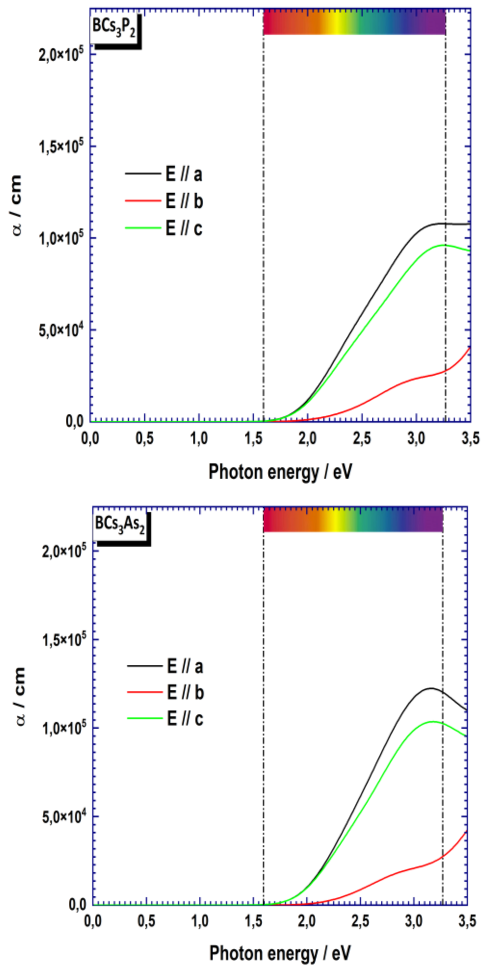

Figure 4. Absorption coefficient of BCs_3Pn_2 (Pn= P, As) compounds.

When compared with the conventional semiconductors $BCs_3Pn_2\left(Pn = P,\ As\right)$ have significantly small effective mass value, making them promising materials for electronic devices.

D. Optical Properties

The optical absorption spectrum of $BCs_3Pn_2\left(Pn = P,\ As\right)$ along all polarization directions is shown in Fig. 4. It is noteworthy that the optical absorption shows significant anisotropy where the light is absorbed more strongly along a and b axis polarizations. Besides, the absorption coefficient is seen to quickly exceed $10^5 cm^1$ after surpassing the value of the bandgap. This behavior of rapid increase of the absorption coefficient at energies above the bandgap is comparable to that of conventional photovoltaics inorganic materials such as Si, CdTe, $CuInGaSe_2$, and GaAs, which are widely used for solar cells. For this reason, these materials could be useful in photovoltaic applications.

IV. CONCLUSION

In summary, we have systematically investigated the structural, electronic and optical properties of the alkali metal dipnictidoborates $BCs_3Pn_2\left(Pn = P,\ As\right)$ using density-functional theory. This study predicts that the ternary $BCs_3Pn_2\left(Pn = P,\ As\right)$ semiconductors could be suitable for photovoltaic solar cell and optoelectronic devices.

ACKNOWLEDGMENT

Financial support by Université Amar Telidji de Laghouat, Algeria, is acknowledged.

REFERENCES

[1] Jodlowski, A., Rodríguez‐Padrón, D., Luque, R., & de Miguel, G. (2018). Alternative perovskites for photovoltaics. *Advanced Energy Materials*, *8*(21), 1703120.

[2] Somer, M., Carrillo‐Cabrera, W., Peters, K., & Schnering, H. G. V. (2000). Darstellung, Kristallstrukturen und Schwingungsspektren von Verbindungen mit den linearen Dipnictidoborat (3−)‐Anionen [P−B−P] 3−,[As−B−As] 3−und [P−B−As] 3−. *Zeitschrift für anorganische und allgemeine Chemie*, *626*(4), 897-904.

[3] Somer, M., Popp, T., Peters, K., & von Schnering, H. G. (1990). Crystal structure of caesium diphosphidoborate, Cs_3 (BP_2). *Zeitschrift für Kristallographie-Crystalline Materials*, *193*(3-4), 297-298.

[4] Somer, M., Popp, T., Peters, K., & von Schnering, H. G. (1990). Crystal structure of caesium diarsenidoborate, Cs_3 (BAs_2). *Zeitschrift für Kristallographie-Crystalline Materials*, *193*(3-4), 295-296.

[5] Clark, S. J., Segall, M. D., Pickard, C. J., Hasnip, P. J., Probert, M. I., Refson, K., & Payne, M. C. (2005). First principles methods using CASTEP. *Zeitschrift für kristallographie-crystalline materials*, *220*(5-6), 567-570.

[6] Perdew, J. P., Burke, K., & Ernzerhof, M. (1998). Perdew, burke, and ernzerhof reply. *Physical Review Letters*, *80*(4), 891.

[7] Heyd, J., Scuseria, G. E., & Ernzerhof, M. (2003). Hybrid functionals based on a screened Coulomb potential. *The Journal of chemical physics*, *118*(18), 8207-8215.

Wind-PV Energy Harvesting for Critical Loads Supported by Electric Spring

Arunava Chatterjee[1], Soumyajit Ghosh[2]

[1]Electrical Engineering Department, Raghunathpur Govt. Polytechnic, India
[2]Electrical Engineering Department, IIT Kanpur, India

Abstract—**Electric springs (ES) are usually employed to provide stable voltage across critical loads. This paper presents a new control strategy for controlling such an electric spring while supplying a critical load in a microgrid. The primary voltage source in the microgrid structure is a wind turbine and it is supported by a photovoltaic (PV) panel. The critical load is a rural health center which is set-up in a grid isolated area. The ES is controlled by a novel dynamic voltage loop-based controller. Suitable simulations backed by laboratory scale experiments substantiates the effectiveness of the proposed strategy.**

Keywords – electric spring, wind power, photovoltaic, microgrid, critical load

I. INTRODUCTION

Wind energy has become a major source of electrical energy especially for its use in grid-connected power systems [1]. Although it is also used for grid-isolated microgrid systems. It is imperative though to use suitable control strategies due to intermittent nature of wind-generation. Previously, wind energy was majorly used for suppling grid-connected loads [2-5] however, with the usage of power electronic devices, they are commonly used for supplying single-phase microgrids [6-8]. The chief demerit associated with wind generation is the voltage regulation problem and suitable control schemes are essential. This also is a major concern for supplying critical loads with only wind energy [9]. Hybrid generation is also another solution to the voltage regulation problem associated with wind energy. Commonly, solar photovoltaic (PV) source is used along with wind energy for supplying microgrids and such a system can be called as a hybrid generation system [10]. Besides PV, usage of hydro [11] and diesel [12] along with battery are also used commonly. However, PV alone can complement wind energy and thus it is a viable option [13].

For supplying critical loads nevertheless, there is always requirement of power irrespective of the generating conditions. Thus, a wind-PV hybrid source is a preferrable one. In this paper, an electric spring (ES) is used along with such hybrid generation for providing power continuity to the grid-isolated critical load [14]. Typically, the ES is connected in series with a non-critical load. This combination is connected in shunt to the critical load. The ES is controlled using a dynamic voltage reference-based control scheme which is detailed later.

II. PROPOSED SCHEME

For the proposed scheme, a wind turbine coupled to a three-phase induction generator is considered. The wind generation is supported by a PV panel. They are connected to a common DC bus using suitable converters.

In the proposed scheme, a common AC bus is considered where, the induction generator-based wind turbine generator (WTG), PV panel, electric spring in series with a non-critical load and the main critical load considered are connected. The critical load considered is mainly a rural health center with LED light bulbs, fans, refrigerator and incubator as loads. These loads will always be supplied from the bus. The non-critical load is a heating load which is connected in series with the electric spring. The proposed scheme is shown in Fig. 1.

ISBN: 978-86-82602-01-9

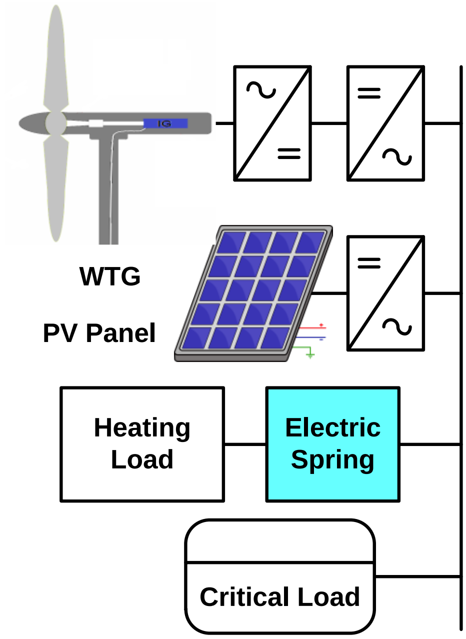

Figure 1. Proposed scheme.

III. Electric Spring Model

The concept of electric spring (ES) is resultant from mechanical spring model. The ES provides voltage support. Applying Hooke's Law, the mechanical spring elastic force is expressed as [15]:

$$F = -kx\,, \tag{1}$$

where, x is the compression/elongation and k is elastic constant. Potential in the spring is therefore,

$$W_m = -\frac{1}{2}kx^2\,. \tag{2}$$

Similarly, an electric spring uses capacitor for energy storage and is similarly expressed as:

$$W_e = -\frac{1}{2}CV^2\,. \tag{3}$$

Fig. 2 shows the model of the electric spring used for the proposed scheme. The ES model shown is also replicated in a laboratory environment after simulation. The ES is usually used in series with a non-critical load like a heating load alike water heater [16]. The same is also used as a utility in the health center as a heating load.

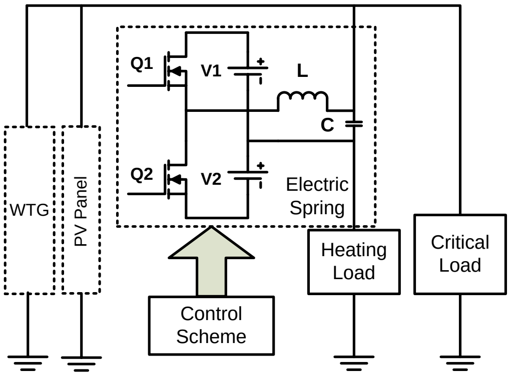

Figure 2. Electric Spring in system.

IV. Proposed System Control

In the proposed scheme, the critical load requires to be supplied at all times irrespective of the generating conditions. The chief impression behind the ES control is transmission of the voltage fluctuation arising due to renewable generation to the non-critical load and supply the critical load at constant voltage. Thus, for controlling the ES, the WTG voltage is sensed. The sensed voltage is compared with a dynamically set reference voltage based on wind speed. The calculated error is fed to a proportional-integral based controller.

The dynamically reference set voltage $V(\omega_r)$ selection is a unique feature of the control of the ES. Depending on the wind speed, the voltage reference and hence the voltage of the bus will be maintained at a constant level. The same is shown in Fig. 3.

When the bus voltage is greater than the reference, the ES will inject a voltage which will lead the non-critical current I_{NC} by 90 degrees. If the system voltage is less than reference, the ES injects a voltage which will lag I_{NC} by 90 degrees.

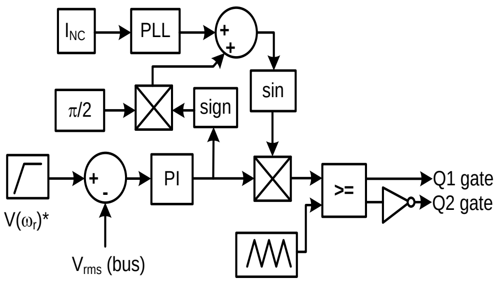

Figure 3. Proposed control scheme for ES.

Thus, the system voltage will be maintained by either absorbing or releasing reactive power dynamically depending on the reference.

The PV panel generation is controlled using incremental conductance based MPPT control for providing power to the bus. The bus frequency is maintained by operating the inverters at constant frequency.

V. Simulation and Experimental Results

The proposed system is simulated in *MATLAB/Simulink* platform. Later, the scheme is verified using a laboratory-based prototype with similar ratings for the devices used in simulation. A three-phase induction generator for the WTG is considered rated at 2kW, 415V, 50Hz and 4-poles in the stator. The PV panel is rated at 500 Watts-peak with output power mean at 130 Watts. The critical load consisting of the health center is rated at 550W at peak with around 7.7 kWh consumed per day. A simple water heater of 1kW is considered as a non-critical load. The IG generated voltage is shown in Fig. 4.

The system voltage is decreased as shown in Fig. 5(a). With the use of the use of ES, the critical load voltage is stable after dip at around 2s as seen from Fig. 5(b).

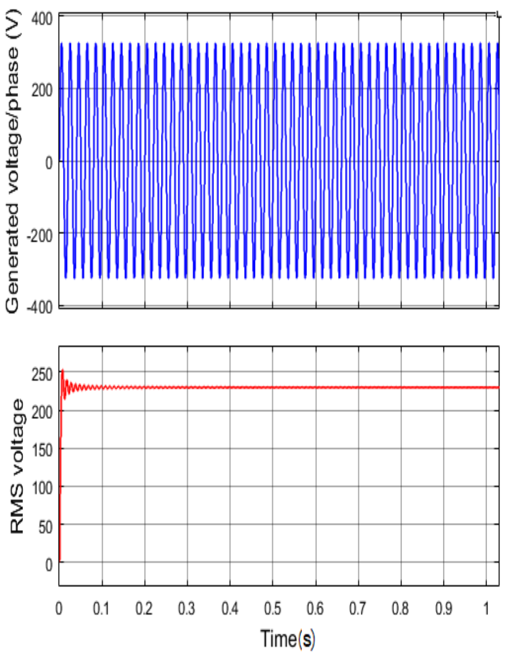

Figure 4. IG generated voltage.

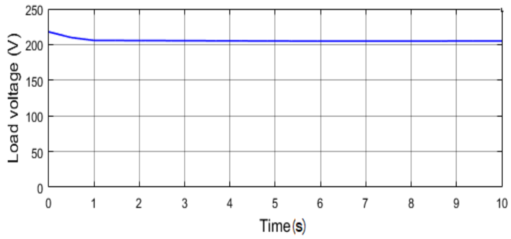

(a)

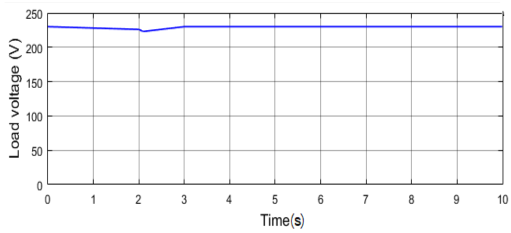

(b)

Figure 5. (a) Decreased system voltage (rms) (b) Critical load voltage with ES control.

The same can be seen when the system voltage increases, the critical load voltage is maintained at a constant level as shown in Fig. 6.

With the ES, the system critical load voltage profile becomes better even after fluctuations in generation. Fig. 7 below shows the experimental system voltage with the ES and without it. The fluctuations due to generation are removed with the use of ES as shown.

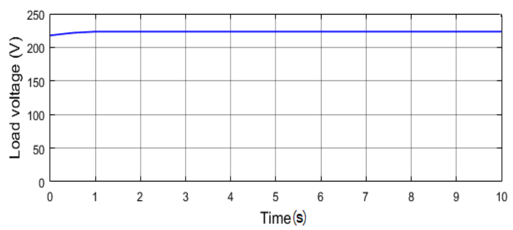

(a)

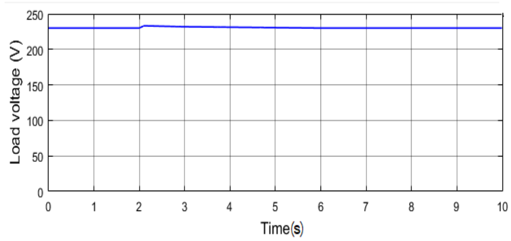

(b)

Figure 6. (a) Increased system voltage (rms) (b) Critical load voltage with ES control.

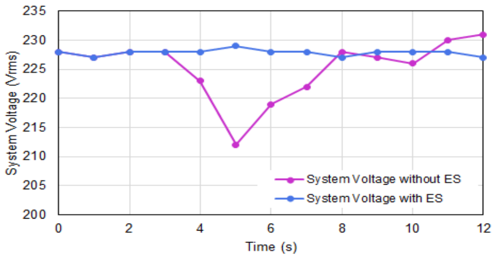

Figure 7. Experimental system voltage with and without ES.

VI. CONCLUSION

This paper presents a hybrid wind-PV based generation scheme supported by electric spring. The system is mainly aimed at operation in isolation from the main grid. The renewable generation mostly has fluctuations and it is stabilized by the use of the electric spring. The spring is controlled using a dynamic voltage-based control loop which is set using the available wind speed for supplying the critical loads connected. The proposed control of the ES can successfully support the load voltage fluctuations and the power profile is improved. In future, the control scheme can be improved to provide added load support and reduction of the load and wind speed transients can also be studied.

REFERENCES

[1] Patel, M. R. (2005). *Wind and solar power systems: design, analysis, and operation*. CRC press.

[2] Roy, K., Chatterjee, A., Chatterjee, D., & Ganguli, A. K. (2015). A photovoltaic-based improved excitation control strategy of three-phase self-excited induction generator suitable for wind power generation. *Electric Power Components and Systems*, *43*(17), 1912-1920.

[3] Bhatti, T. S., Bansal, R. C., & Kothari, D. P. (2003). A bibliographical survey on induction generators for application of non-conventional energy systems. *IEEE Trans. Energy Conversion*, *18*(3), 433-439.

[4] Bansal, R. C. (2005). Three-phase self-excited induction generators: an overview. *IEEE transactions on energy conversion*, *20*(2), 292-299.

[5] Vicatos, M. S., & Tegopoulos, J. A. (1989). Steady state analysis of a doubly-fed induction generator under synchronous operation. *IEEE Transactions on Energy Conversion*, *4*(3), 495-501.

[6] Chatterjee, A., & Chatterjee, D. (2016). Analysis and control of photovoltaic-assisted three-phase induction machine operating as single-phase micro-wind generator. *IET Generation, Transmission & Distribution*, *10*(9), 2165-2176.

[7] Chatterjee, A. (2022). Wind-PV based Generation with Smart Control Suitable for Grid-isolated Critical Loads in Onshore India. *Journal of The Institution of Engineers (India): Series B*, 1-11.

[8] Chatterjee, A., & Chatterjee, D. (2020). An improved current balancing technique of two-winding IG suitable for wind-PV-based grid-isolated hybrid generation system. *IEEE Systems Journal*, *14*(4), 4874-4882.

[9] Arthishri, K., Kumaresan, N., & Gounden, N. A. (2018). Analysis and application of three-phase SEIG with power converters for supplying single-phase grid from wind energy. *IEEE Systems Journal*, *13*(2), 1813-1822.

[10] Hirose, T., & Matsuo, H. (2011). Standalone hybrid wind-solar power generation system applying dump power control without dump load. *IEEE transactions on industrial electronics*, *59*(2), 988-997.

[11] Reznicek, E., & Braun, R. J. (2018). Techno-economic and off-design analysis of stand-alone, distributed-scale reversible solid oxide cell energy storage systems. *Energy Conversion and Management*, *175*, 263-277.

[12] Wang, C., Li, J., & Hu, Y. (2019). Frequency control of isolated wind-diesel microgrid power system by double equivalent-input-disturbance controllers. *IEEE Access*, *7*, 105617-105626.

[13] Chatterjee, A. (2022, February). Analysis of a wind-PV hybrid system with smart control for grid-secluded critical loads in onshore Indian area. In *Proceedings of International Conference on Industrial Instrumentation and Control: ICI2C 2021* (pp.495-503). Singapore: Springer Nature Singapore.

[14] Hui, S. Y., Lee, C. K., & Wu, F. F. (2012). Electric springs—A new smart grid technology. *IEEE Transactions on Smart Grid*, *3*(3), 1552-1561.

[15] Tang, N., Yang, K., Huang, H., & Chi-Kwan, L. (2018, June). The application of electric spring in grid-connected photovoltaic system. In *AIP Conference Proceedings* (Vol. 1971, No. 1, p. 040046). AIP Publishing LLC.

[16] Micallef, A., Ellul, R., & Licari, J. (2020, September). Electric Spring-based Smart Water Heater for Low Voltage Microgrids. In *2020 22nd European Conference on Power Electronics and Applications (EPE'20 ECCE Europe)* (pp. P-1). IEEE.

Demand Response Allocation based on the Customer Cost Function Considering Transmission Network Criteria in the Deregulated Power System

Behrouz Niroomandfam[1], Amir Niromandfam[2]

[1]Islamic Azad University, Miandoab, Iran
[2] Sahand University of Technology, Tabriz, Iran

Abstract—**Recently a massive focus has been made on demand response (DR) programs which have many positive effects such as electricity price reduction, transmission network problems resolving, reliability enhancement and improvement of power market performance. Considering the importance of customer's viewpoint as an essential tool to develop efficient demand side management strategies, this paper proposes a novel method to optimally select the DR resources location based on customer cost function. Existing utility data will be used to predict customer behavior and identity customer cost function versus load curtailment. The method is based on the constrained optimization of multi-objective function formed in terms of EENS (expected energy not supplied), active power loss, customer cost function, and electricity market price enhancement. This multi-objective function is then optimized by applying NSGA-II (non-dominated sorting genetic algorithm) to find the amount and locations of DR programs. Also incremental cost of DR programs will be introduced and calculated in this paper which specifies the value of one additional unit of load reduction in each bus. Further the proposed method can determine incentive payments based on customers' viewpoint which are used in incentive-based program (IBP). The IEEE 24 bus test system is used to demonstrate the effectiveness of the proposed method.**

Keywords - demand response, customer cost function, EENS, active power loss, NSGA-II

I. INTRODUCTION

Nowadays, the power system operation has become more competitive and many challenges will arise. In order to satisfy the reliability and economic criteria, both of the exciting electricity grid and generation units must be utilized more efficiently, or transmission network should be added which are often costly. Economic approach to solve above challenges becomes one of the major interests in power system studies. The use of demand response (DR) programs could be an effective method in solving those problems. DR programs mitigate transmission network capacity limits and reduce power system operation cost by efficient utilization of transmission network and generation units [1].

There are several studies around DR applications on different power system aspects. Most of the current studies have focused on the economic impacts of DR programs on electricity market [2]. On the other hand, in some studies DR programs triggered to enhance network's reliability [3]. Also, DR programs can be used to relief the transmission network criteria such as active power loss problem. Transmission network expansion and power loss reduction have been studied via the price based DR resources in [4]. Utilizing method of loss sensitivity, electricity market model is improved via DR programs in [5]. Demand response modeling based on the concept of demand-price elasticity has been addressed in [6]. Furthermore, authors in [7-8] have modeled the impact of DR implementation by a linear optimization

ISBN: 978-86-82602-01-9

NOMENCLATURE

A. *Variables*

x_k	Load curtailment of *k*th customer type.
Ω_k	Customer sorting variable.
C_i	DR cost in *i*th bus.
C_{total}	Total DR cost.
IC_i	Incremental cost of DR at bus *i*.
$EENS_0$	EENS before implementing DR.
$EENS_{DR}$	EENS after implementing DR.
$\Delta EENS$	EENS improvement by DR.
T_Γ	Interruption duration by outage source *Γ*.
f_Γ	Failure rate by outage source *Γ*.
$Loss_0$	Active power loss before implementing DR.
$Loss_{DR}$	Active power loss after implementing DR.
$\Delta Loss$	Active power loss improvement by DR.
I_{0b}	Electricity current flow among *b*th branch before implementing DR.
I_{DRb}	Electricity current flow among *b*th branch after implementing DR.
$\pi_{0,t}$	Market price before implementing DR.
$\pi_{DR,t}$	Market price after implementing DR
π_t	Local market price at period of *t*.
$\Delta\pi$	Market price improvement by DR.
$P_{G_0 i,t}$	Active power generation at *i*th bus before implementing DR
$P_{G_{DR} i,t}$	Active power generation at *i*th bus after implementing DR
$P_{Gi,t}$	Active power generation at *i*th bus at period of *t*.
$P_{D_0 i}$	Active power demand at *i*th bus before implementing DR
$P_{D_{DR}\ i}$	Active power demand at *i*th bus after implementing DR
$P_{Di,t}$	Active power demand at *i*th bus at period of *t*.
$P_{DRi,t}$	*DR* capacity at *i*th bus at period of *t*.
$P_{Di,t}$	Active power demand at *i*th bus at period of *t*.

B. *Functions*

$c(.)$	Customer curtailment cost function.
$b_c(.)$	Customer benefit function.
$u(.)$	Customer monetary benefit function.
$\xi(.)$	Customer cost function.
$inc(.)$	Incentive payment function.

C. *Parameters*

$k_1,\ k_2$	Customer cost function coefficients.
k_3	Customer motivation factor.
r	Rate of monetary credit
μ_k	0/1 Variable.
Z_b	Branch impedance.
a_n, b_n, c_n	Fuel cost coefficient.
$P_{Gi,t}^{\min}$	Minimum active power generation
$P_{Gi,t}^{\max}$	Maximum active power generation
$P_{DR,i}^{\max}$	Maximum capacity of *DR* resources.

D. *Sets*

N	Number of buses.
N_k	Number of customer types.
N_Γ	Number of outage sources (power line, transformer, switch, etc.).
N_b	Number of branches.
N_G	Number of generation units.

E. *Indices*

i, j	Bus index.
k	Customer type index.
Γ	Outage source index.
b	Branch index.
n	Power generation unit index.

technique considering the customers' behavior. Authors in [9] have employed a multi-object model to find the best size and site of DR programs in which power loss reduction is a one of optimization goal. Also in [10], multi-objective function is solved using NSGA-II to incorporate DR resources and wind farms to expand the transmission capacity by considering tradeoff between investment costs and congestion costs.

Although various DR models have been introduced, but few of the aforementioned studies considered the customers behavioral characteristics. In this paper we have focused on incentive based DR program in which the utility can encourage customers to reduce their load when system reliability, market price or other power system criteria are jeopardized. In this paper, the DR resources are optimally allocated in order to minimize: (1) demand curtailment cost as the customer's behavior aspect, (2) active power loss and EENS as technical goals, (3) electricity market price due to the market index. A key problem in multi-objective function optimization is to select the optimal solution that is the non-inferior one which often referred as the Pareto optimal solution. NSGA-II is one of the most popular multi objective optimization algorithms with the following three characteristics, fast non-dominated sorting approach, fast crowded distance estimation procedure and simple crowded comparison operator. Hence it is widely used in power system researches [11]. In the present paper, NSGA-II is used to solve a multi-objective optimization problem for determining the locations and sizing of DR programs.

The rest of this paper is organized as follows. Section II describes DR model. The other objectives are presented in Section III-V, and Section VI describes the optimization procedure. Section VII presents numerical results of the case study. Finally, section VIII specifies the conclusions.

II. CUSTUMER COST FUNCTION

To consider customer's curtailment cost function, it is safe to assume that the outage costs will grow progressively as demand curtailed increasing. Also, it can be assumed that the marginal benefit of the customer decreases with increased electricity consumption. Fig. 1 shows a possible predicted marginal benefit of a customer with respect to electricity consumption. The dark area shows the loss of surplus as a customer curtails its power because of participation in DR programs [12]. By assumption that the customer marginal benefit function has linear shape, customer curtailment cost function will have quadratic form.

The quadratic curtailment cost functions need to satisfy the sorting condition. This condition is needed to rank the customers in order of increasing or decreasing marginal cost. In this paper, customers are ranked from least willing to most willing which dictates that the customer outage cost function must be nondecreasing in Ω and it can be normalized to be in the interval $0 \leq \Omega \leq 1$. Also the outage cost function must be

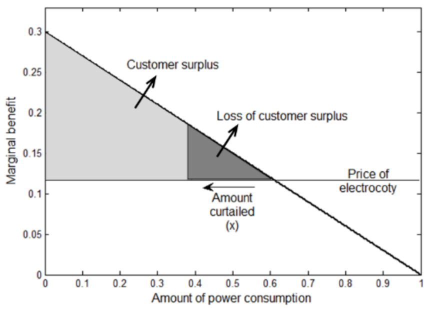

Figure 1. Marginal benefit for a customer [24].

nondecreasing by *x* since it is assumed that the reduction of each extra *kW* brings additional cost to the customer. Finally, it is safe to assume, zero curtailment has zero cost, so all these conditions on the customer outage cost function can be summarized as Eqs. (1) - (4). Hence a general quadratic form of customer curtailment cost function for each type of customer is defined as Eq. (5).

$$\frac{\partial}{\partial \Omega_k}\left(\frac{\partial c(\Omega_k, x_k)}{\partial x_k}\right) < 0 \ , \tag{1}$$

$$\frac{\partial c(\Omega_k, x_k)}{\partial x_k} \geq 0 \ , \tag{2}$$

$$\frac{\partial^2 c(\Omega_k, x_k)}{\partial {x_k}^2} > 0 \ , \tag{3}$$

$$c(\Omega_k, 0) = 0 \ , \tag{4}$$

$$c(\Omega_k, x_k) = k_1 {x_k}^2 + k_2 x_k (1 - \Omega_k) \ , \tag{5}$$

where Ω_k is customer sorting variable. The next step is calibrating the outage cost function coefficients by using realistic data. These data show *x* kW demand each participating customer is willing to reduce against the *r* \$/kW monetary credit. Hence, the benefit function for a customer under a demand management contract is described as (6). Maximization of customer benefit yields the first order conditions yields as Eqs. (7) and (8). By knowing customers load curtailment, amount of monetary credit and base on sorting condition which are described above, we can determine customers cost function.

$$b_c(\Omega_k, x_k) = r x_k - c(\Omega_k, x_k) \ , \tag{6}$$

$$\frac{\partial b_c(\Omega_k, x_k)}{\partial x_k} = r - \frac{\partial c(\Omega_k, x_k)}{\partial x_k} = 0 \ , \tag{7}$$

$$r - 2k_1 x_k - k_2(1 - \Omega_k) = 0 \ . \tag{8}$$

Once the cost function is calibrated, these data can be applied to determine DR allocation problem. One object of the DR allocation is to determine the optimal amount of payment for each customer who agrees to curtail *x* kW via DR contract. Also, customers have other beneficiary from not-paying πx dollars during the DR period when electricity price is π dollar per kW. So the monetary benefit for each customer becomes as Eq. (9). Constraint Eq. (10) is the individual rationality constraint which encourages voluntary customer participation by keeping customer benefit positive.

$$u(x_k) = \xi(x_k) - k_1 x_k{}^2 - k_2 x_k (1-\Omega_i) + \pi_t x_k \quad , (9)$$

$$\xi(x_k) - k_1 x_k{}^2 - k_2 x_k (1-\Omega_k) + \pi_t x_k \geq 0 \quad , (10)$$

To ensure that x kW designed DR will be achieved, utility can add motivation factor to the incentive payments. This motivation payment is paid to customers not to take the adjacent contracts and take the contract designed specifically for them. So based on Eq. (11) customers who are more willing to participate in DR programs are paid more incentives by coefficient k_3. Then, we have:

$$\begin{aligned} \xi(x_k) = k_1 x_k{}^2 + k_2 x_k (1-\Omega_k) + \\ + k_3 x_k (\Omega_k - \Omega_{k-1}) - \pi_t x_k \end{aligned} \quad , \quad (11)$$

$$inc\ (x_k) = \xi(x_k) + \pi_t x_k \quad . \qquad (12)$$

It is safe to assume each bus could have contained different type of customer combination. In order to consider various probabilities of load combination, we use binary variable μ to determine the customers' type in each bus. Hence by using this variable, we can model different scenarios to consider various probabilities of customer combination in different location. For getting the optimal amount of each type of customer's curtailment in each bus, a Lagrangian function with selected lowest DR cost is constructed which determines incremental cost of load curtailment in each bus. Hence Lagrangian function is used to minimize incentive payments described in Eqs. (13)-(20).

$$\min \ C_i = \sum_{k=1}^{N_k} \xi(x_k) \mu_k \quad . \qquad (13)$$

Subject to:

$$\begin{aligned} \xi(x_k) = k_1 x_k{}^2 + k_2 x_k (1-\Omega_k) + \\ + k_3 x_k (\Omega_k - \Omega_{k-1}) - \pi_t x_k \end{aligned} \quad . \quad (14)$$

$$\sum_{k=1}^{N_k} x_k \mu_k = P_{DR,i} \quad , \qquad (15)$$

$$0 \leq P_{DR,i} \leq P_{DR,i}^{\max} \quad , \qquad (16)$$

$$\frac{d\xi(x_k)}{dx_k} \mu_k = IC_i \mu_k , \quad (\Pi_k \in N_K) \quad , \ (17)$$

$$\xi(x_k) \geq 0 \quad , \qquad (18)$$

$$x_k \geq 0 \quad , \qquad (19)$$

$$\mu_k = 0 \ \ or \ 1 \quad . \qquad (20)$$

Equation (14) is the customer cost compatibility constraint, and constraint Eq. (15) represents the sum of load curtailment of various customers which equals to i[th] bus load curtailment. Also, constraint Eq. (17) determines the incremental cost of DR in each bus. Based on the above description, the first goal in this paper is to minimize customers' cost function described by Eq. (21).

$$Objec1 \quad \min : \sum_{i=1}^{N} C_i \quad . \qquad (21)$$

III. EXPECTED ENERGY NOT SUPPLIEDE

With the persistent expanding of power system, any system contingency may impose high cost for power system. Hence, the reliability assessment of bulk power system has become more important. As a reliability assessment index in bulk power system, EENS takes into account the outage duration time which reflects appropriate information about system reliability. The expected energy not supplied is chosen in this paper as an index for composite system reliability of the power system. In order to calculate system expected unsupplied energy due to power outage, the amount of expected energy not supplied to the customers at all load point has to be calculated [13]. The amount of expected energy not supplied is calculated as follows:

$$EENS_0 = \sum_{i=1}^{N} \sum_{\Gamma=1}^{N_\Gamma} P_{D_0\, i} \times T_\Gamma \times f_\Gamma \quad , \qquad (22)$$

$$EENS_{DR} = \sum_{i=1}^{N}\sum_{\Gamma=1}^{N_\Gamma} P_{D_{DR}\,i} \times T_\Gamma \times f_\Gamma \quad , \qquad (23)$$

$$\begin{aligned} Objec2 \quad & \max : \Delta EENS = \\ & = ENNS_0 - EENS_{DR} \end{aligned} \quad . \qquad (24)$$

IV. ACTIVE POWER LOSS

Transmission losses have a significant effect on the active power generation and power transmission cost. So reduction of electrical power losses during transmission in the lines is one of the major priorities of each power system [14]. Active power loss in the transmission network can be defined as follows:

$$Loss_0 = \mathrm{Re}\,al\left\{\sum_{b=1}^{N_B}(Z_b \times I_{0b}{}^2)\right\} \quad , \qquad (25)$$

$$Loss_{DR} = \mathrm{Re}\,al\left\{\sum_{b=1}^{N_B}(Z_b \times I_{DRb}{}^2)\right\} \quad , \qquad (26)$$

$$\begin{aligned} Objec3 \quad & \max : \Delta Loss = \\ & = Loss_0 - Loss_{DR} \end{aligned} \quad . \qquad (27)$$

V. MARKT PRICE

This paper uses OPF based market clearing procedure to determine hourly market price with considering network constrains [15]. As it was mentioned earlier, this method can determine locally price that properly represents both of local load and local generation constrains which is used in customer cost function. So market price before and after DR program implementing is described in Eqs. (28) and (29).

$$\pi_{0,t} = \frac{\sum_{n=1}^{N_G}(a_n P_{G_0 n,t}^2 + b_n P_{G_0 i,t} + c_n)}{\sum_{n=1}^{N_G} P_{G_0 n,t}} \quad , \qquad (28)$$

$$\pi_{DR,t} = \frac{\sum_{n=1}^{N_G}(a_n P_{G_{DR} n,t}^2 + b_n P_{G_{DR} n,t} + c_n)}{\sum_{n=1}^{N_G} P_{G_{DR} n,t}} \quad , \qquad (29)$$

$$Objec4 \quad \max : \Delta\pi = \pi_0 - \pi_{DR} \quad , \qquad (30)$$

VI. MULTI-OBJECTIVE PROBLEM

In many realistic problems, several goals must be simultaneously satisfied to achieve an optimal solution. However, sometimes these multiple objectives have conflict with each other. The multi-objective optimization method is the prevalent approach to solve this type of problem. In the multiple objectives, there may not exist one solution which all the objectives are satisfied optimally. Each typical multi-objective optimization problem usually has a set of solutions which are superior to the others in the search space when all objectives are considered. These solutions are known as Pareto-optimal solutions or non-dominated solutions. As a population-based approach, Genetic Algorithm (GA) is well suited to solve multi-objective optimization problems. The improved genetic algorithm called NSGA-II is considered in this paper. In this approach, to sort a population of size N_{pop} according to the level of non-domination, each solution must be compared with every other solution in the population to determine if it is dominated or not. The procedure is repeated to find the subsequent front. The basic idea of the NSGA-II algorithm is to subdivide the population in each generation into a number of subsets referred to as fronts which are ranked in terms of levels (Fig. 2). For details about the NSGA-II approach, refer to [16].

The decision variables in DR allocation by NSGA-II are the sitting and sizing of responsive demands. After determination of Pareto-optimal solutions, a suitable ranking method should be used to find the best (final) solutions for decision-making. The min-max method is used in this paper for optimal solution selecting. This method tries to minimize the relative deviations of the single objective functions from individual optimum.

VII. NUMERICAL STUDY

The proposed algorithm has been tested on 24-bus IEEE reliability test system (RTS). This system provides appropriate system reliability data in order to compute EENS of the system. Also, the simulations are performed in MATLAB environment and MATPOWER OPF functions. The single-line diagram of the test system is given in Fig. 3 It has 32 generators, 33 transmission lines, 5 transformers, and 17 load buses with the total generation capacity of 3405

MW, and the maximum load of 2850 MW. The generating units' data, load data and transmission lines data can be found in [17]. Table I shows hourly load data on a specific Monday in summer season which are used in this paper as load profile.

In order to determine the coefficients of customer cost function a sample of 10 customers data are taken and modified from [12] which used utility data to specify customer curtailment cost. In order to these data be useful for selected system, we assume all type of customers were paid 10 $ per MW as the monetary credit for a nominal hour of interruption and Table II shows how much curtailment each type of customer is willing to take. Also to consider load location effect on customer cost function, for simplicity, it is assumed only four type customers in each load bus as shown in Table III. Customer type 1, 3, 7 and 10 are selected to calculate total amount of customers curtailment cost and incentive payments. For example at bus 5, only customer type 1 and 3 exist. Hence customer cost coefficients k_1 and k_2 are calculated as 12.723 and 8.499 respectively. Also the incentive motivation factor k_3 is assumed to be 1.

For implementing the proposed algorithm, it is assumed that all load buses could have maximum DR programs capacity equal to 10% of their demand. At the end of evolutionary computation, a Pareto-front which satisfies all objectives is achieved. It includes 200 feasible solutions as shown in Fig. 4. This 3D figure is drawn with respect to EENS, customer cost function and market price objectives. It is clear that all of these points are feasible solutions selected to amend the objectives. Hence by using of these data in min-max method, final solutions can be achieved.

Table V shows the selected buses for DR programs and corresponding incentives. In this table, objectives are customer cost function, EENS reduction, active power loss reduction and market operational price reduction. By investigation of the results, one can observe that in some times the algorithm tries to amend one objective more than the others. In different periods, based on system conditions, the algorithm may select different amount of load as DR resources size or different bus numbers as DR resources site. From Table IV it is obvious that the algorithm could not find any location for

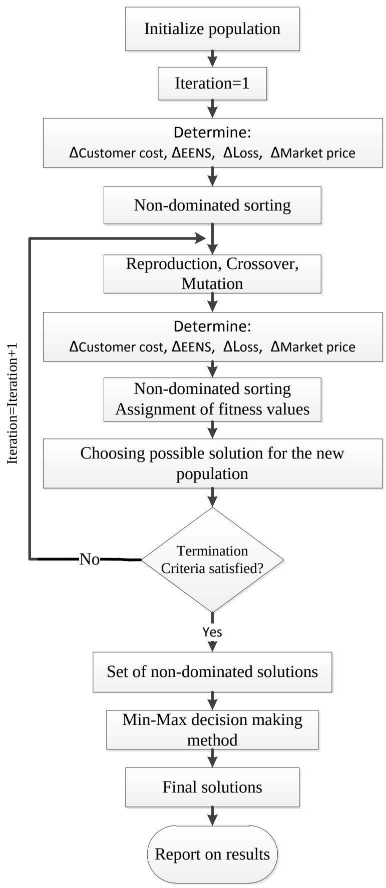

Figure 2. Flowchart of the proposed NSGA-II algorithm.

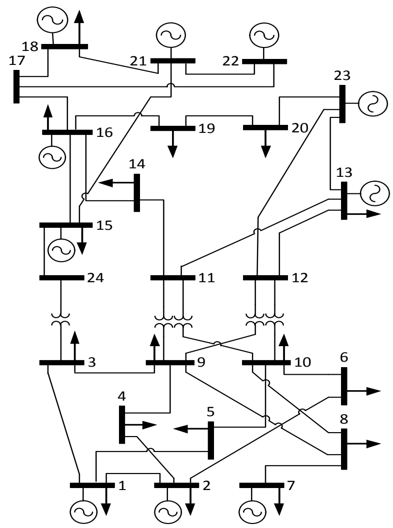

Figure 3. 24-bus IEEE Reliability Test System (RTS).

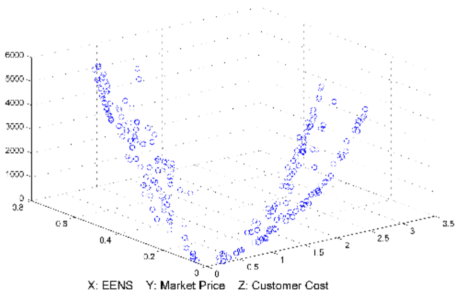

Figure 4. Pareto-optimal front and decision-making results for three-objectives.

DR resources in the period interval from 1 to 7 o'clock, which satisfies objectives properly.

Fig. 6 shows the changes of the load curve in each hours as a result of implementing DR program. By comparing load curves after and before DR implementation, one can observe in peak hours which both of power system demand and power market are in high levels, DR program tries to reduce more load but there may be tangible load reduction even in low market price or low system demand because of enhancing other objectives improvement using DR programs. One of the innovations of this paper is to introduce incremental cost of DR in each bus. By using incremental cost, decision makers can estimate the value of one additional unit of load reduction.

TABLE I. DEMND DATA.

Hour	System demand (MW)	Hour	System demand (MW)
1	1696.3	13	2624.0
2	1590.3	14	2650.5
3	1537.3	15	2650.5
4	1484.3	16	2571.0
5	1484.3	17	2544.5
6	1537.3	18	2544.5
7	1696.3	19	2465.0
8	2014.4	20	2438.5
9	2305.9	21	2438.5
10	2518.0	22	2465.0
11	2624.0	23	2305.9
12	2650.5	24	1908.4

TABLE II. UTILITY DATA OF LOAD CURTAILMENT.

Customer type	Amount of load (kW)	Ω
1	59	0
2	100	0.1229
3	130	0.2127
4	134	0.2247
5	151	0.2755
6	184	0.3743
7	200	0.4222
8	349	0.8668
9	364	0.9132
10	393	1

TABLE III. CUSTOMER TYPES IN EACH BUS.

Load Point	Customer type			
	Ω_1	Ω_3	Ω_7	Ω_{10}
Bus01	1	0	0	0
Bus02	0	1	0	0
Bus03	0	0	1	0
Bus04	0	0	0	1
Bus05	1	1	0	0
Bus06	1	0	1	0
Bus07	1	0	0	1
Bus08	0	1	1	0
Bus09	0	1	0	1
Bus10	0	0	1	1
Bus13	1	1	1	0
Bus14	1	1	0	1
Bus15	1	0	1	1
Bus16	0	1	1	1
Bus18	1	1	1	1
Bus19	1	1	1	1
Load20	1	1	1	1

In order to survey, the results of bus 8 are selected as an example to study. Fig. 7 compares normalized incremental cost of DR in bus 8 with respect to normalized systems demand. By investigation of this figure, one can observe there is significant relationship between incremental cost of DR and systems demand. Results show 85.12% correlation between them because of correlation between system demand, market price and incremental cost of DR. There are incoordination between incremental cost of DR and systems demand in some periods because other objectives than market price are also considered in solving DR allocation problems in this paper.

As an additional benefit, using of DR resources can reduce system operational cost which indicates how much overall financial benefit obtained via DR programs. This benefit contains all customers who are participated in DR

TABLE IV. SELECTED BUSES, AMOUNT OF DR PROGRAM AND THE VALUE OF EACH OBJECTIVE.

Hour	Selected Bus	Incentive payment ($)			
8	5, 7, 8	58	218	192	0
9	5, 7, 8	205	452	126	0
10	6, 7, 8, 10	607	602	652	151
11	8, 10, 13, 15	985	419	1245	929
12	8, 10, 13, 15	1079	133	1342	2571
13	8, 10, 13, 15	1008	872	909	1237
14	7, 8, 10, 13	1280	1330	974	2050
15	7, 8, 10, 13	1550	1389	1520	1535
16	7, 8, 13, 14	651	746	235	1312
17	6, 7, 8, 10	399	435	1047	993
18	6, 7, 8, 14	372	323	1348	825
19	7, 8 , 10 , 18	409	703	405	505
20	7, 8, 16, 18	246	414	91	565
21	7, 10, 16, 18	256	602	84	518
22	7, 8, 14, 18	346	473	293	480
23	5, 6, 7	99	160	295	0
24	5, 7, 8	42	63	147	0

TABLE V. THE COMPARISON BETWEEN BEFORE AND AFTER DR IMPLEMENTATION.

Item	Before DR Implementation	After DR Implementation
System Load (MW)	52745	52112
EENS (MW)	2981.6	2961.6
Power Loss (MW)	917.9	899.1
Operational Cost ($)	647220	636216
Incentive Payments ($)	0.0	43501

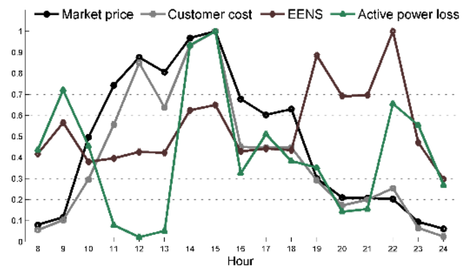

Figure 5. Normalized objectives in different periods.

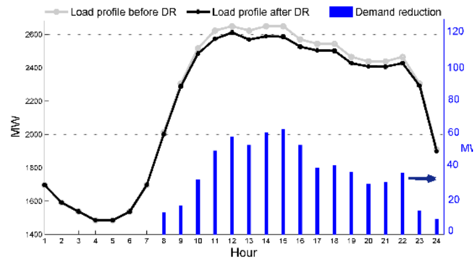

Figure 6. Impact of DR allocation algorithm on load curve in different periods.

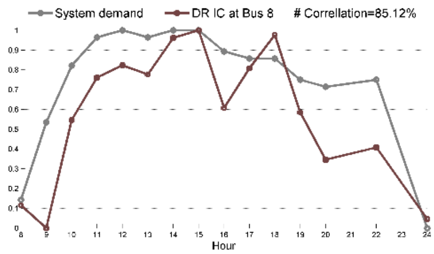

Figure 7. Incremental cost of DR in bus 8 versus system demand.

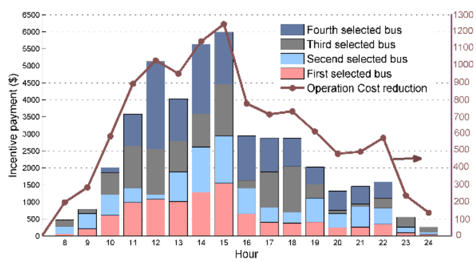

Figure 8. Incentie payments compare with operational cost reduction.

programs or not. Fig. 8 compares the incentive payments paid to participant customers with operational cost reduction in each period. This figure shows high correlation between them. Also it is obvious, much incentive payment is paid when system demand and market price are high and subsequently by implementing DR programs more operational cost will be reduced.

VIII. CONCLUSIONS

An improved demand response allocation model based on the customers' viewpoint has been proposed in this paper. The model takes into account the active power loss reduction and reliability improvement on one hand and electricity market price reduction on the other hand by using the concept of customers' cost function which can be calculated from utility data. The customer cost function is designed to sort the customers in decreasing marginal cost order and identify different customers' viewpoint. Also, NSGA-II algorithm has been applied and presented in this paper for optimal DR allocation. Results showed the proposed algorithm selected the best sizes and sites of DR programs in order to achieve the best solutions which satisfy all objectives. Also by considering the results carefully, sometimes some objectives, which are highly jeopardized, have more effect than the others in DR allocation. By applying the algorithm, incremental cost of DR in each bus is determined. Based on the results, there is significant correlation between incremental cost of DR and market price. Further, determining the optimal amount of incentive payments based on customer cost function was another result of this paper.

REFERENCES

[1] Kazerooni, A. K., & Mutale, J. (2010). Transmission network planning under security and environmental constraints. *IEEE Transactions on Power Systems, 25*(2), 1169-1178.

[2] Niromandfam, A., Yazdankhah, A. S., & Kazemzadeh, R. (2020). Modeling demand response based on utility function considering wind profit maximization in the day-ahead market. *Journal of Cleaner Production, 251*, 119317.

[3] Niromandfam, A., Yazdankhah, A. S., & Kazemzadeh, R. (2020). Design of reliability insurance scheme based on utility function for improvement of distribution grid reliability. *Journal of Operation and Automation in Power Engineering, 8*(3), 257-272.

[4] Özdemir, Ö., Munoz, F. D., Ho, J. L., & Hobbs, B. F. (2015). Economic analysis of transmission expansion planning with price-responsive demand and quadratic losses by successive LP. *IEEE Transactions on Power Systems, 31*(2), 1096-1107.

[5] Hong, M., & Loparo, K. A. (2014, July). An improved electricity market model on demand response considering distribution loss sensitivities. In *2014 IEEE PES General Meeting| Conference & Exposition* (pp. 1-5). IEEE.

[6] Niromandfam, A., Yazdankhah, A. S., & Kazemzadeh, R. (2020). Design of reliability insurance scheme based on utility function for improvement of distribution grid reliability. *Journal of Operation and Automation in Power Engineering, 8*(3), 257-272.

[7] Niromandfam, A., Pour, A. M., & Zarezadeh, E. (2020). Virtual energy storage modeling based on electricity customers' behavior to maximize wind profit. *Journal of Energy Storage, 32*, 101811.

[8] Niromandfam, A., Choboghloo, S. P., Yazdankhah, A. S., & Kazemzadeh, R. (2020). Electricity customers' financial and reliability risk protection utilizing insurance mechanism. *Sustainable Energy, Grids and Networks, 24*, 100399.

[9] Nguyen, T. T., & Yousefi, A. (2011, January). Multi-objective demand response allocation in restructured energy market. In *ISGT 2011* (pp. 1-8). IEEE.

[10] Hu, Y., Bie, Z., Ding, T., & Lin, Y. (2016). An NSGA-II based multi-objective optimization for combined gas and electricity network expansion planning. *Applied energy, 167*, 280-293.

[11] Ahmadi, H., & Akbari Foroud, A. (2016). Design of joint active and reactive power reserve market: a multi- objective approach using NSGA II. *IET Generation, Transmission & Distribution, 10*(1), 31-40.

[12] Fahrioglu, M., & Alvarado, F. L. (2001). Using utility information to calibrate customer demand management behavior models. *IEEE transactions on power systems, 16*(2), 317-322.

[13] Choi, S. B., Nam, K. Y., Kim, D., Jeong, S., Ryoo, H., & Lee, J. (2006). Evaluation of reliability of distribution power system in industrial complex in Korea. In *2006 IEEE PES Power Systems Conference and Exposition* (pp. 718-724). IEEE.

[14] Ogunjuyigbe, A. S. O., Ayodele, T. R., & Akinola, O. O. (2016). Impact of distributed generators on the power loss and voltage profile of sub-transmission network. *Journal of Electrical Systems and Information Technology, 3*(1), 94-107.

[15] Pałka, P. (2017). Derivatives of the nodal prices in market power screening. *Energy Economics, 64*, 149-157.

[16] Deb, K., Pratap, A., Agarwal, S., & Meyarivan, T. A. M. T. (2002). A fast and elitist multiobjective genetic algorithm: NSGA-II. *IEEE transactions on evolutionary computation, 6*(2), 182-197.

[17] Ordoudis, C., Pinson, P., Morales, J. M., & Zugno, M. (2016). An updated version of the IEEE RTS 24-bus system for electricity market and power system operation studies. *Technical University of Denmark, 13*.

Environmental Ranking of the Microgrid's Energy Sources by using ELECTRE Optimization Method

Dario Javor[1]

[1]Faculty of Occupational Safety in Niš, University of Niš, Niš, Serbia

Abstract—**Ranking of microgrid's energy sources is obtained by using the ELECTRE method and environomic (environmental and economic) criteria. Operational & maintenance and fuel costs (OMF costs) as well as CO_2, SO_2, NO_X, CO and particulate matter (PM) emissions are taken as evaluation criteria for the ranking in this multi-criteria optimization. Dispatchable energy sources (diesel engines, microturbines and fuel cells) and main grid as electricity production alternatives are considered in this paper. The results show that microturbines are the best choice from the environomic point of view for the considered data.**

Keywords - environmental criteria, ELECTRE method, microgrids, multi-criteria optimization

I. INTRODUCTION

The microgrid is a self-sufficient local power system with defined electrical boundaries that can operate connected to the main grid or isolated from it. They usually include non-dispatchable energy sources (photovoltaic and/or wind generators), but also dispatchable energy sources (microturbines, fuel cells, gas turbines, gas ICE (Internal Combustion Engine), diesel ICE, etc.). The problem of choosing one of dispatchable energy sources, if photovoltaic panels or wind generators do not provide enough energy at a certain time interval, has to be solved from the environomic point of view. That means that both economic and environmental criteria have to be satisfied. The economic criteria are: capital costs, operational & maintenance costs (that can be fixed or variable), fuel costs, etc. The environmental criteria are emissions of harmful gasses (CO_2, CO, SO_2, NO_X, HC, etc.) and emissions of particulate matter (PM). The weights of these criteria depend on economic strength, the desire to meet the requirements for the protection of the human environment, penalties for the release of harmful gases at the location of the microgrid, the requirements of the owner of the microgrid, government regulations, feed-in-tariff for the generation option, etc. As there are multiple conflicting criteria for this problem, some of the multi-criteria decision making (MCDM) methods has to be used, e.g. ELECTRE (Elimination and Choice Translating Reality) [1], PROMETHEE (Preference Ranking Organization Method for Enrichment of Evaluations) [2-4], TOPSIS (Technique for Order Performance by Similarity to the Ideal Solution), VIKOR (Multicriteria optimization compromise solution), WSM (Weighted Sum Method), WPM (Weighted Product Method), ORESTE (Organization, Storage and Synthesis of Relational Data), or other. In this paper, the ELECTRE method is used to select one of the four energy sources for the microgrid that is optimal according to six criteria.

II. RANKING OF THE MICROGRID'S ENERGY SOURCES BY USING ELECTRE METHOD

In the first step, the Decision-making matrix (DMM) of dimensions m x n is formed. Matrix X is given by (1). Its rows correspond to alternatives a_i, i = 1,2,..., m, whereas its columns correspond to the attributes (criteria) A_j, j =1,2,..., n.

The element of the decision–making matrix is x_{ij}, for i=1,2,3,4, j=1,2,3,4,5,6. The parameters of the considered problem are taken from [5-8] and presented in Table I. The weights of the criteria are given in Table II.

The element of the decision–making matrix is x_{ij}, for i=1,2,3,4, j=1,2,3,4,5,6. The parameters of the considered problem are taken from [5-8] and presented in Table I. The weights of the criteria are given in Table II.

$$
X = \begin{array}{c} \\ a_1 \\ a_2 \\ a_3 \\ a_4 \end{array}
\begin{array}{c} \begin{array}{cccccc} A_1 & A_2 & A_3 & A_4 & A_5 & A_6 \end{array} \\
\begin{bmatrix} x_{11} & x_{12} & x_{13} & x_{14} & x_{15} & x_{16} \\ x_{21} & x_{22} & x_{23} & x_{24} & x_{25} & x_{26} \\ x_{31} & x_{32} & x_{33} & x_{34} & x_{35} & x_{36} \\ x_{41} & x_{42} & x_{43} & x_{44} & x_{45} & x_{46} \end{bmatrix} \end{array}
= \begin{array}{c} \\ a_1 \\ a_2 \\ a_3 \\ a_4 \end{array}
\begin{array}{c} \begin{array}{cccccc} A_1 & A_2 & A_3 & A_4 & A_5 & A_6 \end{array} \\
\begin{bmatrix} 0.15 & 697 & 0.22 & 0.5 & 1 & 0.2 \\ 0.11 & 670 & 0.0036 & 0.186 & 0.4 & 0 \\ 0.242 & 441 & 0.0022 & 0.0136 & 0.01 & 0.01 \\ 0.2 & 889 & 1.8 & 1.6 & 0.01 & 0.3 \end{bmatrix} \end{array} . \quad (1)
$$

TABLE I. DECISION-MAKING MATRIX

Criterion \ Alternative	***a*₁** **Diesel generator (DG)**	***a*₂** **Micro-turbine (MT)**	***a*₃** **Fuel cell (FC)**	***a*₄** **Main grid (MG)**
OMF costs [$/kWh]	0.15	0.11	0.242	0.2
CO_2 [g/kWh]	697	670	441	889
SO_2 [g/kWh]	0.22	0.0036	0.0022	1.8
NO_X [g/kWh]	0.5	0.186	0.0136	1.6
CO [g/kWh]	1	0.4	0.01	0.01
PM [g/kWh]	0.2	0	0.01	0.3

TBALE II. WEIGHTS OF THE CRITERIA

Attribute (criterion)	**Emissions or costs**	**Weight**
A_1	OMF costs	0.6
A_2	CO_2	0.1
A_3	SO_2	0.1
A_4	NO_X	0.1
A_5	CO	0.05
A_6	PM	0.05

In the second step, vector normalization is performed, so that the Normalized matrix N is obtained:

$$
N = \left\lfloor n_{ij} \right\rfloor_{m \times n} , \qquad (2)
$$

for the elements:

$$
n_{ij} = \frac{x_{ij}}{\sqrt{\sum_{i=1}^{m} x_{ij}{}^{2}}}, \quad i = 1,\ldots, m,\ j = 1,\ldots, n. \qquad (3)
$$

The normalized matrix N is:

$$N = \begin{bmatrix} n_{11} & n_{12} & n_{13} & n_{14} & n_{15} & n_{16} \\ n_{21} & n_{22} & n_{23} & n_{24} & n_{25} & n_{26} \\ n_{31} & n_{32} & n_{33} & n_{34} & n_{35} & n_{36} \\ n_{41} & n_{42} & n_{43} & n_{44} & n_{45} & n_{46} \end{bmatrix} =$$

$$= \begin{bmatrix} 0.411053 & 0.50308 & 0.121319 & 0.296446 & 0.928397 & 0.554487 \\ 0.301439 & 0.483592 & 0.001985 & 0.110278 & 0.371359 & 0 \\ 0.663166 & 0.318305 & 0.001213 & 0.008063 & 0.009284 & 0.027724 \\ 0.548071 & 0.641662 & 0.992611 & 0.948627 & 0.009284 & 0.83173 \end{bmatrix}. \quad (4)$$

The weighted normalized matrix V is:

$$V = N \cdot W = \begin{bmatrix} n_{11}w_1 & n_{12}w_2 & n_{13}w_3 & n_{14}w_4 & n_{15}w_5 & n_{16}w_6 \\ n_{21}w_1 & n_{22}w_2 & n_{23}w_3 & n_{24}w_4 & n_{25}w_5 & n_{26}w_6 \\ n_{31}w_1 & n_{32}w_2 & n_{33}w_3 & n_{34}w_4 & n_{35}w_5 & n_{36}w_6 \\ n_{41}w_1 & n_{42}w_2 & n_{43}w_3 & n_{44}w_4 & n_{45}w_5 & n_{46}w_6 \end{bmatrix} =$$

$$= \begin{bmatrix} 0.246632 & 0.050308 & 0.012132 & 0.029645 & 0.04642 & 0.027724 \\ 0.180863 & 0.048359 & 0.000199 & 0.011028 & 0.018568 & 0 \\ 0.397899 & 0.03183 & 0.000121 & 0.000806 & 0.000464 & 0.001386 \\ 0.328842 & 0.064166 & 0.099261 & 0.094863 & 0.000464 & 0.041587 \end{bmatrix}, \quad (5)$$

where W is the matrix of weight coefficients, with dimensions n x n:

$$W = \begin{bmatrix} w_1 & 0 & 0 & 0 & 0 & 0 \\ 0 & w_2 & 0 & 0 & 0 & 0 \\ 0 & 0 & w_3 & 0 & 0 & 0 \\ 0 & 0 & 0 & w_4 & 0 & 0 \\ 0 & 0 & 0 & 0 & w_5 & 0 \\ 0 & 0 & 0 & 0 & 0 & w_6 \end{bmatrix} =$$

$$= \begin{bmatrix} 0.6 & 0 & 0 & 0 & 0 & 0 \\ 0 & 0.1 & 0 & 0 & 0 & 0 \\ 0 & 0 & 0.1 & 0 & 0 & 0 \\ 0 & 0 & 0 & 0.1 & 0 & 0 \\ 0 & 0 & 0 & 0 & 0.05 & 0 \\ 0 & 0 & 0 & 0 & 0 & 0.05 \end{bmatrix}. (6)$$

In the third step, the Concordance interval set C_{pr} and the Discordance interval set D_{pr} are determined for all pairs of alternatives a_p and a_r, for $p \neq r$ and $p, r \in I = \{i \mid i = 1,2,...,m\}$.

Concordance interval set C_{pr} consists of those criteria (attributes) for which the alternative a_p is preferable to a_r:

$$C_{pr} = \{ j \mid x_{pj} \geq x_{rj} \}. \quad (7)$$

Afterwards, the Discordance interval set D_{pr} that is a complementary set for C_{pr} is formed:

$$D_{pr} = \{ j \mid x_{pj} < x_{rj} \} = J / C_{pr}, \quad (8)$$

for $J = \{ j \mid j = 1,2,...,n \}$ the set of all criteria.

In the fourth step, the Concordance interval matrix C is determined. The elements of that matrix consist of c_{pr} concordance indices, which are calculated as the sum of weights corresponding to the elements of the concordance interval set. The concordance index of the alternatives a_p and a_r is:

$$c_{pr} = \sum_{j \in C_{pr}} w_j, \quad (9)$$

so that $0 \le c_{pr} \le 1$. A higher value of the index means a higher desirability of alternative a_p compared to alternative a_r. The concordance interval matrix has zeros on the diagonal, and in the selected example is:

$$C = \begin{bmatrix} 0 & c_{12} & c_{13} & c_{14} \\ c_{21} & 0 & c_{23} & c_{24} \\ c_{31} & c_{32} & 0 & c_{34} \\ c_{41} & c_{42} & c_{43} & 0 \end{bmatrix} = \\ = \begin{bmatrix} 0 & 1 & 0.4 & 0.05 \\ 0 & 0 & 0.35 & 0.05 \\ 0.6 & 0.65 & 0 & 0.65 \\ 0.95 & 0.95 & 0.35 & 0 \end{bmatrix}. \tag{10}$$

In the fifth step, the Discordance interval matrix D is determined. The elements of that matrix are d_{pr} discordance indices which are calculated according to the relation:

$$d_{pr} = \frac{\max\limits_{j \in D_{pr}} \left\{ \left| v_{pj} - v_{rj} \right| \right\}}{\max\limits_{j \in J} \left\{ \left| v_{pj} - v_{rj} \right| \right\}}, \tag{11}$$

so that $0 \le d_{pr} \le 1$. A higher value of the index means a lower desirability of alternative a_p compared to alternative a_r. The discordance interval matrix has zeros on the diagonal, and in the selected example it is:

$$D = \begin{bmatrix} 0 & d_{12} & d_{13} & d_{14} \\ d_{21} & 0 & d_{23} & d_{24} \\ d_{31} & d_{32} & 0 & d_{34} \\ d_{41} & d_{42} & d_{43} & 0 \end{bmatrix} = \\ = \begin{bmatrix} 0 & 0 & 1 & 1 \\ 1 & 0 & 1 & 1 \\ 0.303804 & 0.083414 & 0 & 1 \\ 0.527443 & 0.12234 & 0.696561 & 0 \end{bmatrix}. \tag{12}$$

In the sixth step, the Average concordance index is calculated:

$$\bar{c} = \frac{1}{m(m-1)} \sum_{\substack{p=1 \\ p \ne r}}^{m} \sum_{\substack{r=1 \\ r \ne p}}^{m} c_{pr}. \tag{13}$$

For the selected example $\bar{c} = 0.5$. The elements e_{pr} of the Concordance index matrix E are obtained as:

$$e_{pr} = \begin{cases} 1, & c_{pr} \ge \bar{c} \\ 0, & c_{pr} < \bar{c} \end{cases}, \tag{14}$$

so that the Concordance index matrix is:

$$E = \begin{bmatrix} 0 & 1 & 0 & 0 \\ 0 & 0 & 0 & 0 \\ 1 & 1 & 0 & 1 \\ 1 & 1 & 0 & 0 \end{bmatrix}. \tag{15}$$

In the seventh step, the Average discordance index is determined as:

$$\bar{d} = \frac{1}{m(m-1)} \sum_{\substack{p=1 \\ p \ne r}}^{m} \sum_{\substack{r=1 \\ r \ne p}}^{m} d_{pr}. \tag{16}$$

For the selected example $\bar{d} = 0{,}644463$. The elements f_{pr} of the Discordance index matrix F are obtained based on the criteria:

$$f_{pr} = \begin{cases} 1, & d_{pr} \le \bar{d} \\ 0, & d_{pr} > \bar{d} \end{cases}, \tag{17}$$

so that the Discordance index matrix is:

$$F = \begin{bmatrix} 1 & 1 & 0 & 0 \\ 0 & 1 & 0 & 0 \\ 1 & 1 & 1 & 0 \\ 1 & 1 & 0 & 1 \end{bmatrix}. \tag{18}$$

In the eighth step, the Aggregate dominance matrix G is determined. The elements of the Aggregate dominance matrix are calculated according to the following:

$$g_{pr} = e_{pr} \cdot f_{pr}, \tag{19}$$

so that for the selected example the matrix of aggregate dominance is:

$$
G = \begin{array}{c} \\ a_1 \\ a_2 \\ a_3 \\ a_4 \end{array} \begin{array}{c} \begin{array}{cccc} a_1 & a_2 & a_3 & a_4 \end{array} \\ \begin{bmatrix} 0 & 1 & 0 & 0 \\ 0 & 0 & 0 & 0 \\ 1 & 1 & 0 & 0 \\ 1 & 1 & 0 & 0 \end{bmatrix} \end{array} . \tag{20}
$$

III. Discussion of the Results

Based on the matrix of aggregate dominance, it can be concluded that the third alternative (fuel cell) and the fourth alternative (main grid) have higher emissions and costs than the other two alternatives.

The second alternative (microturbine) has the least emissions and costs, which is concluded based on the results for the second row of matrix *G*.

Based on the elements of the Concordance index matrix *C*, the Net superior value c_p can be obtained for each alternative *p* according to the following equation:

$$
c_p = \sum_{r=1}^{n} c_{pr} - \sum_{r=1}^{n} c_{rp} \ . \tag{21}
$$

Based on the elements of the Discordance index matrix *D*, the Net inferior value d_p for each alternative *p* can be obtained according to the following equation:

$$
d_p = \sum_{r=1}^{n} d_{pr} - \sum_{r=1}^{n} d_{rp} \ . \tag{22}
$$

Table III gives the net superior values and Table IV net inferior values. They both give the results of ranking of the alternatives.

TABLE III. Net Superior Values and Ranking of the Alternatives.

Alternative	**Net superior value**	**Positive rank**	**Negative rank**
Diesel generator (DG)	-0.1	3	2
Microturbine (MT)	-2.2	4	1
Fuel cell (FC)	0.8	2	3
Main grid (MG)	1.5	1	4

TBALE IV. Net Superior Values and Ranking of the Alternatives.

Alternative	**Net inferior value**	**Positive rank**	**Negative rank**
Diesel generator (DG)	0.168754	3	2
Microturbine (MT)	2.794247	4	1
Fuel cell (FC)	-1.30934	2	3
Main grid (MG)	-1.65366	1	4

The positive ranking of the alternatives refers to the maximization, and the negative ranking to the minimization of all criteria.

IV. Conclusion

In this paper, environomic ranking of energy sources as dispatchable sources in the microgrid is obtained by using the ELECTRE method. Operational & maintenance and fuel costs (OMF costs), emissions of CO_2, SO_2, NO_X, CO and particulate matter (PM) are taken as evaluation criteria, so that diesel generator, microturbine, fuel cell and main grid as electricity production alternatives are ranked. The results show that microturbines are the best choice from the environomic point of view for the considered data, but this depends on the weights given to the criteria.

Acknowledgment

This research was financially supported by the Ministry of Education, Science and Technological Development of the Republic of Serbia, according to contract No. 451-03-68/2022-14/ 200148.

References

[1] Roy, B. (1968). Classement et choix en présence de points de vue multiples (la méthode ELECTRE) [Ranking and choice in the presence of multiple points of view (the ELECTRE method)]. *La Revue d'Informatique et de Recherche Opérationelle (RIRO)* (8), 57–75.

[2] Brans, J. P. (1982). L'ingénièrie de la décision; Elaboration d'instruments d'aide à la décision. La méthode PROMETHEE [Decision engineering; Development of decision support tools. The PROMETHEE method]. In R. Nadeau, & M. Landry (Eds*.), L'aide à la décision: Nature, Instruments et Perspectives d'Avenir* (pp. 183-213). Presses de l'Université Laval.

[3] Brans, J. P., Mareschal, B., & Vincke, Ph. (1984). PROMETHEE: A new family of outranking methods in multicriteria analysis. In J. P. Brans (Ed.),

Operational Research '84 (pp. 477-490). North-Holland.

[4] Brans, J. P., & Mareschal, B. (2005). PROMETHEE methods. In J. Figueira, S. Greco, & M. Ehrgott (Eds.), *Multiple Criteria Decision Analysis: State of the Art Surveys* (pp. 163-196). Springer Science + Business Media, Inc.

[5] EPRI report (2003). *Installation, Operation, and Maintenance Costs for Distributed Generation Technologies*. EPRI, Palo Alto, CA: 2003. 1007675.

[6] Marti, B. (2005). *Emissions of Power Delivery Systems.* Semester Thesis PSL0502 EEH – Power Systems Laboratory, Swiss Federal Institute of Technology (ETH) Zurich.

[7] Murty, V. V. S. N., & Kumar, A. (2020). Multi-objective energy management in microgrids with hybrid energy sources and battery energy storage systems. *Protection and Control of Modern Power Systems, 5*(1).

[8] SEE Power EXchange (2022). Available at: http://www.seepex-spot.rs/sr.

Proposal for the Reform of Public Utilities in B&H

Enver Agić[1], Sanel Buljubašić[2]

[1]PIM Univerzitet Banja Luka, Banja Luka, B&H
[2]JP ViK ''Srebrenik" d.d. Srebrenik, Srebrenik, B&H

Abstract—**The paper covers the issues of doing business in certain sectors of utility activities, and points to the situation in public utility companies. Based on the current situation in Bosnia and Herzegovina, and experience in the surrounding countries, proposals have been defined that can be considered by participants in the further process of defining the first steps towards reform of the PUC, in order to: improving the efficiency of the public health service; renewal and development of local infrastructure; achieving quality standards and applying EU regulations (through access to EU grants and other sources). The proposals are aimed at contributing to the initiation of the reform process of public utility companies in Bosnia and Herzegovina, i.e. the preparation, adoption and implementation of regulations that will contribute to the better operations of the PUC.**

Keywords - PUC, reform, privatization, EU standards, prices, quality of service

I. Introduction

Privatization and reform of communal services, along with the mistakes of rapid and comprehensive privatization, is often and the choice of the optimal model is to preserve the "public interest" and operate efficiently. The choice of the optimal model based on the principles of market economy and competitiveness is permanent, respecting the protection of the public interest. Any reform that will be carried out should take into account the specifics and conditions of the negative and positive experiences of others, and at the same time eliminate negative factors in the practice of one's own utility sector, while being careful to protect the future interests of society. In addition to having the prefix "public", in the case of public utility companies and in the case of public assets, there are significant differences between these two types of public companies in the type of activity, size and number, potential interest of foreign partners, profit rate, etc. It is necessary for public utility companies to be considered as a separate unit, due to the complexity of satisfying public functions, special models should be defined for each activity.

In the PUC reform, institutions should define a strategy for vital communal infrastructure, by activity, whether ownership of the same can be subject to privatization or remains in public ownership in order to protect the public interest. When the public sector is defined in the long term, along with the business reform, it is likely that, under certain conditions, donations intended for modernization and harmonization with EU regulatory requirements can be obtained.

Institutions should strategically decide in which utility sector when and to what extent they will allow the entry of private capital from domestic or foreign partners or not at all, with simultaneous institutional regulation. The practice in some countries, regarding the vital and capital-intensive utility sectors, shows that private capital has proven to be effective in reducing business costs, but private capital is not inclined to make significant investments, it is exclusively oriented towards profit, through pressure on prices and reaching a monopoly position, with the reduction of employment and the maximum use of deficiencies in regulation.

A partnership with the private sector or privatization requires a strategy and guidelines, followed by preparatory actions or preconditions such as:

- obligation and transparency of public procurement procedures and criteria,
- legal certainty and public control of contracts,
- regulation of market conditions, etc.

ISBN: 978-86-82602-01-9

The proposal for reform, with a change of ownership, should have property listed, entered in the land register, whose value has been objectively assessed; otherwise, it can be an obstacle for investors or misused during the introduction of the private sector in communal activities. The problems of PUK functioning as a result of inheritance and circumstances that have arisen in the last thirty years are:

- inadequate solution to the issue of ownership and disposal of public property,
- a particularly strong administrative-political influence on the PUC's overall operations,
- accumulation of unresolved issues on that basis,
- growth in business costs and inadequate prices to cover costs,
- low level of collection, large write-off of receivables and outstanding obligations,
- decline in the quality of services, interest in satisfying consumer needs, 7. dilapidated and outdated equipment and infrastructure,
- lack of funds for the renewal and expansion of capacities,
- non-compliance with environmental protection standards,
- absence of business indicators, etc.

The price level of communal services burdens the current operations of the PUC, and the approval of a limited price increase is not based on realistic parameters of cost coverage, but on administrative decisions. Utility companies are looking for the definition of a systematic methodology for price formation, based on the principles of covering all business costs, as well as the necessary investments. When the issue of price is raised, the issue of defining business indicators, quality and responsibility, and the issue of protecting the public from monopolies and sudden price jumps should also be covered in parallel.

With the current purchasing power of the population, with an acceptable price correction, in the short term, it can provide part of the funds to cover business costs, but not the funds for investments. With long-term measures such as: defining the price policy, improving the billing coefficient and reducing network losses (water supply and heating), it is possible to mitigate the price impact, but the problem of providing funds for capacity renewal and standard adjustment remains unsolved due to the required funds.

To obtain precise long-term needs and sources of funds, when the level of funds required for the smooth functioning of the PUC at the current level and the necessary funds for infrastructure expansion and adaptation to EU standards, are verified and put in relation to own funds (PUC, municipality and state funds), information on own self-financing possibilities and the required amount of donations from international institutions can be obtained.

The lack of funds for the modernization and expansion of the infrastructure is an obstacle to the long-term satisfaction of the public interest in quality communal services. The majority of PUKs/municipalities cannot finance their own participation of up to 25% in necessary large-scale investments with their own funds, and the majority must rely on donations from multiple sources and loans for these amounts as well.

Loans for investments require a higher degree of efficiency than donations, the borrower must operate more efficiently and with a profit to cover costs and service loan repayments. To ensure cash flow for annuity repayments, the lender can condition price:

- increases and improve collection rates. If the legal,
- doubts are resolved appropriately, this type of loan,
- represents a relatively safe placement that enables,
- regular repayment of the annuity, because PUK,
- Municipalities - are backed by the state.

The experience of EU countries indicates that one should be careful with loans and privatization arrangements related to them. If the modernization of the infrastructure is financed mainly by borrowing, debt servicing is reflected in the long-term by increasing the price of services and burdening the debtor, i.e. municipality/JKP as well as the state - guarantor. But the basis for access to donations is lost, because they cannot be used to reduce indebtedness, but only for the revitalization of communal infrastructure and reaching standards.

Learned from the experiences of others, modernization of communal infrastructure without a major indebtedness and increased pressure for the entry of private capital, requires parallel with the process of pre-accession and accession to EU integration, orientation of adoption activities and application of EU standards. EU funds for the development of communal infrastructure, i.e. GRANT funds to potential candidates, candidates, were insufficiently used for projects due to the small number of quality individual plans, slowness and ignorance of the methodology of accessing EU funds.

The state of the infrastructure, the required funds, the level of preparation of projects at the local level, do not allow a slow pace of reconstruction and construction, but require a more efficient approach to EU donations. Effective access to donations from EU funds available to potential candidates must be at the state and local level for the use of EU funds, with the participation of own funds.

II. Proposals

1) When defining the reform strategy, competent state institutions should consider PUC separately from PE.

2) Within the PUC reform, communal activities should be viewed separately (water supply, heating,) according to business activities and community needs.

3) When formulating a reform and/or privatization model, PUC institutions should decide and propose regulations on:

a) vital communal infrastructure by activity, i.e. which remains permanently public ownership;

b) define which activities can be subject to ownership transformation;

c) in the case of a partnership with the private sector or privatization, the first step should be strategy and guidelines, and then prepare preconditions such as mandatory and transparent procedures and criteria, legal certainty, public control of contracts, regulation of market conditions and responsibilities, etc.

(Potential positive effects of the mentioned proposals 1, 2 and 3: mistakes of others and “traps” of rapid and comprehensive privatization are avoided while protecting public interest, negotiating position and strategic infrastructure).

4) It is necessary to list, register and realistically assess the value of the property at the disposal (used) of public utility companies.

(Potential positive effects of proposal 4: the records and “fair” value of the property and thus the basis for calculating ownership shares are determined).

5) The first steps of the reform can be the development of measures that lead to more efficient operation of the PUC:

a) completely free the PUC from political influence, with state control in the domain of responsibility for the performance of basic activities and the application of standards;

b) define the methodology of price formation to cover business costs with minimal administrative decision-making. In the first phase of the new price parameters, foresee measures and regulations to protect the public interest from sudden jumps and monopolies. At the same time, the PUC should rationalize operations by internal activities by reducing the loss on the network and increasing the level of collection;

c) consider options for regionalization of inter-municipal systems for options for combining PUCs on a functional basis. The strategy of regionalization should be directed towards the problems of municipalities, as a measure to improve the functionality of PUCs and their economy, and access to external sources of financing.

Potential positive effects of proposal 5:

- Reducing the impact of politics on business efficiency;
- The influence of the regulator in controlling the application of standards and quality improvement;
- Regulation of price policies without administrative influence;

- Regional projects have easier access to financing sources in underdeveloped areas;
- Comparable parameters for evaluating the current state and further needs for indicators in the PUC transformation process are determined.

III. Value of Communal Property

For precise values of communal infrastructure, it must be observed from several aspects by activity. The key is an accurate physical inventory and record of property in property registers, which is often not the case in PUCs/municipalities. In the annual reports, fixed assets are shown in one amount, especially for smaller PUCs, which perform several activities, which creates a problem in delimiting the value of infrastructure by type. From the perspective of policy makers and strategic decisions, the perception of the value of infrastructure is formed on the basis of official data, but when considering future moves, it is also viewed from the perspective of social significance and utility value in the protection of the public interest [1].

IV. Position and Problems in PUC Operations

The problems of the legacy of the previous business system and the position of the PUC are:

- limitation in making key business decisions;
- there is no independence in the disposal of the property they use;
- prices are limited, subsidies to citizens through utility prices and poor billing with rising costs and write-off of receivables, PUCs are financially weak and insolvent;
- administrative division, oversizing and overloading of certain functions within PUC, irrational organization and poorer efficiency in providing services;
- lack of working and investment funds for equipment renewal and expansion;
- there is a strong non-compliance with environmental protection standards;
- objective identification of internal organizational problems is difficult due to the lack of parameters for comparing efficiency within the same activities. [2]

If the problems in PUC operations could be defined by the priorities that should be included in the transformation, then they would be systemic:

- regulation of the appropriate level of prices and business conditions,
- setting of inter-municipal regional systems,
- setting business indicators (“bench marking”),
- development of projects and necessary funds for the reconstruction and development of infrastructure.

V. Utility Service Price

In the public sector, the state determines the prices for services that are produced in the public or private sector, but by the state regulated sector. These services are performed in state-owned public enterprises. Privatization of public companies and the performance of these services in private, but state-regulated companies are increasingly being resorted to. But the state needs to find a model for determining their prices. Such is the practice of price determination in the production and transmission of electricity, various communal services (water supply and sewage), etc. The prices of most of these products and services for several reasons (natural monopoly, external effects, etc.) cannot be determined by the market, but it is up to the state to determine their level.

The pricing policy in the public sector must be guided by three criteria:

- efficiency of resource allocation,
- covering the costs of production of goods and
- service in the public sector and fairness of distribution.

To distinguish them from prices in the private sector, on the one hand, and taxes, on the other hand, prices in the public sector are often given a special name in the economic literature, and are referred to as user charges. With user fees, the state directly determines the level of prices for the services it regulates, while through taxes it indirectly affects the level of prices. In both cases, it determines the final price for the consumer, only in the case of taxes it does so indirectly. The state is trying to determine the optimal amount of taxes, but the optimal level of user benefits should also be determined. This is not always easy to achieve.

A common theoretical recommendation that civil servants should follow when setting prices in the public sector is that prices should be equal to marginal costs, because then the requirement for efficient allocation of resources is satisfied. But in practice, due to several reasons, it is difficult to apply this rule, so it is more considered a general standard to strive for. It is difficult to measure the marginal cost of each service, many public companies operate as natural monopolies and have the characteristics of economies of scale where long-term average costs decline. Marginal costs are then below average costs. If the price were set so that it was equal to the marginal cost, then it would not even cover the average costs and the company would be in a loss.

When the price is lower than the average cost, the company is making a loss. The ideal solution of price equality and marginal cost for determining prices in the public sector can hardly be applied. It is possible to determine the price according to the marginal cost, and the deficit of the public company is financed by subsidies, i.e. increased taxes.

This is an anomaly in the price system, and the question arises as to why taxpayers who do not use a given service bear the cost of its performance-production through taxes.

Another possibility is pricing according to the average cost, that is, according to the principle of fully distributed cost. Then the price represents the intersection of the demand curve and the average cost, and then the company covers its costs and makes neither profit nor loss.

Due to its simplicity, this method is increasingly common in practice. A number of difficulties appear in its application. It is especially difficult to apply this method in companies that produce many products. The third method of pricing is called two-part tariffs. Constant attempts by the state to bring prices as close as possible to the marginal cost, while at the same time the company generates enough income to cover costs, led to the formulation of the principle of two-part tariffs. It is a price system according to which users of a service pay a fixed amount to access its use, and later pay a variable amount according to the principle of price equality and marginal cost for each additional unit of service they use. Although two-part tariffs seem rather complex to implement, they are very widespread in practice.

Some economists accept Ramsey's rule (mathematician F. Ramsey) for pricing in public and regulated companies, that prices should be set slightly above marginal cost in order for the company to survive. However, it is necessary to determine how much above the marginal costs they should be. Ramsey's rule states that prices should be furthest from marginal costs for those products that have the least elasticity of demand. Thus, the rise in prices will produce the smallest distortions in demand.

And when the costs can be determined with certainty, the question remains whether optimal pricing in the public sector should be limited by efficient allocation of resources, or whether it should take into account the need for prices in the public sector to achieve certain shifts towards a fairer distribution.

The PUC's operations are burdened by the fact that the issue of the systematic setting of methodologies for determining and approving the level of service prices is not regulated, at least to the level of covering business costs.

It is usual for requests to increase the prices of communal services to be submitted to the municipality for approval, which puts individual PUCs in an unequal position, because the approval is expressed as a percentage of the current price, adjusted to the inflation rate of the previous year.

The approved increase amount is generally not enough to cover the operating costs. PUCs that (mainly under the influence of local politics) did not submit a request for price increases lag behind other PUCs that did so unjustifiably, from the aspect of covering costs. This is proof that the approval for price increases is not based on realistic parameters of cost coverage, but on administrative interference in PUC operations.

The prices of utility services are insufficient to cover the actual costs of doing business, or the price level is influenced by local politics. The PUC can also choose the option to indirectly increase its revenues, i.e. reduce costs, by reducing the volume or, which is often the case, the quality of services, which is reflected in the volume and quality of service to consumers.

In the case of PUCs whose service prices, despite the approved level of increase, are formed below the level necessary to cover the economic price, business will continue to be burdened with the same problem, because they are not provided with sufficient income to cover all costs. In the case of a number of PUCs whose prices cover costs, there is a lack of incentive for PUC management to influence efficiency in an organized manner, because management is under the direct influence of politics. Respecting the current standard of citizens, an acceptable price correction, as a short-term measure, can provide funds for business expenses, but insufficient for investments. Long-term measures such as:

- defining the price policy,
- improving the level of collection i
- reduction of network losses,

can mitigate the long-term price impact, but the problem of capacity renewal and adaptation to standards remains unsolved.

In the transition of the utility sector, binding principles of price formation methodology should be defined, which enable coverage of business costs, but also funds for investments, with minimal administrative and political interference. In the future, the application of new price parameters should be preceded by a measurable improvement in quality, but foresee measures and regulations to protect consumers from sudden price jumps and monopolies.

VI. STATUS AND SOURCES OF FUNDS FOR THE DEVELOPMENT OF COMMUNAL INFRASTRUCTURE IN B&H

Due to the low level of prices, rising costs and poor billing, PUCs had to reduce the level of necessary investments in the maintenance of communal infrastructure. Chronic illiquidity, as a consequence of a lack of funds, was reflected in the poor condition of the infrastructure. From the point of view of EU standards, the state of municipal infrastructure in B&H is characterized by non-compliance and lagging in development, especially in the wastewater treatment.

In order to start the process of renovation and development of the communal infrastructure, it is necessary to plan (short-term/long-term) the level of funds needed for current operations and the level of funds for investments for modernization and capacity expansion. That is why competent state institutions should prescribe the necessary service standards that must be met, and this will also provide information on technical conditions and necessary investments. Investment needs, in addition to technical criteria and public priorities, must be adapted to EU standards. When priorities are defined and projects are prepared, sources of funding should be urgently sought. Due to the small capacity of municipalities/JKPs and the state, the sources of financing for the reconstruction and construction of infrastructure are limited to a maximum of approx. 25-30% of own participation for priority projects, or from loans from development and commercial banks, while the remaining approx. 70-75% could be provided by donations

Borrowing opportunities for own participation are less than the average remaining credit potential of smaller towns and municipalities, and the position of large cities is better. Cities are a priority due to the number of inhabitants and economic strength, infrastructure projects are large in scope and investments, despite the potential, they must be careful in borrowing, and they must use the benefits provided by donor funds. Loans require a higher degree of efficiency than donations, the borrower must operate efficiently with income that allows him to cover costs and be able to service loan repayments.

When the modernization of the infrastructure is financed mainly by borrowing, the burden of servicing debts for a long period is reflected in the increase in the price of services and the burden on the debtor, i.e. municipality/JKP as well as the state as guarantor. But the need ends and the basis for access to donations is lost, because they cannot be used to reduce indebtedness, but exclusively for the revitalization of infrastructure and reaching standards.

EU funds - grant funds that are planned and allocated, are insufficiently used for specific projects in some countries, due to the small number of high-quality individual plans, slowness or poor knowledge of the methodology of accessing these funds. The state of the infrastructure, the necessary funds for the reconstruction and development of PUC in B&H, as well as the level of project preparation at the local level, require more efficient access to available grant funds. In order for access to grants to be effective and in accordance with the strategy of adaptation to EU standards, preparations must be made at the state and local level for the application of procedures for the use of EU funds.

VII. EU Regulations and Directives

EU directives and standards are an important driver of investments in infrastructure. It is expected that in less developed countries, major investment will be directed towards building networks, and in more developed countries, major investment will be directed towards reducing costs in the process of adapting to EU standards. Building new capacities in some and minor improvements in others require significant funds.

Through the changes, the private sector mostly gave positive results in reducing business costs, but exerted strong pressure on prices due to reaching higher profits, without a motive for significant investments. Multinational companies tend to eliminate competition and create and maintain monopolies, thereby putting pressure on prices for higher profits. Lenders condition the increase in prices due to the security of loan repayment, but they can also influence the conditional privatization of the sector as well as the commercialization of business.

The necessary funds for the development of communal infrastructure, which state funds do not have, and the opportunities provided by pre-accession funds, is the optimal solution for the country, a future member of the EU. Donations, as the most favorable sources of financing, require certain political processes, but also the necessary respect and knowledge of the procedures for accessing those funds.

VIII. Inter – Municipal Cooperation

The advantages of such regional companies are: higher value of fixed assets, stronger creditworthiness, more efficient management, more stable long-term development, easier control by national legislative bodies.

There are possible disadvantages when organizing regional/cantonal companies in the initial phase:

- dissatisfaction of municipalities due to handing over management of municipal PUCs to the regional level;
- dissatisfaction of employees in the municipal PUC due to the possible excess number of employees in the new regional public company;
- dissatisfaction of political factors, because they are losing municipal influence, the number of "political" positions in the PUC is decreasing.

"Reforms of the communal sector require a new framework, control regime and institutions that will implement that regime. Rehabilitation and progress in communal services require a new way of management, which is based on resource conservation and integration with local administration. " [3].

IX. "Benchmarking" as a Technique for Measuring Business Efficiency

"Benchmarking" is the process of finding the best existing product, production process or service on the market, and implementing it as a standard for improving the products, processes and services of a particular company.

The main technique of "benchmarking", when considering the above definition, is measurement. In order to perform a measurement, the one to be measured must have indicators that belong to the same group of indicators that one wants to fix after the measurement.

The following groups of indicators are most often used:

- Performance,
- Processes,
- Product characteristics.

In the case of activities presented in this material, "benchmarking" indicators can be:

For district heating:

- Performance indicators: profit and loss account from the core business, number of connections, calculated/charged ratio, user satisfaction, network length, number of employees per connection, etc.
- Process indicators: heat losses, procedures in case of breakdowns, regular annual maintenance processes expressed in terms of time and monetary units, speed of network expansion, implemented IT processes, etc.
- Indicators of product characteristics: availability of hot water throughout the year, purity of hot water, ability to

regulate the temperature inside heated buildings, etc.

At the beginning of the implementation of “benchmarking”, the most complicated thing is to collect information about the indicators that are taken as relevant for comparison. If that action were to be implemented, a body must be formed to monitor the action. From that aspect, communal services are difficult for “benchmarking”. The reason is the specific characteristics of the utility market, such as: availability of water sources, population size, state of infrastructure, etc.

X. Privatization Process of Utility Sector in New EU Members

The form of PUC reform differs from country to country, due to the motives of competent institutions for formulating change policies. The reason for the reform is to increase efficiency and improve the quality of services. At the beginning of the process, the opinion was that the market-oriented structure of utility companies is much better than the old service distribution system, which was combined with the desire to reduce budget expenditures and transform budget-dependent organizations into economically self-sustainable ones.

In these circumstances, the decisive factor is the lack of investments, which could only be provided from external sources - foreign investments. The only possibility to quickly attract funds was privatization. Some of them lacked transparent market business conditions, such as the regulation of competitiveness of tender conditions and procedures. A lot of mistakes were made due to the lack of legal regulations and imprecise investment conditions, free interpretation of the regulations by the participants, which were later clarified, but which were subsequently difficult to correct. Rapid and thoughtless privatization led to the erosion of municipal property and increased unemployment. The consequences of these moves are still being felt in those municipalities. In each country, there are specificities and differences in the social treatment of public utility services, and in most of the former socialist countries, now members of the EU, the questions of appropriate policy and which options are best are still unclear and unresolved.

Generally speaking, the transformation of the public utility sector took place in 4 phases:

- return of property to local authorities,
- corporatization, public and private sector partnership, commercialization and
- privatization - attracting capital through operational functions, with exceptions in infrastructure privatization,
- regulation.

XI. Mistakes in the Privatization Process

Immediately after the social changes, privatization was the first to sell state property, which was carried out without valid tendering and other regulatory procedures. It was a spontaneous privatization - a search for new owners. At that time, unfavorable contractual arrangements were concluded for users, while at the same time favorable for the private sector. In the absence of regulation, market conditions of business and development of institutions, such phenomena were seen as a natural consequence of privatization.

The most frequently expressed negative features of privatization were:

a) Transformation of natural into private monopolies

- lack of preparation, defined competencies and regulatory bodies;
- large international investors gained a good starting and dominant position on the market before regulatory mechanisms were established, and in order to protect their interests, they opposed market liberalization and competition in the following stages of development.

b) Corruption

- Lack of transparency in public decision-making;
- Inadequate planning of the transformation process;
- Economic and political influence of the private sector on the public sector.

c) Conflict of interest and lack of interest in further changes

- Local politics had no interest in accepting the regulation it prescribes business standards and limits its influence on process transparency.

d) Neglected social aspect

- Price growth, which was not a consequence of improving the volume and quality of services;
- Significantly increased share of utility costs in the average family income;
- Unemployment growth as a consequence of general privatization and slowdown economic activities. The experience of countries that have already gone through the transition process of the utility sector indicates that rapid privatization and loss of control over assets does not yield positive results.

The introduction of the private sector in the utility sector can bring new quality and efficiency of operations from the aspect of costs, but it does not always lead to an improvement in quality. Practice has shown that privatization does not have to be the only solution, but is one of the alternatives. it can also be partial privatization in combination with the introduction of competition, and such a combination can affect the reduction of prices and the improvement of service levels.

The experience of former socialist countries, now members of the EU, show that there was a political need and desire for the transformation and modernization of the utility sector, but there was no need to copy the Western model of privatization of utility services, because the social and economic circumstances were significantly different. The desire to reach the level of development of the EU countries at the time is positive, but it is a complex process, the realization of which requires preparations and a certain time for a planned transition and planned gradual implementation.

In some countries, e.g. In Sweden, the prevailing view is that exclusive 100% public ownership is the best solution for ensuring the satisfaction of necessary public needs, while at the same time allowing "non-core" activities to be separated and privatized.

XII. Recommendations for the Best Practices in Determining Prices

Prices of utility services should:

- be simple and easy for users to understand;
- provide income sufficient to cover the costs of providing the service;
- provide income sufficient to repay long-term obligations;
- prevent ineffective use of resources;
- support investments and activities that will enable quality services for the consumer;
- support investments and activities aimed at environmental protection;
- enable utility services to be affordable to users; and
- reflect the different costs of providing services to different users.

Activities as possible steps towards price redesign:

a) Provision of accurate business books, accounts and files

- Provide quality user data,
- Costs should be related to tasks and activities,
- Ensure reliability of financial data,
- Develop and maintain a performance monitoring system,
- Provide clear parameter definitions.

b) Analyze institutional arrangements

- determine regulatory bodies and their roles

a) Measure the quality of utility services

- Measure the use of utility networks (e.g. flows through sewers, etc.),
- Measure the consumption of end users,
- Monitor the quality of services in all phases.

References

[1] Hyman, D. N. (2014). *Public finance: A contemporary application of theory to policy*. Cengage Learning.

[2] IMF. (1991). *Public Expenditure Handbook*. Washington: International Monetary Fund.

[3] Samuelson, P. A. & Nordhaus, W. D. (1995). *Economics*. New York: McGraw Hill.

Fault Detection of Wind Turbine Gearbox using Time-Domain Features Extraction from Vibration Signal

Chahinez Beldjaatit[1], Hocine Guentri[2]

[1]20 Août 1955 University, Skikda, Algeria
[2]Abdelhafid Boussouf University Center, Mila, Algeria

Abstract—**Premature component failures are a common problem in wind turbine drivetrains, and research has shown that multi-stage gearbox failures result in the longest turbine downtime and consequently the greatest expenditures. According to studies, the majority of gearbox component failures are due to the bearings rather than the gears. Vibration condition monitoring is one of the most crucial equipment maintenance techniques. This is done to identify failing components and improve the machine's safety and reliability. The health of the bearing has an extensive impact on the life of the rotating machine. This is because bearings are the most vital and critical part of rotary equipment. The vibration signal analysis can give us a better understanding of various defects occurring in mechanical systems. The current work focuses on the fault detection of ball bearings using time domain analysis in vibration monitoring. Several statistical features are calculated in this type of analysis for four bearing conditions essentially: healthy, inner race fault, outer race fault, and ball fault condition. When the results from both healthy and defective conditions are compared, it becomes clear that default conditions result in an increase in the majority of the statistical parameter values. The effect of changing the fault diameter and the load on the bearing state is observed through a variation of statistical parameter values. The monitoring results show that time features can clearly distinguish between all bearing situations of wind turbine gearbox.**

Keywords - condition monitoring, fault analysis, rolling element bearing, time domain analysis, wind turbine

I. Introduction

Wind power is considered a clean source of energy and has recently become the world's fastest growing source of renewable energy, with a 591GW installed capacity in 2018 and an expected increase to 908 GW in 2023 [1].

The speed of technological advancement is accelerating daily. This resulted in a demand for any type of work to be faster, and more efficient, systems like compressors, cars, industrial fans, steam turbines and wind turbines perform adequately as a consequence of the numerous applications for rotational mechanical equipment's in various industries [2]. The majority of wind turbine machines are three-blades units with the main parts. The main shaft, which is supported by bearings, transfers wind energy from the blades and rotor to the generator through gearbox where energy of wind is converted into electrical energy by the generator at a speed that is close to ideal as feasible [3].

Notably, certain wind turbine parts breakdown early than anticipated, and because unplanned downtime can be expensive [4]. Wind turbine drivetrains are frequently plagued by premature element failures, with malfunctions in the multi-stage gearbox causing the longest downtime of the turbine and thus the greatest costs [5]. One of the crucial parts of rotating machinery are bearings and studies reveal that the gearbox's bearings failures occur around 76% of the time more than the gears fail 17% of the time [6].

ISBN: 978-86-82602-01-9

The technology for defect identification has taken center stage in prognostics and health management (PHM), it is essential for maintaining mechanically intelligent equipment [7]. Condition monitoring is made up of various sensors and signal processing tools that use techniques like vibration analysis, acoustics, oil analysis, and thermography to give information about the condition of a component [8]. However, vibration analysis is a useful instrument and efficient method for monitoring the state of the rotary machines [9].

A common area of research in mechanical failure identification is bearing fault diagnosis. Fundamentally, there are three types of vibration signal processing techniques used in defect diagnosis: time-domain, frequency domain and time-frequency analysis methods [10]. In time-domain approach, statistical parameters such as RMS, peak value, kurtosis and crest factor are monitored for bearing fault detection [11]. Frequency-based techniques have been widely used for stationary signal analysis like Fast Fourier Transform (FFT) is used for fault location by converting time domain vibration signals into frequency components [12]. Time-frequency techniques are commonly used for non-stationary signals, include Short Time Fourier Transform (STFT) [13], Empirical Mode Decomposition (EMD) [14], Hilbert-Hung Transform (HHT) [15] and Wavelet Transform (WT) [16].

In this paper, time domain analysis has been presented for rolling element bearing fault detection of wind turbine gearbox. It is regarded as one of the most inexpensive and simplest approach to use for defect detection. From vibration signals of healthy and faulty bearings, several time features parameters are extracted and compared under different working conditions, that include change in load and damage diameter. Detection of bearing failures is possible through comparison of time domain statistical features.

II. Experiment Data of Bearing

While real bearing-fault signals for wind turbines are mostly commercially private, the dataset used in this study is obtained from the Case Western Reserve University Bearing Data Center [17] is shown in Fig. 1. It allows access to ball bearing test information for both healthy and damaged bearings. Electro-discharge machining (EDM) was used to collect the vibration signal data under the following four experimental conditions: (a) normal state, (b) inner race fault, (c) outer race fault, and (d) ball fault with fault depths from 0.18 mm to 0.71 mm (0.007 inches to 0.028 inches). The vibration data was recorded using accelerometer with a sampling rate of 12 KHz and 48 KHz for drive end bearing faults. The vibration signals were collected for motor loads of 0 to 3 hp at motor speeds of 1720 to 1797 rpm. In our study, the sampling frequency chosen is 12 KHz for four cases: normal condition, inner race fault, outer race fault, and ball fault. Each fault type bearing includes four kinds of fault degrees (0.18 mm, 0.36 mm, 0.53 mm, and 0.71 mm).

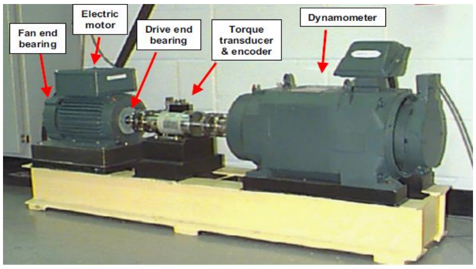

Figure 1. CWRU test rig [18].

III. Time Domain Signal Analysis

Vibration signals provide useful information about the states of the system, and fault detection is based in study of various features collected from system signals [19]. Basically, the process which some characteristics features as well as statistical parameters are computed from vibration data is known as time domain analysis. Feature extraction serves as a crucial stage in the effective fault diagnosis process for high-dimensional datasets. In the current work, the statistical parameters used for time domain analysis are: root mean square (RMS), peak value, kurtosis (Kurt), standard deviation (SD), skewness, and crest factor. The proposed features are described mathematically bellow:

A. Root Mean Square (RMS)

The root mean square (RMS) value displays the vibratory energy level in signal, it is a Gaussian random process with amplitude modulation [20]. RMS is presented as:

$$RMS = \sqrt{1/N\sum_{i=1}^{N}(X_i)^2} \quad , \qquad (1)$$

where X_i is the raw vibration signal, i is the sample number and N is the length of samples.

B. Peak Value

Peak Value is maximum amplitude at some point. The peak value is always used to identify a breakdown with immediate effects [21], it is obtained as:

$$Peak\,value = \max(X_i) \quad . \qquad (2)$$

C. Kurtosis (Kurt)

Kurtosis is the normalized version of the fourth moment of the signal, it is a statistical measure of the random variable distribution. Kurtosis for normal bearing is approximately equal to 3 [22]. When the value is more than or equal to 4, It indicates that there is some level of damage. Kurtosis is given by:

$$Kurt = \frac{\frac{1}{N}\sum_{i=1}^{N}(X_i - \overline{X})^4}{RMS^4} \quad , \qquad (3)$$

$\overline{X}$ is the mean value of vibration time series X_i .

D. Standard Deviation(SD)

The standard deviation displays the degree of signal dispersion from the average. It can also be defined as the signal's RMS. SD is represented as:

$$SD = \sqrt{1/N\sum_{i=1}^{N}(X_i - \overline{X})^2} \quad . \qquad (4)$$

E. Skewness

Skewness is defined as the third statistical moment of vibration signal that is normalized, or more precisely, it is a measure of symmetry. Skewness is presented as:

$$Skewness = \frac{\frac{1}{N}\sum_{i=1}^{N}(X_i - \overline{X})^3}{RMS^3} \quad . \qquad (5)$$

Skewness for a normal distribution is zero since it is highly symmetric. The skewness of the bearing vibration signal reveals the location of the fault [23].

F. Crest Factor(Cf)

Crest factor is the ratio of the signal's peak value to its root mean square (RMS) value. The Cf given by [24]:

$$Cf = \frac{Peak\,value}{RMS} \quad . \qquad (6)$$

Crest factor, which represents the existence of high amplitude peaks in vibration data, is a normalized measurement of signal amplitude.

IV. Results and Discussion

It's always preferable, for condition monitoring reasons, to reduce enormous amounts of data included in the vibration signal to a single indicator or a handful of characteristics that accurately reflect the basic features of signal. Feature extraction is the process used in this. Feature extraction technique is applied on bearing vibration signals of wind turbine gearbox under different motor loads (0 to 3 Hp). All vibration data used for fault diagnosis is implemented for four conditions: healthy, defective ball, defective inner race, and defective outer race. The statistical parameters such as RMS, Peak Value, Kurt, SD, Skewness, and Crest factor are shown graphically in Figs. 2-7.

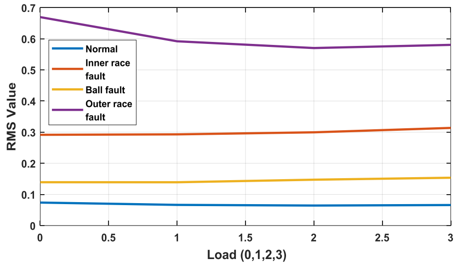

Figure 2. Variation of RMS value for four bearing states.

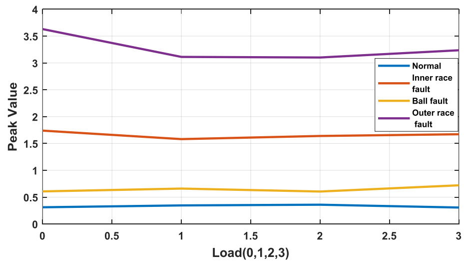

Figure 3. Variation of peak vaue for four bearing states.

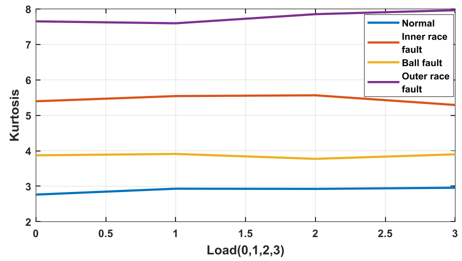

Figure 4. Variation of kurtosis for four bearing states.

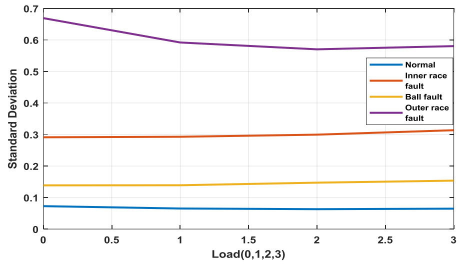

Figure 5. Variation of SD for four bearing states.

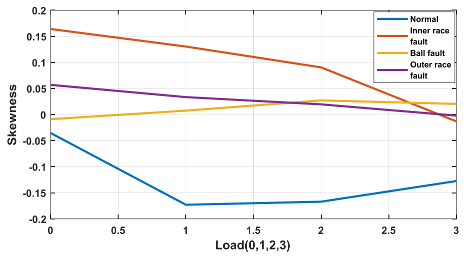

Figure 6. Variation of skewness for four bearing states.

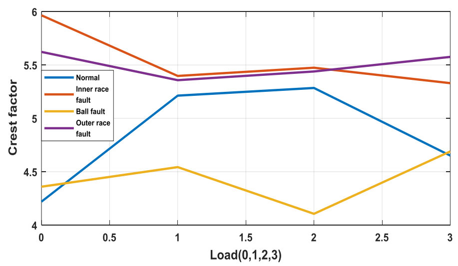

Figure 7. Variation of Cf for four bearing states.

The first essential observation we made from the previous curves of time statistics indicators dependent of different loads (0,1,2,3) was that for defective bearings, when the rolling element passes over the defective zone of the bearing, the time features amplitude rapidly changes and increases. Fig. 2-7 demonstrate that there is a very evident distinction between a normal and faulty bearing. Moreover, we observe that the variation in load has no appreciable impact on the bearing state, and an explanation for that, there is no change in statistical parameters values with the increase in value of load.

Figs. 2-5 display the RMS, peak value, kurtosis, SD respectively for each of the four bearing states that were taken into account for this study. It can easily be seen that the RMS, peak value, Kurt, and SD values are small for healthy bearing and large for abnormal bearings. In addition, there is no overlap in their values for the two cases. Hence, it is clear that these four features offer better results in identifying between normal and faulty bearings. RMS, peak value, Kurt, and SD values for outer race fault are much higher as compared to that of inner race and ball faults, this indicates that the greater energy and asymmetries in the vibration data were caused by the outer race defect.

Variation of skewness of vibration data for different cases is shown in Fig. 6. It can be observed that the values of skewness are negative in healthy state, this refers to the distribution grows a longer tail left of the mean, which these values increase as a fault is introduced. From Fig. 6, we get the conclusion that skewness is an excellent indicator of inner race fault.

In Fig. 7. Can be easily noticed that the crest factor for healthy bearing, bearing with ball fault is overlapping, making it impossible to distinguish between these two situations using the crest factor. Once more, utilizing this time parameter to separate bearing failure types is not very accurate.

To examine the effect of changing the diameter further, the root mean square (RMS), peak value, kurtosis, and standard deviation values for each diameter condition at inner race fault was calculated and compared, like what's shown in the following figures.

Figs. 8, 9, and 11 represent the variation of RMS, peak value, and SD for inner race fault respectively with different diameters of defect. It is clear that the root mean square, peak value and kurtosis values rise when the fault severity level increases. This illustrates that the diameter of fault has a significant effect on the degree of deterioration of bearing condition. It is interesting to note that the increasing in statistical features values refer to the rise in dispersion and number of peaks in vibration signals.

As shown in Fig. 10 the values of kurtosis for bearing with inner race fault are maximum in diameter of 0.36 mm. On the other hand, for

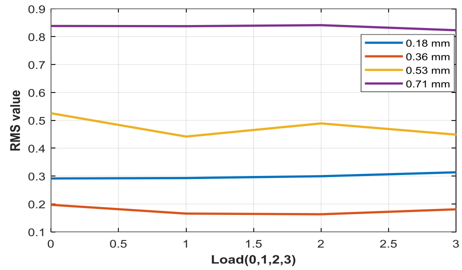

Fig. 8. Variation of RMS value for inner race fault.

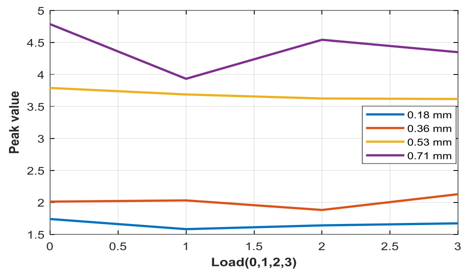

Figure 9. Variation of peak value for inner race fault.

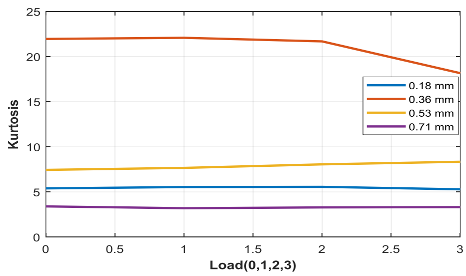

Figure 10. Variation of kurtosis for inner race fault.

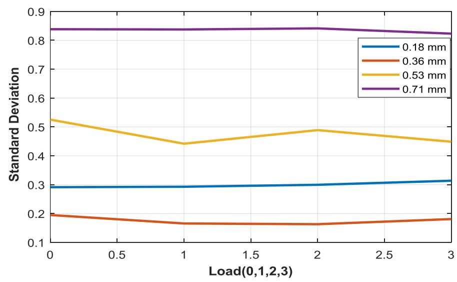

Figure 11. Variation of SD for inner race fault.

faulty condition, an increase in peaks leads to a flattening of the data distribution, which produces a low value of kurtosis.

V. Conclusion

The current paper provides a developed study on the time-domain analysis method for determining the health of wind turbine bearings. This type of analysis evaluates the energy of the vibration signal in time. It was applied to the bearing data under various conditions, which are normal state, inner ring failure, outer ring failure, and ball failure. Statistical methods and feature extraction play a vital role in condition monitoring of gearbox bearings. Thus, time domain signal analysis based on feature extracted is widely used to investigate the random characteristics of a vibration signal generated from a mechanical fault. The main time domain statistical features that were extracted to detect the bearing faults in this work are: RMS, kurtosis, standard deviation, peak value, skewness, and crest factor. Because of the wide variation in these values, it is possible to differentiate between normal and faulty bearings. Hence, it can be concluded that the time domain approach is capable of distinguishing between all bearing states and to reflect the severity of the fault.

References

[1] *Global Wind Report 2018*. *Tethys*. (2018). Available at: https://tethys.pnnl.gov/publications/global-wind-report-2018

[2] Li, Y., Wang, X., Liu, Z., Liang, X. & Si, S. (2018). The Entropy Algorithm and Its Variants in the Fault Diagnosis of Rotating Machinery: A Review. *IEEE Access*, *6*, 66723-66741.

[3] García Márquez, F. P., Tobias, A. M., Pinar Pérez, J. M., & Papaelias, M. (2012). Condition monitoring of wind turbines: Techniques and methods. *Renewable Energy*, *46*, 169–178.

[4] Condition monitoring (2005). Monitoring the wind: reducing kilowatt-hour costs with condition monitoring. *Refocus*, *6*(3), 48–51.

[5] Daniel, S. (2018). *Condition Monitoring of Wind Turbine Drivetrains Using Wavelet Analysis*. Dept. of Engineering Sciences and Mathematics, Luleå University of Technology.

[6] Peeters, C., Guillaume, P., & Helsen, J. (2018). Vibration-based bearing fault detection for operations and maintenance cost reduction in wind energy. *Renewable Energy*, *116*, 74–87.

[7] Wang, D., Tsui, K. L., & Miao, Q. (2018). Prognostics and Health Management: A Review of Vibration Based Bearing and Gear Health Indicators. *IEEE Access*, *6*, 665–676.

[8] Knezevic, J. (1993). *Reliability, Maintainability and Supportability: A Probabilistic Approach*. McGraw-Hill.

[9] Zhang, P., Du, Y., Habetler, T. G., & Lu, B. (2011). A Survey of Condition Monitoring and Protection Methods for Medium-Voltage Induction Motors. *IEEE Transactions on Industry Applications*, *47*(1), 34–46.

[10] Wang, L., Zhang, X., & Miao, Q. (2016). Understanding theories and methods on fault diagnosis for multi-fault detection of planetary gears. In *2016 Prognostics and System Health Management Conference (PHM-Chengdu)*.

[11] Rauber, T. W., de Assis Boldt, F., & Varejao, F. M. (2015). Heterogeneous Feature Models and Feature Selection Applied to Bearing Fault Diagnosis. *IEEE Transactions on Industrial Electronics*, *62*(1), 637–646.

[12] Helmi, H., & Forouzantabar, A. (2019). Rolling bearing fault detection of electric motor using time domain and frequency domain features extraction and ANFIS. *IET Electric Power Applications*, *13*(5), 662–669.

[13] Grebenik, J., Zhang, Y., Bingham, C., & Srivastava, S. (2016). Roller element bearing acoustic fault detection using smartphone and consumer microphones comparing with vibration techniques. In *International Conference on Mechatronics - Mechatronika*.

[14] Camarena-Martinez, D., Osornio-Rios, R., Romero-Troncoso, R., & Garcia-Perez, A. (2015). Fused Empirical Mode Decomposition and MUSIC Algorithms for Detecting Multiple Combined Faults in Induction Motors. *Journal of Applied Research and Technology*, *13*(1), 160–167.

[15] Cheng, G., Cheng, Y. L., Shen, L. H., Qiu, J. B., & Zhang, S. (2013). Gear fault identification based on Hilbert–Huang transform and SOM neural network. *Measurement*, *46*(3), 1137–1146.

[16] Abad, M. R. A. A., Moosavian, A., & Khazaee, M. (2016). Wavelet transform and least square support vector machine for mechanical fault detection of an alternator using vibration signal. *Journal of Low Frequency Noise, Vibration and Active Control*, *35*(1), 52–63.

[17] *Case School of Engineering*. Available at: https://engineering.case.edu/bearingdatacenter

[18] Smith, W. A., & Randall, R. B. (2015). Rolling element bearing diagnostics using the Case Western Reserve University data: A benchmark study. *Mechanical Systems and Signal Processing*, 64–65.

[19] Abid, A., Khan, M. T., & Iqbal, J. (2020). A review on fault detection and diagnosis techniques: basics and beyond. *Artificial Intelligence Review*, *54*(5), 3639–3664.

[20] Nayana, B. R., & Geethanjali, P. (2017). Analysis of Statistical Time-Domain Features Effectiveness in Identification of Bearing Faults From Vibration Signal. *IEEE Sensors Journal*, *17*(17), 5618–5625.

[21] Fu, S., Liu, K., Xu, Y., & Liu, Y. (2016). Rolling Bearing Diagnosing Method Based on Time Domain Analysis and Adaptive FuzzyC-Means Clustering. *Shock and Vibration*, *2016*, 1–8.

[22] Caesarendra, W., & Tjahjowidodo, T. (2017). A Review of Feature Extraction Methods in Vibration-Based Condition Monitoring and Its Application for Degradation Trend Estimation of Low-Speed Slew Bearing. *Machines*, *5*(4), 21.

[23] Azeez, N. I., & Alex, A. C. (2014). Detection of rolling element bearing defects by vibration signature analysis: A review. In *2014 Annual International Conference on Emerging Research Areas: Magnetics, Machines and Drives (AICERA/ICMMD)*.

[24] Sreejith, B., Verma, A., & Srividya, A. (2008). Fault diagnosis of rolling element bearing using time-domain features and neural networks. In *2008 IEEE Region 10 and the Third International Conference on Industrial and Information Systems*.

Real Power Loss Reduction by Enriched Groundhoppers Optimization Algorithm

Kanagasabai Lenin[1]

[1]Department of EEE, Prasad V. Potluri Siddhartha Institute of Technology, Kanuru, Vijayawada, Andhra Pradesh-520007, India

Abstract—**In this paper Enriched Groundhoppers (EG) Optimization Algorithm, is projected to solve the Power loss lessening problem. EG Algorithm imitates the deeds of Groundhoppers. Each Groundhoppers Position symbolizes a candidate solution in the problem. Groundhoppers progression prejudiced by three features: social communication, gravity force, wind advection. Enriched Groundhoppers (EG) Optimization Algorithm has been Modeled by integrating Opposition Based Learning, Levy Flight, and Gaussian Mutation Groundhoppers Optimization Algorithm with for Real Power Loss Reduction. Opposition based learning is one of the influential optimization tools to boost the convergence speed of different optimization techniques. True power loss lessening, voltage divergence curtailing, and voltage constancy index augmentation has been attained.**

Keywords - real, power, groundhoppers

I. INTRODUCTION

Power loss lessening is an authoritative problem in power system. Abundant techniques [1-6] and evolutionary approaches [7-14] are applied for solving Factual power loss lessening problem. Reference [1] done the work on Contribution to à l'étude du dispatching économique problem. Reference [2] did research on optimal power flow solutions. Reference [3] did work on a simple effective heuristic for embedded mixed-integer quadratic programming. Reference [4] solved optimal reactive-power dispatch using differential search algorithm. Reference [5] worked on an enhanced self-adaptive differential evolution based solution methodology for multiobjective optimal power flow. Reference [8] applied Hybrid PSO-Tabu search for solving the problem. Reference [9] used Ant lion optimizer for solving the optimal reactive power problem. Reference [10] solved Optimal reactive power dispatch by using quasi-oppositional teaching learning based optimization.

Reference [12] did research on finding the optimal reactive power dispatch solutions by using a novel improved stochastic fractal search optimization algorithm. Reference [13] solved optimal reactive power dispatch using improved pseudo-gradient search particle swarm optimization. In this paper Enriched Groundhoppers (EG) Optimization Algorithm is projected to solve the Power loss lessening problem. EG Algorithm imitates the deeds of Groundhoppers.

Each Groundhoppers Position symbolizes a candidate solution in the problem. Groundhoppers progression prejudiced by three features: social communication, gravity force, wind advection. Enriched Groundhoppers (EG) Optimization Algorithm has been Modeled by integrating Opposition Based Learning, Levy Flight, and Gaussian Mutation Groundhoppers Optimization Algorithm with for Real Power Loss Reduction.

Opposition based learning is one of the influential optimization tools to boost the convergence speed of different optimization techniques. The thriving implementation of the Opposition based learning engages evaluation of opposite population and existing population in the similar generation to discover the superior candidate solution for the problem. Proposed Enriched Groundhoppers (EG) Optimization Algorithm is appraised in IEEE 30 bus system.

II. PROBLEM FORMULATION

Power loss minimization is defined by:

$$Min\,\tilde{OBF}\left(\bar{r},\bar{u}\right)\ , \tag{1}$$

Subject to:

$$L\left(\bar{r},\bar{u}\right)=0\ , \tag{2}$$

$$M\left(\bar{r},\bar{u}\right)=0\ , \tag{3}$$

$$r=\left[VLG_1,..,VLG_{Ng};QC_1,..,QC_{Nc};T_1,..,T_{N_T}\right]$$
$$u=\begin{bmatrix}PG_{slack};VL_1,..,VL_{N_{Load}};\\ QG_1,..,QG_{Ng};SL_1,..,SL_{N_T}\end{bmatrix}. \tag{4}$$

The fitness function $\left(F_1,F_2,F_3\right)$ is designed for power loss (MW) reduction, Voltage deviation, voltage stability index (*L*-index) is defined by:

$$F_1=P_{Minimize}=$$
$$=Minimize\left[\sum_m^{NTL}G_m\left[V_i^2+V_j^2-2\cdot V_iV_jcos\O_{ij}\right]\right],\tag{5}$$

$$F_2=Minimize\begin{bmatrix}\sum_{i=1}^{N_{LB}}\left|V_{Lk}-V_{Lk}^{desired}\right|^2+\\ +\sum_{i=1}^{Ng}\left|Q_{GK}-Q_{KG}^{Lim}\right|^2\end{bmatrix},\tag{6}$$

$$F_3=Minimize\,L_{MaxImum}$$
$$L_{Maximum}=Maximum\left[L_j\right];\ j=1;N_{LB},$$
$$\begin{cases}L_j=1-\sum_{i=1}^{NPV}F_{ji}\dfrac{V_i}{V_j}\ ,\\ F_{ji}=-\left[Y_1\right]^1\left[Y_2\right]\end{cases}\tag{7}$$
$$L_{Maximum}=Maximum\left[1-\left[Y_1\right]^{-1}\left[Y_2\right]\times\frac{V_i}{V_j}\right].$$

Equality constraints:

$$0=PG_i-PD_i-V_i\cdot\sum_{j\in N_B}V_j\begin{bmatrix}G_{ij}cos\left[\O_i-\O_j\right]+\\ +B_{ij}sin\left[\O_i-\O_j\right]\end{bmatrix},\tag{8}$$

$$0=QG_i-QD_i-V_i\sum_{j\in N_B}V_j\cdot$$
$$\cdot\left[G_{ij}sin\left[\O_i-\O_j\right]+B_{ij}cos\left[\O_i-\O_j\right]\right].\tag{9}$$

Inequality constraints

$$\begin{gathered}P_{gslack}^{minimum}\le P_{gslack}\le P_{gslack}^{maximum},\\ Q_{gi}^{minimum}\le Q_{gi}\le Q_{gi}^{maximum},i\in N_g,\\ VL_i^{minimum}\le VL_i\le VL_i^{maximum},i\in NL,\\ T_i^{minimum}\le T_i\le T_i^{maximum},i\in N_T,\\ Q_c^{minimum}\le Q_c\le Q_C^{maximum},i\in N_C,\\ \left|SL_i\right|\le S_{L_i}^{maximum}\ ,i\in N_{TL},\\ VG_i^{minimum}\le VG_i\le VG_i^{maximum},i\in N_g\ .\end{gathered}\tag{10}$$

$$Multi\,objective\ fitness\left(MOF\right)=$$
$$=F_1+r_iF_2+uF_3=$$
$$=F_1+\begin{bmatrix}\sum_{i=1}^{NL}x_v\left[VL_i-VL_i^{min}\right]^2+\\ +\sum_{i=1}^{NG}r_g\left[QG_i-QG_i^{min}\right]^2\end{bmatrix}+r_fF_3\ ,\tag{11}$$
$$VL_i^{minimum}=\begin{cases}VL_i^{max}\ ,VL_i>VL_i^{max}\\ VL_i^{min},VL_i<VL_i^{min}\end{cases},$$
$$QG_i^{minimum}=\begin{cases}QG_i^{max}\ ,QG_i>QG_i^{max}\\ QG_i^{min},QG_i<QG_i^{min}\end{cases}.$$

III. ENRICHED GROUNDHOPPERS OPTIMIZATION ALGORITHM

Enriched Groundhoppers Optimization Algorithm (EG) has been modeled by integrating Opposition Based Learning, Levy Flight and Gaussian Mutation [14,15] with Groundhoppers Optimization for Real Power Loss Reduction. Groundhoppers Optimization Algorithm imitates the deeds of Groundhoppers. Each Groundhoppers Position symbolizes a candidate solution in the problem. Groundhoppers progression prejudiced by three features: social communication, gravity force, wind advection. Groundhoppers position is given by:

$$X_i=S_i+G_i+A_i\ ,\tag{12}$$

Social communication is computed by:

$$S_i = \sum_{\substack{j=1 \\ j\neq 1}}^{N} s\left(d_{ij}\right)\hat{d}_{ij} ,$$

$$d_{ij} = \left|X_j - X_i\right| , \tag{13}$$

$$\hat{d}_{ij} = \left(X_j - X_i\right) / d_{ij} ,$$

$$S\left(r\right) = fe^{-r/t} - e^{-r} \ . \tag{14}$$

Groundhoppers's gravity force is defined by:

$$G_i = -g\,\hat{e}_g \ . \tag{15}$$

Groundhoppers's wind advection is defined by:

$$A_i = U\,\hat{e}_w \ , \tag{16}$$

$$X_i = \sum_{\substack{j=1 \\ j\neq 1}}^{N} S\left(\left|X_j - X_i\right|\right)\left(X_j - X_i\right) / d_{ij} - -g\,\hat{e}_g + U\,\hat{e}_w \ . \tag{17}$$

In order to adjust the exploration and exploitation Arithmetic model is defined as follows:

$$X_d^i = c\left(\sum_{\substack{j=1 \\ j\neq 1}}^{N} c\frac{ub_d - ib_d}{2}\cdot S\left(\left|X_j - X_i\right|\right)\cdot \cdot\left(X_j - X_i\right)/d_{ij}\right) + \hat{T}_d \ . \tag{18}$$

$$c = c_{maximum} - I\,\frac{c_{maximum} - c_{minimum}}{L}$$

In this work Enriched Groundhoppers Optimization Algorithm Modeled by Opposition Based Learning, Levy Flight, and Gaussian Mutation for Real Power Loss Reduction. Opposition based learning is one of the influential optimization tools to boost the convergence speed of different optimization techniques. The thriving implementation of the OBL engages evaluation of opposite population and existing population in the similar generation to discover the superior candidate solution for reactive power problem.

Let $N\left(N \in \left[x, y\right]\right)$ be a real number and the N^o (opposite number) can be defined as follows:

$$N^o = x + y - N \ . \tag{19}$$

Levy distribution is defined as:

$$L\left(s,\gamma,\mu\right) = \begin{cases} \sqrt{\dfrac{\gamma}{2\pi}}exp\left[-\dfrac{\gamma}{2\left(s-\mu\right)}\right]\cdot \\ \cdot\dfrac{1}{\left(s-\mu\right)^{3/2}} \quad if\ 0 < \mu < s < \infty \\ 0 \quad if\ s \leq 0 \end{cases} . \tag{20}$$

By Levy flight, innovative state is:

$$X^{t+1} = X^t + \alpha \oplus Levy\left(\beta\right) \ . \tag{21}$$

In the projected method "α" is capricious number:

$$X^{t+1} = X^t + random\left(size\left(D\right)\right) \oplus Levy\left(\beta\right) \ . \tag{22}$$

Gaussian mutation will produce a new-fangled offspring close to the original parent since of its constricted tail which permit for each turn of the exploration space to be searched in better mode. In Gaussian mutation the density function is defined by:

$$f_{gaussian\left(0,\sigma^2\right)}{}^{(\alpha)} = \frac{1}{\sqrt{2\pi\sigma^2}}\, e^{-\frac{\alpha^2}{2\alpha^2}} \ . \tag{23}$$

Then,

$$X_d^i = X_i \oplus G\left(\alpha\right) . \tag{24}$$

Then the customized arithmetic model is given by:

$$X_d^i = c\left(\sum_{\substack{j=1 \\ j\neq 1}}^{N} c\frac{ub_d - ib_d}{2}\cdot S\left(\left|X_j - X_i\right|\right)\cdot \cdot\left(X_j - X_i\right)/d_{ij}\right) \oplus G\left(\alpha\right) + \hat{T}_d \ . \tag{25}$$

A new-fangled candidate solution is engendered through Levy flight mechanism by:

$$X_i^{levy} = X_i^* + random(d) \oplus levy(\beta)$$
$$X_i^{t+1} = \begin{cases} X_i^{levy} \; fitness\left(X_i^{levy}\right) > fitness\left(X_i^*\right) \\ X_i^* \quad otherwise \end{cases} . \quad (26)$$

By using the equation below opposition population will be engendered:

$$X_i^{opposition} = LB + UB - T + r\left(T - X_i\right). \quad (27)$$

a. Commence;

b. Initialization of population and parameters;

c. Fix the opposition based points;

d. Fitness value will be evaluated;

e. Modernize "*c*" by:

$$c = c_{maximum} - I\,\frac{c_{maximum} - c_{minimum}}{L};$$

f. For $i < n$;

g. Distance between Groundhoppers are normalized;

h. Modernize the existing search agent position X_i by:

$$X_d^i = c\left(\begin{array}{l}\sum_{\substack{j=1\\ j\neq 1}}^{N} c\,\frac{ub_d - ib_d}{2}\cdot S\left(\left|X_j - X_i\right|\right)\cdot \\ \cdot\left(X_j - X_i\right)/d_{ij}\end{array}\right) \oplus G(\alpha) + \hat{T}_d$$

i. Execute Levy flight stratagem by:

$$X_i^{levy} = X_i^* + random(d) \oplus levy(\beta)$$
$$X_i^{t+1} = \begin{cases} X_i^{levy} \; fitness\left(X_i^{levy}\right) > fitness\left(X_i^*\right) \\ X_i^* \quad otherwise \end{cases}$$

j. Fetch back X_i if it move out from boundary level;

k. End for;

l. Calculate the fitness value;

m. Modernize "*T*" when enhanced solution available;

n. For $i < n$;

o. Compute the position of oppositional value by:

$$X_i^{opposition} = LB + UB - T + r\left(T - X_i\right)$$

p. Fitness of present exploration agent is computed;

q. Fetch the present exploration agent back when it move beyond the boundary level;

r. End for;

s. Modernize "*T*" when enhanced solution available;

t. Modernize the population "*X*" by choosing the most excellent "*n*" exploration agents from

$$X^{opposition} \; and \; X$$

u. l = l + 1;

v. End while;

w. Revisit "*T*" as the optimal stricture;

x. End.

IV. Simulation Results

Projected Enriched Groundhoppers (EG) Optimization Algorithm is corroborated in IEEE 30 bus system. In Table I shows the loss appraisal, Table II shows the voltage aberration evaluation and Table III gives the L-index assessment. Appraisal of loss has been done with PSO, adapted PSO, enhanced PSO, comprehensive learning PSO, Adaptive genetic algorithm, Canonical genetic algorithm, enhanced genetic algorithm, Hybrid PSO-Tabu search, Ant lion, quasi-oppositional teaching learning based, enhanced stochastic fractal search optimization algorithm, harmony search, upgraded pseudo-gradient search particle swarm optimization and cuckoo search algorithm. Power loss abridged competently and proportion of the power loss lessening has been enhanced. Predominantly voltage constancy augmentation attained with minimized voltage deviancy.

TABLE I. COMPARISON OF REAL POWER LOSS.

Technique	Power loss (MW)
Basic PSO-TS [8]	4.5213
Standard TS [8]	4.6862
Basic PSO [8]	4.6862
Ant LO [9]	4.5900
Basic QO-TLBO [10]	4.5594
Standard TLBO [10]	4.5629
Standard GA [11]	4.9408
Basic PSO [11]	4.9239
HAS [11]	4.9059
Standard FS [12]	4.5777
IS-FS [12]	4.5142
Standard FS [14]	4.5275
EG	4.5007

TABLE II. COMPARISON OF VOLTAGE DEVIATION.

Technique	Voltage deviancy (PU)
Basic PSO-TVIW [13]	0.1038
Basic PSO-TVAC [13]	0.2064
Standard PSO-TVAC [13]	0.1354
Basic PSO-CF [13]	0.1287
PG-PSO [13]	0.1202
SWT-PSO [13]	0.1614
PGSWT-PSO [13]	0.1539
MPG-PSO [13]	0.0892
QO-TLBO [10]	0.0856
TLBO [10]	0.0913
Standard FS [12]	0.1220
ISFS [12]	0.0890
Standard FS [14]	0.0877
EG	0.0839

TABLE III. COMPARISON OF VOLTAGE STABILITY.

Technique	(Voltage constancy) (PU)
Basic PSO-TVIW [13]	0.1258
Basic PSO-TVAC [13]	0.1499
Standard PSO-TVAC [13]	0.1271
Basic PSO-CF [13]	0.1261
PG-PSO [13]	0.1264
SWT-PSO [13]	0.1488
PGSWT-PSO [13]	0.1394
MPG-PSO [13]	0.1241
QO-TLBO [10]	0.1191
Standard TLBO [10]	0.1180
ALO [9]	0.1161
ABC [9]	0.1161
Standard GWO [9]	0.1242
Basic BA [9]	0.1252
Standard FS [12]	0.1252
IS-FS [12]	0.1245
Standard FS [14]	0.1167
EG	0.1507

V. CONCLUSION

Enriched Groundhoppers (EG) Optimization Algorithm successfully solved the power loss lessening problem. Enriched Groundhoppers (EG) Optimization Algorithm has been Modeled by integrating Opposition Based Learning, Levy Flight, and Gaussian Mutation Groundhoppers Optimization Algorithm with for Real Power Loss Reduction. Groundhoppers Optimization Algorithm imitates the deeds of Groundhoppers. Each Groundhoppers Position symbolizes a candidate solution in the problem. Groundhoppers's progression prejudiced by three features: social communication, gravity force, wind advection. Proposed Enriched Groundhoppers (EG) Optimization Algorithm is appraised in IEEE 30 bus system. True power loss lessening, voltage divergence curtailing, and voltage constancy index augmentation has been attained.

REFERENCES

[1] Carpentier, J. (1962). Contribution a l'etude du dispatching economique. *Bulletin de la Société Francaise des électriciens*, *3*(1), 431-447.

[2] Dommel, H. W., & Tinney, W. F. (1968). Optimal power flow solutions. *IEEE Transactions on power apparatus and systems*, (10), 1866-1876.

[3] Takapoui, R., Moehle, N., Boyd, S., & Bemporad, A. (2020). A simple effective heuristic for embedded mixed-integer quadratic programming. *International journal of control*, *93*(1), 2-12.

[4] Abaci, K., & Yamaçli, V. (2017). Optimal reactive-power dispatch using differential search algorithm. *Electrical Engineering*, *99*, 213-225.

[5] Pulluri, H., Naresh, R., & Sharma, V. (2017). An enhanced self-adaptive differential evolution based solution methodology for multiobjective optimal power flow. *Applied Soft Computing*, *54*, 229-245.

[6] Heidari, A. A., Abbaspour, R. A., & Jordehi, A. R. (2017). Gaussian bare-bones water cycle algorithm for optimal reactive power dispatch in electrical power systems. *Applied Soft Computing*, *57*, 657-671.

[7] Mugemanyi, S., Qu, Z., Rugema, F. X., Dong, Y., Bananeza, C., & Wang, L. (2020). Optimal reactive power dispatch using chaotic bat algorithm. *IEEE Access*, *8*, 65830-65867.

[8] Sahli, Z., Hamouda, A., Bekrar, A., & Trentesaux, D. (2014, October). Hybrid PSO-tabu search for the optimal reactive power dispatch problem. In *IECON 2014-40th Annual Conference of the IEEE Industrial Electronics Society* (pp. 3536-3542). IEEE.

[9] Mouassa, S., Bouktir, T., & Salhi, A. (2017). Ant lion optimizer for solving optimal reactive power dispatch problem in power systems. *Engineering science and technology, an international journal*, *20*(3), 885-895.

[10] Mandal, B., & Roy, P. K. (2013). Optimal reactive power dispatch using quasi-oppositional teaching learning based optimization. *International Journal of Electrical Power & Energy Systems*, *53*, 123-134.

[11] Khazali, A. H., & Kalantar, M. (2011). Optimal reactive power dispatch based on harmony search algorithm. *International Journal of Electrical Power & Energy Systems*, *33*(3), 684-692.

[12] Van Tran, H., Van Pham, T., Pham, L. H., Le, N. T., & Nguyen, T. T. (2019). Finding optimal reactive

power dispatch solutions by using a novel improved stochastic fractal search optimization algorithm. *TELKOMNIKA (Telecommunication Computing Electronics and Control)*, *17*(5), 2517-2526.

[13] Polprasert, J., Ongsakul, W., & Dieu, V. N. (2016). Optimal reactive power dispatch using improved pseudo-gradient search particle swarm optimization. *Electric Power Components and Systems*, *44*(5), 518-532.

[14] Duong, T. L., Duong, M. Q., Phan, V. D., & Nguyen, T. T. (2020). Optimal reactive power flow for large-scale power systems using an effective metaheuristic algorithm. *Journal of electrical and computer engineering*, *2020*, 1-11.

[15] Wang, G. G., Deb, S., Gandomi, A. H., & Alavi, A. H. (2016). Opposition-based krill herd algorithm with Cauchy mutation and position clamping. *Neurocomputing*, *177*, 147-157.

Impact of Meteorological Conditions and Cu-Water Nanofluid on Thermoelectrical Performance of Hybrid Photovoltaic Thermal Solar Collector Equipped with a Compound Parabolic Concentrator (CPV/T)

Khaled Mouaici[1], Brahim Fersadou[2], Walid Nessab[3], Henda Kahalerras[4]

[1,2,3,4]USTHB, Algiers, Algeria

Abstract—**This work aims to examine the impact of meteorological conditions and a Cu-Water nanofluid on the performance of a hybrid photovoltaic thermal solar collector combined with a compound parabolic concentrator (CPV/T) located in Algiers. The equations, giving the temporal variations of the temperatures in each component of the CPV/T, are established from thermal balances and are solved by the Runge-Kutta method of order 4. The effects of the concentration ratio ($1 \leq CR \leq 4$), the nanoparticles volume fraction ($0.1\% \leq \phi \leq 2\%$), and the wind velocity (1 m/s $\leq V_{wind} \leq 7$ m/s) on the electrical and thermal powers and efficiencies are analyzed. Results showed an efficiency improvement when increasing the nanoparticles' volume fraction and reducing the concentration ratio. It is also found that high wind velocities are beneficial for electrical performance and vice versa for thermal ones. Finally, the limit values of the concentration ratio, to ensure normal functioning of photovoltaic cells, increase with rising nanoparticles volume fraction and wind velocity.**

Keywords - Concentrating Hybrid Collector (CPV/T), nanofluid, meteorological conditions, thermoelectrical performance

I. Introduction

The daily life of human beings requires a permanent consumption of energy, during telephone calls, buying a coffee or during reading the news. Over the last 200 years the world leader in the energy sector increasingly relying on fossil fuels to ensure a good quality of life, however this energy strategy releases huge amounts of carbon dioxide (CO_2) into the atmosphere and also produces pollutants that are harmful to our health and the environment. Today everyone is wondering about the possibility of ensuring the same energy comfort by relying on renewable energies, as a scientific community our duty is to develop consistent technologies that can represent an attractive alternative for energy world leaders in order to lean towards a zero carbon economy. The sun, our main source of renewable energy, its radiation provides light, heat and electricity after a photovoltaic conversion process. Solar energy is clean, environmentally friendly and freely available over the planet. Every day a huge amount of solar radiation shines on the earth and gives life to human beings and all living mechanisms. Thermal photovoltaic hybridization is a technique allowing the optimization of the exploitation of solar energy by means of a photovoltaic thermal collector PV/T. The use of renewable energy and supporting technologies in a judicious and efficient way can lead to achieving the target 75% lesser CO_2 emission by the year 2050 [1]. According to [2] several studies were carried out for the sake of evaluating and comparing this novel technology with standard solar systems such as a solar thermal collector and PV panels. On the other hand, many sundry research works were conducted to analyze and enhance the performance of PV/T

ISBN: 978-86-82602-01-9

using several techniques and methods. Reference [3] found, that desalination using PV/T system offers the most compatibility application of solar energy along with the generation of electrical power. Reference [4] found, experimentally, that the overall efficiency increases from 24% to 58% when using cooling water flow below the PV cells. Reference [5] also performed an exergy analysis on a PV/T system used as water heater. The thermal efficiency increases with the flow rate and decreases with increasing collector temperature [6,7]. Concluded that cooling the back surface of the PV module with water can effectively reduce temperature and enhance electrical conversion efficiency. Reference [8] employed a combination of a photovoltaic/thermal system with a reflector, a distributor, an amplifier and a vacuum tube to produce electricity and hot water. The results showed that using PV/T systems lead to develop higher performance than PV panels. Reference [9] Investigated the PV/T system to run for air conditioning apart from water heating and power generation, experimentally, results showed that the system is efficient in enhancing the efficiency of the pv module in the PV/T system due to the evaporator which bring down the temperature of this last from 325K to 281K, which would not have been possible in heat pump mode of working.

A new design of a glazed and an unglazed inverted absorber partially covered photovoltaic thermal compound parabolic concentrator (PVT-CPC) was proposed and studied by [10]. The results showed that the proposed system can reach higher levels of instantaneous thermal efficiency with a gain factor of 0.67. Reference [11] investigated numerically a parabolic trough concentrating photovoltaic-thermal system (CPV/T). They have found that energy and exergy efficiencies obtained using PV/T are much greater compared to CPV/T system. Besides, they showed that the effect of using nanofluid is more apparent in the case of CPV/T systems than in the case of PV/T systems. Through this brief literature review, it's remarkable that the concentrating photovoltaic-thermal systems present a very interesting performance. This motivated the present study whose the main objective is to define the technological limitations of this type of collectors using a nanofluid as heat transfer mechanism.

II. Mathematical Modeling

A. System Description

The physical system considered and illustrated in Fig. 1 is a hybrid photovoltaic thermal collector (PV/T) equipped with a compound parabolic concentrator (CPC). The hybrid collector, which combines the mechanism of solar thermal absorbers and PV modules, is made essentially of: PV module covered by single glass layer separated by an air gap, an absorber plate and metallic tube in which the fluid is conveyed are attached to the back the PV module through an adhesive layer, a thermal insulation material placed at the bottom and the sides of the collector to minimize heat losses, and finally an enclosure which carry all collector components for mainly protection purpose and ensure correct placement. The incident concentrated solar irradiance by the CPC is partially absorbed by the photovoltaic module. Losses occur at the cover glass due to reflection and at the inner PV module. The PV module absorbs and converts the solar irradiance into electrical power, while its cell temperature begins to rise due to losses and heat of surrounding atmosphere. Some of this heat is transferred back onto the surrounding atmosphere via convection, while the remaining is transferred to the thermal absorber via conduction. The heat transfer fluid, a nanofluid Cu-Water, enters from a fluid source into the PV/T collector and flow within the tube. It will absorb the heat from the walls of the tubes and carry them into the outlet connection.

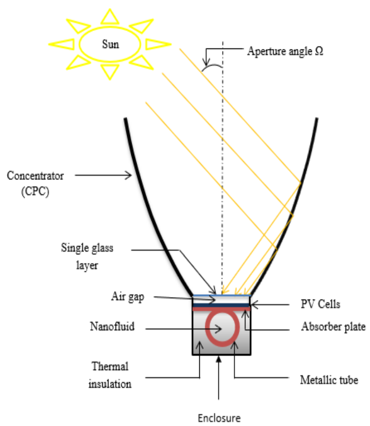

Figure 1. Physical Domain.

III. ASSUMPTIONS

The thermo-electric behavior of the CPV/T system is defined by means of explicit dynamic analysis through solving transient energy balance equations for the various collector components. It must be noted that such a work is extremely difficult due to the presence of the three processes of heat transfer and non-continuity of the studied domain. So, in order to get over these difficulties the sky is supposed as a black body, Employing one dimensional heat transfer, and the thermophysical properties of all components are supposed constant. Each component of the hybrid collector is considered at uniform temperature and it will be represented by node.

IV. MATHEMATICAL FORMULATION

As mentioned earlier in this section, the nodal approach appears appropriate for this study. With mentioned assumptions, the energy equation for each component will be reduced as follows:

A. Glass Cover

$$\begin{gathered} M_g C_{pg}\frac{dT_g}{dt} = \alpha_g G \rho_{con} CR \gamma_t - \\ -(h_{c,g-a} + h_{r,g-s})(\mathrm{T}_g - \mathrm{T}_a) - (\mathrm{h}_{c,g-pv} + \\ + \mathrm{h}_{r,g-pv})(\mathrm{T}_g - T_{pv}) \end{gathered} \quad (1)$$

where G is the global solar irradiation received. ρ, γ_t and α symbolize reflectivity, interception factor and absorptivity respectively. h_r, h_c and T represent the radiation and convection heat transfer coefficients and the temperature respectively. Besides, the subscripts *con*, *g*, *a*, *pv* and *s* refer to the concentrator, glazing, ambient, photovoltaic and sky respectively. *M* and C_p are respectively mass and calorific capacity. CR is the concentration ratio which is defined as follows:

$$CR = \frac{A_{con}}{A_{PV/T}} \quad . \qquad (2)$$

A_{con}, $A_{PV/T}$ refer to concentrator area and hybrid collector area respectively.

B. PV Panel

$$\begin{gathered} M_{pv} C_{ppv}\frac{dT_{pv}}{dt} = \alpha_{pv} G \rho_{con} CR \gamma_t \tau_g - E \\ -(h_{c,g-pv} + h_{r,g-pv})(\mathrm{T}_{pv} - \mathrm{T}_g) - \mathrm{h}_{cond,pv-abs}(\mathrm{T}_{pv} - \\ - \mathrm{T}_{abs}) - \mathrm{h}_{cond,pv-t}(\mathrm{T}_{pv} - \mathrm{T}_t) \end{gathered} \quad ,(3)$$

where τ denotes transmittance; h_{cond} represents the conduction heat transfer coefficient; the subscripts abs and t indicate the absorber and tube respectively. E (W/m^2) is the electrical power produced by the photovoltaic module and given by:

$$E = \alpha_{pv} G \rho_{con} CR \gamma_t \tau_g P A_{PV/T} \eta_r (1 - \beta_r(\mathrm{T}_{pv} - \mathrm{T}_r)) \ .(4)$$

P is the packing factor, η_r and β_r are solar cell efficiency at reference temperature (T_r=298.15 K) and temperature coefficient, respectively.

C. Thermal Absorber Plate

$$\begin{gathered} M_{abs} C_{pabs}\frac{dT_{abs}}{dt} = \\ = h_{cond,pv-abs}(\mathrm{T}_{pv} - \mathrm{T}_{abs}) - \mathrm{h}_{abs-t}(\mathrm{T}_{abs} - \mathrm{T}_t) - \\ - \mathrm{h}_{abs-i}(\mathrm{T}_{abs} - \mathrm{T}_i) \end{gathered} \ . \quad (5)$$

The subscript *i* refers to the thermal insulation.

D. Tube

$$\begin{gathered} M_t C_{pt}\frac{dT_t}{dt} = A_{abs-t} h_{cond,abs-t}(\mathrm{T}_{abs} - \mathrm{T}_t) + \\ + \mathrm{h}_{cond,pv-t}(\mathrm{T}_{pv} - \mathrm{T}_t) - \mathrm{A}_{t-i}\, h_{cond,t-i}(\mathrm{T}_t - \mathrm{T}_i) - \\ - \mathrm{A}_{nf-t}\, h_{nf}(\mathrm{T}_t - \mathrm{T}_{nfm}) \end{gathered} \ .(6)$$

Note that A_{nf-t}, A_{t-i} *and* A_{abs-t} refer respectively to nanofluid/tube, tube/insulation and absorber/tube contact surfaces; h_{nf} is the convective heat transfer coefficient inside the tube.

E. Thermal Insulation

$$M_i C_{pi} \frac{dT_i}{dt} = A_{abs-i} h_{cond,abs-i} (\mathrm{T}_{abs} - \mathrm{T}_i) + \\ + \mathrm{A}_{t-i}\, h_{cond,t-i} (\mathrm{T}_t - \mathrm{T}_i) - \mathrm{A}_{PV/T}\, h_{ai} (\mathrm{T}_i - \mathrm{T}_a) \quad , \quad (7)$$

where h_{ai} is the coefficient that reflects the overall thermal losses between the thermal insulation and the ambient environment.

F. Nanofluid

$$M_{nf} C_{pnf} \frac{dT_{nfm}}{dt} = A_{nf-t} h_{nf} (\mathrm{T}_t - \mathrm{T}_{nfm}) - \\ - \dot{m} C_{pnf} (\mathrm{T}_{nfo} - \mathrm{T}_{nfi}) \quad . \quad (8)$$

Mass flow rate and averaged temperature of nanofluid are $\dot{m}$ and T_{nfm} respectively.

$$T_{nfm} = \frac{T_{nfi} + T_{nfo}}{2} \quad . \quad (9)$$

Equivalent sky temperature [14]:

$$T_s = 0.0552 T_a^{1.5} \quad . \quad (10)$$

The heat transfer coefficients presented in aforementioned energy balance equations are given by [12-16]. The nanofluid properties are computed using the relations found in [16-21].

V. Performance of the CPV/T

Hybrid solar systems are efficient if they develops a good electrical power simultaneously with a considerable thermal yield. The overall thermal and electrical efficiencies of CPV/T are determined respectively by:

$$\eta_{th} = \frac{\dot{m} C_{pnf} (T_{nfo} - T_{nfi})}{GCRA_{PV/T}} \quad , \quad (11)$$

$$\eta_{el} = P \eta_r (1 - \beta_r (\mathrm{T}_{pv} - \mathrm{T}_r)) \quad . \quad (12)$$

VI. Numerical Method

Range-Kutta 4th order method is used to solve the energy balance equations governing the heat transfer process between different PV/T collector components. Before starting the calculation, system data and ambient properties are initialized. The initial temperatures of different hybrid system components are involved in the numerical code. For each time step (0.5 s) the energy equations are solved and then different parameters (temperature and heat transfer coefficients) are estimated and are used in the second time step. The calculations are then continued until required time.

VII. Results and Discussion

This section exhibits the effects of the effects of the concentration ratio ($1 \leq \mathrm{CR} \leq 4$), the nanoparticles volume fraction ($0.1\% \leq \phi \leq 2\%$), and the wind velocity (1 m/s ≤ Vwind ≤ 7 m/s) on the performance of the CPV/T system. The performances of studied device are predicted over a typical day of Algiers city and by keeping fixed the mass flow rate of the nanofluid at 0.01kg/s. It is noteworthy that the maximal value of contraction ratio that could be reached depend strongly on solar cell temperature. So, also in this section we will define the technological limitations obtained by adopting a stop criterion which consist that the system should be shut down immediately if the instantaneous temperature of a PV module is equal at 350 K.

Fig. 2 depicts the variation of mean thermal and electrical efficiencies with concentration ratio for large range of the nanoparticle volume fraction. From the figure it’s clear that increasing concentration ratio affect negatively both of efficiencies with more apparent effect for electrical efficiency than thermal one. This unwanted behavior is related to conversion performance of CPV/T system.

Admitting that the efficiency is only a relationship between what the system receives and what it produces, we can explicitly say that the increase of CR allows to have a greater gain in terms of electrical and thermal power but with a lower conversion rate. Also, it’s remarkable that the use of nanofluids improves the thermoelectric efficiency of hybrid solar systems. This figure also shows an important result concerning the interaction between the nanoparticle volume fraction and concentration ratio. Higher order CR are accessible for $\phi > 1\%$, and therefore the range of use of CPV/T will be expanded.

In order to extract the nature of interactions between different parameters such as interaction velocity and concentration ratio on CPV/T performance we have plotted the curves shown in Fig. 3. It displays the variations of mean electrical and thermal efficiencies with respect to concentration ratio for different levels of wind velocity.

The convective effects governed by the increase in the wind speed represent an additional way of cooling the electrical system in order to make it more efficient, but this affects negatively the thermal performance of the studied system which explains the opposite behavior of electrical and thermal efficiencies revealed in the figure above. The wind speed this exogenous parameter which requires special treatment in order to extract its effects has shown a very attractive result of interacting with the concentration ratio. Despite its undesirable effect

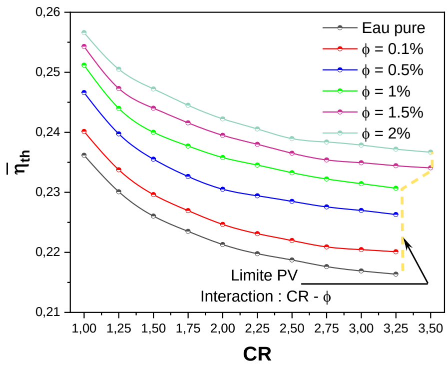

(a) Thermal efficiency

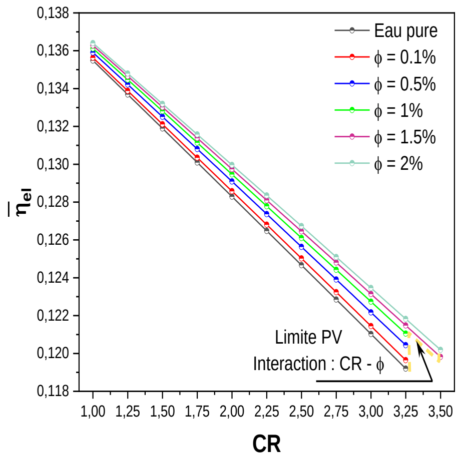

(b) Electrical efficiency

Figure 2. Variations of mean electrical and thermal efficiencies with concentration ratio for different values of nanoparticle volume fraction.

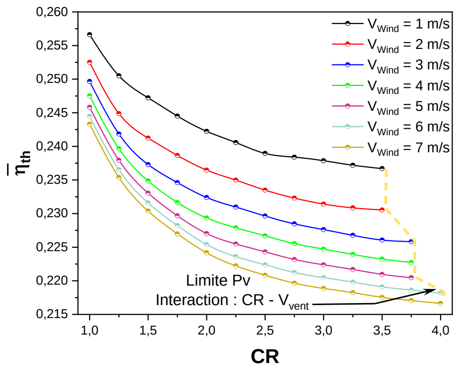

(a) Thermal efficiency

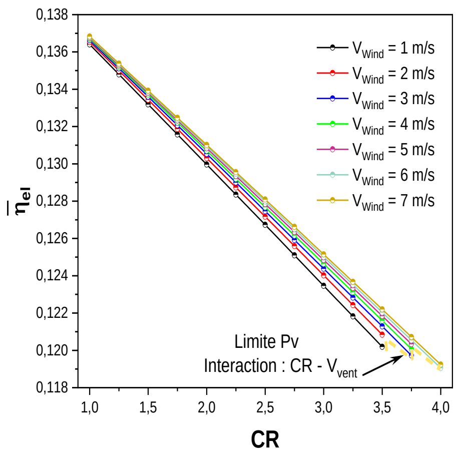

(b) Electrical efficiency

Figure 3. Variations of mean electrical and thermal efficiencies with concentration ratio for different values of wind velocity.

on the thermal quality of the CPV/T system, it offers us the possibility to go further by applying the concentration technique with higher orders of magnitude of CR without damaging the PV cells.

VIII. CONCLUSION

The present work is a scrutiny study which aimed to examine the impact of meteorological conditions and a Cu-Water nanofluid on the performance of a hybrid photovoltaic thermal solar collector combined with a compound parabolic concentrator (CPV/T) located in Algiers. The performance of the CPV/T system is affected by control parameters such as concentration ratio, nanoparticle volume fraction and wind velocity as follows:

The study of the effect of the compound parabolic concentrator, and translated by the concentration ratio, shows that the increase in the value of CR is harmful to the different yields characterizing the rate of electrical and thermal conversion.

The limit concentration ratio, characteristic of a maximum instantaneous temperature T_{pvmax} not exceeding 350 K in order to ensure normal operation conditions of the PV cells, is improved with the increase of nanoparticle volume fraction and wind velocity.

REFERENCES

[1] Johansson, T. B., Kelly, H., Burnham, L., Reddy, A. K., & Williams, R. (Eds.). (1993). *Renewable energy: sources for fuels and electricity*. Island press.

[2] Esfe, M. H., Kamyab, M. H., & Valadkhani, M. (2020). Application of nanofluids and fluids in photovoltaic thermal system: An updated review. *Solar Energy, 199*, 796-818.

[3] Manokar, A. M., et al. (2018). Integrated PV/T solar still-A mini-review. *Desalination, 435*, 259-267.

[4] Tiwari, A., & Sodha, M. S. (2006). Performance evaluation of solar PV/T system: an experimental validation. *Solar energy, 80*(7), 751-759.

[5] Tiwari, A., Dubey, S., Sandhu, G. S., Sodha, M. S., & Anwar, S. I. (2009). Exergy analysis of integrated photovoltaic thermal solar water heater under constant flow rate and constant collection temperature modes. *Applied Energy, 86*(12), 2592-2597.

[6] Bahaidarah, H., Subhan, A., Gandhidasan, P., & Rehman, S. (2013). Performance evaluation of a PV (photovoltaic) module by back surface water cooling for hot climatic conditions. *Energy, 59,* 445-453.

[7] Touafek, K., Haddadi, M., & Malek, A. (2013). Design and modeling of a photovoltaic thermal collector for domestic air heating and electricity production. *Energy and Buildings, 59,* 21-28.

[8] Mohsenzadeh, M., & Hosseini, R. (2015). A photovoltaic/thermal system with a combination of a booster diffuse reflector and vacuum tube for generation of electricity and hot water production. *Renewable Energy, 78*, 245-252.

[9] Fang, G., Hu, H., & Liu, X. (2010). Experimental investigation on the photovoltaic–thermal solar heat pump air-conditioning system on water-heating mode. *Experimental Thermal and Fluid Science, 34*(6), 736-743.

[10] Atheaya, D., Tiwari, A., Tiwari, G. N., & Al-Helal, I. M. (2016). Performance evaluation of inverted absorber photovoltaic thermal compound parabolic concentrator (PVT-CPC): Constant flow rate mode. *Applied Energy, 167*, 70-79.

[11] Yazdanifard, F., Ebrahimnia-Bajestan, E., & Ameri, M. (2017). Performance of a parabolic trough concentrating photovoltaic/thermal system: Effects of flow regime, design parameters, and using nanofluids. *Energy Conversion and Management, 148*, 1265-1277.

[12] Watmuff, J. H., Charters, W. W. S., & Proctor, D. (1977). Solar and wind induced external coefficients-solar collectors. *Cooperation Mediterraneenne pour l'Energie Solaire, 56*.

[13] Duffie, J. A., & Beckman, W. A. (1991). *Solar engineering of thermal processes.* Wiley.

[14] Hollands, K. G. T., Unny, T. E., Raithby, G. D., & Konicek, L. (1976). Free convective heat transfer across inclined air layers. *ASME. J. Heat Transfer., 98,* 189-193.

[15] Chow, T. T. (2003). Performance analysis of photovoltaic-thermal collector by explicit dynamic model. *Solar Energy, 75*(2), 143-152.

[16] Xuan, Y., & Li, Q. (2003). Investigation on convective heat transfer and flow features of nanofluids. *J. Heat transfer, 125*(1), 151-155.

[17] Pak, B. C., & Cho, Y. I. (1998). Hydrodynamic and heat transfer study of dispersed fluids with submicron metallic oxide particles. *Experimental Heat Transfer an International Journal, 11*(2), 151-170.

[18] Xuan, Y., & Roetzel, W. (2000). Conceptions for heat transfer correlation of nanofluids. *International Journal of heat and Mass transfer, 43*(19), 3701-3707.

[19] Brinkman, H. C. (1952). The viscosity of concentrated suspensions and solutions. *The Journal of chemical physics, 20*(4), 571-571.

[20] Maxwell, J. C. (1904). *A treatise on electricity and magnetism.* Oxford University Press, Cambridge.

[21] Hissouf, M., Najim, M., & Charef, A. (2020). Numerical study of a covered Photovoltaic-Thermal Collector (PVT) enhancement using nanofluids. *Solar Energy, 199*, 115-127.

Effects of CdS Buffer Layer Parameters on CIGS Solar Cells Performance

Abderrahim Raidou[1], Abdallah Bendoumou[2]

[1,2]Materials Physics and Subatomic Laboratory, Department of Physics, Faculty of Science, Ibn Tofail University, B.P 133, 14000 Kénitra, Morocco

Abstract—**We studied numerically the performance of the $Cu(In,Ga)Se_2$ (CIGS)-based solar cells using the one dimensional Solar cell Capacitance Simulator (SCAPS-1D) simulation program. This simulated analysis was performed for CIGS solar cells with Mo/CIGS/CdS/i-ZnO/ZnO:Al/MgF_2 structure. We especially investigated the influence of thickness, donor charge carrier concentration and band gap of CdS buffer layer on the output parameters such as J-V characteristic, External Quantum Efficiency, open circuit voltage V_{oc}, short circuit density J_{sc}, fill factor FF and efficiency η. Based on the results, all these photovoltaic parameters decreased with increasing buffer layer thickness and optimum value was 30 nm. We shown also how the performance was affected by the donor charge carrier concentration N_D (cm^{-3}) of CdS buffer layer, there was no change of all performance parameters with buffer layer doping up to carrier concentration N_D of 1×1016 cm^{-3}. However, a further increase in doping concentration affected an increase in efficiency and the optimized value was 1×1018 cm^{-3}. The effect of the band gap was investigated by varying its value from 2.12 to 2.83 eV. The highest efficiency 21.33% was obtained for the high band gap value of 2.83 eV.**

Keywords - $Cu(In,Ga)Se_2$, solar cells, buffer layer, CdS, SCAPS-1D

I. INTRODUCTION

The growing demand for energy and the negative effects of traditional energy sources (fossil fuels) on the environment require us to look for variable sources of sustainable and clean energy that can be a promising alternative to traditional energy. The solar is the most important source of renewable and clean energy; study on solar cells is a major area of interest within the field of energy. Many materials have been developed to produce thin film solar cells such as CdTe, CIGS and CZTS [1]. $Cu(In,Ga)Se_2$-based (CIGS) solar cells are one of the most promising solar cell technologies for cost-effective photovoltaic applications [2]. The efficiency of CIGS solar cell is already reached above 20% for laboratory scale samples [3]. In addition to high efficiencies, CIGS photovoltaic can be made very lightweight and flexible which is desirable for building integrated and portable applications and have also shown high radiation resistance, compared to crystalline silicon and III-V solar cells so they are also promising for space applications [4,5]. New CIGS Solar Cell Record is obtained with an absorber thickness less than 3-μm-thick and by using CdS as buffer layers to play an important role for the pn-junction formation but also to enhance the lattice match between the absorber and the ZnO window layer (doped zinc oxide) [6,7]. The CdS semiconductor material has pulled significant attention as a result of its good electron acceptable and transportable characteristics; what's more, the main 2.4 eV direct band gap makes it more appropriate to be applied in CIGS solar cells [8,9]. Actually, the best efficiency recorded for the CIGS solar cell is where the CdS buffer layer is used [10].

The main objective behind this research work is to study the influence of CdS layer parameters on the CIGS based solar cells performance using the one-dimensional Solar cell Capacitance Simulator (SCAPS-1D) simulation program. We investigated numerically the typical structure Mo/CIGS/CdS/ i-ZnO/ZnO:Al/MgF_2 [11] to get the output solar cell parameters: Short-circuit current density J_{sc}, open-circuit voltage V_{oc}, Fill Factor FF, and efficiency η.

II. EASE OF USE SIMULATION METHODOLOGY

SCAPS is a one dimensional solar cell simulation program developed at the department of Electronics and Information Systems (ELIS) of the University of Gent, Belgium [12]. Our numerical study is done by using this software (with version 3.3.07), which is a valuable tool in modelling polycrystalline thin film solar cells based on CIGS. Comparison between measured and simulated characteristics can lead to a better insight in the internal physical operation of a solar cell [13].

The simulation is reached at ambient temperature of 25°C and under global AM1.5 solar spectrum conditions. The material parameters, of our cell structure Mo/CIGS/CdS/i-ZnO/ZnO:Al/MgF_2, were mined from literature, theoretical, experimental data, either by fitting the simulation to experimental data and values are listed in Table I [14-17]. The molybdenum (Mo) is used as a back metal contact which is characterized by a specific electron work function value 5.0 eV, and for the anti-reflection layer MgF_2 we used

TABLE I. INPUT ELECTRONIC MATERIAL PARAMETERS EMPLOYED IN THE NUMERICAL STUDY FOR THE CIGS-BASED SOLAR CELL.

Parameters	**CIGS**	**CdS**	**i-ZnO**	**ZnO :Al**
Thickness (nm)	3000	50	100	200
Band gap (eV)	1.15	2.4	3.37	3.37
Electron affinity (eV)	4.1	4.2	4.45	4.45
Dielectric permittivity (relative)	13.6	10	9	9
C_B effective density of states (cm^{-3})	2.2E+18	2.2E+18	2.2E+18	2.2E+18
V_B effective density of (cm^{-3})	1.8E+19	1.8E+19	1.8E+19	1.8E+19
Electron thermal velocity (cm/S)	1E+7	1E+7	1E+7	1E+7
Hole thermal velocity(cm /s)	1E+7	1E+7	1E+7	1E+7
Electron mobility (cm^2/Vs)	1E+0	1E+2	1E+2	1E+2
Hole mobility (cm^2/Vs)	2.5E+1	2.5E+1	2.5E+1	2.5E+1
Shallow uniform donor density (N_D cm^{-3})	1E+1	1E+18	1E+18	1E+20
Shallow uniform acceptor density (N_A cm^{-3})	5E+16	0	0	0

the data from SCAPS-1D. We used the same values of the layers thickness, series resistance of 0.23 Ω and shunt resistance of 880 Ω used by the authors [18], who studied the same cell structure experimentally and obtained efficiency up to 20.8%.

III. Results and Discussion

A. Comparison Between Experimental and Simulated CIGS Solar Cells

To carry out our study, we optimized the different electrical parameters, shown in Table I, so as to have the same characteristics J-V of the experimental and simulated studies. The Fig. 1, illustrates the both current density-voltage characteristics of CIGS solar cells, experimental and simulated at ambient temperature of 25°C and under global AM1.5 solar spectrum conditions. It is clear that the simulation result is in good agreement with the experiment [18]. Also the four output parameters: Voltage (V_{oc}), current density (J_{sc}), fill factor (FF) and efficiency (η) are close to the experimental ones.

The simulated energy-band diagram, of ZnO:Al/i-ZnO/CdS/CIGS solar cell under illumination, according to precedent data is shown in Fig. 2. Under illumination the deep donors will be ionized because the Fermi level of holes moves beneath the trap level, and the positively charged fixed donors cause downward band bending in the CdS [19]. Recombination at the interface states and their occupation allows the exchange of electrons between the interface state and the two adjacent conduction bands, and of holes between the state and the two adjacent valence bands. The dominant recombination is between electrons of the n-CdS and holes in the

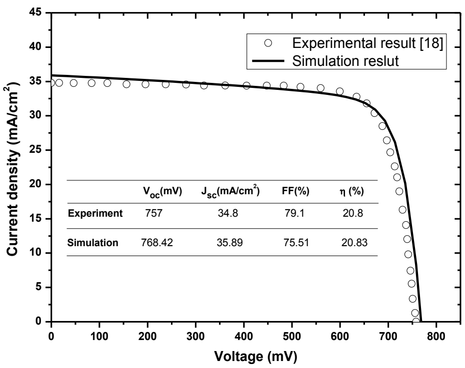

Figure 1. Current density-voltage (J-V) characteristics of experimental and simulated studies of CIGS solar cells.

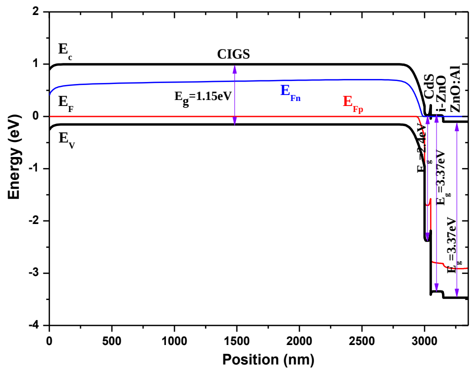

Figure 2. The simulated energy band diagram of CIGS solar cell.

p-CIGS of the interface [13]. The minority-carrier electrons generated in the CIGS bulk become majority carriers when they reach the vicinity of the CdS buffer layer [20].

B. Effect of CdS Buffer Layer Thickness

Buffer layer is an intermediate layer film between the absorber and window layers with two main objectives, to provide structural stability to the device and to fix the electrostatic conditions inside the absorber layer. Cadmium sulphide (CdS) is a prominent candidate to be used as a buffer layer in $Cu(In,Ga)Se_2$ based solar cells [21].

For studying the effect of CdS layer thickness on the photovoltaic performance of CIGS solar cell, it is varied from 0.02 to 0.1 µm while all other electronic parameters listed in Table I are fixed. The simulation results of current density-voltage characteristics are shown in Fig. 3. This figure exhibits the increase of CdS layer thickness affects the decrease in short-circuit

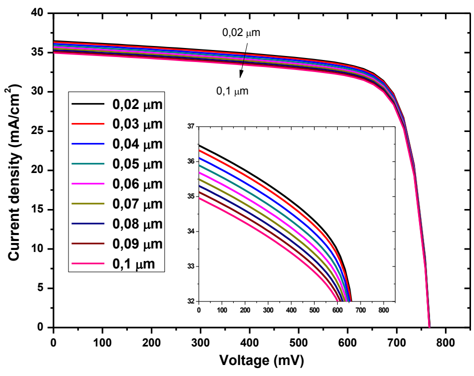

Figure 3. Effect of CdS buffer layer thickness on the current density – voltage (J-V) characteristic.

current density J_{sc}, and also a slight decrease in open-circuit voltage V_{oc}. This is explained by the photons loss, which are absorbed by this buffer layer, that means the decrease in photons is attached to an increase in thickness of buffer layer, which causes decrease in current density.

The CIGS-based solar cells are characterized by high external quantum efficiency. The spectral response is studied under the thickness

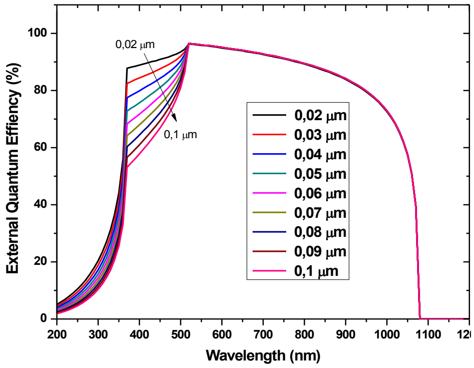

Figure 4. Effect of CdS buffer layer thickness on the External Quantum Efficiency.

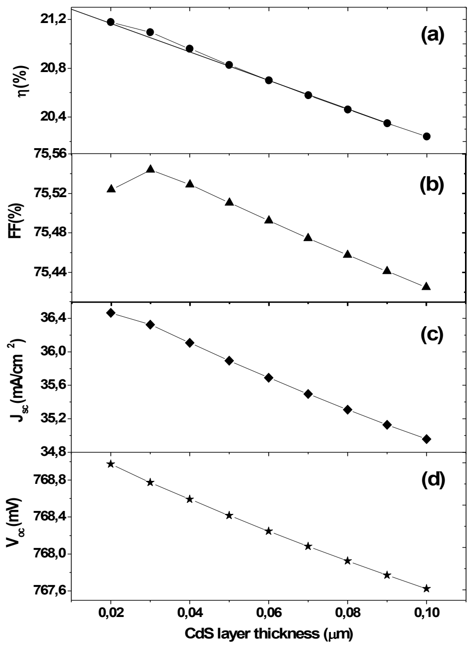

Figure 5. Effect of CdS buffer layer thickness on solar cell parameters: (a) Efficiency, (b) Fill factor (FF), (c) Short-circuit current density (J_{sc}) and (d) Open-circuit voltage (V_{oc}).

effect of the CdS buffer layer, which is illustrated in Fig. 4. It can be observed the affection of the short wavelength response, which decreases with increasing buffer layer thickness. The photon absorption increases with increasing CdS layer thickness. In addition, when the buffer layer is increased, more photons which carry the energy are being absorbed by this layer. Therefore it would lead to a decrease in the photons which have reached the absorber layer. A decrease in the numbers of photons at the absorber layer would decrease the quantum efficiency of the solar cell [22].

The Fig. 5. displays the simulated effect of CdS buffer layer thickness on photovoltaic parameters of CIGS solar cell, namely efficiency (η), fill factor (FF), short circuit density (J_{sc}), and open circuit voltage (V_{oc}). It is observed that the efficiency have a same trend for current density and open-circuit voltage in overall buffer layer thickness range and have strong thickness dependence. And there is a growth of fill factor up to 30 nm and then decreases with the thickness, indicating the optimal value is 30 nm. It is clearly seen that most of the photo-generated carriers are collected by a thinner CdS layer. When the thickness of CdS layer increases, the photons of short wavelengths are absorbed at a further distance of the CdS/CIGS junction. Though the CdS layer is characterized by defect states which act as recombination centers reduce the lifetime of the minority carriers (holes) and consequently the photogenerated carriers recombine before reaching the junction. Therefore, there is a drop of the short circuit current, the open circuit voltage and the efficiency with the increase of the CdS thickness [23].

C. *Effect of CdS Buffer Layer Doping Level N_D*

The donor charge carrier concentration N_D (cm^{-3}) simulation results are depicted in Fig. 6. The CdS buffer layer donor concentration is changed from 1×10^{14} to 1×10^{20} cm^{-3}. It is seen there is no change of all performance parameters with buffer layer doping up to carrier concentration N_D of 1×10^{16} cm^{-3}. However, a further increase in doping concentration affects a slight decrease in V_{oc}, whereas J_{sc}, fill factor and efficiency have an increase with increasing the doping level. The CIGS solar cell efficiency has improved by 2.34% at a higher donor concentration of 1×10^{20} cm^{-3}. Nonetheless, it is desirable to keep the buffer layer as thin as

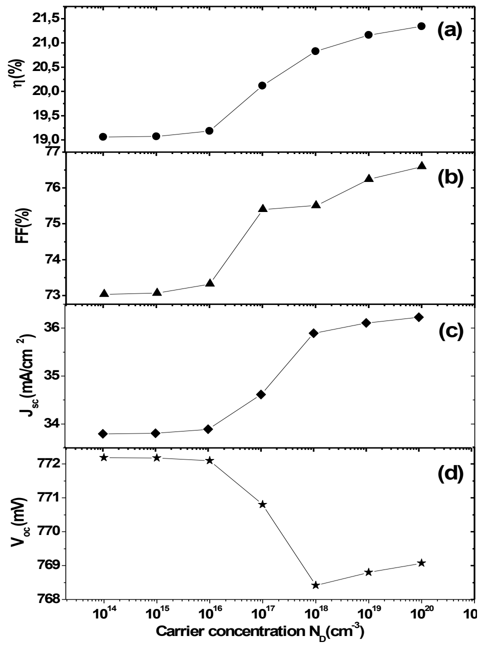

Figure 6. Effect of CdS buffer layer donor charge carrier concentration N_D (cm^{-3}) on solar cell parameters: (a) efficiency, (b) Fill factor (FF), (c) Short-circuit current density (J_{sc}) and (d) open-circuit voltage (V_{oc}).

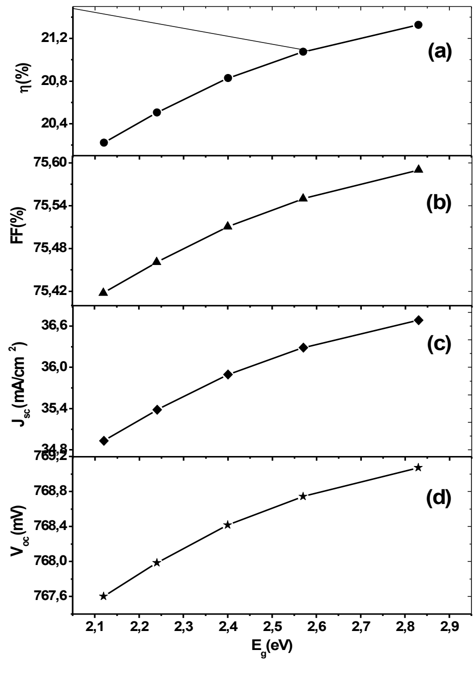

Figure 7. Effect of CdS buffer layer band gap on solar cell parameters: (a) efficiency, (b) Fill factor (FF), (c) Short-circuit current density (J_{sc}) and (d) open-circuit voltage (V_{oc}).

possible with very high doping level to maintain the remarkable overall CIGS-Based solar cells performance. The optimum buffer thickness must be in the range of 30 - 60 nm with doping level of about 1×10^{18} cm^{-3} [24]. On the other hand, when the carrier density of the buffer layer increases the barrier of potential in CdS/CIGS and ZnO/CdS hetero-junctions decreases, and allows an increase in the zone of space charge, from where an improvement of the collection of the photogenerated carriers and thus an increase in the output of conversion [4].

D. *Effect of CdS Buffer Layer Band Gap*

Fig. 7 illustrates the effect of CdS buffer layer band gap on the CIGS solar cell performance, such as open circuit voltage V_{oc}, short circuit density J_{sc}, fill factor FF and efficiency η. The values used for achieving this simulation are obtained experimentally: 2.12 [25], 2.24 [26], 2.4 [25, 27], 2.57 [28,29], and 2.83 [30] eV. As seen in Fig. 7, all the output parameters increase with increasing the buffer layer band gap, indicating an enhancement in the performance of CIGS-based solar cell. The efficiency values at the minimum value 2.12 eV and the maximum value 2.83 eV of CdS buffer layer band gap are 20.22% and 21.33% respectively. The efficiency is improved by 1.11% at higher band gap 2.83 eV. The large band gap buffer layers could possibly provide new insights into the mechanisms behind the metastable effects in CIGS-based devices [31].

IV. CONCLUSION

A numerical study was carried out on the CdS buffer layer parameters for analyzing and improving the performance of CIGS-based solar cells using the SCAPS-1D software. The solar cell output parameters were obtained by varying thickness, donor charge carrier concentration and band gap of the buffer layer. The numerical simulation results illustrated that all output parameters values decreased with increasing thickness, and the suitable value is 30 nm for the buffer layer. The second set of analysis consists of examining the contribution of carrier concentration N_D. The obtained results indicated that was no change of all performance parameters with buffer layer doping up to carrier concentration N_D of 1×10^{16} cm^{-3} and the optimized value is 10^{18} cm^{-3}. The effect of band gap was also studied. It was found that the efficiency improved remarkably with increasing band gap value. It revealed that the highest efficiency is about 21.33% corresponding to a buffer layer of 2.83eV band gap.

ACKNOWLEDGMENT

The authors would like to acknowledge Marc Burgelman and his colleagues at the University of Gent, Belgium, for providing SCAPS-1D simulator.

REFERENCES

[1] Bouabdelli, M. W., Rogti, F., Maache, M., & Rabehi, A. (2020). Performance enhancement of CIGS thin-film solar cell. *Optik, 216*, 164948.

[2] Lin, Y. C., Yen, W. T., Chen, Y. L., Wang, L. Q., & Jih, F. W. (2011). Influence of annealing temperature on properties of Cu (In, Ga)(Se, S) 2 thin films prepared by co-sputtering from quaternary alloy and In2S3 targets. *Physica B: Condensed Matter, 406*(4), 824-830.

[3] Khoshsirat, N., Yunus, N. A. M., Hamidon, M. N., Shafie, S., & Amin, N. (2015). Analysis of absorber layer properties effect on CIGS solar cell performance using SCAPS. *Optik, 126*(7-8), 681-686.

[4] Dabbabi, S., Nasr, T. B., & Kamoun-Turki, N. (2017). Parameters optimization of CIGS solar cell using 2D physical modeling. *Results in physics, 7,* 4020-4024.

[5] Hasoon, F. S., et al. (2001). Microstructural properties of Cu (In, Ga) Se2 thin films used in high-efficiency devices. *Thin Solid Films, 387*(1-2), 1-5.

[6] Boukortt, N. E. I. (2020). Numerical optimization of 0.5‐μm‐thick Cu (In1-xGax) Se2 solar cell. *Optik, 200,* 163409.

[7] Hagiwara, Y., Nakada, T., & Kunioka, A. (2001). Improved Jsc in CIGS thin film solar cells using a transparent conducting ZnO: B window layer. *Solar Energy Materials and Solar Cells, 67*(1-4), 267-271.

[8] Yılmaz, S., Ünverdi, A., Tomakin, M. U. R. A. T., Polat, İ. S. M. A. İ. L., & Bacaksız, E. (2019). Surface modification of CBD-grown CdS thin films for hybrid solar cell applications. *Optik, 185*, 256-263.

[9] Jiang, X., et al. (2010). Effects of molecular interface modification in CdS/polymer hybrid bulk heterojunction solar cells. *Solar Energy Materials and Solar Cells, 94*(12), 2223-2229.

[10] Arbouz, H., Aissat, A., & Vilcot, J. P. (2016). Modeling and optimization of CdS/CuIn1− xGaxSe2 structure for solar cells applications. *International Journal of Hydrogen Energy, 41*(45), 20987-20992.

[11] Jackson, P., et al. (2007). High quality baseline for high efficiency, Cu (In1− x, Gax) Se2 solar cells. *Progress in Photovoltaics: Research and Applications, 15*(6), 507-519.

[12] Burgelman, M., Decock, K., Niemegeers, A., Verschraegen, J., & Degrave, S. (2018). *SCAPS Manual (version: 3.3. 07).* Department of Electronics and Information Systems, University of Gent, Belgium.

[13] Burgelman, M., Nollet, P., & Degrave, S. (2000). Modelling polycrystalline semiconductor solar cells. *Thin solid films, 361,* 527-532.

[14] Nerat, M., Smole, F., & Topič, M. (2011). A simulation study of the effect of the diverse valence-band offset and the electronic activity at the grain boundaries on the performance of polycrystalline Cu (In, Ga) Se2 solar cells. *Thin Solid Films, 519*(21), 7497-7502.

[15] Ouedraogo, S., Sam, R., Ouedraogo, F., Kebre, M. B., Zougmore, F., & Ndjaka, J. M. (2013, September). Optimization of Copper Indium Gallium Di-Selenide (CIGS) based solar cells by back grading. In *2013 Africon* (pp. 1-6). IEEE.

[16] Moradi, M., Teimouri, R., Zahedifar, M., & Saadat, M. (2016). Optimization of Cd1− yZnyS buffer layer in Cu (In, Ga) Se2 based thin film solar cells. *Optik, 127*(8), 4072-4075.

[17] Gharibshahian, I., Sharbati, S., & Orouji, A. A. (2018). Potential efficiency improvement of Cu (In, Ga) Se2 thin-film solar cells by the window layer optimization. *Thin Solid Films, 655*, 95-104.

[18] Jackson, P., Hariskos, D., Wuerz, R., Wischmann, W., & Powalla, M. (2014). Compositional investigation of potassium doped Cu (In, Ga) Se2 solar cells with efficiencies up to 20.8%. *physica status solidi (RRL)–Rapid Research Letters, 8*(3), 219-222.

[19] Köntges, M., Reineke-Koch, R., Nollet, P., Beier, J., Schäffler, R., & Parisi, J. (2002). Light induced changes in the electrical behavior of CdTe and Cu (In, Ga) Se2 solar cells. *Thin Solid Films, 403*, 280-286.

[20] Zheng, X., Li, W., Aberle, A. G., & Venkataraj, S. (2016). Efficiency enhancement of ultra-thin Cu (In, Ga) Se2 solar cells: optimizing the absorber bandgap profile by numerical device simulations. *Current Applied Physics, 16*(10), 1334-1341.

[21] Mostefaoui, M., Mazari, H., Khelifi, S., Bouraiou, A., & Dabou, R. (2015). Simulation of high efficiency CIGS solar cells with SCAPS-1D software. *Energy Procedia, 74,* 736-744.

[22] Chelvanathan, P., Hossain, M. I., & Amin, N. (2010). Performance analysis of copper–indium–gallium–diselenide (CIGS) solar cells with various buffer layers by SCAPS. *Current Applied Physics, 10*(3), S387-S391.

[23] Yaşar, S., Kahraman, S., Çetinkaya, S., Apaydın, Ş., Bilican, İ., & Uluer, İ. (2016). Numerical thickness optimization study of CIGS based solar cells with wxAMPS. *Optik, 127*(20), 8827-8835.

[24] AlZoubi, T., & Moustafa, M. (2019). Numerical optimization of absorber and CdS buffer layers in CIGS solar cells using SCAPS. *Int. J. Smart Grid Clean Energy, 8*(3), 291-298.

[25] Prabahar, S., & Dhanam, M. (2005). CdS thin films from two different chemical baths—structural and optical analysis. *Journal of Crystal growth, 285*(1-2), 41-48.

[26] Priya, N. S., Kamala, S. S. P., Anbarasu, V., Azhagan, S. A., & Saravanakumar, R. (2018). Characterization of CdS thin films and nanoparticles by a simple chemical bath technique. *Materials Letters, 220*, 161-164.

[27] Butt, S., Shah, N. A., Nazir, A., Ali, Z., & Maqsood, A. (2014). Influence of film thickness and In-doping on physical properties of CdS thin films. *Journal of alloys and compounds, 587*, 582-587.

[28] Garcia, L. V., et al. (2015). CdS thin films prepared by laser assisted chemical bath deposition. *Applied Surface Science, 336,* 329-334.

[29] Chander, S., & Dhaka, M. S. (2017). Optical and structural constants of CdS thin films grown by electron beam vacuum evaporation for solar cells. *Thin Solid Films, 638,* 179-188.

[30] Rondiya, S., Rokade, A., Gabhale, B., Pandharkar, S., Chaudhari, M., Date, A., ... & Jadkar, S. (2017). Effect of bath temperature on optical and morphology properties of CdS thin films grown by chemical bath deposition. *Energy Procedia, 110*, 202-209.

[31] Platzer-Björkman, C., Törndahl, T., Hultqvist, A., Kessler, J., & Edoff, M. (2007). Optimization of ALD-(Zn, Mg) O buffer layers and (Zn, Mg) O/Cu (In, Ga) Se2 interfaces for thin film solar cells. *Thin Solid Films, 515*(15), 6024-6027.

Sensorless Performance Enhancements of PMSG Drive by a Wind Turbine

Mohamed Mansouri[1], Mohamed Bey[2], Said Hassaine[3], Ahmed Tahri[4]

[1,2,3,4]Laboratoire de génie informatique et génie énergétique, Université IBN Khaldoun, Tiaret, Algeria

Abstract—**The main objective of this paper is to improve the sensorless performance of PMSG connected to grid drive by a wind turbine. Among the existing observers, the linearly compensated flux observer is selected in this study due its straightforwardness and simplicity where is very adapted to PMSG because the wind turbine drive in medium and high speed. This observer reconstructs the speed and position of PMSG. The compensate part of this observer is modified to achieve the control objectives. The performance of the proposed scheme is very improved compared to original scheme in stator and grid control.**

Keywords – sensorless, PMSG, wind turbine, observer

I. INTRODUCTION

The renewable energy has been greater than before due to control enhancement of different machines, the high-performance control in variable-speed of PMSG received an crucial attention in wind energy conversion system (WECS) [1].

The position information of PMSG plays an important role in terms of the generators control, to eliminate position sensors and to increase the WECS reliability, several technique are developed [2].

Two kinds of signal injection techniques, saturation or magnetic method to detect the rotor's position in zero and low speed operations [3].

According to literature in medium and high-speed ranges, many approaches are developed, such as: estimate the magnitude of electromotive force (EMF) [4], Kalman Filter [5], Sliding Mode Observer (SMO) [6], Phase-Lock Loop (PLL) [7], the high order sliding mode observer (HOSMO) [8], adaptive observers [9], extended state observer [10].

The main objective of this paper is to improve the sensorless performance of PMSG connected to grid drive by a wind turbine. Among the existing observers, the linearly compensated flux observer is selected in this study due its straightforwardness and simplicity where is very adapted to PMSG because the wind turbine drive in medium and high speed. This observer reconstruct the speed and position from the electromotive force of PMSG. The compensate quantity of this observer is modified to achieve the control objectives. The performance of the proposed scheme is very improved compared to original scheme in stator and grid control.

II. THE SYSTEM MODELISATION

A. Turbine Model

The power of the mechanical part of the wind turbine is modeled by:

$$P_m = \frac{1}{2} C_p(\lambda)\rho\pi R^2 V_w^3 \ , \qquad (1)$$

where C_p is the power coefficient, ρ is the air density, R is the blade radius and V_w is the wind speed. The value of C_p depends on the pitch angle (β), the tip speed ratio (λ) and the positive constants c_1 to c_6 [11]:

$$C_p = c_1\left(\frac{c_2}{\lambda_i} - c_3\beta - c_4\right)e^{\frac{-c_5}{\lambda_i}} + c_6\lambda \ , \qquad (2)$$

with

$$\frac{1}{\lambda_i} = \frac{1}{\lambda + 0.08\beta} - \frac{0.035}{\beta^3 + 1} \ , \qquad (3)$$

and

ISBN: 978-86-82602-01-9

$$C_p = 0.38, \beta = 0, \lambda_{opt} = 6.1, c_1 = 0.22,$$
$$c_2 = 116, c_3 = 0.4, c_4 = 5, c_5 = 12.5, c_6 = 0 \quad . \tag{4}$$

The select structure contain a gearbox in order to adapt the generator (speed ω_g and torque T_g) with turbine (speed ω_t and torque $\mathcal{T}_t$). This gear box is described by:

$$\omega_t = \frac{1}{G}\omega_g \ , \tag{5}$$
$$\mathcal{T}_g = \frac{1}{G}\mathcal{T}_t, \tag{6}$$

where G is the gearing ratio [8].

B. PMSG Model

The mathematical model in the park reference of PMSG is derived from the space vector of the stator voltage equation where can be written as:

$$v_d = -R_s i_d - \frac{d\varphi_d}{dt} + \omega_r \varphi_q \ , \tag{7}$$

$$v_q = -R_s i_q - \frac{d\varphi_q}{dt} + \omega_r \varphi_d \ , \tag{8}$$

where R_s indicate the stator resistance, v_{dq} are stator voltages, i_{dq} denote the stator currents, ω_r and $\varphi_{d,q}$ are the rotor speed and magnetic flux respectively.

The electromagnetic torque and the mechanical equation in (d,q) coordinate can be written as:

$$T_{em} = \frac{3n_p}{2}\left[\varphi_d i_q - \varphi_q i_d\right] \ , \tag{9}$$

$$\frac{d\omega_r}{dt} = \frac{3n_p}{2}\left[\varphi_d i_{sq}\right] - \frac{f_v}{J}\omega_r - \frac{T_t}{J} \ , \tag{10}$$

where f_v represents the viscous friction, $\mathcal{J}$ denote the inertia, T_t represents the mechanical torque and n_p denote the pole pair number [11].

III. Stator-Side Control

On dual closed loop control, one controls the flux and other controls the torque. This loop control uses the two components of current. The speed regulation determinate the reference torque by using a maximum power point tracking (MPPT) approach to obtain the maximum power of the turbine.

The MPPT approach impose a reference speed, which depends on the wind speed V_w and the optimal tip speed ratio λ_{opt} where is given by:

$$\omega* = \frac{\lambda_{opt} \times V_w}{R} \ . \tag{11}$$

The sensorless control block is illustrated in Fig. 1. The speed is derived from compensated flux observer. The control loop used the PI regulator [11].

IV. Grid Side Control

The controller of grid-side converter is double-loop structure, including vdc outer loop and dq-axes current inner loop.

Fig. 2 show different block of this part. The vdc loop uses the ant-windup PI regulator; the

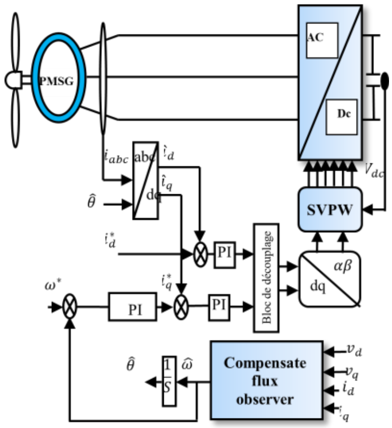

Figure 1. Stator and sensorless control block.

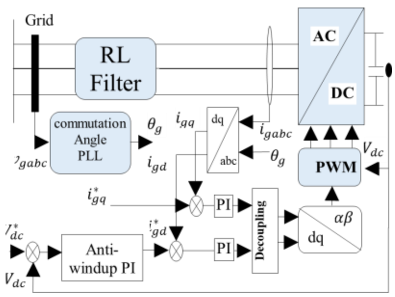

Figure 2. Grid control block.

current loop uses the proportional integral regulator.

The following equation represents the grid voltage:

$$v_{gd} = v_{id} - Ri_{gd} - L\frac{di_{gd}}{dt} + L\omega_g i_{gq} \;, \quad (12)$$

$$v_{gq} = v_{iq} - Ri_{gq} - L\frac{di_{gq}}{dt} + L\omega_g i_{gd} \;, \quad (13)$$

where L and R are the inductor and resistor of grid, v_{gd} and v_{gq} are the grid voltage [12].

V. DC Voltage Model

The DC bus is the quantity between the two converters, which consists of a capacitor, its purpose is to filter the voltage. The DC bus is modeled by the following equation:

$$\frac{dv_{dc}}{dt} = \frac{1}{c} I_{dc} \;, \quad (14)$$

with I_{dc} is the capacitor current [12].

VI. Compensated Flux Observer

In the field-oriented control, the back-EMF vector is aligned with q-axis and designate the rotor position, against the permanent magnet flux is aligned with d-axis.

Fig. 3 shows the schematic block of the observer, this observer is based on the estimation of the electromotive forces to determine the speed of PMSG. The flux permanently positive, so the position angle cannot change its direction [13]. Here, k and Q are positive constant, e is speed error.

In the flux compensation part, the reference [13] uses a gain multiplied by the sign of speed, the speed is positive in wind turbine conversion, so this part cannot improve the speed response.

In this paper we have proposed another trick which this part is modified by including the speed error.

From a liaison between EMF (ed, eq) and flux, we can write:

$$e_d = \frac{d\varphi}{dt}, \; so \; \varphi = \int e_d \;, \quad (15)$$

$$e_q = \omega_r \varphi, \; so \; \omega_r = \frac{e_q}{\varphi} \;. \quad (16)$$

VII. Simulation Results

The simulations with nominal parameters and according to selected trajectories is presented to examine the performance of the proposed sensorless control.

Fig. 4 shows the estimated speed with original and proposed method. From this figure, we can notice that the estimated speed tracks the reference speed very well, however, the zoom show that the speed of original method has an oscillation and small overshoot compared to proposed method.

The direct and quadrature current are displayed in Fig. 5. We can see clearly that the direct current of two method reaches zero, but the current with original method has more oscillation such as speed. The quadrature currents is proportional to the wind speed and have an overshoot in first time.

As it can be seen in Fig.6, that the DC voltage is following with better accuracy the reference. The DC voltage stabilizes with no overshoot.

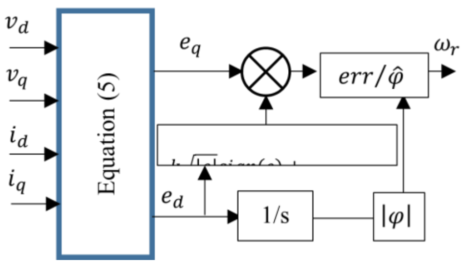

Figure 3. Observer block.

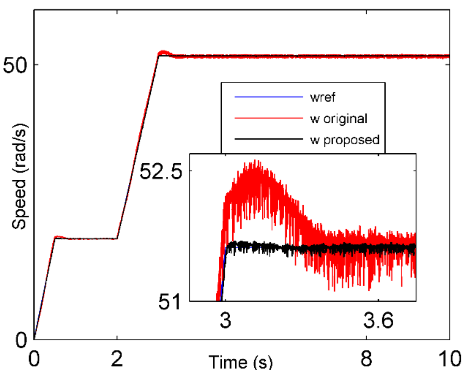

Figure 4. Speed simulation.

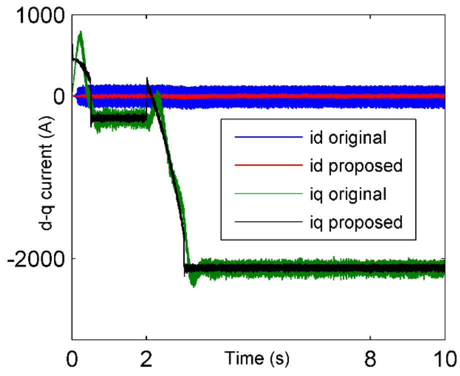

Figure 5. D-q current simulation.

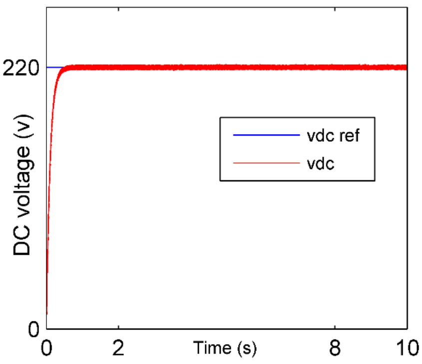

Figure 6. DC voltage simulation.

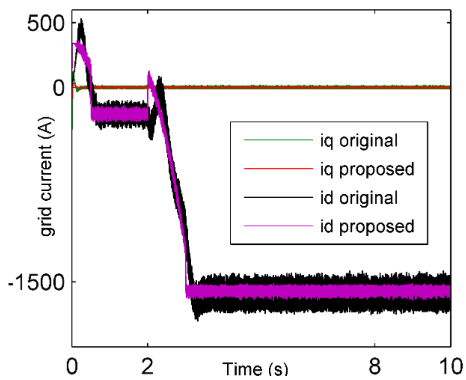

Figure 7. Grid current simulation.

This good performance is due to the integrator anti-windup.

The control strategy kept the q-axis grid current to zero (Fig. 7), a small overshoots appear in iq grid current. The id grid current have a good performance with small backward overshoot. It is clear that the response with proposed method is very improved compared to original method.

VIII. Conclusion

This work deals a sensorless control of PMSG connected to grid and driven by a wind turbine. A modified linearly compensate flux observer is introduce for estimate speed. The proposed scheme provide a satisfactory response in the speed, stator and grid current. The DC voltage have a good response due anti-windup regulator.

References

[1] Li, S., Zhang, K., Li, J., & Liu, C. (2016). On the rejection of internal and external disturbances in a wind energy conversion system with direct-driven PMSG. *ISA transactions*, *61*, 95-103.

[2] Sergeant, P., De Belie, F., & Melkebeek, J. (2011). Rotor geometry design of interior PMSMs with and without flux barriers for more accurate sensorless control. *IEEE Transactions on Industrial Electronics*, *59*(6), 2457-2465.

[3] Chi, W. C., Cheng, M. Y., Li, C. L., Su, K. H., & Li, W. H. (2014, October). Motor parameter auto-identification based on sensorless startup procedure for PMSM drives. In *IECON 2014-40th Annual Conference of the IEEE Industrial Electronics Society* (pp. 3861-3866). IEEE.

[4] Zaim, S., Nahid-Mobarakeh, B., & Meibody-Tabar, F. (2014). Robust position sensorless control of nonsalient pmsm at standstill and low speeds. *IEEE Journal of Emerging and Selected Topics in Power Electronics*, *2*(3), 640-650.

[5] Bindu, V., Unnikrishnan, A., & Gopikakumari, R. (2010). Sensor less vector control of pmsm using a blind system identification approach based on extended kalman filter algorithm. In *IEEE International Conference on Computational Intelligence and Computing Research*.

[6] Chen, S., Luo, Y., & Pi, Y. (2015). PMSM sensorless control with separate control strategies and smooth switch from low speed to high speed. *ISA transactions*, *58*, 650-658.

[7] Olivieri, C., & Tursini, M. (2012). A novel PLL scheme for a sensorless PMSM drive overcoming common speed reversal problems. In *International Symposium on Power Electronics Power Electronics, Electrical Drives, Automation and Motion* (pp. 1051-1056). IEEE.

[8] Mohamed, M., Said, H., Mhamed, L., Mohamed, B., Tayeb, A., Mouloud, D., & Mohamed, M. (2019). New hybrid sensorless speed of a non-salient pole PMSG coupled to wind turbine using a modified switching algorithm. *ISA transactions*, *94*, 187-199.

[9] Hamida, M. A., De Leon, J., Glumineau, A., & Boisliveau, R. (2012). An adaptive interconnected observer for sensorless control of PM synchronous motors with online parameter identification. *IEEE Transactions on Industrial Electronics*, *60*(2), 739-748.

[10] Liu, H., & Li, S. (2011). Speed control for PMSM servo system using predictive functional control and extended state observer. *IEEE Transactions on Industrial Electronics*, *59*(2), 1171-1183..

[11] Porselvi, T., & Muthu, R. (2014). Wind energy conversion system with boost converter and CHB MLI with single DC input. *International Journal of Engineering and Technology, 6*(1), 138-145.

[12] Bouazza, F., Mohamed, M., & Abdelhamid, L. (2020). Control of Grid Connected PMSG-Based Wind Turbine System with Back-To-Back Converter Topology Using Resonant Controller. *International Journal of Mechanical and Mechatronics Engineering, 14*(5), 213-219.

[13] Ma, Z., & Kennel, R. (2012, June). System-on-Chip sensorless control of PMSM combining signal injection and flux observer. In *Proceedings of The 7th International Power Electronics and Motion Control Conference* (Vol. 2, pp. 1201-1205). IEEE..

Model-driven Approach to Smart Grid Stability Prediction in Neo4j

Nenad Petrović[1], Issam Al-Azzoni[2], Abdullah Alqahtani[3]

[1]University of Niš, Faculty of Electronic Engineering, Niš, Serbia
[2]College of Engineering, Al Ain University, Al Ain, UAE
[3]College of Computer Engineering and Science, Prince Sattam bin Abduulaziz University, Alkharj, KSA

Abstract—**Stability is of utmost importance when it comes to smart grid infrastructures. Dramatic parameter variations and fluctuations can lead to wrong decisions, which could lead to fatal consequences. In this paper, we propose a model-driven methodology for highly automated machine learning approach to smart grid stability prediction. Stability prediction is treated as binary classification problem and implemented relying on Neo4j graph database's Graph Data Science Library (GDS). The proposed framework is evaluated on open, publicly available dataset. According to the achieved results, the predictive model shows better performance in terms of accuracy and execution time compared to other solutions based on deep learning. On the other side, the adoption of model-driven approach is beneficial when it comes to reusability and convenient experimentation compared to manual, non-automated design.**

Keywords – stability, smart grid, machine learning, model-driven enginnering, Neo4j

I. INTRODUCTION

Smart grids represent critical infrastructure and have utmost strategical importance for development worldwide [1,2]. They support exploiting combinations of alternative sources like wind and solar power for clean and affordable energy. Unlike traditional power grids, here we have participant nodes (either households or enterprises) which are both energy consumers and producers at the same time, the so-called prosumers [2]. Therefore, the flow of energy in smart grids is considered bidirectional, as the participants which produce more energy than needed can offer and sell it to others for some specific price. However, unexpected fluctuations and changes as consequences of anomalies, failures or malicious attacks that alter the measured data about supply and demand within them could have fatal consequences to the environment. Therefore, smart grid stability determination in dynamic environment is crucial for their successful adoption. The goal is to detect disturbances and fluctuations, considering not only technical aspects, but taking into account the way the participants respond to the changes when it comes associated economic aspects, such as energy price.

In this paper, we focus on adoption of machine learning classification algorithm within Neo4j graph database for purpose of smart grid stability prediction. Moreover, we develop model-driven methodology leveraging code generation on top of it, in order to automatize data importing and writing complex queries, while enabling better reusability.

II. BACKGROUND AND RELATED WORKS

A. Smart Grid Stability Model: 4-Node Star

The stability model assumed in this paper is built upon the works from [2-4]. In what follows, the 4-node star architecture adopted in this paper will be introduced (depicted in Fig. 1).

The mathematical model based on differential equations aiming to identify instability of smart grid in case of 4-node star architecture was presented in [3,4]. This kind of architecture assumes one power generation node that supplies energy to three other nodes which act as consumers. The following features are considered within the model: 1) total power balance – energy produced or consumed for each of the participant nodes; 2) reaction time – the time required to adjust energy production/consumption as response to changes of price 3) elasticity of energy price.

ISBN: 978-86-82602-01-9

Furthermore, in [2], a simulated, augmented dataset based on this model for purpose of evaluating deep learning-based approach to smart grid stability prediction using classification was created.

B. *Neo4j*

The template is used to format your paper and style the text. All margins, column widths, line spaces, and text fonts are prescribed; please do not alter them.

Neo4j [5] is graph-based database management system. The underlying model consists of three main concepts [6]: 1) nodes – represent entities form the domain of interest 2) connections between the nodes 3) properties – refers to key-value pair whose role is to provide further description of characteristics relevant to entities and their relations. It includes Cypher [7], which is a declarative query language used for retrieval of desired data from graph.

However, since the end of the last year, Graph Data Science (GDS) Library [8,9] was added to Neo4j in order to enable functionalities executed over the data stores as graph. As for now, it covers only two machine learning techniques – link prediction and classification. While Community Edition of GDS is free, additional license is required in order to leverage more than 4 cores for further acceleration of calculations. Despite the fact that its set of machine learning-related capabilities is not so wide, it was shown that GDS outperforms several other solutions, especially when it comes to efficiency [9]. In [10], it was shown that classification in Neo4j can be used for hotel cancellation prediction relying on binary classification, while the execution time was superior to other data mining and deep learning-based solutions.

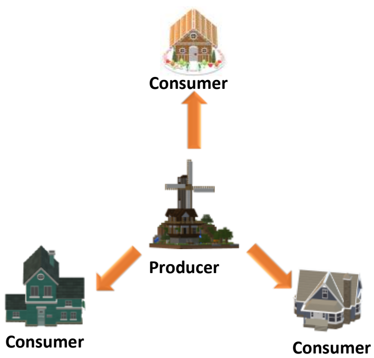

Figure 1. 4-node star smart grid architecture.

C. *Classification and Graph Data Science Library*

In this paper, classification capabilities offered by Graph Data Science Library within Neo4j for purpose of smart grid stability prediction are leveraged. The problem is treated as binary classification with two possible categorical outcomes (1 – stable, 0 – not stable).

Classification problem, in general, represents assignment of the correct label to the sample from collection of observations. For this purpose, a set of input variables known as feature properties is considered, while the output itself produced as outcome of this process is denoted as target property.

However, when it comes to supervised learning (as in this case), predictive model is trained by adjusting its parameters iteratively based on estimations obtained within dataset containing only samples with correct labels (train set). The distance from the correct value is estimated using error function, while the amount of weight parameter modification as a response depends on learning rate (also called penalty in Neo4j). After finishing the training phase, it is possible to evaluate model on either the same training data or dataset with previously unseen samples (test set). Neo4j supports two commonly used metrics in case of classification task:

$$Accuracy = \frac{TP+TN}{TP+TN+FP+FN}, \quad (1)$$

$$F-score = \frac{TP}{TP+\frac{1}{2}(FP+FN)}. \quad (2)$$

In these equations, variables represent different types of observation counts: true positive (TP), true negative (TN), false positive (FP) and false negative (FN).

In order to train a classification model using Neo4j's GDS Library, the method `gds.alpha.ml.nodeClassification.train` [11] is used. Before training, a set of algorithm parameters has to be set, while the most important ones are mentioned: `modelName` – how the model will be stored in catalog; `featureProperties` - names of independent variables; `targetPropery` – class label, the dependent variable name;

holdoutFraction – percentage of dataset used for evaluation; `metrics` – evaluation metric, either f1-score (two variants - `F1_WEIGHTED` and `F1_M ACRO`) or accuracy. Furthermore, it is required to set the model parameter, while GDS gives the ability to define multiple candidate models within `params`.

For each of the candidate models, the following values are adjustable: `penalty` – learning rate; `batchSize` – number of samples processed within one training iteration; `minEpochs` – minimum number iteration through the training set; `maxEpochs` – maximum number of training iterations; patience – maximum number of training iterations without performance improvement before stopping; `tolerance` – minimum acceptable error function value before stopping.

D. Model-Driven Engineering using Eclipse Modelling Framework (EMF)

Model-driven software engineering makes use of domain or system model-based representations with synergy of code generation in order to automatize or speed-up certain phases related to development of software assets. software development phases and usage scenarios [12]. Therefore, models can be used in many different ways and for various purposes, ranging from generation of documentation executable code to system verification and validation.

Ecore [13] within Eclipse Modelling Framework (EMF) [14] for Java programming language provides the capabilities for construction of metamodels that can be further used as templates for user-specified instances, which are structured in a way that complies with the definition provided by the underlying metamodel. Moreover, it gives the ability to generate adapter classes that aid the manipulation of model instances, enabling parsing and traversal, which are crucial steps for retrieval of parameters and code generation. On the other side, we make use of PyEcore [15], which allows handling of EMF/Ecore metamodels and models in Python. It provides an API that is compatible with the original EMF implementation in Java. Using pyecore, the network planning problems can be represented as Ecore model instances. Furthermore, the instance of a model can be verified and imported in form of Python objects, which is suitable for automated solving of network planning problems

In this paper, model-driven approach is leveraged for automatization of two aspects relevant to classification in Neo4j: graph construction and classification query generation.

III. IMPLEMENTATION

A. Classification Workflow in Neo4j

In the first step, data is loaded from CSV file within Neo4j environment by executing `LOAD CSV WITH HEADERS FROM file` query, as it can be seen in Listing 1. We import the dataset under consideration in form of a collection of data rows labelled as "Stability". Within the query, file: parameters is used to specify the corresponding path. On the other side, `MERGE` serves to choose the desired columns from the CSV file and set user-defined node label ("Stability" in this case).

```
LOAD CSV WITH HEADERS FROM
'file:///sg_stability.csv' AS row
WITH row WHERE row.stabf IS NOT NULL
MERGE (s:Stability {tau1: row.tau1,
...
stabf : row.stabf});
```

Listing 1. Loading CSV file into Neo4j as set of nodes.

Furthermore, a graph must be constructed from the loaded rows before classification model is trained. Method `gds.graph.create.cypher` is used for that purpose with corresponding parameters, as it can be seen in Listing 2. There are three mandatory parameters: 1) name of graph 2) Cypher query for node retrieval 3) Cypher query filtering the edges between nodes. However, in this paper we rely only on node properties for classification, while edges between nodes are not leveraged.

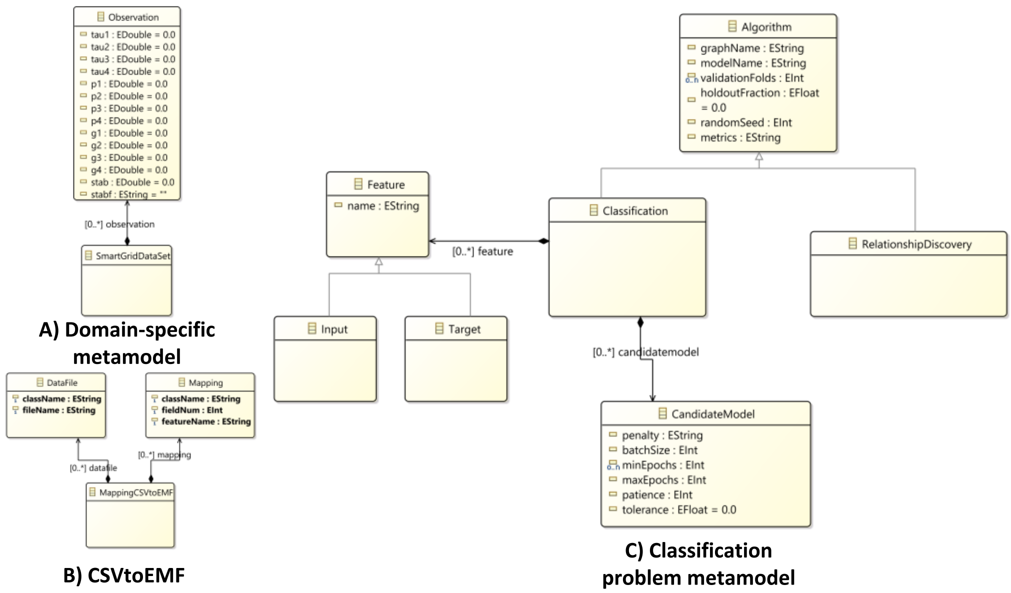

Figure 2. Metamodels: a) Smart grid stability dataset metamodel b) Data import metamodel - CSVtoEMF c) Prediction problem metamodel.

```
CALL gds.graph.create.cypher(
  'StabilityGraph',
  'MATCH (s:Stability) WHERE s.stabf is
NOT NULL RETURN id(s) as id,
   toFloat(s.tau1) as tau1,
   ...
   toInteger(s.stabf) as stabf',
  'MATCH (start:Stability)-[link]-
>(end:Stability)
RETURN ID(link) as link, ID(start) as
source, ID(end) as target'
)
```

Listing 2. Graph construction starting from collection of imported rows in Neo4j.

Once graph is constructed, we train the predictor based on classifier by executing `gds.alpha.ml.nodeClassification.train` procedure from Graph Data Science Library, in a way which is illustrated in Listing 3. The invocation command contains three main parts: 1) specification of classification algorithm's inputs and output – name of the input graph, name of classification model, set of independent variables, dependent variables and desired evaluation metric 2) setting the candidate model parameters 3) best model selection criteria – defining how the candidate models are compared and which one should be selected as the best and stored into Neo4j catalog under `modelName`.

```
CALL
gds.alpha.ml.nodeClassification.train('S
tabilityGraph', {
  modelName: 'stability_prediction',
  featureProperties:
         ['tau1', 'tau2',
           . . .
         'g4'],
  targetProperty: 'stabf',
  randomSeed: 3,
  holdoutFraction: 0.25,
  validationFolds: 5,
  metrics: [ 'ACCURACY'],
  params: [
        {
               penalty: 0.01,
               maxEpochs: 10,
               batchSize: 100
        },
        . . .
        {      penalty: 0.1 }
]
}) YIELD modelInfo
RETURN
  {penalty:
modelInfo.bestParameters.penalty} AS
winningModel,
```

```
  modelInfo.metrics.ACCURACY.outerTrain
AS trainGraphScore,
      modelInfo.metrics.ACCURACY.test AS
testGraphScore
```

Listing 3. Graph-based classifcator training command in Neo4j.

B. *Model-driven Framework*

The proposed model-driven framework covers two aspects – efficient data import [16] and Neo4j query generation. It consists of metamodels and code generation procedures.

Metamodels aiming the automated import of CSV data into Neo4j as depicted in Fig. 2a and 2b. Two of them are relevant for this task: domain-specific metamodel (2a) and CSVtoEMF (2b) [16]. The first one describes the data of interest from a particular domain, which is smart grid stability in our case. The second gives the ability to define mapping between the corresponding CSV file rows and domain-specific features. Based on these two metamodels, the final outcome is to import the raw CSV file into Neo4j by generating the corresponding loading and graph construction queries based on model instances. The output of mapping are Neo4j queries for data import and graph creation, similar to code from Listings 1 and 2.

On the other side, another metamodel describing the classification problems (shown in Fig. 2c) is used for automated generation of machine learning-related queries executable by GDS in Neo4j. For that purpose, user has to provide corresponding parameters relevant to the specific machine-learning task, such as input and target variable or hyperparameters. At the moment, it covers the aspects related to classification-alike problems and relevant parameters. The generated output based on this metamodel is classification train function invocation, structured as shown in code within Listing 3.

In Fig. 3, the model-driven workflow leveraging metamodels and automated code generation is depicted. In the first step, user sets the desired CSV file path and selects which columns from the table to include. Additionally, for purpose of classification, it is also required to distinguish which columns represent input features and which one is the target output. The modeling is done within automatically generated GUI-enabled environment within Eclipse, provided by EMF. After that, the user-created model instance about CSV column mapping is leveraged to construct Cypher queries for data import and graph construction in Neo4j. Moreover, once the data is imported, classification training method invocation code is parametrized. Finally, user can input the generated queries into Neo4j, execute them and functional classifier for smart grid stability prediction will be created and stored into Neo4j catalog. The classifier is ready after that for predictions on previously unseen data.

IV. Experiments and Evaluation

For evaluation of the proposed approach, we used publicly available online dataset from [17]. It contains 60 000 observations from the simulated smart grid environment with the features described in Table I. It was split into training (75%) and test set (25%). Independent variables are in white fields, while the dependent variables are gray. The experiments were executed on a laptop with given capabilities: Intel i7 7700HQ 2.8GHz quad-core CPU, 16GB of DDR4 RAM and M1 SSD.

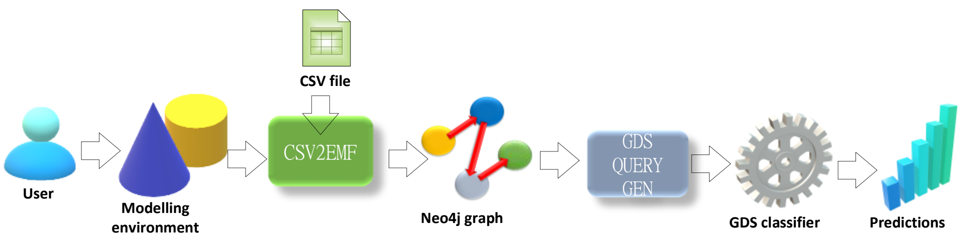

Figure 3. Model-driven framework for machine learning in Neo4j.

TABLE I. STABILITY PREDICTION DATA SET OVERVIEW.

Vari.	Type	Description
τ_1-τ_4	Real [0.5, 10]	Reaction time for each of the participant nodes. The first one (τ_1) is for the supplier node, while the others represent consumers.
p_1-p_4	Real consumers: [-2.0, 0.5]	Nominal power which is consumed (negative) or produced (positive) by participant nodes. Here, p1 denotes producer, while the others are consumers, so the following equation holds: $p_1 = -(p_2 + p_3 + p_4)$
γ_1- γ_4	Real [0.05-1.00]	Coefficient of price elasticity for smart grid nodes.
stab	Real	Characteristic differential equation maximum real part of the root.
stabf	Categorical	if (stab>0) then stabf=1 else stabf=0

Moreover, an overview of experiment results for the proposed approach is shown in Table II. Several different aspects were taken into account, regarding different steps and components: classification model prediction performance, execution time for various steps and speed-up achieved as outcome of adopting model-driven approach. The first column denotes the considered aspect of interest for evaluation. Furthermore, the second column denotes to which component experiment refers to. Moreover, the next column holds the description of relevant conditions for experiment related to the observed aspect. Finally, the last column shows the values obtained as a metric for the considered aspect.

Observing the obtained values, we can notice that classification model gives performance comparable, but slightly worse than approach presented in [3], but outperforms several other solutions based on deep learning discussed in [3]. On the other side, the execution time for training is faster than most of the methods relying on neural networks, confirming the efficiency of Neo4j, when it comes to classification task. Additionally, query execution time increases with the number of candidate models included. On the other side, the benefits of model-driven code generation were measured by comparing the sum of user-defined model instance creation and code generation to manual query construction by medium-skilled professional. The speed-up in our case was a bit more than 4 times.

TABLE II. EXPERIMENT RESULTS OVERVIEW.

Aspect	Component	Condition	Result
Classification perfoamance	Predictive model	Learning rate 0.01 75% train 25% test	F1: 0.98 Acc.: 0.97
Execution time	Import CSV	60 000 records, 12 features	*4 min*
	Training		*8 s*
	ML query generation	5 candidate models	*0.57 s*
		10 candidate models	*0.68 s*
Speed-up	Model creation	User-created in Eclipse tool	283 s
	Auto. query	Code generation algorithm	1.32 s
	Manual query	Medium skill	1149 s
	Speed-up	Manual/ Auto	4.04 [times]

V. CONCLUSION AND FUTURE WORK

According to the experimentally obtained results on publicly available dataset, our approach to model-driven smart grid stability prediction seems promising. Classification model created as outcome of the experiments outperforms several deep learning-based solutions when it comes to both accuracy and execution time. On the other side, the adoption of model-driven code generation is highly beneficial, as it reduces the time necessary for manual query construction by about 4 times.

In future, it is planned to extend the approach for more machine learning tasks applicable in smart grid use cases (such as load forecast using regression), apart from classification and also for other data science frameworks, as well. Moreover, adopting similar approach to smart grid observability is also considered.

ACKNOWLEDGMENT

This work has been supported by the Ministry of Education, Science and Technological Development of the Republic of Serbia.

REFERENCES

[1] Bashir, A. K. et al. (2021). Comparative analysis of machine learning algorithms for prediction of smart grid stability. *International Transactions on Electrical Energy Systems, 31*(9), 1-23.

[2] Breviglieri, P., Erdem, T. & Eken, S. (2021). Predicting Smart Grid Stability with Optimized Deep Models. *SN Computer Science, 2*, 1-12.

[3] Schäfer, B. et al (2016). Taming instabilities in power grid networks by decentralized control. *Eur. Phys. J. Spec. Top. 225,* 569–582.

[4] Arzamasov, V., Böhm, K. and Jochem, P. (2018). Towards Concise Models of Grid Stability. In *2018 IEEE International Conference on Communications, Control, and Computing Technologies for Smart Grids (SmartGridComm)*, (pp. 1-6).

[5] *Neo4j*. Available at: https://neo4j.com/, last accessed: 01/11/2021.

[6] *Graph database concepts*. Available at: https://neo4j.com/docs/getting-started/current/graphdb-concepts/

[7] *The Neo4j Graph Data Science Library Manual v1.7*. Available on: https://neo4j.com/docs/graph-data-science/current/

[8] *Cypher Query Language*. Available on: https://neo4j.com/developer/cypher/

[9] *Announcing: Graph-Native Machine Learning in Neo4j!*. Available at: https://neo4j.com/blog/announcing-graph-native-machine-learning-in-neo4j/

[10] Petrović, N. (2021). Booking Cancellation Prediction Relying on Graph Database in Neo4j. In *IEEESTEC – 14th Student Projects Conference*, (pp. 209-212).

[11] *Node Classification*. Available at: https://neo4j.com/docs/graph-data-science/current/algorithms/ml-models/node-classification/, last accessed: 01/11/2021.

[12] Brambilla, M., Cabot, J., & Wimmer, M. (2017, March 30). *Model-Driven Software Engineering in Practice: Second Edition.*

[13] *Eclipse Modeling Framework*. Available at: https://www.eclipse.org/modeling/emf/, last accessed: 30/11/2021.

[14] *Ecore.* Available at: https://wiki.eclipse.org/Ecore

[15] *PyEcore: A Pythonic Implementation of the Eclipse Modeling Framework* [online]. Available at: https://github.com/pyecore/pyecore

[16] Al-Azzoni, I., Petrovic, N., Alqahtani, A. (2021). A Utility to Transform CSV Data into EMF. In *International Conference on Software Defined Systems (SDS 2021)*, (pp. 1-6).

[17] *Predicting Smart Grid Stability with Deep Learning*. Available at: https://www.kaggle.com/pcbreviglieri/predicting-smart-grid-stability-with-deep-learning

Numerical Analysis of a Tubular Heat Exchanger Efficiency under the Effects of Porous Baffles, Variable Magnetic Field, and Hybrid Nanofluid

Khaled Mouaici[1], Brahim Fersadou[2], Walid Nessab[3], Henda Kahalerras[4]

[1,2,3,4]USTHB, Algiers, Algeria

Abstract—**A numerical study is conducted to analyze the performance of a tubular heat exchanger in which a (Cu-Al_2O_3/Water) hybrid nanofluid flows in the presence of magnetic sources, which generate a variable magnetic field. The hot and the cold fluids, circulating in co-current, flow respectively in the internal tube and the annular space provided with porous baffles arranged in a staggered manner. The Darcy-Brinkman-Forchheimer model is used to describe the fluid flow in the porous regions, and the conservation equations are solved by the finite volume method using the SIMPLE algorithm. The main aim of this work is to analyze the effect of control parameters such as Reynolds, Hartmann, and Darcy numbers, as well as the volume fraction of nanoparticles, on the flow structure and the heat transfer characteristics. The results show that intensifying the magnetic field with a reduction of the fluid velocity in the presence of low-permeability porous baffles improves the heat exchanger's effectiveness. As for pressure drops, they are reduced with the decrease in the magnetic field intensity, the increase in the permeability of porous baffles, and the intensity of the inertial force. The results also showed that increasing the volume fraction of nanoparticles is beneficial for improving the thermal and dynamic performances of the device.**

Keywords – heat exchanger, hybrid nanofluid, porous baffles, magnetic field

I. INTRODUCTION

This Extremely high equipment cooling performance is a significant need for several industrial branches (automotive, naval, food processing, chemical and mechanical units, and so on). With the help of heat exchangers, the overheating of equipment can be prevented and avoided. The heat exchangers are engineered to attain maximum heat transfer rate, minimum volume and weight, low-pressure drop, high efficiency, and low cost. The use of fins is one of the commonly used methods to enhance the heat transfer rate in heat exchangers. However, in parallel to increasing the pressure drop, this method also raises their weight and volume; therefore, its application has many limitations. Other than changes in the geometry of heat exchangers, improving the working fluids' properties can increase the heat exchange rate in these devices. In recent years, the alternative solution of using nanofluids and, more recently, hybrid nanofluids has been widely adopted by researchers. Reference [1] carried out a study of the thermal-hydraulic characteristics of a non-Newtonian Fe_3O_4-Carbon nanotube (CNT). The results indicated an improvement in heat transfer rate up to 53.8% and 28.6% at Reynolds numbers 500 and 2000, respectively. Reference [2] analyzed numerically and in 3D the impact of the volume fraction and the proportion of nanoparticles of an Al_2O_3-Cu/water hybrid nanofluid on the thermal efficiency of a one-pass shell and tube heat exchanger. The outcomes showed that the parameters characterizing the heat transfer increase monotonically with the concentration and proportion of nanoparticles. For example, the rate of growth of the heat exchange coefficient of the hybrid nanofluid is 139% compared to water and 25% compared to a Cu/water nanofluid. Reference [3] proposed a new technique to enhance the hydrothermal performance of a concentric tube heat exchanger by using a tapered wire coil. The experimental study is carried out on a hybrid Al_2O_3-MgO/water nanofluid flowing in a

ISBN: 978-86-82602-01-9

turbulent regime. The effects of using a tapered coil turbulator and a hybrid nanofluid on the hydrothermal behaviors are examined for different coil configurations (converging (C), diverging (D), and converging-diverging (CD)) and various inlet temperatures and flow rates. The findings revealed that the D-type wire coil insert led to the highest hydrothermal efficiency compared to the C and C-D types. Reference [4] experimentally tested the efficiency of a hybrid (water/Fe_3O_4-MWCNT) nanofluide in a plate heat exchanger. They established that when a hybrid nanofluid is used as a coolant, the heat exchanger performance is increased by 10.5% compared to that obtained when employing pure water. The hybrid technique combining nanofluid as a passive method and magnetic field as an active approach has been widely used by researchers.

In heat exchangers, one can quote the work of [5], where the inner tube was corrugated. From a computational analysis in a concentric tube heat exchanger [6], it has been inferred that providing a non-uniform magnetic field could control the motion of a ferrofluid and enhance the thermo-hydraulic performance of the device. To lessen the size of a heat exchanger and preserve energy, an experimental study was conducted employing various enhancing strategies, such as a Fe_3O_4-water-Arabic gum nanofluid, a regulated magnetic field, a curved tube, and a pierced turbulator [7]. Recently, combined effects of a non-uniform magnetic field, nanofluid, and several inner tube geometries (smooth, sinusoidal, trapezoidal, and triangular) on the performance of a double pipe heat exchanger, are examined using the CFD technique [8]. The authors found that the tube with a triangular form performed 15% better than a smooth tube and had a higher heat transmission rate than other configurations.

Although much research has been done on various techniques to improve heat transfer in heat exchangers, the triple combination of a nanofluid-porous medium-variable magnetic field has received little or no attention. To this end, the present work aims to study a tubular heat exchanger's thermal and dynamic characteristics. The porous medium is positioned in the annular space in the form of baffles, the hot and cold fluids are hybrid Cu-Al_2O_3/water nanofluids, and the non-uniform magnetic field is obtained from magnetic sources placed outside the studied device.

II. Mathematical Formulation

A. Physical Domain

The physical domain, illustrated in Fig. 1, is a tubular heat exchanger of length l and inner and outer radius r_i and r_o, respectively. The annular space is provided with porous baffles, arranged in a staggered manner, with the following specifications: porosity ϵ, height h_p, width w, and spacing s. The working fluid is a hybrid nanofluid (Cu-Al_2O_3/Water) with volume fractions of copper and alumina nanoparticles ϕ_{Cu} and ϕ_{Al2O3}, respectively. The same-type hot and cold liquids flow co-currently in the inner tube and the annular space, respectively, and enter the heat exchanger with uniform temperatures T_{hi} and T_{ci} and constant velocities U_{hi} and U_{ci}, respectively. The outer tube wall is thermally insulated, while the inner tube is thin, so the conductive thermal resistance is neglected.

A non-uniform external magnetic field is created by fourteen magnetic sources arranged radially outside the heat exchanger and axially in the middle of each upper baffle. Each of them is an electric wire through which an electric current I flows, thus generating a magnetic field whose axial and radial components are:

$$H_x\left(x,y\right) = \sum_{i=1}^{i=14} -\frac{I}{2\pi}\frac{\left(r-b_i\right)}{\left(x-a_i\right)^2+\left(r-b_i\right)^2}, \tag{1}$$

$$H_r\left(x,y\right) = \sum_{i=1}^{i=14} +\frac{I}{2\pi}\frac{\left(x-a_i\right)}{\left(x-a_i\right)^2+\left(r-b_i\right)^2}. \tag{2}$$

B. Governing Equations

The nanofluid is considered Newtonian, incompressible, and electrically conductor. The flow is two-dimensional, axisymmetric, laminar, and in a steady state. The nanoparticles are smaller than the pore size of the porous medium.

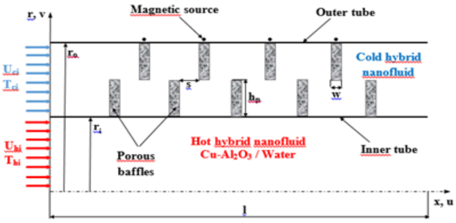

Figure 1. Physical configuration.

They are suspended in the base fluid with surfactants to avoid agglomeration and sedimentation problems. Isotropic and homogeneous porous medium saturated by a hybrid nanofluid with local thermal equilibrium between the nanoparticles, the base fluid, and the porous matrix. Negligible viscous dissipation and no internal heat sources.

The equations of continuity, momentum, and energy in the dimensionless form are written as follows:

$$\vec{\nabla}.\vec{V} = 0\,, \tag{3}$$

$$\begin{aligned}&\frac{1}{\delta^2}\vec{\nabla}.\vec{\nabla}\vec{V} = -\vec{\nabla}P + \\ &+\frac{1}{Re}\frac{R_\mu}{R_\rho}\nabla^2\vec{V} - \frac{1}{ReDa}\frac{R_\mu}{R_\rho}\vec{V} - \\ &-\frac{C}{\sqrt{Da}}\left|\sqrt{U^2+V^2}\right|\vec{V} + \\ &+\frac{R_\sigma}{R_\rho}\frac{Ha^2}{Re}\left(\vec{V}\wedge\vec{H}\right)\wedge\vec{H}\end{aligned}\,, \tag{4}$$

$$\begin{aligned}&\vec{\nabla}.\vec{\nabla}\theta = \frac{1}{RePr}\frac{R_k}{R_{C_p}R_\rho}\nabla^2\theta + \\ &+\frac{R_\sigma}{R_{C_p}R_\rho}\frac{Ha^2Ec}{Re}\left(\vec{V}\wedge\vec{H}\right)^2\end{aligned}\,. \tag{5}$$

Re, Da, Ha, and Ec are the Reynolds, Darcy, Hartmann, and Eckert numbers. C is the inertial coefficient characterizing the inertia effect in the porous medium. The expressions of the other parameters are:

$$\begin{aligned}&R_\rho = \frac{\rho_{hnf}}{\rho_{bf}}, R_\mu = \frac{\mu_{hnf}}{\mu}, R_k = \frac{k_{hnf}}{k_{bf}}, R_\sigma = \frac{\sigma_{hnf}}{\sigma_{bf}} \\ &R_{Cp} = \frac{C_{phnf}}{C_{pbf}}, R_r = \frac{r_o}{r_i}\;; R_{\dot{m}} = \frac{\dot{m}_c}{\dot{m}_h}\end{aligned} \tag{6}$$

The subscripts bf, hnf, h, and c stand for the base fluid, hybrid nanofluid, and hot and cold fluids, respectively. $\dot{m}$ is the mass flow rate.

C. Boundary Conditions

The associated boundary conditions are:

Inlet:

$$0 < R < R_i : U = \frac{R_r^2 - 1}{R_{\dot{m}}}, V = 0, \theta = 1\,, \tag{7}$$

$$R_i < R < R_o : U = 1, V = \theta = 0\,. \tag{8}$$

Outlet:

$$\frac{\partial U}{\partial X} = V = \frac{\partial \theta}{\partial X} = 0\,. \tag{9}$$

Axis:

$$\frac{\partial U}{\partial R} = V = \frac{\partial \theta}{\partial R} = 0\,. \tag{10}$$

Inner tube:

$$U = V = 0, \left.\frac{\partial\theta}{\partial R}\right]_h = \left.\frac{\partial\theta}{\partial R}\right]_c\,. \tag{11}$$

Outer tube:

$$U = V = \frac{\partial\theta}{\partial R} = 0\,. \tag{12}$$

III. Numerical Modeling

The finite volume approach and SIMPLE algorithm [8] are used to solve numerically the system composed of the previously defined equations and the accompanying boundary conditions. The diffusive and convective terms are discretized using the power-law approach, and the obtained algebraic equations are then solved using the line-by-line method. The mesh distribution is not uniform in either direction, becoming narrower at the porous baffles interfaces and solid walls. After multiple testing, an optimal number of nodes of 550 × 80 (in the X and R directions, respectively) has been chosen to guarantee an accurate numerical solution and a suitable computation time. The highest relative error between two successive iterations for the velocity components and temperature, which must be smaller than 10^{-6}, is the chosen convergence condition for the iterative process ends.

IV. Results

Many control parameters govern the current problem, so some have been fixed, while others have been varied. For this purpose, we set the length of the heat exchanger (L = 51), the porosity of the porous medium (ϵ = 0.9), as well as the spacing (S = 2), width (W = 1), and height (H_p = 0.5) of the porous baffles. On the other hand, we varied the Hartmann number ($0 \leqslant$ Ha $\leqslant 50$), Darcy number ($10^6 \leqslant$ Da $\leqslant 10^{-2}$), Reynolds number ($100 \leqslant$ Re $\leqslant 600$), and the volume fraction of each nanoparticle constituting the hybrid nanofluid (1%⩽ϕ_{Cu}⩽3%; 1% ⩽ ϕ_{Al2O3} ⩽ 3%).

Fig. 2 shows the streamlines and isotherms in the annular space of the heat exchanger for different Hartmann numbers. The flow of the hybrid nanofluid is divided into two parts, one flowing through the porous baffles and the other flowing between the baffles, thus extending the path of the nanofluid in the heat exchanger will benefit the heat transfer between the hot and cold fluids. Increasing the magnetic field intensity hardly affects the main flow structure of the flow up to Ha = 15. Above this Hartmann number value, the Lorentz force's slowing effect begins to appear, starting with the heat exchanger's inlet and outlet parts and propagating more to the center as Ha increases. Concerning the thermal field, the heat from the hot fluid flowing in the inner tube is transmitted more efficiently from the lower porous baffles than from the areas of the inner tube surface without baffles; this is probably due to the higher exchange surface because of the porous structure of the baffles. The average temperature of the cold hybrid nanofluid rises as the Hartmann number increases since the area with a high heat exchange rate, which was initially located at the heat exchanger outlet, has widened, and its extent has increased axially and radially.

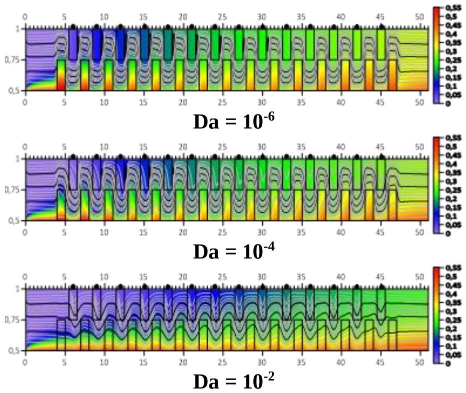

Figure 2. Streamlines and isotherms in the annular space for various Da: Ha = 30, Re = 100, and ϕ_{Cu} = ϕ_{Al2O3}=2.5%.

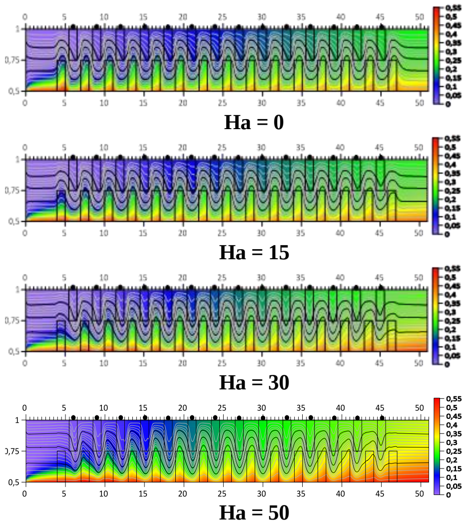

Figure 3. Streamlines and isotherms in the annular space for various Ha: Da = 10^{-3}, Re = 100, and ϕ_{Cu} = ϕ_{Al2O3}=2.5%.

The streamlines and isotherms for different values of the Darcy number are depicted in Fig. 3. The pattern of the streamlines is mainly due to the presence of the porous baffles, which deflect the fluid upwards and downwards and thus prolong the hybrid nanofluid motion in the heat exchanger. At low Darcy numbers, e.g., Da = 10^{-6}, the porous baffles behave like solids, and the flow is essentially between them. When the permeability is increased, the porous medium develops less resistance to the flow, and some of the nanofluids flow inside the baffles, reducing the fluid's path through the heat exchanger. The presence of the porous structures in the annular space and the variation of their permeability brought changes not only in the dynamic aspect but also in the thermal field. Indeed, from this figure, it is clear that the more impermeable the porous substrate becomes, the greater the amount of heat transmitted from the hot fluid to the cold liquid and the greater the extent of its propagation in the annular space, both in length and height. On the other hand, for high Darcy numbers, which correspond to porous baffles with increased permeability, the hot fluid zones will retract at the exchanger outlet and near the inner tube wall.

Fig. 4 displays the changes in the dynamic and thermal field structures caused by the variation of the Reynolds number. The increase of Re is accompanied by an improvement in the inertial force, which allows a greater quantity of cold nanofluid to flow through the porous baffles and subsequently reduces the length of its path through the annulus. The thermal consequence of the acceleration of the fluid flow is a decrease in the propagation of the heat absorbed at the inner tube wall to the whole space due to its rapid evacuation. This behavior leads to a reduction in the average temperature of the cold fluid, which will negatively affect the effectiveness of the heat exchanger.

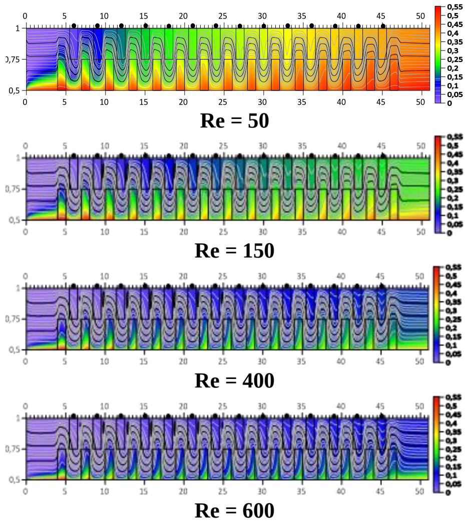

Figure 4. Streamlines and isotherms in the annular space for various Re: Da = 10^{-4}, Ha = 30, and ϕ_{Cu} = ϕ_{Al2O3}=2.5%.

The evolution of the heat exchanger effectiveness with the Hartmann number, illustrated in Fig. 5, shows the same behavior for all the cases considered, ε increases with Ha. This evolution can be explained as follows: in the porous baffles, the increase of the nanofluid velocity with Ha will allow better heat exchange between the hot and cold fluids (see Fig. 2), while in the other regions, the decrease of the velocity will lengthen the nanofluid motion in the annulus, giving it the possibility to absorb more heat. As a result, the average temperature increases and improves effectiveness. It should also be noted that decreasing the permeability of the porous medium, the intensity of the inertial force, and increasing the volume fraction of one of the two nanoparticles by fixing that of the other is beneficial.

The pressure drop in the annulus is shown in Fig. 6. Due to the Lorentz force's slowing effect, the system's hydrodynamic performance is reduced with increasing Ha under all conditions. However, an interesting result appears when examining the impact of nanoparticles' volume fraction. Indeed, raising the volume fraction of one of the two nanoparticles reduces the pressure drop value with a more apparent decrease by growing the concentration of the copper nanoparticles, especially at large values of Ha. As expected, ΔP_c increases with decreasing Darcy and Reynolds numbers.

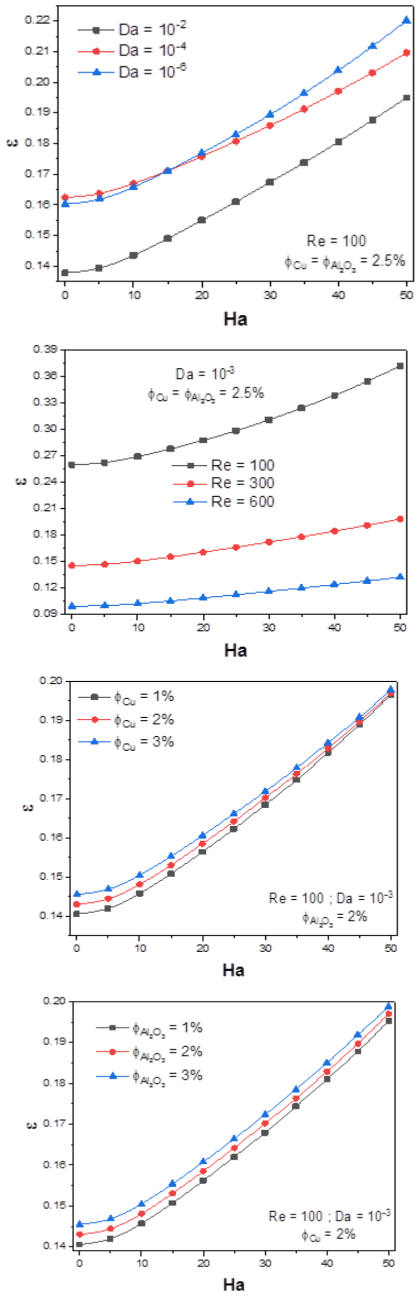

Figure 5. Evolution of ε with Ha for various Da, Re, ϕ_{Cu}, and ϕ_{Al2O3}.

V. CONCLUSIONS

This numerical study aims to assess the contribution of hybrid nanofluids, magnetohydrodynamics (MHD), and porous materials in improving the performance of

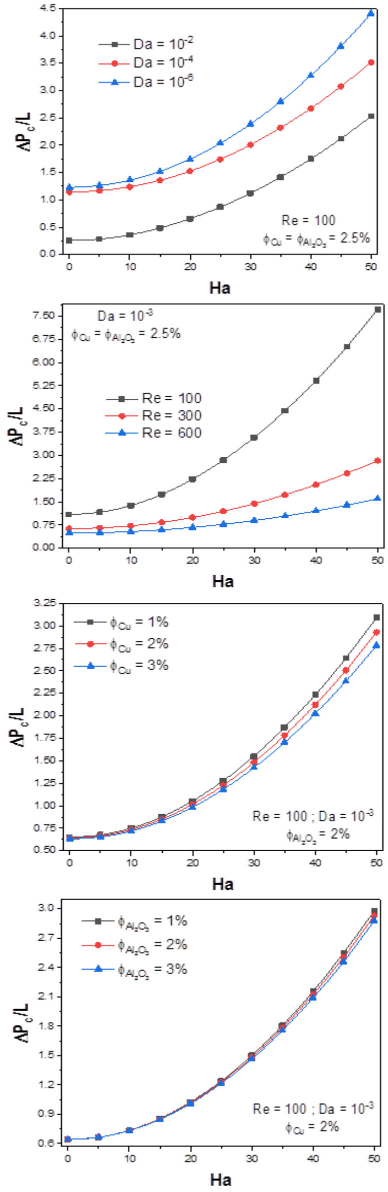

Figure 6. Evolution of $\Delta P_c/L$ with Ha various Da, Re, ϕ_{Cu}, and ϕ_{Al2O3}.

tubular heat exchangers. The main results found can be summarized as follows:

The increase in the magnetic field strength reveals the slowing effect of the Lorentz force, which starts from the inlet and outlet parts of the heat exchanger and propagates more and more to the center as Ha increases. Thermally, the growth in the value of this parameter leads to an enlargement of the zones with high heat exchange rates axially and radially.

The heat exchanger effectiveness is enhanced by increasing the Hartmann number and reducing the Darcy and Reynolds numbers.

The pressure drop is reduced as the magnetic field strength decreases, porous baffles permeability, and inertial force strength increases.

Concerning the interest in hybrid nanofluids, the results concluded that increasing the volume fraction of either type of nanoparticle is beneficial for improving the thermal and dynamic performances of the heat exchanger.

References

[1] Bahiraei, M., Godini, A. & Shahsavar, A. (2018). Thermal and hydraulic characteristics of a minichannel heat exchanger operated with a non-Newtonian hybrid nanofluid. *Journal of Taiwan Institute of Chemical Engineers*, *84*, 149-161.

[2] Anitha, S., et al. (2019). What dominates heat transfer performance of hybrid nanofluid in single pass shell and tube heat exchanger?. *Advanced Powder Technology*, *30*(12), 3107-3117.

[3] Singh, S.Kr. & Sarkar, J. (2020). Improving hydrothermal performance of hybrid nanofluid in double tube heat exchanger using tapered wire coil turbulator. *Advanced Powder Technology*, *31*(5), 2092-2100.

[4] Alklaibi, A.M. et al. (2022). Experimental investigation on the performance of hybrid Fe_3O_4 coated MWCNT/Water nanofluid as a coolant of a Plate heat exchanger. *International Journal of Thermal Sciences*, *171*, 107249.

[5] Mousavi, S.V., et al.(2016). The influence of magnetic field on heat transfer of magnetic nanofluid in a sinusoidal double pipe heat exchanger. *Chemical Engineering Research and Design*, *113*, 112-124.

[6] Shakiba, A. & Vahedi, K. (2016). Numerical analysis of magnetic field effects on hydro-thermal behavior of a magnetic nanofluid in a double pipe heat exchanger. *Journal of Magnetism and Magnetic Materials*, *402*, 131-142.

[7] Fan, F., et al. (2020). A novel thermal efficiency analysis on the thermo-hydraulic performance of nanofluids in an improved heat exchange system under adjustable magnetic field. *Applied Thermal Engineering*, *179*, 115688.

[8] Azizi, Y., Bahramkhoo, M. & Kazemi, A. (2023). Influence of non-uniform magnetic field on the thermal efficiency hydrodynamic characteristics of nanofluid in a double pipe heat exchanger. *Scientific Reports*, *13*, 407.

[9] Patankar, S.V. (1980). Numerical heat transfer and fluid flow. Mc Graw-Hill.

Social Perspective Estimation of the Modern Cities Electricity Customers: Welfare, Satisfaction and Elasticity

Ramin Niromandfam[1]

[1]Azad Islamic University, Bonab, Iran

Abstract—**Nowadays, the vision of electricity energy customers has been changed in such a way that are considered as dynamic and active actors in the modern societies. In such environments, the concept of energy citizenship are proposed where in addition to the economic criteria, energy providers have to consider their customers' viewpoints and behaviors in electricity service providing. To study the socioeconomic aspects of the electricity customers, this paper develops a novel load model based on the concept of the utility function. Utility function is a relative concept that provides a representation to estimate customer satisfaction regarding consuming goods or receiving services. The model can estimate the customers' welfare and viewpoints based on their risk aversion coefficients. Social studies are needed to estimate these coefficients. As an alternative, this paper strives to present these coefficients as a function of elasticity data which is a well-known index and concept in power systems. In addition, a novel incentive-based demand response program is developed based on the proposed load model where the incentives are determined considering the customers' perspectives. In the numerical section, Iranian electricity demand data is utilized to study the efficiency of the proposed model. The results proved that instead of the profit maximizing, electricity consumers consume energy based on their expected utility maximization. In the result section, electricity price and income variation effect on the consumption are measured for the different types of customers.**

Keywords - energy citizenship, social perspective, elasticity, utility function, welfare function

I. INTRODUCTION

In today's societies, the uninterrupted supply of electrical energy is essential for modern human life, where the vast majority of activities are associated directly or indirectly with electricity consumption. Providing electricity via smart grid infrastructure is one of the main features of modern cities. This infrastructure can propagate the electricity price signal to the electricity customers. The signal enables the customers to behave, such as active players, who can modify their consumptions [1]. Hence, the customers' behavior and social perspective identifications are essential to providing efficient electrical services in the modern environment. One of the main outcomes of the consumers' social behavior estimation is modeling the elasticity of the electricity demand. Different demand models have been utilized in the previous studies to analyze consumers' behavior and price elasticity. For example, the almost ideal demand system (AIDS) model [2], ordinary least squares [3], panel data methods [4], artificial neural networks [5], and time-series methods [6] have been employed to predict the consumption behavior and the elasticity data. Most of the previous studies have estimated country-level aggregated elasticity of electricity demand. While such considerations could provide a comprehensive vision into the customers' behaviors of a particular country, they can't determine their individual behaviors against the electricity price changes. The individual behavior is often affected by additional benefits of the consumption like productivity, health, convenience, and aesthetics, which might be difficult to quantification. We employ electricity customers' risk aversion coefficients to model their individual consumption behaviors and estimate elasticity data.

Although electricity customers' social indices have been examined in previous studies, this paper designs a comprehensive behavior model in which social indices can be determined. The main parameter of the model is the customers' risk aversion coefficients. The coefficients are used to estimate the electricity consumption value from the customers' viewpoints. To analyze the customer's behavior, this paper examines the concept of the utility theory from economics to model the customers' welfare function. Then, an economic load model is established based on the welfare function. Employing the load model, electricity customer sensitivity against the electricity price and income variations are estimated. Based on the elasticity model, the optimal incentive will be determined to ensure the customers reduce their demand and participate in the DR program. Fig. 1. illustrates the hierarchy of the proposed model.

The remainder of this paper is organized as follows. Comprehensive reviews around the customers' behavior and utility function are provided in Section II. Section III is dedicated to model the elasticity of electricity demand. Numerical results and conclusion are addressed in Sections IV and V.

II. UTILITY FUNCTION

This paper utilizes the concept of the utility function to measure satisfaction due to electrical energy consumption. Utility function, U, is a function with terms of the consumption, D, and the risk aversion coefficient, a, with the following properties [7]:

Property I. The customer's satisfaction increases as the consumption increases, thus:

$$\frac{\partial U(D,a)}{\partial D} > 0 \,. \tag{1}$$

Property II. Satisfaction margin decreases with increasing consumption, which can be written as:

$$\frac{\partial U^2(D,a)}{\partial D^2} < 0 \,. \tag{2}$$

Property III. No satisfaction is obtained without the consumption, which can be expressed as:

$$U(0,a) = 0 \,. \tag{3}$$

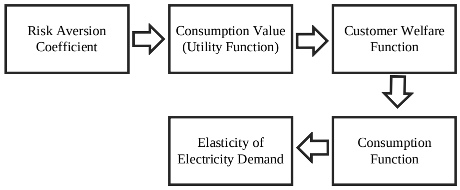

Figure 1. Extracting essential information from the risk aversion coefficient scheme.

Property IV. A high-risk aversion coefficient leads to more satisfaction due to the consumption, which can be formulated as:

$$\frac{\partial U(D,a)}{\partial a} > 0 \,. \tag{4}$$

Utility function can measure the customers' risk aversion behavior in which the higher the curvature of U indicates the higher risk aversion behavior. Each function with the above properties can be used as a utility function which will be concave and saturated by the consumption.

The welfare function of electricity customers, W, can be achieved by deducting the cost of electricity from the satisfaction function, as shown in Eq. (5).

$$W(D,\pi,a) = AU(D,a) - \pi D \,, \tag{5}$$

where, π is the electricity price and A is the calibration coefficient which is used to calibrate the welfare function with the initial consumption and electricity price [8]. A rational customer consumes electrical energy based on his/her welfare maximization, so we have:

$$\begin{gathered} \frac{\partial W(D,\pi,a)}{\partial D} = \\ = \frac{\partial(AU(D,a))}{D} - \pi = 0 \end{gathered} \,, \tag{6}$$

$$A\frac{\partial U(D,a)}{\partial D} = \pi \,. \tag{7}$$

Considering the above equations, the calibration coefficient would be as Eq. (8):

$$A = \frac{\pi_0}{\dfrac{\partial U(D_0, a)}{\partial D_0}}, \tag{8}$$

where, π_0 and D_0 are the initial electricity price and initial consumption level.

In this paper, the exponential forms of utility function is selected from [9], so we have:

$$U(D,a) = 1 - e^{-aD}, \quad a > 0, \tag{9}$$

$$W(D,\pi,a) = A(1 - e^{-aD}) - \pi D, \tag{10}$$

$$A = \frac{\pi_0}{a} e^{aD_0}, \tag{11}$$

$$D = \begin{cases} D_0 - \dfrac{1}{a}\ln(\dfrac{\pi}{\pi_0}), & \pi < \pi_0 e^{aD_0} \\ 0, & \pi \geq \pi_0 e^{aD_0} \end{cases}. \tag{12}$$

III. Price-Elasticity of Electricity Demands

A. Elasticity

Price-elasticity of electricity demand, E, is a normalized measurement of the proportional change of the customer's consumption in response to a change in the electricity price. For single-period demands, only own-price elasticity can be defined in which the demand of Ith period responds only to the Ith price variations. The own-price elasticity would be as in Eq. (13).

$$\mathrm{E} = \frac{\pi}{D} . \frac{\partial D}{\partial \pi}\bigg|_{D = D_0, \pi = \pi_0}. \tag{13}$$

In the following, the own-price elasticity of the single-period electricity demand will be determined considering different utility functions.

Considering Eq. (12), the derivation of consumption concerning the electricity price would be as Eq. (14) for the exponential utility function. Hence, the elasticity would be as Eq. (15). Due to the exponential utility function definition, $a \geq 0$, the own-price elasticity always will be negative.

$$\frac{\partial D}{\partial \pi} = -\frac{1}{a\pi}, \tag{14}$$

$$\mathrm{E} = -\frac{1}{aD_0}. \tag{15}$$

Based on Eq. (15), the risk aversion coefficient plays a critical role in the customer's behavior against the price variations. Table I illustrates different own-price elasticities concerning the value of aD_0 which are described in the following:

Perfect inelastic demand. An infinite risk aversion coefficient leads to perfect inelastic consumption. This means regardless of the price values, the demand remains constant.

Inelastic demand. Demand is inelastic when a change in the price causes a relatively small effect on the demand. To this end, the term aD_0 has to be greater than the unit.

Unit elastic demand. Unit elastic occurs when the percentage change in demand is equal to the percentage change in the price. This happened when aD_0 is equal to the unit.

Elastic demand. Demand is elastic when a change in the price produces a relatively enormous effect on the demand. Demand is elastic when aD_0 is lower than the unit.

Perfect elastic demand. For this case, the customer is risk-neutral due to electrical energy consumption (a=0). Where a small rise (fall) in electricity price leads to zero (infinite) demand. This is a theoretical concept because it requires the consumer consumes electricity energy all available at some price, but none at any other price.

B. Multi-period Elasticity

For multi-period demands, the consumption has multi-period sensitivity which is denoted by cross-price elasticity of demand. The cross-price

TABLE I. Own-price elasticity as a function of aD_0 for exponential utility function.

Perfect inelastic demand	$aD_0 = \infty$	$E_I = 0$
Inelastic demand	$aD_0 > 1$	$0 < E_I < -1$
Unit elastic demand	$aD_0 = 1$	$E_I = -1$
Elastic demand	$aD_0 < 1$	$-\infty < E_I < -1$
Perfect elastic demand	$aD_0 = 0$	$E_I = -\infty$

elasticity of Ith time period demand with respect to Jth time period price can be formulated as in Eq. (16).

$$\mathrm{E}_{I,K} = \frac{\pi_K}{D_I} \cdot \frac{\partial D_I}{\partial \pi_K}\bigg|_{D_I = D_I^0,\, \pi_K = \pi_K^0} . \quad (16)$$

C. *Income Elasticity*

Income elasticity is an economic term that explains the connection between demand and the consumer’s budget. In other words, if a customer's income goes up or down, his/her income elasticity represents how he/she will use the electrical energy. In the following, the income elasticity of electricity demand will be formulated considering different utility functions. Income-elasticity of demand for the exponential utility functions is as Eq. (17).

$$E_{I,B} = \frac{B}{a_I D_I^0 \sum_{J=1}^{T} \frac{\pi_J^0}{a_J}}, \quad (17)$$

D. *DR Model*

In the previous Sections, the impact of price changes on electrical energy consumption was examined. In addition to price changes, providing incentives in the incentive-based DR program will affect electricity consumption. In this Section, an effective incentive-based DR program will be designed based on the welfare maximization concept. We utilize the DR model which is provided by [10]. The model is illustrated in Eq. (18) which determines the incentive rate, *Inc*, as a function of electricity price, elasticity, and demand of each customer.

$$Inc = -\frac{\pi}{E} \frac{\Delta D}{D_0} . \quad (18)$$

This paper expands the proposed single-period DR model to establish a multi-period DR model, which would be as:

$$\begin{bmatrix} \frac{Inc_1}{\pi_1} \\ \cdots \\ \frac{Inc_T}{\pi_T} \end{bmatrix} = \begin{bmatrix} E_{1,1} & & E_{1,T} \\ & \cdots & \\ E_{T,1} & & E_{T,T} \end{bmatrix}^{-1} \begin{bmatrix} \frac{\Delta D_1}{D_1^0} \\ \cdots \\ \frac{\Delta D_T}{D_T^0} \end{bmatrix} . \quad (19)$$

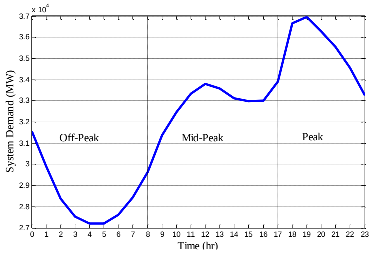

Figure 2. Iranian power grid load curve on 17 December 2019 [11].

IV. Numerical Results

To evaluate the performance of the proposed load model, the Iranian power system load on 17 December 2019, Fig. 2, has been selected for numerical studies [11]. The load curve is divided into three different periods, namely the off-peak period (0:00–8:00), mid-peak period (08:00–17:00), and peak period (17:00–23:00) [12]. Table II illustrates different time periods and corresponding electricity prices for the selected power system, where *Rial* is the monetary unit of Iran.

The customers’ risk aversion coefficients play an important role in the proposed load model. Social studies are needed to estimate these coefficients. As formulated in Eq. (17), the coefficients also can be achieved utilizing elasticity data. Table III illustrates elasticity data for different Iranian electricity sectors which are taken from [13].

Utilizing Eq. (17), risk aversion coefficients for different customers can be determined as shown in Table IV. Critical data are embedded in these coefficients. The customers’ consumption behavior, achieved satisfaction and welfare are some of these data.

TABLE II. Time Periods and Electricity Prices [11].

	Off-peak	**Mid-peak**	**peak**
Time	00:00 to 8:00	8:00 to 17:00	17:00 to 23:00
Electricity price	260 Rials/kW	520 Rials/kW	1040 Rials/kW

TABLE III. Elasticity Data for Different Electricity Sectors [13].

Sector	**Off-peak**	**Mid-peak**	**peak**	**Portion of total demand**
Residential	1.21	0.64	1.01	34%
Industrial	1.72	4.5	0.53	31%
Agricultural	0.87	0.46	0.56	17%
Public	1.57	2.87	1.05	9%
Commercial	1.1	1.99	1.6	9%

TABLE IV. RISK AVERSION COEFFICIENT FOR DIFFERENT ELECTRICITY SECTORS.

Sector	Off-peak	Mid-peak	peak
Residential	0.82	1.56	0.99
Industrial	0.58	0.22	1.89
Agricultural	1.15	2.17	1.78
Public	0.64	0.35	0.95
Commercial	0.91	0.5	0.62

To investigate the customers' consumption behavior due to electricity price and income variations, four scenarios are considered in this Section. The scenarios are:

Scenario I: Only the impact of electricity price variations on consumption is considered.

Scenario II: Only the impact of income variations on consumption is considered.

Scenario III: Simultaneous impact of the electricity price and income variations on consumption is considered.

Scenario IV: An incentive-based DR program is implemented to examine the incentive effect on the customers' social indices.

A. *Scenario I*

In this scenario, the Iranian power system demand variations versus electricity price changes will be studied. Fig. 3-5 illustrate the demand when the price increases 5% in the off-peak, mid-peak, and peak periods. From the figures, the price increment in each time period leads to the consumption decrement in that period. Because of the cross-elasticity, the price increment may affect slightly the other periods' consumption.

B. *Scenario II*

In the previous sections, a comprehensive load model is developed based on the customers' risk aversion coefficients. In addition to own-price elasticity, the model is also capable to estimate income elasticity for electricity demand. Table V illustrates the income-elasticity data for different sectors. Similar the price elasticity, the income elasticity is related to the electricity price and the customers' risk aversion coefficients in different periods. As an example for the industrial sector, although the consumption is highly sensitive to the income variations in the mid-peak, the sensitivity would be small in the peak period.

TABLE V. INCOME-ELASTICITY FOR DIFFERENT SECTORS [13].

Sector	Off-peak	Mid-peak	peak
Residential	1.3	0.68	1.08
Industrial	0.93	2.4	0.28
Agricultural	1.5	0.80	0.97
Public	0.95	1.74	0.64
Commercial	0.68	1.24	0.96

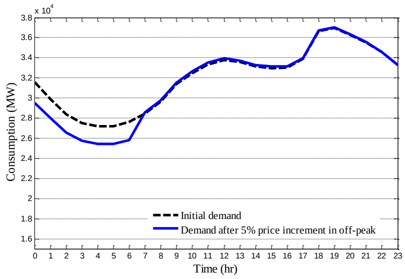

Figure 3. Electricity demand variations versus 5% electricity price increment in the off-peak period.

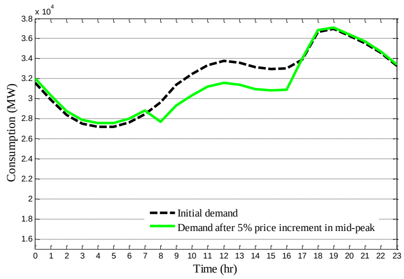

Figure 4. Electricity demand variations versus 5% electricity price increment in the mid-peak period.

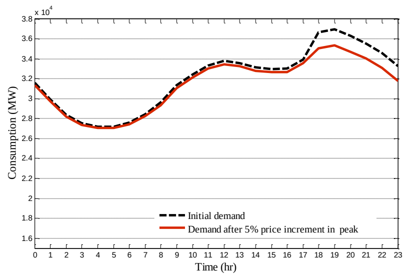

Figure 5. Electricity demand variations versus 5% electricity price increment in the peak period.

This scenario is devoted to studying the income variations' effects on the Iranian electricity sectors. To this end, Fig. 6 illustrates different sectors' consumption variations due to 5% income increment. Because of the different income elasticities, different sectors behave differently versus the income increment. For example, the industrial customers invest a major part of the surplus income on the mid-peak consumption.

C. *Scenario III*

The Iranian power market utilizes the single-side auction method to determine the market-clearing price, while the demand side does not bid into the market. In this market, the electricity price has remained regulated by the customers. Each year, the regulator increases the electricity price based on inflation and the customers' average income increment. In this scenario, we want to examine how the consumption will respond if the regulator increases electricity price as much as the income increases. Fig. 7 illustrates the Iranian power system demand for different scenarios. From the figure, the system demand does not change if the electricity price increment will be equal to the income increment. As a result, it can be concluded to study electricity consumption sensitivity, it is necessary to consider the price and income changes, simultaneously.

Total electricity consumption, budget, satisfaction, and welfare for the different scenarios are compared in Table VI. From the table, the electricity price increment in scenario I leads to load reduction. In this scenario, customers manage the budget through load reduction which results in the low satisfaction and welfare. In scenario II, the customers spend the surplus budget to consume more electrical energy. The consumption increment increases the budget, welfare, and satisfaction values. The consumption will not change in scenario III, when the electricity price increment is equal to the budget increment. For this scenario, although the customers' utility does not change, the budget is increased and the welfare is decreased.

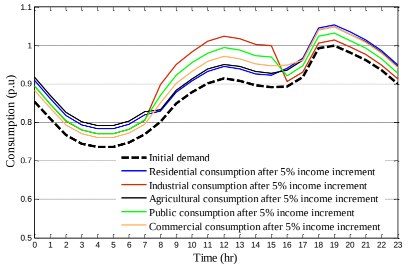

Figure 6. Different sectors' consumption versus 5% income increment.

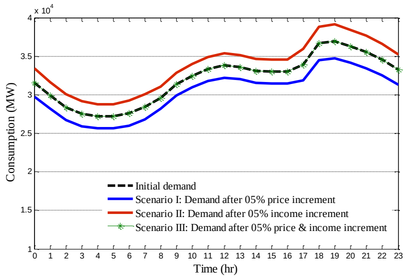

Figure 7. Iranian power system demand considering electricity 5% price and income increment.

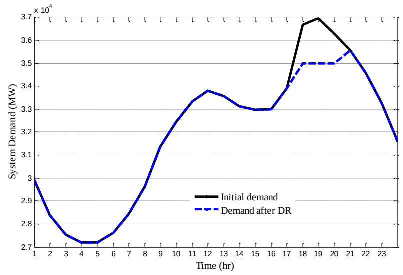

Figure 8. Iranian power system demand after DR program implementation.

TABLE VI. ELECTRICITY DEMAND, BUDGET, UTILITY AND WELFARE CONSIDERING DIFFERENT SCENARIOS.

	Initial State	**Scenario I**	**Scenario II**	**Scenario III**
Demand (MWh/day)	768300	727682	810123	768299
Budget (billion Rials/day)	468.81	468.41	492.71	492.28
Satisfaction (billion Rials/day)	766.44	730.6	808.02	766.52
Welfare (billion Rials/day)	299.63	262.19	315.31	274.24

TABLE VII. EFFECT OF DR PROGRAM ON THE CUSTOMERS' DEMAND, UTILITY AND WELFARE.

Time Period	Sector	Load Reductuin Percent	Incentive Rate (Rials/kW)	Incentive Cost (Million Rials)	Satisfaction Reduction (Million Rials)	Welfare Increment (Million Rials)
Hour 18 (P^{DR}=1673MW)	Residential	13.4%	138	230.874	1857.881	108.393
	Industrial	14.7%	289	483.497	2000.768	220.539
	Agricultural	26.8%	497	831.481	2225.538	342.246
	Public	51%	502	839.846	2250.600	344.520
	Commercial	51%	328	548.744	2059.200	243.210
Hour 19 (P^{DR}=1958MW)	Residential	15.6%	160	313.288	2198.875	153.293
	Industrial	17.1%	335	655.930	2405.970	402.140
	Agricultural	31%	578	1131.724	2701.690	446.093
	Public	59%	582	1139.556	2733.972	449.010
	Commercial	59%	382	747.956	2461.240	325.948
Hour 20 (P^{DR}=1280MW)	Residential	10.4%	107	136.960	1406.190	65.375
	Industrial	11.4%	223	285.440	1484.604	133.839
	Agricultural	20.7%	385	492.800	1603.680	215.263
	Public	39.2%	388	496.640	1609.645	218.023
	Commercial	39.2%	255	326.400	1505.165	152.149

D. Scenario IV

In this scenario, an incentive-based DR program will be designed to reduce demand in the peak time period. The goal of the DR program is to reduce system demand below 35000 MW in peak hours. To this end, it is needed the system demand is reduced to about 1673 MW, 1958 MW, and 1280 MW in hours 18, 19, and 20, respectively. Fig. 8 illustrates the system demand before and after the DR program implementation.

Because of the different risk aversion behavior, different incentives are needed to convince different sectors to reduce their demands. The demand reduction will affect the customers' satisfaction and welfare. Table VII illustrates the DR program's effects on the customers' demand, satisfaction, and welfare. Considering Eq. (16), the incentive rate is related to the load reduction percent, electricity price, and elasticity of electricity demand. The load reduction percent would be equal to the DR needed load reduction, P^{DR}, divided by the load of each sector. From the table, the residential and public sectors request the lowest and the highest incentive rate. Although the load reduction decreases the satisfaction value, receiving incentives increases the welfare value. From the cost minimization perspective, the residential sector is the best selection for the DR program implementation because this sector requests the lowest incentive payment (cost). But from the social perspective, applying the DR program to the public sector would be a better choice because this sector has the highest welfare increment. As a result, the proposed model enables decision-makers to evaluate, in addition to economic considerations, social considerations and consumers' viewpoints of service delivery.

V. CONCLUSION

This paper illustrated critical data are embedded in the electricity customers' risk aversion coefficients. Utilizing the concept of the utility function, the coefficients are used to estimate electricity customers' satisfaction and welfare due to different consumption levels. From the results, electricity consumers achieve more satisfaction from the consumption as the risk aversion coefficient increases. This paper proved the risk aversion behavior is the main parameter of the electrical energy consumption and consumption sensitivity versus electricity price and income variations.

From the results, to manage their budget, the customers have to reduce the consumption as the price increases. The consumption reduction reduces the customers' satisfaction and welfare. On the other hand, as the customers' income increases, they spend the extra budget to consume more electricity energy which increases their satisfaction and welfare. Although electricity price increment can neutralize the income increment effect on the consumption, the customers' satisfaction and welfare would be changed. Hence, to study electricity consumption, the price and income variations should be considered, simultaneously.

Utilizing the customers' risk aversion behavior, a novel incentive-based DR program is designed in this paper. The results illustrated as the risk aversion coefficient increases, more incentive is needed to convince the customers to reduce their demand. In addition to incentive cost measurement, the model can measure the customers' satisfaction variations due to participation in the DR program.

REFERENCES

[1] Niromandfam, A., Choboghloo, S. P., Yazdankhah, A. S., & Kazemzadeh, R. (2020). Electricity customers' financial and reliability risk protection utilizing insurance mechanism. *Sustainable Energy, Grids and Networks, 24*, 100399.

[2] Auray, S., Caponi, V., & Ravel, B. (2019). Price elasticity of electricity demand in france. *Economie et Statistique, 513*(1), 91-103.

[3] Iqbal, M. (1983). Residential demand for electricity and natural gas in Pakistan. *The Pakistan Development Review,* 23-36.

[4] Nakabi, T. A., & Toivanen, P. (2019). An ANN-based model for learning individual customer behavior in response to electricity prices. *Sustainable Energy, Grids and Networks, 18*, 100212.

[5] Silva, S., Soares, I., & Pinho, C. (2018). Electricity residential demand elasticities: Urban versus rural areas in Portugal. *Energy, 144*, 627-632.

[6] Atalla, T. N., & Hunt, L. C. (2016). Modelling residential electricity demand in the GCC countries. *Energy Economics, 59*, 149-158.

[7] Niromandfam, A., Yazdankhah, A. S., & Kazemzadeh, R. (2020). Design of reliability insurance scheme based on utility function for improvement of distribution grid reliability. *Journal of Operation and Automation in Power Engineering, 8*(3), 257-272.

[8] Niromandfam, A., Pour, A. M., & Zarezadeh, E. (2020). Virtual energy storage modeling based on electricity customers' behavior to maximize wind profit. *Journal of Energy Storage, 32*, 101811

[9] Niromandfam, A., Yazdankhah, A. S., & Kazemzadeh, R. (2020). Design of reliability insurance scheme based on utility function for improvement of distribution grid reliability. *Journal of Operation and Automation in Power Engineering, 8*(3), 257-272.

[10] Niromandfam, A., Yazdankhah, A. S., & Kazemzadeh, R. (2020). Modeling demand response based on utility function considering wind profit maximization in the day-ahead market. *Journal of Cleaner Production, 251*, 119317.

[11] Iran Grid Management Company (IGMC). (2019). Available at: http://www.igmc.ir/en.

[12] Iran electric power industry statistic. (2019). Available at: https://www.tavanir.org.ir/en/.

[13] Zin, A.M., Moradi, M., Khairuddin, A., Naderipour, A. and Khavari, A.H., 2015, December. Estimation of elasticity of electricity demand in Iran: New empirical evidence using aggregate data. In *2015 IEEE Student Conference on Research and Development (SCOReD)* (pp. 710-715). IEEE.

Preliminary Research on the Application of Neural Networks to the Combustion Control of Boilers with Automatic Firing

Stefan Popović[1], Dejan Đukić[2], Sonja Đukić Popović[3], Lazar Kopanja[4]

[1,2,4]Alfa BK University, Belgrade, Serbia
[3]Faculty of Mathematics, Belgrade University, Serbia

Abstract—**This paper deals with the importance and application of neural networks for improving the operation of boilers with automatic firing. Although the neural network model was illustrated in the middle of the twentieth century, it is experiencing its full expansion only today. Neural networks have a very wide application, both in complex security systems, improving the quality of life through applications used in everyday life, and in industrial plants. The paper starts from the theoretical foundations for understanding neural networks and provides an overview of research conducted on boilers with automatic firing. The conclusion of the work is that this area is insufficiently researched and that a greater application of neural networks in this area would be of great importance for improving combustion, and thus would lead to significant fuel savings and reduction of environmental pollution.**

Keywords – neural networks, boilers with automatic firing, environmental protection

I. Introduction

Today, when we are faced with uncontrolled pollution, and at the same time, the sale of boilers with automatic firing is expanding, we must take care of saving the fuel that the boiler consumes. By increasing the degree of fuel utilization, we reduce the emission of harmful gases into the atmosphere, reduce the consumption of biomass or fossil fuels that are used, and therefore have a positive effect on the environment and increase the quality of living conditions. Neural networks, although they were presented as a mathematical model in the middle of the twentieth century, are experiencing their full expansion only today, at the end of the first quarter of the twenty-first century. The application of neural networks is very broad, there is almost no area in which they have not played a key role in the functioning of automatic control systems, object recognition, decision systems and many other areas that we are surrounded by [1]. The application of neural networks in the combustion control of boilers with automatic firing is almost negligible. There is almost no research on this topic in works and practical application. The application of neural networks itself could be reflected in the automatic calibration of the combustion control system.

II. Neuron Networks - Theoretical Basics

Interest in neural networks dates back to early 1940s, as illustrated by the work of [2]. As a basis for modeling neural systems, they proposed models of neurons in the form of binary boundary devices and stochastic algorithms that include instant changes from 0 to 1 or from 1 to 0 in the output of the neurons.

The results of [3], dealing with the development of training algorithms for multilayer perceptrons, changed significantly the state of development of neural networks. Their basic method, often called the generalized delta rule for backward propagation learning, provides an effective training method for multilayer networks. Although it cannot be shown that this training algorithm converges to a solution in terms of analogous proof for a single-layer perceptron, the generalized delta rule has been successfully used in a number of problems of practical interest. This success established perceptron-like multilayer machines as one of the major neural network models currently in use.

Perceptron for two classes of patterns in its most basic form, the perceptron learns a linear decision function that discriminates two linearly separable training sets. The response of this elementary decision mechanism is calculated as a weighted sum of its inputs; it is

$$d(x) = \sum_{i=1}^{n} \omega_i x_i + \omega_{n+1} . \qquad (1)$$

This decision function is linear with respect to the components of the pattern vector. The coefficients ω_i , *i = 1, 2, ..., n, n + 1,* called synaptic weights, scale the inputs before they are summed together and passed through a threshold function. In this sense, weights are analogous to synapses in the human neural system. The threshold function that maps the output of the summator to the final output of the device is often called the activation function.

When $d(x) > 0$, the threshold element causes the perceptron output to be +1, indicating that the pattern *k* is recognized as belonging to class *i*. The inverse is true when $d(x) < 0$. When $d(x) = 0$, the input vector lies on the decision surface that separates the two classes of patterns, giving an absence of decision. The decision limit implemented by a perceptron is obtained by equating the previous equation with zero:

$$d(x) = \sum_{i=1}^{n} \omega_i x_i + \omega_{n+1} = 0 \ . \qquad (2)$$

Another form that is often used is to extend the pattern vector by adding an additional unitary value to that vector. That is, an extended sample vector is created from the sample vector *x*. The previous equation then becomes

$$d(y) = \sum_{i=1}^{n} \omega_i y_i = w^t y \ . \qquad (3)$$

This expression is usually more appropriate in terms of notation. However, regardless of the formulation used, the key problem is to find w using a given set of training template vectors from each of the two classes.

In multilayer neural networks, we apply the decision-making functions to recognition problems of multiclass patterns, regardless of whether classes are separable or not. These networks consist multiple layers of perceptron computing elements.

The basic architecture of the neural network model under consideration consists of layers of structurally identical computer nodes (neurons) arranged so that the output of each neuron in one layer is fed to the input of each neuron in the next layer. The number of neurons in the first layer, layer *A*, is N_A . Often, $N_A = n$, i.e. the size of the input sample vector. The number of neurons in the output layer, layer *Q*, is denoted by N_Q . The number N_Q is equal to W , the number of pattern classes that the neural network is trained to recognize. The network recognizes the sample vector x as belonging to class ω_i if the network output for that class is “high”, while outputs for all other classes are “low”, as explained in the following paragraphs.

Each neuron has the same structure as that in the perceptron model we discussed earlier, with the exception that the hard limiter activation function has been replaced by a soft-limiting “sigmoid” function. Differentially along all neural network pathways is required in the development of training rules. The following sigmoid activation function has the necessary differentiability property:

$$h_j\left(l_j\right) = \frac{1}{1 + e^{-\left(l_j + \theta_j\right)/\theta_v}} \ . \qquad (4)$$

When this special function is used, the system gives a high reading for any value of I_i greater than θ_i , and a low reading for any value of I_i , less than θ_i .The sigmoid activation function is always positive and can reach its limit values of 0 and 1 only if the input for the activation element is infinitely negative or positive, respectively. For this reason, values close to O and 1 (say, 0.05 and 0.95) define low and high values at neuron output. In principle, different types of activation functions can be used for different layers or even for different nodes in the same layer of the neural network. In practice, the usual approach is to use the same form of activation function throughout the network.

During training, adjusting the neurons' parameters in the output layer is simple, because the desired output of each node is known. The main problem in training a multilayer network lies in adjusting the weights in the so-called hidden layers. That is, in those that are not the output layer.

Back-propagation training method: We start from the output layer. The total squared error, i.e. the difference between the desired responses, r_q and the corresponding actual responses, O_q, of the nodes in the (output) layer *Q*, is

$$E_Q = \frac{1}{2}\sum_{q=1}^{N_q}\left(r_q - O_q\right)^2, \quad (5)$$

where *Nq* is the number of nodes in the output layer.

All these equations form a generalized delta rule for training a multilayer neural network. The process begins with an arbitrary (but not all equal) set of weights across the network. Then the application of the generalized delta rule in any iterative step involves two basic phases. In the first phase, the training vector is presented to the grid and allowed to propagate through the layers to calculate the output *O*, for each node. The outputs of a node in the output layer are then compared to their desired responses, lp, to generate the error terms. The second phase involves propagating backwards through the network, during which the corresponding error signal is passed to each node and appropriate weight changes are made. This procedure also applies to bias weights of the perceptrons. As previously explained in some detail, they are treated simply as additional weights that modify the sum of inputs of a node in the network.

It is a common practice to monitor the overall classification errors as well as the errors associated with individual patterns. In a successful training session, the classification errors decrease with the number of iterations and the procedure converges to a stable set of weights that show only small fluctuations with additional training. The approach used to determine whether a pattern is properly classified during training is to determine whether the node response in the output layer associated with the pattern class from which the pattern was derived is high, while all other nodes have low outputs, such as previously defined.

Once the system is trained, it classifies the patterns using the parameters established during the training phase. In normal operation, all feedback paths are excluded. Each input sample is then allowed to propagate through all the layers, and the pattern is classified as belonging to the output node class that was high, while all others were low. If more than one output is marked as high, or if none of the outputs is marked as such, the choice is one of declaring a misclassification or simply assigning a pattern to the class of the output node with the highest numerical value. [1]

III. Application of Neuron Networks in Boilers with Automatic Firing

The boiler is one of the three major devices of the thermal power plant. The single-unit capacity of the boilers in power plants is constantly rising, and the boilers are developing toward large capacity and high parameters [4,5]. For large or very large coal-fired boilers (supercritical units), if the combustion instability occurs during combustion, the thermal efficiency of boiler combustion will directly decrease, and a large number of pollution by-products will be generated, even some extreme situations may occur, such as furnace cavity extinction and major furnace safety accidents [6,7].

One of the applications of neural networks in boilers with automatic firing is given in the work of Zhang in 2020, where thermal energy diagnostics of boilers is done using computer recognition of objects and neural networks. The computer image processing and neural network technology are applied to diagnose the thermal energy of boiler plants, i.e., the flame combustion diagnosis, to verify their effectiveness and superiority. Methods: First, the YD-NQ type endoscopic high temperature video acquisition system is used to collect the images of flame combustion. Second, the images are pre-processed by the gray-scale method and the median filtering method. Then the flame combustion parameter features are extracted. The neural network algorithm is improved, and the boiler combustion model based on the improved neural network algorithm is established.

Therefore, the combustion decision base is obtained. Finally, the improved neural network model is compared with the traditional neural network model and the 5-4 model to verify its validity. Results: The experiments have found that the improved neural network model is superior to the traditional neural network model. Meanwhile, its accuracy rate and confidence are relatively higher than those of the traditional model. In addition, a single sample also consumes shorter running time, which is 0.0075 seconds. Comparing with the 5-4 model, the improved neural network model has certain advantages, i.e., its accuracy rate and confidence are relatively higher, which are, respectively 91.28% and 96.69%, however, a single sample consumes longer running time than the 5-4 model. Conclusion: The experimental research has found that the application of computer image processing and neural network technology to the thermal energy diagnosis of boiler plants can effectively determine the stability of flame combustion, timely understand the state of flame combustion, and thus diagnose the thermal energy. Therefore, they have values for applications [8].

Another example of the application of neural networks in boilers with automatic firing is given in the work of Chen Ji in 2022. There is described a random spectral attenuation method proposed to reduce moisture content disturbances. The calibration spectra were replicated and multiplied by random attenuation coefficients to introduce information about the possible interference. All of the simulated attenuated spectra were used to train the artificial neural network (ANN) quantitative model. Compared with direct modeling without random spectral attenuation, the coefficient of determination (R2) was improved from −3.4291 to 0.7102, and the root-mean-square error (RMSE) was reduced from 1.8709% to 0.4786% in the analysis of volatile matter content interfered by moisture. The results showed sufficient ability of the method to detect samples disturbed by moisture without additional sample pretreatment and improve the speed of LIBS analysis [9].

One of the most significant and extensive works describing the application of neural networks in boiler control is Hang Ta Wen's work from 2021. The purpose of his study is to utilize two artificial intelligence (AI) models to predict the syngas composition of a fixed bed updraft gasifier for the gasification of rice husks. Air and steam-air mixtures are the gasifying agents. In the present work, the feeding rate of rice husks is kept constant, while the air and steam flow rates vary in each case. The consideration of various operating conditions provides a clear comparison between air and steam-air gasification. The effects of the reactor temperature, steam-air flow rate, and the ratio of steam to biomass are investigated here. The concentrations of combustible gases such as hydrogen, carbon monoxide, and methane in syngas are increased when using the steam-air mixture. Two AI models, namely artificial neural network (ANN) and gradient boosting regression (GBR), are applied to predict the syngas compositions using the experimental data. A total of 74 sets of data are analyzed. The compositions of five gases (CO, CO_2, H_2, CH_4, and N_2) are predicted by the ANN and GBR models. The coefficients of determination (R2) range from 0.80 to 0.89 for the ANN model, while the value of R2 ranges from 0.81 to 0.93 for GBR model. In this study, the GBR model outperforms the ANNs model based on its ensemble technique that uses multiple weak learners. As a result, the GBR model is more convincing in the prediction of syngas composition than the ANN model considered in this research [10].

IV. CONCLUSION

The safe and stable operation of the boilers often determines the safe and environmentally friendly operation of the entire unit. The most direct indication of the stability of combustion is the combustion flame. Therefore, it is necessary to monitor the combustion state of the flame in the furnace chamber in real-time to ensure the safe and economic operation of the boilers. The way to establish a safe and reliable energy-saving furnace coal combustion system has become a critical issue [11,12]. Until now, the monitoring system has only remained the stage of monitoring whether the coal particles are in the state of being lit or extinguished. Although a boiler flame image monitoring system can be introduced to provide technical support for automatic monitoring and determination of combustion stability, flame stability monitoring requires relevant personnel to perform on-site observations. Therefore, the stabilization of flame images has always been one of the urgent problems to be solved in the automatic monitoring of the state of combustion of boilers. A scientific and effective solution to this problem is important for ensuring the safe and economical operation of boilers [8]. Although there are systems with better results (GBR model), the use of knowledge from the field of neural networks for application in combustion control in boilers with automatic ignition would greatly improve the degree of fuel utilization, ensure more stable operation of boilers, which would lead to significant energy savings, and therefore would help preserve the environment, reduce the emission of harmful gases, reduce the amount of ash and reduce the consumption of biomass and fossil fuels, which are becoming less and less every day on planet Earth.

REFERENCES

[1] Stefan Popovic, Lazar Kopanja, Sonja Djukic Popovic and Dejan Djukic (2022). Neural networks and their application in object recognition. 12th *International Conference on Applied Internet and Information Technologies* (AIIT 2022), Zrenjanin, Serbia.

[2] Gökçe B, Sonugür G. (2022, July) Recognition of dynamic objects from UGVs using Interconnected Neural network-based Computer Vision system. *Automatika: Journal for Control, Measurement, Electronics, Computing & Communications, 63*(2), 244–58.

[3] Bottcher, W., Machado, P., Lama, N., & McGinnity, T. M. (2021, July). Object recognition for robotics from tactile time series data utilising different neural network architectures. In *2021 International Joint Conference on Neural Networks (IJCNN)* (pp. 1-8). IEEE.

[4] Zhu, Y. (2018). Research on the architecture and behavior model of high-speed channel for thermal image processing. *Wireless Personal Communications, 102*(4), 3869-3877.

[5] Rajah, T. T. R., Chiam, Y. K., & Azizul, Z. (2018). Fuzzy-based framework for the selection of image processing software for diagnosis and outcome prediction of cardiac diseases. *Advanced Science Letters, 24*(2), 1109-1113.

[6] Lazić, V., Arsić, D., Nikolić, R. R., Rakić, D., Aleksandrović, S., Djordjević, M., & Hadzima, B. (2016). Selection and analysis of material for boiler pipes in a steam plant. *Procedia Engineering, 149*, 216-223.

[7] Wu, S. (2015). A traffic motion object extraction algorithm. *International Journal of Bifurcation and Chaos, 25*(14), 1540039.

[8] Zhang, J. (2020). Computer image processing and neural network technology for thermal energy diagnosis of boiler plants. *Thermal Science, 24*(5 Part B), 3221-3228.

[9] Chen, J., Li, Q., Liu, K., Li, X., Lu, B., & Li, G. (2022). Correction of moisture interference in laser-induced breakdown spectroscopy detection of coal by combining neural networks and random spectral attenuation. *Journal of Analytical Atomic Spectrometry, 37*(8), 1658-1664.

[10] Wen, H. T., Lu, J. H., & Phuc, M. X. (2021). Applying artificial intelligence to predict the composition of syngas using rice husks: A comparison of artificial neural networks and gradient boosting regression. *Energies, 14*(10), 2932.

[11] Fernández-Alemán, J. L., López-González, L., González-Sequeros, O., Jayne, C., López-Jiménez, J. J., Carrillo-de-Gea, J. M., & Toval, A. (2016). An empirical study of neural network-based audience response technology in a human anatomy course for pharmacy students. *Journal of medical systems, 40*(4), 1-12.

[12] Soltani, A., Battikh, T., Jabri, I., & Lakhoua, N. (2018). A new expert system based on fuzzy logic and image processing algorithms for early glaucoma diagnosis. *Biomedical Signal Processing and Control, 40*, 366-377.

Performance-enhancement of ZnO/ a-Si:H/n a-Si:H/i-c-Si/p /BSF /Al Heterojunction Solar Cells by Optimization of Some Physical Parameters

Naceur Selmane[1], Feriha Afrah Boukhelkhal[2], Ali Cheknane[3], Fakhereddine Khemloul[4]

[1,2,3]Electronic department, Laghouat university, Laghouat, Algeria
[4]Physics department, Laghouat university, Laghouat, Algeria

Abstract—**Heterojunction silicon solar cells, also known as heterojunctions with intrinsic thin layer (HIT) of the type TCO/n-a-Si:H/i-a-Si:H/p–c-Si/p+-a-Si:H/BSF solar cells (where TCO is transparent conducting oxide involving Al-doped ZnO; a-Si:H is hydrogenated amorphous silicon; c-Si:H is hydrogenated crystalline silicon; BSF is back surface field, n- and p- refer to n-type and p-type,respectively; n-a-Si is the emitter layer; i-a-Si is the passivation layer of intrinsic type semiconductor) have attracted special interest due to their suitability and high efficiency. Thickness and work function for the TCO layer are all optimized here. With optimal parameters, TCO/n-a-Si:H/i-a-Si:H/p-c-Si/p+-a-Si:H/BSF solar cells exhibit high simulation characteristics in terms of conversion efficiency (25.62%), open circuit potential (V_{OC}, 744mV), short circuit current density (J_{SC}, 42.43mA/cm^2) and fill factor (*FF*, 83.7%). The Automat for Simulation of Heterostructures (AFORS-HET) program is used. The energy band diagram, current density, quantum efficiency, and charge-carrier generation/recombination behaviours are investigated to find out how heterojunction cell performance enhancement occurs.**

Keywords- solar cells, thickness, work function, high efficiency

I. INTRODUCTION

Solar cells based on thin film silicon/crystalline silicon heterojunctions have attracted interest. They are highly stable with high conversion efficiency [1]. The cells are also not expensive, and their thickness and doping densities can be controlled.

The amorphous and crystalline heterojunctions (a-Si:H/c-Si) were first reported in the early 1980s is formed [2]. Twenty years later, Sanyo invented HIT solar cell using plasma enhanced chemical vapour deposition (PECVD) deposited onto n-type CZ wafer. The multi-layered new cell showed high conversion efficiency (20.7%). Intrinsic buffer layer, back side face (BSF) layer and transparent conductor oxide (TCO) improved properties for the hetero-junction solar cell [3]. Other parameters involved in HIT solar cells, such as thickness, doping concentration, different re-combinations (Radiative, Auger, and SRH) at interface due to surface states, defects distribution type and TCO work function also affect solar cell performance [4-6]. The quality of interfaces between the different layers is another important factor. Amorphous emitter layer, TCO layer and their concentrations, doping, work function and thickness, should also be considered.

ISBN: 978-86-82602-01-9

The TCO work function is a major parameter, responsible for the high performance ofa-Si:H/p c-Si solar cells, that has been studied By numerical simulation, a prospective TCO/n-a-Si:H/i-a-Si:H/p-c-Si/p+a-Si:H BSF solar cell is proposed here with high performance. Photovoltaic characteristics such as the conversion efficiency (η), fill factor (*FF*),open-circuit potential (V_{OC}) and the short circuit current density (J_{SC}), have all been assessed. Simulation helps exploration of solar cells with special characteristics with minimal cost, and helps understand different phenomena that occur in heterojunction solar cells. Automat for Simulation of Heterostructures (AFORS-HET) software is used to optimize parameters, such as thickness, doping concentration and work function to obtain high performance solar cells [3,7]. This work is focused on effects of TCO thickness and work function, and on the emitter layer (n-a-Si) doping concentration. The effects of such parameters on performance of TCO/n -a-Si:H/i-a-Si:H/p- c-Si/p+ a-Si:H BSF solar cells are investigated here.

II. Structure of Heterojunction Solar Cell and Simulation Details

AFORS-HET, based on solving the one-dimensional Poisson and the continuity equations using Shockley–Read–Hall recombination statistics, is useful in studying heterojunction solar cells [3,7,8]. The simulated HIT solar cells have the structure ZnO/ a-Si:H/n a-Si:H/i-c-Si/p /Al BSF /Al, where p-c-Si is the absorber layer, n-a-si is the emitter layer, i-a-Si is the passivation layer of intrinsic type and TCO is the transparent conductive oxide (ZnO in this study). Fig. 1 schematically describes the solar cell used here.

In the present simulation, AM 1.5 radiation was used as the illumination source with a power density of 100 mW/cm^2. For the p-c-Si substrate, oxygen defects with a density of 1×10^{11} cm^{-3} eV^{-1} located at 0.55 eV above EV (EV+0.55) are assumed. The defect states involve similar densities for electrons (1×10^{-14}cm^{-3} and holes (1×10^{-14}cm^{-3}).

The AFORS-HIT software environment, which is one dimensional solar cell device simulator, is employed here. The cell characteristics to be extracted are η, V_{OC}, J_{SC}, and *FF*. Effect of integration of the Al-doped ZnO layer in the heterojunction cell on its performance will also be assessed.

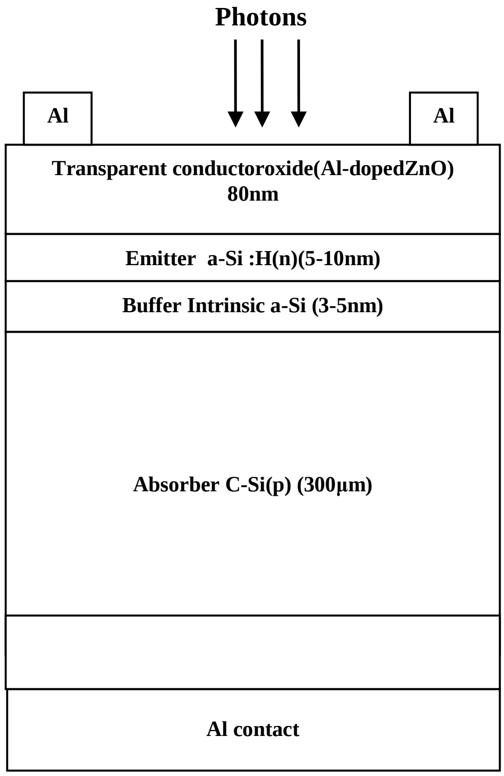

Figure 1. A schematic diagram of a n-a-Si:H/i-a-Si:H/p-c-Si/p$^+$-a-Si:H/BSF solar cell.

III. Results and Discussion

A. Effects of Buffer i-a-Si:H BSF p+-a-Si: Hand TCO Layers on the HIT Solar Cell

The performance of a given solar cell is influenced by addition of each layer. The integration of i-a-Si:H buffer layer and BSF layer has thus been investigated here. Photo-current density vs. applied potential (J-V) characteristics are shown in Fig. 2. The i-a-Si:H layer and BSF layer affect the J-V plots, as compared to the reference a-n–Si/c-p-Si solar cell. The efficiency changes from 13.5% (with no buffer layer) to 17.78% with the intrinsic layer. When the BSF layer is included, the efficiency becomes higher than 20%.It is well known that a high quality i-a-Si:H buffer layer acts as the passivation for the a-Si:H/c-Si interface in HIT solar cells. The middle band diagram in Fig. 3 shows that the i-a-Si:H buffer layer can hinder the photon-generated the short-circuit current density of the solar cell is improved by inserting an i-a-Si:H buffer layer. Moreover, the carrier recombination from the n-a-Si:H emitter layer to the p-c-Si base layer. Thus absorber (bandgap $E_g = 1.12$eV) is

TABLE I. MAIN SIMULATION PARAMETERS USED FOR DIFFERENT LAYERS IN THE HETERO-JUNCTION SOLAR CELL.

	a-Si H(n)	a-Si H(i)	c-Si H(p)	Al-BSF (P^+)
Layer thickness (nm)	10	5	3×10^5	5×10^3
Dielectric constant (dk)	11.9	11.9	11.9	11.9
Band gap E_g(eV)	1.74	1.72	1.12	1.72
Electron affinity(eV)	3.9	3.9	4.05	4.05
Effective conduction band density(cm^{-3})	1×10^{20}	1×10^{20}	2.8×10^{19}	2.8×10^{19}
Effective valence band density(cm^{-3})	5×10^{18}- 1×10^{20}	1×10^{20}	1.04×10^{19}	1.04×10^{19}
Electron mobility($cm^2V^{-1}s^{-1}$)	20	20	1040	20
Hole mobility($cm^2V^{-1}s^1$)	5	5	412	5
Doping concentration of donators (cm^{-3})	1×10^{20}	0	0	0
Doping concentration of acceptors (cm^{-3})	0	0	1.5×10^{19}	1×10^{20}
Thermal velocity of electron (cm^{-3} s^{-3})	1×10^7	1×10^7	1×10^7	1×10^7
Thermal velocity of holes (cm^{-3} s^{-3})	1×10^7	1×10^7	1×10^7	1×10^7
Auger recombination coefficient for electrons(cm^6s^{-1})	0	0	2.2×10^{-31}	2.2×10^{-31}
Auger recombination coefficient for holes (cm^6s^{-1})	0	0	9.9×10^{-32}	9.9×10^{-32}

connected with i-a-Si:Hbuffer ($E_g = 1.72$eV), which is in turn connected with the emitter layer n-a-Si that forms contact for electrons (bandgap $E_{g1} = 1.74$eV) and another contact in the other side for holes with a bandgap $E_{g2} = 1.72$eV.

So the p-c-Si absorber layer has a band gapvalue that is different fromthose ofthe two hetero-interfaces, $E_{g1} = 1.74$eV for the emitter layer, and $E_{g2} = 1.72$eV for i-a-Si:H buffer layer. On the left hand side of the structure, generated mobile electrons are collected in the n-a-Si layer whereas the holes are reflected. On the right hand side of the structure, the mobile holes are collected in the p^+-a-Si:H BSF-contact whereas the electrons are reflected.

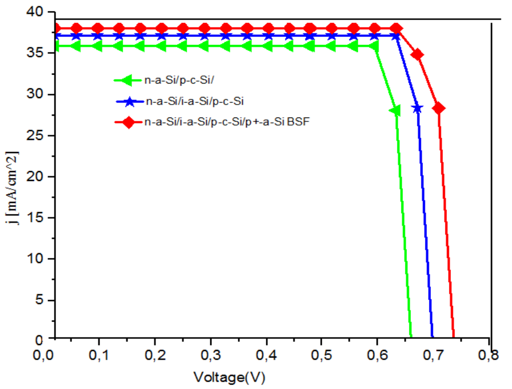

Figure 2. Simulated effects of i-a-Si: and p^+-a-Si:H layers on *J-V*plotsfor the HIT solar cell.

Effect of adding the i-a-Si:H buffer layer or the p+-a-Si:H BSF layer on the band structure for an a-Si:H/c-Si has been simulated as shown in Fig. 3.

The band discontinuities ΔE_C for the conduction band and ΔE_V for the valence band (quantum deep) at both interfaces are caused by the different band gap of c-Si. The front n-a-Si:H/p-c-Si contact is similar to a p-n homo-junction. It also forms a selective n-contact because the band offset in the valence band hinders holes from entering into the a-Si:H emitter. The p^+-a-Si:H back contact forms a BSF, where the electric field forces the electrons away from the interface and attracts the holes.

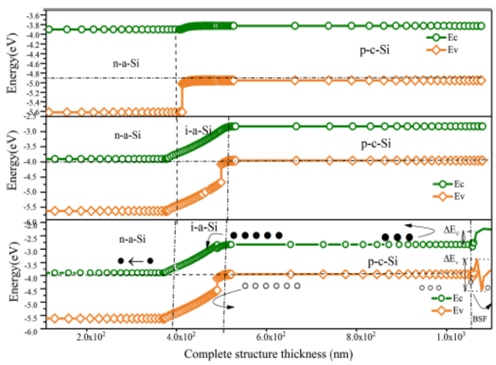

Figure 3. Effects of adding buffer i-a-Si:H and BSF p+-a-Si:H layers on band structure for the HIT solar cell.

Moreover, the band offset in the conduction band ΔE_C hinders the electrons from diffusing into the p+-a-Si:H layer, which limits the V_{OC} from the back contact compared to those without BSF layer.

To further improve the performance of the solar cell, TCO (ZnO) has also been integrated. With a wide band gap (~3.4eV) ZnO increases the probability of absorption of photons with wide wavelength range, and decreases the number of reflected photons. The p-c-Si layer will thus absorb more incident photons, yielding more electron-hole pair formation. The J_{SC} will thus increase. Other characteristics, *FF*, V_{CO}, J_{SC} and η, will consequently be enhanced with the insertion of the ZnO layer [7].

Effects of adding different layers on HIT solar cell performance are summarized in Table II. The following sections describe how varying thickness and doping density for different layers may further enhance the HIT solar cell.

TABLE II. EFFECTS OF INTEGRATINGBUFFER I-A-SI:H AND BSF P+-A-SI:H LAYERS ON HIT SOLAR CELL CHARACTERISTICS.

Solar cell	**J_{SC} (mA /cm^2)**	**V_{OC} (mV)**	**FF**	**η%**
n-a-Si/p-c-Si	36.14	663.7	72	13.5
n-a-Si/i-a-Si/p-c-Si	37.65	699.4	74.2	16.78
n-a-Si/i-a-Si/p-c-Si/P$^+$-a-Si BSF	38.23	738.2	78	19 .4

B. *Effect of Emitter Layer Thickness*

The performance of the solar cell is influenced by the variation of the thickness of each layer in the heterojunction. Effect of emitter layer thickness is simulated here. Fig. 4 shows that when the thickness of the emitter layer varies from 5 to15 nm, the values of *FF*, V_{CO}, J_{SC} and η change. Maximum efficiency of 24% can be observed for the 5nm thickness. Value of *FF* slightly increases by increasing the layer thickness from 5 to 15 nm, while values of J_{SC} and V_{CO} steadily decrease.

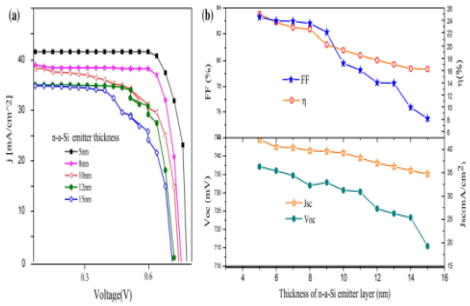

Figure 4. Effect of n-a-Si emitter layer thickness in the HIT solar cell on (a) J-V plots and (b) other extracted cell characteristics V_{OC}, J_{SC}, *FF* and η.

The V_{OC} can be simply expressed as:

$$V_{co} = \frac{KT}{q} \ln\left(\frac{J_{sc}}{j_0} + 1\right) . \quad (1)$$

where K is Boltzmann constant, T is Kelvin temperature, q is element charge, and j_o is leakage current that lowers V_{OC} [9]. V_{OC} does not directly depend on thickness of the *n*-type emitter [10]. In the thickness range 5-15 nm here, the thickness 6nm exhibits maximum V_{OC} value. Based on Fig. 4, J_{SC} increases with lower emitter layer thickness. This is due to lowered recombination rate as discussed above. Over all, the 5nm thickness shows optimal value for cell performance taking into consideration values of *FF*, V_{OC}, J_{SC} and η together. With higher thickness, the generated carriers recombine before reaching the Ohmic contacts (electrodes) at the surface. Excessive minority carriers are prone to undergo the un-wanted recombination. This is because the higher thickness increases the probability that the carriers recombine in the emitter layer before reaching the surface. Moreover, the diffusion length is related to the lifetime τ, which is defined as “the average time between the creation of the carrier and its recombination in a material, without electrical contact”. Life time is related to diffusion length (L) by:

$$L = \sqrt{D\tau} \ , \quad (2)$$

where D is diffusion coefficient .Smaller thickness for n-a-Si emitter thus increases the lifetime of hole and electron minority carriers. Longer lifetimes are desirable to give electron-hole pairs higher chance to reach the surface, and to yield higher photo-current. Moreover, the emitter layer helps create the p-n junction effect, within the charge separating region, essential to produce photo-current in solar cells.

Therefore, the n-a-Si:H emitter layer should be as thin as possible to inhibit recombination on one hand, and to allow absorbed photons reach the c-p-Si absorber layer on the other hand. Most electrons are thus generated in the absorber layer, which leads to higher solar cell performance [10].

C. *Effect of Emitter Layer Doping Density*

The n-a-Si emitter layerdoping density may affect the performance of the solar cell. Fig 5 shows that as doping concentrations decreases below (2×10^{19} cm^{-3}, the V_{OC} value sharply decreases. The J_{SC} also decreases when decreasing doping concentration below $2\text{x}10^{19}$cm^{-3}. At lower doping concentrations, the electric field leads to accumulation of electron and hole carriers at the band offset of the valence and conduction band interface. This results from the different band gap values of the materials involved in the hetero-junctions. Recombinations (Radiative, Auger, and SRH) are encouraged along the n-a-Si emitter and the depletion region which affects efficiency.

Therefore, in a weak electric field, charge accumulation occurs leading to increased recombinations. In case of strong electric field, recombination rate is lowered as holes are driven away from the interface. Electrons, that reach the space charge region, are accelerated by this electric field towards the front contact. Fig. 5 shows that at doping density 2×10^{19}cm^{-3} or higher, in the n-a-Si emitter layer, the J_{SC} reaches higher than 43mA/cm^2, η reaches ~25.54%, and *FF* slightly increases from 78.5% to 83.5%. The results are in congruence with earlier reports [3].

D. *Effect of TCO (Al-doped ZnO) Layer Thickness*

Effect of Al doped ZnO layer thickness on the HIT solar cell performance has been studied here. As discussed in Section III.*A* above, the ZnO layer increases the absorption of the light. Varying the TCO layer thickness from 40 to 100 nm also affects the HIT cell characteristics (V_{OC}, J_{SC}, *FF*, and η), as shown in Fig. 6. The Figure shows that the as the thickness increases from 40 to 80 nm, all parameters are enhanced. After 80 nm thickness, all parameters are lowered. The optimal thickness value is thus 80 nm, which yields V_{OC}, *FF*, J_{SC}, and η values of 738mV, 83.5%, 38.62mA/cm^2 and 24.78%, respectively. The optimal thickness value 80 nm is consistent with earlier reported values [7].

E. *Effect of TCO Work Function*

Effect of the TCO work function on the HIT solar cell characteristics has been simulated here. Fig. 7 show values of J_{SC}, V_{OC}, *FF*, and η are affected by TCO wave function in the range 4.0 – 4.5 eV. The *FF* value steadily decreases with increased wave function, until 4.4eV, after which it sharply decreases.

Values of V_{OC} and η steadily decrease with increased wave function value up to 4.4eV. At values higher than 4.4eV, the V_{OC} and η values decrease more steeply. The J_{SC} values steadily decreases with increased work function, as shown in Fig 7.

Fig. 8 clarifies the influence of TCO work function, together with its thickness, on the HIT solar cell performance. Two work function values (4.0 and 4.4eV) are described. With larger TCO work function (ca. 4.4eV), a potential barrier occurs, which inhibits charge carrier injection in the emitter layer n-a-Si:H.

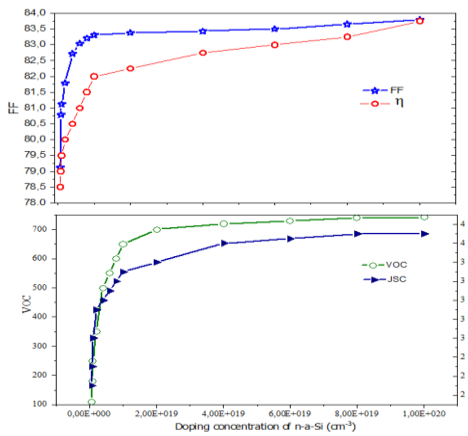

Figure 5.Effect of n-a-Si:H layer doping concentration on HIT solar cell parameters V_{OC}, J_{SC}, *FF* and η.

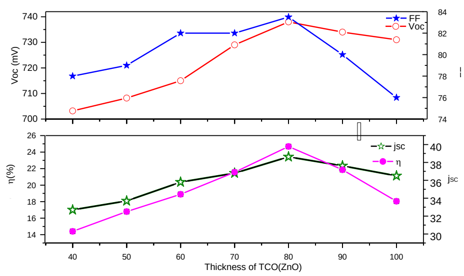

Figure 6. Effect of TCO layer thickness on HIT solar cell characteristics (V_{OC}, J_{SC}, *FF* and η).

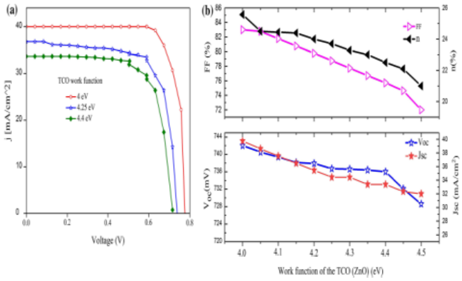

Figure. 7. Effect of work function value of TCO (Al-doped ZnO) in the HIT solar cell on (a) J-V plots and (b) other extracted cell characteristics V_{OC}, J_{SC}, *FF* and η.

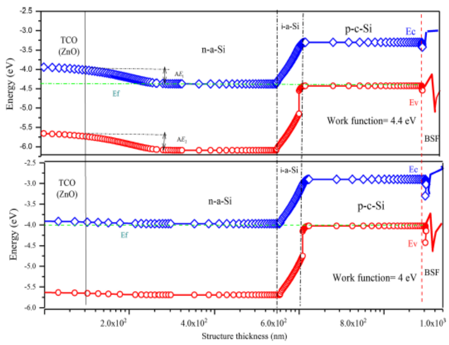

Figure 8. Simulated energy band diagrams for the HIT solar cell using two different TCO work functions 4.0 and 4.4eV.

The minority carriers (electrons) become more difficult to participate in the conduction. Such difficulty is caused by the higher potential barrier with higher wave functions, which decreases for lower work functions. Any lower wave functions (ca. 4.0eV) for the n-a-Si:H layer exhibit lower band bending (closer to flat band), which facilitates minority charge carrier (electron) injection into the emitter layer. Fig. 8 thus predicts higher solar cell performance with the lower TCO work function (4.0 eV).

This is understandable as the work function is commonly defined as the minimum thermodynamic work (energy) needed to remove an electron from a solid to a point in the vacuum immediately outside the solid surface. Higher performance should therefore be expected with lower work functions. Fig. 8 confirms that the optimal value of work function is 4.0eV, yielding maximum values for η (25.62%), *FF* (83.68%), J_{SC} (940.26 mA/cm$_2$) and V_{OC} (739.13mV).

IV. Conclusion

High performance hetero-junction a-Si:H/c-Si solar cells can be constructed. Band discontinuities and different layer parameters (emitter and TCO layers) affect solar cell performance as confirmed here using AFORS-HET simulation program. Layer thickness and doping density of the n-a-Si emitter layer, as well as TCO (ZnO) work function, affect HIT solar cell characteristics, and can be optimized. The effect of adding a-i-Si buffer and P+-a-Si back side face (BSF) layers is studied. Such addition enhances the solar cell performance. Lower n-a-Si:H emitter layer thickness (~5nm) and higher doping density (2×10^{19}cm^{-3} or higher) enhance the HIT solar cell performance. The optimal TCO thickness is ~80 nm with 4.0eV work function. With optimal conditions, high solar cell characteristics (η = 25.62%, V_{OC} = 744 mV, J_{SC} = 42.43mA/cm^2, *FF*: 83.7%) can be reached for the TCO/n-a-Si:H/i-a-Si:H/p-c-Si/p+a-Si:H/BSF solar cell.

References

[1] Masuko, K., Shigematsu, M., Hashiguchi, T., Fujishima, D., Kai, M., Yoshimura, N., ... & Okamoto, S. (2014). Achievement of more than 25% conversion efficiency with crystalline silicon heterojunction solar cell. *IEEE Journal of Photovoltaics*, *4*(6), 1433-1435.

[2] A. Goebtzberger and V.U. Hoffman, *Photovoltaic Solar Energy Generation*, N.Y., Springer (2005).

[3] Liu, J., Huang, S., & He, L. (2015). Simulation of a high-efficiency silicon-based heterojunction solar cell. *Journal of Semiconductors*, *36*(4), 044010.

[4] Izzi, M., Tucci, M., Serenelli, L., Mangiapane, P., Salza, E., Chierchia, R., ... & Veneri, P. D. (2015). TCO optimization in Si heterojunction solar cells on p-type wafers with n-SiOx emitter. *Energy Procedia*, *84*, 134-140.

[5] Selmane, N., Cheknane, A. L. I., & Hilal, H. S. (2020). Optimization of al-doped ZnO transparent conducting oxide and emitter layers for enhanced performance of Si heterojunction solar cells. *Journal of Electronic Materials*, *49*, 2179-2190.

[6] Zhao, L., Zhou, C. L., Li, H. L., Diao, H. W., & Wang, W. J. (2008). Design optimization of bifacial HIT solar cells on p-type silicon substrates by simulation. *Solar Energy Materials and Solar Cells*, *92*(6), 673-681.

[7] Selmane, N., Cheknane, A., Aillerie, M., & Hilal, H. S. (2019). Effect of ZnO-based TCO on the performance of a-Si H (n)/a-Si H (i)/c-Si H (p)/Al BSF (p+)/Al heterojunction solar cells. *Environmental Progress & Sustainable Energy*, *38*(4), 13114.

[8] Selmane, N., Cheknane, A., Khemloul, F., Helal, M. H., & Hilal, H. S. (2022). Cost-saving and performance-enhancement of CuInGaSe solar cells by

adding CuZnSnSe as a second absorber. *Solar Energy*, *234*, 64-80.

[9] Jensen, N., Rau, U., Hausner, R. M., Uppal, S., Oberbeck, L., Bergmann, R. B., & Werner, J. H. (2000). Recombination mechanisms in amorphous silicon/crystalline silicon heterojunction solar cells. *Journal of Applied Physics*, *87*(5), 2639-2645.

[10] Tanaka, M., Taguchi, M., Matsuyama, T., Sawada, T., Tsuda, S., Nakano, S., ... & Kuwano, Y. (1992). Development of new a-Si/c-Si heterojunction solar cells: ACJ-HIT (artificially constructed junction-heterojunction with intrinsic thin-layer). *Japanese Journal of Applied Physics*, *31*(11R), 3518.

Cluster Analysis in Probability - based Multi-objective Optimization

Maosheng Zheng[1], Jie Yu[2]

[1]School of Chem. Eng., Northwest University, Xi'an, China
[2]School of Life Sci., Northwest University, Xi'an, China

Abstract—**The probability - based multi-objective optimization is a novel approach with brand new concept of "preferable probability" and the assessments, which can be used in many fields, including energy planning, programming problem, operation research, etc. However, it needs "independent objective" to be analogical as an "independent event" from the respect of probability theory. In this paper, it discusses the application of cluster analysis to conduct the separation of an "independent objective" from "multiple objectives". The results show that using linear correlation coefficient to distinguish the "similarity" of performances is a rational method, it thus can be used to provide appropriate objective classification for the probability - based multi-objective optimization.**

Keywords - multi – objectives, cluster analysis, independent objectives, linear correlation coefficient, simultaneous optimization

I. INTRODUCTION

In the probability – based multi–objective optimization [1], a brand new concept of "preferable probability" and the assessments for the probability – based multi – objective optimization (PMOO) were proposed. This novel approach can be used in many fields, including energy planning, programming problem, operation research, etc.

The main philosophy of PMOO is that the essence of "multi - objective optimization" is "simultaneous optimization of multiple objectives" from the point of view of system theory, a probability - based method was further proposed on basis of set theory and probability theory, which regarded each objective as an "independent event".

From the perspective of set theory and probability theory, the intersection of independent events and the joint probability of independent events can be used to characterize the simultaneous occurrence of multiple independent events. In this way, when it equates each objective with an independent event, the problem of simultaneous optimization of multiple objectives becomes "rule – based". However, the equating of "each objective" to an "independent event" strongly depends on the separation "independent events" from "multiple objectives", such that the probability - based multi - objective optimization method can be used rationally.

This paper focuses on the problem of separating "independent event" from "multiple objectives" through cluster analysis.

Cluster analysis originated from a branch of biology [2]. By classifying things, people can gradually and deeply understand the deeper problems of the material world. Preliminarily, the classification methods are mostly implemented by experience or professional knowledge, so they can be classified as qualitative methods. Later, mathematical methods were gradually adopted to get a certain quantitative classification with characteristic values. It should be a development trend to use mathematical methods for quantitative and scientific classification. Cluster analysis is also an important branch of multivariate analysis, which develops rapidly. Nowadays, cluster analysis has been widely used in archaeology, biology, geology, industrial and agricultural production, weather forecast, medicine, medicine and other fields. Actually, in the process of cluster analysis, the class is not given in advance, but needs to be determined according to the characteristics of the observed data, and there is no need to make any assumptions about the number and structure of classes. In the clustering results, objects belonging to the same class tend to be similar to each other in a sense, while objects belonging to different classes tend to be dissimilar. The purpose of clustering analysis is to classify objects into several classes according to certain rules [2]. Cluster analysis can be divided into *Q* cluster analysis and *R* cluster analysis according to different classification objects [3]. *Q*-type clustering is for samples, and *R*-type clustering is for performances.

Generally speaking, according to the degree of similarity, the samples (or performances) are classified one by one, and the closely related classes are clustered into a small taxon, and then gradually expanded, so that the alienated ones are clustered into a large taxon, until all the samples (or performances) are clustered, forming a cluster diagram that represents the affinity. Classify the samples (or performances) according to some requirements in turn [3].

The general viewpoint of classification is that the closer the similarity of performances is, the closer their similarity coefficient is to 1 or -l, while the similarity coefficient of unrelated performances is closer to 0.

Those that are similar are classified into one category, and those that are not are classified into different categories. The distance is the "space" characteristic between "points". Each sample is regarded as a point in *P*-dimensional space, and the distance between points is measured by some kind of measurement. The points that are closer to each other belong to one category, while the points that are farther away belong to different categories.

This paper mainly discusses *R*-type cluster analysis. Special attention is paid on appropriate objective classification for the probability-based multi-objective optimization.

II. CHARACTERIZATION OF SIMILARITY

A. *Similarity Coefficient*

Usually, the similarity coefficient is used to characterize the similarity between samples or performances, but through careful analysis of the similarity coefficient, it can be concluded that the similarity coefficient is not a good coefficient to characterize the similarity between samples or performances.

The definition of "similarity coefficient" is:

$$S_{jk} = \frac{\sum_{i=1}^{m} x_{ij} x_{ik}}{[\sum_{i=1}^{m} x_{ij}^{2} \times \sum_{i=1}^{m} x_{ik}^{2}]^{0.5}} \quad . \tag{1}$$

In Eq. (1), S_{jk} is a "similarity coefficient" that was used to represent the "similarity degree" between two attributes x_{ij} and x_{ik} in time or space previously.

Furthermore, the attribute x_{ij} can also be "normalized", that is,

$$y_{ij} = (x_{ij} - A_j) / (\mathrm{B}_j - \mathrm{A}_j) \quad . \tag{2}$$

In (2), $A_j = min\{x_{ij}, i = 1, 2, \ldots, m\}$, $B_j = max\{x_{ij}, i = 1, 2, \ldots, m\}$.

Thus, a "normalized expression" for (1) is,

$$S'_{jk} = \frac{\sum_{i=1}^{m} y_{ij} y_{ik}}{[\sum_{i=1}^{m} y_{ij}^{2} \times \sum_{i=1}^{m} y_{ik}^{2}]^{0.5}} \quad . \tag{3}$$

In fact, the results of Eqs. (1) and (3) are not equivalent in general. In addition, the results of Eqs. (1) and (3) can't even reflect the similarity between two diagraphs, which will be described in the following example. Therefore, the "similarity coefficient" between two attributes obtained from above definition may not be a "good coefficient" to characterize the real similarity between samples or performances.

Example 1

Table I gives the values of three attributes of 7 different samples. Curves 1, 2 and 3 in Fig. 1 show the variations characteristics of these three attributes of different samples, respectively. Now, the problem is to find the "similarity coefficient" between attribute Eqs. (1) and attributes Eqs. (2) and (3).

TABLE I. VALUES OF THREE ATTRIBUTES OF DIFFERENT SAMPLES.

Sample	Attribute 1	Attribute 2	Attribute 3
1	1	4	10
2	2	5	9
3	3	6	8
4	4	7	7
5	5	8	6
6	6	9	5
7	7	10	4

According to Eq. (1), the "similarity coefficient" between attribute 1 and attribute 2 of these seven samples can be obtained,

$$S_{12} = 0.9829 \ . \tag{4}$$

While, according to Eq. (3), the "similarity coefficient" between attribute 1 and attribute 2 of these seven samples can be obtained,

$$S'_{12} = 1 \ . \tag{5}$$

The values given by Eqs. (4) and (5) for the same attributes are not equal! This shows that the "similarity coefficient" defined in such a way may not be a "good coefficient" to characterize the similarity between attributes.

Furthermore, let's study the "similarity coefficient" between attribute 1 and attribute 3 to see what happens.

The "similarity coefficient" between attribute 1 and attribute 3 of these seven samples can be obtained by Eq. (1),

$$S_{13} = 0.7372 \ . \tag{6}$$

However, according to Eq. (3), the similarity coefficient between attribute 1 and attribute 3 of these seven samples can be obtained,

$$S'_{13} = 0.3846 \ . \tag{7}$$

These results fully show that the "similarity coefficient" defined in such a way may not be suitable for characterizing the similarity between attributes.

There are also many literatures that discuss the "similarity coefficient" as well [5-7].

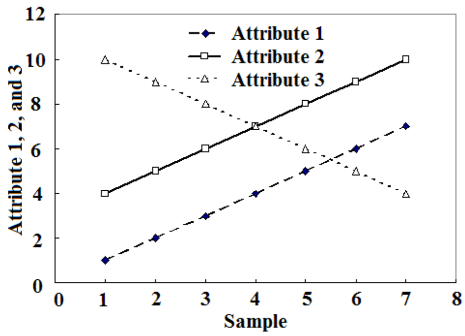

Figure 1. Three attributes of different samples.

B. *Linear Correlation Coefficient*

The definition of "linear correlation coefficient" is,

$$r_{jk} = \frac{\sum_{i=1}^{m}(x_{ij} - \overline{x_j}) \times (x_{ik} - \overline{x_k})}{[\sum_{i=1}^{m}(x_{ij} - \overline{x_j})^2 \times \sum_{i=1}^{m}(x_{ik} - \overline{x_k})^2]^{0.5}} \ . \tag{8}$$

In Eq. (8), r_{jk} is the "linear correlation coefficient" that is used to represent the degree of linear correlation degree between two attributes x_{ij} and x_{ik}, and $\overline{x_j}$ is the average value of the *j*-th attribute and $\overline{x_k}$ the average value of the *k*-th attribute.

Now, the "linear correlation coefficient" is analyzed with an example as well.

Example 2

Find the linear correlation coefficient between the attributes Eqs. (1) and (2) of different samples given in Fig.1 and Table 1.

Here, we use the Eq. (8) to analyze the data of attribute Eq. (1) and attribute Eq. (2) in Table I and Fig. 1. It results in the linear correlation coefficient r_{12} = 1. While the analysis of the data of attribute Eq. (1) and attribute Eq. (3) in Table I and Fig. 1 gets the linear correlation coefficient r_{13} = –1.

Actually, there is only a relative translation between the data of attribute Eq. (1) and attribute Eq. (2) in Table I and Fig.1, that is, *"the data of attribute 1" = "'the data of attribute 2' + 3"* only. Of course, they are fully linearly correlated and completely similar. However, according to the definition for "similarity coefficient" with Eq. (1), its similarity has been "discounted". So it can be said that "similarity coefficient" may not be a "good coefficient" to characterize the similarity between samples or performances. While, for the linear correlation coefficient, it is just the right coefficient to reflect the linear proportional relationship, and it is more reasonable to reflect the similarity between samples or attributes; in addition, the linear correlation coefficient also has the invariance of "normalization" similar to the Eq. (2).

Besides, [8] analyzed the precipitation forecast business and field test of Zhengzhou Meteorological Observatory during the main flood season of Huanghuai in June -August, 2000, and showed that the forecast method with linear correlation coefficient is very useful in precipitation similarity forecast, especially in 24-hour forecast.

C. Distance

The distance between samples is defined. The smaller the distance, the closer they are. The commonly used distances include Minkowski distance, Euclidean distance and Chebyshev distance. Considering the dimensional differences between different attributes, the normalization like Eq. (2) is usually used as well.

III. APPLICATION OF CLUSTERING ANALYSIS IN MULTI-OBJECTIVE OPTIMIZATION

As mentioned earlier, in the probability - based multi - objective optimization, equating "each objective" to an "independent event" depends on the ability to separate "independent event" from "multiple objectives" through cluster analysis. This section discusses the problem of separating "independent goal" from multiple objectives. It is still illustrated by an example.

Example 3

Cao used cluster analysis to analyze the physical and mechanical properties of cutting tool materials [9]. Now, we re-analyze it to fully understand the co-relationship between the physical and mechanical properties of cutting tool materials. Table II shows the physical and mechanical properties of 8 samples of tool materials [9].

TABLE II. PHYSICAL AND MECHANICAL PROPERTIES OF 8 SAMPLES OF TOOL MATERIALS [9]

Material	**Property**		
	Hardness (HRA) × 0.1	***Flexural strength (GPa)***	***Impact toughness (kJ/m²) × 0.1***
W18 Cr4V	8.31	3.2	25
YG6	8.95	1.45	3
YG6x	9.1	1.4	2
YG8	8.9	1.5	4
YT30	9.25	0.9	0.3
YT14	9.05	1.2	0.7
Al_2O_3 AM	9.1	0.5	0.5
Si_3N_4 SM	9.2	0.8	0.4

The analysis of the data in Table II shows that there is a strong linear correlation between the hardness of cutting tool materials, bending strength and impact toughness. As shown in Figs. 2 - 4, their linear correlation coefficients are both greater than 94% and close to 95%.

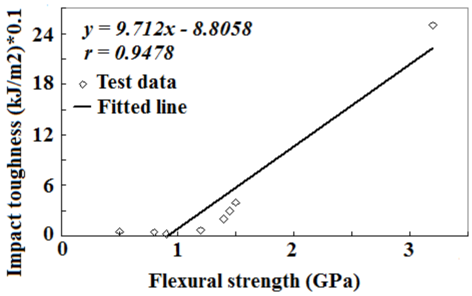

Figure 2. Correlation between flexural strength and impact toughness of tool materials.

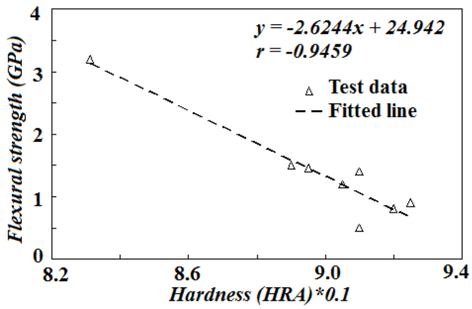

Figure 3. Correlation between hardness and flexural strength of tool materials.

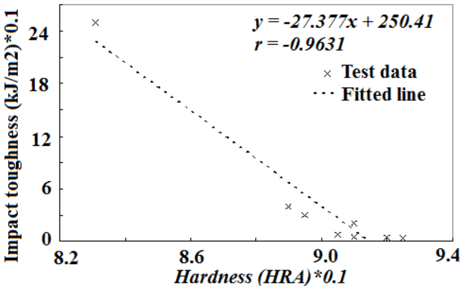

Figure 4. Correlation between hardness and impact toughness of tool materials.

As to this group of materials, when doing multi-objective optimization analysis, they can be classified into one category, and only one of them can be employed as an "independent objective" attribute to participate in the evaluation. However, if more "objectives" than "independent objective" participate in the analysis and evaluation of multi - objective optimization problem, for example, two or three attributes of hardness, bending strength and impact toughness of this group of tool materials participate in the evaluation at the same time, it is equivalent to increase their weighting factors of the relevant objectives.

In addition, there are some clustering analysis methods based on fuzzy theory as well [10-16].

IV. Conclusion

Using linear correlation coefficient analysis method, we can conduct the separation of an independent objective (attribute) from multiple objectives. In the evaluation, if the attributes of "non - independent objectives" are involved instead of only "independent objectives" participating in the analysis and evaluation of multi - objective optimization at the same time, it is equivalent to increase their weighting factors of the relevant objectives.

References

[1] Zheng, M., Teng, H., Yu, J., Cui, Y., & Wang, Y. (2022). *Probability-Based Multi-objective Optimization for Material Selection.* Springer.

[2] Xiao, Z., & Yu, J. (2013). *Multivariate Statistics and SAS Application, 2nd Ed.* Wuhan University Press, Wuhan, China.

[3] Han, M. (2017). *Applied Multivariate Statistical Analysis, 2nd Ed.* Tongji University Press, Shanghai, China.

[4] Yan, X. (2011). Evaluation model of agricultural machinery selection based on similarity coefficient and distance. *Anhui Agricultural Science, 39*(19), 11888-11891.

[5] Xu, D., Xia, M., & Liu, X. (1995). Index synthesis method of similarity coefficient and its application. *Journal of Huazhong Normal University (Natural Science Edition), 29*(2), 155-157.

[6] Xu, B. (1992). Rationality of the definition of similarity coefficient. *Engineering Mathematics, 8*(3), 13-20.

[7] Zhong, M. (1996). Similarity coefficient and distance between component data. *Journal of Mathematical Medicine, 9*(2), 145-147.

[8] Yan, H., Li, S., Huang, Y., & Zhang X. (2003). Test of common similarity criteria and use of comprehensive similarity coefficient. *Meteorology and Technology, 31*(4), 211-215.

[9] Cao, S. (1997). Fuzzy cluster analysis of physical and mechanical properties of cutting tool materials. *Journal of Tianjin Textile Institute of Technology, 16*(5), 26-30.

[10] Yu, S., Zhang, J., & Li, J. (2001). Determination method of mechanical properties of materials based on fuzzy clustering. *Journal of Gansu Sciences, 13*(1), 6-11.

[11] Shao, R. (2002). Application of fuzzy cluster analysis method in eystem analysis. *Liaoning Chemical Industry, 31*(9), 386-389.

[12] Yang, C., & Hong, D. (2005), Multi-objective decision method based on fuzzy cluster analysis. *Journal of Xi'an University of Finance and Economics, 18*(4), 31-34.

[13] Gan, J. (1989). Fuzzy cluster analysis of cutting performance of carbide tools. *Journal of Harbin Institute of Shipbuilding Engineering, 10*(1), 40-53.

[14] Giordani, P., Ferrao, M. B., & Martella, F. (2020). *An introduction to Clustering with R.* Springer, Singapore.

[15] Shitong, W., Chung, K. F., Hongbin, S., & Ruiqiang, Z. (2004). Note on the relationship between probabilistic and fuzzy clustering. *Soft Computing, 8*, 366-369.

[16] Pedrycz, W. (2021). *An Introduction to Computing with Fuzzy Sets*. Springer, Cham, Switzerland.

Energy Waves

Jelenka Savković Stevanović[1]

[1]Faculty of Technology and Metallurgy, The University of Belgrade, Belgrade, Serbia

Abstract—**In this paper quantum energy and, electromagnetic waves were studied. Discrete energy quantity, call quant, and information were considered. In classical physics and chemistry governing opinion that electromagnetic waves emission, transfer, and absorption are performed continuous. However, Planck's assumed that energy emitted discontinuously with break, in energy quant. The quant energy and frequency were examined.**

Keywords - field, waves, lengths, frequency, shield

Notation

c - light velocity, m/s

E - quant energy, J

g -gravity acceleration, m/s^2

F_M - magnetic force, N

$h = 6.62\ \ 10^{-34}\ Js$ -universal Planck's constant

f - frequency, hertz

I_v - information value, $Byte$

m - electrons mass, kg

p - probability of position

q - probability of time

t - time, s

v - electrons speed moving, m/s

v_r - friction speed, m/s

Greek symbols

λ - wave length, m

I. Introduction

In physics electromagnetic radiation refers to the waves of the electromagnetic field propagating through space, carrying electromagnetic radiation energy. It includes radio waves, microwaves, infrared, light, ultraviolet, X-rays and gamma rays.

The electromagnetic (EM) spectrum is the range of all types of EM radiation. Radiation is energy that travels and spread out as it goes-the visible light that comes from lamp in our house and the radio waves that come from the radio station. In physics, electromagnetic radiation (EM radiation or EMR) refers to the waves (or their quanta, photons) of the electromagnetic field, propagating (radiating) are two types of electromagnetic radiation.

The 6G-six generation wireless is the successor the 5G cellular technology. 6G will be able to use higher frequencies than 5G networks and provide substantially higher capacity and much lower latency. One of the goal of 6G internet will be to support one micro-second latency communications representing 1,000 times faster or 1/1000th the latency than one millisecond throughput [1,2].

The 6G technology market is expected to facilitate large improvement in the areas of imaging, presence technology and location awareness. Working in conjunction with artificial intelligence, the computational infrastructure of the 6G will be able to autonomously determine the best location for computing to occur, this includes decisions, about data storages, processing and sharing.

The 5G is the 5th generation mobile network. It is a new global wireless standard after 1G, 2G, 3G and 4G networks. 5G enables a new kind of network that is designed to connect virtually everyone and everything together including machines, objects, and devices. Some 5G pundits contend that the new network generates radiofrequency radiation that can damage DNA and lead to cancer; cause oxidative damage that can cause premature aging; disrupt cell metabolism; and potentially lead to other disease through the generation of stress proteins.

At low frequencies, external electric and magnetic fields induce small circulating currents within the body. The main effect of radiofrequency electromagnetic fields is heating

ISBN: 978-86-82602-01-9

of body tissues. There is no doubt that short-term exposure to very high levels of electromagnetic fields can be harmful to health [3,4].

To protect against 6G and 5G and other electromagnetic fields in our home, the electromagnetic field home adaptor is recommended. The home adaptor will correct the 6G or 5G or 4G signal going to devices like a tablet in our home. It will not fully protect against fields originating out of our home (such as the neighboring routers and cell towards).

Some studies have found a link between electromagnetic field exposure and a higher risk of childhood leukemia, but other studies have not. Other studies have not found proof that electromagnetic field exposure causes other childhood cancers. Studies in adults did not prove that electromagnetic field exposure causes cancer.

In this work electromagnetic waves and information were examined.

II. ELECTROMAGNETIC WAVES PROPERTIES

Electromagnetic waves can be imagined as a self-propagation transverse oscillating wave of electric and magnetic fields. This 3D animation shows a plane linearly polarized wave propagating from left to right. The electric and magnetic fields in such a wave are in-phase with each other reaching minima and maxima together.

Electrodynamics is the physics of electromagnetic radiation, and electromagnetism is the physical phenomenon associated with the theory of electrodynamics. Electric and magnetic fields obey the properties of superposition. Thus, a field due to any particular particle or time-varying electric or magnetic field contributes to the fields present in the same space due to other causes. Further, as they are vector fields, all magnetic and electric field vectors add together according to vector addition. For example, in optics two or more coherent light waves may interact and by constructive or destructive interference yield a resultant irradiance deviating from the sum of the component irradiances of the individual light waves.

The electromagnetic fields of light are not affected by traveling through static electric or magnetic fields in a linear medium such as a vacuum. However, in nonlinear media, such as some crystals, interactions can occur between light and static electric and magnetic fields -these interactions include the Faraday effect and Kerr effect.

In refraction, a wave crossing from one medium to another of different density alters its speed and direction upon entering the new medium. The ratio of the refractive indices of the media determines the degree of refraction. Light of composite wavelengths (natural sunlight) disperses into a visible spectrum passing through a prism, because of the wavelength-dependent refractive index of the prism material (dispersion); that is, each component wave within the composite light is bent a different amount.

EM radiation exhibits both wave properties and particle properties at the same. Both wave and particle characteristics have been confirmed in many experiments. Wave characteristics are more apparent when EM radiation is measured over relatively large timescales and over large distances while particle characteristics are more evident when measuring small timescales and distances. For example, when electromagnetic radiation is absorbed by matter, particle-like properties will be more obvious when the average number of photons in the cube of the relevant wavelength is much smaller than 1. It is not so difficult to experimentally observe non-uniform deposition of energy when light is absorbed, however this alone is not evidence of "particulate" behavior. Rather, it reflects the quantum nature of matter. Demonstrating that the light itself is quantized, not merely its interaction with matter, is a more subtle affair.

Some experiment display both the wave and particle natures of electromagnetic waves, such as the self-interference of a single photon. When a single photon is sent through an interferometer, it passes through both paths, interfering with itself, as waves do, yet is detected by a photomultiplier or other sensitive detector only once.

III. WAVES MODEL

Representing of the electric vector of wave of circularly polarized electromagnetic radiation. In homogeneous, isotropic media, electromagnetic radiation is a transverse wave meaning that its oscillations are perpendicular to the direction of energy transfer and travel.

The electric and magnetic parts of the field in an electromagnetic wave stand in a fixed ratio of strengths to satisfy the two that specify how one is produced from the other. In dissipation-less (lossless) media, these **E** and **B** fields are also in phase, with both reaching maxima and minima at the same points in space. A common misconception is that the **E** and **B** fields in electromagnetic radiation are out of phase because a change in one produces the other, and this would produce a phase difference between them as sinusoidal functions (as indeed happens in electromagnetic induction, and in the near-field close to antennas). However, in the far-field EM radiation which is described by the two source-free Maxwell curl operator equations, a more correct description is that a time-change in one type of field is proportional to a space-change in the other. These derivatives require that the **E** and **B** fields in EMR are in-phase. An important aspect of light's nature is its frequency. The frequency of a wave is its rate of oscillation and is measured in hertz, the SI unit of frequency, where one hertz is equal to one oscillation per second. Light usually has multiple frequencies that sum to form the resultant wave. Different frequencies undergo different angles of refraction, a phenomenon known as dispersion.

A monochromatic waves (a wave of a single frequency) consists of successive troughs and crests, and the distance between two adjacent crests or troughs is called the wavelength. Waves of the electromagnetic spectrum vary in size, from very long radio waves longer than a continent to very short gamma rays smaller than atom nuclei. Frequency is inversely proportional to wavelength, according to the equation:

$$v = f\lambda \ , \tag{1}$$

where v is the speed of the wave, f is the frequency and λ is the wavelength. As waves cross boundaries between different media, their speeds change but their frequencies remain constant. Electromagnetic waves in free space must be solutions of Maxwell's electromagnetic wave equation. Two main classes of solutions are known, namely plane waves and spherical waves. The plane waves may be viewed as the limiting case of spherical waves at a very large (ideally infinite) distance from the source. Both types of waves can have a waveform which is an arbitrary time function (so long as it is sufficiently differentiable to conform to the wave equation). As with any time function, this can be decomposed by means of Fourier analysis into its frequency spectrum, or individual sinusoidal components, each of which contains a single frequency, amplitude and phase. Such a component wave is said to be monochromatic. A monochromatic electromagnetic wave can be characterized by its frequency or wavelength, its peak amplitude, its phase relative to some reference phase, its direction of propagation, and its polarization.

Interference is the superposition of two or more waves resulting in a new wave pattern. If the fields have components in the same direction, they constructively interfere, while opposite directions cause destructive interference. An example of interference caused by EMR is electromagnetic interference (EMI) or as it is more commonly known as, radio-frequency interference (RFI). Additionally, multiple polarization signals can be combined (i.e. interfered) to form new states of polarization, which is known as parallel polarization state generation.

IV. ELECTROMAGNETIC RADIATION

In physics, electromagnetic radiation (EMR) consists of waves of the electromagnetic (EM) field, which propagate through space and carry electromagnetic radiant energy. It includes radio waves, microwaves, infrared, (visible) light, ultraviolet, X-rays, and gamma rays. All of these waves form part of the electromagnetic spectrum (Fig. 1).

Classically, electromagnetic radiation consists of electromagnetic waves, which are synchronized oscillations of electric and magnetic fields. Electromagnetic radiation or electromagnetic waves are created due to periodic change of electric or magnetic field. Depending on how this periodic change occurs and the power generated, different wavelengths of electromagnetic spectrum are produced. In a vacuum, electromagnetic waves travel at the speed of light, commonly denoted *c*. In homogeneous, isotropic media, the oscillations

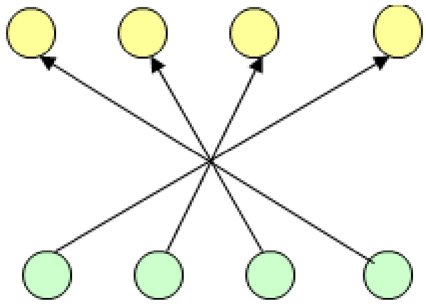

Figure 1. Radiation.

of the two fields are perpendicular to each other and perpendicular to the direction of energy and wave propagation, forming a transverse wave. The position of an electromagnetic wave within the electromagnetic spectrum can be characterized by either its frequency of oscillation or its wavelength. Electromagnetic waves of different frequency are called by different names since they have different sources and effects on matter. In order of increasing frequency and decreasing wavelength these are: radio waves, microwaves, infrared radiation, visible light, ultraviolet radiation, X-rays and gamma rays.

Electromagnetic waves are emitted by electrically charged particles undergoing acceleration, and these waves can subsequently interact with other charged particles, exerting force on them.

EM waves carry energy, momentum and angular momentum away from their source particle and can impart those quantities to matter with which they interact. Electromagnetic radiation is associated with those EM waves that are free to propagate themselves (“radiate”) without the continuing influence of the moving charges that produced them, because they have achieved sufficient distance from those charges. Thus, EMR is sometimes referred to as the far field. In this language, the near field refers to EM fields near the charges and current that directly produced them, specifically electromagnetic induction and electrostatic induction phenomena.

In quantum mechanics, an alternative way of viewing EMR is that it consists of photons, uncharged elementary particles with zero rest mass which are the quanta of the electromagnetic field, responsible for all electromagnetic interactions. Quantum electrodynamics is the theory of how EMR interacts with matter on an atomic level. Quantum effects provide additional sources of EMR, such as the transition of electrons to lower energy levels in an atom and black-body radiation. The energy of an individual photon is quantized and is greater for photons of higher frequency. This relationship is given by Planck's equation $E = hf$, where E is the energy per photon, f is the frequency of the photon, and h is Planck's constant. A single gamma ray photon, for example, might carry ~100,000 times the energy of a single photon of visible light.

The effects of EMR upon chemical compounds and biological organisms depend both upon the radiation's power and its frequency. EMR of visible or lower frequencies (i.e., visible light, infrared, microwaves, and radio waves) is called *non-ionizing radiation*, because its photons do not individually have enough energy to ionize atoms or molecules, or break chemical bonds. The effects of these radiations on chemical systems and living tissue are caused primarily by heating effects from the combined energy transfer of many photons. In contrast, high frequency ultraviolet, X-rays and gamma rays are called *ionizing radiation*, since individual photons of such high frequency have enough energy to ionize molecules or break chemical bonds [5]. These radiations have the ability to cause chemical reactions and damage living cells beyond that resulting from simple heating, and can be a health hazard. Electromagnetic energy travels in waves and spans a broad spectrum from very long radio waves to very short gamma rays. The human eye can only detect only a small portion of this spectrum called visible light. A radio detects a different portion of the spectrum, and an X-ray machine uses yet another portion.

V. ADVANTAGE OF THE 6G OVER THE 5G

The 6G is expected to support 1 terabyte per second. The 6G is expected to support 1 terabyte per second (Tbps) speeds. This level of capacity and latency will be unprecedented and will extend the performance of 5G applications along with expanding the scope of capabilities in support of increasingly new and innovative applications across the realms of wireless cognition, sensing and imaging. The 6G's higher frequencies will enable much faster sampling rates in addition to providing significantly better throughput. The combination of sub-mmWave (e.g. wavelengths smaller than one millimeter) and the use of frequency selectivity to determine relative electromagnetic absorption rates is expected to lead to potentially significant advances in wireless sensing solutions.

Additionally, whereas the addition of mobile edge computing – MEC is a point of consideration as an addition to 5G networks, MEC will be built into all 6G networks. Edge and core computing will become much more seamlessly integrated as part of a combined communications/computation infrastructure framework by the time 6G networks are deployed. This will provide many potential advantages as 6G technology becomes operational, including improved access to artificial intelligence (AI) capabilities.

The 6G is expected to launch commercially in 2030. The 6G is being developed in response to the increasingly distributed radio access network - RAN and the desire to take advantage of the terahertz - THz spectrum to increase capacity and lower latency. While some early discussions have taken place to define 6G, research and development - R&D activities will start in earnest in 2020. Many of the problems associated with deploying millimeter wave radio for 5G new radio are expected to be solved in time for network designers to address the challenges of 6G. It's expected that 6G wireless sensing solutions will selectively use different frequencies to measure absorption and adjust frequencies accordingly. This is possible because atoms and molecules emit and absorb electromagnetic radiation at characteristic frequencies and the emission and absorption frequencies are the same for any given substance.

VI. QUANTUM ENERGY

The word quantum derives from the meaning "how great" or "how much". The discovery that particles are discrete packets of energy with wave - like properties led to the branch of physics dealing with atomic and subatomic systems which is today called quantum mechanics. In physics, a quantum is the minimum amount of any physical entity (physical property) involved in an interaction. The fundamental notion that a physical property can be "quantized" is referred to as "the hypothesis of quantization". This means that the magnitude of the physical property can take on only discrete values consisting of integer multiples of one quantum. For example, a photon is a single quantum of light or of any other form of electromagnetic radiation. Similarly, the energy of an electron bound within an atom is quantized and can exist only in certain discrete values. Indeed, atoms and matter in general are stable because electrons can exist only at discrete energy levels within an atom. Quantization is one of the foundations of the much broader physics of quantum mechanics. Quantization of energy and its influence on how energy and matter interact (quantum electrodynamics) is part of the fundamental framework for understanding and describing nature.

Quant mechanical moving of electrons in atoms make magnetic field permanent feromagnets. Electrical particles with spin also have magnetic moment. Some electrical neutral particles, for example neutron, which have spin, also have magnetic moment because of distribution electricity in their inner structure. Particles without spin never have magnetic moment.

The magnetic field of permanents magnets can be quite complicated, especially near the magnet. The magnetic field of a small straight magnet is proportional to the magnet's strength (called its magnetic dipole moment). The equations are non-trivial and also depend on the distance from the magnet and the orientation of the magnet. For simple magnets, m points in the direction of a line drawn from the south to the north pole of the magnet. Flipping a bar magnet is equivalent to rotating its m by 180 degrees.

The magnetic field of larger magnets can be obtained by modelling them as a collection of a large number of small magnets called dipoles each having their own m. The magnetic field produced by the net magnetic field of identical (to a multiplicative constant) so that in many cases the distinction can be ignored. This is particularly true for magnetic fields, such as those due to electric currents, that are not generated by magnetic materials.

Equation of electron moving in magnetic field:

$$m\frac{dv}{dt} = m(g + v_r) \ , \qquad (2)$$

$$F_M = m\frac{dv}{dt} - m(g + v_r) \ , \qquad (3)$$

where v electrons speed moving, m electron's mass, g gravity acceleration, v_r friction acceleration, t time and F_M magnetic force. In this way is defined magnetic force and magnetic moment. By Eq. (3) can control and seek out conditions for wished force of magnetic field. If more magnetic field fixed in set then is obtained resulted magnetic force as shown in the following equation:

$$F_M = F_{M_1} + F_{M_2} + F_{M_3} + ...F_{M_N} \ . \qquad (4)$$

Magnetic force F_M is expressed in SI system.

In classical physics and chemistry is opinion that electromagnetic waves emission, transfer and absorption are performed continuous. Max Planck introduce assumption that electromagnetic radiation emitted in discrete energy quantity called energy quant [6]. It means energy emitted discontinuously, with break, in energy package (Fig.1). Energy of one quant proportional is frequency radiation f .

$$E = hf = h\frac{c}{\lambda} \ , \qquad (5)$$

where $h = 6.62 \cdot 10^{-34}\ Js$ universal Planck's constant, a c light velocity, f frequency and λ wave length of electromagnetic waves which emitted.

The photon energy formula is used to compute radiant energy in joules based on Planck's constant and a frequency of radiation in hertz.

Einstein is proved Planck's hypothesis on quant applying to describing photo effect. Einstein extended Planck's hypothesis that energy electromagnetic radiation transferring in quant to some obstacle which it absorbed. Instead Planck's name quant (small pieces), Einstein suggested name photon (light pieces) [7].

Idea about photons (quant) means the following: electromagnetic waves energy have discontinuous structure. These small energy pieces are rely photons (quant). Planck's formula for energy one photon shows that. If different electromagnetic waves have photons non-equal energy. Since photon's energy in opposition proportion with radiation waves length then minimal energy of photons have electromagnetic waves with maximum waves length, and such as radio waves, until maximum photons energy have path of specter which have minimal waves lengths and those are cosmic waves [8].

If electromagnetic waves emitted in the form of quant, with that energy each quant $E = hf$, than all emitted energy:

$$E = nhf \ , \qquad (6)$$

where $n = 1, 2, 3, 4.....$

According to Eq. (6) follows that:

- The smallest energy which can emitted equal energy one quant (energy cannot be less from this energy but cannot be emitted).
- All amount emitted energy must be equal integer product of energy of one quant.

Equation (5) can be write in the following form:

$$\begin{aligned} &If\ \omega = 2\pi f,\ f = \frac{\omega}{2\pi}, \\ &E = h\frac{\omega}{2\pi} = \frac{h}{2\pi}\omega = h^{\bullet}\omega . \qquad (7) \\ &h^{*} = 1.05 \cdot 10^{-34}\ Js \end{aligned}$$

Electromagnetic waves emitted in the form of quant, with total emitted energy $E = nhf$ to the final product. When these quant energies are high density then becomes substance. Thus substance in the high density energy.

The quant energy term can be derived according to the following equation:

$$\Delta p \Delta q = E \Delta t \ , \qquad (8)$$

where p probability of position, q is probability of time, E is quant energy and t is time. This formula includes no determine principle. Vibration change can be defined as:

$$\Delta f = \frac{E}{h} \ , \qquad (9)$$

where f frequency.

Like other waves, electromagnetic waves have properties of speed, wavelength, and frequency.

Information quant is:

$$I_v = -\sum_{i}^{n} p_i \log_2 p_i \ . \qquad (10)$$

The new information value can be expressed as:

$$I_v^{NEW} = -\sum_{i=1}^{n} p_i(out/in)\log_2 p_i(out/in) \ , \ (11)$$

where I_v information value and p_i probability.

VII. How Shield From Electromagnetic Waves

Some frequency of electromagnetic waves are harmful for biochemical processes in the human body.

Typical materials used for electromagnetic shielding include sheet metal, metal screen, and metal foam. Any holes in the shield or mesh must be significantly smaller than the wavelength of the radiation. Electromagnetic shielding that blocks radio frequency. Electromagnetic radiation is also known as radio frequency shielding. The shielding can reduce the coupling of radio waves, electromagnetic fields, and electrostatic fields. A conductive enclosure used to block electrostatic fields is also known as a Faraday cage at is being kept out, or the enclosure will not effectively approximate unbroken conducting surface.

Thin amounts of plastic wrap, was paper, cotton and rubber are not likely to interfere with radio waves. However, aluminum foil, and other electrically conductive metals such as copper, can reflect and absorb the radio waves and consequently interferes with their transmission.

The polymer 11 percent gold by weight, and the gold atoms in the substance efficiently scatter or absorb most forms of radiation, including X-rays. Chemically incorporated into a polymer, gold is less poisonous than other heavy metals that also block radiation.

The stop frequency is the end (highest) frequency of the frequency band to analyze. For information and other ways to set the start frequency. The maximum stop frequency can measure by the measurement hardware.

VIII Conclusion

In this paper properties of the electromagnetic waves and information were examined. Quantum electrodynamics of energy and its influence on how energy and matter interact is part of the fundamental framework for understanding nature. The quant energy term and information terms were derived.

Health shielding from electromagnetic waves was studied.

References

[1] Stratton, J. A. (1941). Chapter V Planex waves in unbounded, isotropic media. *ElectromagneticTheory*. McGraw Hill Book Company, New York, N.Y.

[2] Jeansi, J. (1947). *The growth of Physical Science*. Cambridge University Press, London.

[3] Pursell Morin (2013). *Electricity and Magnetism (3rd ed.).* Cambridge University Press, New York, N.Y.

[4] Savković Stevanović, J. (2019). Magnetic field. *Computers and Ecological Engineering Journal, 15*(3), 93-98.

[5] Savković Stevanović, J. (2019). Quantum energy and chemical reaction kinetics. *Computers and Ecological Engineering Journal*, *15*(1), 1-6.

[6] Planck, M. (1901). Ueber das Gesetz der Energieverteilung im Normalspectrum (On the Law of Distribution of Energy in the Normal Spectrum). *Annalen der Physik, 309*(3), 553. doi:10.1002/andp.19013090310.

[7] Einstein, A. (1905). Über einen die Erzeugung und Verwandlung des Lichtes betreffenden heuristischen Gesichtspunkt. *Annalen der Physik (in German), 17*(6), 132–148.

[8] Brown, T., LeMay, H., & Bursten, B. (2008). *Chemistry: The Central Science*. Upper Saddle River, NJ, Pearson Education. ISBN 0-13-600617-5.

Providing Effective Marketing Strategies for Local Energy Communities' Resources, Renewable Energy and Demand Side Management

Behrouz Niroomandfam[1], Amir Niromandfam[2]

[1]Islamic Azad University, Miandoab, Iran
[2]Sahand University of Technology, Tabriz, Iran

Abstract—**Nowadays, the concept of local energy communities (LEC) is proposed in the modern societies in which, not only the goal is satisfying the technical constraints, but also is providing the service based on the citizens' preferences. To answer the environmental concerns and in response to the urgent demand of energy generation, these communities strive to employ the renewable energy sources (RESs) and demand side resources (DSRs). The first objective of this paper is providing a mathematical model for the energy citizens' viewpoints which enables the LEC to employ optimally the DSRs. The second objective is establishing an energy marketing scheme which enables the small size end-use consumers to participate optimally in the electricity market. In addition to participation in the market, this DSRs will be also utilized to cover RESs' marketing challenges. The main challenge of RESs is their intermittent nature of energy sources which limits their participation in the electricity market. In exchange of covering the RERs output power uncertainty, the participated citizens receive incentive based on their behavior model. In the numerical section three scenarios are considered to cover the RES generation's uncertainty. At first, second and third scenarios, the RES's operator utilizes trading with the imbalance energy market, employs the proposed DSRs and uses both of them. The results illustrate that although for less output power mismatch of RER utilizing the DSRs has the lowest cost, by increasing the mismatch incentive cost will be increased hence the third scenario will be economic.**

Keywords - demand side management, renewable energy, electricity market, local energy communities

I. INTRODUCTION

Due to the lack of sufficient quantity of fossil fuels and environmental concerns, the need of renewable energy sources has become an important issue in electric power system. The main feature of many RESs is the random nature of these resources which causes uncertainty in scheduling their output power, therefore they cannot participate with full capacity in electricity power market [1]. To enable RESs be compatible in power market, supportive policies have been designed and implemented in many countries. Increasing the penetration of renewable energy sources in one hand, and achieving to the objectives of power system restructuring on the other hand make the supportive policies lower and lower, so they have to adapt themselves to the power market conditions [2]. To relief market problems of RESs such as Wind-PV generation, numerous researches have been done and divided in two main categories: 1) various researches survey methods to improve RESs forecasting models and thereby reduce the uncertainty in a day-ahead scheduling, 2) some other researches implement renewable sources in the joint with energy storage units or suitable demand side management (DSM) approach to compensate renewable power generation uncertainty [3-4].

In this paper, Wind-PV energy are scheduled via LEC concept to contribute in a day-ahead

ISBN: 978-86-82602-01-9

NOMENCLATURE

A. *Variables*

x_k	Load curtailment of kth customer type.
Ω_k	Customer sorting variable.
C_i	DR cost in ith bus.
C_{total}	Total DR cost.
IC_i	Incremental cost of DR at bus i.
$EENS_0$	EENS before implementing DR.
$EENS_{DR}$	EENS after implementing DR.
$\Delta EENS$	EENS improvement by DR.
T_Γ	Interruption duration by outage source Γ.
f_Γ	Failure rate by outage source Γ.
$Loss_0$	Active power loss before implementing DR.
$Loss_{DR}$	Active power loss after implementing DR.
$\Delta Loss$	Active power loss improvement by DR.
I_{0b}	Electricity current flow among bth branch before implementing DR.
I_{DRb}	Electricity current flow among bth branch after implementing DR.
$P_{D_0 i}$	Active power demand at ith bus before implementing DR
$P_{D_{DR}\, i}$	Active power demand at ith bus after implementing DR
$P_{Di,t}$	Active power demand at ith bus at period of t.
$P_{DRi,t}$	*DR* capacity at ith bus at period of t.
λ_t^+	Positive imbalance marketprice at period of t.
λ_t^-	Negative imbalance market price at period of t.
λ_t^D	Day-ahead electricity price at period of t.
λ_t^{UP}	Positive compensating imbalance prices
λ_t^{DW}	Negative compensating imbalance prices

B. *Functions*

$c(.)$	Customer curtailment cost function.
$b_c(.)$	Customer benefit function.
$u(.)$	Customer monetary benefit function.
$\xi(.)$	Customer cost function.
$inc(.)$	Incentive payment function.

C. *Parameters*

$k_1,\ k_2$	Customer cost function coefficients.
k_3	Customer motivation factor.
r	Rate of monetary credit
μ_k	0/1 Variable.
Z_b	Branch impedance.
$P_{DR,i}^{\max}$	Maximum capacity of *DR* resources.

D. *Sets*

N	Number of buses.
N_k	Number of customer types.
N_Γ	Number of outage sources (power line, transformer, switch, etc.).
N_b	Number of branches.

E. *Indices*

i, j	Bus index.
k	Customer type index.
Γ	Outage source index.
b	Branch index.

power market. Also, DR resources is utilized to cover RESs' output uncertainty. A multi-objective optimization problem is solved using improved non-dominated sorting genetic algorithm (NSGA-II) to: 1) determine the best locations of DR resources based on the technical objectives such as EENS and power loss reduction; 2) minimize customer cost function as customer behavior aspect. To maximize the profit, LEC offers based on optimistic RESs generation scenario in the day-ahead market where the output mismatch is compensated via the DR resources.

The rest of this paper is organized as follows: Section II provides a description of proposed method. In Section III, DR model will be described. Section IV and V are dedicated to describe EENS and power loss model. Section VI presents numerical results of the case study. Finally, Section VII specifies the conclusions.

II. Problem Description

A power producer owning a Wind-PV units faces uncertainty referenced by the nature of these resources, wind velocity and solar irradiance. This uncertainty affects the participation strategy in energy market and also the profit of these resources. Thus, the market strategy for Wind-PV units must take into account these uncertainties and imbalance power in order to capture the most possible profit from the market. Power imbalance is defined as the difference between the level of actual delivered energy and the level of contracted energy in the day-ahead market which can be negative, zero or positive [5]. In this market, negative imbalance price (λ^-) corresponds to shortage generation and

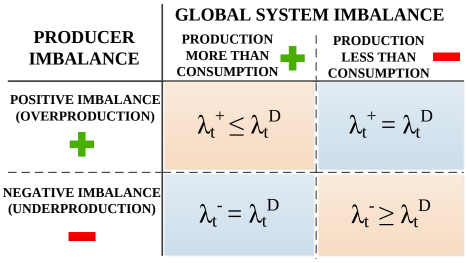

Figure 1. Imbalance prices depending on producer and global system conditions.

positive imbalance price (λ^+) represents excess generation price. In European electricity markets, λ^{UP} and λ^{DW} are the compensating imbalance prices comes from real-time market [6]. Fig. 1 demonstrates imbalance prices for different possible cases. With the producer and global system imbalances are in different status (one positive and the other negative), the imbalance price is the same as the day-ahead market price (λ^D). When of them are in the same status, the imbalance price may be different from the day-ahead market price as shown in this figure. For positive (negative) global system imbalance, the power producers have the possibility of selling (buying) its excess (shortage) generation at a price smaller (higher) than the day-ahead market-clearing price. If the system imbalance is positive or negative, the imbalance prices are defined as Eqs. (1) and (2).

$$\begin{cases} \lambda_t^+ = \min(\lambda_t^D, \lambda_t^{DW}) \\ \lambda_t^- = \lambda_t^D \end{cases}, \qquad (1)$$

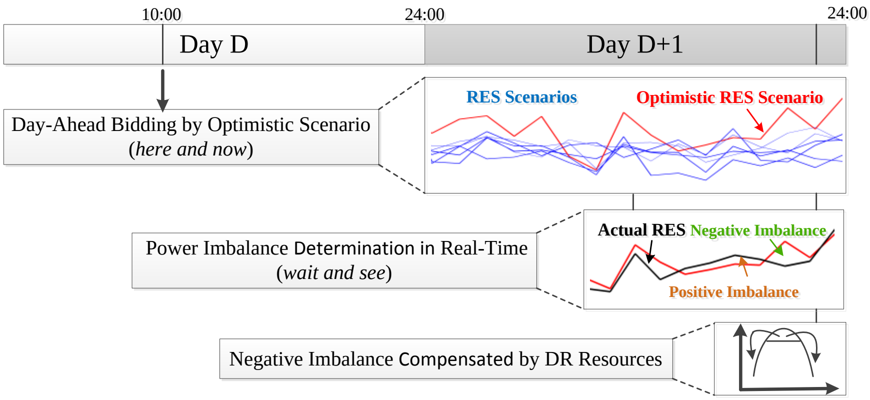

Figure 2. Two-step RESs bidding procedure in day-ahead market.

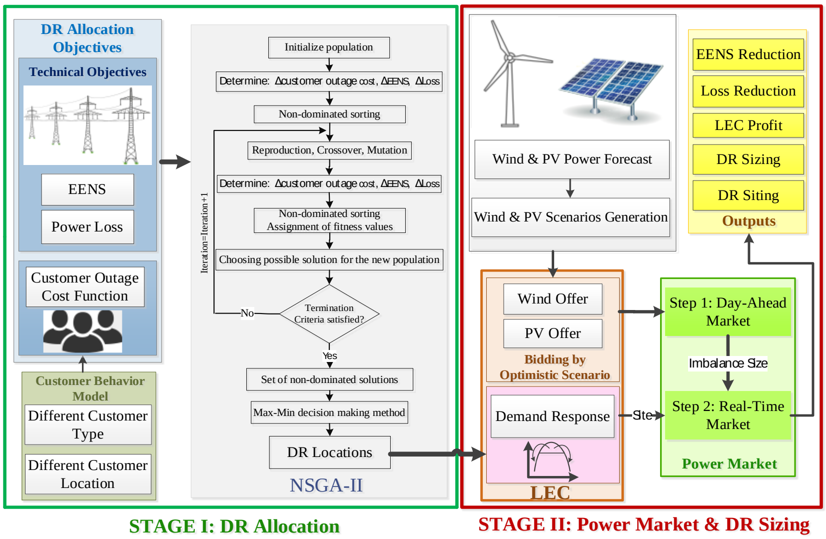

Figure 3. Hierarchy of proposed method.

$$\begin{cases} \lambda_t^+ = \lambda_t^D \\ \lambda_t^- = \max(\lambda_t^D, \lambda_t^{UP}) \end{cases}. \quad (2)$$

The main goal of this paper is obtaining the maximum profit from wind-PV units in the day-ahead market. Market participation procedure of these sources will be performed in two steps as shown in Fig. 2. At the first step (here and now step), wind-PV generation scenarios will be forecasted as the LEC resources. Because of the intermittent nature of RESs, the existence of a mismatch between the forecasted generation and physical delivered energy is predictable. In order to obtain maximum profit from the market, this paper will use the most optimistic renewable generation scenario for bidding in day-ahead power market. Bidding with optimistic scenarios, positive energy imbalance (actual generation more than the one offered) will have the lowest level, so maximum profit can be obtained from day-ahead auction. But it is obvious that the negative energy imbalance will be increased. In the second step (wait and see step), LEC can update wind-PV generation data in few minutes before of clearing time. Therefore, DR resources alleviate the negative imbalance of renewable energy. The proposed model needs DR resources with a quick response, hence this paper uses incentive-based DR program which allows LEC operator directly controls the customers' consumption. The other main goal of this paper is to relieve transmission network problems such as EENS and active power loss. Customer behavior is another attracted criteria which will be taken into account.

Based on the above description, Fig. 3 illustrates the two-stage programming model in which, DR resources will be allocated via NSGA-II multi-objective model at the first stage. In the second stage, the LEC operator will offer wind-PV energy in day-ahead market based on the optimistic generation scenario, and determine the size of DR resources to meet the energy mismatch.

III. DR Model

Customers will participate in DR programs, if they are offered appropriate incentives. These incentives would be optimized if the utility can estimate the outage costs of the customers [7-8]. Several functions can be used as customer outage cos function but it is necessary that calibrated the cost function with the real data obtained from demand side management programs [9]. The main goal of this calibration process is to find coefficients for real-word customers' cost functions.

The first step is identifying customer outage cost function based on utility existing data. It is safe to assume the cost of customer outage will grow progressively as the demand curtailment increased. Also, the marginal benefit of the customer will be decreased by increasing electricity consumption. For linear marginal benefit function, the outage cost function will have a quadratic form. This paper uses quadratic form of the outage cost function which is proposed in [10]. This function sorts the customers in the order of the least willing to the most willing to participate in DR program. A general quadratic form of customer outage cost function can be formulated as Eq. (3).

$$c(\Omega_k, x_k) = k_1 x_k{}^2 + k_2 x_k (1 - \Omega_k) \cdot \quad (3)$$

The next step is calibrating the outage cost function with the real-word data considering x as load curtail amount (kW) of kth customer type with the rate of r \$ monetary credit. Hence, the benefit function for a customer under a demand management contract is described as Eq. (4). Maximization of the benefit function yields conditions Eqs. (5) and (6). Coefficients k_1 and k_2 are determined based on the customer load curtailment, amount of monetary credit and sorting condition.

$$b_c(\Omega_k, x_k) = r x_k - c(\Omega_k, x_k), \quad (4)$$

$$\frac{\partial b_c(\Omega_k, x_k)}{\partial x_k} = r - \frac{\partial c(\Omega_k, x_k)}{\partial x_k} = 0, \quad (5)$$

$$r - 2k_1 x_k - k_2 (1 - \Omega_k) = 0. \quad (6)$$

To ensure that the designed DR level will be implemented, the utility can add motivation factor to incentive customers. This motivation payment makes sure the customers do not try to take the adjacent contracts. So based on Eq. (7), customers who are more willing to participate in DR are paid more incentives trough the coefficient k3.

$$\begin{aligned} c(\Omega_k, x_k) = k_1 x_k{}^2 + k_2 x_k (1 - \Omega_k) + \\ + k_3 x_k (\Omega_k - \Omega_{k-1}) \end{aligned}. \quad (7)$$

Each bus could have combination of different types of customer. Binary variable µk determines the customers' type in each bus. To obtain the optimal curtailment level of each customers' type in each bus, a Lagrangian function is utilized which determines incremental cost of load curtailment in each bus. Lagrangian function is used to minimize incentive payments which are paid to the customer Eqs. (8)-(15).

$$\min \; C_i^{DR} = \sum_{k=1}^{N_k} c(x_k)\mu_k , \tag{8}$$

Subject to:

$$\begin{aligned} c(x_k) = k_1 {x_k}^2 + k_2 x_k (1-\Omega_k) + \\ + k_3 x_k (\Omega_k - \Omega_{k-1}) \end{aligned} , \tag{9}$$

$$\sum_{k=1}^{N_k} x_k \mu_k = P_{DR,i} \;, \tag{10}$$

$$0 \le P_{DR,i} \le P_{DR,i}^{\max} \;, \tag{11}$$

$$\frac{dc(x_k)}{dx_k}\mu_k = IC_i \mu_k , \quad (\Pi_k \in N_K) \;, \tag{12}$$

$$c(x_k) \ge 0 \;, \tag{13}$$

$$x_k \ge 0 \;, \tag{14}$$

$$\mu_k = 0 \;\; or \; 1 . \tag{15}$$

Equation (9) is the customer cost compatibility constraint, and Eq. (10) represents the sum of load curtailment of various customers in each bus. Incremental cost of DR is determined by Eq. (12). Based on the above description, the first goal in DR allocation is to minimize customers' outage cost function as DR programs cost described by Eq. (16).

$$Objec1: \;\; \min \;\; C_t^{DR} = \sum_{i=1}^{N} C_i^{DR}, \quad \forall t . \tag{16}$$

IV. Expected Energy Not Supplied

The expected energy not supplied is chosen in this paper as the reliability index for composite power system which takes into account the outage duration time. In order to calculate system expected unsupplied energy due to power outage, the amount of expected energy not supplied to the customers at all load point has to be calculated as follows [10]:

$$EENS_0 = \sum_{i=1}^{N}\sum_{\Gamma=1}^{N_\Gamma} P_{D_0\, i} \times T_\Gamma \times f_\Gamma \;, \tag{17}$$

$$EENS_{DR} = \sum_{i=1}^{N}\sum_{\Gamma=1}^{N_\Gamma} P_{D_{DR}\, i} \times T_\Gamma \times f_\Gamma \;, \tag{18}$$

$$\begin{aligned} Objec2: \; \max : \Delta EENS = \\ = ENNS_0 - EENS_{DR} \end{aligned} . \tag{19}$$

V. Active Power Loss

Transmission losses have a significant effect on active power generation and power transmission cost, so finding a method which reduces these effects is essential to improve economic efficiency of the electric energy market. Minimizing active power loss in the transmission network can be modelled as follows [11]:

$$Loss_0 = \mathrm{Re}\,al\left\{\sum_{b=1}^{N_B}(Z_b \times {I_{0b}}^2)\right\} \;, \tag{20}$$

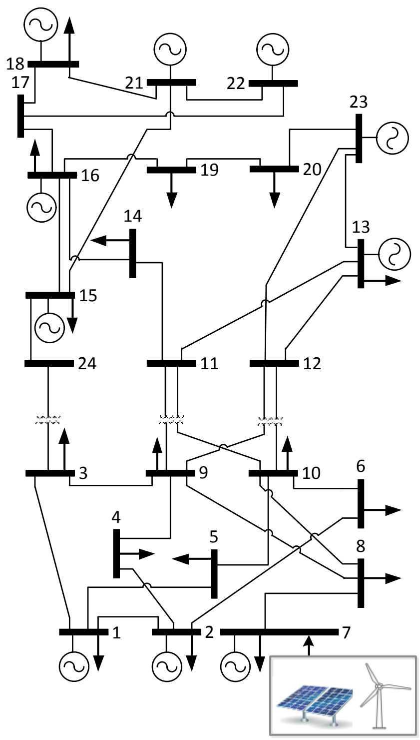

Figure 4. 24-bus IEEE Reliability Test System (RTS) with wind-PV units.

$$Loss_{DR} = \mathrm{Real}\left\{\sum_{b=1}^{N_B} (Z_b \times I_{DRb}{}^2)\right\}, \quad (21)$$

$$\begin{aligned} Objec3: \ \max: \Delta Loss = \\ = Loss_0 - Loss_{DR} \end{aligned} . \quad (22)$$

VI. NUMERICAL STUDY

The proposed algorithm has been tested on 24-bus IEEE reliability test system (RTS) [12]. The simulations for the first and second stages are performed in MATLAB environment by MATPOWER OPF functions and GAMS software environment, respectively. The single-line diagram of the test system is given in Fig. 4 where Wind-PV units are installed in bus 7. The historic and prognosis data of wind farm power are extracted from Nord Pool market (Latvia) in February 23, 2017 [12]. This paper uses different cases as the optimistic scenarios which are generated by adding different positive percentage to forecasted data and showed in Figs. 5 and 6. Also Fig. 7 shows positive and negative energy deviations of RESs for each case.

In order to determine the coefficients of customer outage cost function, customers' data are taken from [10]. Table I demonstrates utility data of load curtailment. In order to these data be useable for selected power system, this paper assumes these customers are currently on a DR program that pays them a fixed rate of 10$ per

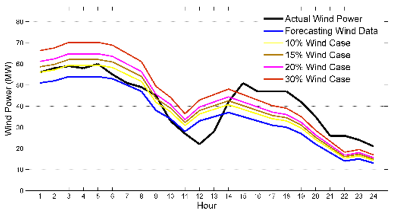

Figure 5. Different bidding cases of wind energy and actual wind power.

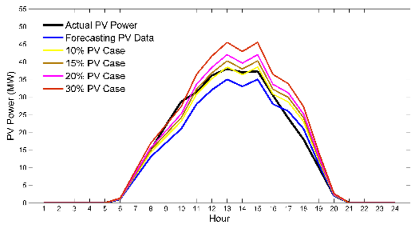

Figure 6. Different bidding cases of PV energy and actual PV power.

available MWh for curtailment. Also, for simplicity, it is assumed only four types customers (customer type 1, 5, 8 and 10) exist in each load bus as shown in Table II. For example at bus 5, only customer type 1 and 5 exist. Hence customer cost coefficients k_1 and k_2 are calculated as 6.41 and 9.243 respectively. Also the incentive motivation factor k_3 is assumed to be 1.

TABLE I. UTILITY DATA OF LOAD CURTAILMENT [11].

Customer type	**Amount of load (kW)**	**Ω**
1	59	0
2	100	0.0529
3	130	0.0916
4	134	0.0968
5	151	0.1187
6	184	0.1613
7	200	0.1819
8	349	0.3741
9	364	0.3935
10	780	1

TABLE II. CUSTOMER TYPES IN EACH BUS.

Load Point	**Customer type**			
	Ω_1	**Ω_5**	**Ω_8**	**Ω_{10}**
Bus01	1	0	0	0
Bus02	0	1	0	0
Bus03	0	0	1	0
Bus04	0	0	0	1
Bus05	1	1	0	0
Bus06	1	0	1	0
Bus07	1	0	0	1
Bus08	0	1	1	0
Bus09	0	1	0	1
Bus10	0	0	1	1
Bus13	1	1	1	0
Bus14	1	1	0	1
Bus15	1	0	1	1
Bus16	0	1	1	1
Bus18	1	1	1	1
Bus19	1	1	1	1
Load20	1	1	1	1

For implementing the proposed algorithm, it is assumed that all load buses could have maximum DR capacity equal to 5% of their demand. To determine DR resources locations, NSGA-II method is performed for 24 hours at first stage. At the end of evolutionary computation, a Pareto-front which satisfies all objectives is achieved as shown in Fig. 8. This 3D figure is drawn with respect to EENS, customer cost function and power loss reduction objectives. Finally, bus 8, 10, 13 and 14 are determined as DR locations. Based on the above description, the locations are determined by NSGA-II multi-objective method but size of the DR resources depends on the price of the negative power imbalance. Fig. 9 shows day-ahead market price, downward and upward.

LES has options to sell (buy) energy to (from) imbalance market or use DR resources to compensate its energy imbalance. Fig. 10 shows the amount of LEC profit enhanced by selling the positive imbalance energy to the imbalance market when generated energy is higher than bidding energy for each scenario.

Negative imbalance cost includes two parts, one part is related to DR costs and the other is related from buying energy from balancing market. So, Fig. 11 illustrates negative imbalance and DR cost. For negative imbalance compensation, DR resources are used until the Incremental Cost (IC) of DR be less than the negative imbalance price. For the higher IC, the LEC has to buy energy from the imbalance market. Using The IC data, the LEC can estimate the cost of one additional MW of DR resources. Negative imbalance market price and DR IC are shown in Fig. 12.

EENS and active power loss reduction used as technical objectives of LEC, so Figs. 13 and 14 illustrate EENS and active power loss reduction of the power system as the results of DR program implementation. By surveying these results, one can observe EENS and loss reduction don't have strict relation with DR levels, for example in hour 11 and for 10% positive RESs case, EENS and active power loss reduction are high with respect to DR resources.

As mentioned earlier, LEC has the goal to get maximum profit. Two types of profit could be available, one comes from day-ahead market bidding and the other comes from selling excess power. As shown in Fig.15, by increasing optimistic scenarios, DR cost and negative imbalance cost will be saturated and increased

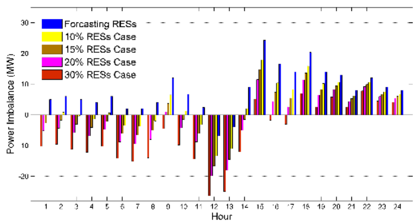

Figure 7. Positive and negative energy deviations of different RESs cases.

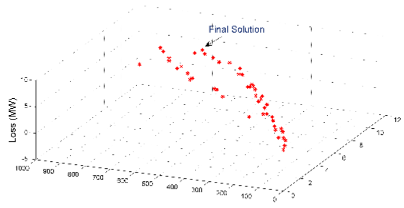

Figure 8. Pareto-optimal front for DR allocation.

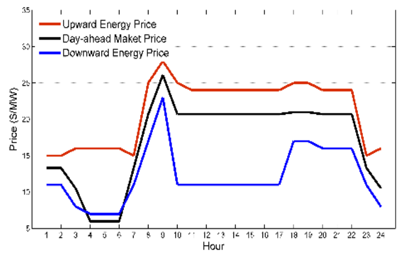

Figure 9. Day-ahead market and downward/upward energy prices.

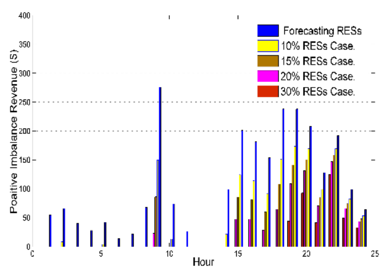

Figure 10. Positive imbalance revenue of different cases.

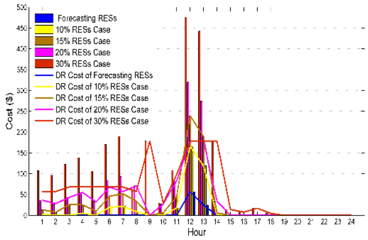

Figure 11. Negative imbalance and DR cost of different cases.

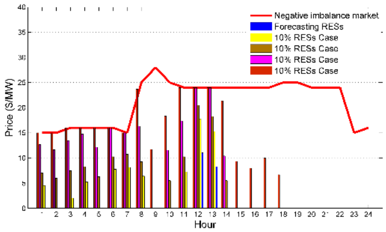

Figure 12. Negative imbalance market price versus IC of DR.

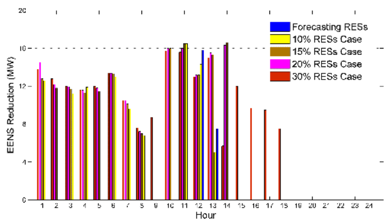

Figure 13. EENS reduction by DR resources of different cases.

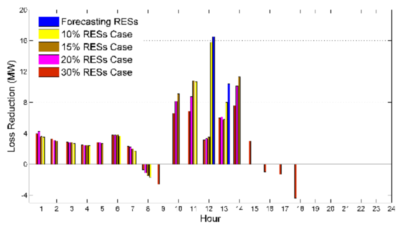

Figure 14. Active power loss reduction by DR resources of different cases.

exponentially, respectively. Fig. 16 illustrates the day-ahead trading and overall profits of the LEC versus different optimistic cases. Finally, Table III represents different technical objectives versus different optimistic cases.

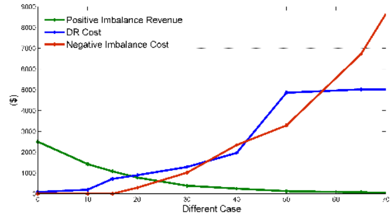

Figure 15. Imbalance profit/cost and DR cost versus different cases.

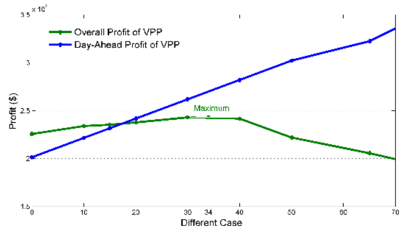

Figure 16. Total profit and day-ahead trading profit versus different cases.

VII. Conclusions

A new method proposed in this paper to support local energy communities who faces wind and PV generation uncertainty. The proposed LEC uses DR resources to add the flexibility to RESs and enables them to participate efficiently in the day-ahead market. LEC bids RESs' energy with the optimistic scenarios in day-ahead market to restrict the problem of output power mismatch of RESs to only negative imbalance, where DR resources were used to address the problem of the negative power mismatch. An improved DR allocation model has been used in this paper which takes into account the power loss reduction and reliability improvement and the concept of customers outage cost function. By utilizing of customers' outage cost function, incentive to customers could be determined optimally.

TABLE III. Summary of Technical Results.

Case	EENS Reduction (MW)	Power Loss Reduction (MW)
0% RESs Case	26.9	23.3
10% RESs Case	46.7	100.9
15% RESs Case	56.2	157.1
20% RESs Case	59.5	170.2
30% RESs Case	41.5	206.1

REFERENCES

[1] Niromandfam, A., Pour, A. M., & Zarezadeh, E. (2020). Virtual energy storage modeling based on electricity customers' behavior to maximize wind profit. *Journal of Energy Storage, 32*, 101811.

[2] Niromandfam, A., Yazdankhah, A. S., & Kazemzadeh, R. (2020). Modeling demand response based on utility function considering wind profit maximization in the day-ahead market. *Journal of Cleaner Production, 251*, 119317.

[3] Amrouche, S. O., Rekioua, D., Rekioua, T., & Bacha, S. (2016). Overview of energy storage in renewable energy systems. *International journal of hydrogen energy, 41(*45), 20914-20927. Anderson, C. L., & Cardell, J. B. (2014). A decision framework for optimal pairing of wind and demand response resources. *IEEE Systems Journal, 8*(4), 1104-1111.

[4] Wang, X., Palazoglu, A., & El-Farra, N. H. (2015). Operational optimization and demand response of hybrid renewable energy systems. *Applied Energy, 143*, 324-335.

[5] Gomes, I. L., Pousinho, H. M. I., Melicio, R., & Mendes, V. M. F. (2017). Stochastic coordination of joint wind and photovoltaic systems with energy storage in day-ahead market. *Energy, 124*, 310-320.

[6] Guerrero-Mestre, V., de la Nieta, A. A. S., Contreras, J., & Catalao, J. P. (2015). Optimal bidding of a group of wind farms in day-ahead markets through an external agent. *IEEE Transactions on Power Systems, 31*(4), 2688-2700.

[7] Niromandfam, A., Choboghloo, S. P., Yazdankhah, A. S., & Kazemzadeh, R. (2020). Electricity customers' financial and reliability risk protection utilizing insurance mechanism. *Sustainable Energy, Grids and Networks, 24*, 100399.

[8] Niromandfam, A., Yazdankhah, A. S., & Kazemzadeh, R. (2020). Design of reliability insurance scheme based on utility function for improvement of distribution grid reliability. *Journal of Operation and Automation in Power Engineering, 8*(3), 257-272.

[9] Niromandfam, A., Yazdankhah, A. S., & Kazemzadeh, R. (2020). Design of reliability insurance scheme based on utility function for improvement of distribution grid reliability. *Journal of Operation and Automation in Power Engineering, 8*(3), 257-272.

[10] Fahrioglu, M., & Alvarado, F. L. (2001). Using utility information to calibrate customer demand management behavior models. *IEEE transactions on power systems, 16*(2), 317-322.

[11] Ogunjuyigbe, A. S. O., Ayodele, T. R., & Akinola, O. O. (2016). Impact of distributed generators on the power loss and voltage profile of sub-transmission network. *Journal of Electrical Systems and Information Technology, 3*(1), 94-107.

[12] Ordoudis, C., Pinson, P., Morales, J. M., & Zugno, M. (2016). *An updated version of the IEEE RTS 24-bus system for electricity market and power system operation studies.* Technical University of Denmark.

Investigation of Structural, Microstructural and Optical Properties of ZnO, Zn0.90Co0.05M0.05O (M= Na, Al, Cd, Cu) Thin Films by USP Method for Photovoltaic Applications

Sabrina Roguai[1], Abdelkader Djelloul[2]

[1,2]Department of Science of the Matter, Abbes Laghrour University Khenchela, Algeria

Abstract—**Pure and codoped nanocrystalline single-phase films of Zn0.90Co0.05M0.05O (M=Al, Cd, Na, Cu) were successfully synthesized by the ultrasonic spray pyrolysis technique. Structural analysis by X-ray diffraction shows that all films have a hexagonal wurtzite structure with an average crys-tallite size in the range of 19-25 nm. SEM analysis revealed that Cd and Na preserve the shape of the nanopetals observed with the ZnO films, while doping with Al or Cu promotes the for-mation of dense films consisting of nanorods. For optical properties, by applying the Le-ven-berg-Marquardt least squares method, the experimental transmittance data were perfectly fitted with the transmittance data calculated via a combination of the Wemple-DiDomenico model, the bandgap energy, thickness and refractive index are calculated.**

Keywords - thin films, microstructure, optical properties

I. INTRODUCTION

Zinc oxide based semiconductors showed a great interest in recent years because of their wide range applications, in particular in the field of spintronics. ZnO is a semicon-ductor with a large bandgap ($Eg = 3.31\,eV$), large exciton binding energy ~60 meV at room temperature [1] and a transmittance of approximately 0.9 in the visible region. Among these semiconductors, ZnO that is doped with a small amount of transition metal ions, in particular Co-doped ZnO system has been highly investigated. It is important to note that the defect environment can be altered when a dopant atom M (Co, Al, Cd, Cu and Na) substitutes a Zn atom. Therefore, it is worth investigating the doping effect on various properties of ZnO: M system.

In this work, of ZnO, Zn0.90Co0.05M0.05O (with M=Al, Cd, Na and Cu) thin films are deposited by ultrasonic spray pyrolysis (USP) technique. The effectsof the nature of the co-doping element M on structure, microstructure properties are discussed.

II. EXPERIMENTAL METHODS

A. Film Preparation

In this study were prepared by ultrasonic spray pyrolysis. The solution used for the investigated films has the following composition: 0.01 M of zinc acetate; 50 ml deionised water; 20 ml CH3OH; and 30 ml C2H5OH. Cobalt nitrate hexahydrate 5% (Co, at.%), cop-per acetate 5% (Cu, at.%), cadmium acetate 5% (Cd, at.%), aluminium nitrate hexahydrate 5% (Al, at.%)] and sodium chloride 5% (Na, at.%) has been used as the Co, Cu, Cd, Al and Na source. A small amount of acetic acid was added to the aqueous solution for adjusting the pH value to about 4.8, in order to prevent the

ISBN: 978-86-82602-01-9

formation of hydroxides. Thin films were deposited onto glass substrates at the temperature of 450 °C and the deposition time was fixed at 30 and 45 min [2-4].

B. *Characterization Techniques*

X-ray diffraction patterns were recorded using high resolution Rigaku Ultima IV powder X-ray diffractometer equipped with Cu Ka radiation ($k = 1.5418\,Å$). The film morphology was examined using a (Quanta™ 250 FEG-SEM from FEI company) scanning electron microscope.

III. Results and Discussion

A. *Structure Analysis*

X-ray diffraction patterns of as-prepared pure ZnO, 5% Co-doped ZnO and co-doped Zn0.90Co0.05M0.05O with M=Na, Al, Cu, and Cd system (Fig. 1) reveal the formation of pure single wurtzite phase as confirmed with JCPDS Card No. 00-036-1451. The intensity of diffraction peaks varies considerably and non-homogeneously, depending on the nature (its atomic number) of the doping element and its real concentration within the films after deposition (which will be discussed in SEM/EDX section).

A preferred orientation along (0 02) direction for all compositions is observed, but the grains orientation along this direction is dependent as well on the nature of the doping element. This was associated with the value of the surface free energy, which might be minimum for ZnO (0 02) plane during the growth process.

The results of structural parameters are reported in Table I, the obtained values in this study are slightly smaller than the values $a = 3.2521\,Å$ and $c = 5.2078\,Å$ of ZnO

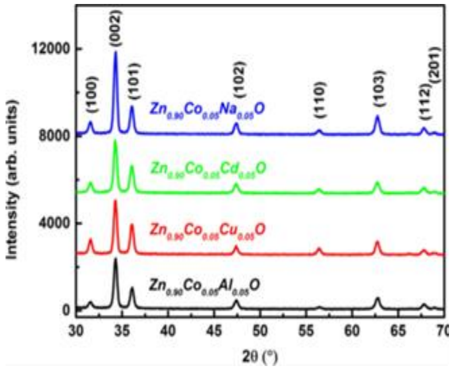

Figure 1. XRD patterns of Zn0.90Co0.05M0.05O (M=Na, Al, Cu, and Cd).

powder synthesized by an auto-combustion method [5].

The values for Co-doped ZnO are higher than that of pure ZnO, which are similar to our results. Moreover, it is observed that the variation of lattice parameters after codoping is in agreement with the change of the ionic radius of the substituting element ($r[Co2+] = 0.079\ nm$; and $r[Cu2+] = 0.087\ nm$; $r[Na+] = 0.116\ nm$; $r[Al3+] = 0.068\ nm$; and $r[Cd2+] = 0.109\ nm$) by occupying $Zn2+ (r = 0.088\ nm)$ sites within ZnO crystal attice. The crystallite size seems to not being affected by the nature and the ionic radius of the doping element (M=Na, Al, Cu and Cd), the average value is around 20 nm. However, the value of microstrain varies considerably with M, which can be attributed to its valence and ionic radius.

TABLE I. X-RAY DIFFRACTION RESULTS.

Composition	Crystallite size (nm)	Microstrain (%)	Lattice parameters (Å)
ZnO	25	0.266	3.2542
$\mathbf{Zn_{0.90}Co_{0.05}Na_{0.05}O}$	23	0.163	3.2603
$\mathbf{Zn_{0.90}Al_{0.05}Na_{0.05}O}$	21	0.212	3.2571
$\mathbf{Zn_{0.90}Cu_{0.05}Na_{0.05}O}$	22	0.126	3.2592
$\mathbf{Zn_{0.90}Cd_{0.05}Na_{0.05}O}$	19	0.194	3.2601

B. Microstructural Observations

Images of the surface of the films is reported in Fig. 2. To study the effect of the co-dopant type, SEM images were compared to those recorded on pure ZnO (Fig. 3) and Co-doped ZnO (Fig. 4). The doping with Co seems to preserve the ZnO microstructure characterized by the presence of nanopetals emerging perpendicularly to the film surface.

One can notice a slight effect of Co-doping on reducing the size and length of nanopetals which is in good agreements with the reduction of crystallite size observed by XRD data. For these two films, the nanopetals have a thickness of 20 nm and a length (or size) of 200–350 nm.

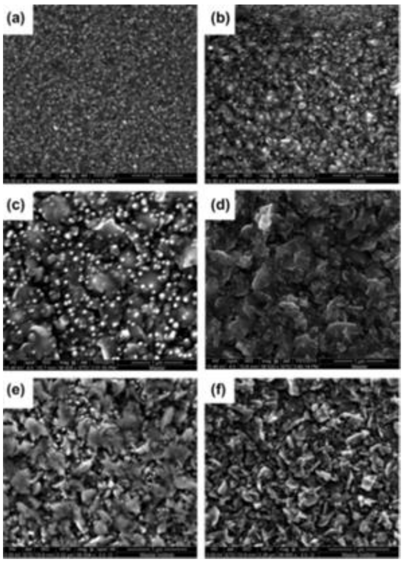

Figure 2. XRD patterns of $Zn_{0.90}Co_{0.05}M_{0.05}O$ (M=Na, Al, Cu, and Cd) films.

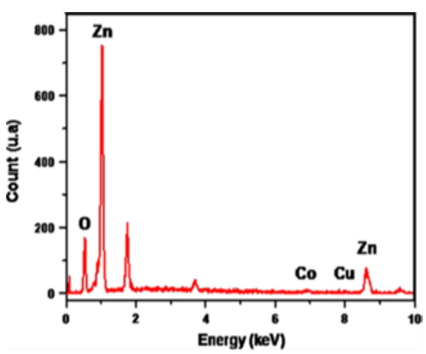

Figure 3. Example of EDAX spectra of co doped $Zn_{0.9}Co_{0.05}Cu_{0.05}O$ thin films.

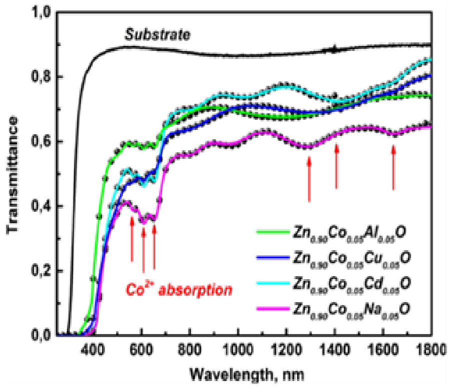

Figure 4. Transmittance of the bare glass substrate, TSbstrate, is also shown. Measured (full circles) and calculated (solid lines).

In addition to that, a population of nanosized spherical features with a size of 30–60 nm can be observed.

C. EDX Analysis

The SEM is equipped with Genesis Energy-dispersive X-ray (EDX) spectroscopy system that was used to determine the chemical composition of the films. An example of EDX spectra of Cu/Co co-doped ZnO film is shown in Fig. 3. In particular, EDX data are analyzed in order to reveal the co-doping effectiveness as well as to check the stoichiometry of the as-prepared oxide films.

D. Optical Properties

The solid curve in Figs. 4 corresponds to the curve fitting and the symbol represents the experi-mental data [5]. The Figure reveal a reasonable good fitting to the experimental data, The values of d, Eg, and n, extracted by fitting.

The optical energy band-gap of pure ZnO film was estimated as 3.26 eV. This value is slightly smaller than the bulk value of 3.31 eV [1] and in good agreement with previously reported data of ZnO thin films [6]. An obvious red shift of the absorption edges can be observed in $Zn_{0.95}Co_{0.05}O$ and co-doped $Zn_{0.90}Co_{0.05}M_{0.05}O$ with M=Na, Al, Cu, and Cd films. The value of the direct optical band-gap is reduced from 3.26 to 2.94 eV. The s-d and p-d exchange interac-tions lead to a negative and positive correction to the conduction band and the valence band edges, resulting into band-gap narrowing. The interaction leads to corrections in the energy bands; the conduction band is lowered

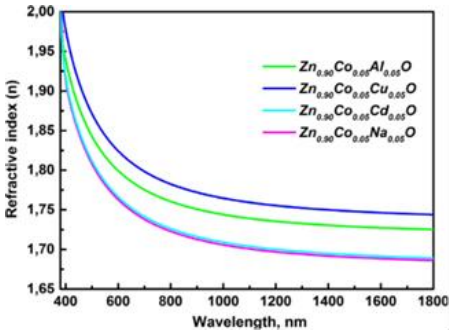

Figure 5. Refractive index of $Zn0.90Co0.05M0.05O$ films.

while the valence band is raised thereby causing the band-gap to shrink [7,8].

The calculated refractive indices of ZnO, Zn0.95Co0.05O and Zn0.90-Co0.05M0.05O (with M=Al, Cd, Na and Cu) films (Fig. 5) exhibit a function of the wavelength. It is found that the refractive indices at 598 nm of ZnO, Zn0.95Co0.05O and Zn0.90Co0.05Cu0.05O films are equal to 1.77, 1.84 and 1.82, respectively. It can be noticed that the above calculated refractive indices are equal or a little greater than that of ZnO film prepared under the same conditions. This might be due to the fact that the index of refraction is sensitive to structural defects (for example voids, dopants, in-clusions), thus it can provide an important information concerning the microstructure of the material.

IV. Conclusions

X-ray diffraction analysis using the Rietveld method shows that the as-deposited ZnO, co-doped Zn0.90Co0.05M0.05O (M=Na, Al, Cu, and Cd) films are pure single wurtz-ite phase. The lattice parameters vary linearly with increasing ionic radius of the doping element. The nature of the co-dopant element is found to influence considerably the film morphology, grain size and stoichiometry of the formed oxides. The doping effectiveness was revealed by EDX analysis of the chemical composition of the films. While the co-doping with Cu appears to be effective and leads to the expected film composition, the co-doping with Na was not successful. The addition of Al and Cd are found to lead to the formation of oxide films with a slight shift of its stoichiometry. The morphology of Cd and Na codoped films is similar to ZnO films characterized by the formation of nanopetals, whereas Cu and Al additions change the morphology and lead to the growth of dense films characterised by the presence of nanorods or nanowires. An optical model, which combines the Wemple–DiDomenico model, absorption coefficient of an electronic transi-tion and Tauc–Urbach model, has been proposed to simulate the optical constants and thicknesses of ZnO and co-doped Zn0.90Co0.05M0.05O (M=Na, Al, Cu, and Cd) films from normal incidence transmittance. It is found that the simulated transmittance is well consistent with the measured transmittance. The dispersion parameters and optical con-stants of the films were determined. These parameters changed with Co, Al, Cd, Cu and Na dopants.

Acknowledgment

The authors would like to thank the National Project Research (PNR) and LASPI2A Laboratory of Khenchela University (Algeria) for their financial support of this research project.

References

[1] Oktik, S. (1988). Low cost, non-vacuum techniques for the preparation of thin/thick films for photovoltaic applications. *Progress in Crystal Growth and Characterization*, *17*(3), 171-240.

[2] Yang, H., & Nie, S. (2009). Preparation and characterization of Co-doped ZnO nanomaterials. *Materials Chemistry and Physics*, *114*(1), 279-282.

[3] Yang, M., Guo, Z., Qiu, K., Long, J., Yin, G., Guan, D., ... & Zhou, S. (2010). Synthesis and characterization of Mn-doped ZnO column arrays. *Applied surface science*, *256*(13), 4201-4205.

[4] Raoufi, D., & Raoufi, T. (2009). The effect of heat treatment on the physical properties of sol–gel derived ZnO thin films. *Applied surface science*, *255*(11), 5812-5817.

[5] Roguai, S., Djelloul, A., Nouveau, C., Souier, T., Dakhel, A. A., & Bououdina, M. (2014). Structure, microstructure and determination of optical constants from transmittance data of co-doped Zn0. 90Co0. 05M0. 05O (MAl, Cu, Cd, Na) films. *Journal of alloys and compounds*, *599*, 150-158.

[6] Ashour, A., Kaid, M. A., El-Sayed, N. Z., & Ibrahim, A. A. (2006). Physical properties of ZnO thin films deposited by spray pyrolysis technique. *Applied Surface Science*, *252*(22), 7844-7848.

[7] Qiu, X., Li, L., & Li, G. (2006). Nature of the abnormal band gap narrowinzzzzzzzg in highly crystalline Zn 1− x Co x O nanorods. *Applied physics letters*, *88*(11), 114103.

[8] Pankove, J. I. (1975). *Optical processes in semiconductors*. Courier Corporation.

Using C++ and CPLEX to Optimize Multigeneration Systems in the Residential Sector

Danielle Bandeira de Mello Delgado[1], Iderval da Costa e Silva Neto[2], Monica Carvalho[3]

[1]Graduate Program in Mechanical Engineering, Center of Technology, Federal University of Paraiba(UFPB), João Pessoa, Brazil
[2]Department of Informatics, Center of Informatics, Federal University of Paraiba (UFPB), João Pessoa, Brazil
[3]Department of Renewable Energy Engineering, Center of Alternative and Renewable Energy, Federal University of Paraiba (UFPB), João Pessoa, Brazil

Abstract—**Decentralized energy production based on the combination of heating and cooling technologies is becoming increasingly common in grid-connected applications. These decentralized systems are especially attractive when a wide range of energy resources is available, such as natural gas, solar energy, biomass, and biofuels. This study presents a new, user-friendly optimization interface to ensure that a wide range of energy consumers in Brazil can take advantage of multi-generation schemes. The main objective is to develop the economic optimization of an energy system for the residential sector in Brazil. To this end, a C++ based optimization model is built encompassing solar collectors and fuel cells to achieve minimal annual costs (equipment + operation). The energy demands considered are heating (hot water), cooling, and electricity (encompassing an electric vehicle charging station). In the case study herein presented, the optimal system presented high capital costs but achieved a reduction of 22.27% in the total annual cost when compared to a reference system (separate production of energy services).**

Keywords- linear programming, polygeneration, economics

I. Introduction

The adoption of multigeneration systems is mainly motivated by the energy needs of factual society. Solutions that involve intelligent heating and cooling systems are becoming essential due to the low levels of energy consumption achieved, with significant environmental advantages. Some of the sectors positively affected are transportation/urban mobility (electric and hybrid cars) and the energy sector, through the more rational use of energy resources in buildings.

Multigeneration technologies provide substantial socioeconomic and environmental benefits that relate to the efficient use of energy resources. Overall system efficiency increases significantly if system design considers energy integration concepts. In addition, various alternative fuels can be used to improve resource utilization through fuel switching or blending [1].

The new, more decentralized energy paradigm requires adequate economic signaling for services capable of attracting new investments in new energy services and stimulating consumers to respond actively, optimizing operation and costs [2].

In the case of Brazil, the industrial, residential and commercial sectors consumed 79% of the electricity available in the country in 2021[3]. Distributed micro- and mini-generation of electricity increased by 84% in 2021 (compared to 2020). This growth was encouraged by regulatory actions, such as the possibility of compensating the surplus energy produced by smaller systems (net metering) [4].

The optimization of multigeneration systems for energy supply is still a complex operational problem, due to the wide variety of technological options for energy supply and conversion, large daily and annual variations in energy demands,

ISBN: 978-86-82602-01-9

as well as gaps in legislation and variations in energy tariffs. Against this complexity, simplification is necessary, using appropriate techniques and models.

Reference [5] proposed a free economic structural and parametric optimization model for a hospital in Paraíba. Optimization was based on Mixed Linear Integer Programming (MILP), to obtain the optimized solution (configuration and operation) using LINGO software. The economic optimization suggested the use of biomass as a resource in boilers for the production of hot water and steam, and when compared to a conventional system, it presented an annual cost 10.99% lower. A previous study by [6] used environmental information from Life Cycle Assessment (LCA) for the optimization. The optimized environmental solution indicated trigeneration to minimize the environmental impacts produced by the energy supply and conversion system.

Reference [7] presented an alternative energy source in a hotel, located in an area with high power outages in Colombia. Photovoltaic solar energy was gradually introduced and combined with conventional power supply to meet energy demand at peak consumption times. The optimization problem was implemented in a computer program known as HOGA, version 2.2, which considered economic parameters associated with the photovoltaic system. The simulations showed that the combination of diesel and photovoltaic solar energy was a good alternative to meet the demand for lighting energy in the hotel, even at night, using battery storage. In this work, the optimization was not performed freely, as it already indicated the equipment that would be used.

Reference [8] developed methodologies for the synthesis and optimization of polygeneration systems in residential/commercial buildings considering their dynamic behavior and local restrictions, approaching multi-objective optimization models with balanced objective functions; accurate representation of dynamic operating conditions; realistic representation of the thermal requirements of supply and demand in the superstructure; and cost allocation proposals for fair distribution among end consumers. Complex polygeneration systems were proposed for two case studies, a multifamily building in Zaragoza (Spain) and a university hospital in Campinas (Brazil). A multi-objective optimization procedure was developed based on MILP to determine the optimal system configuration (based on real equipment available on the market) and economic (total annual cost) and environmental (total CO_2 emissions).

Reference [9] presented a new integrated approach to determine the optimal capacity and dispatch profile of combined heat and power microsystems in residential buildings, considering different operating strategies, objective functions and component inclusion. The optimization was based on MILP, implemented in MATLAB and several essential specifications such as inverter efficiency for micro combined heat and power units based on direct current, charge, discharge, and storage losses as well as excess heat dump were considered. The developed model was applied to four types of residential buildings with different heat and electricity consumption patterns. The model reduced total annual cost and greenhouse gas emissions by up to 62.5% and 14.9%, respectively, compared to separate generation.

The objective of this study is to present the structural and parametric optimization of a multigeneration system, from an economic perspective, for a residential building. Commercially available technologies and resources are employed, to verify the installation potential of these pieces of equipment. Besides traditional energy demands (hot water, cooling, and electricity, a charging station is considered at the building for vehicles. These results will be inputs for subsequent evaluations at different end-user locations in Brazil, in remote and urban communities and in different climatic situations.

This study differs from the others, as it aims to create a simulation tool for the optimization of multigeneration systems with a friendly interface and easy to use by users of residential consumer units to serve as a subsidy in the analysis of economic feasibility and decision making for acquisition and installation of these systems.

II. METHODOLOGY

A. Energy Demands

The study case is a 30-story building located in João Pessoa (Northeast Brazil). Energy demands are specified hour by hour, considering two representative days per month (working day, holiday) as shown in Table I.

Determination of electricity demands followed Brazilian standard

NBR 5410:2005 [10]. The area of the rooms were considered to dimension the lighting load, along with the perimeter for the dimensioning of the general use sockets and the active powers of equipment used in elevators, pool pumps and water reservoirs (specific use). Specification of demand factors followed the procedure set out in item 16 of the Unified Distribution Standard NDU – 001 [11] published by the electric energy concessionaire.

For the cooling load, the degree-day method was used, which is a static calculation method to determine the thermal needs of a space. Daily use of air-conditioning in the apartment units occurred between 9 pm and 7 am (on weekdays and weekends). The front desk of the building (reception area) employed air-conditioning 24 hours a day and the entertainment area (for parties, etc.) required cooling from 4pm to 10pm on weekends only.

To calculate the hot water demands, the amount of useful energy was calculated, expressed in kilowatt hours per day (kWh/day).

TABLE I. ENERGY DEMANDS OF RESIDENCIAL CONSUMER.

Month/ Representative day	**Electricity**	**Hot Water**	**Cooling**	**Charging station**
	kWh/day			
Jan	4113	1160	306	88
Feb	4113	1664	287	88
Mar	4113	1678	632	88
Apr	4113	1705	419	88
May	4113	1739	602	88
Jun	4113	1801	577	88
Jul	4113	1862	159	88
Aug	4113	1896	481	88
Sep	4113	1882	512	88
Oct	4113	1807	818	88
Nov	4113	1732	688	88
Dec	4113	1692	185	88
MWh/year				
Annual	732	330	85	16

Calculations followed the ABNT 15569 [12] standard, considering two showers a day, at 6 am and 8 pm on weekdays and at 8 am and 8 pm on weekends.

There is also an electric vehicle charging station at the building, which operates 24 hours a day. Simultaneous charging of two vehicles was considered, twice a day (22 kW per charge).

B. *Superstructure*

The superstructure shown in Fig. 1 is proposed to meet the demands of electricity, cooling and hot water.

The available energy utilities are:

- EE - Electricity Energy resource that can be produced (+) or consumed (-) by some equipment. Electricity also appears in the superstructure as demand (-) of the consumer unit. The surplus production of electricity (+) by the SIFV (Photovoltaic System) may be compensated by consumption or demand;
- DI -Diesel Energy resource that can be consumed (-) by some equipment;
- BM -Biomass Energy resource that can be consumed (-) by some equipment;
- GN –Natural Gas Energy resource that can be consumed (-) by some equipment;
- AQ –Hot Water Corresponds to the demand (-) for hot water presented by the consumer unit;
- AG –Cooling Water Corresponds to the demand (-) for cooling presented by the consumer unit;
- AR –Refrigeration Water Used to reject heat to the environment in the cooling tower (energy balance);
- AA–Ambient air Waste to the environment (energy balance).

The available technologies (equipment) are:

- SIFV - Photovoltaic System Electricity production (+) system composed of solar modules and inverters;
- GDGN - Natural Gas Generator Equipment for the production of electricity (+), hot water (+) and cooling water (-), from the consumption of natural gas (-);

- GDDI–Diesel Generator Equipment for the production of electricity (+), hot water (+) and cooling water (+), from the consumption of diesel (-);
- CADI–Diesel boiler Equipment for producing hot water (+) from diesel consumption (-);
- CAGN–Natural Gas boiler Equipment for the production of hot water (+) from the consumption of natural gas (-);
- CABM - Biomass boiler Equipment for producing hot water (+) from the consumption of biomass (-);
- CAEE– Electric boiler Equipment for producing hot water (+) from electricity consumption (-);
- CHAQ -Single effect absorption chiller Equipment for the production of chilled water (+) and cooling water (+), from the consumption of electricity (-) and hot water (-);
- CHEE - Mechanical chiller Equipment for the production of chilled water (+) and cooling water (+), based on electricity consumption (-);
- TRAR–Cooling tower Equipment to reject heat from chillers. produces ambient air (+), from the consumption of electricity (-) and cooling water (-);
- TCAQ - Heat Exchanger (Hot Water - Cooling Water) Equipment to perform heat exchange. Produces cooling water (+), from the consumption of hot water (-);
- CCOM - Fuel Cell Equipment for the production of electricity (+) and hot water (+), from the consumption of natural gas (-);
- SITS - Thermosolar System for the production of hot water (+) composed of solar collectors and boiler, from solar irradiation;
- RDEE - Electricity Network Conventional electricity supply system (+).

Technical parameters of the equipment were obtained from equipment data sheet and are displayed in Table II along with capital costs.

C. *Optimization Model*

The model was implemented in C++, using the CPLEX solver, being developed with the objective of facilitating the interface with the end user and allowing a better understanding of the simulation and analysis results. The MILP-based optimization problem allows knowing the value of all energy flows. The solution also provides the result of an economic evaluation, identifying system configuration (type and number of equipment) and operation to obtain the minimum cost.

All input data for the model were included in electronic spreadsheets (one for demand, one for the list of technical coefficients, costs of investment, maintenance and operation and another for tariff costs).

The economic objective function considers annual costs: fixed costs (initial investment in equipment) and variable costs (purchase of energy resources to meet demands, maintenance and operation costs), as shown in Eqs. (1)–(3).

$$Min C_{total} = C_{fix} + C_{var} \,, \tag{1}$$

$$C_{fixo} = \left[f_{rc} \cdot (1 + f_{ci}) \cdot \sum_i NE(i) \cdot CE(i) \right] + \\ + SIFV + SITS \,, \tag{2}$$

$$C_{var} = \left[\sum_d \sum_h p(d,h) \cdot t(d,h) \right] + O\&M \,. \tag{3}$$

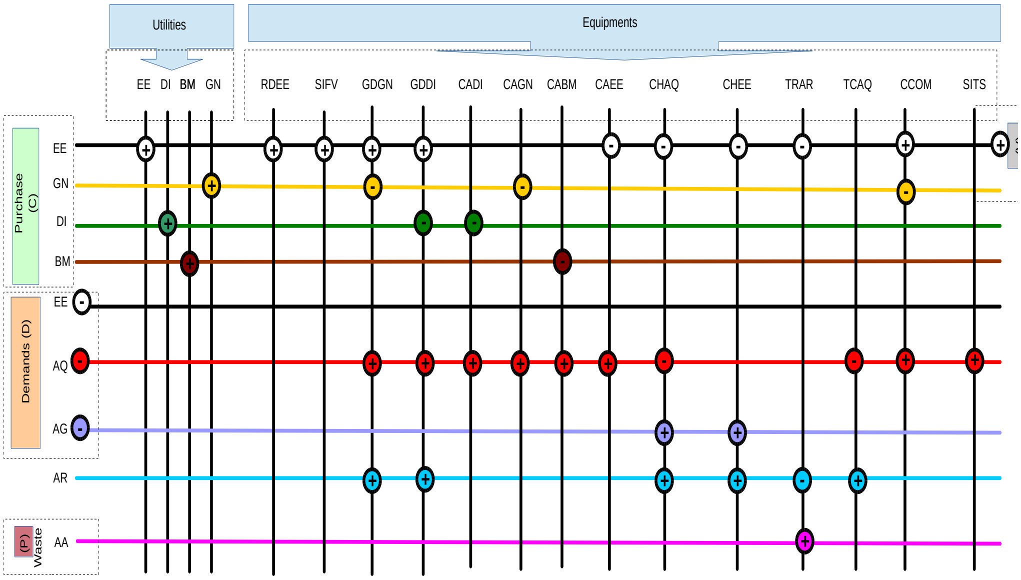

Figure 1. Superstructure of the residential consumer.

TABLE II. TECHNICAL COEFFICIENTS AND INVESTMENT, MAINTENANCE AND OPERATION COSTS.

Technical coefficients										Equipment		
	EE	*DI*	*BM*	*GN*	*AQ*	*AG*	*VA*	*AR*	*AA*	*Investment Cost CINV (10^3 R$)*	*Cost O&M (R$/h)*	*Nominal Pow (MW)*
RDEE	1.00									0.00	0.00	0.07
SIFV	1.00									13.36	0.50	0.45
GDGN	1.00			- 3.70	2.95			2.12		158.10	3.69	0.17
GDDI	1.00	- 2.03			1.45			1.48		73.05	1.70	0.33
CADI		- 1.09			1.00					49.30	1.15	0.38
CAGN				- 1.09	1.00					49.30	1.15	0.38
CABM			- 1.25		1.00					56.52	1.32	0.37
CAEE	- 1.10				1.00					28.20	0.66	0.35
CHAQ	- 0.01				- 1.26	1.00		2.23		150.00	3.50	0.10
CHEE	- 0.32					1.00		1.32		145.00	2.61	0.06
TRAR	- 0.01							- 0.98	1.00	23.99	0.56	0.36
TCAQ					- 1.10			1.00		7.40	0.17	0.40
CCOM	1.00			- 2.75	1.03					3500.00	81.67	0.20
SITS					1.00					10.52	0.50	0.02

Tables III and IV present the parameters of the optimization problem.

TABLE III. OPTIMIZATION PROBLEM PARAMETERS.

Variable	Representation	Type
$NE(i)$	number of technology equipment i	integer
$c_e(d,h)$	purchase in period (d,h), of electricity	continuous
$c_g(d,h)$	purchase in period (d,h), of natural gas	continuous
$c_d(d,h)$	purchase in period (d,h), of diesel	continuous
$c_b(d,h)$	purchase in period (d,h), of biomass	continuous
$X(i,j,d,h)$	energy flows	continuous
$PIN(i)$	installed Power of Technology i	continuous
$p(d,h)$	costs with the purchase of electricity and/or fuel for period h of the representative day d	continuous
$PRODT(d,h,i)$	total production of the set of equipment of a given technology i in a period (d,h)	continuous
$K(i,j)$	absolute value of production coefficients	continuous
INDCOM	possibility of purchase	binary
INDDEM	possibility of demand	binary
INDVEN	possibility of sale	binary
INDDES	possibility of waste	binary

The restrictions of the problem are:

1. $PRODT(d,h,i) \le PIN(i)$ - Restriction: The total production of the set of equipment of a given technology i in a period (d,h) is limited by the total installed capacity of the equipment;

2. $X(i,j,d,h) = K(i,j) \cdot PRODT(d,h,i)$ - Production restriction: X is the energy flow of utility j, produced or consumed by technology i, and K is the absolute value of the production coefficients;

3. $$Prod(j,d,h) - Cons(j,d,h) + C(j,d,h) - \\ -V(j,d,h) - D(j,d,h) - P(j,d,h) = 0$$
Energy balance equations for each utility j;

TABLE IV. OPTIMIZATION PROBLEM VARIABLES.

Parameter	Representation
i	technology - equipment
j	utility - fuel
d	day
h	hour
f_{rc}	capital recovery factor
f_{ci}	indirect cost factor
$O\&M$	equipment operation and maintenance cost
$t(d,h)$	number of hours of operation, for the period h of the representative day d
$PIN(i)$	nominal power of each equipment
$CE(i)$	cost of technology equipment i
$SIFV$	cost of the photovoltaic system
$SITS$	cost of the thermosolar system
V_e	electricity tariff value
V_g	natural gas tariff value
V_d	diesel tariff value
V_b	biomass tariff value
$Prod(j,d,h)$	production of utility j,on day$d$ hour h
$Cons(j,d,h)$	consumption of utility j,on day$d$ hour h
$C(j,d,h)$	purchase of utility j,on day$d$ hour h
$V(j,d,h)$	sale of utility j,on day$d$ hour h
$D(j,d,h)$	demand of utility j,on day$d$ hour h
$P(j,d,h)$	waste of utility j,on day$d$ hour h
$VTUP(i,j)$	is 1 when the coefficient of production (table II) is positive, that is, when technology $i$produces utility j.
$VTUC(i,j)$	is 1 when the production coefficient is negative, that is, when technology i consumes utility j

4. $Prod(j,d,h) = \sum_i X(i,j,d,h) \cdot YTUP(i,j)$
with $YTUP(i,j) \in \{0,1\}$ - Energy balance equations for each utility j – Production;

5. $Cons(j,d,h) = \sum_i X(i,j,d,h) \cdot YTUC(i,j)$
com $YTUC(i,j) \in \{0,1\}$ - Energy balance equations for each utility j– Consumption;

6. $$C(j,d,h) \le INDCOM(j) \cdot \\ \cdot (Cons(j,d,h) + D(j,d,h))$$
with $INDCOM(j) \in \{0,1\}$ - Purchase restriction;

7. $P(j,d,h) \leq INDDES(j) \cdot Prod(j,d,h)$

with $INDDES(j) \in \{0,1\}$ - Waste restriction;

8. $D(j,d,h) \leq INDDEM(j) \cdot$
$\cdot (Prod(j,d,h) + C(j,d,h))$

with $INDDEM(j) \in \{0,1\}$ - Demand restriction.

III. RESULTS

Initially a reference system is established for comparison purposes, when the optimization model excludes combined energy production and renewables.

Only traditional technologies such as the conventional electricity grid, natural gas and diesel boiler, heat exchangers, mechanical chiller, and cooling tower are considered. The optimal system is a free optimization, using all the utilities and technologies provided in the superstructure except solar energy.

In addition, there an optimal system that includes photovoltaic solar panels and solar collectors for hot water production (mandatory inclusion of these equipment).The results of the optimization are presented in Table V.

The reference system is based on the purchase of electricity to meet the electricity and hot water demands directly, and indirectly, the cooling demand through the mechanical chiller.

The optimal economic scenario includes the photovoltaic, but don´t include the thermosolar generation systems. However the optimal economic solution included biomass to produce hot water in a boiler, because of the low cost of the fuel used.

Although the optimal system presented a higher initial investment in equipment (higher capital costs), it achieved a 27.02% reduction in total annual cost when compared to the reference system (separate production of energy services) however with an initial investment 41.69% higher. 22.27% less electricity was imported from the grid with the internal use of electricity generated by the SIFV for consumption of equipment and to meet demand.

TABLE V. ECONOMIC OPTIMIZATION RESULTS.

Equipments	**Economic Optimization**	
	Reference System	***Optimal System***
	Quantity of Equipment (Individual Power)	
RDEE	1 (300kW)	1 (300kW)
GDGN	-	-
GDDI	-	-
CADI	-	-
CAGN	1 (385W)	-
CABM	-	1 (370kW)
CAEE	-	-
CHAQ	-	-
CHEE	1 (60kW)	1 (60kW)
TRAR	1 (360kW)	1 (360kW)
TCAQ	-	-
CCOM	-	-
SIFV	-	102 panels (0.455kW)
SITS	-	-
Energy flows (MWh/year)		
Imported electricity	824.66	641.04
Purchase of natural gas	238.83	-
Purchase of biomass	-	345.32
Purchase of diesel	-	-
Useful cogenerated heat	-	-
Annual Costs (R$/year)		
Investment in equipments	27.701,60	47.509,81
Equipment maintenance and operation	25.974,20	29.574,64
Purchase of electricity	294.293,51	228.599,51
Purchase of natural gas	107.806,00	-
Purchase of diesel	-	-
Purchase of biomass	-	26.934,90
Total Annual Cost (R$/year)	**455.775,31**	**332.618,86**

IV. CONCLUSION

The economic optimal solution suggested the use of the photovoltaic system and the biomass in boilers for the production of hot water, reaching an annual cost that was 27.02% lower than the separate production of energy.

Input data as well as results are displayed in spreadsheets, highlighting the ease of use of the software and the implemented model.

Future work can focus on a sensitivity analysis of the system based on the application of the most recent Brazilian regulations, to evaluate the system in conditions of surplus generation and possibility of compensation.

ACKNOWLEDGMENT

The authors wish to acknowledge the financial support of the National Council for Scientific and Technological Development (CNPq), for productivity grant 309452/2021-0.

REFERENCES

[1] Jana K., Ray A., Majoumerd M. M., Mohsen A. & de S. (2017). Polygeneration as a future sustainable energy solution – A comprehensive review. *Applied Energy*, 202, 88–111.

[2] Brazil. (2020). *EPE - Empresa de Pesquisa Energética.Final report of PNE 2050*. Available at: http://www.link.com https://www.epe.gov.br/sites-pt/publicacoes-dados-abertos/publicacoes/PublicacoesArquivos/publicacao-227/topico-563/Relatorio%20Final%20do%20PNE%202050.pdf.

[3] Brazil. (2022). *EPE - Empresa de Pesquisa Energética. National Energy Balance 2022: Base year 2021*. Available at: https://www.epe.gov.br/sites-pt/publicacoes-dados-abertos/publicacoes/PublicacoesArquivos/publicacao-675/topico-638/BEN2022.pdf.

[4] Brazil. (2022). *EPE - Empresa de Pesquisa Energética. National Energy Balance 2022: Base year 2021*. Available at: https://www.epe.gov.br/sites-pt/publicacoes-dados-abertos/publicacoes/PublicacoesArquivos/publicacao-675/topico-638/BEN2022.pdf.

[5] Delgado, D., Carvalho, M., Coelho Junior, L. M., Abrahão, R., & Chacartegui, R. (2018). Photovoltaic solar energy in the economic optimisation of energy supply and conversion. *IET Renewable Power Generation*, *12*(11), 1263-1268.

[6] Carvalho, M., de Mello Delgado, D. B., & Chacartegui, R. (2016). Life cycle analysis as a decision criterion for the implementation of solar photovoltaic panels in as Northeast Brazil hospital. *Energy, Transportation and Global Warming*, 295-310.

[7] Garcia, Y., Diaz, O., & Guzman, R. (2017). Design and optimization of PV/diesel hybrid power system in a hotel. *International Journal of Energy Production and Management*, *2*(1), 52-59.

[8] Pina, E. A. (2019). Thermoeconomic and environmental synthesis and optimization of polygeneration systems supported with renewable energies and thermal energy storage applied to the residential-commercial sector. *Thesis* .Mechanical Engineering Department, University of Zaragoza, Zaragoza.

[9] Mohammadi, H., & Mohammadi, M. (2020). Optimization of the micro combined heat and power systems considering objective functions, components and operation strategies by an integrated approach. *Energy Conversion and Management*, *208*, 112610.

[10] ABNT. Brazilian Association of Technical Standards (2005). NBR 5410: Low Voltage Electrical Installations.

[11] ENERGISA (2019). NDU – 001 – version 6.2 - Unified Distribution Standard. João Pessoa.

[12] ABNT. Brazilian Association of Technical Standards (2020). NBR 5410: Direct Circuit Solar Water Heating System.

A Study of the Nonlinear and Linear Behavior of a Gantry Crane System

Muthanna M. Al-Hadeethi[1], Abdulmuttalib A. Muhsen[2], Bashar Hassan Attiya[3]

[1,2,3]Haditha Hydropower Station, Ministry of Electricity, Haditha, Iraq
[2]Faculty of Power and Aeronautical Engineering, Warsaw University of Technology, Warsaw

Abstract— **This work presents a study of the nonlinear and linear behavior of a gantry crane system. The Lagrange equation was used to derive the model of the nonlinear system, and the Taylor series approximation was used to get the linearized model. The system was simulated using MATLAB. PID and PD controllers were used to control the oscillation of the load during the movement of the trolley within the specified displacement. The MATLAB simulation results were presented to demonstrate the effect of model parameters such as cable length, mass of trolley and payload on the trolley displacement and payload oscillation, as well as the effect of the controllers on system response.**

Keywords - Nonlinear model, gantry crane, Lagrange, simulation, PID controller.

I. INTRODUCTION

The growing need for large items and equipment necessitates the employment of modern, rapid, effective, and dependable cranes for transporting, loading and unloading heavy goods from one place to another. In industries, warehouses, seaports, building sites mining sites, and power plants, among others, a gantry crane system is a straightforward solution for transporting, loading, and unloading various types of products [1].

Two or more legs usually support the gantry crane, and the trolley is designed to move and deliver large goods right or left along the crane's horizontal bridge rail until they reach their destination [2].

During normal operation or in the presence of external disturbance such as high wind, gantry crane system (GCS) are susceptible to vibration and payload deflection. This resulted in incorrect load positioning, task delays, and perhaps system or operational environment damage [3]. In addition, the oscillation of the payload increases with the speed of movement of the crane [2]. However, the speed of movement is required because it affects productivity. Therefore, many researchers have been working on constructing a mathematical model of the system for exact dynamic analysis and effective control to improve system Productivity, ensure environmental safety, and reduce maintenance costs due to system breakdown [1,3,4].

In order to control the trolley position and the oscillation of payload, many researchers have been applied various control strategies such as Fuzzy Logic, Linear Quadratic Regulator and PID controllers [3,5]. PID controllers are frequently employed in industrial control systems because of its simple form, ease of adjustment, and outstanding stability [6].

In this work, the behaviour of linear and non-linear for the crane system will be analyzed and studied when changing the system parameters as well as the effect of using PID and PD controllers on the response of the system.

II. GANTRY CRANE SYSTEM DESCRIPTION

The gantry crane system (GCS) shown in Fig.1, the trolley moves horizontally along the jib. A pair of legs hold the jib in place. A payload is hung from a trolley by a suspension cable. The schematic diagram of the gantry crane system in Fig.2 shows that the force required to move the trolley is denoted by (F). The trolley mass is (m_2), the payload mass is (m_1), the payload oscillation angle is (θ), the trolley displacement is (x), and the payload cable length is (l). The force supplied to the trolley (F) is the GCS's input, while the desired outputs are the displacement (x) and the payload oscillation angle (θ) [1].

ISBN: 978-86-82602-01-9

Figure 1. Gantry Crane System.

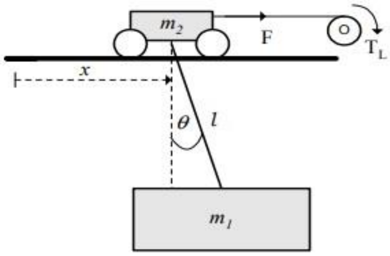

Figure 2. Schematic diagram of gantry crane system.

TABLE I. SYSTEM PARAMETERS

Parameter	Symbol	Value
Mass of payload	m_1	0.5 kg
Mass of trolley	m_2	2 kg
length of cable	l	0.5 m

III. MODELLING OF GCS

The system consists of two subsystems. The electrical part is represented by the DC motor, which represents the applied force (*F*). The trolley and the payload represent the mechanical part.

A. Modelling of Mechanical Part

This part was derived by using Lagrange equation [1-3] with some assumptions such as neglecting trolley friction, cable mass and external disturbances.

$$\frac{d}{dt}\left(\frac{\partial L}{\partial q_i}\right) - \frac{\partial L}{\partial q_i} = Q_i \ , \qquad (1)$$

$$L = T - V \ , \qquad (2)$$

$$\begin{gathered} q_1 = x,\ q_2 = \theta,\ Q_i = F \ , \\ T = \frac{1}{2} m_1 v_1^2 + \frac{1}{2} m_2 v_2^2 \ , \\ v_1 = \dot{x} \ . \end{gathered} \qquad (3)$$

Using the cosine rule, the velocity analysis of Fig.2 yields:

$$\begin{gathered} v_2^2 = \dot{x}^2 + (L\dot{\theta})^2 - 2\dot{x}L\dot{\theta}\cos(180 - \theta) \ , \\ v_2^2 = \dot{x}^2 + (L\dot{\theta})^2 + 2\dot{x}L\dot{\theta}\cos\theta \ , \\ T = \frac{1}{2} m_2 \dot{x}^2 + \frac{1}{2} m_1 \left[\dot{x}^2 + (L\dot{\theta})^2 + 2\dot{x}L\dot{\theta}\cos\theta \right] . \end{gathered} \qquad (4)$$

$$\begin{gathered} V = V_e + V_g \ , \\ V_e = 0 \ , \\ V_g = mgh \ , \\ V = -mgL\cos\theta \ . \end{gathered} \qquad (5)$$

Substituting Eqs. (4) and (5) into Eq. (2), yields:

$$\begin{aligned} & L = \frac{1}{2} m_1 \left(\dot{x}^2 + L^2\dot{\theta}^2 + 2\dot{x}L\dot{\theta}\cos\theta \right) + \\ & + \frac{1}{2} m_2 \dot{x}^2 + m_1 gl\cos\theta \ , \\ & for\ q_1 = x \\ & \frac{\partial L}{\partial x} = 0 \ . \end{aligned} \qquad (6)$$

$$\begin{aligned} & \frac{\partial L}{\partial \dot{x}} = m_1\dot{x} + m_2\dot{x} + m_1 L\dot{\theta}\cos\theta = 0 \ , \\ & \frac{d}{dt}\left(\frac{\partial L}{\partial \dot{x}}\right) = m_1\ddot{x} + m_2\ddot{x} - \\ & -m_2 L\theta\sin\theta + m_2 L\theta\cos\theta \ , \\ & \frac{d}{dt}\left(\frac{\partial L}{\partial \dot{x}}\right) = \left(m_1 + m_2\right)\ddot{x} + \\ & + m_1 l\ddot{\theta}\cos\theta - m_1 l\dot{\theta}^2\sin\theta \ . \end{aligned} \qquad (7)$$

Substituting Eqs. (6) and (7) into Eq. (1) where $Q_i = F$, the result is:

$$\left(m_1 + m_2\right)\ddot{x} + m_1 l\ddot{\theta}\cos\theta - m_1 l\dot{\theta}^2\sin\theta = F \ . \qquad (8)$$

For $q_2 = \theta$:

$$\begin{aligned} & L = \frac{1}{2} m_2\dot{x}^2 + \frac{1}{2} m_1\left[\dot{x}^2 + (L\dot{\theta})^2 + 2L\dot{x}\dot{\theta}\cos\theta \right] + \\ & + mgL\cos\theta \ , \\ & \frac{\partial L}{\partial \dot{\theta}} = m_1 L^2\dot{\theta} + m_1 L\dot{x}\cos\theta \ , \\ & \frac{d}{dt}\left(\frac{\partial L}{\partial \dot{\theta}}\right) = m_1 L^2\ddot{\theta} - m_1 L\dot{x}\dot{\theta}\sin\theta + m_1 L\ddot{x}\cos\theta \ . \end{aligned} \qquad (9)$$

$$\frac{\partial L}{\partial \theta} = -m_1 L\dot{x}\dot{\theta}\sin\theta - m_1 gL\sin\theta \;, \qquad (10)$$

Substituting Eqs. (9) and (10) into Eq. (1) where $Q_i = 0$, the result is:

$$\begin{aligned} & m_1 L^2\ddot{\theta} - m_1 L\dot{\theta}\dot{x}\sin\theta + m_1 L\ddot{x}\cos\theta + \\ & + m_1 L\dot{x}\dot{\theta}\sin\theta + m_1 gL\sin\theta = 0 \;, \qquad (11) \\ & m_1 L^2\ddot{\theta} + m_1 L\ddot{x}\cos\theta + m_1 gL\sin\theta = 0 \;. \end{aligned}$$

Thus, Eqs. (8) and (11) represent the nonlinear model.

B. *Linearization*

Using Taylor series expansion:

$$F(x) = f(x_0) + (x - x_0) f' + \frac{(x - x_0)^2}{2!} f''(x_0) + \\ + \frac{(x - x_0)^3}{3!} f'''(x_0) + \ldots + \frac{(x - x_0)^n}{n!} f''(x_0)$$

Linearize the nonlinear terms $\sin\theta$, $\cos\theta$ at the operation points $(\bar{x}, \bar{\theta}) = (0,0)$:

$$\begin{aligned} & \sin\theta \approx \sin\bar{\theta} + \frac{d}{d\theta}\sin\theta\Big|_{\theta=\bar{\theta}} \cdot \Delta\theta \;, \\ & \sin 0 = 0 \;\; and \;\; \cos 0 = 1 \;, \\ & \sin\theta \approx 0 + \cos\bar{\theta} \cdot \Delta\theta = \Delta\theta \;, \\ & \cos\theta \approx \cos\bar{\theta} + \frac{d}{d\theta}\cos\theta\Big|_{\theta=\bar{\theta}} \cdot \Delta\theta \;, \\ & \cos\theta \approx 1 - (\sin 0) \cdot \Delta\theta = 1 \;, \\ & Thus, \; \sin\theta \approx \theta \;\; and \;\; \cos\theta = 1 \;, \\ & \theta \approx 0, \; \sin\theta = 0 \;\; and \;\; \Delta\theta \approx \theta \approx 0 \;, \\ & \dot{\theta} \approx 0 \;. \end{aligned}$$

Thus, Eq. (8) become:

$$(m_1 + m_2)\ddot{x} + m_1 L\ddot{\theta} = F \;. \qquad (12)$$

Similarly, Eq. (11) become:

$$m_1 L^2\ddot{\theta} + m_1 L\,\ddot{x} + m_1 gL\theta = 0 \;. \qquad (13)$$

Eqs. (12) and (13) represent the approximation of nonlinear model can then be rearranged as follows:

$$\ddot{x} = \frac{m_1 g}{m_2}\theta + \frac{1}{m_2}F \;, \qquad (14)$$

$$\ddot{\theta} = \frac{-(m_1 + m_2)g}{m_2 L}\theta - \frac{1}{m_2 L}F \;, \qquad (15)$$

C. *Modelling of DC Motor*

The force (F) required to move the trolley is produced using a DC motor, Fig.3 shows the circuit diagram of the motor. DC motor force equation was derived in [5] as below:

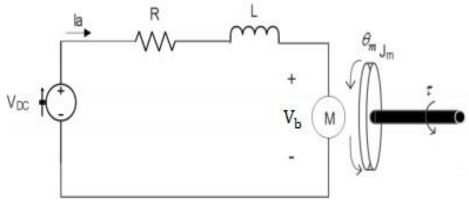

Figure 3. DC Motor circuit diagram.

$$T_m = J_m\left[\frac{d^2\theta_m}{dt^2}\right] + D_m\left[\frac{d\theta_m}{dt}\right] \;, \qquad (16)$$

where T_m is motor torque, J_m is the moment inertia θ_m is rotor angle position, and D_m is the equivalent viscous value of armature and the load reflected to the armature.

Since the moment inertia (J_m) is very small, Eq. (14) become:

$$T_m = D_m\left[\frac{d\theta_m}{dt}\right] = \frac{T_L}{r} \;, \qquad (17)$$

$$T_L = F\,r_p \;, \qquad (18)$$

where T_L is load torque and r_p is radius of pulley.

$$\theta_m = \frac{r}{r_p}x \;, \qquad (19)$$

where r is gear ratio:

$$V = Ri + L\frac{di}{dt} + V_b \;, \qquad (20)$$

where V is an input voltage, i is armature current, V_b is back electromotive force and L is inductance that is neglected, Eq. (18) become:

$$V = Ri + V_b \;, \qquad (21)$$

$$V = R\left[\frac{T_m}{K_T}\right] + K_E\left[\frac{d\theta_m}{dt}\right], \qquad (22)$$

where K_T is torque constant and K_E is back *emf* constant:

$$V = R\left[\frac{\frac{T_L}{r}}{K_T}\right] + K_E\frac{d}{dt}\left[\frac{r}{r_P}x\right], \qquad (23)$$

$$V = \frac{RFr_P}{K_T r} + \frac{K_E r}{r_P}\dot{x}, \qquad (24)$$

$$F = \frac{VK_T r}{Rr_P} - \frac{K_E K_T r^2}{Rr_P^2}\dot{x}, \qquad (25)$$

IV. Simulation Process

A. Simulation of Nonlinear and Linear System

MATLAB was used to simulate the system where FCN block used for simulation nonlinear system that is represented by Eqs. (8) and (11) as shown in Fig. 4. Eqs. (14) and (15) were used to simulate the linear system as shown in Fig.5, while Fig.6 shows the simulation of bang bang input (± 5 Nm) which used to energize the system.

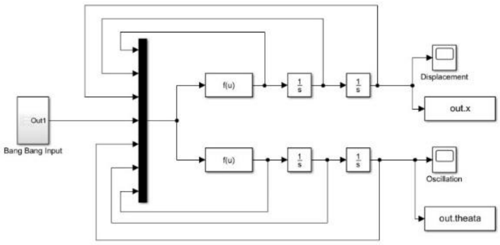

Figure 4. Simulink diagram for the nonlinear system.

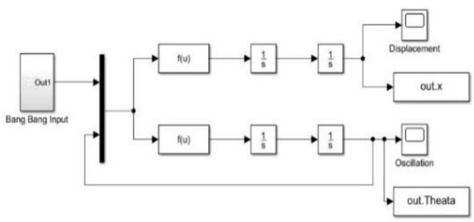

Figure 5. Simulink diagram for the linear system.

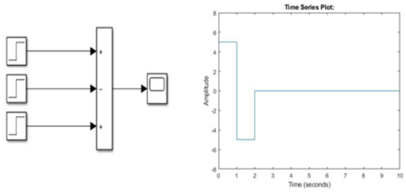

Figure 6. Simulink diagram of bang bang input.

B. Results of Simulation and Discussion

Different masses of trolley (m_2) (2,4,6)Kg were used for simulation with bang bang input equal to ± 5 Nm, the responses of the system as shown in Figs. 7 and 8 for trolley displacement and payload oscillation respectively. The displacement of the trolley is inversely proportional to its mass as the mass of the trolley increases, its displacement decreases. In addition, the smaller the payload oscillation angle, the larger the trolley mass.

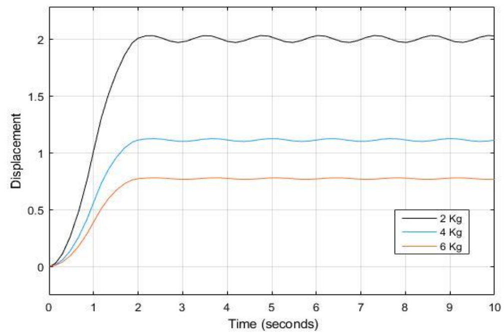

Figure 7. Trolley displacement with different masses of trolley.

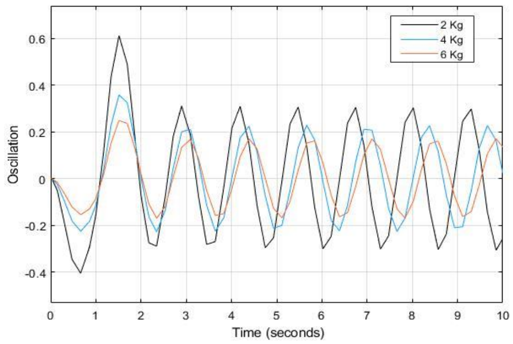

Figure 8. Payload oscillation with different masses of trolley.

Then, the payload mass (m_1) was changed to different values (0.5,0.75,1)Kg with same bang bang input ±5 Nm, the different responses obtained as shown in the Figs. 9 and 10, which are shown that increasing the mass of the payload reduces both the trolley displacement and the payload oscillation angle.

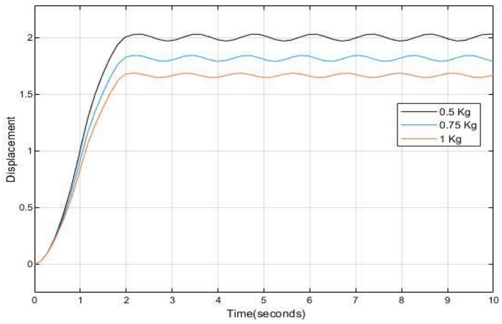

Figure 9. Trolley displacement with different masses of trolley.

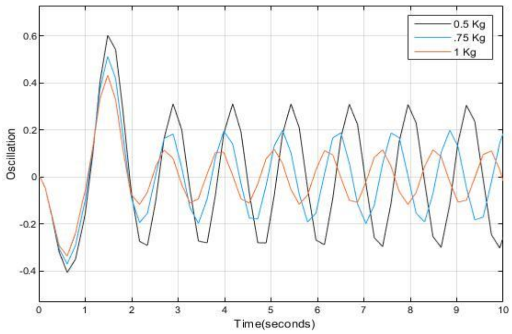

Figure 10. Payload oscillation with different masses of trolley.

Next, different values of cable length (0.5, 0.75, and 1) meter were used with same bang bang input ± 5 Nm. Figs. 11 and 12, show that the length of the cable has less effect on displacement. However, the relationship between the length of the cable and the payload oscillation angle is direct, as increasing the length of the cable leads to an increase in the angle of oscillation and vice versa.

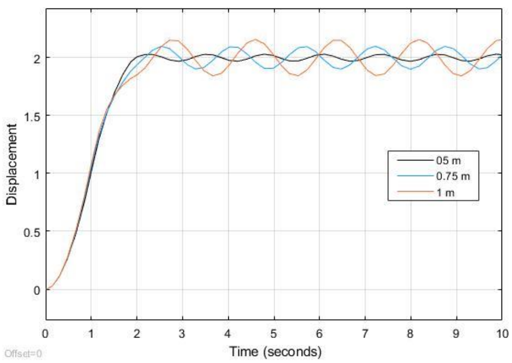

Figure 11. Trolley displacement with different length of cable.

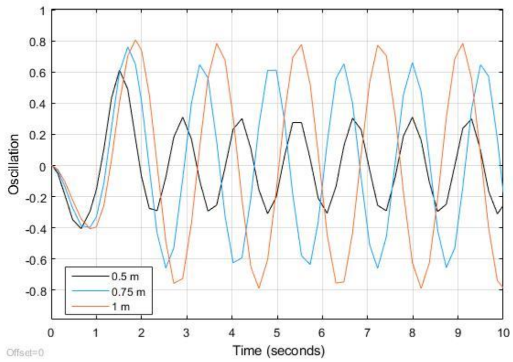

Figure 12. Payload oscillation with different length of cable.

Finally, the bang bang input was changed to different values (± 2.5, ± 5, and ± 7.5) Nm. Figs.13 and 14 show that the displacement of the trolley and the angle of oscillation of the payload is proportional to the input force.

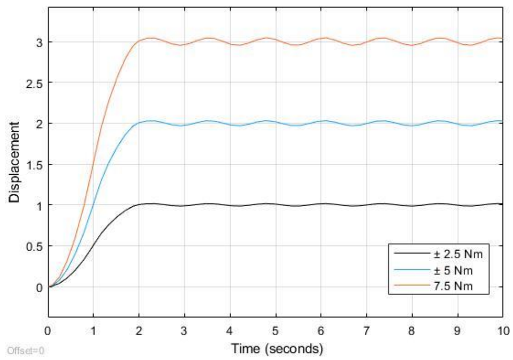

Figure 13. Trolley displacement with different input.

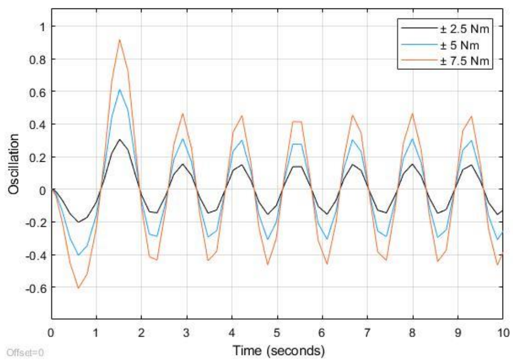

Figure 14. Payload oscillation with different input.

V. PID CONTROLLER

Two controllers (PID and PD) were used to control the movement of the trolley and the oscillation of the payload. Fig.15 shows the simulation of the system with the controllers and Figs. 16 and 17 show the responses of the trolley displacement and payload oscillation. The controllers were manually tuned to show the effect of the controller on the response of the system.

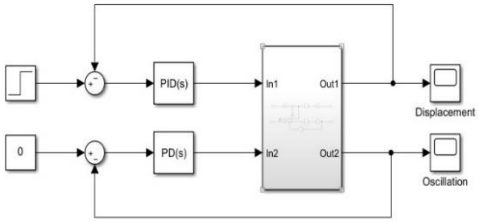

Figure 15. Simulink diagram of the system with controllers.

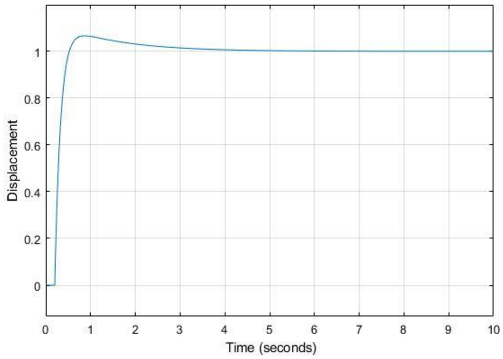

Figure 16. Trolley displacement with controller.

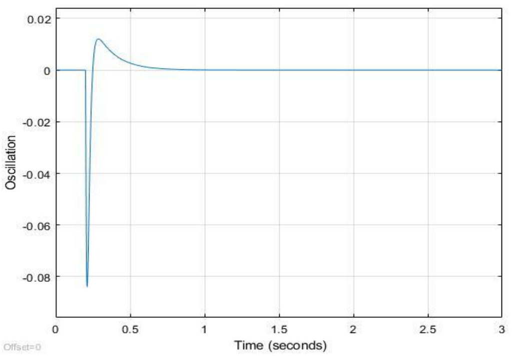

Figure 17. Payload oscillation with controller.

VI. Conclusion

In this work, a dynamic model of the gantry crane system has been studied and analyzed. The Lagrange equation have been used to derive the system's nonlinear differential equations. The responses of the system, such as trolley displacement and payload oscillation, have been studied. Various GCS system parameters have been investigated. The performance response of GCS is particularly sensitive to parameter setting adjustment, according to simulation results. PID and PD controllers have been applied to the system with manual tuning to show their effect on the system response. The study and analysis of systems is very useful in developing control mechanisms for gantry crane systems.

References

[1] Alhassan, A. B., Muhammad, B. B., Danapalasingam, K. A., & Sam, Y. M. (2015, May). Optimal analysis and control of 2D nonlinear gantry crane system. In *2015 International Conference on Smart Sensors and Application (ICSSA)* (pp. 30-35). IEEE.

[2] Jaafar, H. I., Mohamed, Z., Jamian, J. J., Abidin, A. F. Z., Kassim, A. M., & Ab Ghani, Z. (2013). Dynamic behaviour of a nonlinear gantry crane system. *Procedia Technology*, *11*, 419-425.

[3] Alhassan, A., Danapalasingam, K. A., Shehu, M., Abdullahi, A. M., & Shehu, A. (2016). Closed-loop schemes for position and sway control of a gantry crane system. *International Journal of Simulation: Systems, Science and Technology*, *17*, 1-8.

[4] Solihin, M. I., Legowo, A., & Akmeliawati, R. (2009, May). Robust PID anti-swing control of automatic gantry crane based on Kharitonov's stability. In *2009 4th IEEE Conference on Industrial Electronics and Applications* (pp. 275-280). IEEE.

[5] Hussien, S. Y. S., Ghazali, R., Jaafar, H. I., & Soon, C. C. (2015, November). Robustness analysis for PID controller optimized using PFPSO for underactuated gantry crane system. In *2015 IEEE International Conference on Control System, Computing and Engineering (ICCSCE)* (pp. 520-525). IEEE.

[6] Sun, Z., Wang, N., Bi, Y., & Zhao, J. (2015, July). A DE based PID controller for two dimensional overhead crane. In *2015 34th Chinese Control Conference (CCC)* (pp. 2546-2550). IEEE.

Utilization and Kientic Parameters Study of Mg and Ti-doped Lithium Fluoride-based Thermoluminescent Material

Chahra-Zed Benkhelifa[1], Faycal Kharfi[2]

[1,2]Department of Physics, Ferhat Abbas-Sétif1 University, Setif-19000, Algeria
[1,2]Laboratory of Dosing, Analysis, and Characterisation with high resolution, Ferhat Abbas-Sétif1 University, Setif-19000, Algeria

Abstract—**Even though a variety of materials are still used for dosimetry applications i.e. individual monitoring, environmental monitoring, radiological research, and other different dosimetric applications. Lithium fluorides have dominated these over the past three decades, first with LiF: Mg, Ti (TLD-100) and most recently with the high-sensitivity LiF: Mg, Cu, P. The aim of this work is the establishment of the TLD-100 TL response to radiation dose and radiation energy. Then, to study the thermoluminescence kinetics through the main kinetic parameters determination of the studied material, such as TL peak temperature *T*, activation energy *E*, and frequency factor *s* by using a suitable theoretical trap model and computerized glow curve deconvolution (CGCD) technique. Experimental TL glow curves (signals) were recorded around the Riso TL/OSL reader DA-20. The experimental data fitting and glow peaks deconvolution were performed by GlowFit software. The obtained results show that the studied dosimeter responds correctly and linearly to X-ray dose in the considered interval from 0 to 10Gy. The results of the CGCD technique give entire satisfaction when compared to the literature.**

Keywords - environment, thermoluminescence (TL), TLD-100, X-rays, CGCD

I. INTRODUCTION

The TLD-100 dosimeter based on Lithium Fluoride doped with both Magnesium and Titanium (LiF: Mg, Ti) is common in dosimetry such as individual monitoring, environmental monitoring, radiological research, and other different dosimetric applications [1-8] due to its approximate tissue equivalence, linearity over a wide dose range and high sensitivity [9]. The TL glow curve of TLD-100 is characterized by at leats five peaks. However, its glow curve is complicated because of its complex dynamics of traps. The TLD-100 main peak also known as dosimetric peak is located at ∼ 250°C, which coresponds to a stable trap level [9-10].

In this work, the study was conducted on the analysis of the TLD-100 glow curve after being irradiated with X-rays through the determination of the main kinetic parameters such as TL peak temperature (T_m), activation energy (E), and frequency factor (s) by using suitable theoretical trap model and computerized glow curve deconvolution (CGCD) technique.

II. GLOW-FIT DECONVOLUTION TOOL

The software developed for glow-curve analysis is based on Randall and Wilkins' first-order kinetics model. As given in Eq. (1), the TL intensity of a glow-peak in the TL glow-curve is:

$$I(T) = I_m exp\left(\frac{E}{kT_m} - \frac{E}{kT}\right)\cdot \\ \cdot exp\left(-\frac{E}{kT_m^2}\int_{T_m}^{T} exp\left(\frac{E}{kT_m} - \frac{E}{kT'}dT'\right)\right), \quad (1)$$

where I is the intensity of the glow peak, E is the activation energy or trap's depth, k represents the Boltzmann constant, T is the absolute temperature, I_m and T_m are the intensity and the

ISBN: 978-86-82602-01-9

temperature of the maximum. Since the exponential integral of Eq. (1) is not analytically solvable, different approximations and functions have been proposed and discussed by [11-13] to describe a single glow peak.

The exponential integral in this case can be approximated as follows:

$$\begin{aligned}&\int_0^T exp\left(-\frac{E}{kT'}\right)dT' \approx \\ &\approx \frac{E}{k}\int_x^{\infty} x'^{-2} exp\left(-x'\right)dx' = , \\ &= \frac{E}{k}\frac{1}{x}E_2\left(x\right) \ ,\end{aligned} \tag{2}$$

where $x = \frac{E}{kT}$, $x' = \frac{E}{kT'}$ and $E_2\left(x\right)$ represents the second exponential integral function that can be evaluated: $E_2\left(x\right) = \alpha\left(x\right)\exp\left(-x\right)$, $\alpha\left(x\right)$ is 4th order polynomials quotient that can be given as follows [14]:

$$\alpha\left(x\right) = 1 - \frac{\alpha_0 + \alpha_1 x + \alpha_2 x^2 + \alpha_3 x^3 + x^4}{b_0 + b_1 x + b_2 x^2 + b_3 x^3 + x^4} \ . \tag{3}$$

The following expression is used for describing a single glow peak [13]:

$$\begin{aligned}&I\left(T\right) = I_m exp\left(\frac{E}{kT_m} - \frac{E}{kT}\right)\cdot \\ &\cdot exp\left(\frac{E}{kT_m}\left(\alpha\left(\frac{E}{kT_m}\right) - \frac{T}{T_m} exp\left(\frac{E}{kT_m} - \frac{E}{kT}\right)\alpha\left(\frac{E}{kT}\right)\right)\right)\end{aligned} \ . \tag{4}$$

The glow curve, as shown above, is a nonlinear function of I_m, T_m and E parameters. The best-fitted values of peak parameters can be found by using an iterative procedure. GlowFit can deconvolve up to ten glow peaks from the TL glow-curve at the same time. The number of unknown parameters for ten glow peaks is thirty three; the three additional parameters are used in background expression, which is $a + b\cdot exp\left(T/c\right)$, where a, b, and c are the background parameters that are unknown. The best-fit parameters can be determined by the minimization of χ^2 function which must be defined. Trial values are used to start the minimization process. A Levenberg-Marquardt method for non-linear function minimization was adapted in this program [15].

The quality of the fitting was judged by the Figure-Of-Merit (FOM), which is given by [16]:

$$FOM = \sum_i \frac{\left|Y_{exp} - Y_{fit}\right|}{A} \ , \tag{5}$$

where Y_{exp} and Y_{fit} are the experimental and fitted curve data points, and A is the fitted area of the curve.

The frequency factors were estimated following formula for first-order kinetics:

$$s = \frac{\beta E}{kT_m^2} exp\left(\frac{E}{kT_m}\right). \tag{6}$$

III. Materials and Methods

A. Description of the Dosimeter

The dosimeter is manufactured as square-shaped chips with a size of approximately 3.0 mm × 3.0 mm and a thickness of 0.89 mm.

B. TL Measurments

The TL measurements were performed using Risø TL/OSL-DA-20 reader (Risø National Laboratory, Denmark), equipped with a Varian VF-50J (50 kV/1 mA) X-ray source with an average dose rate of 2 Gy/s and a bialkali EMI 9235QB PM tube with a maximum detection efficiency of 200–400 nm. TL measurements were performed in temperature range from 0-450°C at a linear heating rate of 5°C/s in the N_2 atmosphere.

C. TL Deconvolution Method

The obtained experimental data were fitted and glow peaks were deconvoluted by GlowFit software tool.

IV. Discussion of Results

Before irradiation, we read the TL signal to determine the background reading (reading to a zero dose).

As seen from Fig. 2, all the glow curves are comparable only with regard to their shapes and not their intensities. The intensity of TL signals is increasing with an increase in the delivered dose. According to the graphs, the glow peaks are sensitive to the radiation dose.

The detailed results of the evolution of the TL signal as a function of dose are shown in the Table I.

TABLE I. DETAILED RESULTS OF TLD-100 EXPOSURE TO DIFFERENT X-RAY DOSES.

Dose (Gy)	TL integral	Peak position (°C)
2	76155	250
4	154864	250
6	230412	247
8	311495	248
10	391817	248

A. TLD-100 Dose-Response

On the basis of the previous results, the response curve (TL = f (D)) of the chosen dosimeter is reproduced by the graph of Fig. 3.

The TLD-100 dosimeter has a linear response over the dose range under study, according to the previous curve. When all of the experimental conditions are met and the used equipment is properly calibrated, this result agrees well with the known TLD-100 response in the dose interval under consideration.

B. Kinetic Parameters Determination Results by the CGCD Method

The TL glow deconvolution and the obtained fit curve as well as the residue of fitting work (difference between the two curves) are presented in Fig. 4.

The fit of TL glow curve is done with an FOM of 2.69 and residue is below an average of 5% in the stable peaks region between 400 °K and 530°K.

Table II shows the results and data of TL glow curve deconvolution and fitting by separated TL peaks revealed. When the obtained results are compared to the literature, they provide complete satisfaction.

TABLE II. THE USED PEAKS DATA FOR CURVE FITTING.

Peak	I_m	T_m (°K)	*E(eV)*	$s(s^{-1})$
1	711.71	335.08	0.72	2.32×10^{10}
2	681.08	360.40	0.95	7.16×10^{12}
3	2341.39	421.34	1.39	2.09×10^{16}
4	2950.99	461.27	1.50	1.13×10^{16}
5	3612.18	490.40	1.67	2.64×10^{16}
6	10569.65	519.95	2.15	3.25×10^{20}
7	772.76	574.43	0.78	3.80×10^{5}

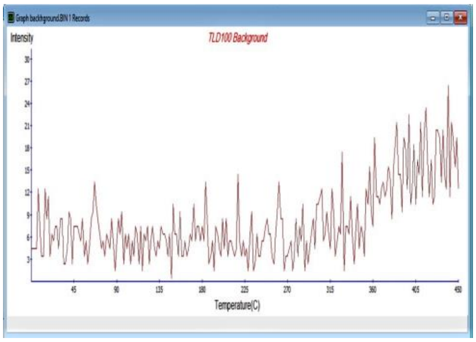

Figure 1. Thermoluminescence background of TLD-100.

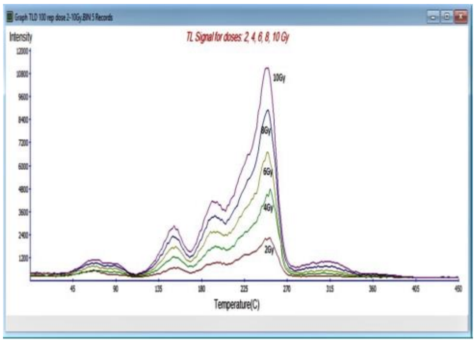

Figure 2. TL glow curves for different X-ray doses.

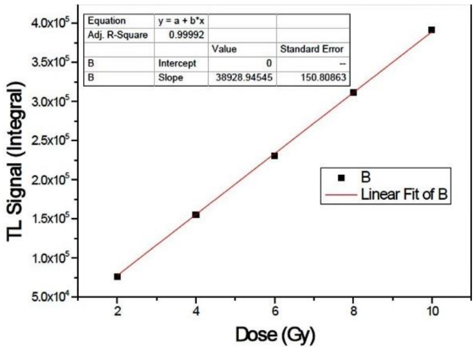

Figure 3. TL signal as a function of X-ray doses.

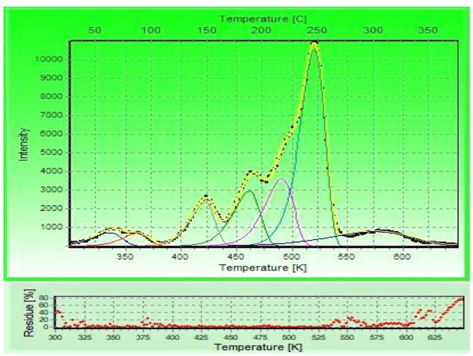

Figure 4. TLD-100 CGCD results.

Indeed, data relating to the main TL peak N°6 agree well with the findings presented in [17-21]. This peak is commonly used in thermoluminescence dating and radiation dosimetry.

V. Conclusion

The thermoluminescence phenomanon and its kinetics were investigated in this work.

Thus, the thermoluminescence mechanism and signal reading were thoroughly explained. The thermoluminescence dose-response of LiF:Mg,Li (TLD-100) was established and was found to be linear in the considered interval of doses between 2 and 10 Gy. It was possible to study the thermoluminescence kinetics of the studied material and determine its main kinetics parameters by selecting the experimental data of the TL signal obtained with an exposure X-ray dose of 10 Gy.

The Randal and Wilkins first-order kinetic model is used to deconvolve the TL glow curve. The deconvolution results obtained on the experimental TL peaks allowed us to calculate the trap's activation energies and frequencies. Thus, the LiF:Mg,Li (TLD-100) main TL peak was observed at a maximum temperature of 519.95 °K (246.95 °C), with an activation energy of 2.15 eV and a frequency of 3.25×10^{20} s^{-1}.

References

[1] Faghihi, R., Mehdizadech, S., Sina, S., Alizadeh, F.N., Zeinali, B., Kamyab, G.R., Aghevlin, S., Khorramdel, H., Namazi, I., Heirani, M., Moskhriz, M., Mahani, H., & Sharifzadeh, M. (2012). Radiation dose to neonates undergoing X-ray imaging in special care baby units in Iran. Radiat. *Prot. Dosimetry,150*(1),55-9.

[2] Sina, S., Zeinal, B., Karimipoorfard, M., Lotfalizadeh, F., Sadeghi, M., Zamani, E., & Faghihi, R. (2014). Investigation of the entrance surface dose and dose to different organs in lumbar spine imaging. *J. Biomed. Phys. Eng,4*(4):119-26.

[3] Berni, D., Gori, C., Lazzari, B., Mazzocchi, S., Rossi, F., & Zatelli, G. (2002). Use of TLD in evaluating diagnostic reference levels for some radiological examinations. *Radiat. Prot. Dosim, 101*, 411-3.

[4] His, W.C., Fagundes, M., Zeidan, O., Hug, E., & Schreuder, N. (2013). Image-guided method for TLD-based in vivo rectal dose verification with endorectal balloon in proton therapy for prostate cancer. *Med. Phys, 40*:051715.

[5] Lambert, J., Nakano, T., Law, S., Elsey, J., Mckenzie D.R., & Suchowerska, N. (2007). In vivo dosimeters for HDR brachytherapy: a comparison of a diamond detector. *Med. Phys,34*:1759-65.

[6] Sina, S., Faghihi, R., Meigooni, A.S., Mehdizadeh, S., Mosleh, Shirazi, M.A., & Zehtabian, M. (2011). Impact of the vaginal applicator and dummy pellets on the dosimetry parameters of Cs-137 brachytherapy source. *J. Appl. Clin. Med. Phys,12*:3480.

[7] Mosleh Shirazi, M.A., Faghihi, R., Siavashpour, Z., Nedaie, H.A., Mehdizadeh, S., & Sina, S. (2012). Independent evaluation of an in-house brachytherapy treatment planning system using simulation, measurement and calculation methods. *J. Appl. Clin. Med. Phys, 13*:3687.

[8] Biran, T., Weininger, J., Malchi, S., Marciano, R., & Chisin, R. (2004). Measurements of occupational exposure for a technologist performing 18F FDG PET scans. *Health. Phys, 87*:539-4.

[9] Mckeever, S.W.S. (1988). Thermolumiescence of solids. *Cambridge.*

[10] Azor, J., Furett, C., & Scacco, A. (1993). Preparation and properties of thermoluminescent materials. *Phys. Stat. Sol. (a), 138*: 10-46.

[11] Bos, A.J.J., Piters, T.M., Gomez Ros, J.M., & Delgado, A. (1993). An intercomparison of glow curve ananlysis computer programs: I. synthetic glow curves. *Radiat. Prot. Dosim, 47*:473-477.

[12] Bos, A.J.J., Piters, T.M., Gomez Ros, J.M., & Delgado, A. (1994). An intercomparison of glow curve ananlysis computer programs: II. Measured glow curves. *Radiat. Prot. Dosim, 51*:257-264.

[13] Horowitz, Y.S., & Yossian, D. (1995). Computerized glow curve deconvolution: application to thermoluminescence dosimetry. *Radiat. Prot. Dosim, 60*.

[14] Abramowitz, M., & Stegun, I.A. (1972). Handbook of of mathematical functions. New York:Dover.

[15] Brandt, S. (1998). Analiza danych. Wydawnictwo Naukowe PWN.

[16] Balian, H.G., & Eddy, N.W. (1977). Figur-Of-Merit (FOM), an improved criterion over the normalized chi-squared test for assessing goodness-of-fit of gamma-ray spectral peaks. *Nucl. Inst. Method, 145*:389-395.

[17] Taylor, G.C., & Lilley, E. (1978). The analysis of thermoluminescent glow peaks in LiF (TLD-100). *J. Appl. Phys. D,11*:567.

[18] Fairchild, R.G., Mattern, P.L., Lengweiler, K., & Levy, P.W. (1978). Thermoluminescence of LiF TLD-100: glow-curve kinetics. *J. Appl. Phys,49*(8):4523.

[19] Mckeever, S.W.S. (1980). Thermoluminescence in LiF: analysis of the glow-curves. *Nucl. Instr. and Meth, 175*:19.

[20] Hoogenboom, J.E., de Vries, W., Dielhof, J.B., & Bos, A.J.J. (1988). Computerized analysis of glow curves from thermally activated processes. *J. Appl. Phys, 64*:3193.

[21] Sohrabi, M., Jafarizadeh, M., & Zahedifar, M. (1998). Analysis of kinetics and trapping parameters of LiF: Mg, Ti thermoluminescent dosimeters by general order model. *Nucl. Instr. and Meth,416*(2-3):446-451.

Optimal PV Distributed Generation Planning for Benefit Maximization in Distribution Network Considering Time-varying Load Demand Models

Mohamed Zellagui[1], Nasreddine Belbachir[2], Adel Lasmari[3], Samir Settoul[3]

[1]Department of Electrical Engineering, University of Batna 2, Algeria
[2]Department of Electrical Engineering, University of Mostaganem, Algeria
[3]Department of Electrical Engineering, University of Constantine 1, Algeria

Abstract—**In this paper, the African Vulture Optimization (AVO) algorithm is employed to find the optimum size and location of multiple PV-DGs depending on solar PV panels (PV) connected to EDS. This algorithm is used to maximize the multi-objective function (MOF) using the active power losses level (APLL), net saver level (NSL), short circuit level (SCL), and voltage deviation level (VDL), while accounting for the impact of various time-varying load demand models, such as constant, commercial, residential, and industrial loads, which have a significant influence on the optimal location and size of the DG. The effectiveness of the proposed AVO algorithm is validated on the standards IEEE 33 and 69-bus distribution systems while comparing to other metaheuristic optimization algorithms. This paper examines the effect of time-varying voltage-dependent simulation tools on PV-DG unit planning studies. Multiple DG units are assigned to the identified bus, and load flow analysis is performed. The performance indices for different load models show a reduction in power loss, an improvement in voltage profile, and an increase in line capacity.**

Keywords - Photovoltaic distributed generation, electrical distribution system, time-varying load models, multi-objective function, African vulture optimization algorithm.

I. Introduction

Due to the sudden rise in demand for electricity, finding a balance between consumption and production has become a critical challenge for researchers. Among solutions, the conventional solution is to build new power plants, but this involves major investment opportunities and expenses, along with the environmental implications of using fossil fuels [1]. Because of these benefits, interest in integrating DG sources into the EDS is significantly increasing around the world, owing to technological advancements that have resulted in lower electricity costs [2].

In reality, the practical system has three types of loads; additionally, in the majority of distribution system planning research, Reactive and real power demand are presumed to really be constant values, and substantial quantities are presumed to just be voltage-independent; however, different types of loads exist depending on the load voltage [3].

Recently, several algorithms and methods have been implemented to resolve the problem of the optimum sizing and setting of the PV-DG considering different load models, these algorithms, and methods are Firefly Algorithm (FA) to minimize APL and QPL losses using loss sensitivity factor [4], Crow Search Algorithm (CSA) applied to practical Egyptian EDS for the maximization the VSI and the annual savings in the losses cost [5], Strength Pareto Evolutionary Algorithm 2 (SPEA 2) to minimizing APL, annual operating costs and pollution gas emission [6], Teaching Learning Based Optimization (TLBO) for the aim of minimizing the APL, and the VDI [7], and Biogeography-Based Optimization (BBO) algorithm to reduced APL with an effective power factor mode [8]. In 2019, applied Analytical Method (AM) to minimize APL and approved the voltage stability margin index [9], Mixed integer linear programming (MILP) to minimize energy cost, and balance unsymmetrical loading [10], and Gravitational Search Algorithm (GSA) to minimize APL and maximize annual cost savings with uncertainties of DG and load demand [11]. In 2020, applied Adaptive modified whale optimization algorithm (AMWOA) to maximize VSI and minimize APL [12], the Salp Swarm Algorithm (SSA) minimizes the voltage deviation, power losses and voltage stability indices [13], Phasor PSO (PPSO) algorithm to a reduction in APL and yearly economic loss in practical EDS in Portuguese [14] , Proposed new VSI index with basic PSO technique for optimal DG based wind and solar sources [15], and finally implanted multi-objective WOA for the reliability index and the profit of company of distribution system [16].

The utility and consumers benefit from the integration of distributed generation (DGs) based renewable energy sources (RESs) in electrical distribution systems (EDS) represented in a number of ways, including improved voltage profile and stability, lower system losses, and decreased reliance on fossil fuels. However, due to the accompanying volatility in load demand and generation capacity, RES integration is a significant problem. The demand for RESs has increased due to the satisfaction of power consumers and the implemented environmental restrictions.

In recent years, optimization techniques have been used for power industry deregulation, enabling the best presence of PV-DG units in EDS. The electrical loads have been simulated employing their reactive and active power elements, which react differently to adjustments in the frequency and voltage of the power system.

This paper addresses an efficient implementation of AVO algorithm considering various loads. Furthermore, the effectiveness of the proposed AVO algorithm is validated on the standards IEEE 33 and 69-bus distribution systems while comparing it to other metaheuristic optimization algorithms.

II. FORMULATING THE LOAD MODEL

This part goes over the time-varying depending on voltage load modeling. The depended voltage load model's mathematical expression is as follows: [4,13]:

$$P_i(t) = P_{oi}(t) \cdot V_i^{n_p}(t) \ , \tag{1}$$

$$Q_i(t) = Q_{oi}(t) \cdot V_i^{n_q}(t) \ . \tag{2}$$

P_i and Q_i are active and reactive power, P_{oi} and Q_{oi} are active and reactive operated locations and V_i refer to voltage. n_p and n_q, are presumed as in Table I [15-19]:

TABLE I. DIFFERENT VOLTAGE-DEPENDENT LOAD MODEL.

Load Type	n_p	n_q
Constant	0	0
Industrial	0.18	6.00
Residential	0.92	4.04
Commercial	1.51	3.40

III. PROBLEM FORMULATION

A. Multiple-objective Functions

By assigning a weight to any level, the multiple-objective level that this research considers again for optimum utilization of PV-DG under various loading model planning can be expressed as follows:

$$MOF = Max \sum_{i=1}^{N_{Bus}} \sum_{j=2}^{N_{Bus}} \begin{pmatrix} \alpha_1.APLL_{i,j} + \alpha_2.VDL_j + \\ \alpha_3.ISCL_{i,j} + \alpha_4.NSL_{i,j} \end{pmatrix} , \tag{3}$$

where, α_1, α_2, α_3, and α_4 are the weighting factors. Their choice is depending on the cruciality of any objective function, in several research the higher weighting factor was considered for the minimizing of P_{Loss} [14,15,16] than for the other technical factor such as voltage deviation, short circuit level, so, for reason to the cruciality of APL mitigating for system reliability and its direct influence on cost minimization in this paper, α_1 is proposed as 0.40, additionally, due the technical reason, each of α_2, α_3 and α_4 is set to 0.20. The discussed levels are given as:

Firstly, is the Active Power Loss (APLL), as follows:

$$APLL = \frac{P_{Loss}^{Before\ DG}}{P_{Loss}^{Before\ DG} + P_{Loss}^{After\ DG}} \times 100 \ , \tag{4}$$

where, the active power loss (P_{Loss}) can be represented as follows [17-19]:

$$P_{Loss} = R_{ij}\frac{\left(P_{ij}^2 + Q_{ij}^2\right)}{V_i^2} \ . \quad (5)$$

Where, R_{ij}, P_{ij}, and Q_{ij} are the resistance, real and reactive power between branch i, j respectively.

The Voltage Deviation (VDL) is the second level, and it may be donated as follow: [17]:

$$VDL = \frac{VD_{Before\ DG}}{VD_{Before\ DG} + VD_{After\ DG}} \times 100\,, \quad (6)$$

where,

$$VD = \left|1 - V_j\right| . \quad (7)$$

The Short Circuit Level (SCL) expression may be represented as in below [18- 20]:

$$SCL = \frac{SC_{After\ DG} - SC_{Before\ DG}}{SC_{Before\ DG}} \times 100 \,. \quad (8)$$

Here,

$$SC = \frac{V_j}{Z_{ij}}\ , \quad (9)$$

where, V_j is the voltage magnitude at bus j, and Z_{ij} is the impedance of the distribution line.

Finally, the Net Saving Level (NSL), where may be defined as follow:

$$NSL \ = \frac{ALC_{Before\ DG} - ALC_{After\ DG}}{ALC_{Before\ DG}} \times 100\,, \quad (10)$$

where, the annual losses cost (ALC), which is dependent on P_{Loss}, and is expressed as in [21, 22]:

$$ALC = P_{Loss} \times K_P \times T\ , \quad (11)$$

where, K_p is the incremental power loss cost (\$/kW), and T is number year's hours.

B. Power Balance Constraint

Equality constraints considered in this study are represented as follows [23, 24]:

$$P_G + P_{DG} = P_D + P_{Loss}\ , \quad (12)$$

$$Q_G = Q_D + Q_{Loss}\ , \quad (13)$$

where, P_G, and Q_G are the real, and reactive power injected by substation, P_D, P_G are real and reactive load power.

C. Constraints of Distribution Line

Inequality constraint of the distribution line is shown in the following equations [25,26]:

$$V_{\min} \le \left|V_i\right| \le V_{\max}\,, \quad (14)$$

where V_{min}, and V_{max} are the allowable limits of the voltage.

The voltage dropping limits are presented by the next equations:

$$\left|V_1 - V_j\right| \le \Delta V_{\max}\,, \quad (15)$$

where ΔV_{max} represents the upper limits of voltage drop at each branch.

The line capacity constraint can be represented as:

$$\left|S_{ij}\right| \le \left|S_{\max}\right|, \quad (16)$$

where S_{max} is the maximum limits of apparent power and S_{ij} is the apparent power between branch i, j.

D. PV-DG Constraints

The PV-DG constraint considered in this paper are represented in the equations below [27,28]:

$$P_{DG}^{\min} \le P_{DG} \le P_{DG}^{\max}\,, \quad (17)$$

where P_{DG} is the real power supplied by the DG unit, and P_{DG}^{max}, P_{DG}^{min} are the upper and lower limits of P_{DG}.

$$2 \le DG_{Position} \le N_{Bus}\ . \quad (18)$$

Where, DG Position is the position of DG, and N_{Bus} is the network bus numbers.

$$N_{DG} \le N_{DG.\max}\ . \quad (19)$$

Where, N_{DG}, and $N_{DG.max}$ are the number of DG units and the maximum number of DG.

$$n_{DG,i} \,/\, Location \le 1\ . \quad (20)$$

IV. AFRICAN VULTURE OPTIMIZATION ALGORITHM

The African vultures optimization algorithm is a society method adopted by the African continent's vultures' food search and competition. Benyamin Abdollah Zadeh [29] introduced it in 2021 for problems involving global optimization. Algorithm 1 represents the pseudo-code of the AVOA algorithm.

Algorithm 1. Pseudo-code of AVO algorithm

1. Generate the initial population P_i (i = 1, 2, ..., N)
2. **While** ($k < k_{max}$)
3. Calculate fitness values of Vulture
4. Set P_{best} Vulture 1 as the location of Vulture (First best location Best Vulture Category 1)
5. Set P_{best} Vulture 2 as the location of Vulture (Second location Best Vulture Category 2)
6. for (each Vulture (P_i)) do
7. Select R(i)
8. Update F
9. if (/F/ ≥1) then
10. if ($P_1 \geq$ rand P_1) then
11. Update the location of Vulture
12. else
13. Update the location of Vulture
14. if (/F/ < 1) then
15. if ($P_2 \geq 0.5$) then
16. if ($P_2 \geq$ rand P_i) then
17. Update the location of Vulture
18. else
19. if ($P_3 \geq$ rand P_3) then
20. Update the location of Vulture
21. else
22. Update the location of Vulture

Return $P_{Best\ Vulture1}$

V. OPTIMAL RESULTS, IMPACTS AND COMPARISONS

A. Test Systems

The proposed algorithm was carried out in MATLAB 2017. In addition, the AVOA algorithm was applied to two standards IEEE, distribution system which is used to evaluate the integration of PV-DG units.

The first test system, shown in Fig.1. a, is the standard of IEEE 33-bus EDS, composed of 33 buses, and 32 distribution line branches.

Different load model is considered, where the real power loads of each of constant, industrial, commercial, and residential are: 3.7150, 3.6794, 3.4299, and 3.5337 MW, moreover the reactive power loads are 2.3000, 1.6370, 1.8891, and 1.6370 MVar respectively, with a nominal base voltage of 12.66 kV [18].

The second test system, shown in Figure 1.b, is the standard IEEE 69-bus EDS, composed of 69 buses, 68 distribution line branches. Different load model is considered, where the real power loads of each of the constant, industrial, commercial, and residential are: 3.7919, 3.7579, 3.5210, and 3.6230 MW, while the reactive power loads are: 2.6941, 2.0473, 2.2265, and 2.2911 MVar respectively, with a nominal base voltage of 12.66 kV [18].

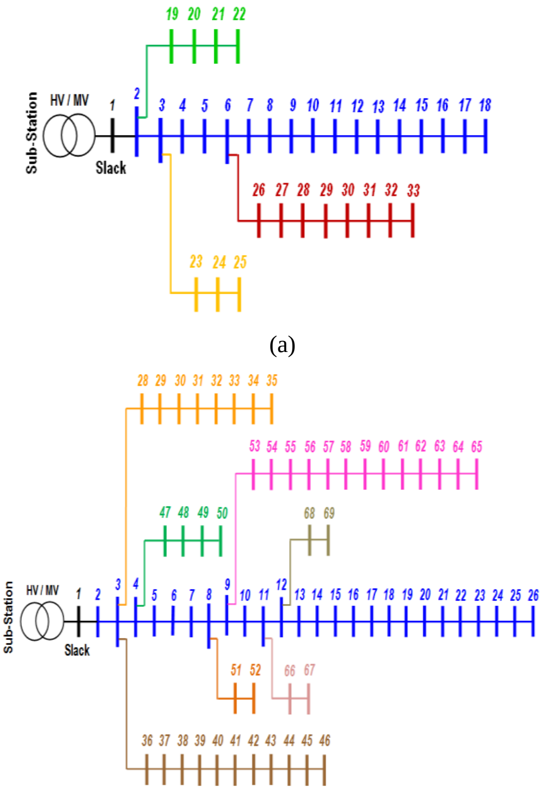

(a)

(b)

Fig.1. Single diagram of distribution systems: a). IEEE 33-bus, b). IEEE 69-bus.

The convergence curves characteristics of the AVOA for different types of loads are shown in Fig.2.

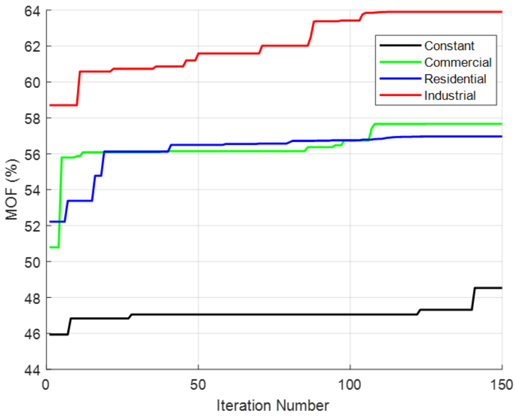

(a)

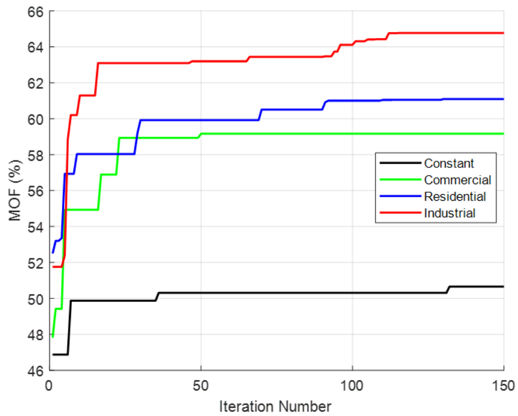

(b)

Fig.2: Convergence characteristic of AVO algorithm: a). IEEE 33-bus, b). IEEE 69-bus.

Fig.2.a shows so each sort of load necessitates a unique number of iterations to achieve the best solution, in addition, it is noticed that the industrial, residential, and commercial loads converge lately with more than 110 iterations whereas, the constant load exhibits the long time to converge compared to other loads, which is shown to be less than 140 iterations.

For the second test system, it is clearly shown that the commercial load reaches their best solution after iteration number 50, on the contrary, the residential, constant, and industrial loads converge lately, more than 100 iterations, with a rapid converge of the commercial load compared to other loads, in addition, the results of residential, and commercial loads are very close to each other.

B. Impact of PV-DG on Load Model Parameters

The bus voltage profiles of the three EDSs for different load models are represented in Fig.3. Noticed a considerable increase in voltage profiles of the three EDSs, which be within the allowable limits for all types of loads.

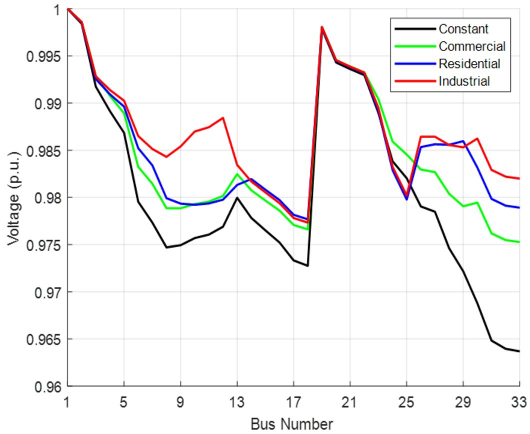

(a)

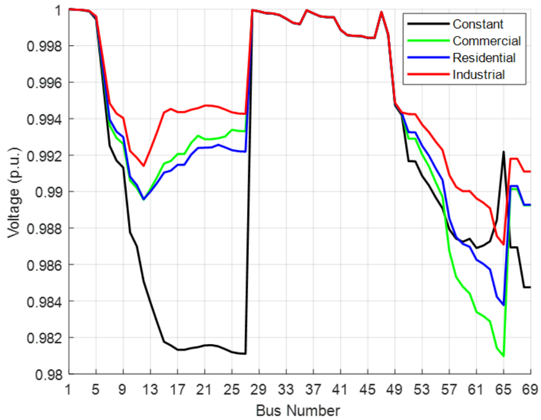

(b)

Fig.3. The bus voltage profiles:
a). IEEE 33-bus, b). IEEE 69-bus.

The analysis of Fig.3.a. shows that the integration of PV-DG in the first test system is affecting the voltage profile. It can be noted that the voltage is maintained within permissible limits.

We can also observe, that except for the constant loads the voltage profiles for the other types of loads are identical because the placements and sizes of multiple PV-DG units are so close.

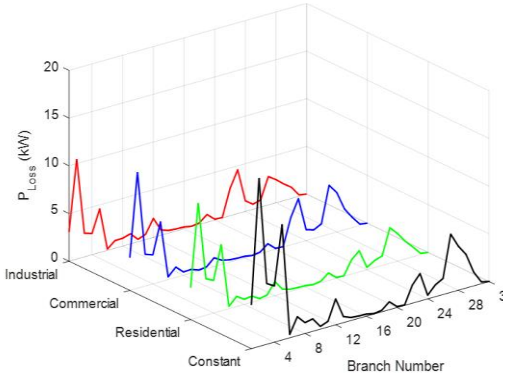

(a)

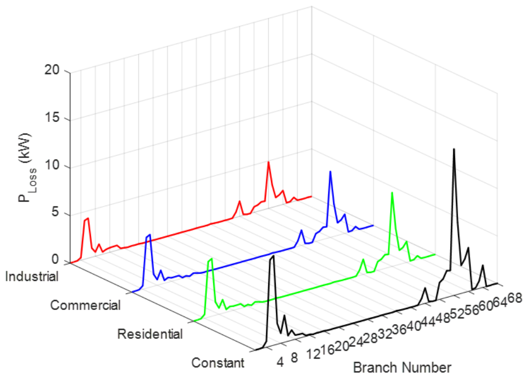

(b)

Fig.4. Real power losses of distribution system: a). IEEE 33-bus, b). IEEE 69-bus.

For the second test system, there is a small deviation in some placements, which appears especially in the buses 10 to 27, and between 50 to 69 where the industrial load has the highest value of voltage compared to other types of loads, on the contrary, the worst voltage profiles has obtained for the constant load.

Fig.4 shows the contribution of the incorporation of multiple PV-DG units for reduced P_{Loss} in all branches, which has different influences depending on the type of load. For both IEEE 33-bus and 69-bus EDSs, the maximum P_{Loss} per branch is obtained for the constant load, whereas the minimum results have occurred for the industrial load.

Moreover, a high amount of P_{Loss} per branch is obtained for the industrial load, noting that the amount of P_{Loss} for the first test system is 49.191 kW, whereas, for the second test system is 30.49 kW. The results tabulated in Table II represent the optimization results obtained by the proposed method before and after the integration of multiple PV-DG units for all test systems.

TABLE II. DIFFERENT LEVELS OF VALUE FOR ALL TEST SYSTEMS

(A) IEEE 33-BUS

Type of Load Model	Cases Studies	DG Parameters		P_{Loss} (kW)	V_{min} (p.u.)	*APLL* (%)	*VDL* (%)	*SCL* (%)	*NSL* (%)	*MOF* (%)
		Bus	DG (MW)							
Constant Load	Without DG	---	---	210.98	0.903	---	---	---	---	---
	With DG	13 25 29	0.944 0.260 1.044	81.52	0.963	72.13	64.76	6.39	61.36	48.53
Commercial Load	Without DG	---	---	152.61	0.919	---	---	---	---	---
	With DG	13 25 30	0.7559 0.3000 0.9797	51.35	0.975	74.82	66.49	5.46	66.35	57.66
Residential Load	Without DG	---	---	159.11	0.917	---	---	---	---	---
	With DG	8 14 29	0.0113 0.6905 1.3202	57.18	0.977	73.56	67.86	5.75	64.06	56.96
Industrial Load	Without DG	---	---	163.68	0.916	---	---	---	---	---
	With DG	12 25 30	0.9701 0.0119 1.1547	49.191	0.977	76.89	71.25	6.16	69.94	60.23

(B) IEEE 69-BUS

Type of Load Model	Cases Studies	DG Parameters		P_{Loss} (kW)	V_{min} (p.u.)	*APLL* (%)	*VDL* (%)	*SCL* (%)	*NSL* (%)	*MOF* (%)
		Bus	DG (MW)							
Constant Load	Without DG	---	---	224.94	0.909	---	---	---	---	---
	With DG	22 61 65	0.2598 1.3260 0.6530	77.93	0.981	74.26	63.31	0.914	65.35	50.65
Residential Load	Without DG	---	---	164.89	0.921	---	---	---	---	---
	With DG	20 23 61	0.2651 0.2100 1.6067	39.82	0.983	80.54	66.64	1.036	75.84	61.09
Commercial Load	Without DG	---	---	156.95	0.924	---	---	---	---	---
	With DG	20 25 61	0.3857 0.1098 1.4602	43.61	0.981	78.25	64.78	1.013	72.21	59.16
Industrial Load	Without DG	---	---	171.40	0.919	---	---	---	---	---
	With DG	16 21 61	0.2854 0.2700 1.7388	30.49	0.987	84.89	69.97	1.147	82.20	64.76

As depicted in Table II, for the first test system, the best placement obtained by the applied algorithm is for the residential, industrial, and commercial loads at different buses. This integration of multiple PV-DG units allows to increase in the APLL to 72.13, 74.82, 73.56, and 76.89 %, also, the NSL is increased to 61.36, 66.350, 64.060, and 69.94 % respectively for the constant, industrial, commercial, and residential.

Generally, this maximization is due to the minimization of P_{Loss}. Moreover, the VDL is maximized to 64.76, 66.49, 67.86, and 71.251 % for each of residential, constant, industrial, and commercial loads. For the second IEEE 69-bus test system, the integration of multiple PV-DG units allows minimizing the P_{Loss} to 77.93, 39.82, 57.18, and 30.49 kW. moreover, the APLL is maximized to 72.13, 74.82, 73.56, and 76.88 % respectively for the constant, industrial, commercial, and residential loads.

Furthermore, the best results of SCL are obtained by the constant load that is maximized to 6.39 %.

VI. CONCLUSIONS

This paper addresses the maximization of the technical-economic levels, which formulated the multi-objective function (MOF) based on APLL, VDL, SCL and NSL, through the optimum presence of PV-DG units based on the AVOA algorithm and tested on the standards IEEE 33-, and 69-bus EDSs considering various load models, outcomes show that each type of loads can significantly impact on the planning of PV-DG units.

The obtained results proved the efficient behavior of the AVOA algorithm by mitigating power losses and enhancing voltage profiles; additionally, we may conclude that AVOA can be easily applied to different practical and large EDS, where real power losses are minimized to 77.93, 39.82, 57.18, and 30.49 kW % respectively.

Additionally, the results demonstrate the superiority and accuracy of the proposed AVOA algorithm in determining the optimal placement of the PV-DG units. Where the results obtained in the two standers IEEE EDSs proves the superiority of the proposed AVOA algorithm in term of achieving the minimum power losses compared to other algorithms in the literature, where the percentage of reduction is up to 45.63 %, and 62.99 % respectively for the IEEE 33-, and 69-bus.

In reality, the electric loads are dynamic also, they have significant influences on the planning of incorporation of multiple PV-DG units in real power systems, where the optimal sizing and setting of multiple PV-DG units is depending on the types of the load, so studying the realistic loads gives more accuracy and efficiency for the optimal sizing and setting of PV-DG units.

References

[1] Truong, K. H., Nallagownden, P., Elamvazuthi, I., & Vo, D. N. (2020). A quasi-oppositional-chaotic symbiotic organisms search algorithm for optimal allocation of DG in radial distribution networks. *Applied Soft Computing*, 88, 106067.

[2] Kazeminejad, M., Banejad, M., Annakkage, U., & Hosseinzadeh, N. (2019). The effect of high penetration level of distributed generation sources on voltage stability analysis in unbalanced distribution systems considering load model. *Journal of Operation and Automation in Power Engineering*, 7(2), 196-205.

[3] Qian, K., Zhou, C., Allan, M., & Yuan, Y. (2011). Effect of load models on assessment of energy losses in distributed generation planning. *International Journal of Electrical Power & Energy Systems*, 33(6), 1243-1250.

[4] Sudabattula, S. K., & Muniswamy, K. (2018). Optimal Allocation of Photo Voltaic Arrays in Radial Distribution System with Various Load Models. *Gazi University Journal of Science*, 31(4), 1123-1139.

[5] Ismael, S. M., Aleem, S. H. A., & Abdelaziz, A. Y. (2018, February). Optimal sizing and placement of distributed generation in Egyptian radial distribution systems using crow search algorithm. In 2018 International Conference on Innovative Trends in *Computer Engineering (ITCE)* (pp. 332-337). IEEE

[6] Hamida, I. B., Salah, S. B., Msahli, F., & Mimouni, M. F. (2018). Optimal network reconfiguration and renewable DG integration considering time sequence variation in load and DGs. *Renewable energy*, 121, 66-80.

[7] Barik, S., & Das, D. (2018). Determining the sizes of renewable DGs considering seasonal variation of generation and load and their impact on system load growth. *IET Renewable Power Generation*, 12(10), 1101-1110.

[8] Ravindran, S., & Victoire, T. A. A. (2018). A bio-geography-based algorithm for optimal siting and sizing of distributed generators with an effective power factor model. *Computers & Electrical Engineering*, 72, 482-501.

[9] Essallah, S., Khedher, A., & Bouallegue, A. (2019). Integration of distributed generation in electrical grid: Optimal placement and sizing under different load conditions. *Computers & Electrical Engineering*, 79, 106461.

[10] Mehrjerdi, H. (2019). Simultaneous load leveling and voltage profile improvement in distribution networks by optimal battery storage planning. *Energy*, 181, 916-926..

[11] Murty, V. V. V. S. N., & Kumar, A. (2019). Optimal DG integration and network reconfiguration in microgrid system with realistic time varying load model using hybrid optimisation. *IET Smart Grid*, 2(2), 192-202.

[12] Uniyal, A., & Sarangi, S. (2021). Optimal network reconfiguration and DG allocation using adaptive modified whale optimization algorithm considering probabilistic load flow. *Electric Power Systems Research*, 192, 106909.

[13] Ahmed, A., Nadeem, M. F., Sajjad, I. A., Bo, R., & Khan, I. A. (2020, January). Optimal allocation of wind DG with time varying voltage dependent loads using bio-inspired: Salp swarm algorithm. In 2020 3rd *International Conference on Computing, Mathematics and Engineering Technologies (iCoMET)* (pp. 1-7). IEEE.

[14] Ullah, Z., Elkadeem, M. R., Wang, S., & Akber, S. M. A. (2020). Optimal planning of RDS considering PV uncertainty with different load models using artificial intelligence techniques. *International Journal of Web and Grid Services*, 16(1), 63-80.

[15] Parizad, A., Baghaee, H. R., Yazdani, A., & Gharehpetian, G. B. (2018, February). Optimal distribution systems reconfiguration for short circuit level reduction using PSO algorithm. In 2018 *IEEE Power and Energy Conference at Illinois (PECI)* (pp. 1-6). IEEE..

[16] Tan, W. S., Hassan, M. Y., Majid, M. S., & Rahman, H. A. (2012, December). Allocation and sizing of DG using cuckoo search algorithm. In 2012 *IEEE international conference on power and energy (PECon)* (pp. 133-138). IEEE.

[17] Ameli, A., Bahrami, S., Khazaeli, F., & Haghifam, M. R. (2014). A multiobjective particle swarm optimization for sizing and placement of DGs from DG owner's and distribution company's viewpoints. *IEEE Transactions on power delivery*, 29(4), 1831-1840.

[18] El-Zonkoly, A. M. (2011). Optimal placement of multi-distributed generation units including different load models using particle swarm optimisation. *IET generation, transmission & distribution*, 5(7), 760-771.

[19] Belbachir, N. Zellagui, M. Bekkouche, B. (2022). Optimal location and sizing of multiple distributed generators in radial distribu-tion network using metaheuristic optimization algorithms. *FACTA Universitatis Series Electronics and Energetics*. (2022), 35 (2), 229-242.

[20] M., Lasmari, A., Alaboudy, K., Settoul, S., & Hassan, H. A. (2022). Enhancing energy efficiency for optimal multiple photovoltaic distributed generators integration using inertia weight control strategies in PSO algorithms. *Polityka Energetyczna*, 25.

[21] Zellagui, M., Belbachir, N., Lasmari, A., Bekkouche, B., & El-Bayeh, C. Z. (2022). Application hybrid chaotic maps and adaptive acceleration coefficients PSO algorithm for optimal integration photovoltaic distributed generation problem in distribution energy network. *In Control Applications in Modern Power Systems* (pp. 27-39). Springer, Singapore.

[22] Belbachir, N., Zellagui, M., Lasmari, A., El-Bayeh, C. Z., & Bekkouche, B. (2021, March). Optimal PV sources integration in distribution system and its impacts on overcurrent relay based time-current-voltage tripping characteristic. In 2021 *12th International Symposium on Advanced Topics in Electrical Engineering (ATEE)* (pp. 1-7). IEEE.

[23] Belbachir, N., Zellagui, M., Lasmari, A., El-Bayeh, C. Z., & Bekkouche, B. (2021). Optimal integration of photovoltaic distributed generation in electrical distribution network using hybrid modified PSO algorithms. *Indonesian Journal of Electrical Engineering and Computer Science*, 24(1), 50-60.

[24] Lopez, E., Opazo, H., Garcia, L., & Bastard, P. (2004). Online reconfiguration considering variability demand: Applications to real networks. *IEEE Transactions on Power systems*, 19(1), 549-553.

[25] Lasmari, A., Settoul, S., Zellagui, M., & Chenni, R. (2020, October). Optimal hourly scheduling of PV sources in EDS considering the power variability of load demand and DG using MOGWO algorithm. In 2020 6th *International Conference on Electric Power and Energy Conversion Systems (EPECS)* (pp. 85-90). IEEE.

[26] Zellagui, M. Settoul, S. Lasmari, A, El-Bayeh, C. Z. and Belbachir, N. (2022). Arithmetic optimization algorithm for optimal instal-lation of DSTATCOM into distribution system based on various voltage stability indices. 9th International Conference on Modern Power Systems (MPS), Cluj, Romania, 16-17 June 2021.

[27] Belbachir, N. Zellagui, M. Settoul, S., El-Bayeh, C. Z., Bekkouche, B (2021). Simultaneous optimal integration of photovoltaic distributed generation and battery energy storage system in active distribution network using chaotic grey wolf optimization. Electrical Engineering & Electromechanics, (2021), 2021 (3), 52–61.

[28] Zellagui, M. Belbachir, N. and El-Bayeh, C. Z (2021). Optimal allocation of RDG in distribution system considering the seasonal uncertainties of load demand and solar-wind generation systems. IEEE 19th International Conference on Smart Technologies (EUROCON), Lviv, Ukraine, 6–8 July (2021).

[29] Abdollahzadeh, B., Gharehchopogh, F. S., & Mirjalili, S. (2021). African vultures optimization algorithm: A new nature-inspired metaheuristic algorithm for global optimization problems. *Computers & Industrial Engineering*, 158, 107408.

Autor index

V

Y

Z

Š

Ž

www.energetics.cosrec.org

ISBN: 978-86-82602-01-9